# Principles of Non-Equilibrium Self-Assembly

## A kinetic theory

**Florian Gartner**

A dissertation
submitted to the Faculty of Physics
at the Ludwig–Maximilians–Universität München
for the degree of
DOCTOR RERUM NATURALIUM


München 2022

# Principles of Non-Equilibrium Self-Assembly

## A kinetic theory

Dissertation
an der Fakultät für Physik
der Ludwig–Maximilians–Universität München

vorgelegt von
Florian Manuel Gartner
aus Vilsbiburg

München, den 02.02.2022

Erstgutachter: Prof. Dr. Erwin Frey
Zweitgutachter: Prof. Dr. Ulrich Gerland
Tag der mündlichen Prüfung: 25.03.2022

# Zusammenfassung

Lebende Materie unterscheidet sich von toter Materie auf fundamentale Weise dadurch, dass lebende Systeme über sämtliche Größenordnungen bis hin zur molekularen Ebene (selbst-) organisiert sind. Ebene diese Selbstorganisation über viele Größenordnungen ist es, die dem Leben solche erstaunlichen und einzigartigen Eigenschaften verleiht, wie zu adaptieren und zu evolvieren, zu wachsen und sich zu reproduzieren, zu lernen, zu heilen sowie auf vielfältige Art und Weise mit der Umgebung zu interagieren. Um die Verbindung von der molekularen Ebene zu größeren Längenskalen herzustellen, ist die Fähigkeit lebender Systeme größere funktionelle Strukturen aus kleineren Bestandteilen herzustellen von zentraler Bedeutung. Da dieser Prozess in biologischen Systemen typischerweise selbstorganisiert abläuft, wird dieses Phänomen als *Self-Assembly* bezeichnet. Das Konzept von Self-Assembly spielt demnach eine zentrale Rolle sowohl für unser Verständnis lebender Systeme als auch für die Frage, wie das Leben ursprünglich entstehen konnte.

Neben der rein wissenschaftlichen Faszination für das Phänomen Self-Assembly besteht jedoch auch ein großes technologisches und medizinisches Interesse daran. Bei einem System wie dem menschlichen Körper, welches bis zur molekularen Ebene selbstorganisiert ist, besteht womöglich die effizienteste Möglichkeit unfunktionelles Verhalten zu korrigieren und bestimmte Krankheiten zu heilen darin, direkt auf der kleinsten Längenskala einzugreifen. Im Grunde ist das bereits das Prinzip nach dem übliche Pharmazeutika in der Regel den Organismus beeinflussen. Self-assembly in diesem medizinischen Kontext könnte jedoch das Tor zur Herstellung von Arzneimitteln öffnen, die ein wesentlich komplexeres Verhalten haben als übliche Pharmazeutika; die in der Lage sind Entscheidungen zu treffen, mit höherer Präzision zu agieren und sich den Besonderheiten eines speziellen Problems anzupassen. Zum Beispiel wäre es möglich, dass in der Zukunft komplexe Operationen minimalinvasiv von funktionellen Nanorobotern vorgenommen werden, und dass Krankheiten wie Krebs, Multiple Sklerose oder Erbkrankheiten von “intelligenten” Pharmazeutika geheilt werden. In diesem Zusammenhang ist Self-Assembly so wichtig, weil es zusammen mit Sequenz-Faltung (z.B. DNA Origami) vermutlich die einzige Möglichkeit darstellt um komplexe Strukturen auf dieser kleinen Längenskala herzustellen. Andere Techniken, wie zum Beispiel das 3D-Drucken, die auf externer Kontrolle anstatt auf Selbstorganisation beruhen, sind nicht in der Lage auf solch kleinen Längenskalen zu agieren und können daher für diesen Zweck nicht eingesetzt werden.

Dieser Aspekt, der es erlaubt grundlegende Prinzipien des Lebens zu erforschen und gleichzeitig die Aussicht zu haben, zum Fortschritt von Technologie und Medizin beitragen zu können, ist es, was meiner Meinung nach Biophysik im Allgemeinen und Self-Assembly im Speziellen zu einem so reichen und großartigen Forschungsfeld macht. Darüber hinaus ist das Feld Self-Assembly sehr interessant weil es durch eine sehr schöne und reichhaltige Physik beschrieben wird: Die analytischen Methoden, die benutzt werden um Self-Assembly Phänomene zu

verstehen und zu beschreiben, reichen dabei von einfachen heuristischen Argumenten und Dimensionsanalyse über nichtlineare Dynamik, die Theorie kinetischer Ratengleichungen und stochastischer Mastergleichungen bis hin zu Symmetrieprinzipien, Skalierungskonzepten und Renormierungsgruppentheorie. Darüber hinaus ist natürlich die Numerik ein unverzichtbares Werkzeug bei der Erforschung von Self-Assembly Systemen. So ist es in unserer Forschung mehrere Male vorgekommen, dass wir sehr überrascht waren von dem Ergebnis einer numerischen Studie, das wir intuitiv ganz anders erwartet hätten.

Diese Thesis untergliedert sich in drei Teile, die jedoch stark miteinander verbunden sind und sich mit unterschiedlichen Aspekten von Self-Assembly Systemen beschäftigen: der Zeiteffizienz von Self-Assembly-Prozessen, stochastischen Effekten in Self-Assembly-Systemen sowie einer möglichen Kopplung von Self-Assembly mit Genexpression.

1. **Zeiteffizienz von Self-Assembly.**
Der erste Teil der Dissertation beinhaltet drei Projekte und untersucht die Zeiteffizienz von Self-Assembly-Prozessen. Genauer fragen wir uns, wie lange es dauert bis ein substanzieller Ertrag (Yield) vollständiger Strukturen in einem Self-Assembly-Prozess erreicht werden kann und wie die Zeiteffizienz kontrolliert und optimiert werden kann.
In dem ersten Projekt führen wir zu diesem Zweck ein konzeptionelles Modell ein, welches es uns erlaubt vier Schlüsselstrategien (Szenarien) von Nichtgleichgewichts-Self-Assembly-Prozessen zu beschreiben, die der Vermeidung unerwünschter Nukleationsereignisse und kinetischer Fallen dienen. Wir charakterisieren dabei die Zeiteffizienz der vier Szenarien durch ihre jeweilige Zeitkomplexität, also die Abhängigkeit der Dauer des Assembly-Prozesses von der Größe der Zielstruktur. Ähnlich wie bei Computeralgorithmen erlaubt uns diese Charakterisierung mittels der Zeitkomplexität, die vier Szenarien aussagekräftig miteinander zu vergleichen. Darüber hinaus offenbart die Zeitkomplexitätsanalyse, dass sowohl die Assemblyzeitdauer als auch der optimale Wert des Kontrollparameters robust mit der Größe der Zielstruktur skalieren. Wir erwarten, dass die Robustheit dieser Skalierungsgesetze die Formulierung von Gesetzmäßigkeiten ermöglicht, mit deren Hilfe der Ertrag und die Zeiteffizienz in experimentellen Self-Assembly-Systemen besser vorhergesagt und kontrolliert werden können.
Speziell interessant ist in diesem Zusammenhang eine Strategie, die effizientes Self-Assembly erzielt indem die Verfügbarkeit der Bausteine reguliert wird (Supply Regulation), wohingegen die Feinjustierung von Ratenkonstanten und molekularer Eigenschaften der Bausteine hinfällig wird. Wir denken, dass diese Strategie eine ergänzende Möglichkeit in der Nanotechnologie darstellen könnte um Self-Assembly effizient umzusetzen.
Auf Grund der möglichen Bedeutung dieser Strategie für die Nanotechnologie, widmen wir ein separates Projekt der Analyse und Bewertung möglicher Implementierungen von Supply Regulation in Self-Assembly Systemen. Zu diesem Zweck haben wir ein spezielles theoretisches Modell entwickelt, welches es uns erlaubt die Zeitkomplexitätsexponenten verschiedener Supply-Strategien analytisch zu berechnen. Der Vergleich der betreffenden Zeitkomplexitätsexponenten ermöglicht es uns dabei, eine der Strategien eindeutig als das zeiteffizienteste Verfahren für Supply Regulation zu identifizieren.
Die Skalierungsanalyse, die wir in dem ersten Projekt durchgeführt haben, legt nahe, dass eines der vier Szenarien, nämlich jenes welches auf reversiblem Binden der Bausteine basiert, auch sensitiv im Bezug auf die Morphologie der Bausteine sein könnte. Aus diesem Grund untersuchen wir im dritten Projekt, wie die Morphologie der Bausteine die benötigte Assemblyzeit beeinflusst, und ob die Zeiteffizienz optimiert werden kann indem man die Form

der Bausteine verändert. In der Tat finden wir, dass die Form der Bausteine einen erheblichen Einfluss auf die Zeiteffizienz sowie die Zeitkomplexität hat und dass durch die Wahl einer "günstigen" Morphologie die Zeiteffizienz und Robustheit (im Bezug auf "Variabilität" des Kontrollparameters) signifikant verbessert werden können. Die Abhängigkeit der Kinetik von der Morphologie der Bausteine sehen wir in dem Umstand begründet, dass die Gestalt der Bausteine relevante Eigenschaften wie die effektive Nukleationsgröße der Strukturen sowie die effektive Ordnung der Bindereaktionen bestimmt, von denen wir wiederum zeigen können, dass sie einen starken Einfluss auf die Assemblykinetik und deren Zeiteffizienz haben. Da das Szenario, welches auf reversiblem Binden basiert, als Standardszenario der Nanotechnologie angesehen wird, könnte dieses Resultat wichtige technologische Konsequenzen haben.
Ein Manuskript über die Resultate des ersten Projektes wurde im Journal PNAS publiziert und ist in Kapitel 2 abgedruckt. Ein Manuskripts zu den Ergebnissen des dritten Projekts ist derzeit in Vorbereitung. Der Manuskriptentwurf ist in Kapitel 4 abgedruckt. In beiden Projekten bin ich der einzige Erstautor.

2. **Stochastische Effekte in heterogenen Self-Assembly Systemen.**
Der zweite Teil meiner Arbeit beinhaltet drei Projekte und untersucht die Rolle stochastischer Effekte in Self-Assembly-Prozessen im Falle beschränkter Teilchenzahlen. Allgemeiner fragen wir uns, unter welchen Bedingungen Self-Assembly robust und resilient funktionieren kann, wie seine Genauigkeit kontrolliert und stochastische Effekte abgeschwächt werden können. Diese Fragen sind maßgeblich für Self-Assembly-Prozesse in Zellen relevant, da Zellen gewisse Strukturen nur in relativ geringer Anzahl herstellen und daher stark von Stochastizität bzw. Fluktuationen in den Teilchenzahlen betroffen sein können.
In dem ersten Projekt beschreiben und quantifizieren wir einen stochastischen Effekt, den wir auch als "stochastische Ertragskatastrophe" bezeichnen. Wir zeigen, dass dieser Effekt speziell in heterogenen Self-Assembly Systemen auftritt und dass er von demographischen Fluktuationen in den Teilchenzahlen verursacht wird. Interessanterweise kann dieser Effekt zu einer starken Reduktion bis hin zur vollständigen Unterdrückung des Ertrages führen, obwohl die deterministischen Ratengleichungen einen perfekten Yield vorhersagen. Es zeigt sich, dass die stochastische Ertragskatastrophe im Limes großer Teilchenzahlen vernachlässigbar wird, dass jedoch die minimale Anzahl an Teilchen, die benötigt wird um robust einen bestimmten Ertrag erzielen zu können, stark mit der Größe der Zielstruktur anwächst. Wir zeigen außerdem, dass höhere Homogenität der Bausteine, eine höhere Nukleationsbarriere sowie erhöhte Reversibilität der Bindereaktionen die stochastische Ertragskatastrophe abschwächen oder sogar vollständig aufheben. Es ist daher anzunehmen, dass Zellen derartige Mechanismen nutzen um Self-Assembly-Prozesse makromolekularer Strukturen robust ablaufen zu lassen.
Wie ist es möglich, dass demographische Fluktuationen in den Teilchenzahlen einen so starken und schädlichen Effekt bewirken, selbst bei relativ hohen Gesamtteilchenzahlen? Ein genaueres Verständnis der zugrundeliegenden Mechanismen kann dabei helfen weitere Strategien zu finden, mit denen stochastische Effekte abgewendet und die Robustheit von Self-Assembly-Prozessen verbessert werden kann. Zu diesem Zweck beschäftigen wir uns in dem zweiten Projekt damit eine effektive Theorie zu formulieren, die in der Lage ist die stochastische Dynamik in unserem konzeptionellen Modell zu erfassen. Im Wesentlichen erklärt die effektive Theorie wie Fluktuationen in den heterogenen Konzentrationen zu einer effektiv erhöhten Nukleationsrate führen, welche das System in kinetische Fallen treibt. Basierend auf diesen Erkenntnissen beschreiben wir fünf weitere Mechanismen, die es erlauben, durch Regulierung

des Levels von Teilchenzahlfluktuationen, deren schädlichem Effekt zu entkommen.
Neben der Problematik kinetischer Fallen, die auf Grund einer zu hohen Nukleationsrate entstehen und zu vermehrtem Zusammenbau von unvollständigen Strukturen führen, ist auch das Auftreten von Fehlern, welche zu einem inkorrekten Zusammenbau der Strukturen führen, eine entscheidende Problematik in Self-Assembly-Prozessen. Aus diesem Grund beschäftigen wir uns in dem dritten Projekt mit der Frage, wie Fehler in dem Assembly-Prozess effektiv vermieden werden können. Wir erweitern hierbei das Modell, indem wir eine endliche Fehlerrate einführen und betrachten die finale Anzahl von fehlerfrei zusammengebauten Strukturen in den verschiedenen irreversiblen Szenarien. Wir finden dabei, dass die finale Anzahl fehlerfreier Strukturen typischerweise exponentiell mit der Fehlerrate und der Größe der Strukturen abnimmt und zusätzlich durch einen weiteren stochastischen Effekt verringert werden kann, den wir auch als "stochastische Defektkatastrophe" bezeichnen. Die Regulation der Verfügbarkeit der Bestandteile (Supply Regulation) könnte jedoch eine effiziente Methode sein, um die Fehlerrate zu minimieren und stochastische Effekte zu vermeiden. Wir betrachten hierbei einen Supply Mechanismus, der auf Selbstregulation der Bausteine beruht und in seiner prinzipiellen Funktionsweise daher auch in biologischen Systemen realisiert werden könnte. Wir zeigen außerdem, dass dieser auf Selbstorganisation basierende Regulationsmechanismus dieselbe Zeitkomplexität besitzt als wenn die Verfügbarkeit der Bausteine extern kontrolliert wird.
Ein Manuskript über die Resultate des ersten Projektes wurde im Journal eLife publiziert und ist in Kapitel 5 abgedruckt. Für dieses Projekt teile ich mir die Erstautorenschaft mit Isabella Graf und Patrick Wilke. Manuskripte zu den Ergebnissen des zweiten und dritten Projekts sind derzeit in Vorbereitung. Die entsprechenden Manuskriptentwürfe sind in den Kapiteln 6 und 7 abgedruckt. Für das zweite Projekt teile ich Erstautorenschaft mit Isabella Graf, in dem dritten Projekt bin ich der einzige Erstautor.

3. **Self-Assembly und Genexpression.**
Der letzte Teil meiner Arbeit untersucht mit Hilfe eines hypothetischen Modells, wie Self-Assembly und Genexpression in Zellen gekoppelt sein könnten, um Self-Assembly von großen Strukturen zu koordinieren.
Alle Bestandteile, die sich zu makromolekularen Strukturen in Zellen zusammen setzen, werden zunächst durch Genexpression gebildet. Solche Strukturen wie Flagellae, Ribosome oder Kernporen werden darüber hinaus üblicherweise in kontrollierter Anzahl in der Zelle benötigt. Es stellt sich daher die Frage, wie Zellen in der Lage sind relativ präzise eine bestimmte Anzahl von Molekülen herzustellen, die sich anschließend in eine bestimmte Struktur zusammensetzen, ohne dabei zu viel Energie zu verschwenden. Darüber hinaus haben wir aus den vorherigen Projekten gesehen, dass durch eine entsprechende Regulation der Verfügbarkeit der Bausteine die Effizienz des Assembly-Prozesses gesteigert und die Fehlerrate signifikant verringert werden kann. In diesem Projekt erforschen wir einen möglichen, hypothetischen Mechanismus wie Genexpression und Self-Assembly gekoppelt sein könnten, sodass von jeder Spezies eine kontrollierte Anzahl von Molekülen in einer bestimmten zeitlichen Reihenfolge bereitgestellt wird. Durch eine geeignete Approximation können wir das System analytisch beschreibbar machen und dadurch einige relevante Eigenschaften berechnen. Wir finden dabei, dass der Mechanismus durch besondere Robustheitseigenschaften gekennzeichnet ist sowohl im Bezug auf Variation der Ratenkonstanten als auch im Bezug auf Teilchenzahlfluktuationen, die in einem biologischen Kontext sehr wichtig sind. Obwohl das Modell ursprünglich als hypothetisches Modellsystem entwickelt wurde, ergeben sich auffällige Gemeinsamkeiten zwischen dem

zentralen Netzwerkmotiv, das die Expression der Monomere in der richtigen Anzahl reguliert, mit dem regulatorischen Netzwerk, das in gramnegativen Bakterien die Expression der Flagellenmotorproteine kontrolliert.
Eine Publikation zu diesem Projekt ist geplant, ein Manuskriptentwurf dazu existiert jedoch noch nicht.

Im letzten Kapitel dieser Arbeit führe ich die Ergebnisse der verschiedenen Projekte, vor allem der ersten beiden Teile, zusammen um eine kinetische Theorie von Self-Assembly-Prozessen zu formulieren. Die Theorie unterscheidet dabei vier grundlegende Self-Assembly Szenarien und beschreibt für jedes dieser Szenarien das Skalierungsverhalten wichtiger Parameter und Observablen in Abhängigkeit von der Größe der Zielstruktur. Ich hoffe, dass diese Theorie einen Beitrag zum besseren Verständnis von Self-Assembly Phänomenen, insbesondere der benötigten Zeitdauer von Self-Assembly-Prozessen leisten wird. Darüber hinaus motiviert die Theorie einen speziellen “Skalierungsansatz” der Nanotechnologie, der auch die benötigte Assemblyzeit explizit berücksichtigt und es erlaubt diese zu minimieren.

# Synopsis

Living matter is fundamentally different from dead matter in that it is (self-)organized over all length scales down to the molecular scale. It is exactly this self-organization over many length scales, which provides life with its fantastic and unique properties to adopt and evolve, to grow and reproduce, to learn, heal and interact with its environment in a myriad of possible ways. In order to bridge the gap from the molecular scale to larger length scales, the ability of living systems to generate larger functional structures from smaller subunits plays a key role. Because this formation typically proceeds in a self-organized way in a biological system, we term this phenomenon *self-assembly*. The concept of self-assembly therefore plays a crucial role for our understanding of living systems as well as for the question of how life could have emerged originally.

Beside the pure scientific fascination of self-assembly, there is also huge technological and medical interest in the subject: Given that life and, in particular, the human body is organized down to the molecular scale, the most effective way to correct dysfunctional behaviour and cure certain diseases may be to intervene directly on this smallest length scale. Basically, this is how most pharmaceuticals already affect the organism. However, self-assembly in this medical context could open the path to generate medicals that exhibit a much more complex behavior than usual pharmaceuticals, being able to take decisions, operate with higher precision and adopt to the specificities of the concrete problem. For example, it can be envisioned that, in the future, complex surgery will be performed in a minimally invasive way by functional nano agents and that diseases like cancer, multiple sclerosis or congenital disorders are healed by 'clever' pharmaceuticals. In this context, self-assembly is so important because self-assembly together with sequence folding (e.g. DNA origami) are supposedly the only possibilities to generate such complex structures at this small length scale. Other techniques like 3D printing, which rely on external control rather than self-organization, fail to operate on such small length scales and hence cannot be used for this purpose.

This combination of exploring the basic principles of life paired with the prospect of contributing to the advancement of technology and medicine, is, in my opinion, what makes biophysics in general and self-assembly in particular such a rich and formidable field of research. Moreover, what makes this field even more stirring is that self-assembly gives rise to very beautiful physics: The analytical methods used to describe and understand this phenomenon range from simple heuristic arguments and dimensional analysis, over nonlinear dynamics, the theory of kinetic rate- and stochastic master equations, to symmetry principles, scaling concepts and the renormalization group. Furthermore, numerics is, of course, an indispensable tool in the theoretical study of self-assembling systems. Such being the case, it occurred several times in our research that we were completely surprised by the outcome of a numeric simulation,

which, intuitively, we had anticipated completely differently.

This thesis is divided into three parts, which, however, are strongly interconnected and deal with different aspects of self-assembly: the time efficiency of self-assembly processes, stochastic effects in self-assembly systems as well as possible couplings between self-assembly and gene expression.

1. **Time efficiency in self-assembly.**
The first part of this thesis contains three projects and deals with the time efficiency of self-assembly processes. Specifically, we ask how long it takes for a self-assembling system to realize a substantial yield and how this time efficiency can be controlled and optimized.
In the first project, we introduce a conceptual model that allows us to describe four key strategies (scenarios) for non-equilibrium self-assembly, which can be used to avoid spurious nucleation and overcome kinetic traps. We characterize the time efficiency of each of the four scenarios by its time complexity, i.e. the dependence of the assembly time on the size of the target structure. Similar as for computer algorithms, this characterization via the time complexity allows us to informatively compare the four scenario. Furthermore, the time complexity analysis reveals robust power law dependencies of both the assembly time and the optimal value of the control parameter on the structure size. We claim that the robustness of these scaling laws can be used to formulate reliable laws that allow to better predict and control the yield and time efficiency in self-assembly experiments. Especially interesting in this context is a strategy that induces efficient self-assembly by regulating the supply of constituents and, therefore, does not require fine-tuning of rate constants or other molecular properties. We suggest that this strategy might be a complementary way to realize efficient self-assembly in nanotechnology.
Due to the supposed importance of this strategy for nanotechnology, we dedicated a separate project to the analysis and evaluation of different possible implementations of supply regulation in self-assembly systems. To this end, we developed a specific theoretical model that allows us to analytically compute the respective time complexity exponents for various supply strategies. By comparing the pertinent time complexity exponents, we are thus able to identify the most time efficient implementation of supply regulation.
Our scaling analysis performed in the first project suggests that one of the four scenarios, namely the one that relies on reversible binding of the constituents, might also be sensitive to the morphology (shape) of the constituents. Therefore, in the third project, we investigate how the morphology of the constituents influences the assembly time in this scenario and whether the time efficiency can be optimized by altering the shape of the constituents. Indeed, we find that the shape of the building blocks crucially impacts the time efficiency and time complexity and that, by choosing a 'favorable' morphology, the time efficiency and robustness (with respect to 'variability' in the control parameter) can be significantly improved. The reason is attributed to the fact that the morphology of the constituents determines relevant properties like the effective nucleation size and the effective order of attachment reactions, which, in turn, can be shown to strongly influence the assembly kinetics and its time efficiency. Since the scenario that is based on reversible binding reactions is considered as the current standard in nanotechnology, this finding can have considerable technological consequences.
A manuscript discussing the results of the first project has been published in PNAS and is reprinted in chapter 2. A draft of the manuscript for the third project, which is still in prepa-

ration for submission, is reprinted in section 4. In both projects I am the single first author.

2. **Stochastic effects in heterogeneous self-assembly.**
The second part of my thesis contains three parts and investigates the role of stochastic effects in self-assembly if the particle number is limited. More generally, we ask under which conditions self-assembly is robust and resilient, how its fidelity can be controlled and stochastic effects can be mitigated. These questions are important in a cellular context, because cells often build structures in relatively low copy numbers and hence could be strongly affected by stochasticity or fluctuations in the particle numbers.
In the first project, we describe and quantify a stochastic effect which we termed 'stochastic yield catastrophe'. We show that this effect occurs specifically in heterogeneous self-assembly systems and it results from demographic noise in the particle numbers. Interestingly, this effect can lead to a strong reduction or even a complete suppression of the assembly yield, although the deterministic rate equations may predict a perfect yield. We find that the stochastic yield catastrophe becomes negligible in the limit of large particle numbers but that the minimal particle number that is required to achieve a fixed yield strongly increases with the size of the target structure. We furthermore show that increased homogeneity of the building blocks, an enhanced nucleation barrier as well as increased reversibility of the binding reactions mitigates stochastic effects or even leads to their complete elimination. Therefore, it is to be expected that cells rely on such mechanisms in order to enable the robust self-assembly of macromolecules.
How is it possible that demographic noise in the particle numbers provokes such a strong detrimental effect even for relatively larger particle numbers? Understanding the mechanisms at work can help identify strategies to alleviate the stochastic yield catastrophe and to increase resilience in assembly processes. To this end, in the second project, we formulate an effective theory that is capable of capturing the stochastic dynamics in our conceptual model. Essentially, the effective theory explains how fluctuations in the heterogeneous concentrations lead to an effectively increased nucleation rate, which drives the system into kinetic trapping. Based on these insights, we propose five additional mechanisms that allow to prevent the detrimental stochastic effect by regulating the effective noise level in the particle concentrations.
Beside the problem of kinetic traps that arise due to an enhanced nucleation rate, resulting in the assembly of incomplete structures, another key challenge to overcome in self-assembly is the avoidance of errors that would lead to incorrectly assembled or malformed structures. Therefore, in the third project, we ask how the emergence of assembly errors can effectively be avoided and the fidelity of self-assembly be optimized. To this end, we extend the model by introducing a finite error rate with which particles bind incorrectly and we consider the final number of correctly assembled structures in the various irreversible scenarios. We find that, typically, the number of correctly assembled structures decreases exponentially both with the error rate and the size of the structures and, in addition, can be significantly reduced by another stochastic effect, which we refer to as 'stochastic defect catastrophe'. However, regulation of the availability of the building blocks (supply regulation) might be an efficient method in order to minimize the error probability and to avoid stochastic effects. In this context, we investigate a supply mechanism that relies on self-regulation by the building blocks themselves and, therefore, could principally also be realized in a biological system. Furthermore, we show that this mechanism based on self-organization exhibits the same time

complexity as a scenario in which the availability (supply) of the building blocks is controlled externally.
A manuscript that discusses the results of the first project has been published in eLife and is reprinted in chapter 5. For this project I share co-first authorship with Isabella Graf and Patrick Wilke. Manuscripts on the results of the second and third project are currently in preparation for submission. The corresponding manuscript drafts are reprinted in chapters 6 and 7. For the second project I share co-first authorship with Isabella Graf while for the third project I am the single first author.

3. **Self-assembly and gene-expression.**
The last part of my thesis, with the help of a hypothetical model, investigates how self-assembly and gene-expression could be coupled in cells in order to coordinate the self-assembly of large structures.
All components that self-assemble into macromolecular structures inside cells are created via gene-expression. Furthermore, these macromolecular structures like flagellae, ribosomes or nuclear pore complexes are typically built in well-controlled numbers. This raises the question how cells are able to precisely count the number of molecules they need to produce in order to assemble a specific number of structures without wasting too much energy. Furthermore, we have seen from the previous projects that, by properly regulating the availability of the building blocks, self-assembly efficiency can be increased and the error probability significantly reduced. In this project, we investigate a possible, hypothetical mechanism that couples gene-expression with self-assembly, so that monomers of the different species are provided in well-controlled amounts in a temporal sequence. Through an appropriate approximation, the system can be made analytically tractable, which allows us to analytically access certain key characteristics of the mechanism. In this way, we find that the mechanism fulfils special robustness criteria both with regard to variations in the rate constants as well as to particle number fluctuations, both of which would be crucially important in a biological context. Although the model was originally conceptualized as a hypothetical model system, its central network motif, which regulates expression of the building blocks in the correct amount, shows some striking similarities with the regulatory network that controls the expression of flagellar motor proteins in Gram-negative bacteria.
A publication on the results of this project is planned, however, a corresponding manuscript does not yet exist.

In the last chapter of this thesis, I combine the results obtained from the various projects, primarily of the first two parts, to formulate a concise kinetic theory of self-assembly processes. The theory distinguishes four key scenarios for self-assembly and, for each of these scenarios, characterizes the scaling behavior of important parameters and observables in dependence of the size of the target structure. I hope that this theory will contribute to the better understanding of self-assembly phenomena, in particular, of the time required by self-assembly processes. Furthermore, the theory motivates a special 'scaling approach' to nanotechnology, which also takes the required assembly time explicitly into account and thus allows one to minimize it.

# Contents

# List of publications

### Publications directly relevant to this thesis

1. Gartner*, F. M., Graf*, I. R., Wilke*, P., Geiger, P. M., & Frey, E. (2020). *Stochastic yield catastrophes and robustness in self-assembly.* **eLife**, 9(e51020), 1-37. DOI: 10.7554/eLife.51020. [1]
2. Gartner, F. M., Graf, I. R., & Frey, E. (2022). *The time complexity of self-assembly.* **PNAS**, 119(4). DOI: 10.1073/pnas.2116373119. [2]
3. Gartner, F. M., & Frey, E. (2022). *Self-assembly efficiency strongly depends on the morphology of the constituents.* In preparation. [3]
4. Gartner, F. M., Graf, I. R., & Frey, E. (2022). *Controlling fidelity and time-efficiency in self-assembly.* In preparation. [4]
5. Graf*, I. R., Gartner*, F. M., & Frey, E. (2022). *Understanding and guiding robust self-assembly of heterogeneous structures.* In preparation. [5]

### Other publications

6. Träuble, F., Gartner, F. M., Graf, I. R., & Frey, E. (2022). *Topological properties of self-assembly reaction networks determine robustness to stochastic effects.* In preparation. [6]
7. Würthner*, L., Gartner*, F. M., Muramatsu*, D., & Frey, E. (2022). *Anomalous kinetic roughening of bulk-coupled growing interfaces.* In preparation. [7]
8. Muramatsu, D., Gartner, F. M., & Frey, E. (2022). *Immune cells as active matter system.* In preparation. [8]
9. Angerpointner, S., Kohler, K., Gartner, F. M., Frey, E. & Trapp, O. (2022). *Kinetic models of the formose reaction in alkaline environments reveal (un)identifiable reaction pathways.* In preparation. [9]
10. Gaimann, M., Gartner, F. M., & Frey, E. (2022). *In silico evolution of biological conditional memory using sequential transcription logic.* In preparation. [10]
11. Dass*, A. V., Wunnava*, S., Langlais*, J., von Esch, B., Krushe, M., Ufer, L., Chrisam, N., Dubini, R. C. A., Gartner, F. M., Angerpointer, S., Dirscherl, C. F., Rovó, P., Mast, C. B., Šponer, J., Ochsenfeld, C., Frey, E., & Braun, D. (2022). *RNA autopolymerisation from 2',3'–cyclic nucleotides at air-water interface.* In preparation. [11]

# 1 Introduction: Self-assembly in biology and nanotechnology

The purpose of this first chapter is to give an overview over the most important research directions in the field self-assembly, both on the experimental and the theory side.

Many macromolecular protein complexes in biology, in order to be able to perform sophisticated functions, reveal highly heterogeneous and complex architectures. These architectures are typically formed from smaller subunits and they vary broadly in size: Some structures, like small protein complexes [12], consist of only a few components, while others, like for example large virus capsids [13] or complex organelles like the bacterial flagellum [14], can comprise more than a thousand up to several thousand subunits. Since function is closely related to structure in biology, building up such complex architectures is essential for living systems in order to be able to perform sophisticated functions. A highly fascinating aspect of the emergence of these structures is that they typically form in a self-organized way, without external control and without a 'blueprint' or a template. A blueprint could be, for example, an RNA sequence, which is translated into a corresponding sequence of amino acids, that then folds into a protein. In contrast, building larger structures from individual subunits has the central advantage that the same subunits can be repeated several times in the structure, which reduces the total amount of information that needs to be stored. Furthermore, the degree of complexity that can be realized by assembling independent constituents appears to be significantly higher than the structural complexity that can be achieved by folding a single sequence of amino acids. We generically refer to this process of the self-organized arrangement of individual subunits into larger structures as *self-assembly*.

Although there is not always a sharp distinction in the literature, self-assembly should be clearly delimited from aggregation. Aggregation [15] also refers to a process in which larger structures form irreversibly from smaller subunits, however, the structures that emerge are typically not defined by a specific subunit composition, subunit arrangement or size but rather appear as random conglomerations of particles. These aggregates typically do not fulfil a (complex) function and their formation is often even undesirable (for example some protein aggregates that cause neurodegenerative diseases [16, 17, 18]). Correspondingly, binding reactions between the subunits that form these aggregates are typically non-specific and reactions of larger clusters are common. Instead, self-assembly - at least according to our perception - describes the formation of ordered structures of a specific subunit composition, which are typically able to perform some biological function.
Furthermore, in the literature, the term 'biogenesis' is often used instead of 'self-assembly' in order to denote highly regulated and complex assembly processes that involve a large number of 'helper' molecules, also called assembly factors. The reasoning thereby is that

the principle of self-organization appears to be violated if the assembly process does not run spontaneously but depends on a large number of associated assembly factors and, thus, the term self-assembly might be unjustified. Indeed, for example, a eukaryotic ribosome consists of roughly 80 building blocks, whereas the assembly process in total involves more than 200 different molecules [19, 20]. In the literature, one therefore often uses the term 'biogenesis of the ribosome' [21, 22] instead of 'self-assembly of the ribosome'.
However, whether a system is self-organized or externally controlled, largely depends on the definition of the system. Furthermore, a distinction of assembly processes based on whether or not molecules are involved that do not form part of the final structures, might not be very conducive in understanding basic principles of the underlying processes that lead to the formation of complex structures. We therefore take a pragmatic point of view in this respect and generally consider processes that rely on assembly factors or other control factors as belonging to the field of self-assembly as well - at least as long as single molecules do not contain a complete blueprint of the entire structure and, thus, information is only stored locally.

The reliability and efficiency with which intracellular self-assembly processes create complex structures, based only on local information, poses several questions: How can complex structures like ribosomes [19, 20], flagellae [14, 23, 24] or virus capsids [25, 26] be built up within short time with such high accuracy? If information is stored only locally, how can be ensured that complete structures emerge and not only pieces or fragments of the structures are formed? How can the number of assembly errors be minimized, which might have devastating consequences for an organism (see introduction to chapter 7 for examples)? Finally, what sets a limit to the resource and time efficiency of self-assembly processes and which conditions must be met in order for those efficiencies to be maximized?
A putative answer to these questions might be given by assuming that the desired structures emerge as free energy minima of the system and thus the self-assembly process constitutes the system's approach to thermodynamic equilibrium [27, 28, 25, 29]. This perception of self-assembly, also referred to as equilibrium self-assembly, is heavily used in the literature, in particular, for example, on virus capsid assembly [30, 27, 31, 32, 33, 25, 34, 35]. While this approach can be quite useful in some contexts for reversible self-assembling systems, it generally does not account for local minima of the free energy, also called kinetic traps [36, 31, 37, 34, 29, 38], which might be encountered while the system approaches the global free energy minimum. In other words, equilibrium self-assembly disregards the time it takes the system to approach the global free energy minimum through those local minima. If this time scale is long compared to the biologically relevant time scale of the system, then the equilibrium approach might be futile and transient states can be realized which do not correspond to a global free energy minimum.
Therefore, in order to better understand the emergence of kinetic traps, kinetic self-assembly models based on rate equations have been studied [39, 40, 36] and particle-based simulations have been performed [41, 42, 43, 44, 45, 46]. These investigations show that a particular kind of kinetic trap, which is also called depletion trap, can arise if in the initial phase of the assembly process too many structures get initiated and thereby the resources run out before the structures can be completed. In order to avoid such depletion traps, a fundamental principle has been established, stating that, in order to obtain a high assembly yield, nucleation of new structures must be significantly slower than the growth of existing structures ('slow nucleation principle') [40, 47, 48, 49, 50, 51, 52, 53].

Other kinds of kinetic traps, which have been described particularly in virus capsid assembly, arise due to an incorrect arrangement of the subunits and can usually be ruled out by adjusting the binding strengths between the subunits [54, 55, 25]. In general, it has been suggested that weak and reversible interactions between the subunits might be a key requirement in order to overcome kinetic traps [56, 57, 58, 59, 45, 60, 25, 34, 61]. Contrary to this, however, it is broadly assumed that in the assembly of cellular structures like ribosomes, flagellae, nuclear pore complexes etc., most binding reactions between the subunits are strong and effectively irreversible, suggesting that other ways to circumvent kinetic traps must exist. In this thesis, we will characterize a broad range of possible strategies by which kinetic traps can be overcome and, in particular, we will study a general framework that allows us to analyze the time that these different strategies require in order to avoid kinetic traps.

In the following, we will more closely discuss two particular subfields of self-assembly that have arisen and that play a prominent role in the exploration of self-assembly phenomena: Virus capsid assembly and DNA-based nanotechnology. While the first subfield studies the formation of virus capsids as an example of biological self-assembly processes, the second subfield investigates principles of self-assembly with the help of artificial systems, which are realized by exploiting the properties of DNA molecules. Another important difference between both subfields concerns the heterogeneity of the building blocks: While virus capsids are typically built from a very limited number of different types of building blocks, artificial self-assembly processes are often realized with a large number of different types of constituents. Despite those differences, basic principles like the slow nucleation principle discussed above have emerged equivalently in both fields.

## 1.1 Virus capsid assembly

Virus capsids are a paradigmatic example of self-assembling systems: Once a cell gets infected, the genetic material of the virus causes the cell to produce virus proteins, which then assemble completely autonomously into new virions. Understanding this self-assembly process of viruses is thus pivotal in getting a more thorough understanding of human diseases and their spreading.
Most viruses have either an icosahedral or helical capsid structure and they differ broadly in size [62]: One of the smallest viruses, the satellite tobacco mosaic virus, consists of a singe-stranded RNA with 1059 nucleotides encapsidated by 60 identical capsid proteins [26]. In contrast, the Megavirus, which is larger than some bacteria, consists of a double-stranded DNA molecule with more than 1.2 million base pairs and a capsid that is built from more than 1000 capsid proteins [13]. It has been shown that if a virus capsid would be made from a single polypeptide chain, this capsid could impossibly be large enough in order to carry the entire genetic information necessary to built the peptide [63]. Hence, in order for viruses to be able to reproduce, it is necessary that the capsids self-assemble from inpedependent and largely identical subunits. Typically, the capsids are built from many identical copies of a small number of different types of constituents, which are arranged in a highly symmetrical and regular fashion. In 1962, Caspar and Klug developed a classification scheme in order to characterize the structure and symmetries of icosahedral capsids [64]. They found that icosahedral capsids are built from multiples of 60 subunits. Three so-called asymmetric units

thereby form each of the 20 identical triangular facets of the icosahedron. The triangulation number (T-number) is mathematically defined as the squared length of an edge of a triangular facet when the unfolded structure of the virus is mapped onto a two-dimensional hexagonal lattice [65, 25]. Typically, the T-number corresponds to the number of subunits forming one asymmetric unit, so that the total number of subunits forming the capsid is $60T$. For example, Herpesviridae form capsids with a T=16 icosahedral symmetry [66] and the capsids of Turriviridae exhibit T=31 symmetry [65]. Also bacterial carboxysomes exhibits an icosahedral symmetry corresponding to a triangulation number of T=75 [67].

In 1955 Fraenkel-Conrat and Williams demonstrated experimentally that active virions of the tobacco mosaic virus assemble spontaneously from RNA and capsid proteins in vitro [68]. This finding opened the path to in-depth experimental investigation of virus capsid self-assembly and entailed a number of theoretical studies and computational models intended to describe the self-assembly process of the capsids [69, 39, 40, 57, 36, 59, 70, 45, 71]; where we listed just a few examples. Some of the main insights gained from these experimental studies are discussed in the following:
The observations suggest that virus capsid assembly can essentially be described as a nucleation and growth process [69, 40, 36, 72]. According to the slow nucleation principle, it is thereby crucial that nucleation is slow compared to growth, since otherwise only incomplete fragments of capsids would form. This retardation of nucleation is generally achieved by weak binding interactions mainly due to hydrophobic interactions among the constituents [57, 59, 45], resulting in a highly reversible self-assembly dynamics and an effective nucleation size, similarly to nucleation phenomena in crystal growth or condensation [73].
Further observations from the experiments show that the assembly yield only sets in after a so-called lag phase and then exhibits a characteristic sigmoidal dependence on time [69, 70, 48]. Moreover, under physiological conditions, only complete capsids and free subunits are typically present in detectable concentrations, whereas concentrations of larger intermediates are very low and escape detection, for example, in size-exclusion chromatography experiments [69, 45, 48, 25]. For this reason, it is still difficult to characterise the detailed assembly pathways, as these intermediates are so transient and rare. It remains a major open question to determine the precise mechanisms of the fast and robust growth phase.

From the theory side there are mainly three different approaches, namely by analysing the self-assembly process with the help of thermodynamics, by kinetic rate equations and with particle based simulations, as we will briefly outline in the following. Interesting reviews on virus capsid assembly and these various theoretical approaches can be found, for example, in [74, 75, 25, 34, 76].

### Thermodynamics of virus capsid assembly

In the thermodynamic description, the final state of the system is characterized by minimization of the free energy under the constraint that the total subunit concentration is fixed [27, 34, 35]. This leads to the well-known law of mass action [77, 78, 25, 79], relating the concentration $c_n$ of n-mers to the concentration of monomers $c_1$:

$$c_n = (c_1 e^{-\beta\epsilon(n)})^n \,, \tag{1.1}$$

where $\beta = (k_B T)^{-1}$ and $\epsilon(n)$ is the aggregation free energy per subunit in an n-mer. Due to mass conservation, the concentrations are subject to the constraint $\sum_{n=1}^{S} n c_n = C$, where $C$ is the initial concentration of monomers and $S$ the size of complete capsids. For spherical capsids, the per subunit aggregation free energy $\epsilon(n)$ will typically be minimal for some intermediate size $n < S$, while $\epsilon(n)$ increases particularly strongly for the last subunits that are added completing the capsid [72, 25, 34]. Therefore, under the constraint of mass conservation, the law of mass action predicts a large concentration only for monomers and complete capsids, while intermediate concentrations are rather low, consistent with the experimental findings [39, 25]. Based on this observation that intermediate concentrations are negligible at equilibrium, the equations for capsid assembly thermodynamics can be simplified considerably by neglecting all intermediates except free subunits and complete capsids, so that the mass conservation constraint reduces to

$$C = c_1 + S c_S \,. \tag{1.2}$$

Combining this condition with the law of mass action and assuming $S \gg 1$, it can be shown that the fraction of subunits bound in capsids, $f = \frac{S c_S}{C}$, becomes large if the total subunit concentration is above a pseudo-critical concentration $C^* \approx e^{\beta \epsilon(S)}$ [30, 25, 34]:

$$f \approx \left(\frac{C}{C^*}\right)^S \ll 1 \qquad \text{for } C \ll C^* \tag{1.3}$$

$$\approx 1 - \frac{C^*}{C} \qquad \text{for } C \gg C^* \,. \tag{1.4}$$

Note that the transition between the two regimes becomes sharper with increasing capsid size $S$. This result suggests that, increasing the total subunit concentration $C$ or the magnitude of the binding energy (i.e. decreasing $C^*$), increases the fraction of subunits in complete capsids $f$ at equilibrium. However, due to the finite time scale in experiments, increasing the binding energy can lead to kinetic trapping, implying that the equilibrium cannot be reached [25]. On the other hand, we will show in this thesis (primarily in chapter 4) that irreversible intermediate assembly steps can be beneficial in that they allow to achieve high yields in parameter regimes in which thermodynamics would not predict good yields.

It has furthermore been argued that also under optimal conditions virus capsid assembly will not reach thermodynamic equilibrium because the last assembly steps, when the capsid is completed, are effectively irreversible on the relevant time scale. In fact, the time scale of dissociation of complete capsids has been estimated to 50 days or more [80, 81, 25]. Moreover, substantial hysteresis has been measured for the dissociation of HBV capsids under denaturant, indicating that the capsids are not at thermodynamic equilibrium [82]. Of course, irreversible steps, especially in the late stages of the assembly process, make sense from a biological point of view as they could significantly prolong the time over which the virus can remain intact in infinitely diluted and unfavorable environments (also see our discussion in the motivation for part I) [25]. It has been shown that, even if there are irreversible steps in the assembly process, for times longer than the lag time, the same relation as in Eq. (1.3) may hold but with a different value for the critical concentration $C^*$ [47]. This relation is then also called the *pseudo law of mass action*.

Hence, it is likely that virus capsid assembly generically does not reach thermodynamic equilibrium on the relevant time scales, although it can still be described by a (pseudo) law of mass action. Fitting the aggregation free energy $\epsilon(S)$ to $C^*$, however, might lead to a false

value if this is not properly taken into account [25].

In summary, while the thermodynamic description leads to some qualitatively correct results about virus capsid assembly, its assumptions are not strictly justified, likely causing quantitative discrepancies. Furthermore, thermodynamics ignores the important aspect of time, which is why it is unable to predict kinetic traps and generally the time efficiency of self-assembly schemes.

### Rate equation models for capsid assembly

In order to study the dynamics of virus capsid self-assembly processes, rate equation models have been investigated [39, 40, 36]. These models typically describe the evolution of the concentrations of the polymer sizes by associating each polymer size with a typical configuration of an unfinished capsid (a similar approach will be used in chapter 4). The first step in these models is typically described by a nucleation event with a specified nucleation size, whereupon the structures grow reversibly by attachment and detachment of single monomer subunits until they reach the size of a complete capsid. The rates for attachment and detachment can thereby either be chosen generically [47] or be specifically related to the associated capsid configurations [40, 36]. Conceptually, this approach is similar to the one used by Becker and Döring in order to describe crystallization phenomena [73], with the important difference that in the case of virus assembly the final structures have a fixed, finite size. In more extensive models, several configurations per cluster size have been taken into account, with transitions between these configurations being specified accordingly [83, 84]. On the other hand, rate equation models could be made analytically tractable by approximating the state space (described by the cluster size variable) as a continuum [30, 47].
These rate equation models have generally shown good agreement with experimental kinetic data [40, 85, 70] and have thus helped to develop a better understanding of the kinetics of virus capsid assembly. In particular, they enabled a better understanding of depletion traps, which could not be predicted with the thermodynamic approach, and thereby contributed essentially to the establishment of the slow nucleation principle. Furthermore, the models explain the origin of the lag time and the sigmoidal time dependence of the assembly yield [70, 48]. The main insight thereby is that during the initial phase of the assembly process, the cluster size distribution propagates as a travelling wave front and yield sets in as soon as the wave reaches the final size $S$ of the capsids [47]. If nucleation is too fast, free subunits will deplete before the wave reaches the final size and thus the system becomes kinetically trapped. A comparison with kinetic data moreover suggested the existence of an activation step of the subunits prior to binding [70].
Some of the analytical models studied in this thesis will build upon kinetic rate equation models as well.

### Particle-based simulations of capsid assembly dynamics

A drawback of rate equation models is that, in order to be feasible, they require the complexity of the state space to be simplified drastically (typically to a one-dimensional variable

that characterizes the size of intermediates)[1]. Particle-based simulations, in contrast, allow to explore the entire state space and do not require any further assumptions to be made about the assembly pathways. Furthermore, in contrast to rate equation models, these simulations also account for misbinding between subunits, which may result in the assembly of malformed structures. For those reasons, various groups have performed particle-based simulations that track the positions and orientations of each subunit [41, 42, 43, 44, 45, 46]. Simulations at atomic resolution are practically impossible or would entail an extreme computational demand [87], since already a single capsid protein typically has several hundred amino acids. Hence, the different groups have developed various coarse-grained, excluded-volume models for the subunits, representing them either as 'patchy-spheres' [88, 89], trapezoids consisting of spherically symmetric 'pseudoatoms' [90, 91, 92] or as subunits with polygonal interaction directions [93, 94].
An important insight gained from particle-based simulations concerns the 'malformed capsid trap' that arises if subunit addition to growing capsids occurs more quickly than already associated subunits can anneal defective or strained interactions [25], thereby leading to malformed capsids. Generally, this trap occurs for large binding energies (annealing of defective interactions is slow) and large subunit concentrations (addition of subunits is fast) but it also significantly depends the binding specificity of the subunits. Malformed capsid traps have also been observed experimentally [54, 95, 55].

## 1.2 DNA nanotechnology

The aim of nanotechnology is to control and manipulate matter on the molecular scale. Being able to build artificial functional structures on the nanometer scale could allow to realize groundbreaking technological and medial advancements. For example, a few potential applications of artificial nanostructures and nanotechnology are: pin-point drug delivery systems and tissue engineering, nano-sized robotics and diagnostics in medicine; optical, electronic, catalytic or sensing devices, e.g. in solar cells, light emitting diodes or electronic circuits [96, 97, 98, 99, 100].
It has turned out that DNA molecules have very favorable chemical and mechanical properties in order to be used as building material for artificial nano structures [101, 102, 103]. Furthermore, exploiting the properties of Watson-Crick base pairing between the four different nucleotides A, T, G and C, allows to design highly specific, predictable and programmable interactions among different substrands [102, 49]. Because A only binds with T and G with C, varying a subsequence of $n$ bases allows for the creation of $4^n$ uniquely binding domains of length $n$. Hence, with only a rather small sequence length $n$, a huge number of uniquely binding sequence strands can be created. This 'richness' of the sequence space together with the well-suited mechano-chemical properties of DNA molecules is at the very heart of DNA nanotechnology and makes the approach so very versatile.

[1] For example, an icosahedral virus capsid composed of only 12 subunits already allows for 750 possible intermediate configurations [86], whereby this number of possible configurations grows exponentially with the structure size.

### DNA origami

One particular direction of DNA nanotechnology is DNA origami, which has been introduced by Rothemund in 2006 [104] but relies on ideas put forward by Seeman already in 1982 [101]. Analogous to the ancient art of origami, in which a two-dimensional sheet of paper is folded into three-dimensional objects, in DNA origami a long single-stranded DNA molecule is folded into complex two- [104], or three-dimensional structures [105, 106, 107]. In order to fold the long DNA strand (which is also called the scaffold strand), a large number of short staple strands is inserted, which bind specifically to two distinct regions of the scaffold strand and thereby fold it into the desired structure [102, 103, 100]. While the scaffold strand can be any generic DNA strand of sufficient length (typically the genome of the M13 phage is used for that purpose), the short staple strands have to be specifically designed and synthesized so that they bind to the correct positions of the scaffold. There are computer algorithms available that automatically calculate the set of required staple strands in order to fold a given scaffold strand into any desired target structure [108]. Subsequent annealing of a mixture consisting of the scaffold strands together with an excess of synthesized staple strands typically allows to achieve high yields close to 100%.
The approach is very elegant and it is astonishing how well it works, given that DNA has not been optimized for this kind of application. However, there are two major limitations to this approach: First, DNA origami is hard to be scaled up, as the overall dimensions of these nanostructures are limited by the length of the scaffold strand, and ssDNA scaffolds significantly longer than the traditionally used M13 genome are technically challenging to acquire and mechanically fragile [100]. Second, each time the shape of the structure needs to be changed, even only slightly, a complete new set of staple strands has to be designed and synthesized [49]. Both of these limitations can be overcome with DNA-brick based assembly.

### DNA-brick based assembly

In DNA-brick based assembly, instead of using a single long scaffold strand, the structures are build in a modular way from several smaller strands (also called 'bricks' or 'tiles'). These bricks can either be rather complex, folded structures themselves that connect via junctions [106, 105, 109, 110], smaller double-stranded bricks with two 'crossovers' that connect by their 'sticky ends' [111, 112, 113] or tiny single-stranded bricks consisting e.g. of only 32 base pairs each [49, 50]. Independently of the specific nature of the bricks, these approaches have in common that the bricks self-assembly into higher order structures without any template. In this way, DNA assemblies of more than one gigadalton and a size of almost 500 nm in diameter could be assembled [2] [109, 110].
The large versatility of the brick-based approach in assembling three-dimensional structures of complex shapes is nicely demonstrated by the works of Ke and Wei [49, 50]. In this approach, which is also called 'tile lego', hundreds or thousands of distinct, single-stranded tiles

[2] Since this is significantly larger than the size of most viruses, one particular very promising application of these large-scale nanostructures aims to build artificial capsid shells with an aperture, which are equipped with antibodies (or other virus-binding moities) on the shell's interior surface [110]. In this way, if a virus enters the capsid, it gets trapped inside and is thus prevented from interacting with the cells of an organism. Due to the large number of antibodies in the interior, an individual antibody does not need to bind overly strongly in order to trap the virus. Thus, the hope is that these virus traps can be used as a broad-spectrum platform against virus infections.

of 32 or 42 base pairs, respectively, in length assemble a cubic 'canvas'. Each brick within the canvas is unique and binds only with four specific neighbors. By selecting subsets of bricks from this canvas, a large plethora of different shapes can readily be assembled.
This demonstrates a central advantage of the brick-based approach over DNA origami: While in DNA origami, new staple strands must be designed and synthesized if a new structure is to be build, the brick-based approach is much more versatile in that the same set of strands can be used with only a different subset of strands being selected. Key to the functionality of this approach is the large heterogeneity of DNA bricks, which allows to address each brick within the canvas individually: In an improved method [114], which uses slightly longer strands of a length of 52 base pairs, a canvas consisting of 30000 unique components and a side length of more than 100nm could be created, which allowed for the creation of even more intricate 3D structures. These examples therefore illustrate nicely how structure heterogeneity, which will also play an important role in several projects of this thesis, can be achieved in nanotechnological applications.
A drawback of the brick-based approach, however, is that the yields are currently still rather low: in particular, for those very large structures with 30000 components, the yield is only $\sim 1\%$ but reaches up to 24% for smaller structures [49, 115, 114].
It was originally believed that self-assembly with heterogeneous DNA tiles was hard to be realized, since it was expected that deviations from the stoichiometric ratios of the bricks would lead to partial structure formation and kinetic trapping [115, 116, 53]. Kinetic trapping, however, is presumably suppressed to a large extent due to a putative slow nucleation step of the tiles followed by fast growth of the assemblies [49, 50, 51]. It might thus be this nucleation barrier which renders brick-based nanotechnology possible. However, it can not be excluded that the yield drop for larger structures might be due to an excess of nucleation events.
We hope that the results of this thesis will contribute to establish additional strategies to control DNA-brick based self-assembly allowing to improve the yield and time efficiency of these applications.

For reviews and perspectives on DNA nanotechnology please refer to [102, 116, 115, 103, 117, 100, 118]. Reviews on algorithmic self-assembly, which is another highly interesting subfield of DNA nanotechnology, although not discussed in depth here, can be found in [119, 120, 121].

# Part I

# Time efficiency of self-assembly

## General motivation

In a discussion with Hendrik Dietz[3] from the Technical University of Munich in November 2020, Hendrik told us about their work on the self-assembly of artificial capsids from DNA-bricks [110], following the example of biological virus capsid assembly. Generally, artificial shells have important potential biotechnological and medical applications, ranging from pin-point drug delivery systems to compartmentalizations for chemical reactions [122, 123]. The experiments of the Dietz group, in particular, aim to assemble capsids with an aperture at one side, that will be equipped with antibodies in the interior. In this way, the capsids can be used to trap virus particles inside an organism and prevent them from interacting with the organism's cells. The hope is that in this way a broadly applicable antiviral platform can be created, which can be utilized to combat a broad range of viral infections. Rebuilding viral shells with artificial components can furthermore help to shed light on yet poorly understood aspects of the formation of viral capsids in vivo.
While the Dietz group - quite remarkably - managed successfully to assemble various capsid shells consisting of up to 180 DNA bricks, when I asked how long the assembly processes would typically take, Hendrik's answer was the following: The smallest capsids, which consist of only 8 components, assemble quasi instantaneously. The T=1 capsids, consisting of 60 components, still assemble rather quickly in the course of a few hours. The T=3 capsids with 120 components need roughly a day and the T=4 capsids with 180 components require 10 to 14 days to assemble with sufficiently high yield[4].
This illustrates two important aspects of self-assembling systems: First, the required assembly time apparently increases with the size of the target structure; and second, this increase can be quite drastic, so that the required assembly time can easily become a limiting factor for the self-assembly of large objects. After all, the T=4 capsid is by far not among the largest capsids that appear in nature, where we find structures like the T=75 bacterial carboxysome that consists of $\sim$ 4500 components [124, 125]. The bacterial flagellum is even bigger and consists of roughly $\sim$ 30000 proteins [126]. Extrapolating the trend observed in the experiment, it would probably take decades to assemble a structure as large as the carboxysome or the flagellum. This shows that natural assembly processes are very likely optimized not only with respect to resource efficiency but also with respect to time efficiency. Consequently, this implies that for a comprehensive understanding of biological as well as artificial self-assembly processes, the time component plays an essential role.

Nevertheless, in the literature on self-assembly so far, much more attention has been put on understanding structural determinants of the resulting assemblies rather than on kinetic aspects determining their assembly processes. The reasons for this bias are presumably manifold. However, an important aspect is probably the fact that it is very difficult to extract any information on self-assembly kinetics from experiments, since on the one hand it is impossible to directly observe the dynamics, and on the other hand it is rare to even observe intermediate products like unfinished capsid shells, which might allow one to infer the underlying dynamics: Typically, the distribution of assembly states is double-peaked with a high concentration

[3] Hendrik Dietz is professor for biomolecular nanotechnology at the Technical University of Munich and a leading expert in the field. Together with his team he has the goal of building functional artificial nanodevices via self-assembly and sequence folding.
[4] This data can also be found in Figure 3 in reference [110]

of monomers on the one hand and a large concentration of finished products on the other hand, while intermediate states exist only in very low concentrations [127, 36, 47].
As most theory in the field has been developed close to experiments, one has therefore rather focused on structural aspects of the resulting assemblies, which could be compared and backed with experimental data. To this end, thermodynamics provides a useful theoretic description, that has been used extensively [35, 121, 128, 33, 27, 32, 78, 34], as it conveniently allows one to characterize the structure of the assembly products without the need to specify the underlying dynamics.
Usually, thermodynamics provides a valid description of a system that has reached thermodynamic equilibrium and fulfils detailed balance. As has been discussed in the introduction, however, it is very unlikely that self-assembling systems like virus capsids will reach thermodynamic equilibrium on biologically or experimentally relevant time scales [47, 129, 25]. Supposing, for example, virus capsid assembly would reach thermodynamic equilibrium, this would imply that the chemical potential of a subunit in solution and as part of a capsid would adopt the same value. Hence, releasing the virus particle from the infected cell into its surrounding like the blood stream, which is depleted of free subunits, would inevitably lead to the virus's disassembly. Apparently, this does not happen, implying that virus assembly is intrinsically out-of-equilibrium. The reason why thermodynamics can still be applied in order to describe the final assembly state is owed to the fact that reversible self-assembling systems can be shown to often obey a 'pseudo-law of mass action' [47]. This means that, despite the presence of irreversible assembly steps, the distribution of assembly products may qualitatively behave as if it were in equilibrium.
For those reasons, although the prerequisites for a thermodynamic description are usually not strictly fulfilled, thermodynamics has become a prevalent theoretical tool in the study of self-assembly systems [27, 32, 33, 25, 35]. The drawback of this theoretical approach, however, is that it does not allow to investigate the underlying kinetics of the system; In particular, it does not inform about the time the system requires to reach the (quasi-)equilibrium state.
For this reason, coarse-grained molecular dynamics simulations have been performed extensively in order to gain a better understanding of kinetic aspects of self-assembly systems [45, 43, 130, 131, 132, 133, 134]. However, since these simulations are typically computationally expensive - in particular if the assembly dynamics is strongly reversible - only rather small structures have been simulated so far. As the experiments of the Dietz group suggest, however, time efficiency becomes critical especially for the self-assembly of large objects. Hence, detailed molecular dynamics simulations are presumably not very well suited to test the efficiency of self-assembly schemes for large objects and thereby are probably not the optimal method either to establish a holistic understanding of self-assembly kinetics.

The difficulty or incapability of the prevalent analytical, numerical and experimental approaches to describe and quantify kinetic features of the self-assembly of large objects might be important reasons why kinetics has largely been neglected against structural properties in self-assembly[5] [136]. As the experiments of the Dietz group suggest, however, both aspects

[5] As has been discussed in the introduction, kinetic models for virus capsid assembly do exist, though. For example, Zlotnik and coworkers [135, 36] developed a model of rate equations analogous to the Becker-Döring equations for a system undergoing crystallisation [73], that describes the evolution of capsid intermediates. However, these models have primarily been used to study qualitative aspects of (reversible) self-assembly kinetics like the origin of lag phase, the reason for the sigmoidal shape of temporal yield curves or the

are essential for a proper understanding of self-assembling systems.

The goal of the first part of this thesis therefore comprises the development of conceptual, analytical and numerical tools suitable to describe the time required by self-assembly processes and to formulate a concise theory of their time efficiency.
Specifically, the first chapter analyzes and compares the time efficiency of various, reversible and irreversible self-assembly schemes. To this end, we introduce the concept of time complexity, which quantifies the dependence of the assembly time on the size of the target structure, analogous with the concept of time complexity in computer science. The time complexity thereby allows for a simple and informative characterization of the time efficiency of self-assembly processes and hence plays an important role also in the following chapters. Furthermore, we describe analytical methods that allow one to calculate the exponent that characterizes the scaling of the assembly time and we discuss methods to efficiently simulate the self-assembly processes. Equipped with these tools and concepts, we characterize the time efficiency of four different self-assembly scenarios.
In the second chapter, we analyze one of the irreversible assembly scenarios more in depth and discuss a few different ways to implement this scenario. The concept of time complexity thereby again provides a reliable and powerful tool to characterize the efficiency of these different implementations.
Finally, in the last chapter of this first part, we discuss how the morphology of the constituents influences the time efficiency of reversible self-assembly processes. Thereby we determine how the scaling of the assembly time as a function of the detachment rate and the structure size is affected by the morphology of the constituents.

In all studied cases, our findings suggest that time plays a critical role in self-assembly and that certain changes, for example concerning the way in which nucleation events are controlled or in the morphology of the constituents, can have a big effect on the assembly time. The concept of time complexity thereby provides a simple and informative description of the assembly time and hence constitutes a powerful tool to characterize these effects. We hope that these insights into the time efficiency of self-assembly processes will help to speed up self-assembly experiments and contribute to a better understanding of biological self-assembly processes.

emergence of kinetic traps. Furthermore, these models have typically only been considered for rather small capsids. In contrast, the goal of this thesis is to develop a comprehensive theory of the time required by self-assembly processes on a broader perspective, by examining also different kinds of assembly schemes or assembly control scenarios.

# 2 The time complexity of self-assembly

The goal of this chapter is to summarize the most important findings of our project on the time complexity of self-assembly. The corresponding manuscript has been published in PNAS 119(4) (2022). This chapter is based on and uses parts of this publication [2], which is also reprinted in section 2.7.

## 2.1 Motivation

Self-assembly experiments, like the one of the Dietz group discussed in the general motivation, often rely on reversibility of the binding reactions in order to overcome kinetic traps. This implies that single bonds are rather weak and hence can easily be broken up again. In this way, assembly errors that occur at early stages in the assembly process can be corrected and kinetic traps be avoided due to the reversibility of the reactions. Many experimental and some biological self-assembly systems, like virus capsids, therefore rely on this scheme [56, 57, 58, 59, 60, 25, 61] and reversibility has become a paradigm for virus capsid assembly [45]. However, as we show in this project, a disadvantage of this method is that, in order to be time efficient, fairly precise fine-tuning of a control parameter (which can be either the temperature, binding energy, monomer concentration, salt concentration, etc.) is necessary. Because it is not a priori clear what the optimal value for the control parameter is, time optimization is presumably a rather difficult task. This might explain the difficulties and the poor time efficiency in the experiments of the Dietz group.
But is it possible that there is also a completely different, maybe simpler approach to artificial self-assembly that allows to optimize time efficiency more easily? A very suggestive idea would be to supply the constituent species in a specified sequence in order to favour a specific assembly pathway and thereby avoid kinetic traps. Experimentally, this could be a very feasible strategy, as it would only require the various constituents to be added to the system in a specified temporal order. In analogy with just-in-sequence supply for industrial assembly processes, we therefore call this assembly scheme *just-in-sequence scenario*. But how can we tell which of the two scenarios, the one relying on reversibility of binding reactions or the one based on just-in-sequence supply, is more time efficient?
A similar problem of evaluating different strategies based on their time efficiency, frequently occurs in computer science when different algorithms are available to solve a particular kind of computational problem. Often it thereby occurs that a particular algorithm is fast if the amount of input data is small, but it becomes very inefficient if the 'size' of the problem increases. Therefore, rather than quantifying the efficiency of an algorithm by the time it requires to solve a particular problem, one evaluates it by how its runtime *scales* with the size of the problem. This important parameter is called the *time complexity* of the algorithm. The time complexity has another central advantage, namely, that it can typically be computed or estimated quite easily. This means that, while it is generally difficult to predict the exact

runtime of an algorithm, the scaling of the runtime in dependence of the size of the problem can usually be accessed much more easily. The time complexity thus allows to informatively compare different algorithms with respect to their efficiency in solving large computational problems and it has thus become an essential concept in computer science.
Hence, it is suggestive to apply the same concept to quantify and compare the time efficiency of different self-assembly schemes. To this end, we quantify the efficiency of the different self-assembly schemes by how the minimal time required to achieve a demanded yield of 90% scales with the size of the target structure. Beside the reversible binding scenario and the just-in-sequence scenario, we also examine two other irreversible scenarios that are relevant in a biological and, potentially, in an artificial context. In these two scenarios, kinetic traps are avoided either with the help of a (slow) activation step of the monomers or by reducing the dimerization rate, which might be realized, for instance, with the help of allosteric effects. We call these two scenarios *activation scenario* and *dimerization scenario*, respectively. The idea is that most biological and artificial self-assembly systems can qualitatively be characterized as one of these four key scenarios or a superposition of them.
Just as for computer algorithms, the concept of time complexity turns out to be very useful in characterizing and comparing the time efficiency of these different self-assembly schemes: The time complexity scaling can be accessed analytically, it is a very robust measure and, most importantly, it reveals a huge discrepancy in the time efficiency of the different self-assembly scenarios for large sizes of the target structure. This implies that, depending on the strategy that is used in order to avoid kinetic traps, the time required by the assembly process can vary by orders of magnitude.
In particular, the analysis shows that the scenario that relies on reversible binding and the scenario based on just-in-sequence supply are competitive in their time efficiency but depend critically on different kinds of parameters: While for the reversible binding scenario fine-tuning of rate constants is essential in order to achieve high efficiency, the just-in-sequence scenario requires adjustment of the particle numbers supplied in order to function efficiently and robustly. Hence, we conclude that the just-in-sequence scenario might indeed be a promising complementary approach to artificial self-assembly and it would be very interesting to test this strategy in experiments.

## 2.2 Model

The conceptual model that we used to investigate the time complexity of self-assembly processes is illustrated in Fig. 8.1. The model allows us to simulate four key scenarios for self-assembly that we will specify in detail below. We consider the assembly of $N$ particles of $S$ different species into one-, two- or three dimensional target structures of variable size $S$ as depicted in the figure. Beside the size of the target structure, also the dimensionality of the structure may be relevant for the required assembly time and, therefore, we vary the dimensionality as well. We assume that particles start in an inactive state from which they get activated at constant total rate $N\alpha$. The inactive state can represent an assembly inactive configuration of the molecules, or, more generally, it could also represent a state before the particles have entered the system or before they have been produced via gene-expression etc. Once particles are active, they start to self-assemble. Assembly takes place in a well-mixed

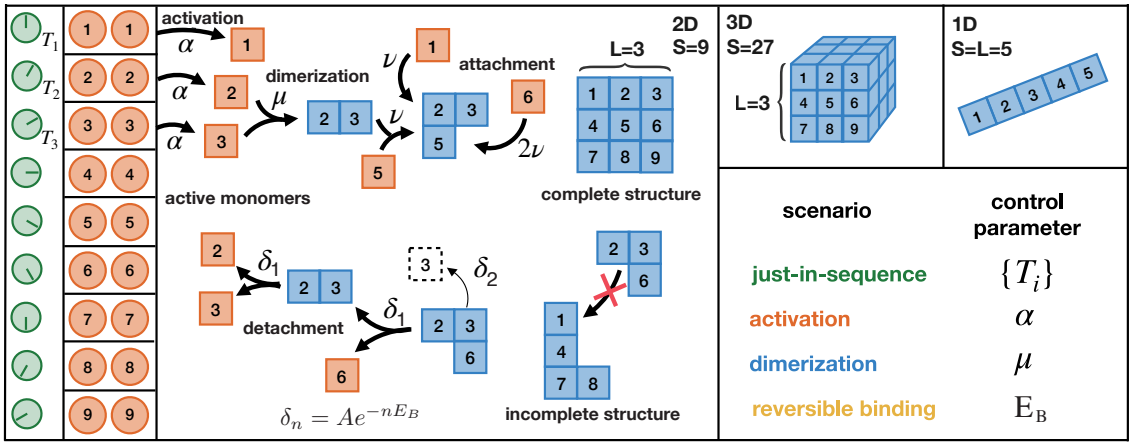


**Figure 2.1** | Illustration of the model (slightly adapted from [2]). $N$ identical copies of $S$ different species of monomers assemble into one- (1D), two- (2D) or three-dimensional (3D) heterogeneous structures of volume $S$ (only the 2D case is illustrated explicitly). A constant influx of monomers of species $i$ takes place during the time interval $[T_i, T_i + \frac{1}{\alpha}]$ with net influx rate $N\alpha$. Once added to the system (activated), monomers start to self-assemble. A monomer of a bulk species has 2 (1D), 4 (2D) or 6 (3D) possible binding partners as illustrated in the figure. Any two fitting monomers can dimerize with rate $\mu$. Subsequent to dimerization, structures grow by attachment of single monomers with rate $\nu$ per binding site. Furthermore, monomers can detach from a cluster with rate $\delta_n = Ae^{-nE_B}$, where $n$ is the number of bonds that need to be broken assuming a binding energy $E_B$ per bond. Our goal is to minimize the time $T_{90}$ until 90% of all resources are assembled into complete structures. To this end, we control particular elements of the assembly process (control parameters) and distinguish four scenarios which are defined through the respective control parameter(s). Each scenario can be used to elude kinetic traps and achieve a high assembly yield but how do these different strategies differ regarding their time efficiency?

fluid environment. Furthermore, we assume that all particles bind specifically only with their neighboring species. This means that erroneous binding events that would otherwise lead to incorrectly assembled structures are neglected. Following the assumptions of ideal aggregation theory, we only consider attachment of monomers and neglect interactions of larger polymers [70, 77, 35].

The assembly process starts with a dimerization event followed by subsequent attachment of further monomers. We assume that dimerization between two fitting monomers happens at a rate $\mu$ which may be smaller than the general growth rate $\nu$. Biophysical reasons for why the dimerization rate may be significantly smaller than the growth rate could be allosteric binding effects or the action of enzymes (assembly factors) that guide biologcial assembly processes. Indeed, it has been observed that several biomolecules like, for example, flagellin, the components of ribosomes or some viruses, do not assemble spontaneously but preferentially attach to a preexisting structure [137, 20, 138]. Furthermore, we also consider detachment processes of particles from partially assembled structures. We assume that the detachment rate of a particle decreases exponentially with the binding energy or, more generally, the energy barrier that needs to be overcome, according to the Arrhenius law. The total binding energy (energy barrier) of a particle is assumed to be proportional to the number of bonds of the particle. Sufficiently low binding energies induce an effective nucleation barrier similarly as a decreased dimerization rate. However, the underlying biophysical mechanisms of both nucleation scenarios are completely different. The nucleation mechanism induced by a

low binding energy is related to the nucleation process in crystal growth and described by standard nucleation theory. On the other hand, conformational switching is the essence of the much more sophisticated mechanisms leading to a direct reduction of the dimerization rate [137, 138]. Accordingly, we will also find that the time complexity is quite different for both scenarios. Finally, in order to describe the just-in-sequence scenario as anticipated in the motivation, we allow for the different species to be activated at distinct time points. This allows to provide the various species in a specific sequence and thereby favor a designated assembly pathway.

In order to achieve efficient self-assembly, nucleation must be significantly slower than growth [34, 31, 139]. Otherwise, too many structures would emerge and the resources would run out before all structures can get finished. The system is then said to be kinetically trapped [31, 60]. The model allows us to study four different mechanisms or *scenarios* to avoid such kinetic traps. In the *reversible binding* and the *dimerization scenario*, the frequency of nucleation events is regulated by controlling the binding energy $E_B$ (relative to the thermal energy scale $k_BT$) or the dimerization rate $\mu$, respectively. In the *activation scenario*, a slow activation rate $\alpha$ reduces the momentary concentration of active monomers and thereby regulates the effective dimerization rate (which depends quadratically on the concentration of monomers). Note that the activation scenario does not discriminate between the different species, i.e. all species are activated simultaneously. In contrast, the just-in-sequence scenario distinguishes the time points $T_i$ when the different species $i$ get activated and thereby favours specific assembly pathways. We denote the interval between the equidistant time points $T_i$ by $\Delta T$. Hence, each of the four scenarios can be described by a single control parameter $E_B$, $\mu$, $\alpha$ or $\Delta T$, respectively. For each of the four scenarios, we identify the optimal value of the respective control parameter, which minimizes the time $T_x$ required to achieve a fixed yield $x$ of completely assembled structures. Typically in the paper, we demand a fixed yield of $x = 90\%$.

We defined the model as a completely heterogeneous self-assembly system where each species occurs only once in a completely assembled structure. However, for the activation, dimerization and reversible binding scenario, the heterogeneity of the structure is actually irrelevant. Because these three scenarios treat all species equivalently, the governing chemical rate equations are invariant under relabelling the species and, therefore, the dynamics can be shown to be independent of the heterogeneity of the system (see Supplement [1] and [2]). Hence, the results of the time complexity analysis for these three scenarios are actually valid in a much more general sense.

Some other idealizations and specific choices were made in defining the model (for example, it was assumed that the attachment rates for all species are identical). Therefore, in the supplement, we analyze a number of modifications of the original model and show that the results of the time complexity analysis mostly remain invariant to such variations.

## 2.3 Key challenges

A major challenge in this project was the simulation of the reversible binding scenario for two- and three-dimensional target structures. In order to avoid kinetic traps and achieve a high yield, it turned out that for some systems the detachment rate had to be chosen a factor of $10^2 - 10^4$ larger than the typical reaction rate $C\nu$ (where $C$ is the initial concentra-

tion of monomers). Consequently, due to the high level of reversibility, most of the time the simulation just jumps back and forth between repeated attachment and detachment events. Hence, many Gillespie steps are required in total until a yield of 90% is achieved. For some simulations, several billion Gillespie steps were necessary to perform only a single run. Particularly expensive are simulations with large target structures and especially if detachment rates deviate considerably from the optimal rate (such as for the plot in Fig. 3B in the paper). Furthermore, many individual runs are necessary in order to reliably determine averages and to perform the optimization of the parameter. Due to a high effort in optimizing the C++ code of the simulation, the program could be improved to perform approximately one million Gillespie steps per second on a 3,1 GHz CPU. By parallelizing individual runs and exploiting the computational capabilities of the LRZ Cluster, all simulations necessary to determine the parameter- and time complexity exponent for a specified scenario could be performed approximately within 5 days.
Another challenge concerned the simulation of the activation scenario because, as we will see later in this thesis, the activation scenario is affected by strong stochastic effects, unless the number of particles $N$ is very large ($N > 10^7$ for the largest simulated structures with $S = 1000$). However, this problem can be bypassed by exploiting the deterministic independence of the activation scenario from the heterogeneity. In other words, in the limit of large particle numbers, the heterogeneous system behaves deterministically like an equivalent homogeneous system. The homogeneous system, in contrast, is not affected by such strong stochastic effects if the particle number is small and thus can be simulated with much lower particle number (typically N=1000 is totally sufficient). We termed this method of simulating a heterogeneous system as an equivalent homogeneous system as 'method of homogenization' (see [2] Supplement).
A more conceptual challenge was the determination of the optimal strategy for the two- and three dimensional just-in-sequence scenario. As described in detail in the paper, time efficiency and robustness in the just-in-sequence scenario for higher dimensional target structures are jeopardized by increasing competition for resources caused by a growing number of complexes. Hence, additional regulation is necessary to down-regulate the level of competition. While at least three suitable regulatory mechanisms exist theoretically (see next chapter), varying the concentrations of the different species in specific, non-stoichiometric ratios, is seemingly the most efficient and experimentally feasible strategy. Determination of the optimal ratios for the concentrations therefore was another challenge that appears straight-forward in hindsight but was not obvious at the beginning of the project.

## 2.4 Results and discussion

An important result of this project is that for sufficiently large particle number $N$ and structure size $S$, the optimal parameter value in all four scenarios as well as the minimal assembly time exhibit power law dependencies on $S$. We denote the corresponding scaling exponents as the control parameter exponent $\phi$ and the time complexity exponent $\theta$, respectively. Importantly, these exponents do not depend on details and specific assumptions of the model and are invariant to modifications of the assembly kinetics. For example, we verified robustness of the exponents for different boundary conditions of the structures, for heterogeneous binding rates and for different thresholds $x$ of the yield in the definition of the assembly time $T_x$. Fur-

thermore, the simulation of more sophisticated experimental protocols like annealing[1] in the reversible binding scenario or alternative forms of monomer input in the activation scenario (also see section 2.6.1) leave the exponents invariant.
The identification of these robust scaling laws suggests that the characterization of self-assembly processes via the parameter- and time complexity exponent is informative and useful in an experimental context: Often, as in the experiments of the Dietz group, a similar system of building blocks is used to assemble structures of different sizes. The assembly of small structures is typically fast. Hence, one could identify the optimal parameter for the small system and, with the help of the simulated parameter exponent, estimate the optimal parameter (and the expected assembly time) for the larger system. Hence, in this 'scaling approach' to experimental self-assembly, one would first explore the small system and then 'scale up' to the larger system. Importantly, the derived scaling laws are not limited only to the optimal parameter and minimal assembly time but they can be shown to imply a general relation between the parameter $P$, the yield $x$ and the assembly time $T_x$. Precisely, it can be stated that, upon altering the size $S$ of the target structure, if the respective control parameter $P$ is scaled with $S^{\phi}$, then the assembly time $T_x$ scales with $S$ to the power of $\theta$:

$$P \sim S^{\phi} \qquad \Rightarrow \qquad T_x C\nu \sim S^{\theta}\,. \tag{2.1}$$

This relation implies, of course, that the same yield $x$ will be achieved again if the parameter is adapted in the prescribed way. We demonstrate in section 2.6.2 that the scaling relation holds in this general form. To this end, we show that, in a plot of the assembly time versus the parameter value, rescaling the y-axis by the minimal assembly time and the x-axis by the optimal parameter enforces a collapse of the curves.
The time complexity analysis furthermore enables us to compare the different scenarios with respect to their efficiency. We find that controlling the dimerization rate $\mu$ is the most efficient strategy. Reversible binding is very inefficient for one-dimensional structures because for one dimensional structures there is no effective nucleation barrier in contrast to the higher dimensional cases. For two- and three-dimensional structures, reversible binding is efficient and competitive with the JIS scenario, provided the detachment rate is fine-tuned precisely (see Fig. 3B in [2]). The just-in-sequence scenario could be an alternative strategy for artificial heterogeneous self-assembly. Because it only relies on temporal control of the constituent supply and does not require fine-tuned rate constants or other sophisticated molecular properties, it might be a more versatile and practicable approach compared to reversible binding. However, key for the efficiency and the robustness of the just-in-sequence scenario is that the different species are supplied in concentrations of specific ratios, which must be met with sufficient precision. Therefore, precise molecular counting mechanisms could open up an alternative route to nanotechnology.

[1] 'annealing' refers to the experimental procedure of slowly reducing the temperature during the experiment in order to keep the ratio between the detachment rate and the reaction rate (which depends on the concentration of (unbound) monomers) at a constant level. [140]

## 2.5 Key results

In my opinion, there are three key results of this project:

- Optimization of time efficiency plays a crucial role for self-assembling systems. Different assembly strategies, despite all of them being highly resource efficient (high final yield), can nevertheless differ in their time efficiency by several orders of magnitude. Suboptimal parameter settings can also lead to an increase of the assembly time by many orders of magnitude.
- The time complexity analysis yields a simple but informative characterization of the time efficiency of self-assembly processes. It allows us to informatively compare different self-assembly scenarios and it identifies robust scaling laws for the optimal parameter settings in these scenarios.
- Regulation of the temporal supply of constituents defines a time-efficient strategy for heterogeneous self-assembly. Specifically, the 'just-in-sequence' scenario, in which constituents are provided in specific concentrations in a specified sequence, could be a complementary, highly versatile approach to artificial self-assembly. Robust molecular counting mechanisms are key to the successful implementation of this strategy.

The concept of time complexity turned out to be very useful in characterizing the time efficiency of self-assembly processes. An interesting question for future research would be whether other self-organization processes, like pattern formation or self-organization of active matter systems, can likewise be characterized by their time complexity in an informative way.

## 2.6 Additional material

In this section we provide additional material that is not covered in the paper or in the supplementary material but that is important in the context of time complexity and also for later chapters in this thesis. First, we show analytically that the time complexity of the activation scenario is independent of the form of the input. Second, we show that the derived scaling laws describe dependencies of the assembly time on the structure size also for non-optimal parameter values and independent of the yield. To this end we demonstrate that upon rescaling the parameter by the optimal parameter and the assembly time by the minimal assembly time, the assembly time curves collapse onto Master curves.

### 2.6.1 Independence of the time complexity of the activation scenario from the form of monomer input

The activation scenario is characterized by a slow input of monomers that does not discriminate between the different species. In the paper we assumed that the influx of monomers is constant over a finite time interval, which is supposed to mimic the experimental act of 'pipetting' solute particles into the system. By contrast, in our project on stochastic effects in self-assembly [1] (see chapter 5), we assume that inactive particles get activated independently at a constant per capita rate and hence the total input decreases exponentially. Of course, in principle, there are arbitrary many possible choices for the input function in the activation scenario. Another biologically relevant example has been analyzed in the Supplementary Material of this project. Thereby we assumed that activation of monomers is reversible and that the switching between the active and inactive state is fast and thus can be assumed to be at equilibrium. We showed numerically that the time efficiency indeed can be increased by this special form of input relative to the constant influx scenario, but the time complexity exponent remains invariant.
In this section, we show analytically that the parameter- and time complexity exponent in the activation scenario are independent of the form of the input. This 'robustness result' will justify the nomenclature 'activation scenario' for all forms of monomer input and establishes the connection between the different implementation of the scenario in this project and in the later projects. It shows that the only inherent characteristic of the activation scenario is that the species are supplied indiscriminately.
In the supplement of the paper, we used analytic scaling arguments in order to derive estimates for the exponents. Here we choose a different, more rigorous analytic approach, which will also from the basis of analytic considerations in later chapters of this thesis. For a rigorous derivation of the basic ansatz, for which we just give intuitive arguments here, please refer to the later chapters (4 and 5).

The basic assumption is that the optimal parameter exhibits the same scaling as the threshold parameter at which the onset of the yield occurs. The reason behind this assumption is that, in the limit of large structure sizes, the yield transition curves have a constant shape and both the threshold and the optimal parameter are at fixed positions on these curves. Hence, we will determine the scaling of the threshold parameter.
To this end, we exploit the equivalence of the heterogeneous to a homogeneous system in which

particles are indistinguishable and we only consider the case of one-dimensional target structures. The exponents for the higher-dimensional cases can be related to the one-dimensional case by a simple rescaling argument (see main text in [2]).
As long as the yield is zero, the dynamics can be reduced to a two-component system that describes the evolution of the concentration of monomers $m(t)$ and the total concentrations of complexes $K(t)$:

$$\frac{d}{dt}m = F(t) - \nu m K\,, \tag{2.2}$$

$$\frac{d}{dt}K = \mu m^2\,. \tag{2.3}$$

Here $F(t)$ is the input function that fulfils the constraint $\int_0^\infty F(t)dt = N$, so that in total $N$ monomers are supplied. The second term in the first line describes attachment of monomers to complexes with rate $\nu$ and the second line accounts for nucleation (dimerization) of complexes with rate $\mu$. Because the yield is zero, all complexes in the system have a constant growth rate and it is not necessary to keep track of their sizes. Therefore, the reduction to this two-component system is possible.
We assume that the input function $F$ can be written in the form $F(t) = N\alpha f(\alpha t)$, where $\alpha^{-1}$ is a parameter that determines the time scale of the input function and $f$ is an arbitrary function that integrates to 1: $\int_0^\infty f(x)dx = 1$. For example, monomer input caused by the irreversible activation of inactive particles is described by the input function $f(x) = e^{-x}$, and constant influx over a finite time interval $1/\alpha$, as assumed in the paper, is described by the rectangular input function $f(x) = \Theta(x)\Theta(1-x)$.
Measuring time in units of $(N\nu)^{-1}$ and particle numbers relative to $N$, the system can be written in dimensionless form:

$$\frac{d}{dt}m = \omega f(\omega t) - mK\,, \tag{2.4}$$

$$\frac{d}{dt}K = \eta m^2\,, \tag{2.5}$$

where $\omega = \alpha/(N\nu)$ and $\eta = \mu/\nu$.
The crucial insight that enables us to determine the scaling from Eq. (2.4) and (2.5) is that, asymptotically, in the limit of small $\omega$ (corresponding to large structure sizes $S$), the term $\frac{d}{dt}m$ becomes negligible against the terms on the right hand side. We will therefore neglect $\frac{d}{dt}m$ and then show a posteriori that this approximation is indeed justified. The system thereby simplifies to

$$m = \frac{\omega f(\omega t)}{K}, \tag{2.6}$$

$$\frac{d}{dt}K = \eta\omega^2\frac{f^2(\omega t)}{K^2}\,. \tag{2.7}$$

The second equation can be solved by separation of variables and gives

$$K(t) = \left(3\eta\omega\int_0^{\omega t} f^2(x)dx\right)^{\frac{1}{3}}\,, \tag{2.8}$$

and hence for the monomer concentration we obtain

$$m(t) = \frac{f(\omega t)\omega}{\left(3\eta\omega\int_0^{\omega t} f^2(x)dx\right)^{\frac{1}{3}}}\,. \tag{2.9}$$

Taking the time derivative of $m(t)$, we find $\frac{d}{dt}m \sim \omega^{\frac{5}{3}}\eta^{-\frac{1}{3}}$, while $mK \sim \omega$. Consequently, for constant $\eta$, in the limit of small $\omega$, the term $\frac{d}{dt}m$ becomes indeed negligible against the right hand side of Eq. (2.4), showing that the approximation was justified (see [141] Supplement for a more rigorous argument).
The growth rate of complexes is proportional to the momentary concentration of monomers. Hence, a dimer that emerges at time $t = 0$ will finally reach an expected size of $s_0 = \int_0^\infty m(t)dt$ (in scaleless units). Since the complexes that emerge at $t = 0$ will finally represent the largest complexes in the system, $s_0$ approximately equals the final position of the foremost front of the density profile[2]. In other words, in the limit $s_0 \to \infty$, the travelled distance of the density profile equals $s_0$. Therefore, the condition for the onset of the yield for structures of size $S$ is determined by setting $s_0 = S$:

$$S = s_0 = \int_0^\infty m(t)dt = \left(\frac{\omega^2}{3\eta}\right)^{\frac{1}{3}} \int_0^\infty \frac{f(\omega t)}{\left(\int_0^{\omega t} f^2(x)dx\right)^{\frac{1}{3}}}dt = \left(\frac{1}{3\omega\eta}\right)^{\frac{1}{3}} \int_0^\infty \frac{f(y)}{\left(\int_0^{y} f^2(x)dx\right)^{\frac{1}{3}}}dy\,. \tag{2.10}$$

The integral term is independent of $\eta$ and $\omega$ and thus gives a constant while the prefactor determines the scaling. Using the above definitions for $\omega$ and $\eta$, it follows for the scaling of the threshold parameter,

$$\alpha_{\text{th}} \sim \frac{\nu}{\mu} N\nu S^{-3}\,, \tag{2.11}$$

yielding the control parameter exponent $\phi = -3$. Since the parameter $\alpha$ determines the time scale of the input, the total time required by the process will scale inversely with $\alpha$: $T \sim \alpha^{-1} \sim S^3$, and thus the time complexity exponent follows as $\theta = 3$. Note that the result (2.11) coincides[3] in this more general form with the result that we obtained in a different way from the scaling analysis in the supplement of the paper ([2]). The scaling exponents for two- and three-dimensional target structures are obtained by substituting $\nu \to \nu S^{(d-1)/d}$ in Eq. (2.11), as described in the main text of the paper.
This shows that for any input function that depends on a single time scale parameter, the control parameter exponent and the time complexity exponent are invariant to the form of the input as long as all species are supplied indiscriminately. The only possibility to reduce the time complexity with a supply strategy is by discriminating the different species as is done in the just-in-sequence scenario.
An interesting scenario would also be the case when active particles decay irreversibly into a waste product as it occurs, for example, in the systems studied by the group of Job Boerkhoven [142]. This scenario corresponds to an input function whose time integral is not constrained to give $N$ but can also be smaller. It is, however, very unlikely that the time- or resource efficiency can be improved by the irreversible wasting of monomers.

[2] the correspondence is only approximate because the tip of the wave front corresponds to the maximal size reached by the early dimers not their average size. In the limit $s_0 \to \infty$, however, the difference becomes negligible; see [141] Supplement.

[3] to reproduce the exact result, the particle number $N$ must be replaced with the concentration $C$ and the units of the rate constants must be adapted accordingly

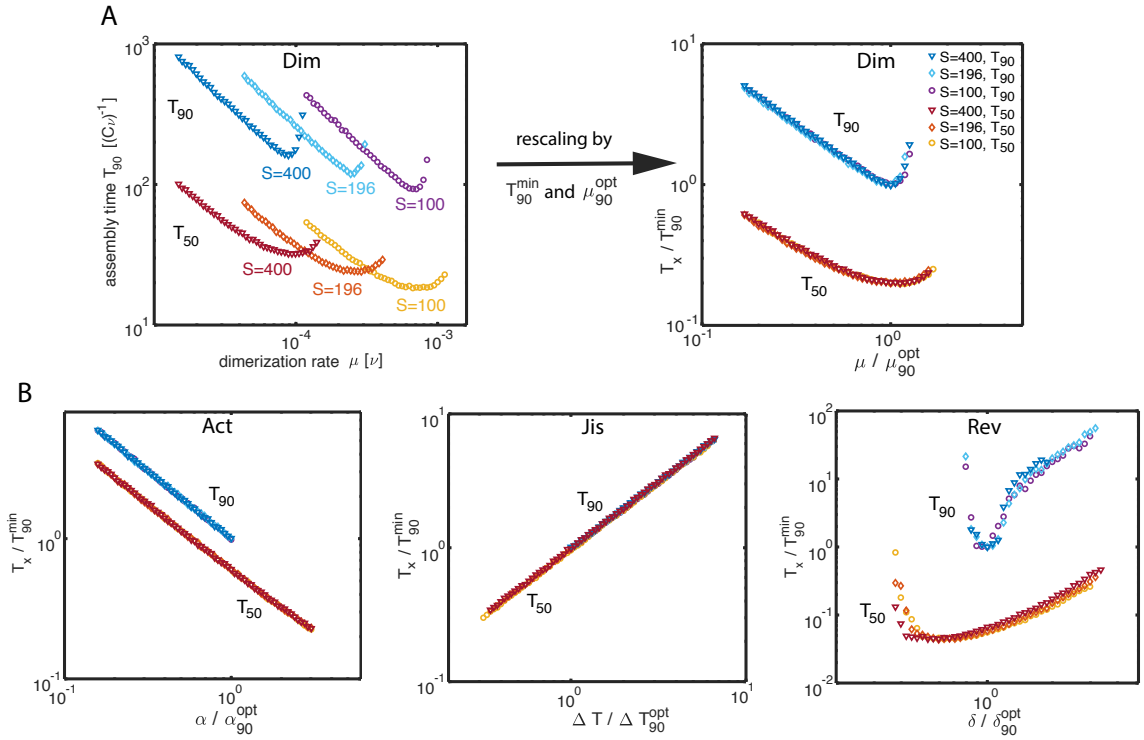


**Figure 2.2** | Collapse of the $T_x$-curves. **A** The $T_{90}$ and $T_{50}$ curves in the dimerization scenario are plotted against the dimerization rate for two-dimensional target structures of three different sizes $S = 100$, $S = 196$ and $S = 400$. Rescaling the x-axis for each system size by the optimal dimerization rate to obtain 90% yield, $\mu_{90}^{\text{opt}}$, and the y-axis by the minimal assembly time $T_{90}^{\text{opt}}$ leads to a collapse of the $T_{90}$ and $T_{50}$ curves. **B** Analogous to A, the rescaled assembly time is plotted against the respective control parameter for the activation, just-in-sequence and reversible binding scenario (only the rescaled plot is shown in each case). The $T_{90}$ and $T_{50}$ curves similarly collapse onto Master curves. The collapse of the curves shows that the scaling that were derived for the optimal parameter and the minimal assembly time in dependence of the structure size $S$, actually holds for *all* points on the curve and independently of the yield threshold $x$ in the definition of the assembly time $T_x$. Thereby, the law that describes the scaling of the assembly time with structure size for the different scenarios holds in the much more general sense given by Eq. (2.12).

## 2.6.2 Collapse of the time curves

In the paper, we only analyzed the scaling of the optimal parameter and the minimal assembly time, which allowed us to informatively compare the different self-assembly scenarios. However, the significance of the scaling laws, as described by the exponents $\phi$ and $\theta$, actually goes much further. Indeed, we show in this short section that the scaling applies not only for the optimum but for any point in the parameter space. To this end, we rescale the assembly time ($T_{90}$ and $T_{50}$) for different sizes of the target structure by the corresponding minimal assembly time $T_{90}^{\text{min}}$, and the respective control parameter by the optimal parameter to obtain 90% yield, see Figure 2.2. The rescaled plots show that in all four scenarios the curves for the 50% and 90% assembly times collapse onto two Master curves. This implies that the same scaling as for the optimum can be applied to *all* points on the curve that achieve the required yield $x$. Furthermore, since also the 50% yield curves collapse despite being rescaled with the

90% optimum, the scaling appears to be independent of the required yield $x$. In essence, the theory that results from this data collapse can concisely be summarized as the following scaling law: If, upon altering the size $S$ of the target structure, the respective control parameter $P$ is scaled with $S^{\phi}$, then the assembly time $T_x$ scales with $S^{\theta}$:

$$P \sim S^{\phi} \qquad \Rightarrow \qquad T_x C\nu \sim S^{\theta} \,. \tag{2.12}$$

Note that $P$ refers to the dimensionless control parameter, i.e. $\frac{\alpha}{C\nu}$, $\frac{\mu}{\nu}$, $\frac{\delta}{C\nu}$ and $\Delta T C\nu$ for the activation, dimerization, reversible binding and just-in-sequence scenario, respectively.
The parameter exponents therefore describe the 'canonical way' of controlling assembly processes in dependence of the size of the target structure and the time complexity exponents predict how the assembly time will behave in response to such control. Hence, the time complexity analysis describes optimal control strategies for self-assembly systems in dependence on the size of the target structure.
In practice, this control theory could be useful for experiments that use the same system of building blocks to assemble structures of different sizes as in the experiments of the Dietz group discussed in the introduction. Once a good setting is found for the small system, the theory can then predict how the control parameters should optimally be adopted for the larger system ('scale-up approach'). Thereby, the theory can be useful to increase the time efficiency of self-assembly experiments.

## 2.7 Publication reprint: The time complexity of self-assembly, PNAS (2022)

This section is a publication reprint of the following manuscript published in PNAS 119(4) (2022).

### The time complexity of self-assembly

by

Florian M. Gartner,[1] Isabella R. Graf,[1,2] and Erwin Frey[1]
[1] *Arnold-Sommerfeld-Center for Theoretical Physics and Center for NanoScience, Department of Physics, Ludwig-Maximilians-Universität München*
[2] *Present address: Department of Physics, Yale University, New Haven, CT 06520, USA.*

DOI: 10.1101/2021.04.01.437956

# The time complexity of self-assembly

Florian M. Gartner[a,b], Isabella R. Graf[a,b,1], and Erwin Frey[a,b,2]

[a]Department of Physics, Arnold-Sommerfeld-Center for Theoretical Physics, Ludwig-Maximilians-Universität München, D-80333 München, Germany; and [b]Center for NanoScience, Ludwig-Maximilians-Universität München, D-80333 München, Germany

Edited by Christopher Jarzynski, University of Maryland, College Park, MD; received September 24, 2021; accepted December 8, 2021

**Time efficiency of self-assembly is crucial for many biological processes. Moreover, with the advances of nanotechnology, time efficiency in artificial self-assembly becomes ever more important. While structural determinants and the final assembly yield are increasingly well understood, kinetic aspects concerning the time efficiency, however, remain much more elusive. In computer science, the concept of time complexity is used to characterize the efficiency of an algorithm and describes how the algorithm's runtime depends on the size of the input data. Here we characterize the time complexity of nonequilibrium self-assembly processes by exploring how the time required to realize a certain, substantial yield of a given target structure scales with its size. We identify distinct classes of assembly scenarios, i.e., "algorithms" to accomplish this task, and show that they exhibit drastically different degrees of complexity. Our analysis enables us to identify optimal control strategies for nonequilibrium self-assembly processes. Furthermore, we suggest an efficient irreversible scheme for the artificial self-assembly of nanostructures, which complements the state-of-the-art approach using reversible binding reactions and requires no fine-tuning of binding energies.**

nonequilibrium self-assembly | time efficiency | time complexity | self-assembly scenario | supply control

Time efficiency of self-assembly plays an important role in biology. For example, virus assembly must be fast to produce many virus particles before the infected cell is eliminated by the host's immune system (1–3). Moreover, as larger and ever more complex nanostructures are to be realized for technological or medical applications, time efficiency in artificial self-assembly becomes vital (4, 5). Designing self-assembly schemes that are fast and resource efficient is, however, challenging. The task amounts to finding strategies that avoid the formation of large numbers of incompatible and incomplete fragments of the desired target structure. Such kinetic traps (6–10) arise even when all building blocks have a high binding specificity and erroneous binding is negligible, and they become more prominent with increasing structure size. Consequently, assembly time increases with structure size.

But how exactly does the assembly time scale with the size of the target structure, and how does this scaling depend on the self-assembly scheme? What kinds of schemes optimize the assembly time? Answers to these questions will enable assembly strategies to be identified that are optimally suited for the production of large, functionally complex macromolecular structures via artificial self-assembly, a major goal in nanotechnology (4, 5, 11–13). Here, we address these questions by studying the time complexity (as opposed to structural complexity) (14–17) of four prototypical self-assembly scenarios, using scaling arguments and in silico modeling of the stochastic dynamics. Three of these scenarios have well-established realizations in biological and artificial self-assembly processes. The fourth strategy is a distinct idea conceptualized to achieve efficient self-assembly in a technological context by effectively regulating the supply of building blocks.

## General Model and Self-Assembly Scenarios

To explore these questions in their simplest form, we consider an assembly process involving $N$ identical copies of $S$ different species of building blocks (monomers) and assume chemical reaction kinetics in a well-mixed fluid environment. By $C = N/V$ we denote the concentration of monomers per species, where $V$ is the reaction volume. As we expect the time efficiency of the assembly process to depend on the dimensionality of the structure, we investigate the assembly of linear polymers, two-dimensional sheets, and three-dimensional cubes of edge length $L$ (volume $S$) (Fig. 1). We specify the system as a fully heterogeneous system with $S$ distinct species because this case defines the most general self-assembly process that allows for the largest set of different assembly strategies to be applied. Our analysis shows, however, that for three of the four strategies we consider, the heterogeneity of the building blocks is indeed irrelevant in the limiting case of large particle numbers $N$ and therefore our results hold independently of the heterogeneity of the structures. We assume that all binding reactions are specific and take place only between "neighboring" species as illustrated in Fig. 1. Erroneous binding between the constituents that would lead to malformed structures is thereby not taken into account. Following the assumptions of classical aggregation theory, we furthermore neglect interactions among oligomers (17, 18).

Specifically, we assume the following reaction kinetics: Any two compatible monomers can bind at rate $\mu$, forming a dimer that serves as a nucleus for further growth by sequential addition of monomers at rate $\nu$ per binding site. Analyses of more complex reaction schemes including heterogeneous binding rates are discussed in *SI Appendix* and show that our conclusions are

### Significance

**An important limiting factor for self-assembly processes is the time it takes to assemble large structures with high yield. While equilibrium self-assembly systems slowly relax toward a state of minimal free energy, nonequilibrium systems offer various ways to control assembly processes and to optimize their time efficiency. We show that these different control scenarios can informatively be characterized by their time complexity, i.e., their scaling of the assembly time with the structure size, analogous to algorithms for computational problems. Especially for large structures, differences in the time complexity of the scenarios lead to strongly diverging time efficiencies. Most significantly, we show that by effectively regulating the supply of constituents, high resource and time efficiency can be achieved for self-assembly processes.**

Author contributions: F.M.G., I.R.G., and E.F. designed research, performed research, analyzed data, and wrote the paper.

The authors declare no competing interest.

This article is a PNAS Direct Submission.



[1]Present address: Department of Physics, Yale University, New Haven, CT 06520.

[2]To whom correspondence may be addressed. Email: frey@lmu.de.

This article contains supporting information online at https://www.pnas.org/lookup/suppl/doi:10.1073/pnas.2116373119/-/DCSupplemental.

Published January 18, 2022.

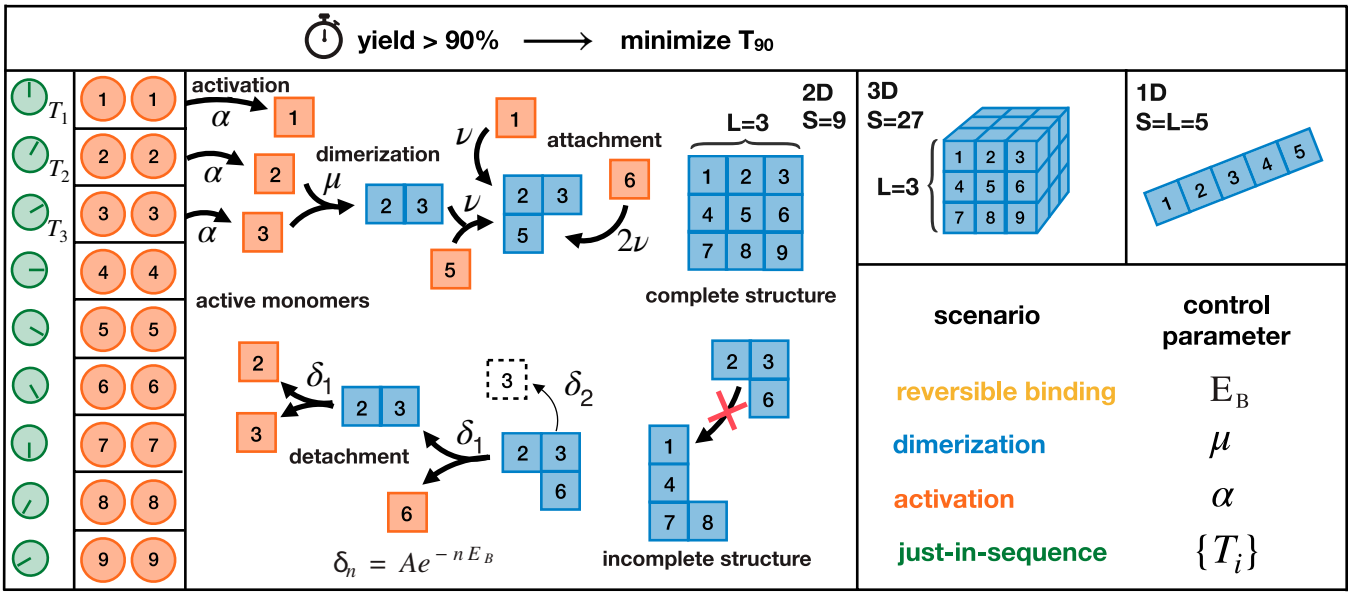


**Fig. 1.** Schematic description of the model. *N* identical copies of *S* different species of monomers assemble into one- (1D), two- (2D), or three-dimensional (3D) heterogeneous structures of edge length *L* (only the 2D case is illustrated explicitly). A constant influx of monomers of species *i* takes place during the time interval $[T_i, T_i + \frac{1}{\alpha}]$ with net influx rate $N\alpha$. Once added to the system (activated), monomers start to self-assemble. A monomer of a bulk species has two (1D), four (2D), or six (3D) possible binding partners as shown. In the 1D case, we assume periodic boundary conditions, i.e., species 1 and *S* can bind as well and the final structures form closed rings. In the higher-dimensional cases, we assume open boundaries, implying that the species located at the boundary have a reduced number of binding partners. Any two fitting monomers can dimerize with rate $\mu$. Subsequent to dimerization, structures grow by attachment of single monomers with rate $\nu$ per binding site. Furthermore, monomers can detach from a cluster with rate $\delta_n = Ae^{-nE_B}$, where *n* is the number of bonds that need to be broken and $E_B$ the binding energy per bond. We set $A = 10^{18} C\nu$, with $C = N/V$ denoting the concentration of monomers per species. Our aim is to minimize the assembly time $T_{90}$ when 90% of all resources are assembled into complete structures. To this end, we control particular elements of the assembly process (control parameters) and distinguish four scenarios that are defined through the respective control parameter(s). The other parameters are fixed from the following set of "default" values: $T_i = 0$, $\alpha = \infty$, $\mu = \nu$, $E_B = \infty (\delta_n = 0)$. Each scenario can be used to elude kinetic traps and achieve a high assembly yield but how much time do these different strategies require?

robust against model modifications. We mainly consider irreversible processes, in which structures can only grow. To assess the relevance of reversible binding, we also discuss a scenario in which individual monomers may detach from the edges of incomplete structures at a finite detachment rate $\delta_n$ that decreases exponentially with the number *n* of bonds that need to be broken: $\delta_n = Ae^{-nE_B}$ (Arrhenius' law). Here $E_B$ is the binding energy per contact (bond) in units of $k_B T$ and the constant $A$ can typically be assumed to be large relative to the rate of reactions (19, 20). Note that we consider only the detachment of single monomer units. In the special case of one-dimensional structures, this implies that the structures grow and shrink only at the ends but do not break up in the middle. This assumption can be justified if some mechanism stabilizes linear structures in the middle (for example, if allosteric effects stabilize the interior bonds). Otherwise, fragmentation of one-dimensional structures would strongly reduce the time efficiency of their self-assembly and the result of our analysis below must be interpreted as an upper limit for the efficiency.

Once a structure contains all *S* species it is considered complete, and no further attachment or detachment processes occur (absorbing state). The yield of the assembly process is defined as the number of complete structures relative to their maximum possible number *N*.

In artificial self-assembly systems, the temporal supply of components can usually be controlled externally. This offers effective ways of regulating the assembly dynamics. To examine the potential of such supply-control strategies, we study two diametrically opposed cases. In the first case, all building blocks are supplied (activated) uniformly over a fixed time interval $\tau = 1/\alpha$ at a constant influx rate $N\alpha$. By controlling $\alpha$ one can regulate the concentrations of monomers and hence the effective dimerization rate. In the second case, the different species are added in a defined temporal sequence (Fig. 1), which allows one to favor specific assembly pathways by altering the order of the time points $T_i$ at which a species *i* is added (supply order).

Besides the binding rate $\nu$ that fixes the timescale, we are left with four control parameters, $E_B, \mu, \alpha, \{T_i\}$, which define different assembly scenarios (Fig. 1). In the reversible binding scenario, kinetic traps are avoided by "designing" monomers with an optimal binding energy $E_B$ and resulting detachment rates $\delta_n$. This strategy is considered as the state of the art in DNA-brick–based self-assembly (21–24) but it also plays an important role in biology, for instance for virus capsid assembly (25). In the dimerization scenario, the assembly process is controlled by the dimerization rate $\mu$. A nucleation barrier $\mu/\nu < 1$ can be implemented for example by allosteric effects or with the help of enzymes (assembly factors) and is known to play a central role in many instances of biological self-assembly (26–29). In the activation scenario, the assembly efficiency is controlled by an overall influx rate $\alpha$ without discrimination between species. Such a control of the availability of active monomers has been suggested as a means to effectuate the self-assembly of some virus capsids (26), as well as other cellular macromolecular structures like the membrane attack complex (30). Finally, in the just-in-sequence (JIS) scenario, the monomers are supplied just in sequence with a favorably chosen assembly path by appropriate design of the supply order $\{T_i\}$. We therefore expect that these four key scenarios cover the underlying mechanisms of a large class of biologically and experimentally relevant self-assembly processes.

## Time Complexity Analysis

For each of the four scenarios, we investigated the minimal time required to achieve a target yield of 90% (denoted as $T_{90}^{\min}$). This requires us to identify the optimal value of the respective control

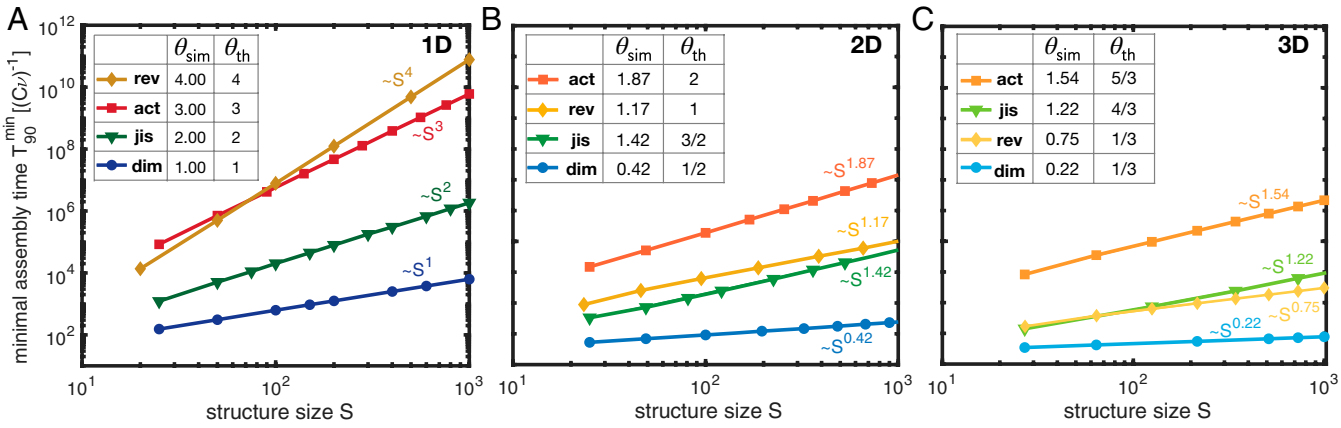


**Fig. 2.** Time complexity. (*A–C*) The minimal assembly time $T_{90}^{\min}$ in the four scenarios in dependence of the size $S$ of the target structure as obtained from stochastic simulations for different dimensionalities of the structures: (*A*) 1D, (*B*) 2D, and (*C*) 3D. The reactive timescale $(C\nu)^{-1}$ defines the basic timescale in the system, which depends on the initial concentration $C$ of monomers per species. Hence, the minimal assembly time is measured in units of $(C\nu)^{-1}$. Each data point represents an average over several independent realizations of the stochastic simulation for the same (optimal) parameter value, determined by a parameter sweep (*SI Appendix*, section 1). We find power-law dependencies of the minimal assembly time on the size of the target structure. The corresponding time complexity exponents $\theta_{sim}$ resulting from the simulations are summarized in the tables in *A–C* together with their theoretic estimates $\theta_{th}$ (which we derive in *SI Appendix*, section 3). We indicate the scenarios as rev, reversible binding; act, activation; jis, just-in-sequence; and dim, dimerization.

parameter that maximizes the time efficiency. We are interested in the asymptotic dependence of $T_{90}^{\min}$ on the structure size $S$ for $S, N \gg 1$. In particular, while we have shown previously (31) that for small copy numbers $N$, the activation scenario is strongly influenced by stochastic effects, we here assume $N$ to be large enough so that stochastic effects can be considered irrelevant.

Maximal time efficiency can then be obtained by a proper choice of the relative frequency of nucleation and growth events: Initiation of new structures must be sufficiently retarded relative to the growth of existing structures to avoid kinetic traps ("slow nucleation principle") (31–33). The larger the target structure is, the smaller the ratio between the effective nucleation and growth rate has to be to achieve a yield of 90%. However, too small a nucleation rate severely limits the required assembly time on the other hand. The various scenarios (with the exception of the one-dimensional reversible-binding scenario, which constitutes a special case) represent different mechanisms to control the ratio between the nucleation and growth rate and therefore allow one to tune it to an optimal value.

However, the effectiveness with which the ratio is controlled, and thus the minimum assembly time that can be achieved, varies greatly between the different strategies. In all cases, we find numerically that both the optimal control parameter and the minimal assembly time exhibit power-law dependencies on the size $S$ of the target structure (Fig. 2). The corresponding exponents are referred to as the control parameter exponent $\phi$ and the (time) complexity exponent $\theta$, respectively. Both exponents are scenario specific and, moreover, depend on the dimensionality of the assembled structure, as is discussed in detail below for each scenario.

To derive analytical estimates for the exponents, we use that the optimal ratio between nucleation and growth rate should approximately scale inversely with the structure size,

$$\frac{\text{number of nucleation events per time}}{\text{number of attached monomers per time}} \sim S^{-1}. \qquad [1]$$

A detailed mathematical evaluation of the scaling of the terms on the left-hand side with the system parameters can be found in *SI Appendix*, section 3. In the main text, we restrict ourselves to a discussion of the phenomenology of our numerical results and use heuristic scaling arguments.

**Reversible-Binding Scenario.** In the reversible-binding scenario, the time complexity strongly depends on the dimensionality of the structure. For one-dimensional structures, the rate of monomer detachment is the same for all unfinished structures. Hence, it is not possible to selectively disfavor nucleation of new structures relative to the growth of existing structures by varying the binding energy $E_B$. In this respect, the one-dimensional reversible-binding scenario constitutes a special case among all scenarios, since it realizes a profoundly different self-assembly mechanism. We find that structures are initially formed in such an amount that the overall attachment and detachment processes of the monomers balance out and the concentration of monomers becomes stationary. Growth and shrinkage of a structure then become approximately equally likely and the cluster sizes evolve (approximately) diffusively, with diffusion constant given by $D = \nu m + \delta$, where $m$ denotes the stationary monomer concentration. Hence, varying the detachment rate $\delta$ allows one to maximize the diffusive flux. We show in *SI Appendix*, section 3 that the optimal detachment rate and the resulting effective diffusion constant scale like $\delta_{\text{opt}} \sim D \sim \frac{\nu}{\mu}(C\nu)S^{-2}$. This implies that the assembly time for one-dimensional structures scales like the diffusive timescale (to diffusively transverse a distance $S$) $T_{90}^{\min} \sim S^2/D \sim \nu^{-2}S^4$ with time complexity exponent $\theta = 4$, which agrees very well with the results obtained from stochastic simulations (Fig. 2*A*).

In higher dimensions, large clusters are typically bound more tightly and hence become energetically favored over clusters of small size, as illustrated in Fig. 3*A*. This creates an effective nucleation barrier, which allows one to strongly enhance the time efficiency compared to the one-dimensional case. Essentially, the monomer concentration is thereby much larger than in the one-dimensional case, which enables nucleated structures to grow quickly. However, to guarantee both high resource efficiency (high yield) and time efficiency, the binding energy must be fine-tuned to within few percent of its optimal value (Fig. 3*B*). Larger binding energies imply a lower nucleation barrier and lead to kinetic trapping, whereas lower binding energies progressively reduce the effective nucleation rate. By fine-tuning of the binding energy $E_B$, we obtain the time complexity exponents $\theta_{2D} \sim 1.19$ and $\theta_{3D} \sim 0.75$, respectively, for the two-dimensional (2D) and three-dimensional (3D) cases (Fig. 2 *B* and *C*). Both exponents can also be estimated analytically from

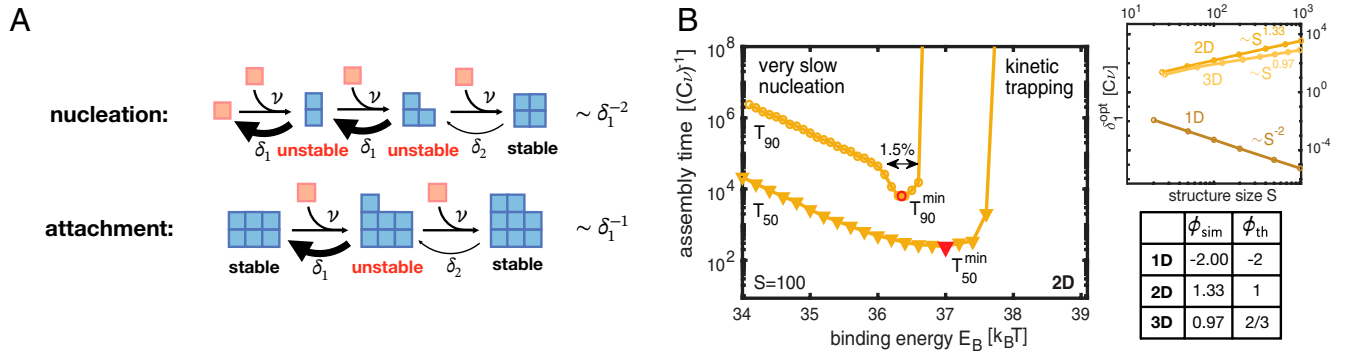


| | $\phi_{sim}$ | $\phi_{th}$ |
|---|---|---|
| **1D** | -2.00 | -2 |
| **2D** | 1.33 | 1 |
| **3D** | 0.97 | 2/3 |

**Fig. 3.** Reversible-binding scenario. (*A*) In the reversible-binding scenario (if $\delta_2 \ll \delta_1$), the cluster evolution typically proceeds via stable intermediate states (in which all constituents form two or more bonds), whereas unstable intermediates are short lived. Hence, nucleation is disfavored relative to growth because nucleation proceeds via two unstable intermediate states whereas attachment proceeds only via one. (*B*) Assembly time to achieve 50% yield ($T_{50}$) and 90% yield ($T_{90}$) plotted against the binding energy $E_B$ for two-dimensional target structures of size $S = 100$ (with preexponential factor $A = 10^{18} C\nu$). To achieve high yield with maximal time efficiency, $E_B$ must be fine-tuned to a narrow range (here ≈1.4%) around its optimal value. In *Inset*, the optimal detachment rate $\delta_1^{\text{opt}}$ exhibits a power-law dependence on the structure size with exponent characterized by the dimensionality of the structure. The control parameter exponents $\phi_{\text{sim}}$ together with their theoretic estimates $\phi_{\text{th}}$ are summarized in the table.

Eq. **1** by deriving effective rates for nucleation and attachment reactions (*SI Appendix*, section 3 and tables in Fig. 2 *B* and *C*). Note that the binding energy $E_B$ is measured in units of $k_B T$ and the detachment rate relative to the reaction rate $(C\nu)$. Hence, the most feasible way to fine-tune the control parameter in experiments will be to adapt either the temperature or the monomer concentration $C$.

**Dimerization Scenario.** We then analyzed the remaining irreversible assembly scenarios, setting $\delta_n = 0$. In the dimerization scenario, decreasing the dimerization rate $\mu$ disfavors initiation of new structures relative to the growth of existing structures. Fig. 4*A* shows the corresponding transition from zero to perfect final yield, with $\mu_{90}$ indicating the rate at which a final yield of 90% is achieved. We find that the optimal rate $\mu_{\text{opt}}$ that minimizes the time required to achieve 90% yield is only slightly lower than $\mu_{90}$ and, for linear structures, scales as $\mu_{\text{opt}} \sim \nu S^{-2}$ (Fig. 4 *A*, *Inset*). This dependence of $\mu_{\text{opt}}$ on $S$ for linear structures can be explained as follows: According to Eq. **1**, when increasing the structure size $S$, the ratio between nucleation (= dimerization) and growth rate must be reduced to allow the structures to grow to the larger size. However, to achieve the desired scaling, $\mu_{\text{opt}}$ must scale quadratically with $1/S$, because the number of dimerization events per time increases with the number of possible dimerization partners ($\sim S$) leading to an additional factor of $1/S$.

Since dimerization is the rate-limiting step, we expect that the assembly time will predominantly be determined by the total dimerization rate $T_{90}^{\text{min}} \sim (C\mu_{\text{opt}} S)^{-1} \sim (C\nu)^{-1} S$. This estimate correctly predicts the time complexity exponent $\theta = 1$ for linear structures (Fig. 2*A*). For target structures of higher dimension, the effective growth rate of clusters is increased compared to the one-dimensional case because structures grow radially. This allows for a simple possibility to relate the exponents for target structures of higher dimension to the one-dimensional case by rescaling the binding rate $\nu$: Note that the number of possible binding partners of a globular structure with $s$ particles is proportional to its surface area and thus scales approximately as $s^{(d-1)/d}$, where $d$ is the dimensionality of the structure. Thus, defining an effective average binding rate $\nu_S \sim \nu S^{(d-1)/d}$ for a target structure size $S$ allows one to map higher-dimensional growth processes to an effective one-dimensional process along the radial coordinate. Replacing $\nu \to \nu_S$ therefore translates the scaling laws for linear objects into approximate scaling laws for higher-dimensional structures. This scaling idea for the dimerization scenario accurately yields the control parameter exponents for higher-dimensional structures (table in Fig. 4*A*) and only slightly overestimates the time complexity exponents in higher dimensions (Fig. 2 *B* and *C*). These deviations may be attributed to the subleading contribution of the growth process to the total assembly time, which becomes more pronounced in higher dimensions. The dimerization scenario is the most time-efficient scenario because reducing the dimerization rate allows one to specifically control the effective nucleation speed without simultaneously affecting the attachment rate. In contrast, changing the binding energy in the reversible-binding scenario at the same time reduces the effective attachment speed and therefore renders this strategy less efficient.

**Activation Scenario.** In the activation scenario, nucleation is inhibited by controlling the concentration of available (or active) monomers. Decreasing the influx rate $\alpha$ reduces the momentary concentration of active monomers and therefore reduces the effective dimerization rate. As in the dimerization scenario, this leads to a transition from zero to perfect final yield (Fig. 4*B*). The transition is not strictly monotonic but exhibits some small-scale peaks, whose origin is not entirely clear. From the stochastic simulations and scaling analysis (*SI Appendix*, section 3) we infer for linear structures an optimal influx rate scaling as $\alpha_{\text{opt}} \sim \frac{\nu}{\mu}(C\nu) S^{-3}$ (Fig. 4 *B*, *Inset*). The dependence of $\alpha_{\text{opt}}$ on $S$ can be explained similarly to that for the dimerization scenario: When increasing $S$, according to Eq. **1**, the ratio between effective nucleation and growth rate must be reduced, while the increase of the total nucleation rate with increasing number of species must be balanced. Together, this accounts for a factor of $1/S^2$ in $\alpha_{\text{opt}}$, analogous to the dimerization scenario. Additionally, however, increasing $S$ would enhance the total influx of particles and thus the momentary concentration of monomers. This again would increase the nucleation rate and needs to be balanced, thus explaining the third factor of $1/S$. The control parameter exponents $\phi$ for higher-dimensional structures can again be derived with our rescaling argument, $\nu \to \nu S^{(d-1)/d}$, and are found to be only slightly larger than those obtained from simulations (table in Fig. 4*B*). As the monomers are activated over a time span $1/\alpha$, the time complexity exponents are the reciprocals of the parameter exponents (Fig. 2).

We expect that the exponents for the activation scenario remain the same if other forms of monomer input are considered. For example, monomers could (reversibly or irreversibly) switch between an assembly inactive and active state. In

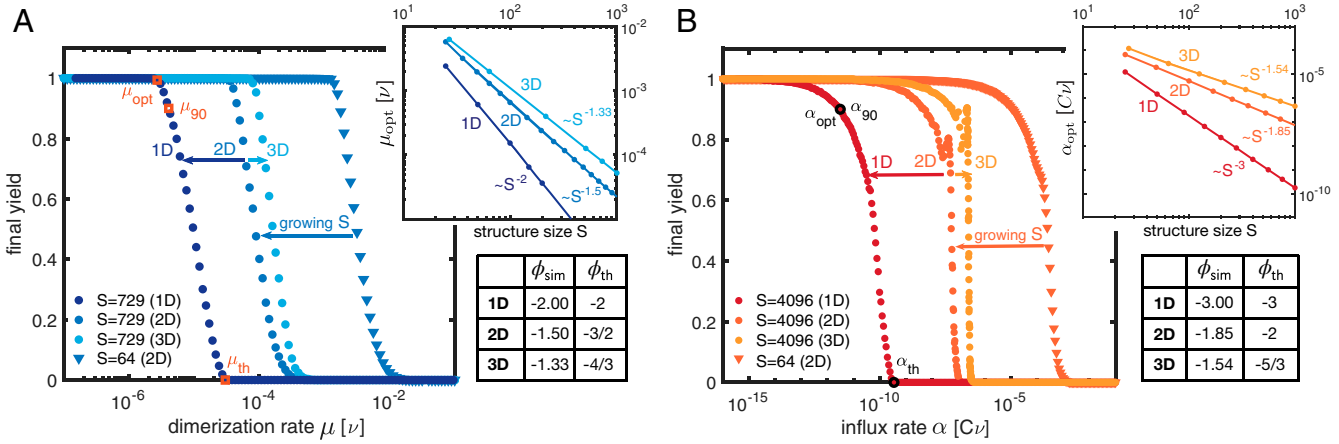


| | $\phi_{sim}$ | $\phi_{th}$ |
|---|---|---|
| 1D | -2.00 | -2 |
| 2D | -1.50 | -3/2 |
| 3D | -1.33 | -4/3 |

| | $\phi_{sim}$ | $\phi_{th}$ |
|---|---|---|
| 1D | -3.00 | -3 |
| 2D | -1.85 | -2 |
| 3D | -1.54 | -5/3 |

**Fig. 4.** Dimerization and activation scenario. (*A* and *B*) The final yield in dependence of the dimerization rate (*A*) and the activation or influx rate (*B*) for different sizes (symbols) and dimensionality (color shading) of the target structure. Data points represent averages over at least 20 independent realizations. Upon decreasing either the dimerization or the activation rate, perfect final yield is achieved. For the leftmost transition we indicate the optimal parameter value $\mu_{opt}$ or $\alpha_{opt}$ that minimizes the time to achieve a yield of 90%. *Insets* show the dependence of the optimal parameter value on the structure size for different dimensionality. The corresponding control parameter exponents $\phi_{sim}$ are summarized in the tables together with their theoretic estimates $\phi_{th}$ (main text).

*SI Appendix*, section 4, we simulate the reversible case explicitly, assuming that the switch is fast so that active and inactive monomers are at equilibrium. This case might indeed be relevant in virus capsid assembly (26) and it exhibits the same scaling as the constant influx scenario (*SI Appendix*, Fig. S5*C*). Controlling the switching rate between particle configurations (for example with light) (34) could also be a feasible way to implement the activation scenario experimentally.

**Just-in-Sequence Scenario.** In the irreversible assembly scenarios discussed so far, all species are made available simultaneously. Consequently, excess nucleation of structures can only be suppressed by using a low dimerization or activation rate. In contrast, the JIS scenario favors specific assembly paths by regulating the order in which building blocks are supplied. The species supplied first in this temporal sequence define the nuclei for subsequent growth. Formation of other competing nuclei (dimers) during the assembly process is suppressed by the sequential delivery of building blocks, which ensures that mutual binding partners are supplied successively. Binding of newly added monomers to existing structures is therefore more likely than formation of new dimers. The frequency of competing nucleation events can be controlled by adjusting the interval $\Delta T$ between the equidistant time points $T_i$ at which subsequent "batches" of monomers are provided. Longer time intervals increase the yield at the cost of a lower time efficiency.

To minimize the total number of batches, we chose an "onion" supply protocol, which allows structures to grow radially from the inside out, like the skins of an onion (Fig. 5*C*). Furthermore, the time efficiency can be enhanced by using increasing, nonstoichiometric concentrations for the monomers in successive batches (Fig. 5*B*). Nonstoichiometric concentrations in a properly chosen ratio (*SI Appendix*, section 1, *Just-in-sequence scenario*) reduce competition for resources between growing structures (Fig. 5*A*) and thereby greatly enhance the time efficiency, as well as robustness to extrinsic noise in the particle numbers supplied, especially for higher-dimensional structures (Fig. 5*D* and *E*). Therefore, nonstoichiometric concentrations are the key to successful implementation of the JIS strategy for higher-dimensional structures. Since we assume equidistant time intervals $\Delta T$ between subsequent batches, the total assembly time is the product of $\Delta T$ ($\sim S$) and the total number of batches ($\sim L \sim S^{1/d}$), yielding the complexity exponents $\theta = 1 + 1/d$, as shown in Fig. 2. To demonstrate the broad experimental applicability of the JIS supply strategy with a concrete example, we discuss in detail in *SI Appendix*, section 5 how the JIS strategy could efficiently be used to assemble artificial $T = 1$ capsids. Artificial capsids have important potential technological and medical applications (35–37) and the simulations show that the JIS strategy might indeed be a feasible and efficient way to assemble these structures.

## Discussion

Fig. 2 shows the dependence of the minimal assembly time on target structure size, together with the resulting time complexity exponents for the different scenarios and dimensionalities. All exponents decrease with increasing dimensionality of the target structure and can even change their relative order. For the dimerization, activation, and reversible-binding scenario, one can show that the analysis is independent of the heterogeneity of the building blocks (*SI Appendix*, section 2). Remarkably, the exponents are furthermore robust to various modifications of the model such as heterogeneous binding rates, modified boundary conditions, or altered definitions of the assembly time (*SI Appendix*, section 4). Similarly, advanced protocols like annealing or different forms of monomer input in the activation scenario leave the exponents invariant. This invariance shows that the time complexity analysis yields a reliable and robust characterization of self-assembly processes. Furthermore, the invariance of the parameter exponents allows for an optimal control strategy to be identified in dependence of the size of the target structure in each of the four scenarios.

The dimerization scenario turns out to be the most time-efficient scenario in all dimensions. Controlling the dimerization rate is efficient as it allows one to initiate just as many structures as are needed, followed by a rapid growth phase if all particles are readily available. For linear structures, the supply-control strategies rank second and third, with coordinated supply in the JIS scenario being more efficient than uncoordinated supply in the activation scenario. Reversible binding is the least efficient approach to assembling large linear structures, but it is efficient for the assembly of higher-dimensional structures and then becomes competitive with the JIS scenario, slightly outperforming it for large structure sizes.

The reason why reversible binding is inefficient for one-dimensional structures is that for linear objects—in contrast to higher-dimensional objects—nucleation cannot be slowed

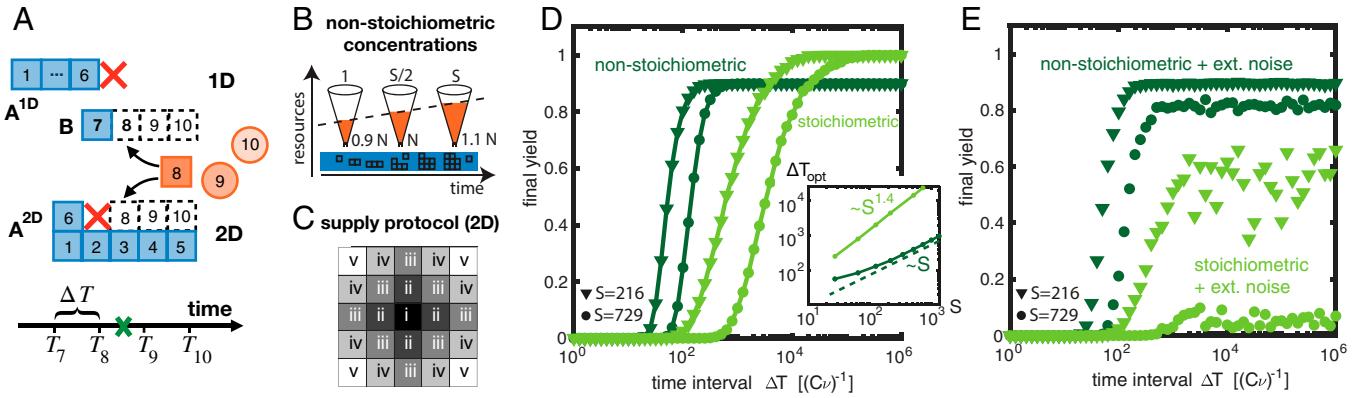


**Fig. 5.** JIS scenario. (*A*) In the JIS scenario, the different species are added sequentially; here, for illustration, they are in a linear sequence ($T_1 < T_2 < T_3 < \dots$). Along the regular assembly paths, $A_{1D}$ (1D) or $A_{2D}$ (2D), additional dimers B can form, competing for resources with the regular structures and thereby disrupting their growth. While for one-dimensional structures a disruption event prevents a structure $A_{1D}$ from further growth, in higher dimensions both defective structures $A_{2D}$ and B continue to grow, thereby increasing competition for resources. (*B*) Competition for resources can be alleviated by enhancing the amount of resources with each assembly step (nonstoichiometric concentrations; *SI Appendix*, section 1). For example, providing the first species in concentration $0.9N$ and increasing linearly up to $1.1N$ for the last species strongly enhances assembly efficiency (*D*) and robustness (*E*). (*C*) Parallel supply protocol illustrated for a 2D structure of size $S = 25$ causing the structures to grow radially in an "onion-skin"–like fashion. Roman numbers indicate the order in which species are supplied. Species with identical numbers ("onion skins") are supplied simultaneously in "batches." (*D*) When using nonstoichiometric concentrations, high yield can be achieved with a shorter time span $\Delta T$ between subsequent batches, exhibiting a smaller control parameter exponent (*Inset*) compared to the case of stoichiometric concentrations. Simulations were performed for 3D structures with $N = 10^4$ to $10^5$. (*E*) External noise in the concentrations jeopardizes the yield when stoichiometric concentrations are used, whereas nonstoichiometric concentrations are much more robust. Here, for each species we assumed a coefficient of variation CV = 0.1% with average particle numbers as in *D*.

down relative to growth by increasing the detachment rate. This strong dependence of the efficiency on the dimensionality implies that, generally, the morphology of the assembled structures plays an important role for the reversible-binding scenario. For example, assembling quasi-linear objects with two (or more) layers of subunits instead of a one-layered linear object might significantly increase the assembly efficiency. Identifying and designing those morphologies that are particularly favorable and assemble efficiently could therefore be an interesting direction for future research.

In conclusion, our time-complexity analysis of self-assembly describes lower bounds for the required assembly time as a function of the target structure size. Furthermore, it provides a robust description of how the parameters of the system must be controlled to achieve optimal time and resource efficiency. The analysis enables us to compare the efficiency of different self-assembly scenarios. In computer science, the complexity of a computational problem is defined as the complexity of the fastest algorithm available to solve it (38). Among the assembly scenarios discussed here, limiting the dimerization rate defines the fastest assembly process and might thereby determine the time complexity of self-assembly (of course, we cannot exclude the possibility of even faster assembly strategies). Experimentally, however, controlling the dimerization rate is difficult, as it effectively requires building blocks that exhibit allosteric binding effects. So far, experiments have typically resorted to rendering binding reactions reversible (21–23, 25, 39, 40). Our analysis shows that this common approach is time efficient for the assembly of higher-dimensional structures. However, to be truly competitive, fairly precise tuning of bond strengths, temperature, and the concentration is required. Our analysis suggests that a supply-control strategy like the JIS scenario is a promising alternative that offers similar or better time efficiency using irreversible self-assembly. As a significant advantage, this strategy does not rely on sophisticated properties of the building blocks (like allosteric effects or fine-tuned bond strengths) but only on temporal supply control and hence on parameters that might be more amenable to regulation and adaptation in experiments: In its simplest implementation, the different species could just be added manually to the system in the designated temporal sequence.

Compared to the current state-of-the-art approach via reversible reactions, irreversible assembly schemes might thus provide a complementary and more versatile strategy for assembling complex structures, requiring control over relative concentrations, rather than fine-tuning of the molecular details. Importantly, the idea underlying the JIS scenario entails a rather specific design principle for efficient irreversible assembly protocols of complex nanostructures ("batches without mutual binding partners"); we demonstrate in *SI Appendix*, section 5 how this principle is applied exemplarily for the assembly of artificial $T = 1$ capsids. This design principle thereby provides a clear path toward the experimental realization of the JIS scenario, suggesting that the strategy will be broadly applicable to the assembly of artificial structures.

An interesting question for future research concerns the prospects for spatiotemporal supply control, i.e., controlling not only the time interval but also the site at which monomers are injected into a spatial system, for further enhancement of the time efficiency. Moreover, it would be interesting to consider the time complexity of assembly schemes like hierarchical self-assembly (41–44), which include polymer–polymer interactions, or assembly schemes in which interactions among the particles allow for multiple self-assembly states. Finally, other potentially important aspects of self-assembly include susceptibility to errors in the case of reduced binding specificities or defective particles, as well as robustness to stochastic effects for small copy numbers. If particle numbers are large and nonspecific bonds are sufficiently weak and reversible, we expect that these factors will not considerably affect the assembly dynamics. Otherwise, it might be instructive to test how the different assembly scenarios are influenced by these factors and compare the robustness of the various strategies in this respect.

## Materials and Methods

This paper is accompanied by a detailed *SI Appendix* file, which discusses the numerical and analytical methods that were used to simulate the four scenarios and to determine their time complexity exponents. Specifically, *SI Appendix*, section 1 shows the details of the numerical simulation and, in particular, explains how the concentrations for the various species in the just-in-sequence scenario were determined. *SI Appendix*, section 2 analyzes the master equation and shows mathematically that the heterogeneity

(distinguishability) of the building blocks is irrelevant for the dynamics in the limit of large particle numbers. *SI Appendix*, section 3 is dedicated to the mathematical scaling analysis and explains how the analytic estimates for the time complexity and control parameter exponents are derived. Furthermore, *SI Appendix*, section 4 demonstrates the robustness of the time complexity exponents to various modifications of the model and variations in the parameters. Finally, *SI Appendix*, section 5 illustrates how the just-in-sequence supply strategy can be used in practice for the concrete example of artificial $T = 1$ capsid assembly and thereby demonstrates the broad applicability of the just-in-sequence scenario.

**Data Availability.** C++ code for simulations and data have been deposited in GitHub (https://github.com/FloGat88/Self_Assembly.git) (45).

**ACKNOWLEDGMENTS.** We thank Patrick Wilke and Philipp Geiger for stimulating discussions. This research was supported by the German Excellence Initiative via the program "NanoSystems Initiative Munich" and was funded by the Deutsche Forschungsgemeinschaft (DFG) (German Research Foundation) under Germany's Excellence Strategy, EXC-2094–390783311, as well as under Project ID 364653263–TRR 235. F.M.G. and I.R.G. were supported by a DFG fellowship through the Graduate School of Quantitative Biosciences Munich.

1. A. Zlotnick, Theoretical aspects of virus capsid assembly. *J. Mol. Recognit.* **18**, 479–490 (2005).
2. J. D. Perlmutter, M. F. Hagan, Mechanisms of virus assembly. *Annu. Rev. Phys. Chem.* **66**, 217–239 (2015).
3. M. F. Hagan, Modeling viral capsid assembly. *Adv. Chem. Phys.* **155**, 1–68 (2014).
4. J. M. Stewart, E. Franco, Self-assembly of large RNA structures: Learning from DNA nanotechnology. *DNA RNA Nanotechnol.* **2**, 23–35 (2015).
5. P. Chidchob, H. F. Sleiman, Recent advances in DNA nanotechnology. *Curr. Opin. Chem. Biol.* **46**, 63–70 (2018).
6. E. J. Deeds, J. A. Bachman, W. Fontana, Optimizing ring assembly reveals the strength of weak interactions. *Proc. Natl. Acad. Sci. U.S.A.* **109**, 2348–2353 (2012).
7. S. Whitelam, R. L. Jack, The statistical mechanics of dynamic pathways to self-assembly. *Annu. Rev. Phys. Chem.* **66**, 143–163 (2015).
8. D. Endres, A. Zlotnick, Model-based analysis of assembly kinetics for virus capsids or other spherical polymers. *Biophys. J.* **83**, 1217–1230 (2002).
9. W. M. Jacobs, D. Frenkel, Self-assembly of structures with addressable complexity. *J. Am. Chem. Soc.* **138**, 2457–2467 (2016).
10. M. F. Hagan, O. M. Elrad, R. L. Jack, Mechanisms of kinetic trapping in self-assembly and phase transformation. *J. Chem. Phys.* **135**, 104115 (2011).
11. H. Ramezani, H. Dietz, Building machines with DNA molecules. *Nat. Rev. Genet.* **21**, 5–26 (2020).
12. N. C. Seeman, H. F. Sleiman, DNA nanotechnology. *Nat. Rev. Mater.* **3**, 1–23 (2017).
13. L. Cademartiri, K. J. Bishop, Programmable self-assembly. *Nat. Mater.* **14**, 2–9 (2015).
14. S. E. Ahnert, I. G. Johnston, T. M. Fink, J. P. Doye, A. A. Louis, Self-assembly, modularity, and physical complexity. *Phys. Rev. E Stat. Nonlin. Soft Matter Phys.* **82**, 026117 (2010).
15. D. Soloveichik, E. Winfree, Complexity of self-assembled shapes. *SIAM J. Comput.* **36**, 1544–1569 (2007).
16. C. G. Evans, E. Winfree, Physical principles for DNA tile self-assembly. *Chem. Soc. Rev.* **46**, 3808–3829 (2017).
17. C. Chen, C. C. Kao, B. Dragnea, Self-assembly of brome mosaic virus capsids: Insights from shorter time-scale experiments. *J. Phys. Chem. A* **112**, 9405–9412 (2008).
18. A. Ben-Shaul, W. M. Gelbart, "*Statistical thermodynamics of a mphiphile self-assembly: Structure and phase transitions in micellar solutions*" in *Micelles, Membranes, Microemulsions, and Monolayers*, W. M. Gelbart, A. Ben-Shaul, D. Roux, Eds. (Springer, New York, NY, 1994), pp. 1–104.
19. P. D. Schnier, J. S. Klassen, E. F. Strittmatter, E. R. Williams, Activation energies for dissociation of double strand oligonucleotide anions: Evidence for Watson-Crick base pairing in vacuo. *J. Am. Chem. Soc.* **120**, 9605–9613 (1998).
20. K. Bielec *et al.*, Kinetics and equilibrium constants of oligonucleotides at low concentrations. Hybridization and melting study. *Phys. Chem. Chem. Phys.* **21**, 10798–10807 (2019).
21. G. M. Whitesides, B. Grzybowski, Self-assembly at all scales. *Science* **295**, 2418–2421 (2002).
22. S. Zhang, Fabrication of novel biomaterials through molecular self-assembly. *Nat. Biotechnol.* **21**, 1171–1178 (2003).
23. F. Hong, F. Zhang, Y. Liu, H. Yan, DNA origami: Scaffolds for creating higher order structures. *Chem. Rev.* **117**, 12584–12640 (2017).
24. R. Freeman *et al.*, Reversible self-assembly of superstructured networks. *Science* **362**, 808–813 (2018).
25. D. C. Rapaport, Role of reversibility in viral capsid growth: A paradigm for self-assembly. *Phys. Rev. Lett.* **101**, 186101 (2008).
26. G. R. Lazaro, M. F. Hagan, Allosteric control of icosahedral capsid assembly. *J. Phys. Chem. B* **120**, 6306–6318 (2016).
27. J. A. Marsh, S. A. Teichmann, Structure, dynamics, assembly, and evolution of protein complexes. *Annu. Rev. Biochem.* **84**, 551–575 (2015).
28. A. Zlotnick, S. Mukhopadhyay, Virus assembly, allostery and antivirals. *Trends Microbiol.* **19**, 14–23 (2011).
29. D. L. Caspar, Movement and self-control in protein assemblies. Quasi-equivalence revisited. *Biophys. J.* **32**, 103–138 (1980).
30. C. Leung *et al.*, Stepwise visualization of membrane pore formation by suilysin, a bacterial cholesterol-dependent cytolysin. *eLife* **3**, e04247 (2014).
31. F. M. Gartner, I. R. Graf, P. Wilke, P. M. Geiger, E. Frey, Stochastic yield catastrophes and robustness in self-assembly. *eLife* **9**, 1–37 (2020).
32. A. Y. Morozov, R. F. Bruinsma, J. Rudnick, Assembly of viruses and the pseudo-law of mass action. *J. Chem. Phys.* **131**, 155101 (2009).
33. A. Murugan, J. Zou, M. P. Brenner, Undesired usage and the robust self-assembly of heterogeneous structures. *Nat. Commun.* **6**, 6203 (2015).
34. A. A. Gil *et al.*, Optogenetic control of protein binding using light-switchable nanobodies. *Nat. Commun.* **11**, 4044 (2020).
35. J. G. Heddle, S. Chakraborti, K. Iwasaki, Natural and artificial protein cages: Design, structure and therapeutic applications. *Curr. Opin. Struct. Biol.* **43**, 148–155 (2017).
36. B. Schwarz, M. Uchida, T. Douglas, Biomedical and catalytic opportunities of virus-like particles in nanotechnology. *Adv. Virus Res.* **97**, 1–60 (2017).
37. C. Sigl *et al.*, Programmable icosahedral shell system for virus trapping. *Nat. Mater.* **20**, 1281–1289 (2021).
38. M. Sipser, *Introduction to the Theory of Computation* (Thomson Learning, Boston, MA, 2006).
39. G. M. Whitesides, M. Boncheva, Beyond molecules: Self-assembly of mesoscopic and macroscopic components. *Proc. Natl. Acad. Sci. U.S.A.* **99**, 4769–4774 (2002).
40. A. Zlotnick, Are weak protein-protein interactions the general rule in capsid assembly? *Virology* **315**, 269–274 (2003).
41. T. K. Haxton, S. Whitelam, Do hierarchical structures assemble best via hierarchical pathways? *Soft Matter* **9**, 6851 (2013).
42. S. Whitelam, Hierarchical assembly may be a way to make large information-rich structures. *Soft Matter* **11**, 8225–8235 (2015).
43. W. Pfeifer, B. Saccà, From nano to macro through hierarchical self-assembly: The DNA paradigm. *ChemBioChem* **17**, 1063–1080 (2016).
44. J. E. Baschek, H. C. R. Klein, U. S. Schwarz, Stochastic dynamics of virus capsid formation: Direct versus hierarchical self-assembly. *BMC Biophys.* **5**, 22 (2012).
45. F. M. Gartner, Stochastic simulation of self-assembly scenarios (C++ code). GitHub. https://github.com/FloGat88/Self_Assembly.git. Deposited 24 September 2021.

PNAS
www.pnas.org

# Supplementary Information for

# The time complexity of self-assembly

**Florian M. Gartner, Isabella R. Graf and Erwin Frey**

**Erwin Frey**
**E-mail: frey@lmu.de**

## This PDF file includes:

Supplementary text
Figs. S1 to S7 (not allowed for Brief Reports)
SI References

# Contents

# Supporting Information Text

In this Supporting Information (SI), we first discuss the numerical methods that were used in order to simulate the four scenarios and to determine their time complexity exponents. In particular, in the paragraph 'Just-in-sequence scenario', we show how the concentrations for the various species in the just-in-sequence scenario were determined. In the next section, we discuss the Master equation of the system and show that the heterogeneity (distinguishability) of the building blocks is irrelevant for the dynamics in the limit of large particle numbers. Subsequently, we derive analytic estimates for the time complexity and control parameter exponents using mathematical calculations and scaling arguments. These analytic estimates for the exponents are the basis for the 'theoretical values' presented in the main text. Afterwards, we demonstrate that our results, in particular the time complexity and control parameter exponents, are robust to modifications of the model and variations in the parameters. Finally, in order to demonstrate the broad applicability of the just-in-sequence scenario, we show how the supply strategy can be used in practice for the concrete example of artificial T=1 capsid assembly.

## 1. Numerical methods and implementation of the scenarios

**Simulation.** Particle-based, stochastic simulations of the reaction kinetics of the system were performed using Gillespie's algorithm (1). In the simulation, we store the numbers of active and inactive monomers of the various species in two separate linear arrays of length $S$. We only consider binding reactions of a species $i$ with species $i \pm 1$ in the one-dimensional case, additionally with $i \pm L$ in the two-dimensional case and additionally with $i \pm L^2$ in the three-dimensional case, see Fig. 1. All other binding rates are assumed to be 0. In the one-dimensional case, periodic boundary conditions were implemented by allowing binding reactions also between species 1 and $S$. Hence, the final structures represent closed rings. In the higher dimensional cases, open boundaries were implemented by reducing the number of possible binding partners of the boundary species accordingly.

When a complex is initiated from the dimerization reaction of two monomers, we reserve for the complex a boolean array of size $S$, which contains ones for the species that are contained in the complex and zeros for all other species. When additional species subsequently attach to (or detach from) the complex, the respective sites are set to one (zero) until the complex is complete and contains no more zeros. In this way, the simulation respects all possible configurations of clusters that can emerge. In order to speed up the simulation, we store for each species $i$ an array which references all complexes to which species $i$ can attach. The total attachment rate of species $i$ is thereby given by the product of the rate $\nu$ with the number of active monomers of species $i$ and the total number of binding sites in complexes that species $i$ can bind to. Likewise, the total dimerization rate of species $i$ is given by the product of the dimerization rate with the number of monomers of species $i$ and the total number of monomers species $i$ can bind to. Note that in summing the dimerization rates of individual species in order to calculate the total dimerization rate of all species, a factor of $1/2$ has to be included in order to avoid double counting. Whenever a species dimerizes or attaches to a complex, its number of monomers is reduced by one unit and when a species detaches from a complex, its number is increased by one unit.

In order to keep track of the detachment rates of the constituents of each complex, we associate with each complex additional arrays that store the indices of the constituents that detach, respectively, with rate $\delta_1$, $\delta_2$, $\delta_3$... . Depending on the chosen values for $A$ and $E_B$, however, typically some $\delta_n = Ae^{-nE_B}$ become so small that they effectively do not influence the assembly dynamics and can therefore also be neglected in order to increase efficiency. For example, rates can be set to zero if

the expected total number of events they will invoke during the simulated time span is much lower than 1. In any case, we assumed that constituents that have the maximum number of neighbors in a structure are always stable by setting $\delta_{2d}$ to zero (where $d$ is the dimensionality of the structure). This ensures that complete structures are always stable, which allows us to directly compare the various self-assembly strategies. Note that for one-dimensional structures, $\delta_{2d} = 0$ implies that the structures do not break up in the middle but only grow and shrink by adding/detaching single monomer units at the ends. This is a reasonable assumption because by allowing structures to also break up in the middle, the assembly process would be extremely inefficient as larger structures would become increasingly more unstable. With the detachment events for a complex organized in the above-mentioned array structures, it is straight forward to calculate the total detachment rate for each complex and with it the total detachment rate for the system.

This was a description of the basic structure of our simulation. Additional cross-references between the various data structures were implemented to enable efficient updating of the respective rates and events after an event has happened. Optimizing the efficiency of the simulation was necessary because, for example, the reversible binding scenario generally requires a large number of Gillespie steps (up to several billion per run for the large systems) due to the reversibility of binding reactions. With these optimizations, the simulation written in C++ was able to perform more than one million Gillespie steps per second on a 3.1 GHz CPU. The C++ code of the simulation is available online.

**The method of 'homogenization'.** We show in chapter 2 of this supplement, that in the case of periodic boundary conditions of the structures, the distinguishability (heterogeneity) of the species is irrelevant for the dynamics of the activation, dimerization and reversible binding scenario in the limit of large particle numbers. Therefore, these systems can also be simulated with only a single species that can occupy any site within a cluster (homogeneous system). The advantage of simulating a homogeneous rather than a heterogeneous system is that stochastic effects arising from fluctuations in the concentrations of the different species are thereby suppressed (2). Hence, in order to observe deterministic behavior, a smaller total number of particles is required for homogeneous systems, increasing the efficiency of simulations. We exploit this increase of efficiency in our simulations of the activation scenario, where stochastic effects are particularly strong. In order to simulate the system as a homogeneous system while leaving the structure of the simulation and all data types unchanged, two simple steps can be performed:

- Make monomer creation and annihilation act on all species simultaneously (i.e. if a monomer of one species is added or subtracted, add or subtract one for all other species as well),
- rescale the influx rate $\alpha$ and dimerization rate $\mu$ by $S^{-1}$.

The first step constrains all species to equal concentrations while the second rescales the rates as if there were only a single species. Computationally, however, it is more efficient to count only the monomers of one species explicitly instead of acting on $S$ species simultaneously.

Note, in particular, that in this way complexes are still represented by the same data structure (i.e. arrays of length $S$ filled with zeros and ones as described above) but any site can now be occupied by any monomer, irrespective of its species.

In the case of periodic boundary conditions of the structures, the homogeneous system is shown in chapter 2 to behave *exactly* like the heterogeneous system in the limit of large $N$. Hence, for one-dimensional structures, which we implemented with periodic boundary conditions, this approach is exact. In the case of non-periodic boundary conditions, however, the 'homogenized' system is only an approximation to the heterogeneous dynamics because not all species are equivalent any

more due to the presence of the boundary. Nevertheless, Figure S2 shows that this approximation is indeed very accurate for higher dimensional structures by comparing the deterministic behavior for systems with small structure size $S$. The overall accuracy of the approximation in the case of non-periodic boundaries is consistent with the finding that the boundary conditions as such do not have a big impact on the assembly time (see Fig. S5). We refer to this method of approximating a heterogeneous system as a homogeneous system as 'method of homogenization´. We used this method in particular for the simulations of the activation scenario in order to reduce stochastic effects and thereby avoid the necessity of simulating huge numbers of particles for the heterogeneous systems.

Note that, in order to investigate the system's deterministic behavior, in principle, one could also formulate and solve the chemical rate equations (ordinary differential equations). However, this approach would require a characterization of all possible cluster configurations. In other words, each state of the boolean array which describes a possible cluster configuration must be represented by a separate differential equation ('state-based' approach). Due to the large number of possible configurations for higher dimensional structures, this is not feasible without further approximations. In contrast, 'homogenization' allows to stick with a particle-based description and hence is significantly more efficient as it requires only the specification of a subset of all possible configurations (limited by the total number $N$ of particles present in the system).

In the following, we discuss the parameter settings and some particularities of the individual scenarios that are relevant for their simulation. In the subsequent section, we discuss the Master equations of the system and we show the equivalence between the heterogeneous and the homogeneous system for large particle numbers.

**Reversible binding scenario.** For the reversible binding scenario, the parameters were set as follows: $\mu = \nu = 1,\ \alpha = \infty$ (i.e. all monomers are available right from the outset), $T_i = 0\ \ \forall i$ and a variable binding energy per contact $E_B$ that fixes the detachment rates according to $\delta_n = Ae^{-nE_B}$ (Arrhenius' law). We fixed the pre-exponential factor at $A = 10^{18}C\nu$, which appears to be a realistic choice in the light of typical experimentally measured values for A (3, 4). However, we confirmed that the choice of the constant $A$ does not qualitatively affect our results (in particular it does not affect the exponents) as long as $A$ is large, and hence $\delta_1 \gg \delta_{n>1}$. If $A$ is small (for example $A = 10^6C\nu$ or smaller), or when $\delta_n$ values are chosen independently of one another, the minimal assembly time and the measured exponents can differ slightly, as then $\delta_2$ is no longer negligible compared to $\delta_1$ (see Fig. S1).

We simulated the reversible binding scenario with particle number $N = 500$. It is important that $N$ is chosen large enough, because for small $N$ the measured assembly time fluctuates very strongly between independent runs and the average assembly time increases with $N$. Only if $N$ is large enough does the average assembly time (measured relative to the reactive timescale $C\nu$ as in Fig. 2) converge and become independent of $N$. We verified that for $N = 500$ the remaining $N$-dependence is negligible. Alternatively, the method of homogenization described above can be used to reduce the role of fluctuations resulting from finite particle numbers and therefore allows the system to be simulated with fewer particles. In particular, the reversible binding scenario in one dimension can be simulated faster and more accurately in this way with a five-fold lower total particle number ($N_{\mathrm{tot}} = 100S$).

Generally, simulation of the reversible binding scenario is computationally much more expensive than that of the irreversible scenarios, since many more steps are generally needed owing to the fast detachment processes. Partly, a single run needed several billion Gillespie steps to complete. It is therefore useful to reduce the particle number in the simulations, as long as the results remain

accurate.
We found that with $N = 500$, the standard deviation in the assembly time between different runs is already rather small compared to the mean. Thus, averaging over a rather small number of independent runs (between 1 and 10) is usually sufficient. We generally found that self-averaging of the system by choosing a large particle number $N$ is usually more effective than averaging over a large number of independent runs. The quality of the statistics can be controlled either with the help of the empirical standard deviation in the interesting observable (yield or assembly time) or visually by verifying that neighboring data points line up into smooth curves as in Fig. 3B.

**Dimerization scenario.** For the dimerization scenario we used $\alpha = \infty$, $T_i = 0\ \forall i$, $\delta_n = 0$ and a variable dimerization rate $\mu$ as well as $N = 1000$. The dimerization scenario can be simulated most efficiently, because far fewer steps are needed due to the irreversibility of binding reactions. Furthermore, stochastic effects do not play an important role (2), so $N$ can be chosen to be relatively small. Conversely, fluctuations in the assembly time between independent runs decrease with increasing $N$, allowing for greater accuracy in the determination of the exponents.

**Activation scenario.** We defined the activation scenario by $\mu = \nu = 1$, $T_i = 0\ \forall i$, $\delta_n = 0$ and a variable influx rate $\alpha$. Since the momentary concentration of active monomers is generally small for a low influx rate, the activation scenario is strongly affected by stochastic effects (see Ref. (2) for details). Furthermore, the magnitude of these stochastic effects strongly depends on the number of species, and hence on the size $S$ of the target structure. Consequently, depending on $S$, a large number of particles $N$ may be required to achieve a yield $\geq 90\%$ in the activation scenario. By "homogenizing" the system, i.e. treating species as indistinguishable and simulating a homogeneous system instead of a heterogeneous system as described above, the computational cost of the simulation can be drastically reduced using a much smaller total number of particles.

In the case of one-dimensional structures, which were implemented with periodic boundary conditions, the homogenized simulation is exact, in the sense that it reproduces the same yield and assembly time as obtained for the heterogeneous system in the limit of large $N$. In the case of open boundaries of the structures which have been implemented for the higher dimensional cases, "homogenization" yields an accurate approximation (see Fig. S2). We exploited this method to simulate the activation scenario efficiently with a total number of particles $N_{\mathrm{tot}} = 1000S$, as in the dimerization scenario.
Note that for two-dimensional structures in the activation scenario, apparently the approximation slightly underestimates the minimal assembly time (see Fig. S2). Hence, the time complexity exponent for heterogeneous 2D structures might in reality be even closer to its theoretic value than predicted by the approximation.

**Just-in-sequence scenario.** For the JIS scenario, we set $\mu = \nu = 1$, $\alpha = \infty$, $\delta_n = 0$ and control the time points $T_i$ at which the different species are supplied. Species with identical $T_i$ define a 'batch'. We only considered the case of equidistant intervals $\Delta T$ between successive batches. The supply protocol (see Fig. 5C) assigns the species to the batches and specifies the concentrations in which the species are supplied. In this work, we exclusively used the "onion-skin supply protocol" depicted in Fig. 5C, where structures grow radially from the center outwards. This protocol minimizes the total number of batches. As discussed in the main text, in the JIS scenario, choosing the concentrations of the species in specific, non-stoichiometric ratios is crucial in reducing competition for resources among the growing structures and enhancing the efficiency of assembly. In order to compensate for the increasing number of clusters that form through excess dimerization events, the number of

resources supplied is increased with each batch. This comes at the price, insofar as the maximum yield is limited to a value less than 1 corresponding to the number of initial seeds. The desired effect is that each species can be provided in an amount that allows all the structures currently present in the system to grow, thus reducing competition for resources to a minimum. The most efficient usage of resources is therefore achieved if all species are provided in the minimal amount so that all existing structures can grow. If a single species is provided in excess, additional nucleation events will be triggered and, consequently, all subsequent species must also be supplied in larger amounts in order to keep competition at a minimum. This would result in a lower resource- and time efficiency. The optimal concentration of a species, which allows to achieve maximal time efficiency, is therefore determined by the total number of structures formed during previous assembly steps that are capable of binding the species that has just been supplied. More precisely, for each species provided in the $b^{\text{th}}$ batch, we supply a number

$$N_b = (1-p)N + pSN\frac{Z_b}{Z_{\text{tot}}} \qquad [1]$$

of monomers, where $Z_1 = 0$ and $Z_i < Z_j$ for $i < j$, see below. The first contribution, $(1-p)N$, which is identical for all species, is the basal particle number, which defines the maximum number of complete structures that can be built. The second contribution is the excess concentration, which provides additional resources for the growing total number $\sim Z_b$ of complexes that have already formed through excess dimerization events. Here, pSN with $p < 1$ is the total amount of resources that is distributed unevenly among the species, and $Z_b/Z_{\text{tot}}$ is the fraction of that amount assigned to the individual species supplied in the $b^{\text{th}}$ batch. The normalization factor $Z_{\text{tot}} := \sum_{i=1}^{S} Z_{b(i)}$, with $b(i)$ denoting the batch number of species $i$, sums the $Z_b$ over all species, and thereby fixes the average particle number $\overline{N}$ per species: $\overline{N} = \frac{1}{S}\sum_{i=1}^{S} N_{b(i)} = (1-p)\,N + pN = N$. The basal fraction of resources $(1-p)$ determines the maximum yield, and hence should be at least 0.9 to meet our criterion for the assembly time. We found that $p = 0.07$ minimizes the assembly time $T_{90}$ and, therefore, we used this value in the simulations.

The success of the JIS strategy crucially depends on the choice of the numbers $Z_b$. Optimally, in order to minimize competition and achieve maximal time efficiency, the excess concentrations $Z_b$ should reflect the number of the excess complexes relevant for a species supplied in the $b^{\text{th}}$ batch (see Fig. S3). Approximately, the number of previous excess dimerization events will be proportional to the total number of species supplied previous to the $b^{\text{th}}$ batch, i.e. provided by the batches 1 to $b-1$. Since in the onion-skin protocol, species with batch number less than $b$ form a $d$-dimensional volume (see Fig. 5C), for large $b$ we obtain approximately: $Z_b \sim b^d$. Correcting this count for small $b$ (see Fig. S3) we can further improve the efficiency by setting:

$$Z_b \sim \begin{cases} 0 & \text{if } b = 1 \\ (b+1)^d & \text{if } b > 1 \end{cases} \qquad [2]$$

for two- and three- dimensional structures and $Z_b \sim (b-1)$ in the 1D case. It might be possible to improve the efficiency further by assigning particle numbers $N_s$ individually for each species, rather than identically for all species in the same batch. However, we already achieve very good results with this choice of $Z_b$. On the other hand, with all species in a batch being supplied in identical particle numbers, those species could likewise be indistinguishable. In this way, a regular target structure could be designed with only two distinct species, which alternately assemble the "skins of the onion" (the "homogenized" version of the JIS scenario; also see the example on capsid assembly

in section 5 of this SI). Furthermore, note that, if the particle numbers $N_b$ for the different species are chosen appropriately on average, the system becomes robust to external noise up to a certain limit (see Fig. 5E and Fig. S7B).

For reasons of computational efficiency, we would like to simulate the system with a small (average) particle number $N$. Note, however, that the implementation of non-stoichiometric concentrations requires a minimum $N$ due to the discreteness of particle numbers: In order to ensure that the right-hand side of Eq.(1) reasonably maps onto integer values for the numbers $N_b$, the factor $pSN/Z_{\mathrm{tot}}$ that multiplies $Z_b$ should be of the order at least $\mathcal{O}(1)$. In order to find a rough condition for $N$, we therefore estimate the normalization factor $Z_{\mathrm{tot}}$:

$$Z_{\mathrm{tot}} := \sum_{i=1}^{S} Z_{b(i)} = \sum_{b=1}^{b_{\max}} m(b) Z_b \approx \int_0^{b_{\max}} m(b) b^d \mathrm{db} \ , \qquad [3]$$

where in the second step we change the sum over *species* to a sum over *batches*, with $m(b)$ denoting the number of species in the $b^{\mathrm{th}}$ batch ('density of species') and $b_{\max} = \frac{d}{2}L$ being the total number of batches (see Fig. 5C). Note that, in the onion-skin protocol, species with the same batch number lie on rhomboidal shapes around the center species. Furthermore, the densities are symmetric about $\mathrm{b}_{\max}/2$ (batches ii and iii have the same densities as v and vi, respectively, in the supply protocol depicted in Fig. 5C). Hence, we approximate the density of species by

$$m_b \sim \begin{cases} a b^{d-1} & b \leq \frac{b_{\max}}{2} \\ a(b_{\max} - b)^{d-1} & b > \frac{b_{\max}}{2} \end{cases} \ , \qquad [4]$$

where the constant $a$ is determined from the condition $\int_0^{b_{\max}} m\,(b) = S$. Performing the calculation yields $Z_{\mathrm{tot}} \sim S^2$. Hence, in order to guarantee that the prescribed ratios of the particle numbers $N_b$ can be met, the average particle number should be $N \gtrsim \frac{S}{p}$.

We used $N = 10^4$ in our simulations of the JIS scenario with non-stoichiometric concentrations, with $p = 0.07$ and a structure size $S$ of maximally $10^3$. By simulating individual runs with a larger particle number $N = 10^5$, we verified that the $N$-dependence of the assembly time is negligible for $N \geq 10^4$. The simulations of the JIS scenario with stoichiometric concentrations were performed with $N = 10^5$, because the larger time intervals $\Delta T$ led to very small momentary concentrations, and hence required a larger overall particle number to achieve $N$-independent assembly times.

**Determination of $T_{90}^{\mathrm{min}}$ and the optimal parameter.** In order to determine the minimal assembly time for a specified scenario and target structure, we first varied the respective control parameter roughly to find an estimate for its optimal value that minimizes the assembly time in the simulation. Afterwards, we sampled the parameter range around the estimated parameter value thoroughly by varying the control parameter in equidistant increments of approximately 2-4 percent precision. For each parameter value, the assembly time was averaged over several independent runs (50-100 for the irreversible scenarios and 5-50 for the reversible binding scenario). The minimal assembly time $T_{90}^{\mathrm{min}}$ was then determined as the minimum of the averaged assembly times, and the corresponding parameter value was chosen as the optimal parameter value. If the minimum of the assembly times was attained at the boundary of the sampled parameter range, we increased the range in the direction of the respective boundary and simulated additional parameter values. We repeatedly increased the range (or modified the parameter estimate) until we found a minimum that was attained somewhere in the middle of the sampled range to ensure that the global minimum has been identified.

## 2. Master equation and the irrelevance of the heterogeneity of the system

Here we show the moment equations resulting from the stochastic Master equation that describe the assembly kinetics for one-dimensional structures. The higher dimensional cases are conceptually similar to the one-dimensional case but do not allow for a simple representation of all possible cluster configurations. Therefore, we restrict ourselves to illustrating the mathematical framework only for the 1D case. The moment equations are subsequently used to show that for structures with periodic boundaries, the heterogeneity (distinguishability of species) is irrelevant in the limit of large $N$. This is the basis of our 'method of homogenization', which exploits the equivalence between heterogeneous and homogeneous systems in order to increase the efficiency of the simulations.

For one-dimensional structures, each possible kind of polymer can be characterized by two variables: the length $\ell$ of the polymer, and the monomer species $s$ at its right end which will be referred to as the species of the polymer. We denote by $n_\ell^s(t)$ with $2 \leq \ell < L$ and $1 \leq s \leq S$ the number of polymers of size $\ell$ and species $s$ in the system at time $t$. Furthermore, $n_0^s$ and $n_1^s$ denote the number of inactive (not yet added) and active monomers of species $s$, respectively, and $n_L$ the number of complete structures.

The subsequent set of equations can then be interpreted in two different ways: Either all terms with a species index (upper index) outside the range $1 \leq s \leq S$ are considered as zero or species indices are taken modulo S. The first case describes the self-assembly of structures with an open, non-periodic boundary. In contrast, the second case describes the assembly process of a periodic structure, i.e. a ring in this 1D case (the case considered in the main text). We show in section 4 of this SI that the choice of the boundary condition only has a small effect on the assembly time and, in particular, does not affect the control parameter and time complexity exponents. By $\langle ... \rangle$ we indicate (ensemble) averages. The system governing the evolution of the first moments (the averages) of the $\{n_\ell^s\}$ is then given by:

$$\frac{d}{dt}\langle n_0^s\rangle = -\alpha\,\Theta(t-T_s)\langle\Theta(n_0^s)\rangle\,, \tag{5a}$$

$$\begin{aligned}\frac{d}{dt}\langle n_1^s\rangle &= \alpha\,\Theta(t-T_s)\,\langle\Theta(n_0^s)\rangle - \mu\left(\langle n_1^s n_1^{s+1}\rangle + \langle n_1^s n_1^{s-1}\rangle\right)\\ &\quad - \nu\sum_{\ell=2}^{L-1}\left(\langle n_1^s n_\ell^{s+\ell}\rangle + \langle n_1^s n_\ell^{s-1}\rangle\right) + \delta\sum_{\ell=2}^{L-1}\left(\langle n_\ell^{s+\ell-1}\rangle + \langle n_\ell^s\rangle\right)\,,\end{aligned} \tag{5b}$$

$$\frac{d}{dt}\langle n_2^s\rangle = \mu\,\langle n_1^{s-1}\,n_1^s\rangle - \nu\,\left(\langle n_1^{s-2}\,n_2^s\rangle + \langle n_2^s\,n_1^{s+1}\rangle\right) + \delta\,\left(\langle n_3^s\rangle + \langle n_3^{s+1}\rangle - 2\langle n_2^s\rangle\right)\,, \tag{5c}$$

$$\begin{aligned}\frac{d}{dt}\langle n_\ell^s\rangle &= \nu\,\left(\langle n_1^{s-\ell+1}\,n_{\ell-1}^s\rangle + \langle n_{\ell-1}^{s-1}\,n_1^s\rangle - \langle n_1^{s-\ell}\,n_\ell^s\rangle - \langle n_\ell^s\,n_1^{s+1}\rangle\right)\\ &\quad + \delta\,\left(\langle n_{\ell+1}^s\rangle + \langle n_{\ell+1}^{s+1}\rangle\right)\mathbf{1}_{\{\ell\leq L-2\}} - 2\delta\langle n_\ell^s\rangle\,, \qquad 3\leq\ell<L\,,\end{aligned} \tag{5d}$$

$$\frac{d}{dt}\langle n_L\rangle = \nu\,\sum_{s=1}^{L}\left[\langle n_1^{s-L+1}\,n_{L-1}^s\rangle + \langle n_{L-1}^{s-1}\,n_1^s\rangle\right]\,. \tag{5e}$$

Eq. (5a) and the first term in Eq. (5b) describe the influx of monomers of species $s$ into the system starting at time $T_s$ with a constant rate $\alpha$ until all inactive monomers have been added (which, on average, will be at time $T_s + \frac{1}{\alpha}$). Here, $\Theta$ denotes the Heaviside function. Besides the influx of monomers, the temporal change in the number of active monomers (Eq. (5b)) is governed by the following processes: dimerization of monomers at rate $\mu$, binding of monomers to the left and to the right end of existing polymers at rate $\nu$ and detachment of monomers from the left and right end of polymers with rate $\delta$.

Equations (5c) and (5d) describe the dynamics of dimers and larger polymers of size $3 \leq \ell < L$, respectively. The terms account for dimerization of active monomers as well as all possible kinds of reactions of polymers with monomers, together with detachment of monomers from polymers. The indicator function $\mathbf{1}_{\{\ell \leq L-2\}}$ in Eq. (5d) (which equals 1 if the condition $\ell \leq L-2$ is satisfied and 0 otherwise) excludes source terms that would account for detachment from completed structures, which are assumed to be stable. Finally, the complete structures form an absorbing state and, therefore, include only the respective gain terms (cf. Eq (5e)).

For sufficiently large particle numbers $N$, correlations between the particle numbers $\{n_\ell^s\}$ in Eq. (5) can be neglected and the two-point correlator can be approximated as the product of the corresponding mean values (mean-field approximation):

$$\langle n_i^s n_j^k \rangle = \langle n_i^s \rangle \langle n_j^k \rangle \ \forall s, k \tag{6}$$

Note that, in the case of periodic boundary conditions and if $T_i = T_j \ \forall i, j$, all species are equivalent. Mathematically, this is reflected by the invariance of Eq. (5) with respect to relabelling the upper indices if $T_i = T_j$. This symmetry of the system allows us to drop the distinction by species and to define the homogeneous concentrations

$$\langle n_\ell^s \rangle = \langle n_\ell^k \rangle := c_\ell \, V \quad \forall s, k, \tag{7}$$

where $V$ is the reaction volume. Setting $T_i = T_j = 0$ and rescaling the rate constants $\mu$ and $\nu$ by a factor of $V$, Eq. (5) thereby reduces to a set of rate equations for a homogeneous (one species) system in the deterministic limit $N \to \infty$:

$$\frac{d}{dt} c_0 = -\alpha \, \Theta(c_0) \,, \tag{8a}$$

$$\frac{d}{dt} c_1 = \alpha \, \Theta(c_0) - 2\mu c_1^2 - 2\nu \sum_{\ell=2}^{L-1} c_\ell c_1 + 2\delta \sum_{\ell=2}^{L-1} c_\ell \,, \tag{8b}$$

$$\frac{d}{dt} c_2 = \mu \, c_1^2 - 2\nu \, c_1 c_2 + 2\delta \, (c_3 - c_2) \,, \tag{8c}$$

$$\frac{d}{dt} c_\ell = 2\nu \, (c_1 c_{\ell-1} - c_1 c_\ell) + 2\delta \, c_{\ell+1} \mathbf{1}_{\{\ell \leq L-2\}} - 2\delta c_\ell \,, \qquad 3 \leq \ell < L \,, \tag{8d}$$

$$\frac{d}{dt} c_L = \nu \, c_1 c_{L-1} \,. \tag{8e}$$

Note that, in transforming Eq. (5e), we had to multiply by a factor of $L^{-1}$ because the complete rings on the left hand side of Eq. (5e) are not distinguished into species. Therefore, in the deterministic limit, the heterogeneous system decouples into $S$ independent homogeneous assembly processes for the $S$ different species. This means that, in the case of periodic boundary conditions and if the particle number $N$ is large, the heterogeneity (distinguishability of species) is irrelevant; also see ref. (2) for more details. This holds true for the activation, dimerization and reversible binding scenario where $T_i = T_j$.

The equivalence of species no longer holds exactly in the absence of periodic boundary conditions because then the species at the boundary of the structure violate the symmetry. However, the symmetry still holds approximately and the heterogeneous system can well be approximated by a corresponding homogeneous system for large $N$ as described in the previous section. Figure S2 shows that in the case of non-periodic boundaries, this approximation is still quite accurate by comparing the deterministic behavior for systems with small structure size $S$.

This result shows that our time complexity analysis of the activation, dimerization and reversible binding scenario does not depend on the heterogeneity of the system and therefore applies to a broad range of natural and artificial self-assembling systems. Furthermore, the (approximate) deterministic equivalence between heterogeneous and homogeneous systems can be exploited in order to speed up the simulations: While heterogeneous systems may be strongly affected by stochastic effects arising from fluctuations in the concentrations of the different species (for example in the activation scenario), homogeneous systems suppress these stochastic effects (2). Hence, in order to observe deterministic behavior, a smaller total number of particles is required for homogeneous systems, increasing the efficiency of simulations. We exploit this behavior in our 'method of homogenization' as described in the previous section.

## 3. Scaling theory

In this section, we provide a mathematical scaling analysis in order to derive the characteristic exponents for the four scenarios analytically, supporting our numerical findings. We first discuss the reversible binding scenario for one-dimensional structures, followed by a unified approach to the irreversible scenarios as well as the reversible binding scenario for higher dimensional structures. Note that only the one-dimensional reversible binding scenario is fully reversible, while in the higher dimensional cases one can identify quasi-stable intermediate assembly products that form irreversibly. Exploiting the (stepwise) irreversibility of the assembly kinetics allows to analyze reversible binding for higher dimensional structures together with the irreversible scenarios in a unified approach, whereas reversible binding in one dimension needs to be analyzed separately.

### Reversible binding for 1D structures

To mathematically analyze the scaling behavior of the one-dimensional reversible binding scenario, we need to identify the optimal value of the detachment rate $\delta := \delta_1$ that minimizes the time taken to achieve a yield of 90%, depending on the size of the target structure. Since generally several unfinished structures exist at the same time and thereby compete for resources when growing, an exact analysis requires knowledge of the full temporal evolution of the polymer size distribution, which is very hard to obtain. Therefore, we will make two simplifying assumptions to obtain the scaling behavior: First, we employ a quasi-stationarity assumption, $\partial_t m = 0$, for the monomer concentration. While this may seem to be a rather drastic postulate, the idea is rather intuitive: During the assembly process, structures grow by consumption of monomers and, vice versa, the number of monomers increases due to their detachment from structures. As a result, in the limit of large structure sizes where many attachment and detachment events occur before any structure is completed, the concentration of monomers adjusts itself over time in such a way that attachment and detachment roughly balance and the monomer concentration is constant. As we will show more explicitly below, in this case the polymer size distribution corresponds to a random walk on a one-dimensional lattice with constant hopping rates. To proceed, we then make a second, important assumption: We postulate that the scaling of the time to obtain a yield of 90% is the same as the scaling of the mean first-passage time of the approximate random walk to reach the absorbing boundary at $x = S$ (complete structure). This amounts to assuming that growth of structures is the time-limiting step and that the corresponding timescale does not change considerably over the course of the assembly process, e.g. the times to obtain 50 or 90% yield scale similarly with the structure size. With these assumptions, we identify the time complexity exponent to be 4 and the control parameter exponent to be -2, as we will outline in more detail in the following.

In the reversible binding scenario, we have $T_s = 0 \ \forall s$ and $\alpha \to \infty$. With the reaction rate $\nu$, the dimerization rate $\mu$ and the detachment rate $\delta$, the deterministic equations for the temporal evolution of the concentrations are (see Eqs. (5) for the general case):

$$\begin{aligned}
\partial_t m &= -2\mu m^2 - 2\nu m \sum_{j=2}^{S-1} c_j + 2\delta \sum_{j=2}^{S-2} c_j \\
\partial_t c_2 &= \mu m^2 - 2\nu m c_2 - \delta c_2 + 2\delta c_3 \\
\partial_t c_i &= 2\nu m (c_{i-1} - c_i) - 2\delta (c_i - c_{i+1}) \quad i = 3, \dots, S-2 \\
\partial_t c_{S-1} &= 2\nu m (c_{S-2} - c_{S-1}) - 2\delta c_{S-1} \\
\partial_t c_S &= 2\nu m c_{S-1}
\end{aligned} \tag{9}$$

where $m$ is the number of monomers per species and $c_i$ the number of $i$-mers. Defining $K = \sum_{j=2}^{S-1} c_j$ to be the number of unfinished complexes, the temporal evolution for the monomers is given by

$$\partial_t m = -2\mu m^2 - 2(\nu m - \delta)K.$$

In the quasi-stationary limit, $\partial_t m = 0$, the evolution of the polymer-size distribution $\partial_t c_i$ can be identified with a random walk on a one-dimensional lattice with constant hopping rates $2\nu m$ to the right and $2\delta$ to the left, corresponding to monomer attachment and monomer detachment, respectively (see also the deterministic analogue in Eq. (9)). Since completed structures are stable, the right end at $i = S$ is absorbing, implying that $c_S = 0$ or, in the continuum limit, $c(l = S) = 0$. Furthermore, we assume that all particles are provided at $t = 0$ at the left end $l = 0$*. The last two points imply that the polymer concentration $c(t, l)$ decreases over time. As a measure for the quasi-stationary properties of the system, we therefore consider the temporally integrated concentration $I(l) = \int_0^\infty \mathrm{d}t\ c(t, l)$.

In the continuum limit, Eq. (9) becomes $\partial_t c(t, l) = -2(\nu m - \delta)\partial_l c(t, l) + (\nu m + \delta)\partial_l^2 c(t, l)$. Using that $c(t \to \infty, l) = 0 \forall l$ and $c(0, l) = 0 \forall l > 0$, the integrated concentration satisfies $v\partial_l I(l) = D\partial_l^2 I(l)$ where

$$v = 2(\nu m - \delta)$$

is the drift coefficient and

$$D = \nu m + \delta$$

is the diffusion constant of the random walk. Its solution is given by

$$I(l) = C(1 - e^{v(l-S)/D})$$

where $C$ is an integration constant that is related to the number of injected particles. It will, however, not be relevant for the calculation of the first-passage time.

We will use the integrated concentration to calculate the time-averaged mean size of unfinished polymers. This quantity is helpful to determine the number of monomers self-consistently as conservation of particles requires $m + \sum_{j=2}^{S} jc_j = N$. Before yield sets in this can be rewritten as $m + \sum_{j=2}^{S-1} jc_j = N$. Furthermore, the sum can be expressed in terms of the average polymer size of unfinished polymers $\langle j \rangle$ as $\sum_{j=2}^{S-1} jc_j = \langle j \rangle \sum_{j=2}^{S-1} c_j = \langle j \rangle K$. In the continuum limit, we find the following self-consistency equations:

$$N = m + \langle l \rangle K \quad [10]$$

$$\langle l \rangle = \frac{\int_0^S \mathrm{d}l\ lI(l)}{\int_0^S \mathrm{d}l\ I(l)} = -\frac{D}{v} + \frac{S^2 v}{2(Sv + D(-1 + e^{-Sv/D}))}. \quad [11]$$

From the quasi-stationarity condition $\partial_t m = 0$, we furthermore find

$$m^2 + \frac{\mu}{\mu} mK - \frac{\delta}{\mu} K = 0. \quad [12]$$

Taken together, we have three conditions (10), (11) and (12) to determine three unknown variables $m$, $K$ and $\langle l \rangle$ self-consistently (for fixed $\delta$). Furthermore, we have another unknown, the optimal

*Since we are interested in the limit of large $S$, we approximate $S - 2 \approx S$ and, thus, do not distinguish whether particles are injected at $l = 0$, $l = 1$ or $l = 2$.

monomer detachment rate $\delta_{opt}$. So, we need another equation, namely by minimizing the first-passage time. The mean first-passage time for the above random walk is given by

$$\langle T\rangle = \frac{L}{v} - \frac{D}{v^2}(1 - e^{-vL/D}). \quad [13]$$

What is left to do is to determine $m$, $K$, $\langle l\rangle$ and $\delta_{opt}$ self-consistently from (10), (11) and (12) and from minimizing the mean first-passage time (13).

As a first step, we use condition (12) to write $\delta = \nu m + \mu\frac{m^2}{K}$. Correspondingly, we find

$$D = 2\nu m + \mu\frac{m^2}{K}$$
$$v = -2\mu\frac{m^2}{K}$$

for the drift and diffusion constant in terms of $m$ and $K$. Using condition (11) together with the particle conservation condition (10) and with the mean-first passage time (13), we end up with the two defining equations for $m$ and $K$:

$$N = m + \frac{\nu}{\mu}\frac{K^2}{m} + \frac{K}{2} + \frac{S^2K}{2(S + (\frac{\nu}{\mu}\frac{K}{m} + \frac{1}{2})(1 - e^{\frac{Sm}{\frac{\nu}{\mu}K + \frac{m}{2}}}))}$$
$$\langle T\rangle = -\frac{K}{2\mu m^2}(S + (\frac{\nu}{\mu}\frac{K}{m} + \frac{1}{2})(1 - e^{\frac{Sm}{\frac{\nu}{\mu}K + \frac{m}{2}}})).$$

To make progress, we make a last approximation, namely that $m \ll K$. This assumption is justified a posteriori and leads to

$$N = \frac{\nu}{\mu}\frac{K^2}{m} + \frac{S^2K}{2(L + \frac{\nu}{\mu}\frac{K}{m}(1 - e^{S\frac{\mu m}{\nu K}}))}$$
$$\langle T\rangle = -\frac{K}{2\mu m^2}(S + \frac{\nu}{\mu}\frac{K}{m}(1 - e^{S\frac{\mu m}{\nu K}}))$$

or, in slightly rewritten form,

$$\frac{(S\frac{\mu m}{\nu K})^2}{2(1 - \frac{\mu m N}{\nu K^2})} = e^{S\frac{\mu m}{\nu K}} - 1 - S\frac{\mu m}{\nu K} \quad [14]$$

$$\langle T\rangle = \frac{S^2K^2}{4\mu m(\frac{\nu}{\mu}K^2 - Nm)}. \quad [15]$$

Intriguingly, the first condition (14) is recast in terms of two dimensionless variables $a = \frac{S\mu m}{\nu K}$ and $b = \frac{N\mu m}{\nu K^2}$ as

$$e^a - 1 - a = \frac{1}{2(1-b)}a^2 \quad [16]$$

whose possible solutions are independent of all other parameters of the system and, in particular, independent of $S$. Furthermore, the average first-passage time then becomes

$$\langle T\rangle = \frac{\mu}{\nu^2}\frac{S^4}{4N}\frac{b}{a^2(1-b)}. \quad [17]$$

In order to minimize $\langle T \rangle$, thus, the term $b/(a^2(1-b))$ has to be minimized under the constraint (16). This minimization procedure is entirely independent of $S$ and we conclude that the average first-passage time scales as

$$\langle T \rangle \sim \frac{\mu S^4}{4\nu^2 N}. \tag{18}$$

Similarly, $m$ and $K$ behave as

$$m = \frac{\nu}{\mu}\frac{N}{S^2}\frac{a_{opt}^2}{b_{opt}} \sim \frac{\nu N}{\mu S^2}$$
$$K = \frac{N}{S}\frac{a_{opt}}{b_{opt}} \sim \frac{N}{S}.$$

From these scaling functions, we can finally determine the scaling of $\delta_{opt}$ from (12):

$$\delta_{opt} = \frac{\nu^2}{\mu}(m + \frac{m^2}{K}) = \frac{\nu^2}{\mu}(\frac{N}{S^2}\frac{a_{opt}^2}{b_{opt}} + \frac{N}{S^3}\frac{a_{opt}^3}{b_{opt}}) \sim \frac{\nu^2}{\mu}\frac{N}{S^2},$$

where we neglected the higher-order scaling $\sim \frac{N}{S^3}$. This yields the parameter exponent $\phi = -2$.

As a last step, we can actually determine $a_{opt}$ and $b_{opt}$ numerically from minimizing $b/(a^2(1-b))$ under the constraint (16). This procedure yields

$$a_{opt} \approx 2.687$$
$$b_{opt} \approx 0.672$$

and plugging in these values into the formulas for $\langle T \rangle$ and $\delta_{opt}$ we get:

$$\langle T \rangle \approx 0.07\frac{\mu S^4}{\nu^2 N} \tag{19}$$
$$\delta_{opt} \approx \frac{\nu^2}{\mu}(10.74\frac{N}{S^2} + 28.87\frac{N}{S^3}) \approx 10.74\frac{\nu^2}{\mu}\frac{N}{S^2}. \tag{20}$$

Combining the scaling behavior of $m$ and $\delta_{opt}$, we find that the drift coefficient $D$ vanishes to lowest order and the polymer size distribution behaves as a purely diffusive process. Intriguingly, this is true not only in the optimal case but follows more generally from the quasi-stationarity assumption: the system self-organizes into a diffusion process without drift where growth of structures and detachment of monomers balance. The optimal parameter choice thus corresponds to maximizing the diffusive flux through the system.

## Universal approach to the irreversible scenarios and reversible binding for 2D/3D structures

For the irreversible scenario as well as the reversible binding scenario in higher dimensions, one can use a unified scaling approach by demanding a specified ratio between the total nucleation and attachment rate. For reversible binding in higher dimensions, this approach works as well because during their growth processes, clusters pass through stable intermediate stats whose decay rate is negligible against their growth rate. Hence, transitions between these stable intermediates can effectively be considered as irreversible. Consequently, the reversible binding scenario for

higher dimensional structures is fundamentally different from the reversible binding scenario for one-dimensional structures, whose dynamics was described by a random walk. After we introduce the general ansatz, we will first use it to derive the parameter and time complexity scaling for the irreversible scenarios and afterwards for the higher-dimensional reversible binding scenario.

It is possible to derive simple scaling relations for the time efficiency, because the simulations show that in the irreversible scenarios, the respective control parameter is optimal (achieving a minimal $T_{90}$ assembly time) close to where the *final* yield is approximately 90% (see main text Fig. 4A,B). This is plausible because in all scenarios the control parameter defines the rate limiting time scale and hence the parameter is optimal close to where the desired yield is barely reached. Therefore, the scaling of the optimal parameter can be determined by identifying a scaling relation that fixes a constant final yield. In order for the final yield to be independent of the size $S$ of the target structure, the ratio between the total nucleation and total attachment rate must scale inversely with $S$. To put it simply: if the size of the target structure is doubled, in order to achieve a constant yield, there need to be twice as many growth events relative to the same number of initiation events.

$$\frac{\text{total number of nucleation events per time}}{\text{total number of attached monomers per time}} := \frac{\mu_{\text{tot}}}{\nu_{\text{tot}}} \overset{!}{\sim} \frac{1}{S}\,. \tag{21}$$

(By the exclamation mark we indicate that we demand the relation to hold in order to guarantee a constant yield.) This formula provides the starting point of our argument. In the following paragraphs we identify the total nucleation rate $\mu_{\text{tot}}$ and total attachment rate $\nu_{\text{tot}}$ for the three irreversible scenarios as well as for the reversible binding scenario in higher dimensions.

## Dimerization scenario

In the dimerization scenario, we focus on one-dimensional structures only. The higher dimensional cases are related to the one-dimensional case via rescaling of the reaction rate $\nu \to \nu S^{(d-1)/d}$ as explained in the main text.

The total nucleation rate depends quadratically on the momentary concentration of active monomers $m$ per species and linearly on $S$ (number of possible dimerization partners).

$$\mu_{\text{tot}} = \mu m^2 S \tag{22}$$

The total attachment rate is given by the product of the total concentration of complexes $K$ in the system and the concentration of monomers per species.

$$\nu_{\text{tot}} = \nu K m \tag{23}$$

Note that the total concentration of complexes $K$ will scale with $C = \frac{N}{V}$ (which sets the scale for all concentrations in the system) but can be assumed to be independent of $S$ as we demand a constant yield (note that a constant yield implies a constant fraction of complexes $K/C$). Therefore,

$$\frac{\mu_{\text{tot}}}{\nu_{\text{tot}}} \sim \frac{\mu S m}{\nu C} \overset{!}{\sim} \frac{1}{S}\,, \tag{24}$$

in order to obtain a constant yield. In the dimerization scenario, all particles are active from the outset, hence $m \sim C$ and therefore, $\mu^{\text{opt}} \sim \frac{\nu}{S^2}$. Because dimerization is the time-limiting process in the dimerization scenario, this implies for the minimal assembly time

$$T_{90}^{\text{min}} \sim \frac{C}{\mu_{\text{tot}}^{\text{opt}}} \sim \frac{1}{SC\mu^{\text{opt}}} \sim \frac{S}{C\nu}. \tag{25}$$

So, the argument reproduces the control parameter exponent $\phi = -2$ and the time complexity exponent $\theta = 1$ for the dimerization scenario for one-dimensional structures. By rescaling $\nu \to \nu S^{(d-1)/d}$ the respective parameter- and time complexity exponents for the higher dimensional cases are obtained.

## Activation scenario

In the activation scenario, we focus again on one-dimensional structures and obtain the scaling laws for higher dimensional structures by our rescaling argument. In contrast to the dimerization scenario, in the activation scenario the monomers are not active right from the outset. Instead, there is a constant influx of monomers that balances a steady consumption of monomers due to binding. Hence, the stationary concentration $m$ of active monomers is determined from the condition that the total influx of monomers equals their consumption due to binding:

$$\text{total influx rate of monomers} = \text{total consumption of monomers due to binding.} \quad [26]$$

With the total influx rate of monomers given by $\alpha CS$, this translates into

$$\alpha CS = \nu_{\text{tot}} \sim \nu K m, \quad [27]$$

where we neglected the consumption of monomers due to dimerization, because for large $S$ dimerization is negligible compared to attachment (compare Eq. (21)). Demanding a constant yield, we can again assume $K \sim C$ (constant yield implies a constant fraction of complexes $K/C$), and hence, $m \sim S\frac{\alpha}{\nu}$. The total nucleation and attachment rate are again given by Eqs. (22) and (23), respectively, and therefore Eq. (24) applies identically, yielding

$$\alpha^{\text{opt}} \sim \frac{\nu^2 C}{\mu}\frac{1}{S^3} \ . \quad [28]$$

Furthermore, because the influx rate limits the assembly time,

$$T_{90}^{\text{min}} \sim \frac{1}{\alpha^{\text{opt}}} \sim \frac{\mu}{C\nu^2}S^3 \ , \quad [29]$$

confirming the control parameter exponent $\phi = -3$ and time complexity exponent $\theta = 3$ for the one-dimensional activation scenario, as well as a quadratic dependence on $\nu$ that is relevant for the rescaling procedure: Replacing $\nu \to \nu S^{(d-1)/d}$, the respective exponents for the higher dimensional cases are obtained in the usual way. Note that Eqs. (28) and (29) were derived for a general dimerization rate $\mu$, although the activation scenario was originally defined with $\mu = \nu$. Performing the argument with a general $\mu$ is, however, crucial in order to obtain the correct quadratic dependence on $\nu$ to execute the rescaling argument. This is important because the dimensionality affects the typical growth rate of clusters but has no effect on the rate at which clusters nucleate. Therefore, $\mu$ and $\nu$ must be distinguished in order to correctly perform the rescaling to higher dimensionality.

## JIS scenario

In the JIS scenario the different species are provided sequentially in consecutive batches. In order to estimate the total nucleation and attachment rate in Eq. (21), we calculate the total number of nucleation and binding events per species in a single assembly step. The number of nucleation events will crucially be determined by the number of active monomers that are still unbound when the

next batch is supplied: Since the subsequent batch is supplied when most monomers of the previous batch have already bound, the remaining monomers encounter many partners to form dimers while there are only few remaining binding sites in the clusters. Therefore, the remaining monomers will dimerize to the largest extent. In order to estimate the total dimerization rate per assembly step, we therefore need to estimate the concentration of remaining monomers in relation to $\Delta T$. We do this in the following by considering the dynamics of the concentration of monomers of an arbitrary species in the sequence.

Let $m$ denote the concentration of monomers of a species $i$ and $k$ the concentration of structures (binding sites) to which species $i$ can attach. We assume that at time $t = 0$, species $i$ is supplied in initial concentration $m(0) = M \approx C$. Each binding event involving species $i$ reduces both the concentration of binding sites $k$ and the concentration of monomers $m$ by one unit. Therefore, $u := m - k = \text{const}$ is a constant which denotes the excess concentration (i.e. the amount by which the total number of monomers $M$ exceeds the number of binding sites $k(0) := K$). Indeed, $u$ corresponds to the increase in concentration from one batch to the next if species are provided in non-stoichiometric concentrations. For the dynamics of $m$ it then follows that

$$\frac{d}{dt}m = -\nu m k = -\nu m^2 + \nu u m. \qquad [30]$$

By solving the differential equation, we find the monomer concentration $m$ at time $t = \Delta T$:

$$m(\Delta T) = \frac{1}{\frac{1}{u} + \left(\frac{1}{M} - \frac{1}{u}\right) e^{-u\nu\Delta T}} \approx \frac{1}{\frac{1}{u} + \left(\frac{1}{M} - \frac{1}{u}\right)(1 - u\nu\Delta T)} \approx \frac{1}{\nu\Delta T}, \qquad [31]$$

where in the second step we assumed $\Delta T \sim 1/(M\nu) \ll 1/(u\nu)$ (because $u \ll M$) and in the last step we again used $1/M \ll 1/u$. Note that according to Eqs. (1) and (2), the excess concentration will be of order $u \sim (N_{b+1} - N_b) \sim pCS^{-1/d}$, with $p \approx 0.1$, and hence can be assumed to be small compared to $C$ and the initial monomer concentration: $u \ll M$.

The total number of dimerization events during one assembly step can now be estimated as the concentration of monomers of species $i$ that are still unbound at time $\Delta T$ when the next binding partner, species $i + 1$, is supplied (in concentration $\approx M$). More specifically, the total number of dimerization events per assembly step is $\sim m(\Delta T)M \sim \mu_{\text{tot}}$, while the total number of attachment events per assembly step is $\sim KM \sim \nu_{\text{tot}}$ where $K := k(0) \sim C$. Therefore, with Eq. (21),

$$\frac{\mu_{\text{tot}}}{\nu_{\text{tot}}} \sim \frac{1}{\nu C \Delta T} \overset{!}{\sim} \frac{1}{S}. \qquad [32]$$

and thus,

$$\Delta T^{\text{opt}} \sim \frac{S}{C\nu}, \qquad [33]$$

yielding the control parameter exponent $\phi = 1$. In order to obtain the total assembly time, $\Delta T$ must be multiplied by the total number of batches, which is $b_{\max} \sim S^{1/d}$ in the case of the 'onion-skin' supply protocol (see Fig. 5C). Therefore,

$$T_{90}^{\min} \sim \Delta T^{\text{opt}}\, S^{1/d} \sim \frac{S^{1+\frac{1}{d}}}{C\nu}, \qquad [34]$$

yielding the time complexity exponent $\theta = 1 + \frac{1}{d}$, where $d$ is the dimensionality.

## Reversible binding for 2D and 3D structures

For the reversible binding scenario in two and three dimensions we can use the same approach as for the irreversible scenarios, starting from Eq. (21). The key insight is that during the assembly process stable intermediate assembly products form that decay only with rate $\delta_2 \ll \delta_1$ or $\delta_3 \lll \delta_1$ and hence are considered as long-lived on the relevant timescale. In contrast, intermediate states that decay with rate $\delta_1$ are highly unstable and decay quickly as $\delta_1$ is typically large compared to the reactive timescale $C\nu$ in the reversible binding scenario. Figure S4 shows how the resulting total nucleation rate $\mu_{\text{tot}}$ ($\mu_{\text{tot}}$ here denotes the total nucleation rather than dimerization rate) and total attachment rate $\nu_{\text{tot}}$ can be estimated. Here nucleation is an effective four-particle reaction that proceeds via two unstable intermediate states. If the detachment rate $\delta_1$ is large, the effective per capita rate for the four-particle reaction can be approximated as $\mu\nu^2/\delta_1^2$ and the total nucleation rate is given by $\mu_{\text{tot}} \sim \frac{\mu\nu^2}{\delta_1^2} m^4 S$ (the factor $S$ accounts for the fact that there are S possible combinations of species that can form a nucleus). Attachment typically proceeds in two steps. The first step, analogous to the nucleation process, can be approximated as an effective two-particle reaction passing through an unstable intermediate state (see Figure S4). The effective total rate for the first step is therefore $\sim \frac{\nu^2}{\delta_1^2} K m^2 S^{\frac{d-1}{d}}$, where $K$ is the total concentration of complexes and the factor $S^{\frac{d-1}{d}}$ estimates the number of possible binding sites for the first monomer (surface area of an average cluster). Once a new stable state has formed, a cascade of subsequent stable states can be traversed by attachment of additional monomers. Because in this second step the complex only passes through stable states, the second step can be assumed to be fast compared to the first step. We estimate the average number of monomers attaching in the second step to scale again proportionally to the cluster surface $\sim S^{\frac{d-1}{d}}$. This yields an additional stoichiometric factor to be accounted for in the total attachment rate, resulting in $\nu_{\text{tot}} \sim \frac{\nu^2}{\delta_1} K m^2 S^{(2-\frac{2}{d})}$. With Eq. (21), it follows that

$$\frac{\mu_{\text{tot}}}{\nu_{\text{tot}}} \sim \frac{\mu C}{\delta_1} S^{(\frac{2}{d}-1)} \overset{!}{\sim} \frac{1}{S} \ , \tag{35}$$

and, therefore,

$$\delta_1^{\text{opt}} \sim \mu C S^{\frac{2}{d}}, \tag{36}$$

with a control parameter exponent $\phi = \frac{2}{d}$. Since nucleation is the slowest step, we expect the minimal assembly time to scale approximately as the timescale of nucleation:

$$T_{90}^{\text{min}} \sim \frac{C}{\mu_{\text{tot}}} \sim \frac{C}{\mu\left(\frac{\nu}{\delta_1^{\text{opt}}}\right)^2 m^4 S} \sim \frac{\mu}{\nu(C\nu)} S^{\frac{4}{d}-1} \ , \tag{37}$$

yielding a time complexity exponent $\theta = \frac{4}{d} - 1$. Although the theoretical estimates for the exponents in the reversible binding scenario in higher dimensions do not coincide perfectly with the simulated values (compare main text Fig. 2B,C and Fig. 3B), their tendency and the dependence on the dimensionality of the structure are correctly predicted and explained. We suspect that the main reason for the deviations is a slight actual dependence of the average monomer concentration $m$ on $S$, which has been neglected in this scaling argument.

In conclusion, note that for all four scenarios, the scaling exponents for one-dimensional structures could be derived exactly from our scaling analysis. In contrast, for higher dimensional structures, the theoretical estimates generally do not fit the simulated values exactly. This may have various reasons like, for example, deviations from the presumed effective growth rate $\nu_S \sim \nu S^{\frac{d-1}{d}}$ that we used to rescale the exponent for the dimerization and activation scenario.

Furthermore, note that in the scaling argument applied to the reversible binding scenario in higher dimensions we used some specificities of the structure, most importantly, the number of unstable intermediate states in the processes of nucleation and attachment. This suggests that the exponents and the time efficiency of the reversible binding scenario are not fully generic but depend on the shape of the structure and the constituents. In contrast, the scaling arguments for the other scenarios are fully generic, so we do not expect a significant dependence of the time efficiency on specificities of the structure in the irreversible scenarios.

## 4. Robustness to model modifications

To verify that our time complexity analysis is robust to model modifications, we investigated three variants of the original model and the assembly kinetics. Figure S5 shows the minimal assembly time for these variants in all four scenarios. The results of the analysis are discussed in the following.

**Structures with periodic boundaries.** First we simulated the minimal assembly time for structures with periodic boundaries. While in the main text we only considered higher dimensional structures with an open boundary, some typical examples of self-assembling systems comprise the formation of closed structures with periodic boundaries, for instance, two-dimensional shells and capsids such as, for example, virus capsids (5, 6). To assess the relevance of the boundary, we simulated the minimal assembly time for two-dimensional periodic structures or tori. In all scenarios we measured almost the same time complexity exponent as in the original model. Only in the reversible binding scenario the exponent appears to be slightly larger. In the activation, dimerization and reversible binding scenario, the time efficiency increases as a consequence of the modified boundary condition since a closed boundary effectively enhances the possibility of a cluster to grow, thereby increasing the effective binding rate. In the JIS scenario, the time efficiency slightly decreases because the species at the boundary induce an increased excess dimerization rate compared to the case with non-periodic boundary. Also note that, in the JIS scenario, we simulated periodic structures only with an even edge length $L$, since for odd $L$ it would have been necessary to modify the supply order of our protocol in order to make sure that species supplied in the same batch do not bind each other. Moreover, we increased the excess concentrations $Z_n$ (see Eqs. (1) and (2)) of the species at the boundary by a factor of 2 or 4, respectively, to achieve optimal efficiency for the modified boundaries.

**Heterogeneous binding rates.** Next, we investigated the impact of heterogeneous binding rates on the assembly time. Considering a heterogeneous system, the assumption of identical binding rates for all species is an idealization. More realistically, the rates will vary to a certain extent. We therefore simulated the system with heterogeneous rates for the different species, drawn independently from a (truncated) normal distribution with a coefficient of variation of 50%. We truncated the normal distribution for values that are below 20% of the mean in order to guarantee that individual rates do not become negative or very small. For each run the binding rates were chosen independently and the assembly times were averaged over 10-100 independent runs. We did not perform the simulations for the activation scenario since the simulation of the activation scenario is based on the homogeneous approximation and the results would thus not be reliable for heterogeneous rates of the species. In the other scenarios, the measured time complexity exponents are almost identical to those of the original model with homogeneous rates. Only in the dimerization scenario the time complexity exponent seems somewhat smaller, probably because heterogeneity in the rates influences the typical shapes in which clusters grow. In all cases, the time efficiency was reduced as a consequence of heterogeneous rates because small rates influence the overall effective timescale more significantly than the large rates.

**Reduced resource efficiency.** Finally, we altered the definition of the assembly time and explored its effect on the time complexity. In the main text we chose 90% yield as termination criterion for the assembly process. Here, we asked whether the exponents are invariant if a lower resource efficiency of only 50% yield is demanded. In all scenarios, the minimal time $T_{50}^{\min}$ required to achieve 50% yield is significantly smaller than $T_{90}^{\min}$. With the exception of the activation scenario, however, the corresponding time complexity exponents are indistinguishable from those determined for $T_{90}^{\min}$.

For the activation scenario, the exponent appeared to be a bit larger, very close to the theoretical value $\Theta_{\text{th}} = 2$. We relate this slight discrepancy between the two exponents to the fact that the yield transition curves in the activation scenario (compare main text Fig. 4B) become steeper if S is increased. This indicates that the real asymptotic exponent for the activation scenario lies between the exponents measured for $T_{50}^{\min}$ and $T_{90}^{\min}$. Note that, among the four scenarios, the time efficiency of the reversible binding scenario increases the most if lower resource efficiency is demanded.

**Annealing (reversible binding scenario).** The reversible binding scenario is controlled by the ratio between the detachment rate and the growth rate, given by the product of the binding rate $\nu$ and the concentration of monomers (see main text, paragraph reversible binding scenario). However, when more and more particles get attached during the assembly process, the concentration of monomers - if not replenished - gradually decreases. Consequently, the controlling parameter increases during the assembly process. In order to counteract this effect, a frequently used experimental approach consists in 'annealing' the system by decreasing the temperature (7). Typically, one starts at high temperature and gradually cools the system down to room temperature. Since the detachment rate decreases with decreasing temperature, $\delta \sim e^{-E_B/(k_B T)}$, if applied optimally, annealing allows to keep the ratio between detachment rate and growth rate constant during the assembly process. Here we ask how the time efficiency in the reversible binding scenario behaves under an optimal annealing protocol. To this end, we assume that the temperature adapts instantaneously to the momentary concentration of monomers such that the ratio between detachment rate and monomer concentration remains constant throughout the simulation. By varying this fixed ratio we determine the minimal assembly time $T_{90}^{\min}$ as in the main text. Indeed we find that the assembly efficiency can be significantly increased with an optimal annealing protocol, however, the time complexity exponent remains invariant (see Figure S5A, star marker).

**Alternate input functions (activation scenario).** For the activation scenario in the main text we assumed a constant influx of active monomers until all inactive monomers are depleted. Hence, the input as a function of time has a rectangular shape. A natural question that arises is whether the efficacy of the activation scenario can be altered by changing the temporal form of the input. To answer this question we simulated various different input functions which correspond to different biophysical processes providing the active monomers. Here we discuss one particular example for such a differing form of the temporal input which plays an important role in biology (8). Specifically, we assume that activation of monomers is no longer irreversible but, instead, monomers can switch back and forth between an assembly-active and inactive configuration (reversible activation cycle). Furthermore, we assume that this switching dynamics is fast compared to the assembly time scale and hence can be considered to be at equilibrium. The control parameter is the equilibrium constant $K$, which describes the ratio between the concentrations of active and inactive monomers. By measuring the minimal assembly time in the usual way, we find that the activation scenario becomes slightly more efficient through the reversible activation cycle but that the time complexity exponent remains invariant (see Fig. S5C, star marker).

Theoretically, the input can be described by any arbitrary function that integrates to the total particle number $N$. Note that input via fast reversible activation has a special significance because through equilibration it allows the net influx rate to dynamically adopt to the current state of the assembling system (fast binding of active monomers $\rightarrow$ fast net influx, and vice versa). We also tested some other input functions and observed that it generally seems to be favourable for the time efficiency if the input is higher at the beginning of the assembly process and lower towards the end. The measured time complexity exponents however remained invariant for all tested input functions.

This leads us to hypothesise that the time complexity exponent cannot be altered by the form the monomer input as long as all species are treated indifferently.

In conclusion, we tested how robust our results are with respect to modifications of the model, affecting the boundary of the structures, heterogeneities in the rates or the demanded resource efficiency. Furthermore, we investigated differing experimental protocols like annealing or variable input functions for the activation scenario. We found that while the assembly time does indeed depend on details of the model and the assembly protocol, the time complexity exponents - apart from minor deviations - remain invariant to such variations. Furthermore, the general trend in response to a particular model variation is typically the same in the different scenarios (an exception is the modification of the boundary condition in the JIS scenario). This confirms that the general conclusions in the main text on the time efficiency of the different scenarios and their relative ranking remain largely valid if details of the system are changed. On a broader perspective, this shows that the time complexity analysis yields a reliable, robust and informative characterization of self-assembly processes and the distinction of the four scenarios, characterized by different time complexity exponents, is meaningful and useful.

## 5. Experimental JIS supply protocol for the assembly of an artificial T=1 capsid

In this last chapter we aim to demonstrate the applicability of the just-in-sequence supply strategy for actual experimental problems of interest by proposing a specific supply protocol for the assembly of an artificial $T = 1$ capsid.

Artificial shells and capsids have important potential biotechnological applications ranging from the compartmentalization of chemical reactions to the usage as vesicles that enable pinpoint delivery of drugs or other material to specific loci within an organism (9, 10). Other applications intend to use artificial shells with an aperture in order to trap virus particles inside and thereby prevent them from interacting with the host cells (11). The hope is that in this way a broadly applicable antiviral platform can be created that can be utilized to combat a broad range of viral infections. Due to these promising applications, we illustrate the usage of the Jis strategy for the asssembly of artificial capsids.

The simplest icosahedral capsid is the $T = 1$ capsid (classification by Caspar and Klug (12)), which is assembled from 60 proteins. In the following, we discuss two possibilities to assemble artificial T=1 capsids irreversibly with high yield solely by regulating the supply of constituents. These strategies thereby avoid the necessity of fine-tuning the binding strengths or other molecular properties. The first possibility assumes a partly homogeneous design of the capsid (see Fig. S6A), while the second possibility relies on a fully heterogeneous design (Fig. S6C) of the structure.

In principle, the $T = 1$ capsid can be build fully homogeneously out of 60 identical units. However, in order to use the just-in-sequence supply strategy as described in the main text, some degree of heterogeneity is necessary: constituents that are provided in the same batch should not be able to bind each other but only to the existing structures. We therefore propose the partly heterogeneous design depicted in Fig. S6A, which exploits the symmetry of the target structure. Components that are indicated by the same letter are identical and bind specifically only with those species that are adjacent to them.

Designing structures as homogeneously as possible has three practical advantages. First, a lower number of different components needs to be produced and counted, which reduces the experimental effort. Second, self-assembly is faster if a single type of constituent can bind to several distinct sites in the structure and finally, as we discuss below, the absolute tolerance to external noise in particle numbers increases if structures are more homogeneous.

Note, however, that for the assembly of spherical objects like the T=1 capsid, a difficulty arises concerning the upper and the lower "cap", denoted here by A and L, respectively: If the caps are composed of several copies of a single species, these copies would be able to form homo-multimers when they are supplied, thereby undermining the JIS strategy. This challenge can be circumvented either by designing the caps heterogeneously or by making the respective bonds between the cap-species weak and reversible, thereby preventing spurious nucleation. Another possibility is to produce the caps A and L separately and supply them as single, complete units. In the following, for the assembly of the partly homogeneous capsid, we further discuss the second possibility, considering the caps A and L as single units.

Figures S6B and D show possible supply protocols for the assembly of the partly homogeneous and the heterogeneous T=1 capsid, respectively. Both of these protocols were found by maximizing the yield in the simulation. The second column in the tables indicates the species that are supplied in the respective batch, while the third column shows the numbers $Z_b$ that describe the excess concentrations supplied for the species in the respective batch, see Eqs. (1) and (2). The total number $N_b$ of particles for each species supplied in the $b^{\text{th}}$ batch (fourth column) is given by (compare

Eq. (2))

$$N_b = \deg \cdot \left( (1-p)N + pSN \frac{Z_b}{Z_{\text{tot}}} \right) , \qquad [38]$$

where deg is the *degeneracy* of the species, denoting the number of distinct binding positions per structure for this species in the respective assembly step. For the partly homogeneous capsid, the degeneracy is deg = 5 for all species except for the caps which are provided as complete units with degeneracy deg = 1. It is likely that the efficiency of the supply strategy can be further improved by allowing the pairs of species C and D, F and G, as well as I and J, which are supplied in the same batches, to be assigned different particle numbers. For simplicity, however, in this example we assign particle numbers only in correspondence to the batch number.

Figure S7A shows the yield plotted against the interval $\Delta T$ between successive batches both for the partly homogeneous and the heterogeneous $T = 1$ capsid. Black circles indicate the position of the optimal interval $\Delta T_{\text{opt}}$ that minimizes the time required to achieve 90% yield. The partly homogeneous capsids can be assembled in shorter time (provided that the same number of structures is assembled) because the binding speed is larger roughly by a factor of 5 compared to the fully heterogeneous $T = 1$ capsid.

In applications, particle numbers can only be determined with limited accuracy. Hence, it is an essential question how robust this approach is to extrinsic noise in the particle numbers. In order to test the robustness to extrinsic noise we choose particle numbers randomly from a Gaussian distribution and quantify the noise level in terms of the coefficient of variation (CV), defined as the standard deviation of the particle numbers relative to their respective mean. For simplicity, we assume that the CV is the same for all species. Figure S7B shows the yield plotted against the time interval $\Delta T$ for the partly homogeneous $T = 1$ capsid depending on the coefficient of variation. The inset shows the maximum yield (achieved for sufficiently large $\Delta T$) plotted against the CV, both for the partly homogeneous and the heterogeneous design. As a rough estimate, for the two supply protocols discussed here, particle numbers would need to be chosen with an accuracy of about 1% in order to achieve high yield. For a fixed relative strength of noise compared to the mean (CV), the partly homogeneous capsid is slightly more robust than the heterogeneous structure. This implies that the absolute tolerable variability in the number of particles per species is larger by at least a factor of 5 for the partly homogenous capsid compared to the heterogeneous capsid.

In conclusion, we found that both the partly homogeneously as well as the heterogeneously designed $T = 1$ capsid could be assembled efficiently with an irreversible just-in-sequence supply strategy provided that particle numbers can be determined accurately enough. The supply protocols discussed here still leave space for improvement, for example, by assigning particle numbers individually for each species rather than only in correspondence to the batch number. Furthermore, the excess concentrations were chosen in order to guarantee maximal yield for $\Delta T \to \infty$ but have not been optimized for maximal robustness to external noise. Those improvements might allow to even further improve the efficiency and robustness of the approach. Hence, provided that experimental methods for the accurate counting of molecules can be established, the JIS scenario offers a versatile strategy for the realization of biotechnologically relevant macromolecular structures. Our work therefore highlights how new experimental strategies to control concentrations could advance nanotechnology and its applications.

# Supplementary Figures

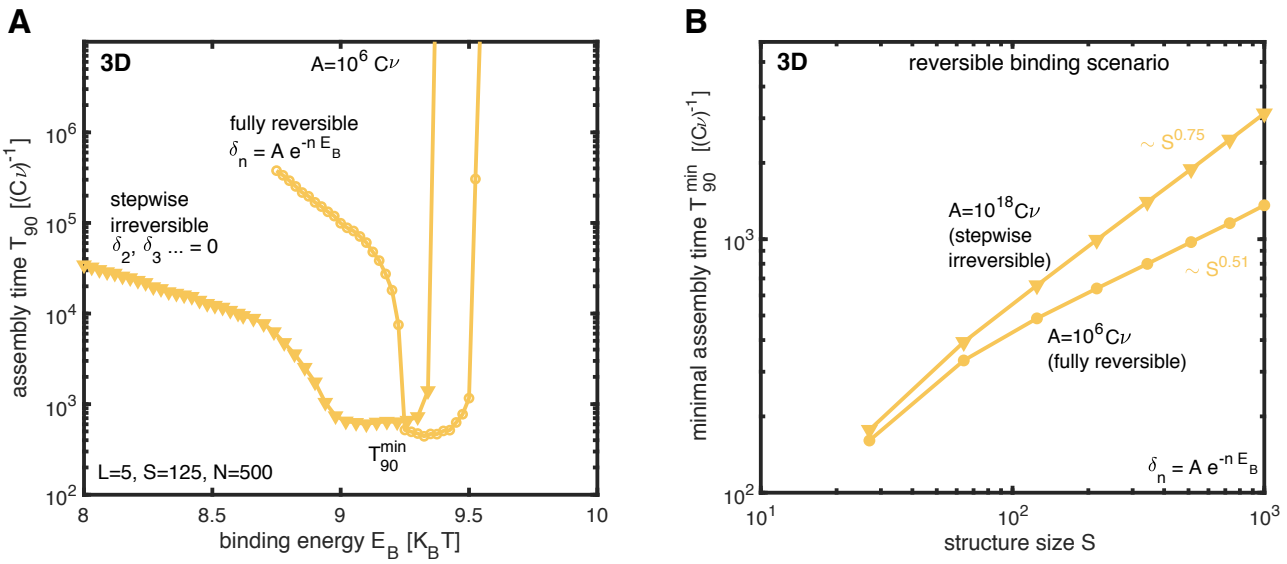


**Fig. S1. Reversible binding scenario: influence of the preexponential factor on the assembly time. A**, assembly time $T_{90}$ versus the binding energy $E_B$ for small preexponential factor $A = 10^6 C\nu$ (marker: circle) for three-dimensional structures of size $S = 125$. For comparison, we also plotted the stepwise irreversible case (marker: triangle) setting all detachment rates except for $\delta_1$ to 0. The stepwise irreversible case is equivalent to choosing $A$ large (in the main text: $A = 10^{18} C\nu$) as in both cases only $\delta_1$ is effectively larger than 0 and all other detachment rates are negligible at close-to-optimal binding energies. Hence, a small preexponential factor $A$ slightly decreases the minimal assembly time (compared to large $A$) at the cost of a reduced variability in the binding energy (fine tuning of $E_B$ (or of the concentration $C$) becomes more critical with small $A$). **B**, minimal assembly time $T_{90}^{\text{min}}$ versus the structure size $S$ for large (stepwise irreversible) and small (fully reversible) preexponential factor $A$. The minimal assembly time that can be achieved as well as the time complexity exponent are slightly smaller for a small preexponential factor.

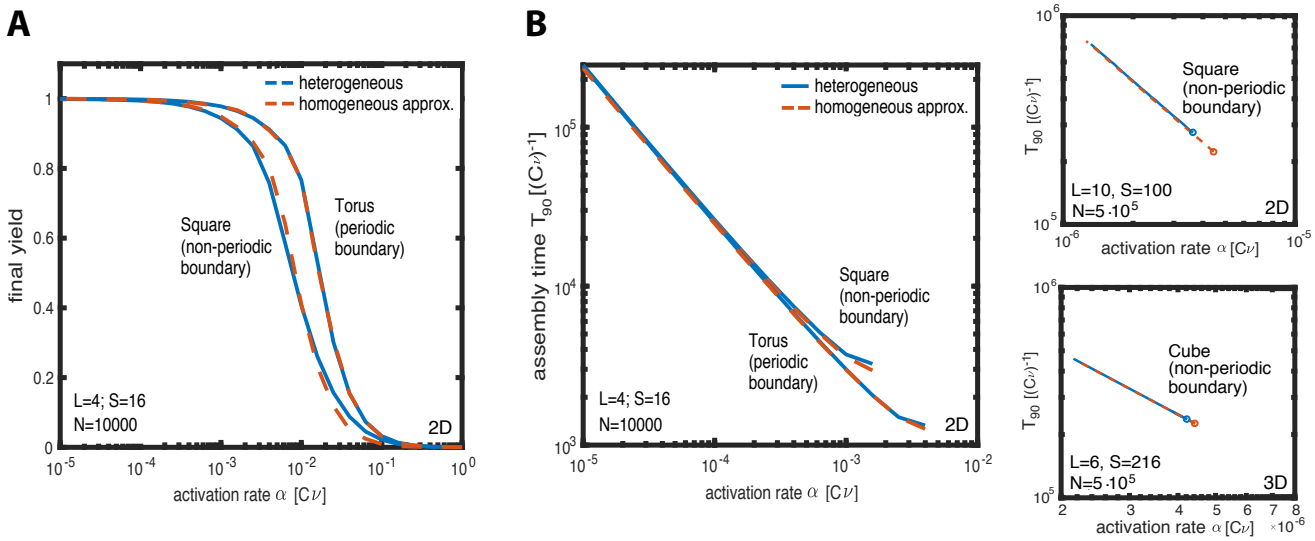


**Fig. S2. Accuracy of the homogeneous approximation in the activation scenario.** Final yield (**A**) and assembly time $T_{90}$ (**B**) versus the activation rate. Both quantities were simulated for two-dimensional structures with and without periodic boundaries as well as with distinguishable (heterogeneous, blue drawn line) and indistinguishable particle species (homogeneous approximation, red dashed line). For structures with periodic boundaries and large particle number $N$, the homogeneous and heterogeneous simulation coincide exactly as predicted by the theory. For structures with non-periodic boundaries, the homogeneous system yields an accurate approximation of the heterogeneous system, in particular if the target structure is small. For larger target structures in 2D, small deviations in the minimal assembly time are observed. For three-dimensional structures, these deviation are extremely tiny even for large target structures. We exploited this equivalence to reduce the computational cost by simulating the activation scenario as a homogeneous system with lower particle number. Generally, the heterogeneous system is subject to stochastic effects arising from fluctuations between the concentrations of the different species, unless the particle number $N$ is large (see (2)). The homogeneous system, in contrast, can be simulated with a much smaller total number of particles. The observed deviations suggest that the approximation slightly underestimates the time complexity exponent for two-dimensional heterogeneous structures by a few percent.

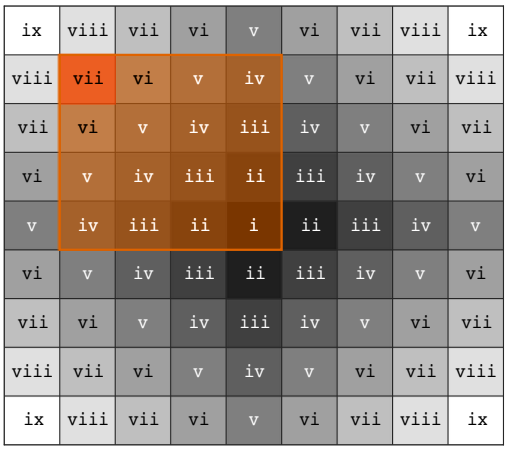


**Fig. S3. Assigning particle numbers in the Jis scenario.** The just-in-sequence scenario requires specified ratios between particle numbers in order to avoid excessive competition for resources (see Eq. (1)). Shown is the onion supply protocol (analogous to Fig. 5C) for a two-dimensional structure of size L=9 (S=81). Roman numbers indicate the batch number (assembly step) in which species are supplied. The shaded square marks all species that can initiate a complex potentially able to bind the species highlighted in red in the seventh assembly step. In order to minimize competition for resources, the species in the seventh batch must hence be supplied in excess concentration $Z_7$ proportional to the area of the square to allow all clusters present at the seventh assembly step to grow. Generalizing, we hence find the excess concentration $Z_n \sim \left(\frac{(n+1)}{2}\right)^2$ for a species supplied in the $n^{\text{th}}$ batch (compare Eq. (2)).

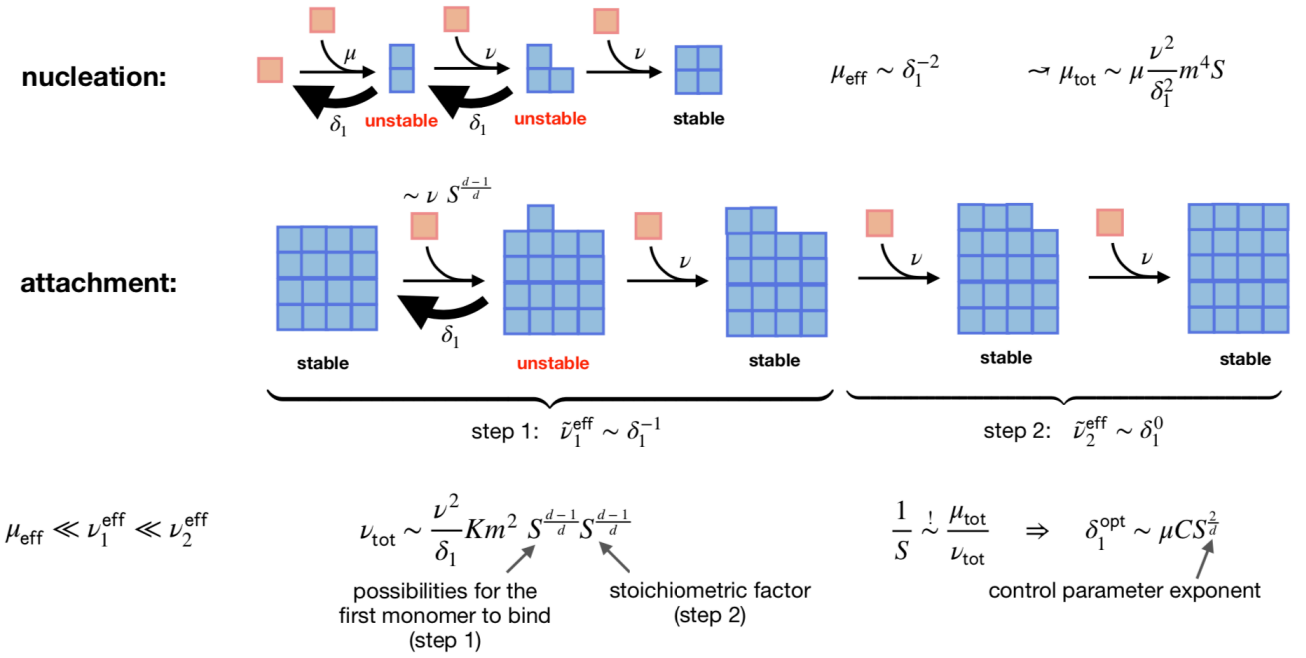


**Fig. S4. Scaling analysis of the reversible binding scenario.** In the reversible binding scenario, a stable nucleus forms by passing through two unstable intermediate states that decay with rate $\delta_1$. Hence, the effective rate for the nucleation process is $\mu_{\text{eff}} \sim \delta_1^2$. Attachment typically proceeds in two steps. In the first step, a monomer first binds reversibly and must subsequently be stabilized by a second monomer. Because one unstable state is passed, the first step effectively happens at rate $\nu_1^{\text{eff}} \sim \delta_1^1$. Subsequently to the first step, additional monomers can attach 'filling the row', while the configuration is continuously stable. Therefore, the second step can be assumed to be fast compared to the first step which, in turn, is fast compared to nucleation: $\mu_{\text{eff}} \ll \nu_1^{\text{eff}} \ll \nu_2^{\text{eff}}$. By setting the total nucleation rate into relation with the total effective attachment rate as detailed in section 3 of this SI, a rough estimate for the control parameter exponent and for the time complexity exponent can be derived.

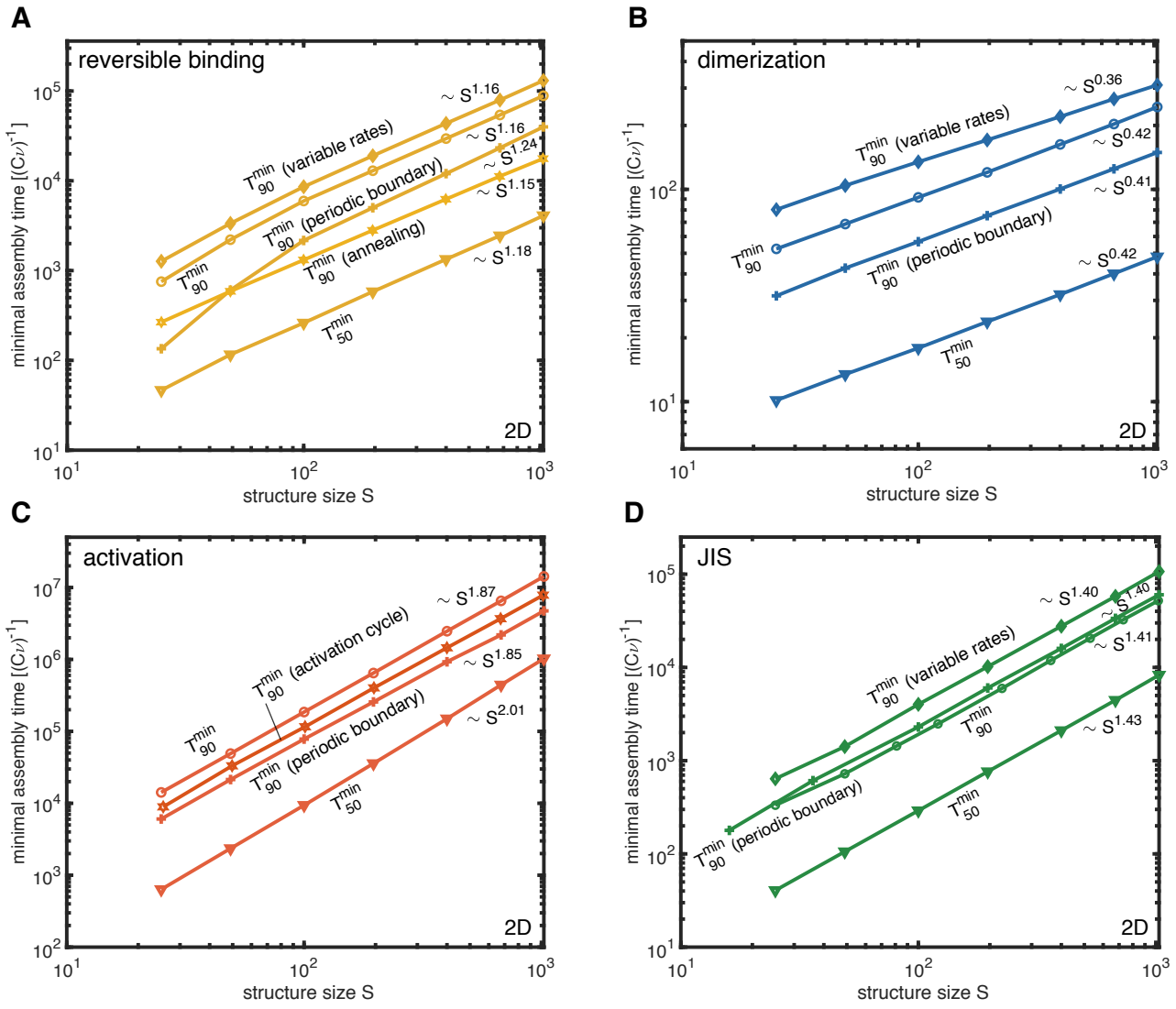


**Fig. S5. Scaling of the minimal assembly time for variants of the model and assembly kinetics.** The minimal time required to achieve 90% ($T_{90}^{\min}$) or 50% yield ($T_{50}^{\min}$) in the different scenarios (**A,** reversible binding; **B,** dimerization; **C,** activation and **D,** just-in-sequence scenario) is shown in dependence of the target structure size $S$ for two-dimensional structures and different variants of the original model. In each subpanel (scenario), the curve labeled $T_{90}^{\min}$ corresponds to the assembly time in the original model. Furthermore, each subpanel shows $T_{90}^{\min}$ for 2D structures with periodic boundary (tori) as well as for variable or heterogeneous rates of the constituent species (not available for the activation scenario), see section 4 of this SI. The curve labelled $T_{50}^{\min}$ shows the minimal assembly time for a lower resource efficiency of only 50% yield. While the assembly time varies for the different model variants, the measured time complexity exponents are, aside from small deviations, largely invariant. This indicates that the time complexity analysis of the self-assembly scenarios is robust and independent of many details of the model.

**A**

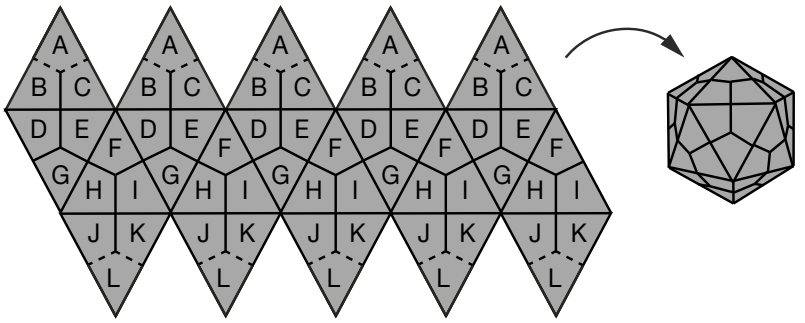


**B**

| batch number | supplied species | excess conc. $Z_b$ | particle number $N_b$ |
|---|---|---|---|
| 1 | A | 0 | 0.9N |
| 2 | B | 1 | 4.59N |
| 3 | C,D | 2 | 4.69N |
| 4 | E | 4 | 4.88N |
| 5 | F,G | 5 | 4.97N |
| 6 | H | 7 | 5.16N |
| 7 | I,J | 10 | 5.45N |
| 8 | K | 18 | 6.20N |
| 9 | L | 40 | 1.66N |

**C**

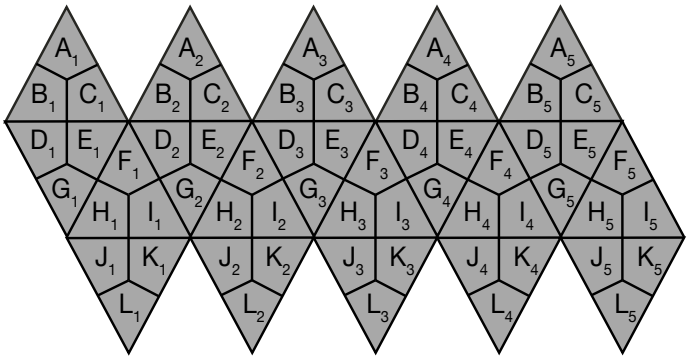


**D**

| batch number | supplied species | excess conc. $Z_b$ | particle number $N_b$ |
|---|---|---|---|
| 1 | $A_2$ | 0 | 0.930N |
| 2 | $A_1$, $A_3$ | 1 | 0.932N |
| 3 | $A_4$ | 3 | 0.935N |
| 4 | $A_5$ | 4 | 0.937N |
| 5 | B | 5 | 0.939N |
| 6 | C,D | 10 | 0.948N |
| 7 | E | 20 | 0.966N |
| 8 | F, G | 25 | 0.975N |
| 9 | H | 35 | 0.993N |
| 10 | I,J | 50 | 1.02N |
| 11 | K | 90 | 1.09N |
| 12 | $L_1$ | 95 | 1.10N |
| 13 | $L_2$, $L_5$ | 130 | 1.16N |
| 14 | $L_4$ | 170 | 1.24N |
| 15 | $L_3$ | 200 | 1.29N |

**Fig. S6. Capsid structure and supply protocols. A**, Partly homogeneous design of the T=1 capsid consisting of 60 subunits and 12 different species. Species of subunits are indicated by capital letters. It is assumed that each species binds specifically only with those species adjacent to it. Furthermore, we assume that the caps, each consisting of 5 subunits of A and L, respectively, are assembled separately and are supplied as complete single units. **B**, Just-in-sequence supply protocol that was simulated in order to assemble the capsid with the structure defined in (A). Columns indicate the species that are supplied in a respective batch, their excess concentration and their resulting total particle numbers assuming a fraction of unevenly distributed resources of $p = 0.07$ (cf. Eq. (38). Here, $N$ is the number of complete structures to be built if the yield were 100%. **C**, Heterogeneous design of the T=1 capsid consisting of 60 subunits and 60 different species. Each species occupies a single specified position in the structure. **D**, Just-in-sequence supply protocol for the heterogeneous structure described in (B). Letters without indices in the protocol represent all 5 corresponding species (for example $\mathrm{B} = \{\mathrm{B}_1, \mathrm{B}_2, \mathrm{B}_3, \mathrm{B}_4, \mathrm{B}_5\}$), which are supplied simultaneously. Note that for the heterogeneously designed capsid the caps are assembled from monomers as well.

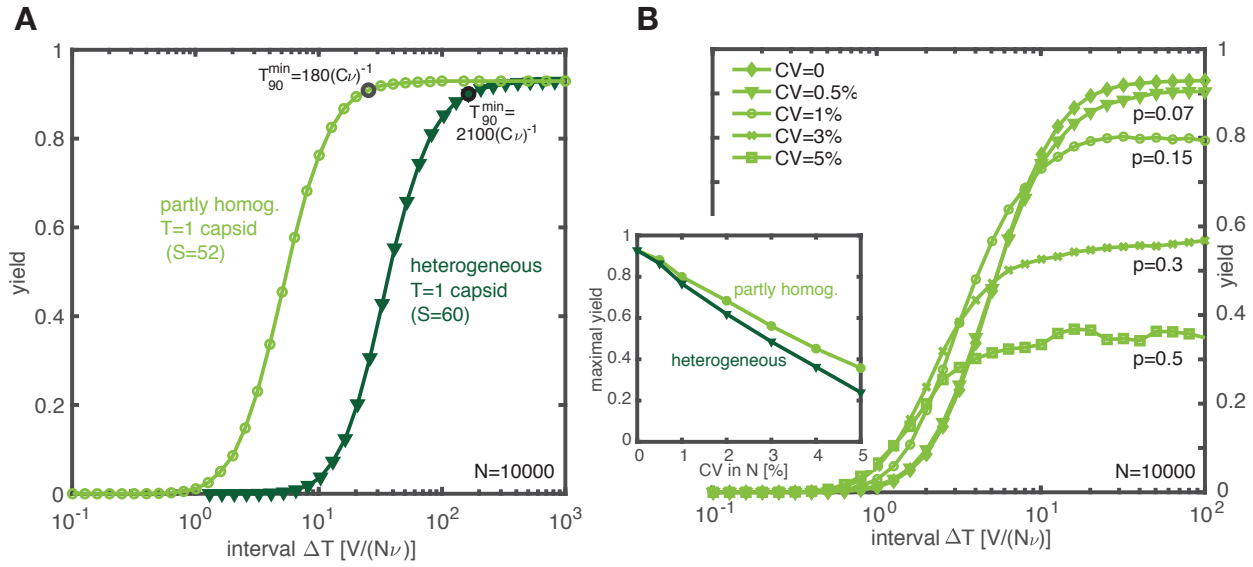


**Fig. S7. Jis scenario for the T=1 capsid. A**, Final yield plotted against the interval $\Delta T$ between subsequent batches both for the partly homogeneous and the heterogeneous capsid (see Fig. S6). Black circles indicate the position of the optimal interval $\Delta T_{\text{opt}}$ and the corresponding minimal assembly time $T_{90}^{\text{min}}$. Simulations were performed for a maximal number of complete structures $N = 10^4$ and a fraction of resources that are distributed unevenly of $p = 0.07$ (cf. Eq. (38), which limits the yield to 93%. The partly homogeneous structure can be assembled faster than the heterogeneous structure, mainly because the binding speed is larger by a factor of 5 in the partly homogeneous capsid. **B**, Yield plotted against the interval $\Delta T$ for different levels of external noise in the particle numbers for the partly homogeneous capsid. For each species, the particle number from the protocol was perturbed independently with a specified coefficient of variation (CV := Gaussian standard deviation / mean). Inset shows the maximal yield for sufficiently large $\Delta T$ plotted against the coefficient of variation for the partly homogeneous and the heterogeneous structure. The fraction $p$ of resources that were distributed unevenly was chosen as follows: $p = 0.07$ for CV$\leq$0.5%, $p = 0.15$ for CV=1%, $p = 0.2$ for CV=2%, $p = 0.3$ for CV=3%, $p = 0.36$ for CV=4% and $p = 0.5$ for CV=5%.

## References


1. DT Gillespie, Stochastic simulation of chemical kinetics. *Annu. Rev. Phys. Chem.* **58**, 35–55 (2007).
2. FM Gartner, IR Graf, P Wilke, PM Geiger, E Frey, Stochastic yield catastrophes and robustness in self-assembly. *Elife* **9**, e51020 (2020).
3. PD Schnier, JS Klassen, EF Strittmatter, ER Williams, Activation energies for dissociation of double strand oligonucleotide anions: Evidence for watson- crick base pairing in vacuo. *J. Am. Chem. Soc.* **120**, 9605–9613 (1998).
4. K Bielec, et al., Kinetics and equilibrium constants of oligonucleotides at low concentrations. Hybridization and melting study. *Phys. Chem. Chem. Phys.* **21**, 10798–10807 (2019).
5. D Endres, A Zlotnick, Model-based analysis of assembly kinetics for virus capsids or other spherical polymers. *Biophys. journal* **83**, 1217–1230 (2002).
6. JM Almendral, Assembly of simple icosahedral viruses. *Struct. physics viruses* **68**, 307–328 (2013).
7. CG Evans, E Winfree, Physical principles for dna tile self-assembly. *Chem. Soc. Rev.* **46**, 3808–3829 (2017).
8. GR Lazaro, MF Hagan, Allosteric control of icosahedral capsid assembly. *The J. Phys. Chem. B* **120**, 6306–6318 (2016).
9. JG Heddle, S Chakraborti, K Iwasaki, Natural and artificial protein cages: design, structure and therapeutic applications. *Curr. opinion structural biology* **43**, 148–155 (2017).
10. B Schwarz, M Uchida, T Douglas, Biomedical and catalytic opportunities of virus-like particles in nanotechnology. *Adv. virus research* **97**, 1–60 (2017).
11. C Sigl, et al., Programmable icosahedral shell system for virus trapping. *Nat. Mater.* **20**, 1281–1289 (2021).
12. DL Caspar, A Klug, Physical principles in the construction of regular viruses in *Cold Spring Harbor symposia on quantitative biology.* (Cold Spring Harbor Laboratory Press), Vol. 27, pp. 1–24 (1962).

# 3 A conceptual model of the just-in-sequence scenario

The goal of this chapter is to summarize our studies on the just-in-sequence scenario using a conceptual model. We plan to publish these results in the near future but a draft for a publication does not yet exist at the time of the original submission of this thesis.

## 3.1 Motivation

It was an essential finding of the last chapter and of our publication [2] that time efficient self-assembly can be achieved in heterogeneous systems by effectively regulating the temporal supply of the constituents. This is an important finding because supply control is, in principle, a simple strategy as it does not require fine-tuning of rate constants or rely on other sophisticated binding properties. This makes this approach particularly interesting for artificial self-assembling systems.
We called the scenario that implements such an effective supply control strategy 'just-in-sequence' scenario (Jis scenario). We described that in order to achieve efficient self-assembly with the Jis scenario for higher-dimensional target structures, it is essential that the species are provided in specific, non-stoichiometric concentrations. The underlying reason is that for two- and three-dimensional structures, an increasing number of complexes in the system continuously increases competition for resources. For one-dimensional target structures, on the other hand, it is not necessary that species are provided in non-stoichiometric concentrations because one-dimensional structures have a self-regulatory mechanism that keeps competition for resources at a constant level.
In this chapter, we study a conceptual model of the just-in-sequence scenario, which quantifies the underlying reason and the effect of this self-regulatory mechanism for one-dimensional structures and the difference to the higher-dimensional systems. The insights gained from this model will enable us to conceive three possible strategies to regulate competition in the higher-dimensional cases. The first strategy tries to mimic the self-regulatory mechanism of one-dimensional structures by selecting a very special assembly pathway. The second strategy stipulates that a small fraction of complexes is removed from the system after each assembly step in order to decrease competition among the remaining complexes. Complementarily, in the last strategy, species are provided in increasing concentrations with each assembly step in order to avoid competition. The effects of these strategies on the assembly process can easily be tested with the model. In particular, the model allows us to calculate the resulting parameter- and time complexity exponents analytically. We find that providing the constituents in increasing, non-stoichiometric concentrations leads to the lowest time complexity exponent and hence promises to be the most efficient implementation of the just-in-sequence scenario for higher-dimensional structures.

## 3.2 Model

The basic idea behind the Jis scenario is that the different species get activated in a sequence and assemble in consecutive assembly steps. Optimally, all structures should get initiated (dimerized) in the first assembly step and should only grow during the subsequent assembly steps. Hence, in the subsequent assembly steps, binding to the existing structures must be favoured and dimerization of additional complexes prohibited. There are two possible ways in order to reduce the dimerization probability in the subsequent assembly steps. One possibility consists in providing the different species in copy number of $N$ particles at fixed, equidistant time points $i\Delta T$, as was assumed in the previous chapter:

$$\frac{dA_i}{dt} = N\delta(t - i\Delta T)\,, \tag{3.1}$$

where $A_i$ denotes the concentration of active monomers of species $i$. By increasing the interval $\Delta T$, a larger fraction of the monomers of species $i$ will have bound before species $i+1$ gets activated. Consequently, the dimerization probability of species $i$ with species $i+1$ will be reduced by increasing $\Delta T$.
A different implementation of the Jis scenario stipulates that inactive monomers $I_i$ of species $i$ get activated slowly with rate $\alpha$ as soon as a fixed fraction $(1-q)$ of the monomers of species $i-1$ has bound:

$$\frac{dA_i}{dt} = \alpha I_i \Theta(qN - (I_i + A_i))\,, \tag{3.2}$$

$$\frac{dI_i}{dt} = -\alpha I_i \Theta(qN - (I_i + A_i))\,, \tag{3.3}$$

with initial condition $A_i(0) = 0$ and $I_i(0) = N$. We typically fix the fraction $q$ below which activation of the subsequent species starts as $q = 0.1$. Similar as in the activation scenario, the dimerization probability is then controlled by the activation rate $\alpha$: Reducing $\alpha$ decreases the momentary concentration of active monomers of species $i$ and $i+1$ and therefore prevents dimerization. This implementation of the Jis scenario will also play an important role in chapter 7 of this thesis. It is motivated rather in a cellular than in an experimental context. The idea is that via regulatory feedback, constituent species $i$ inhibits activation of species $i+1$ and only if the concentration of species $i$ drops below a threshold concentration, activation of species $i+1$ can start. In order to verify our results in this chapter, we use this second implementation of the Jis scenario.
In both implementations, however, the dimerization probability $p_d$ per assembly step is the basic quantity that needs to be controlled in order to achieve efficient self-assembly. Indeed, it can be shown that, in both implementations, the time required for an individual assembly step is inversely proportional to the dimerization probability[1] [2, 143]. Hence, in order to determine the time complexity exponent, it is enough to understand the dependence of the

[1] Precisely, for the first implementation, Eq. (31) in the Supplement of [2] shows that the concentration of unbound monomers at time $\Delta T$ (which corresponds to the amount of monomers that will dimerize when the subsequent species is supplied) is inversely proportional to $\Delta T$: $A_i(\Delta T) \sim \Delta T^{-1}$. Hence, the dimerization probability is inversely proportional to $\Delta T$. Similarly, for the second implementation, Eq. (3) in [143] states that the dimerization probability obeys $p_d = \frac{\alpha}{c\nu} \ln\left(\frac{\nu}{q\alpha}\right)$. Hence, by neglecting the logarithm and since $\alpha$ is inversely proportional to the time an individual assembly step takes, approximately, the assertion $p_d \sim \alpha \sim \Delta T^{-1}$ follows for this case as well.

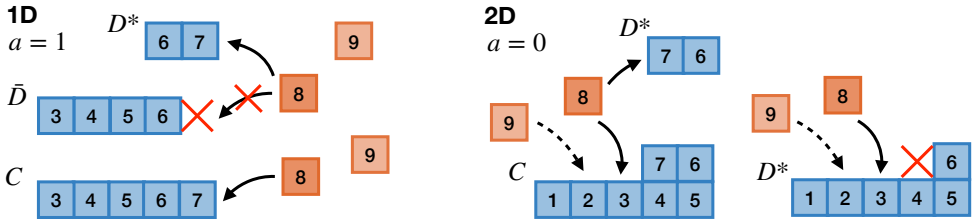


**Figure 3.1 | Competition in the 1D and 2D Jis scenario.** The illustration shows a snapshot of the assembly dynamics at the 8th assembly step for one- (left) and two-dimensional structures (right). In both cases, we assume that in the previous assembly step a monomer of species 6 has formed a dimer with species 7, which, in turn, has led to a shortage in the supply of species 7 causing a defect in one of the other complexes. In the one-dimensional case, due to the missing species 7, the defective complex is unable to bind species 8 or any other species supplied subsequently. Hence, this complex is *latent defective* ($\bar{D}$). In contrast, in the two-dimensional case, the defective complex can continue to grow (*active defective* ($D^*$)). This increases the number of active complexes and competition for resources: As there are more active complexes than supplied monomers in the 8th step, the remaining complete complex ($C$) has to compete with the two defective complexes for the resources to grow. In contrast, in the 1D case, the number of active complexes remains constant and there is no increased competition for resources in subsequent steps. The *defect exclusion factor* $a$ measures the tendency of a complex to become either latent or active defective upon suffering a defect.

yield on $p_d$. This reduction facilitates a simplified description of the Jis scenario, which we will introduce next.

In the simplified model for the Jis scenario, we distinguish three states of complexes, $C(s)$, $D^*(s)$, $\bar{D}(s)$, which denote, respectively, the concentrations of complete-, active defective- and latent defective complexes at the $s^{\text{th}}$ assembly step. A complex is called complete if it incorporates all species supplied up to the current assembly step. Otherwise, a complex is active defective if at least one species $j \leq s$ is missing but the complex can further grow in subsequent assembly steps (see Fig. 3.1). If a complex has a defect that disrupts its growth, it is called latent defective. Latent defective complexes are irrelevant for the subsequent assembly dynamics because they can no longer bind monomers. By $y := C + D^*$ we denote the total concentration of active complexes. All concentrations are measured in units of the (average) initial concentration of monomers per species. At each assembly step, there is a flux between these states: If a complete complex does not bind species $s$ in the $s^{\text{th}}$ assembly step, it becomes either active defective or latent defective, depending on whether a defect excludes the complex from further growth, see Fig. 3.1. Similarly, an active defective complex with a certain probability becomes latent defective if it misses a species in an assembly step. The *defect exclusion factor* $a$ quantifies the probability with which a defect disrupts the growth of a complex (excludes it from further growing). The parameter $a$ depends on the dimensionality of the structure and can be affected by the supply sequence (see below). For one-dimensional structures, a defect always leads to exclusion and hence $a = 1$ in the 1D case (see Fig. 3.1). For higher-dimensional structures, in contrast, a defect usually does not exclude a complex from further growth, yielding $a < 1$ or typically even $a = 0$.
The probability $\chi = \chi(s)$ for a complex to miss species $s$ in the $s^{\text{th}}$ assembly step is given by the shortage of the supply, $y(s) + p_d(s) - r(s)$, divided by the number of active complexes

$y(s)$, where $r(s)$ denotes the amount of resources put in in the corresponding assembly step. For example, suppose that there are $y = 90$ active complexes in the system and $p_d = 10$ additional dimerization events occur during the assembly step but only $r = 70$ monomers are provided. Then 30 complexes out of the 90 will miss a monomer in the assembly step and hence, a fraction $\chi = \frac{30}{90} = \frac{1}{3}$ of all complexes will get a defect.
On the other hand, spurious dimerization events create additional defective complexes. Unless dimerization happens between species 1 and 2, these newly formed complexes will necessarily be defective as they have no possibility to incorporate the previously supplied species. Sometimes, however, a newly emerging dimer will also not be able to incorporate *all* species supplied in subsequent assembly steps (see Fig. 3.3). Therefore, the *dimer growth factor* $b$ measures the extend to which a new dimer will be able to grow in subsequent steps. In other words, it quantifies the fraction of all subsequent species that the dimer will principally be able to incorporate. Effectively, this is taken into account by assigning only a fraction $b$ of newly emerging dimers to the active defective complexes and the remaining fraction $1 - b$ to latent defective complexes. For one-dimensional structures, we always have $b = 1$ while for higher-dimensional structures $b$ may be smaller than 1.

A diagram depicting the transitions between the three states of complexes together with the corresponding transition probabilities is shown in Figure 3.2. The transition probabilities describe the fluxes between these states at each assembly step. The system undergoes $S$ subsequent assembly steps, each of which is characterized by the same dynamics. Hence, we can interpret the variable $s$ as time and describe the whole process by an ordinary differential equation (ODE) in $s$. The resulting system of differential equations is shown in the box in Fig. 3.2. With the convention of measuring concentrations relative to the average initial concentration of monomers per species, the final yield is then identical to the concentration of complete complexes after the last assembly step: $\mathit{yield} = C(s = S)$. We can use this system of ODEs to describe different schemes and protocols for the Jis scenario. All relevant characteristics of the structure and the assembly protocol are thereby combined into the exclusion and growth factor $a$ and $b$.
The model can also be used to describe 'parallel' assembly protocols in which individual assembly steps are executed simultaneously (like the 'onion' protocol, see Fig. 3.3 and chapter 2). In this case, the assembly steps are treated by the model as if they were executed sequentially and the effect of parallelization is accounted for by appropriate choices of the parameters $a$ and $b$ (this will become clear below when we apply this explicitly to the onion protocol).

## 3.3 Results

We now use the simplified model in order to analyze different schemes of the Jis scenario and to understand how these variations affect the time complexity of the assembly process. First, we investigate the assembly of one-dimensional and higher-dimensional target structures using simple supply protocols. The insights gained from this analysis will enable us to bring forth more sophisticated assembly schemes and protocols that will optimize the time efficiency of the assembly process. In order to predict the yield, it is enough to know the concentration $C$ of complete complexes at the end of the assembly process. Since the dynamics of $C$ depends

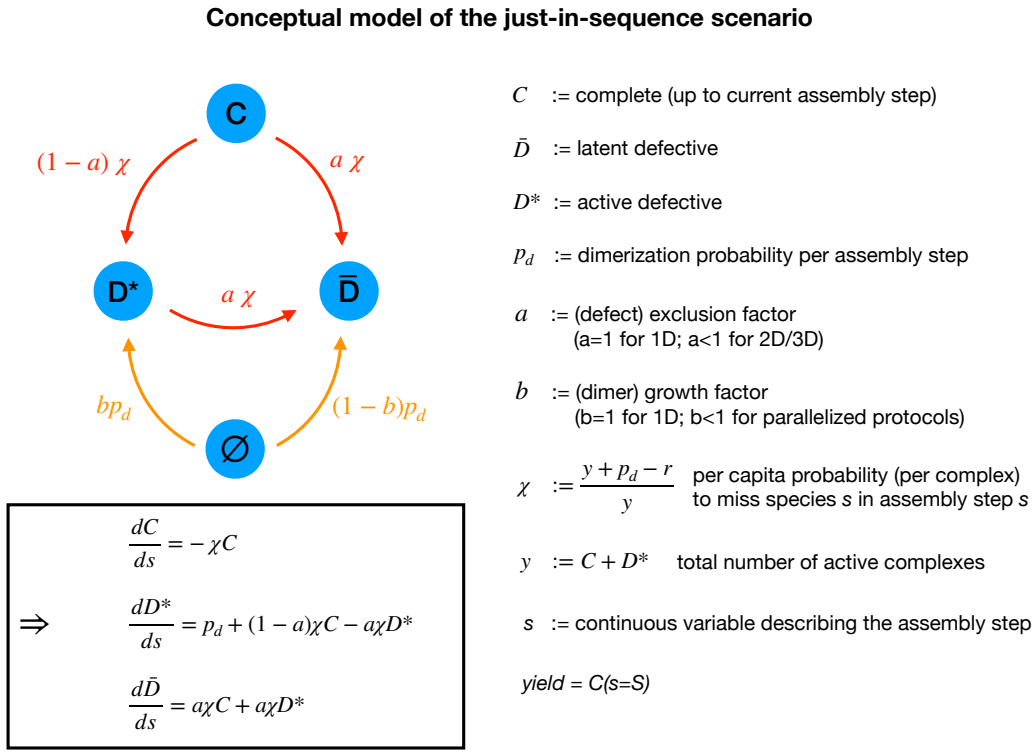


**Figure 3.2 | Conceptual model of the just-in-sequence scenario.** We describe the just-in-sequence scenario by a set of equations governing the flow between three states of complexes: $C$, complexes that are complete up to the current assembly step; $D^*$, defective complexes that are able to grow in subsequent assembly steps (active defective); and $\bar{D}$, defective complexes that are unable to grow in subsequent steps (latent defective); The flow between these states is determined by the probability $\chi$ for a complex to miss a species in an assembly step and the defect exclusion factor $a \in [0, 1]$. The defect exclusion factor measures the probability that a complex that has acquired a defect will be able to grow in subsequent steps. Furthermore, $p_d$ denotes the dimerization probability per assembly step, which creates a steady influx of defective complexes. The dimer growth factor $b \in [0, 1]$ measures to which extent a newly emerging dimer will be able to grow in subsequent assembly steps. The dynamic equations resulting from of the flows depicted in the diagram are shown in the box. The variable $s$, which we interpret as time, quantifies the number of the assembly step. The yield is then given by the concentration of complete complexes at $s = S$ (all concentrations are measured relative to the (average) concentration of particles supplied per species). Solving the dynamic equations in the following allows us to easily calculate the parameter and time complexity exponents for different schemes of the Jis scenario.

only on the concentration $y$ of active complexes (see box in Fig. 3.2), the system can be reduced to two coupled ODEs:

$$\frac{dy}{ds} = \frac{dC}{ds} + \frac{dD^*}{ds} = bp_d - a\chi(C + D^*) = bp_d - a(y + p_d - r)\,, \tag{3.4}$$

$$\frac{dC}{ds} = -\frac{y + p_d - r}{y} C\,, \tag{3.5}$$

where $r = r(s)$ is the amount of resources put in in the $s^{\text{th}}$ assembly step. First, we assume that all species are supplied in equal amounts, i.e. $r = 1$, and we apply the initial conditions $C(0) = y(0) = 1$. We start by analyzing the assembly of one-dimensional target structures.

### 3.3.1 One-dimensional target structures ($a = 1$, $b = 1$)

One-dimensional structures are characterized by $a = b = 1$, see Fig. 3.1. Hence, the dynamics of $y$ simplifies to

$$\frac{dy}{ds} = 1 - y\,. \tag{3.6}$$

With the initial condition $y(0) = 1$, this has the solution $y(s) = 1$. Hence, for one-dimensional structures, the concentration of active complexes remains constant throughout the assembly process. Using this result in the equation for $C$ gives

$$\frac{dC}{ds} = -p_d C\,, \tag{3.7}$$

which, with $C(0) = 1$, is readily solved by $C = e^{-p_d s}$. Thus we obtain for the final yield

$$\text{yield} = C(s = S) = e^{-p_d S} \approx (1 - p_d)^S\,. \tag{3.8}$$

This result for the yield is consistent with our result in [4] (see chapter 7). Solving the equation for the dimerization probability yields

$$p_d = \frac{-\log(\text{yield})}{S}\,. \tag{3.9}$$

Therefore, in order to obtain a constant yield, the dimerization probability must scale inversely proportional with the structure size, $p_d \sim S^{-1}$. Because the time that an individual assembly step takes scales inversely with $p_d$ (see footnote above), the total assembly time for $S$ subsequent assembly steps scales as $T \sim S^2$. This yields a time complexity exponent of $\theta = 2$ for the 1D Jis scenario, in accordance with [2] and [143]. The characteristic property for one-dimensional structures is that, due to $a = 1$, the concentration of active complexes remains constant throughout the assembly process and hence competition for resources does not increase.

### 3.3.2 Higher-dimensional target structures ($a = 0$, $b = \text{const}$)

Next, we consider the assembly of two- and three-dimensional structures with the snake and onion supply protocol, both of which are characterized by $a = 0$ and $b = \text{const}$ (see Fig. 3.3). In this case, the dynamics of $y$ (Eq. (3.4)) reduces to $\frac{dy}{ds} = b\,p_d$, which has the solution $y(s) = 1 + sbp_d$. Hence, because the growth exclusion factor is 0, any dimerization probability larger than 0 will lead to a steady increase of the number of active complexes. Consequently, it follows for the dynamics of $C$ (Eq. (3.5)),

$$\frac{dC}{ds} = -\frac{sbp_d + p_d}{1 + sbp_d} C\,, \tag{3.10}$$

which is solved by separation of variables to give $\log(C) = -s - \frac{p_d - 1}{bp_d} \log(1 + bp_d s)$, and hence it follows for the yield,

$$\log(\text{yield}) = -S - \frac{p_d - 1}{bp_d} \log(1 + bp_d S)\,. \tag{3.11}$$

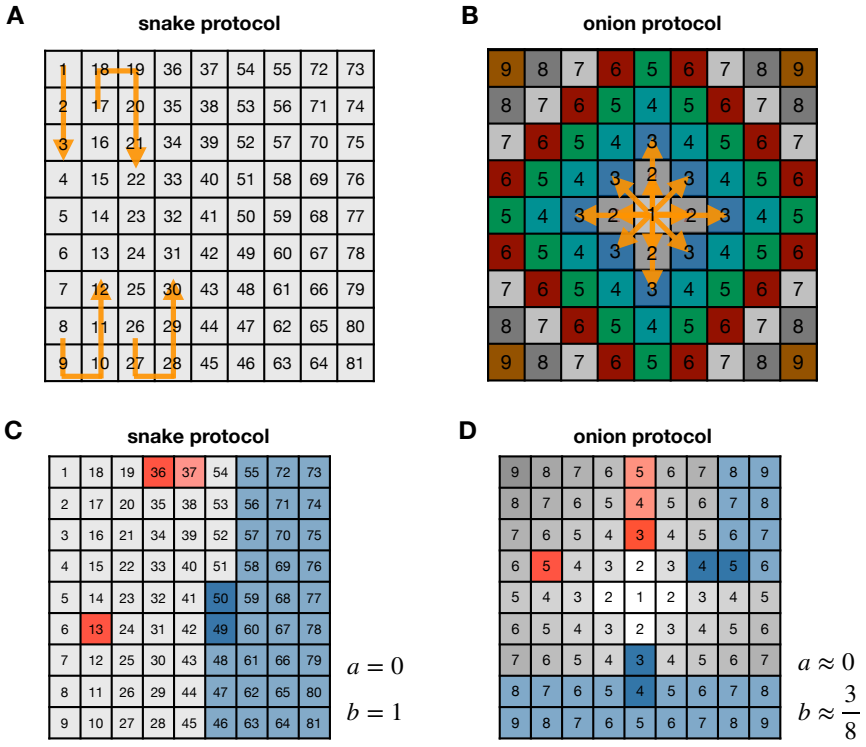


**Figure 3.3 | Snake and onion protocol.** **A**, **B**, supply sequences in the snake and onion protocol for 2D structures are represented by roman numbers (numbers do *not* indicate the species but the batch in which a species is supplied, also see previous chapter). In the snake protocol (A), the species are supplied sequentially one at a time and the structure is assembled column-wise from the left to the right. In the onion protocol (B), the structure is assembled radially from the inside outward. Species that are indicated by the same roman number and marked by the same color (forming the 'skins of the onion') are supplied simultaneously. Hence, a much lower total number of batches is needed for the onion protocol compared to the snake protocol. **C**, **D**, Illustration of the effect of a defect (red shading) and dimerization (blue shading). In bright red, we mark the species that are excluded from being incorporated into a structure as a consequence of a defect (intense red shading) and the specific supply order. Similarly, in light blue, we mark all species that can be incorporated by a newly formed dimer (intense blue). The defect exclusion factor $a$ (dimer growth factor $b$) can be interpreted as the average proportion of excluded species (species that can be incorporated by the dimer) on the number of species yet to be supplied. Hence, the sizes of the shaded regions (when averaged over all species) provide information about the exclusion and growth factor. In the onion protocol, we find that only defects on the horizontal or vertical axis exclude other species from being incorporated while in all other regions a defect has no further effect. Since the proportion of the two axes on the whole square vanishes in the limit $S \to \infty$, we can set $a = 0$ in order to investigate the time complexity for large structures. Similarly, when calculating $b$ in this way we obtain a value between $\frac{1}{4}$ and $\frac{3}{8}$.

We consider the limit $S \to \infty$ and $p_d \to 0$ assuming that $p_d S \to 0$ (which we will verify a posteriori). Expanding the logarithm on the right hand side to second order in $p_d S$, we obtain

$$\log(\text{yield}) = -S - (p_d - 1)S + \frac{1}{2}(p_d - 1)bp_d S^2 + O(p_d^2 S^3) \approx -\frac{1}{2}bp_d S^2 \tag{3.12}$$

to leading order. Hence, it follows that in the limit of large $S$,

$$p_d = \frac{-2\log(\text{yield})}{bS^2}\,, \tag{3.13}$$

and thus $p_d \sim S^{-2}$. This confirms our above assumption $p_d S \to 0$. Because the snake protocol requires $\sim S$ batches and the onion protocol $\sim S^{\frac{1}{2}}$ (2D structures) or $\sim S^{\frac{1}{3}}$ (3D structures) batches, we expect $T \sim S^3$ (snake protocol) and $T \sim S^{2.5}$ (2D onion protocol) or $T \sim S^{2.33}$ (3D onion protocol). Hence, despite the possibility of using parallel assembly protocols in higher dimensions like the onion protocol, which require a lower number of batches, the time efficiency is significantly reduced compared to the one-dimensional case. This inefficiency is a consequence of the steady increase of the number of active complexes in the higher-dimensional Jis scenario.

Intuitively, the negative effect of enhanced competition due to an increasing number of active complexes can be understood as follows: Suppose that in the $s^{\text{th}}$ assembly step an additional active complex is formed. Hence, in all $S - s$ subsequent assembly steps there is one more active complex than monomers that will be provided. In the worst case, in each subsequent assembly step the additional complex can 'take' a monomer from a different complete complex and interrupt its growth. Therefore - on average - the total reduction of the final yield induced by only one additional complex scales like $\sim S$. Consequently, in order to obtain a high yield, the dimerization probability must be controlled $\sim S$ times more tightly than in the one-dimensional case. This explains why the time complexity exponent for the snake protocol $\theta = 3$ is by 1 larger than the time complexity exponent for 1D structures $\theta = 2$.

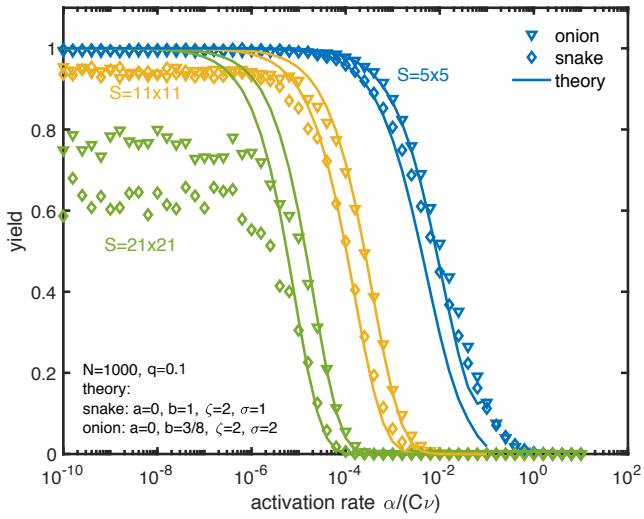


**Figure 3.4 | Testing the theory.** The yield from stochastic simulations (markers) of the snake and onion protocol for two-dimensional target structures of different sizes is compared to the theoretical prediction of the model (drawn lines). To this end, for each activation rate $\alpha$, the corresponding dimerization probability $p_d$ has been calculated numerically using the theory presented in chapter 7 [4]. Subsequently, the ODE system 3.4 has been integrated numerically with the given dimerization probability. The theory describes the onset of the yield very well for large structure sizes. However, it does not capture the stochastic yield drop resulting from a finite particle number.

In order to verify our results and the general validity of the model, we compare in Figure 3.4 the results of the stochastic simulation with the prediction of the model. Specifically, we simulated the onion and the snake protocol for two-dimensional structures of different sizes

(see last chapter for details of the simulation) and plotted the final yield against the activation rate for the implementation of the Jis scenario as given by Eq. (3.2)). In order to make the theoretic prediction for the yield, we first calculated the expected dimerization probability $p_d$ from the activation rate by using the theory that is presented in chapter 7 [4]. Subsequently, we integrated the system (3.4) and (3.5) numerically in order to calculate the final yield. Indeed, for larger structures, the theory predicts the onset of the yield very well. However, in the limit of small $\alpha$, the yield in the simulation does not reach the predicted maximal value of 1. This phenomenon can be attributed to stochastic effects because the particle number $N$ is too small. Because this is a finite size effect, the yield drop is not captured by the deterministic theory (see chapter 7 for more details). Thus, we conclude that the model predicts the yield correctly under the condition that the particle number $N$ is large enough.

### 3.3.3 Higher-dimensional target structures with $0 < a < 1$ and $b = \text{const}$

We have found that the growth exclusion factor $a$ is an important determinant for the efficiency of the assembly process. For one-dimensional structures the exclusion factor is always 1, while for higher-dimensional structures it is typically 0, which results in the low efficiency of the process. Hypothetically, how would the assembly time behave for a constant exclusion factor larger than 0 but smaller than 1? And could such a scenario be realized, for example with the help of a special supply protocol for higher-dimensional target structures? First, we will apply the usual formalism to calculate the time complexity for the hypothetical case with $0 < a = \text{const} < 1$. Afterwards we try to answer whether such a solution could exist in practice.
For a constant exclusion factor $a$ it follows from Eq.(3.4) for the dynamics of $y$:

$$\frac{dy}{ds} = bp_d - a(y + p_d - 1)\,, \tag{3.14}$$

which is solved by $y(s) = 1 + p_d \frac{b-a}{a}(1 - e^{-as})$. Hence, in the limit of large $s$, the concentration of active complexes converges to a constant.

$$y(s) \xrightarrow[s\to\infty]{} 1 + p_d \frac{b-a}{a} =: 1 + p_d w = \text{const.} \tag{3.15}$$

Using this result for the dynamics of $C$ in Eq.(3.5), we obtain

$$\frac{dC}{ds} = -\frac{y + p_d - 1}{y} C = -\frac{p_d w + p_d}{1 + p_d w} C\,, \tag{3.16}$$

which gives $\log(C) = -\frac{p_d w + p_d}{1 + p_d w} s$, and hence, with $C(S) = \text{yield}$,

$$p_d = \frac{-\log(\text{yield})}{S\left(w + 1 + w\frac{\log(\text{yield})}{S}\right)} = \frac{-\log(\text{yield})}{\frac{S}{a}\left(b + (b-a)\frac{\log(\text{yield})}{S}\right)} \xrightarrow[S\to\infty]{} -\frac{a}{b}\frac{\log(\text{yield})}{S} \sim S^{-1}\,. \tag{3.17}$$

Therefore, the time complexity for a hypothetical case with $1 > a > 0$ will be the same as for the one-dimensional case with $a = 1$. For example, an exclusion factor of $a = \frac{1}{2}$ might signify that only every other species, if missing in a complex, prevents the complex from further growing. In the following, we refer to these species as *disruptive species*. The calculation

shows that, theoretically, even a small fraction of disruptive species would suffice to regulate the number of active complexes and hence to induce the same time complexity exponent as for 1D structures. How could such a supply protocol be realized?

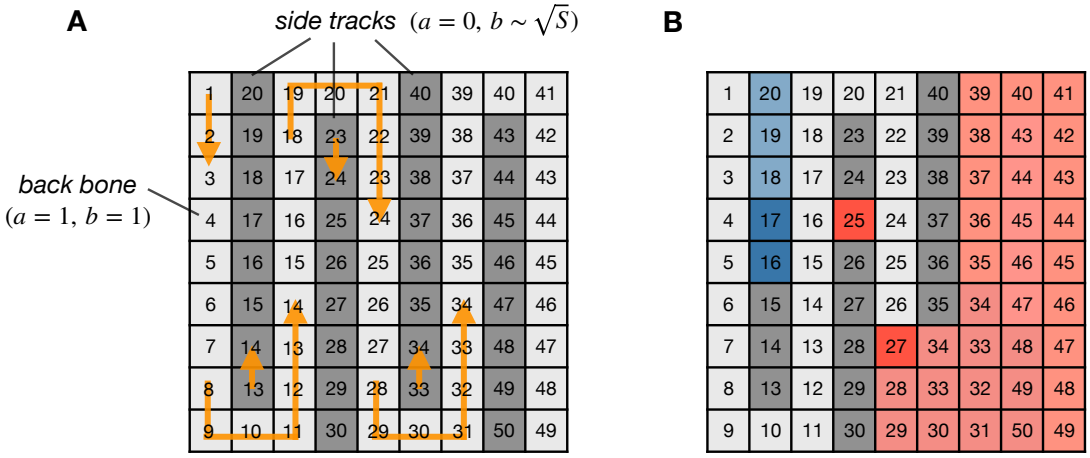


**Figure 3.5 | Back bone protocol. A,** Supply order in the back bone protocol. The structure is divided into two parts: The *back bone*, which follows a similar supply path as the snake protocol but leaves out every second column in the structure. These left-out columns are called the *side tracks*, which are assembled independently from the back bone. Importantly, the supply order is such that assembly of the back bone is always slightly ahead of the respective side track. In this way, if a defect occurs in the back bone, the growth along the back bone cannot be resumed through the side tracks, as the side tracks are assembled afterwards. Since the back bone itself is effectively a one-dimensional structure, this implies that the growth along the back bone will break up and without the back bone as scaffold, the subsequent side tracks can also not be assembled any more. Hence, a defect in the back bone disrupts the growth entirely. On the other hand, a defect in the side track has no effect. The effects of a defect and a dimerization event are illustrated in **B**, analogously to Fig. 3.3. Because the growth exclusion factor $a$ for defects on the back bone is 1, we expect the back bone protocol to be more time efficient than the snake protocol.

In order to investigate the potential of such a self-regulatory mechanism for higher-dimensional structures, we study the *back bone* protocol for 2D structures, see Fig. 3.5. In the back bone protocol, we distinguish two different regions of the structure, the back bone and the side tracks. The back bone forms the scaffold into which the species of the side tracks integrate. The supply oder is depicted in Figure 3.5. As a consequence of the supply order, assembly of the back bone is always slightly ahead of the side tracks. Therefore, if a defect occurs in the back bone, the structure cannot continue to grow[2]. Hence, all species that form the backbone are disruptive species. On the other hand, if a defect occurs in the side tracks, the structure will continue to grow. Thus, we have $a \approx 1$ for the back bone and $a = 0$ for the side tracks. On average, as there are roughly as many back bone species as side track species, we have $a_{\text{av}} \approx \frac{1}{2} = \text{const}$ and hence we would expect $p_d \sim S^1$. However, the simulation shows that the scaling is not as good as expected and the back bone protocol is only slightly more efficient than the snake protocol (see Fig. 3.6). The apparent reason why it is less efficient than expected is because averaging $a$ between the back bone and the side tracks is not valid. The real exponent is revealed by calculating the yield of the back bone and the side tracks

[2] only parts of the adjacent side tracks can still be finished if a defect occurs in the back bone but then the growth will stop

independently. The final yield is then the product of the yield of the back bone and the yields of the side tracks. Since the back bone has $a = 1$ and consists of roughly $S/2$ species, its yield, according to Eq. (3.8), is $e^{-p_d \frac{\sqrt{S}}{2}}$. Each side track is a structure with $a = 0$ and consists of $\sim \sqrt{S}$ species and hence, according to Eq. (3.12), has a yield $e^{-\frac{1}{2}p_d S}$. Because there are $\sim \frac{\sqrt{S}}{2}$ side tracks in total, the final yield is given by

$$\text{yield} = e^{-\frac{1}{2}p_d\sqrt{S}} \cdot \left(e^{-\frac{1}{2}p_d S}\right)^{\sqrt{S}/2} = e^{-\frac{1}{2}p_d S - \frac{1}{4}p_d S^{3/2}} . \tag{3.18}$$

Hence,

$$p_d = \frac{-\log(\text{yield})}{\frac{1}{2}S + \frac{1}{4}S^{3/2}} \sim S^{-\frac{3}{2}} , \tag{3.19}$$

to leading order, instead of $p_d \sim S^{-1}$ as predicted by the calculation above with an average $a_{\text{av}} = \frac{1}{2}$. The time complexity exponent $\theta = -\frac{3}{2}$ for the back bone protocol is confirmed by the stochastic simulation, see Fig. 3.6. Hence, we conclude that simply averaging $a$ is not valid if there are non-disruptive regions in the structure that increase in size with $S$. In other words, averaging $a$ is only valid if the 'distance' between any non-disruptive and the next disruptive species in the assembly path is independent of $S$. In the back bone protocol, the side tracks are connected non-disruptive regions of increasing size and hence, their size-scaling limits the scaling of the time efficiency. Because we did not find a way to construct a supply protocol without any increasing non-disruptive regions, we claim that, with this approach, the time complexity cannot be improved beyond $T \sim S^{\frac{5}{2}}$. Still it is remarkable that the time complexity of the snake protocol can be improved only by slightly changing the supply order.

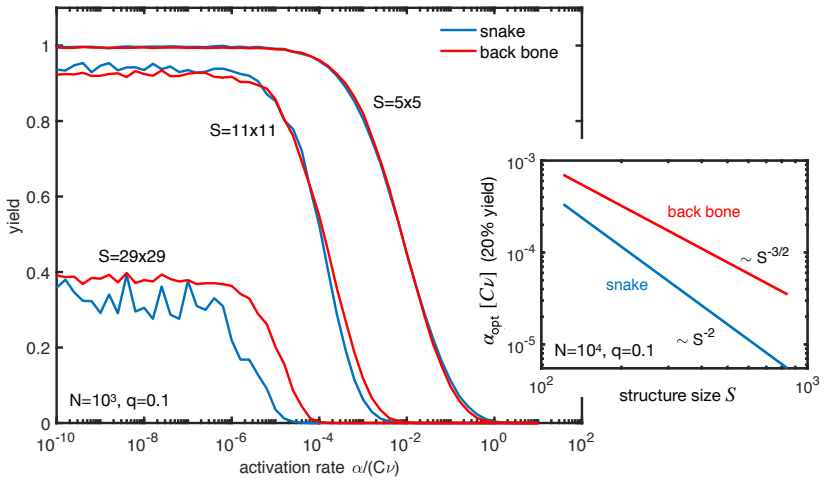


**Figure 3.6 | Comparison between back bone and snake protocol.** The yield obtained from stochastic simulations with the back bone and the snake protocol is plotted against the activation rate for different sizes of the target structure. Inset shows the scaling of the optimal activation rate (to achieve 20% yield) with the structure size. For the back bone protocol we measure a parameter exponent of $\phi = -1.5$ versus $\phi = -2$ for the snake protocol. Hence the back bone protocol is more time efficient than the snake protocol for large structure sizes.

### 3.3.4 Increasing assembly efficiency by removing complexes

Even though generic supply protocols with an effective average $0 < a < 1$ presumably do not exist, the regulatory mechanism behind this idea could be implemented differently. The underlying mechanism to make supply protocols with $a = \text{const} > 0$ efficient is that intermediate disruptive species would regulate competition by converting active complexes into latent defective complexes. Instead of converting active complexes into latent complexes, one could likewise remove them entirely from the system, for example, by some outflux. In order to test this idea with our formalism, we assume that after each assembly step, there is a constant (per capita) outflux rate $\delta$ for all kinds of complexes. The dynamics of active complexes then has to be extended by this outflux term:

$$\frac{dy}{ds} = bp_d - a(y + p_d - 1) - \delta y\,. \tag{3.20}$$

Optimally, the outflux should be such that the concentration of active complexes is held constant throughout the process: $\frac{dy}{ds} = 0$ and hence $y = y(0) = 1$. From this condition, it follows that

$$\delta = p_d(b - a)\,. \tag{3.21}$$

The dynamics of the complete complexes (assuming $y = 1$) also has to be extended by the outflux term:

$$\frac{dC}{ds} = -p_d C - \delta C = -C p_d(1 + b - a)\,, \tag{3.22}$$

which can be solved to give: $\text{yield} = e^{-p_d(1+b-a)S}$. Therefore,

$$p_d = \frac{-\log(\text{yield})}{(1 + b - a)S} \sim S^{-1}\,. \tag{3.23}$$

For the snake protocol we thus expect a time complexity of $T \sim S^2$. It seems paradoxically that by removing complete complexes during the assembly process, the assembly efficiency can be increased and the time complexity exponent be reduced. The explanation of this apparent paradox is that the effect of increased competition due to additional complexes is way worse than the effect of losing a few complexes in each assembly step. Figure 3.7A shows the yield plotted against the activation rate for the snake protocol with ($\delta > 0$) and without ($\delta = 0$) removing complexes after each assembly step. We find that if complexes are removed, the assembly process is significantly more efficient and more robust to stochastic effects for large structure sizes. The simulation also confirms the expected parameter scaling $\alpha_{\text{opt}} \sim p_d \sim S^{-1}$ for the snake protocol for large $S$ (Fig. 3.7 inset).

The hope is that the same strategy of removing complexes can also be applied for the onion protocol. If the parameter scales identically, due to the lower number of batches in the onion protocol, this would imply a time complexity exponent of $\theta = \frac{3}{2}$ for 2D structures. However, from the simulation, we only find a parameter exponent of $\frac{3}{2}$, implying a time complexity exponent of 2 (see Fig. 3.7 inset). The reason for the deviant scaling is that removing complexes only reduces competition between species that are supplied consecutively, but not between species that are supplied simultaneously in the same batch. Hence, since the average size of the batches increases like $\sim S^{\frac{1}{2}}$ in the onion protocol, the parameter scales with $\sim S^{\frac{3}{2}}$ instead of $\sim S^1$.

Thus, removing complexes during the assembly process works fine for the snake protocol but

does not have the desired effect for parallel protocols like the onion protocol because there is still competition for species that are provided simultaneously (in the same batch). Both for the snake and the onion protocol we thus obtain a time complexity of $T \sim S^2$.

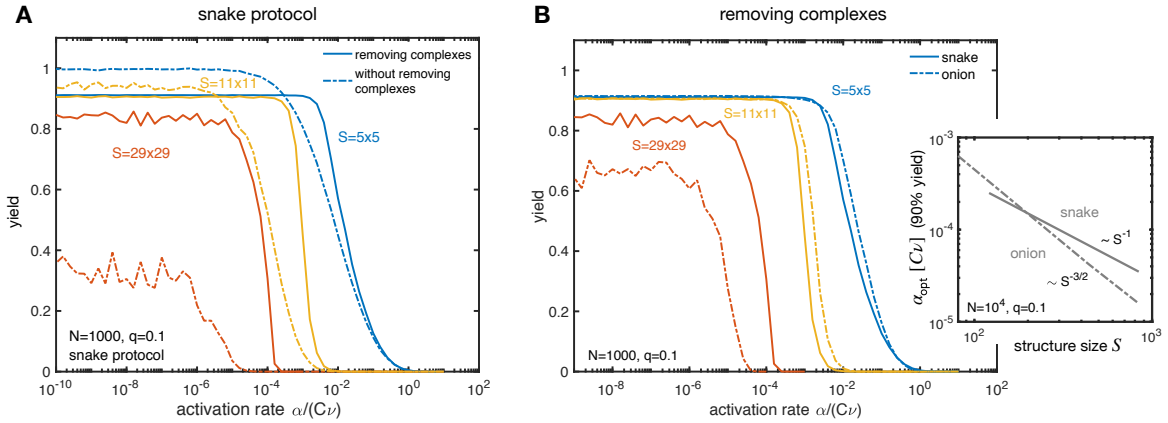


**Figure 3.7 | Removing complexes to enhance assembly efficiency. A,** The yield obtained from stochastic simulations is plotted against the activation rate for the snake protocol both with a finite outflux ($\delta = 0.1\frac{1}{S} > 0$) of complexes (drawn lines) and without outflux ($\delta = 0$; dash-dotted lines). The outflux was implemented by removing a fraction $\delta$ of all complexes after each assembly step. Due to the outflux of complexes, the yield that can maximally be achieved for this choice of $\delta$ is roughly 90%. Nevertheless, for any yield smaller than 90%, self-assembly is found to be significantly more time efficient and robust to stochastic noise if complexes are removed. **B**, Comparison between the snake and the onion protocol with outflux rate $\delta = 0.1\frac{1}{S}$. Inset shows the scaling of the optimal activation rate (to achieve 90% yield) with the structure size for large particle number $N$. We measure a parameter exponent of $\phi \approx -1$ for the snake and $\phi \approx -1.5$ for the onion protocol.

### 3.3.5 Increasing assembly efficiency with non-stoichiometric concentrations

Instead of continuously decreasing the number of complexes in the system, one could approach the problem of reducing competition the other way round, namely by increasing the amount of resources put in with each assembly step. In this way, despite the number of active complexes increases continuously, as species further downward in the assembly sequence are provided in larger concentrations, all active complexes can nevertheless be permitted to grow in each assembly step. Therefore, competition is reduced to a minimum. Furthermore, because resource consumption is an individual process for each species, there is the hope that this strategy is also fully compatible with parallel supply protocols like the onion protocol. In order to calculate the time complexity exponent of this strategy with our formalism, we assume that the resource input $r(s)$ in Eq. (3.4) and (3.5) increases linearly with $s$,

$$r(s) = (1 - \Delta) + s\frac{2\Delta}{S}. \tag{3.24}$$

Here, $\Delta$ is the total fraction of resources that is distributed unevenly. The amount of resources increases linearly from $C(0) = 1 - \Delta$ in the first step to $1 + \Delta$ in the last step, so that the average amount of resources is 1. Because there cannot be more complete complexes than there are initial nuclei, the yield is bounded by $1 - \Delta$. To achieve optimal efficiency, the

dimerization probability needs to be controlled such that the number of complete complexes remains constant throughout the assembly process:

$$\frac{dC}{ds} = -\frac{y + p_d - r}{y} C \stackrel{!}{=} 0\,, \tag{3.25}$$

which implies $p_d = r(s) - y(s)$. In other words, the dimerization probability is controlled such that the surplus of resources in each assembly step compensates the consumption of monomers due to dimerization. It follows for the dynamics of active complexes,

$$\frac{dy}{ds} = bp_d - a(y + p_d - r) = b(r - y)\,, \tag{3.26}$$

which is solved by $y(s) = r(s) - \frac{2\Delta}{bS}$ and thus yields

$$p_d = r - y = \frac{2\Delta}{bS} \sim S^{-1}\,. \tag{3.27}$$

For $\Delta$ close to 0 (yield close to 1), approximately $\Delta \approx -\log(1-\Delta) \approx -\log(\text{yield})$ and hence $p_d \approx \frac{-2\log(\text{yield})}{bS}$. Comparing this result with Eq. (3.23) shows that the strategy of increasing the amount of resources is even more efficient than removing complexes. Furthermore, by plotting the optimal parameter against the structure size (see Fig. 3.8B), we verify that $p_d$ scales like $\sim S^{-1}$ both for the snake and the onion protocol. Hence, we conclude that the strategy is also compatible with parallel supply protocols. Consequently, we expect a time complexity of $T \sim S^2$ for the snake protocol and $T \sim S^{\frac{3}{2}}$ (2D) or $T \sim S^{\frac{4}{3}}$ (3D) for the onion protocol, consistent with the result from the last chapter and with [2]. Hence, the onion protocol with increasing, non-stoichiometric concentrations represents the most efficient strategy for the Jis scenario that we could identify for higher-dimensional structures. It is the only strategy that achieves a lower time complexity exponent than the one-dimensional Jis scenario.

## 3.4 Conclusion

The idea behind the just-in-sequence scenario is that the different species are supplied in a specified sequence in order to favor a specific assembly pathway and to avoid spurious nucleation. While this basic idea is simple, for its efficient implementation additional considerations are necessary. In this chapter, we analyzed an effective model for the just-in-sequence scenario, which allowed us to explore its intricacies and to conveniently calculate parameter- and time complexity exponents for different implementations of the scenario.
We found that the central difference between the one-dimensional and the higher-dimensional Jis scenario can be quantified by a single parameter $a$, which we call the *growth exclusion factor*, and which measures the extent to which a defect in the structure prevents the structure from further growing. While the parameter $a$ is 1 for one-dimensional structures (a defect always disrupts the growth (disruptive)), it is typically 0 for higher-dimensional structures (a single defect never disrupts the growth (non-disruptive)). Therefore, competition continuously increases in the higher-dimensional case and makes a naive implementation of the Jis scenario very time inefficient exhibiting a large time complexity exponent. We studied three potential strategies to regulate the level of competition and to enhance the efficiency of the

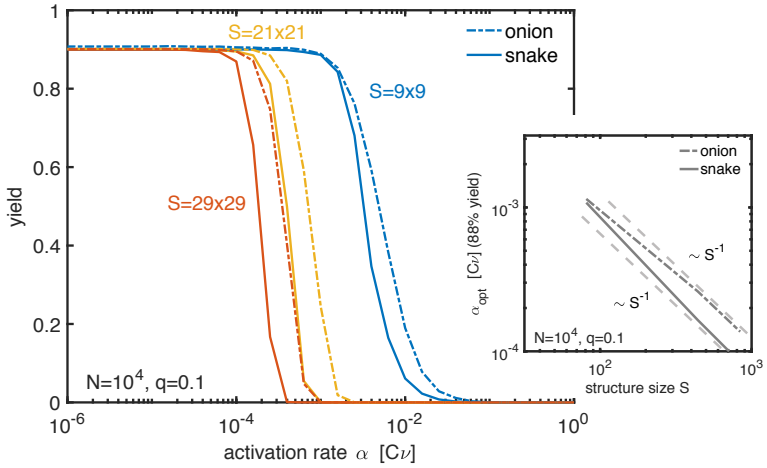


**Figure 3.8 | Just-in-sequence scenario with non-stoichiometric concentrations.** The yield is plotted against the activation rate for the snake and onion protocol when using increasing, non-stoichiometric concentrations for the different species. The inset shows the scaling of the optimal activation rate with the target structure size for large average particle number $N$. Asymptotically, we measure a parameter exponent of $\phi \approx -1$ both for the snake and the onion protocol.

| **implementations of 2D Jis scenario** | control parameter exponent $\phi$ | time complexity exponent $\theta$ |
|---|---|---|
| naive | 2 (s)<br>2 (o) | 3 (s)<br>2.5 (o) |
| special assembly path (back bone protocol) | 1.5 (b) | 2.5 (b) |
| removing complexes | 1 (s)<br>1.5 (o) | 2 (s)<br>2 (o) |
| non-stoichiometric concentrations | 1 (s)<br>1 (o) | 2 (s)<br>1.5 (o) |

(s): snake protocol; (o): onion protocol; (b): back-bone protocol

**Table 3.1 | Summary of parameter and time complexity exponents for the different strategies.** The table summarizes the control parameter- and time complexity exponents for the four implementations of the two-dimensional Jis scenario discussed in this chapter. The corresponding assembly protocol to which each exponent refers is indicated in brackets.

Jis scenario for higher-dimensional structures. The resulting control parameter- and time complexity exponents that we found for these different assembly schemes are summarized in Table 3.1.

First, we tried to mimic the self-regulatory mechanism of one-dimensional structures by using a very special supply sequence (back bone protocol) such that about half of all species become disruptive. The problem with this strategy is that, in order to significantly improve the time efficiency, it would be required that the distance between non-disruptive and disruptive species remained constant for all structure sizes. This, however, apparently cannot

be achieved in practice. Consequently, the strategy only leads to a small improvement of the time complexity.
The second strategy relies on an external control mechanism, which removes a small fraction of the complexes from the system after each assembly step. In this way, competition for resources among the remaining complexes can be reduced and the time efficiency be enhanced. Unfortunately, the favorable parameter scaling can not be maintained if a parallel supply protocol like the onion protocol is used.
Finally, the last strategy reverses the approach of the second strategy and - instead of reducing the number of complexes - stipulates that the amount of resources is increased with each assembly step. In this way, competition for resources can be minimized. In contrast to the strategy of removing complexes, the parameter scaling of this strategy remains the same if parallel supply protocols are used. Hence, the onion protocol with increasing non-stoichiometric concentrations can be identified as the most time efficient strategy for the Jis scenario.

The analysis shows that a naive implementation of the Jis scenario is very time-inefficient but the efficiency can be largely improved by using an additional strategy in order to reduce competition for resources. The time complexity analysis proved very useful in this context: With the help of the simplified model, it was easily possible to calculate the parameter and time complexity exponents, which allowed for a simple quantification and comparison of the time efficiency of the different strategies. This demonstrates again the general usefulness of our time complexity analysis for the study of self-assembling systems.

Another important aspect of the Jis scenario, which has not been considered here explicitly, is robustness to intrinsic and extrinsic noise. By intrinsic noise we mean noise originating intrinsically from the stochastic dynamics. This kind of noise is responsible for the yield drop observed in Figs. 3.4, 3.6 and 3.7, and its effect vanishes for $N \to \infty$. On the other hand, extrinsic noise refers to variations in the supplied numbers of particles, as has been exemplified in the last chapter and in [143]. In all studied cases, higher time efficiency seems to correlate with increased robustness to noise. However, it would still be instructive to quantify the effect of noise in a systematic way for these different implementations of the Jis scenario.

# 4 The role of the morphology of the constituents in reversible self-assembly

The goal of this chapter is to summarize the most important findings of our project on the dependence of the time efficiency of reversible self-assembly processes on the morphology of the constituents. The corresponding manuscript is currently in preparation for submission. This chapter is based on and uses parts of the manuscript preprint in section 4.5.

## 4.1 Motivation

In the previous two chapters we have investigated the time efficiency of different self-assembly schemes or self-assembly scenarios. In contrast, in this chapter, we will analyze the influence of the geometry of the constituents on the efficiency of reversible self-assembly processes. While for the irreversible scenarios discussed in chapter 1 we do not expect a qualitative dependence of the dynamics on the shape of the constituents, our scaling analysis in chapter 2 ([2]) suggests that, in the reversible binding scenario, the geometry of the constituents might play an important role. In the later case, we expect such a dependence because, according to our scaling analysis, the parameter- and time complexity exponents for the reversible binding scenario depend on the effective order of nucleation and attachment reactions, which, in turn, are largely determined by the geometry of the constituents. If a dependence of the time complexity exponent on the geometry of the constituents can indeed be verified, this could have important consequences for experiments as well as for our understanding of biological self-assembly processes. For example, in experiments, designing constituents with a specific geometry appears to be a feasible task and might be significantly simpler to realize than using sophisticated protocols or alternative assembly schemes (for instance, the just-in-sequence scenario discussed in the last two chapters can only be used for heterogeneous systems and requires fine-tuning of the supplied concentrations). In particular, hierarchical self-assembly could offer a simple and efficient way in order to optimize the geometry of the constituents: Making certain bonds stronger than others can induce the particles to first form larger constituents with a favourable geometry so that, subsequently, these larger constituents can self-assemble significantly more efficiently. Additionally, these insights might shed light on the kinetics of virus capsid assembly or other reversible biological self-assembly processes. As stated in the introduction, the kinetics of these systems are still rather poorly understood because intermediate assembly products are typically present in concentrations so low that they escape detection in an experiment. Hence, a proper understanding of the geometry dependence of the time complexity might be helpful, for example, by suggesting possible ways in which the monomers could assemble hierarchically that would optimize the time efficiency. Afterwards, it can be tested specifically if the suggested assembly path is consistent either with experimental data or with other specificities of the system like, for instance, the binding

strengths of the various binding sites of the constituents. In this way, a more comprehensive understanding of the kinetics of biological self-assembly processes might be established.
As a second research question in this chapter, we investigate how self-assembly efficiency depends on the 'degree' of reversibility, i.e., for example, whether or not particles that have formed two or more bonds are still unstable and can detach from a structure at a sufficiently large rate. While reversibility in general has been attributed great importance both for biological and artificial self-assembling systems [58, 56, 61, 57, 60, 59, 45, 25, 34], we do not know of any study that has investigated the effect of reversibility systematically and specified the role of the 'degree of reversibility'. Typically, the meaning of reversibility is seen in the purpose that it allows the system to approach the (quasi-)equilibrium state [27, 28, 25, 29, 31, 35]. However, a system with a low degree of reversibility can have irreversible reactions and is hence inherently out-of-equilibrium. Therefore, by investigating reversibility systematically, we also want to understand the relation between the equilibrium (high degree reversible) and non-equilibrium (low degree reversible) nature of self-assembly processes and which of the two is ultimately more time efficient.
Generally, particle geometries that have a higher number of binding sites, in principle allow for a larger degree of reversibility while the final assembly products (and possibly also some intermediate states) may still be stable. Therefore, both research questions - on the role of the morphology of the constituents and the optimal degree of reversibility - are closely related.

## 4.2 Model

In order to investigate how the time efficiency of reversible self-assembly processes depends on the geometry of the constituents and the 'degree' of reversibility, we explicitly simulate three different particle systems (square, trigonally and hexagonally shaped particles), which self-assemble into two-dimensional structures of a specified size. The model we use is illustrated in Fig. 4.1 and it is simpler than the model that was introduced previously in chapter 2 for the following reasons: First, instead of four different scenarios in chapter 2, here we simulate only the reversible binding scenario. Second, since in the limit of large particle numbers the dynamics of the reversible binding scenario is independent of the heterogeneity of the building blocks [1, 2], we only consider homogeneous systems here (i.e. monomers are indistinguishable). Third, we constrain ourselves only to two-dimensional target structures because all concepts can be illustrated more easily in the 2D case. We expect, however, that our scaling results apply to the self-assembly of three-dimensional objects as well.
The dynamics of the model is then specified as follows: Any two monomers can bind with rate $\mu$ along any edge to form a dimer, which can subsequently grow by further attachment of monomers at any free, neighboring site with rate $\nu$, see Fig. 4.1B. We formally distinguish the dimerization rate from the attachment rate in the analysis because cooperative binding effects might disfavour dimerization against growth in biological or experimental systems [137, 20, 138]. In the simulations, however, we typically set $\mu = \nu$. Following the assumptions of classical or ideal aggregation theory, interactions among larger oligomers are neglected and it is assumed that structures grow only by the attachment of single monomers [70, 77, 35]. In the paper, we evaluate to which extent this assumption is reasonable, specifically for the simulated morphologies, and we also estimate the effect when interactions of larger oligomers are additionally taken into account.

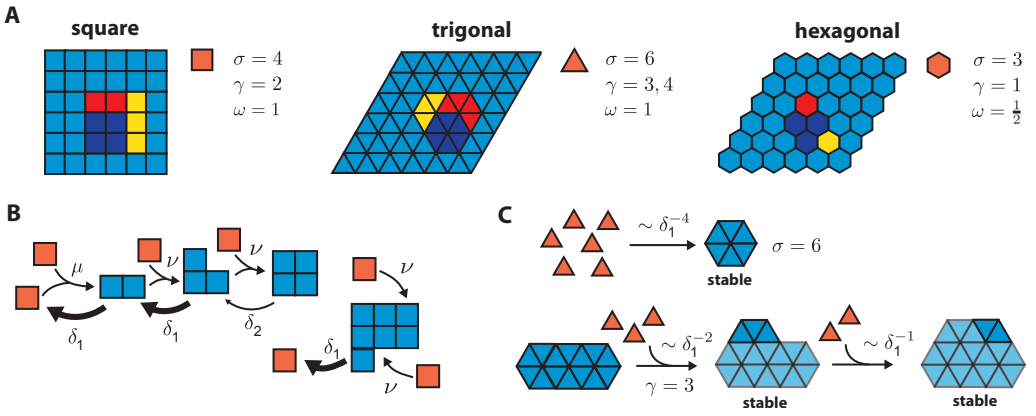


**Figure 4.1** | Illustration of the model. **A** We consider the self-assembly of two-dimensional structures of volume $S$ from square-, trigonally or hexagonally shaped particles and investigate the time the assembly processes take in order to reach 90% yield. The blue, red and yellow shaded regions illustrate the first three stable configurations (in which each particle has two or more bonds) along a typical assembly path. The dynamics is effectively described by the three parameters $\sigma$, $\gamma$ and $\omega$, which are listed for the three particle systems and denote the nucleation size, attachment order and growth exponent, respectively (see C and main text). **B** Self-assembly dynamics is modelled as follows (illustrated for the square system): Two monomers dimerize at rate $\mu$ along any of their edges. Subsequently, particles attach at rate $\nu$ to any free neighboring site until a square of volume $S$ (edge length $\sqrt{S}$) is completed assuming periodic boundary conditions. Furthermore, particles detach from the structure at rate $\delta_n \sim e^{-nE_B}$, with $n$ being the number of bonds between the particle and the structure. **C** Coarse-grained effective dynamics (illustrated for the trigonal system): Assembly starts with the formation of a stable nucleus (blue shaded states in A), which requires a minimum number of $\sigma$ particles. The effective nucleation rate scales as $\sim \delta_1^{-(\sigma-2)}$ because $\sigma - 2$ unstable states must be traversed in order to form the nucleus. Analogously, attachment processes are initiated by an effective reaction of order $\gamma$, after which a succession of reactions of smaller order may follow.

In order to model reversibility of the binding reactions, we furthermore assume that single monomers detach from a structures at a rate $\delta_n$ that decreases exponentially with the number $n$ of bonds that need to be broken in order for the particle to detach: $\delta_n = Ae^{-nE_B}$ (Arrhenius' law). Here $E_B$ is the binding energy per contact in units of $k_BT$ and the constant $A$ is called preexponential factor. The dynamics of the assembly process can be controlled by changing the ratios between the frequencies of detachment and attachment events, $\frac{\delta_n}{C\nu} = \frac{A}{C\nu}e^{-nE_B}$ (with $C$ denoting the initial concentration of monomers), which therefore define our general control parameters. Analogous as $\delta_n$ is measured in units of $C\nu$, time is always measured relative to the reactive time scale in units $(C\nu)^{-1}$.

We define the yield as the fraction of monomers that are bound into complete structures and the assembly time $T_{90}$ as the time at which the yield first surpasses a value of 90%. In particular, we are interested in how the minimal assembly time $T_{90}^{\min}$ scales with the structure size $S$, as is described by the time complexity exponent $\theta$, and in how $\theta$ depends on the particle morphology.

## 4.3 Results and discussion

In the analysis, we first study the case in which all higher order detachment rates except $\delta_1$ vanish. This case can be considered the 'leading order' effect in an expansion that subsequently takes detachment rates of higher order into account. Since the ratio between detachment rates of consecutive order is typically small: $r := \delta_{n+1}/\delta_n = e^{-E_B} \ll 1$, we expected this heuristic expansion to be useful in some sense. Indeed, it turned out that, while the higher order attachment rates do have an important effect on the assembly time in general (see below), they only slightly affect the minimum of the assembly time at least as long as the ratio $r$ (which we also call the *reversibility ratio*) is not too big. This implies that the minimal assembly time $T_{90}^{\min}$ and optimal detachment rate $\delta_1^{\text{opt}}$ are informative parameters that can, in general, be well described by the first order theory. Plotting the assembly time $T_{90}$ against the detachment rate $\delta_1$ for the three different particle systems with $\delta_{n\geq 2} = 0$, thereby reveals a typical behavior (Fig. 4.2): While for small values of $\delta_1$ (fast nucleation), the systems gets kinetically trapped, the minimum is attained in a pronounced U-shape, and for large values of $\delta_1$ the assembly time increases proportional to $S^{\sigma-2}$. Importantly, the minimal assembly time strongly differs between the three particle systems and - even more importantly - it scales differently with the structure size $S$, see Fig 4.2B). This implies that differences in the assembly times of the various particle systems become ever more pronounced with increasing size of the target structure. Consequently, for the self-assembly of large objects, the morphology of the building blocks plays an important role as it crucially determines the time efficiency of their self-assembly.

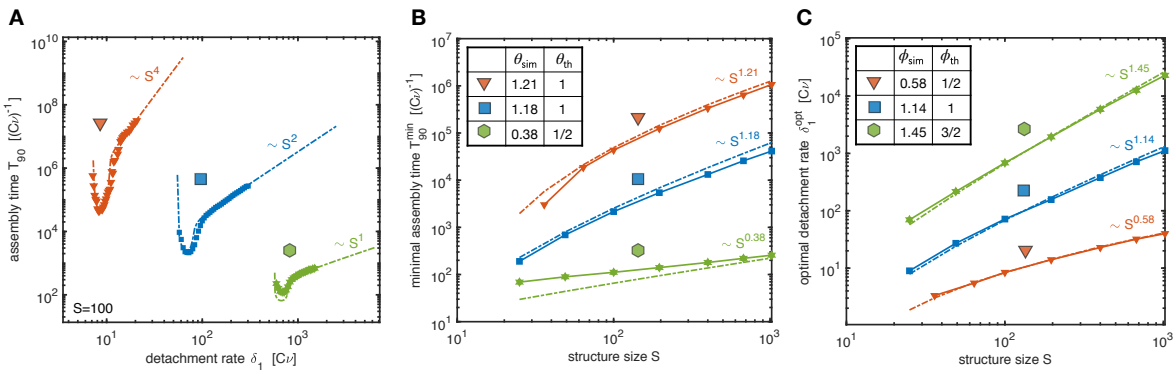


**Figure 4.2 |** Assembly time and optimal parameter for vanishing $\delta_{n\geq 2} = 0$. **A** The time required to achieve 90% yield in the stochastic simulation (markers) is plotted against the detachment rate for the trigonal- (red), square- (blue) and hexagonal (green) system for target structure size $S = 100$. Dash-dotted lines represent the prediction of the effective theory. For large detachment rates, the assembly time scales proportional to $\delta_1^{\sigma-2}$, while for small detachment rates the assembly time diverges. **B, C** The minimal assembly time (B) and optimal detachment rate (C) inferred from the stochastic simulation (markers) and effective theory (dash-dotted lines) are plotted against the size of the target structure and exhibit approximate power-law dependencies for all three particle systems. Tables show the scaling exponents $\theta_{\text{sim}}$ and $\phi_{\text{sim}}$ inferred from the last three data points of the stochastic simulation in comparison with their theoretical asymptotic values $\theta_{\text{th}}$ and $\phi_{\text{th}}$ obtained from Eq. (4.1).

The first order theory brings about a number of simplifications which make it amenable to a mathematical treatment. Most importantly, if higher order detachment rates $\delta_2, \delta_3, ...$ are all zero, intermediate assembly states in which each particle forms at least two bonds are stable and do not decay any more. Since the assembly process proceeds via these stable intermediate states, this allows us to describe the dynamics with a coarse-grained kinetic model based on effective, irreversible rate equations.
The coarse-grained model depends on three parameters: $\sigma, \gamma$ and $\omega$, which denote, respectively, the nucleation size, the effective order of attachment reactions as well as the scaling of the average growth rate of a cluster with its size. The three parameters differ for the three particle systems (see Fig. 4.1) and they uniquely characterize the dynamics of the self-assembly processes (apart from a numerical constant that can be estimated analytically or fitted). The predictions of the effective model for the assembly time and the optimal parameter are plotted in Fig. 4.2 and coincide very well with the data obtained from the stochastic simulations. Hence, the effective theory identifies the three parameters $\sigma, \gamma$ and $\omega$ as the major determinants of self-assembly kinetics.
The irreversibility of the effective model furthermore allows us to simplify the system and to calculate the asymptotic time complexity exponent $\theta$ and parameter exponent $\phi$ analytically. In dependence of the above parameters, we find

$$\theta = \frac{(1-\omega)\sigma + \gamma + 2\omega - 3}{\sigma - \gamma - 1} \qquad \text{and} \qquad \phi = \frac{2-\omega}{\sigma - \gamma - 1}\,. \tag{4.1}$$

In general, the formulas yield good estimates for the exponents inferred from the stochastic simulation (see tables in Fig. 4.2B,C) but do not reproduce them exactly, presumably because the asymptotic scaling regime is not quite reached for the simulated system sizes and the real growth exponent $\omega$ deviates slightly from its estimated value.
Equation (4.1) shows that if the attachment order $\gamma$ is 1 (and consequently $\omega = 1/2$), as it holds for example for the hexagonal system, then $\theta = \frac{1}{2}$ independently of $\sigma$. We suppose that this is the most time efficient scenario that can be achieved[1]. The reason why the hexagonal system is so efficient is because $\gamma = 1$ guarantees a constant growth rate of the clusters, independent of $\delta_1$, and, therefore, the ratio between the effective nucleation rate and cluster growth rate can be controlled most efficiently. Note that the hexagonal system has the same time complexity exponent as the dimerization scenario discussed in chapter 2.
If the attachment order $\gamma$ is larger than 1, according to Eq. (4.1), an increasingly large nucleation size $\sigma$ is required in order to constrain the complexity exponent. However, a large nucleation size leads to a strong increase of the assembly time for detachment rates larger than the optimal value (where $T_{90} \sim \delta_1^{\sigma-2}$) and might therefore necessitate fine-tuning of the control parameter in an increasing manner.
The problem of fine-tuning, however, can be avoided by increasing higher order detachment rates, predominantly $\delta_2$. Plotting the assembly time against $\delta_1$ for fixed, nonzero reversibility ratio[2] $r$ (Fig. 4.3) reveals an important difference: While in the case $\delta_{n\leq 2} = 0$ the assembly

[1] Note that for $\gamma > 1$ and large $\sigma$, Eq. (4.1) would predict a value of $\theta$ even smaller than 1/2. However the approximations that led to Eq. (4.1) become inaccurate if the difference between $\sigma$ and $\gamma$ becomes too large. Hence, we expect that the time efficiency of the hexagonal system cannot be exceeded by a system with $\gamma > 1$.

[2] this control scenario (fixed $r = \delta_{n+1}/\delta_n$ and variable $\delta_1$) corresponds to the common experimental scenario in the which (for example) the monomer concentration is steadily increased while the temperature (and binding energy) is kept fixed.

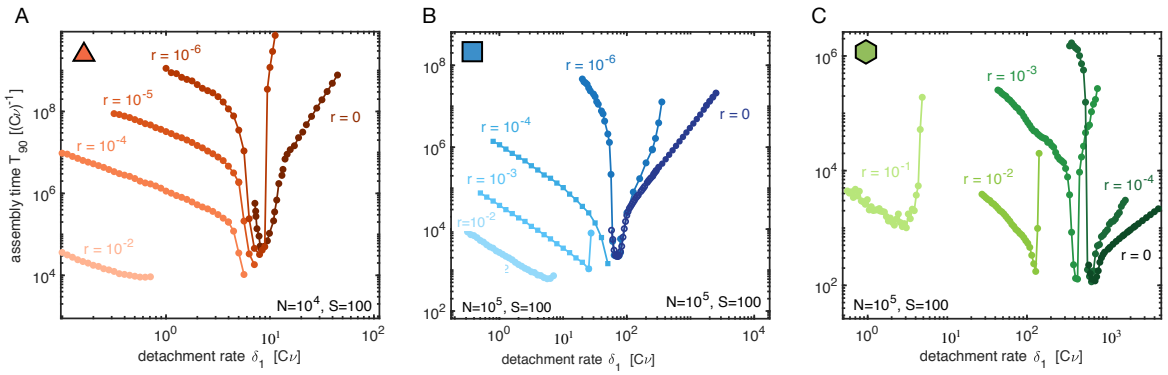


**Figure 4.3** | The effect of higher order reversibility on the assembly time. The assembly time $T_{90}$ obtained from stochastic simulations is plotted against the detachment rate $\delta_1$ for different reversibility ratios $r = \delta_{n+1}/\delta_n = e^{-E_B}$ for the trigonal (A), square (B) and hexagonal (C) system with structure size $S = 100$ and $N = 100S$ or $N = 1000S$. For $r > 0$, the assembly time scales inversely proportional to $\delta_1$ for sufficiently small $\delta_1$ and diverges at large $\delta_1$. In contrast, for $r = 0$ the assembly time diverges at small $\delta_1$ but scales with $\sim \delta_1^{\sigma-2}$ for large $\delta_1$. The minimal assembly time is noticeably affected by higher order reversibility only if $r$ is large.

time diverges at small $\delta_1$ due to kinetic trapping, for $r > 0$ all intermediate structures can be dissolved again and, consequently, the assembly time only increases linearly with decreasing $\delta_1$. Hence, while the minimal assembly time is not strongly affected by higher order detachment rates, the problem of fine-tuning of $\delta_1$ can possibly be avoided if $r$ is large enough, due to the slow increase of $T_{90}$ with decreasing $\delta_1$.
Overall, the effect of the particle morphology on the assembly time must be evaluated as more important than optimizing the reversibility ratio (which may not become too large since otherwise the stability of the final assembly product is jeopardized). On the other hand, if the reversibility ratio is too small (but $\delta_2$ still large enough), the assembly time typically increases very strongly to both sides of the optimum and extreme fine-tuning is necessary.

Hence, our study shows that the geometry of the constituents has a huge impact on the time efficiency of reversible self-assembly processes. In two dimensions, hexagonally shaped particles thereby assemble particularly efficiently and robustly. Indeed, it could be shown that some viruses like the picornaviruses as well as the shells of carboxysomes assemble from hexameric and pentameric building blocks of the form of hexagons and pentagons [144, 145]. In both cases, while the basic subunits have a triangular shape, the pentagons and hexagons assemble as a hierarchical intermediate product. It is thinkable that it is only thanks to this particular morphology of the intermediates that a structure as large as the carboxysome (which consists of 12 pentameric and 740 hexameric capsomeres) can still assemble fast and efficiently. Maybe this hierarchical organisation of the assembly process, by which pentamers and hexamers are generated first, applies even more generically to the assembly of icosahedral viruses and shells. However, larger viruses typically assemble in the presence of a scaffold and hence their assembly kinetics might follow slightly different rules. In any case, an important conclusion of our work is that in experiments like the ones of the Dietz group discussed in the introduction, which build structures from artificial subunits, the time efficiency will most likely be able to be significantly improved by choosing suitable particle geometries or

by organising the assembly process hierarchically. As far as we know, the Dietz group used triangular particles, possibly even with a suboptimal reversibility ratio, which might explain the poor time efficiency of their experiments.

## 4.4 Key results

In my opinion, there are four key results of this project:

- The time efficiency and time complexity of reversible self-assembly processes (as well as robustness/variability in the control parameter) strongly depend on the morphology of the constituents. Particle systems in which the effective order of attachment reactions is 1, as is the case for the hexagonal system studied here, generally assemble most efficiently. The time complexity is found to depend primarily on three 'topological' parameters (nucleation size, attachment order and growth exponent) that characterize the morphology.
- Furthermore, the degree of reversibility (quantified by the reversibility ratio $r = \delta_{n+1}/\delta_n$) plays an essential role: Depending on the morphology of the constituents, a large reversibility ratio can be either beneficial or detrimental (primarily regarding robustness/variability in the control parameter) compared to very small $r$ or $\delta_{n\geq 2} = 0$, while an intermediate reversibility ratio seems to be always very unfavorable.
- A simple, effective model based on kinetic rate equations successfully describes the dynamics of reversible self-assembly processes and can be used to investigate the dependence of the time efficiency on the morphology of the constituents. The 'reversibility order expansion' thereby allows for a systematic analysis of reversible self-assembly kinetics and enables the analytic computation of the asymptotic parameter- and time complexity exponent.
- Hierarchical self-assembly (or deliberate design of constituents with suitable geometries) might offer a simple way to profit from these insights in order to strongly enhance the time efficiency of self-assembly experiments.

## 4.5 Publication preprint: Self-assembly efficiency strongly depends on the morphology of the constituents

This section is a publication preprint of the following manuscript.

**Self-assembly efficiency strongly depends on the morphology of the constituents**

by

Florian M. Gartner,[1] and Erwin Frey[1]
[1] *Arnold-Sommerfeld-Center for Theoretical Physics and Center for NanoScience, Department of Physics, Ludwig-Maximilians-Universität München*

# Self-assembly efficiency strongly depends on the morphology of the building blocks

Florian M. Gartner and Erwin Frey*
*Ludwig-Maximilians-Universität München, Department of Physics,*
*Arnold-Sommerfeld-Center for Theoretical Physics (ASC) and Center for NanoScience (CeNS),*
*Theresienstrasse 37, D-80333 München, Germany.*
(Dated: February 1, 2022)

Self-assembly is a fundamental concept in biology and of significant interest for nanotechnology. Big advances have been made both experimentally and theoretically in characterizing and controlling properties of the resulting structures. Much less is still known, however, about kinetic constraints and determinants of dynamical properties like the time efficiency of self-assembly processes, although these can become a severe limiting factor in experiments. Therefore, we here investigate how the time efficiency and other dynamical properties of reversible self-assembly processes depend on the shape (morphology) of the constituents and the 'degree' of reversibility. To this end, we explicitly simulate three different particle systems (triangularly, square and hexagonally shaped particles), which self-assemble into two-dimensional structures of a specified size. We find that these particle systems differ strongly in their required assembly time, which is predominantly determined by three 'topological' parameters defining the morphologies. This characterization allows us to identify general scaling laws that describe the assembly time as a function of the structure size and detachment rate. We expect that these results can be used to significantly increase the time efficiency of self-assembly experiments.

## I. INTRODUCTION

Self-assembly is an essential concept in biology that explains the formation of large functional structures from smaller subunits and thereby 'bridges the gap' between different lengths scales. Furthermore, artificial self-assembly evokes great interest as it promises plentiful significant applications in nanotechnology, medicine and biology [1–5].

Typically, the formation of these artificial structures as well as of many biological structures like virus capsids is promoted by weak, reversible interactions between the subunits [3, 6–13]. As a consequence, single bonds between subunits are usually unstable, and only a large number of mutual interactions between subunits stabilizes the structure as a whole. In this way, kinetic traps are eluded that would arise if too many stable intermediates are formed which cannot be completed with the available amount of resources [13–18].

While there are various strategies to overcome kinetic traps even in irreversible self-assembly processes [19–21], here we focus exclusively on the reversible case, which plays a pivotal role in nanotechnology and biology [9, 11, 22]. Reversible self-assembly (in thermal equilibrium systems) amounts to a process in which the system minimizes its free energy and thereby reaches a state in which a large fraction of the monomers are tied to complete structures [12, 17, 23, 24]. This conception motivates the use of ensemble theory from statistical physics in order to characterize the final state [15, 25–27]. Indeed, equilibrium methods have been applied successfully to a broad class of self-assembling systems [23, 28–30] and – when applicable - represent powerful and convenient tools to characterize the resulting structure and the yield.

An obvious drawback of equilibrium methods, however, is that they do not allow to draw conclusions on the dynamics of the underlying processes. In particular, they do not inform about the time the system requires to achieve a specified yield. As a consequence, kinetic aspects of self-assembly processes are significantly less understood than structural properties of the resulting assembly products. However, experiments suggest that the time required for completion of self-assembly processes can become a severe obstacle, especially when the structures are large [5]. Hence, it is indispensable for the advancement of the field to gain a deeper understanding also of those factors that control kinetic features like the time efficiency of self-assembly.

A very basic property of self-assembling systems is given by the morphology of the constituents. In this work, we therefore investigate how the shape of the constituents and the 'degree' of reversibility of their binding reactions influence the time efficiency and other dynamical properties, like the role of interactions between intermediate structures, in reversible self-assembly processes. To this end, we perform stochastic simulations for particles of different shapes, that self-assemble into two-dimensional structures of a specified size. We characterize the time efficiency of the self-assembly processes by how the minimally required assembly time scales with the size of the target structure ('time complexity'). A similar concept was applied previously by us in order to quantify the time efficiency of different self-assembly strategies but with a generic morphology of the constituents [21]. A major benefit of this characterization is that the exponent that describes the scaling of the assembly time with the structure size ('time complexity exponent') can be computed analytically.

We find that the time efficiency and, in particular, the

* frey@lmu.de

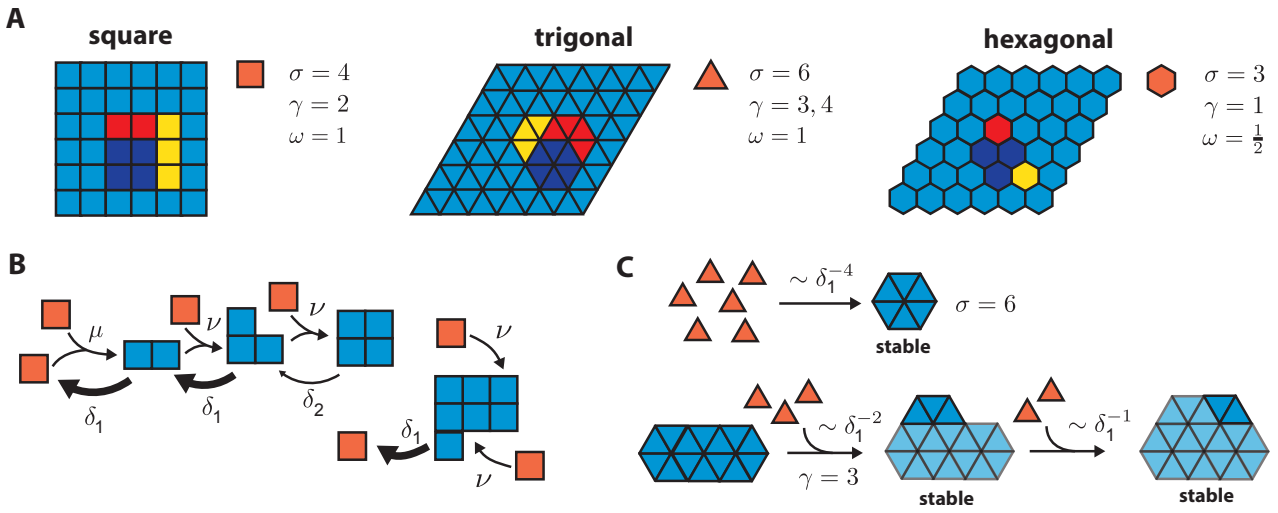


FIG. 1. Illustration of the model. **A** We consider the self-assembly of two-dimensional structures of volume $S$ from square, triangularly or hexagonally shaped particles and ask for the time the assembly processes take in order to reach substantial yields. The blue, red and yellow shaded regions illustrate the first three assembly steps (stable configurations, in which each particle has two or more bonds) along a typical assembly path. The dynamics is effectively described by the three parameters $\sigma$, $\gamma$ and $\omega$, which are listed for the three particle systems and denote the nucleation size, attachment order and growth exponent, respectively (see C and main text). **B** Self-assembly dynamics is modelled as follows (illustrated for the square system): Two monomers dimerize at rate $\mu$ along any of their edges. Subsequently, particles attach at rate $\nu$ to any free neighboring site until a square of volume $S$ (edge length $\sqrt{S}$) is completed assuming periodic boundary conditions. At the same time, particles detach from the structure at rate $\delta_n \sim e^{-nE_B}$, with $n$ being the number of bonds between the particle and the structure. **C** Coarse-grained effective dynamics (illustrated for the triangular system): Assembly starts with the formation of a stable nucleus (blue shaded states in A), which requires a minimum number of $\sigma$ particles. The effective nucleation rate scales as $\sim \delta_1^{-(\sigma-2)}$ because in order to form the nucleus $\sigma - 2$ unstable states must be traversed. Analogously, attachment processes are initiated by an effective reaction of order $\gamma$, after which a succession of reactions of smaller order may follow.

time complexity depend strongly on the morphology of the constituents as well as the 'degree' of reversibility. Our analysis identifies three relevant parameters that determine the time efficiency and allows us to quantify the time complexity exponent for arbitrary monomer morphologies. From this result we derive a number of conclusions regarding biological self-assembly, e.g. of virus capsids, and suggest possible ways in order to optimize artificial self-assembly processes.

## II. MODEL DESCRIPTION

We consider the self-assembly of $N$ identical particles of triangular, square or hexagonal shape into two-dimensional structures of volume $S$, assuming chemical reaction kinetics in a well-mixed fluid environment (Fig. 1). For simplicity of the analysis, we assume that the final structures have periodic boundary conditions, i.e. they from closed tori. In this case, it can be shown that in the limit of large particle numbers, it is irrelevant for the assembly dynamics whether the particles are heterogeneous and bind only with specific neighbors or whether all particles are identical and form unspecific bonds [21, 31]. For convenience, we therefore assume homogeneous systems in which the monomers are indistinguishable but note that our results identically apply for heterogeneous ('information-rich') systems as well. The initial concentration of monomers is denoted by $C = N/V$, with $V$ being the reaction volume.

Specifically, we assume the following reaction kinetics: Any two monomers can bind with rate $\mu$ along any edge to form a dimer, which can subsequently grow at rate $\nu$ by further attachment of monomers at any free neighboring site; see Fig. 1B. We formally distinguish the dimerization rate from the attachment rate because cooperative binding effects might disfavour dimerization of monomers over the attachment of monomers to larger structures in biological or experimental systems. In the simulations, however, we generally set $\mu = \nu$. Following the assumptions of classical or ideal aggregation theory [27], we assume that structures grow only by the attachment of single monomers, while interactions among larger oligomers are neglected [32, 33]. This assumption is generally justified since the concentration of monomers is usually much larger than the concentrations of oligomers. However, we will assess below to which extent ideal aggregation theory is a reasonable assumption specifically for the different morphologies.

Furthermore, in order to account for the reversibility of the binding reactions, it is assumed that single monomers detach from existing structures at a rate $\delta_n$ that decreases

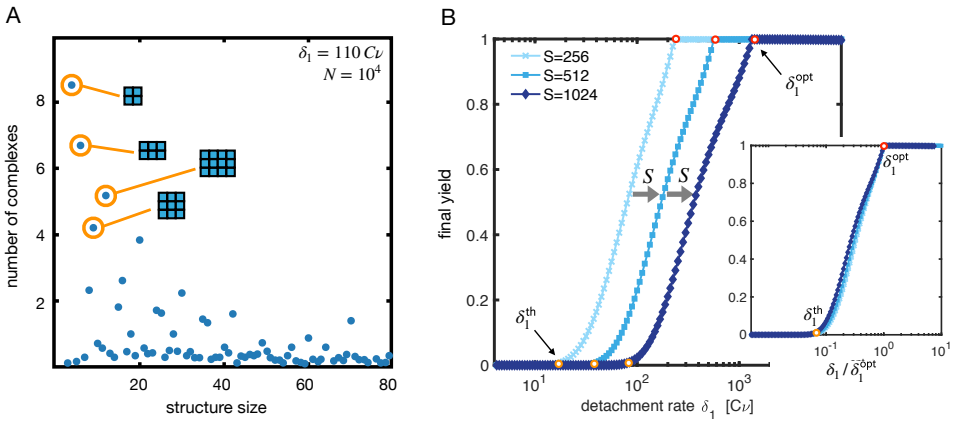


FIG. 2. Cluster size distribution and final yield for vanishing $\delta_{i\geq 2} = 0$. **A** Shown is the cluster size distribution at a fixed, early time point averaged over 100 independent simulations of the square system with target structure size $S = 80$. Structure sizes that allow for a stable configuration are significantly more frequent on average than those which do not allow for a stable configuration. A few of these stable configurations are illustrated explicitly. Our effective theory describes only the most likely assembly pathway connecting these stable configurations. **B** The final yield is plotted against $\delta_1$ for different target structure sizes. Rescaling the x-axis by the optimal detachment rate $\delta_1^{\rm opt}$ minimizing the assembly time leads to a collapse of the yield curves. In particular, this shows that the minimal assembly time scales identically as the threshold rate $\delta_{\rm th}$ to obtain nonzero yield, a fact which we exploit in the mathematical analysis of the scaling behavior (see Methods).

exponentially with the number $n$ of bonds that need to be broken: $\delta_n = A\, e^{-nE_B}$ (Arrhenius' law). Here, $E_B$ is the binding energy per contact in units of $k_BT$ and A is a constant which sets the overall scale of the unbinding rate. The building blocks of triangular, square, and hexagonal shape differ in the maximum number $d$ of bonds they can form: $d = 3$, 4, and 6, respectively. In particular, if complete structures are to be stable, the binding energy must be large enough so that the detachment rate $\delta_d$ is sufficiently small.

The yield at time $t$ is defined as the fraction of monomers that are bound into complete structures. Furthermore, in order to quantify the time efficiency of the self-assembly processes, the assembly time $T_{90}$ measures the time at which the yield first surpasses a value of 90%. In particular, we will investigate how the minimal assembly time $T_{90}^{\rm min}$ that can be achieved depends on the structure size and we will quantify its asymptotic scaling behavior.

The dynamics of the assembly process can be controlled by changing the ratio between the frequencies of detachment and attachment events, i.e., by changing the detachment rates relative to the overall scale of the reaction kinetics: $\delta_n/(C\nu) = \frac{A}{C\nu} e^{-nE_B}$. Assuming detailed balance, the control parameter can also be written as $\frac{1}{C} e^{\Delta G_n}$, where $\Delta G_n$ is the free energy difference between an n-fold bound subunit and a free subunit. Experimentally, this implies various possibilities in order to control the assembly process. For example, it can be controlled thermodynamically, by changing parameters that affect the free energy difference $\Delta G_n$ like temperature, binding energy, pH value or salt concentration, in addition to changing the monomer concentration $C$. Additional possibilities to control the assembly process kinetically can be created by assuming that the monomers have different internal states among which they switch under consumption of energy, whereby detailed balance may be broken. In this kinetic approach, therefore, we describe the behavior of the system in its most general form in terms of the dimensionless control parameters $\delta_n/(C\nu)$. The resulting assembly time is likewise measured relative to the reactive time scale in units $(C\nu)^{-1}$.

## III. REVERSIBLE SELF-ASSEMBLY IN THE LIMIT $\delta_1 \gg \delta_2$

If the binding energy $E_B$ is sufficiently large, the detachment rate $\delta_1$ is significantly larger than the higher order detachment rates $\delta_2, \delta_3, \ldots$ and therefore predominantly determines the assembly dynamics. Consequently, cluster configurations in which each particle has at least two bonds are significantly more stable than intermediate states in which particles are connected with only one bond. This leads to specific intermediate states of enhanced stability via which the self-assembly process typically proceeds (Fig. 1C).

Hallmarks of this dynamics can be inferred from Figure 2A, which shows the polymer size distribution at a specified time, averaged over 100 independent simulation runs. Here, we simulated the assembly of square-shaped building blocks with a target size of $S = 80$. Structure sizes which allow for a configuration of enhanced stability are thereby significantly more common on average than those that do not. In the following, we first consider the case where $\delta_2$ is so small that it effectively does not alter the assembly dynamics on the relevant time scales and can therefore be neglected. This case can be un-

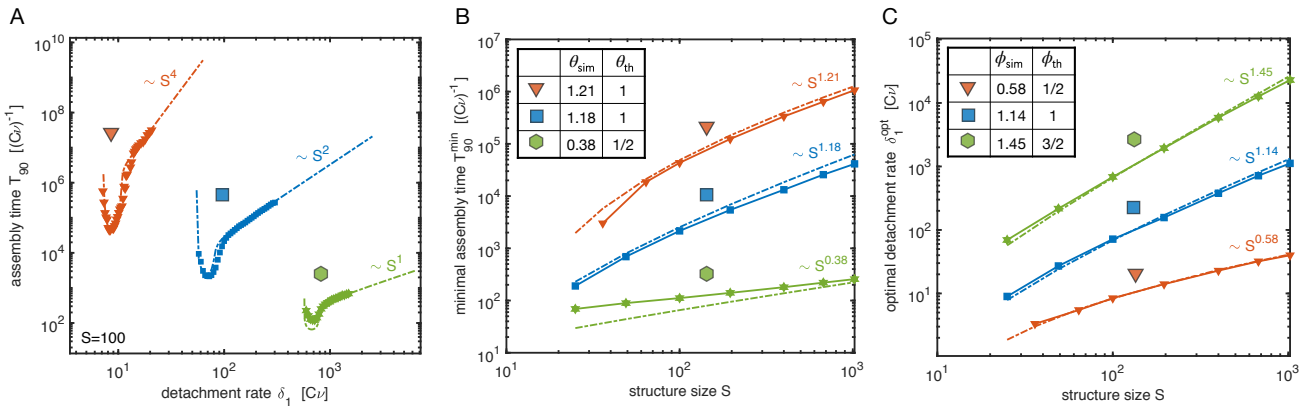


FIG. 3. Assembly time and optimal parameter for vanishing $\delta_2 = \delta_3 = ... = 0$. **A** The time required to achieve 90% yield in the stochastic simulation (markers) is plotted against the detachment rate for the triangular- (red), square- (blue) and hexagonal (green) system for target structure size $S = 100$. Dash-dotted lines represent the prediction of the effective theory (by numerically integrating Eq. (1)). For sufficiently large detachment rates, the assembly time scales proportional to $\delta_1^{\sigma-2}$, while for small detachment rates the assembly time diverges. **B, C** The minimal assembly time (B) and optimal detachment rate (C) inferred from the simulation (markers) and effective theory (dash-dotted lines) are plotted against the size of the target structure and exhibit approximate power-law dependencies for all three particle systems. Tables show the scaling exponents $\theta_{\rm sim}$ and $\phi_{\rm sim}$ inferred from the last three data points of the stochastic simulation in comparison with their theoretical asymptotic values $\theta_{\rm th}$ and $\phi_{\rm th}$ derived by the mathematical analysis (see Eq. (2) and Methods).

derstood as the 'leading order' effect in an expansion in which one truncates the sequence of detachment rates $\delta_1 \ll \delta_2 \ll \delta_3 \ldots$ at successively higher order. The idea is that the leading order effect in which higher order detachment rates $\delta_2, \delta_3, ...$ are neglected might already describe essential features of the kinetics of self-assembly processes. Thereafter, we will investigate how the assembly dynamics is affected by the higher order rates $\delta_2, \delta_3, ....$

If $\delta_{n\leq 2} = 0$, stable intermediate configurations do not decay any more and the assembly process thus contains irreversible steps. Consequently, the system will eventually reach an absorbing state in which all monomers are bound either into complete structures or stable intermediate states. The process can therefore be unambiguously characterized by its final yield, which is a monotonic function of $\delta_1$ (Fig. 2B): If the detachment rate $\delta_1$ is too small, structures nucleate too quickly and the system falls into a kinetic trap, resulting in a poor final yield. Increasing $\delta_1$ slows nucleation relative to cluster growth, thereby increasing the number of structures that get completed but also the time required to reach the final state. The optimal values of $\delta_1$, with which a yield of 90% can be achieved in the smallest amount of time, are indicated on the curves in Fig. 2B for the different target structure sizes.

The assembly time $T_{90}$ as a function of $\delta_1$ is displayed in Fig. 3A for the different morphologies of the monomers and is found to exhibit a characteristic shape: For small $\delta_1$, the assembly time exhibits a U-shape with a pronounced minimum, followed by a power law scaling $\sim \delta_1^{\sigma-2}$ as $\delta_1$ increases. Notably, the minimal assembly times for the three monomer morphologies differ by almost three orders of magnitude. Even more importantly, the minimal assembly times behave differently as a function of the structure size (Fig. 3B): For triangular- and square-shaped monomers, the minimum assembly time as a function of the structure size (for $S \gg 1$) increases approximately as a power law with exponent $\theta \approx 1.2$, while for the hexagonal system it increases only with an exponent of $\theta \approx 0.4$. Similarly, the optimal detachment rates show approximate power law dependencies on the target structure size with characteristic exponents $\phi$. We will refer to the (asymptotic) exponents $\theta$ and $\phi$ as *time complexity-* and *control parameter exponent*, respectively [21]. Differences in the time complexity exponents imply that the disparities in the assembly times of the various monomer morphologies become ever more pronounced with increasing size of the target structure. Consequently, for the self-assembly of large objects, the morphology of the building blocks plays a crucial role, as it decisively determines the time efficiency of their self-assembly process.

## IV. ANALYSIS WITH AN EFFECTIVE MODEL

In order to understand the parameters that influence the assembly time and to predict the time complexity exponent for arbitrary morphologies, we formulate an effective theory of the assembly dynamics. To this end, we exploit the fact that the assembly process typically follows a specific path that passes through a sequence of stable intermediate states, as illustrated in Fig. 2A. The larger the number of unstable states that must be traversed to reach a new stable configuration, the less

likely the particular path will be. In order to formulate the effective theory we therefore only consider the most probable assembly pathways that link stable configurations by the smallest number of unstable intermediate steps. If the detachment rate $\delta_1$ is large compared to the assembly rate $C\nu$, transitions between two subsequent stable states of size $n$ and $n+\gamma$ can then be considered as effective $\gamma+1$-particle reactions involving $\gamma$ monomers as well as the cluster (see Methods for details).

Initially the assembly process starts with the formation of a stable nucleus, which requires a minimal number of $\sigma$ monomers, where $\sigma$ is called the *nucleation size* (see Fig. 1). Subsequent attachment processes proceed in two steps as illustrated in Fig. 1C: First, a leading order reaction that involves $\gamma$ monomers, where $\gamma$ is called the *attachment order*, must occur in order to reach a new stable configuration. Subsequently, a number of subleading order reactions may follow that allow the complex to traverse further stable configurations until another reaction of leading order $\gamma$ is required (see Fig. 1C).

Besides $\sigma$ and $\gamma$, we introduce a third parameter $\omega$, which we call the *growth exponent*, and that quantifies how the average growth rate of a cluster scales with its size. The growth rate of a cluster typically increases with its size $s$ for two reasons: First, the leading order reaction can occur at any site along the boundary of the cluster and, therefore, its rate scales proportional with the boundary. Second, the number of subleading order reactions following a leading order reaction typically increases with the size of the boundary as well. For example, in the case of the triangular and square system, since the cluster boundary scales approximately like $\sim s^{1/2}$, the effective growth rate scales with $\sim s^1$, yielding $\omega = 1$. In contrast, in the case of the hexagonal system, there are no subleading order reactions (because $\gamma = 1$) and hence, approximately $\omega = 1/2$.

The three parameters $\sigma$, $\gamma$ and $\omega$ are summarized in Fig. 1A for the three particle systems.

In the limit where the detachment rate $\delta_1$ is large compared to the reaction rate $C\nu$, the assembly dynamics can be described by the following effective theory for the concentrations $c_n$ of $n$-mers (see Methods for details):

$$\begin{aligned} \partial_t c_1 &= -\sigma\bar{\mu}c_1^\sigma - \bar{\nu}c_1^\gamma \sum_{s=\sigma}^{S-1} s^\omega c_s \,, \\ \partial_t c_\sigma &= \bar{\mu}c_1^\sigma - \bar{\nu}\sigma^\omega c_\sigma c_1^\gamma \,, \\ \partial_t c_s &= \big((s-1)^\omega c_{s-1} - s^\omega c_s\big)\bar{\nu}c_1^\gamma \,. \end{aligned} \tag{1}$$

The three equations describe the temporal evolution of the concentration of monomers, stable nuclei of size $\sigma$ and larger complexes of size $\sigma < s < S$, respectively. Since pre-nucleation states are unstable they are not explicitly considered and the growth of larger clusters is described in terms of effective average growth rates $\sim \bar{\nu}s^\omega c_1^\gamma$, where unstable states have been 'integrated out' (see argument above and Methods). Specifically, the terms on the right hand side of the first line account for the loss of monomers due to nucleation with rate $\bar{\mu}$ and attachment of monomers to complexes with rate $\bar{\nu}$. Similarly, the second line accounts for the gain and loss of stable nuclei due to nucleation as well as growth of stable nuclei, respectively, and the last line describes gain due to the growth of smaller complexes and loss due to growth of complexes of the same size $s$. The effective rate constants for nucleation and attachment are given by $\bar{\mu} := \mu\left(\frac{\nu}{\delta}\right)^{\sigma-2}$ and $\bar{\nu} := a\,\nu\left(\frac{\nu}{\delta}\right)^{\gamma-1}$, respectively (see Methods). Fitting the constant prefactor $a$ in $\bar{\nu}$ for a specified structure size $S = 100$, we find a very good agreement between the stochastic simulation and the effective theory for all three particle systems; see Fig. 3. Hence, the effective theory identifies the three topological parameters $\sigma, \gamma, \omega$ (plus a numerical constant $a$) as the major determinants of self-assembly kinetics. Since the above kinetic approach is completely general, we expect it to accurately describe the self-assembly dynamics of arbitrary systems, for instance, also of three-dimensional structures.

The theory also allows us to analytically compute the asymptotic scaling exponents of the optimal detachment rate and minimal assembly time characterizing their dependence on the structure size. To this end, we exploit the fact that the optimal detachment rate $\delta_1^{\text{opt}}$ scales identically as the threshold rate $\delta_{\text{th}}$ to obtain a fixed yield, which is a consequence of the collapse of the yield curves in Fig. 2B. This permits us to strongly simplify Eq. (1) as a two-variable system, which considers only the concentration of monomers and the total concentration of incomplete structures. From this simplified system, the asymptotic parameter exponent can be determined with a scaling ansatz (see Methods) and we find the optimal detachment rate scaling as $\delta_1^{\text{opt}} \sim S^\phi$ with $\phi = \frac{2-\omega}{\sigma-\gamma-1}$. Furthermore, since nucleation is the time limiting step, the total assembly time approximately equals the time it takes for $0.9N/S$ nucleation events to happen: $T_{90}^{\min} \sim \frac{C}{S}/(\bar{\mu}_{\text{opt}}C^\sigma) \sim S^\theta$, with time complexity exponent

$$\theta = \frac{(1-\omega)\sigma + \gamma + 2\omega - 3}{\sigma - \gamma - 1}\,. \tag{2}$$

The theoretical estimates of the exponents for the three particle systems are displayed in the tables in Fig. 3B,C in comparison with their values inferred from stochastic simulations. In general, the theoretical exponents yield good estimates for the numerically determined exponents. Remaining differences may be attributed to the circumstance that the asymptotic scaling regime is not fully reached for the simulated system sizes and the actual growth exponent $\omega$ slightly deviates from its estimated value.

As can be seen from the definitions of $\phi$ and $\theta$, the exponents are defined only if $\sigma \geq \gamma + 2$ and they tend to decrease with increasing difference between the nucleation size $\sigma$ and attachment order $\gamma$. This implies that in order for self-assembly to be efficient, in general, $\gamma$ should be small and $\sigma$ large. This makes sense intuitively because a large difference between these parameters allows to reduce the nucleation rate by chang-

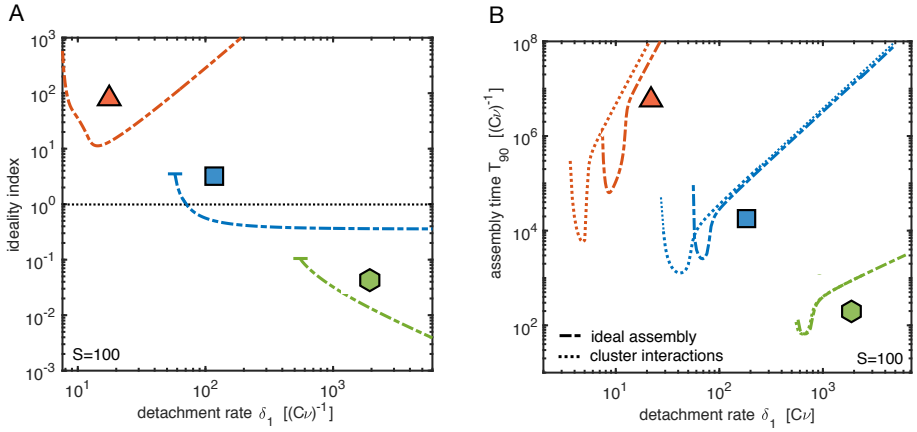


FIG. 4. **Beyond ideal self-assembly: The role of cluster interactions. A** The ideality index $I$, which estimates the number of interactions of an oligomer with other oligomers until time $T_{90}$ (see definition Eq. (3)), is plotted against the detachment rate $\delta_1$ for the three particle systems ($S = 100$). The index has been calculated numerically by integrating the effective model, Eq. (1). Values of $I$ larger than 1 (dotted line) indicate that cluster interactions can potentially be important and affect the assembly dynamics. A strong dependence of the potential role of cluster interactions on the particle morphology is thus revealed. **B** Assembly time $T_{90}$ with (dotted) and without (dash-dotted) cluster interactions plotted against the detachment rate $\delta_1$. In order to simulate the system with cluster interactions, we extended the effective theory by additional terms that account for all possible cluster reactions $c_s + c_p \xrightarrow{\nu} c_{s+p}$ subject to the constraint $s + p \leq S$ (see Methods for details). As in the ideal case, the assembly time in the model with cluster interactions increases like $T_{90} \sim \delta_1^{\sigma-2}$ for large $\delta_1$ but the minimal assembly time is smaller and shifted towards smaller detachment rates. Since the model most likely overestimates the rate of reactions between clusters, the resulting curve must be considered an upper bound for the effect that is to be expected in a real system.

ing $\delta_1$ without simultaneously affecting the attachment rate. Thereby, the ratio between the effective nucleation and attachment rate can be increased efficiently, which permits the assembly products to grow to a larger size [21]. In the hexagonal system, the minimal attachment order $\gamma = 1$ even guarantees a constant growth rate independent of $\delta_1$, which explains the high efficiency of the hexagonal system. Note, however, that if $\sigma$ is much larger than $\gamma$, the theoretical estimates for the exponents may lose their validity because $\delta_1^{\text{opt}} \gg C\nu$ then no longer holds. If $\sigma = \gamma + 1$, the ratio between the effective nucleation and attachment rate cannot be tuned any more since both rates depend identically on $\delta_1$ (the same number of unstable intermediate states must be transversed in both processes). The exponents are thus undefined if $\sigma = \gamma + 1$.

All results so far have been derived under two simplifying assumptions; namely, first, that clusters do not interact and grow only by attachment of single monomers (ideality assumption), and, second, that all higher order detachment rates $\delta_2, \delta_3, \ldots$ vanish. In the following, we will relax both of these assumptions and see how this affects the assembly dynamics.

## V. THE ROLE OF CLUSTER-CLUSTER INTERACTIONS

In order to estimate the extent to which interactions among oligomers can potentially influence the dynamics, we define the *assembly ideality index*

$$I := \frac{S}{C}\,\nu \int_0^{T_{90}} K^2 dt\,, \tag{3}$$

with $K(t) := \sum_{s=\sigma}^{S-1} c_s(t)$ being the total concentration of incomplete complexes in the system at time $t$. The ideality index therefore estimates the expected number of cluster interactions per completed structure until time $T_{90}$ (note that the concentration of completed structures at 90% yield is $0.9C/S \approx C/S$), assuming the same reaction rate $\nu$ between two clusters as between a cluster and a monomer. This assumption for the reaction rate between clusters most likely strongly overestimates their real reaction rate because larger clusters would typically diffuse and thus react more slowly than monomers and only a fraction of their interactions would lead to stable configurations. Furthermore, geometric deformations of larger assemblies might strongly decrease the reaction rate between clusters. Therefore, the ideality index must be interpreted as an upper limit for the expected number of reactions between clusters. Small values $I \ll 1$ indicate that cluster interactions can safely be neglected ('sufficient condition'), whereas large values $I > 1$ indicate that they may potentially have an effect on the dynamics, depending on the specifics of the system.

Figure 4 shows the ideality index plotted against the detachment rate $\delta_1$ for the three particle systems. The index reveals a strong dependence of the role of clus-

ter interactions on the morphology of the constituents: While cluster interactions can be safely neglected for the hexagonal system ($I \ll 1$), the index for the triangular system suggests a large potential role for these interactions. Away from the optimal detachment rate, the role of cluster interactions further decreases for the hexagonal system but increases strongly in the triangular system. We attribute those differences in the ideality index primarily to variations in the attachment order $\gamma$: Small values of $\gamma$ indicate that growth of clusters is comparatively fast and hence the concentration of incomplete structures is rather low, enabling only a small number of cluster encounters.

In order to estimate the effect that cluster interactions can have on the assembly time more accurately, we extended the effective model by additional terms accounting for reactions of any two clusters of sizes $i, j \geq \sigma$ with $i + j \leq S$ to a cluster of size $s = i + j$ at rate $\nu$:

$$\partial_t c_s = ... + \frac{1}{2}\nu \sum_{\substack{i,j\geq\sigma \\ i+j=s}} c_i c_j - \nu c_s \sum_{\substack{i\geq\sigma \\ i+s\leq S}} c_i \,, \qquad (4)$$

for all $\sigma \leq s \leq S$. The factor of $\frac{1}{2}$ in front of the first sum avoids double counting and serves as stoichiometric factor in the case $i = j$. As before, assuming that clusters react at the same rate $\nu$ as monomers will strongly overestimate the effect that cluster interactions have on the assembly time and thus the model can only describe an upper limit for the effect that is to be expected by cluster interactions. Figure 4B compares the assembly time of the ideal system with that obtained from simulating the extended model accounting for cluster interactions. The comparison shows that cluster interactions can potentially reduce the assembly time in the triangular and to a much lesser extent also in the square system. Given that the model most likely overestimates the reaction rate between clusters, however, the reduction of the assembly time will presumably be rather small in reality. Operating at ideality is therefore probably desirable for general self-assembly systems because cluster interactions could additionally promote the emergence of assembly errors and defects. The morphology of the constituents could therefore also be an important determinant of the robustness of the system against errors.

## VI. HIGHER ORDER REVERSIBILITY

Finally, we return to the assumption of an ideal assembly process and study the regime in which the higher order detachment rates $\delta_2, \delta_3, \ldots$ are non-negligible for the dynamics. Specifically, in the following, we quantify the role of higher order detachment rates by the ratio $r$ between detachment rates of consecutive order, $r := \delta_{n+1}/\delta_n = e^{-E_B}$. Small values of $r$ indicate that the higher order detachment rates, which are given by $\delta_n = \delta_1\, r^{n-1}$, are small compared to the leading order detachment rate $\delta_1$ and the assembly process can effectively be considered as irreversible on some relevant time scale (for example on the time scale of the minimal assembly time $T_{90}^{\min}$). We therefore call $r$ also the *reversibility ratio*. For sufficiently small $r$, we assume that the dynamics is well described by Eq. (1) in some parameter regime around the minimum but the question is how the system is affected if $r$ is sufficiently large. Note that if the final structures are required to be sufficiently stable, the reversibility ratio needs to be small enough so that the rate $S\delta_d = S\delta_1 r^{d-1}$, at which a monomer dissociates from a completed structure is sufficiently small. This stability requirement might set an upper limit for the reversibility ratio in practice.

Figure 5 shows the assembly time for the various particle morphologies as a function of $\delta_1$ (in units $(C\nu)^{-1}$) for different reversibility ratios $r$. Here, variation of $\delta_1$ at constant $r$ corresponds to an experimental control scenario where, for example, the concentration $C$ is changed while the temperature (and binding energy) is kept constant. Our numerical results show that the key new feature arising from higher order reversibility is that the range of $\delta_1$ in which a yield of 90% is achieved is now bounded from above when $r > 0$, whereas it is bounded from below when $r = 0$ (in the plot, we indicate divergences of the assembly time at a finite $\delta_1$ by upward arrows in cases where the divergence does not become apparent otherwise). Accordingly, the assembly time diverges at finite $\delta_1^{\text{div}}$ either above the optimal rate, i.e. $\delta_1^{\text{div}} > \delta_1^{\text{opt}}$, $(r > 0)$ or below the optimal rate, i.e. $\delta_1^{\text{div}} < \delta_1^{\text{opt}}$, $(r = 0)$. The reason is that for $r > 0$ the self-assembly process does not become kinetically trapped even if $\delta_1$ is small, because higher order detachment processes can always disassemble any structure. Interestingly, we find that for sufficiently small detachment rates, for all three particle morphologies, the assembly time scales inversely proportional to the detachment rate, independently of $r > 0$. In contrast, if $\delta_1$ is large, higher order detachment processes permit the system to realize a stationary concentration profile. The weight of the profile is shifted more and more towards small structure sizes as $\delta_1$ increases until a yield of 90% can no longer be achieved. If $\delta_{i\geq 2} = 0$, stable intermediate states block the reflux of density to structures of smaller size and thus prevent the system from becoming stationary, thereby explaining why the $T_{90}$-curves do not diverge at large but finite $\delta_1$ in the case $r = 0$.

By decreasing the reversibility ratio, the $T_{90}$-curves gradually change over from the shape that diverges at a finite rate above the optimal rate to the shape that diverges at a finite rate below the optimum. Interestingly, there is typically a range of intermediate ratios $r$ where the minimum is in a deep funnel and the assembly time increases sharply to either side. From an experimental point of view, such a reversibility ratio would be very unfavorable, as it requires extreme fine-tuning of $\delta_1$ to achieve a high yield in a reasonable time. However, depending on the monomer morphology, a sufficiently large reversibility ratio can be quite advantageous to reduce

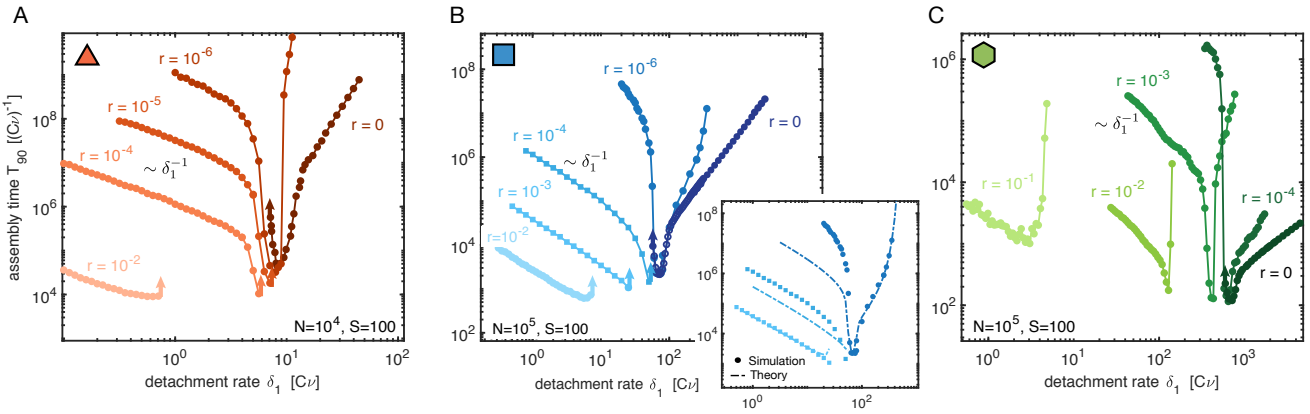


FIG. 5. The effect of higher order reversibility on the assembly time. The assembly time $T_{90}$ obtained from stochastic simulations is plotted against the detachment rate $\delta_1$ for different reversibility ratios $r = \delta_{n+1}/\delta_n = e^{-E_B}$ for the triangular (A), square (B) and hexagonal (C) system with structure size $S = 100$ and $N = 100S$ or $N = 1000S$. Divergences of $T_{90}$ at finite values of $\delta_1$ are indicated by upward pointing arrows if these would otherwise not be evident from the plot. For $r > 0$, the assembly time scales inversely proportional to $\delta_1$ for sufficiently small $\delta_1$ and diverges at large finite $\delta_1$. In contrast, for $r = 0$ the assembly time diverges at small finite $\delta_1$ but scales with $\sim \delta_1^{\sigma-2}$ for large $\delta_1$. The minimal assembly time is noticeably affected by higher order reversibility only if $r$ is large. The inset in B compares the assembly time obtained from stochastic simulations for the square system with the prediction of the effective theory (cf. Eqs. (1) and (5)).

the assembly time and increase the range of variability of the control parameter for which self-assembly is efficient due to the slow increase of $T_{90}$ with decreasing $\delta_1$. Note, in particular, that, as both the control parameter and the assembly time are measured relative to $(C\nu)$ and $(C\nu)^{-1}$, respectively, the assembly time in physical units as a function of the monomer concentration $C$ is constant throughout the range in which $T_{90} \sim \delta_1^{-1}$. This implies that in an experimental control scenario in which the monomer concentration is increased to trigger self-assembly, the assembly time becomes constant for sufficiently large monomer concentrations.

To include higher-order reversibility in the effective kinetic theory, we note that its main effect is the dissociation of structures which are stable against disassembly by $\delta_1$, i.e., structures in which each component has two or more bonds. Decay of these structures is mainly driven by the subleading rate $\delta_2$. For example, in the system with square-shaped monomers, each stable state of rectangular shape decays at rate $\bar{\delta} \approx 4\delta_2$, since there are four edge-particles each detaching at rate $\delta_2$. Hence, in order to account for higher order reversibility in the effective theory, Eq. (1) needs to be extended by the following terms accounting for the disassembly of structures:

$$\begin{aligned} \partial_t c_1 &= \ldots + \sigma\bar{\delta} c_\sigma + \bar{\delta} \sum_{s=\sigma+1}^{S-1} c_s \\ \partial_t c_\sigma &= \ldots + \bar{\delta}\,(c_{\sigma+1} - c_\sigma) \\ \partial_t c_s &= \ldots + \bar{\delta}\,(c_{s+1} - c_s)\ . \end{aligned} \tag{5}$$

The terms on the right hand side of the first line account for the influx of monomers due to the disassembly of nuclei as well as detachment of monomers from larger complexes. Similarly, the terms in the second and third line account for the gain of complexes of size $s \leq \sigma$ due to disassembly of larger complexes and loss due to disassembly of complexes of the same size $s$. Note that, while Eq. (1) describes self-assembly as an irreversible process, only the additional terms in Eq. (5) render the process fully reversible.

Integrating the extended model, we find that the theory correctly describes the qualitative behavior of the system (Fig. 5) but underestimates the assembly time for small $\delta_1$ and small nonzero $r$. We attribute those quantitative differences mainly to the averaging of attachment rates in the effective model, which leads to an overestimation of the rate of transfer of monomers between complexes.

This approach of expanding the theory gradually by terms that account for the heuristic effect of higher order reversibility thus offers a systematic way to describe reversible self-assembly processes. The first order theory, Eq. (1), can thereby be treated analytically by exploiting its irreversibility in order to derive analytic scaling exponents. The theory approximately predicts the minimal assembly time that can be achieved. The higher order corrections lead to important qualitative differences compared to the first order theory, but typically do not significantly alter the minimal assembly time unless $r$ is large.

## VII. DISCUSSION

In this work we found that in the self-assembly of two-dimensional structures, the morphology of the building blocks crucially determines dynamic properties of the self-assembly processes, most importantly their time ef-

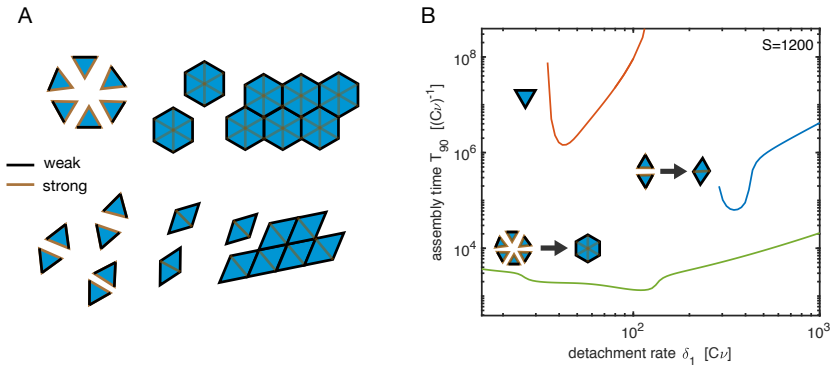


FIG. 6. Hierarchical self-assembly as a way to optimize the morphology. Organizing the assembly process in a hierarchical way can increase self-assembly efficiency significantly by optimizing the morphology of intermediate assembly products. **A** In order to induce triangular particles to assemble hierarchically, bonds between edges indicated in brown are assumed to be more stable than bonds between black edges. As a result of this variation of the binding strengths, particles first form hexamers (hexagons) or dimers (rhomboids) which subsequently assemble into the structures more efficiently than the original triangles. **B** The assembly time is plotted against the detachment rate $\delta_1$ for the triangular particle system in comparison with the two hierarchical schemes illustrated in A and a target structure of size $S = 1200$. Simulations were performed with the effective model (see Methods), assuming a constant ratio $r_h = 10^{-4}$ between the detachment rates of strong and weak bonds. Since self-assembly of particles with the hexagonal morphology is particularly efficient, the assembly time can thus be reduced by three orders of magnitude and variability in the control parameter is enhanced significantly.

ficiency. The dynamic effect of the particle morphology can thereby be expressed by three topological parameters: the nucleation size and attachment order, which describe the effective order of reactions by which clusters nucleate and grow, respectively, as well as the growth exponent, that determines how the growth rate scales with the structure size. Most importantly, the time complexity exponent, which characterizes the scaling of the assembly time with target structure size, is approximately a function only of these three parameters. Monomer morphologies like the hexagonal system, with an attachment order of 1 (and nucleation size larger than 2) are thereby particularly efficient, as they allow to control the nucleation speed without affecting the growth rate when tuning the control parameter. In contrast, an attachment order larger than 1 requires an increasingly large nucleation size in order to keep the time complexity exponent $\theta$ small. A large nucleation size, however, implies a strong increase of the assembly time for detachment rates larger than the optimal rate and might hence necessitate fine-tuning of the control parameter.

This necessity of fine-tuning can possibly be avoided by increasing the reversibility ratio, i.e. the ratio between detachment rates of consecutive order, which amounts to reducing the binding energy between the constituents. We found that a sufficiently large reversibility ratio induces a slow increase of the assembly time for small detachment rates and therefore allows one to achieve high efficiency in a large parameter range. However, too large a reversibility ratio would require a very low binding energy and might hence not conform with the stability of the final assembly products. On the other hand, intermediate reversibility ratios can lead to a very unfavorable situation in which the assembly time increases sharply to both sides of the optimum and extreme fine-tuning is necessary in order to achieve efficient self-assembly.

Our study suggests that understanding kinetic features of self-assembly processes is crucial for a holistic perception of the phenomenon and highly useful when it comes to experimentally realizing self-assembling systems. Specifying structural determinants and conditions under which high yield is achieved might not be sufficient, because the time it takes could be extremely long. Here we found that the morphology of the constituents is an important kinetic determinant, which strongly impacts self-assembly efficiency. We demonstrated that, depending on the particle morphology, the time it takes to achieve a high yield for large target structures can vary by several orders of magnitude. These insights can be used to optimize self-assembly experiments, for example, by suggesting highly efficient ways to implement hierarchical self-assembly. For instance, Fig. 6 shows two possibilities in order to significantly enhance the self-assembly efficiency of triangular monomers by optimizing their morphology with a hierarchical assembly step. Making certain bonds more stable than others enables the monomers to first form squares or hexagons, which subsequently assemble into the final structures much more efficiently than the original triangles. We simulated this hierarchical scenario by modifying the effective theory (see Methods) and find that for structures of size $S = 1200$, a reduction of the minimal assembly time by 3 orders of magnitude can be achieved and robustness in the control parameter is greatly enhanced (Fig. 6B).

Furthermore, our results may contribute to a better understanding of the kinetics of biological self-assembly processes. For example, several icosahedral virus capsids assemble from triangular-shaped particles [34] but

the mechanisms underlying their self-assembly are still largely unknown. Our results would suggest that either a hierarchical step or higher order reversibility is required in order for large capsids to assemble time-efficiently. However, an additional problem concerns the icosahedral symmetry of spherical capsids: At 12 precise positions the capsid proteins must form pentamers while everywhere else they form hexamers. Consequently, it has been suggested that large virus capsids can only assemble in the presence of a scaffold [35] coordinating their formation and thus our results might not apply directly in this case as a consequence of the scaffolding. Otherwise, assuming that icosahedral shells assembled without a scaffold with nucleation size $\sigma = 5$, Eq. (2) would predict a time complexity exponent of $\theta = 2$, implying that self-assembly of large icosahedral capsids would be even significantly less efficient than self-assembly of the planar triangular system ($\theta = 1$). Hence, beside structural aspects, enhancement of time efficiency could be another essential reason for the requirement of a scaffold in the formation of large icosahedral viruses. In contrast, alpha-carboxysomes, which also form large icosahedral structures, were shown to assemble also in the absence of a scaffold and are composed of proteins with hexameric and pentameric quaternary structure (CsoS1ABC and CsoS4AB) [36]. Hence, carboxysome capsids represent the icosahedral analogue of the hexagonal particle system studied here. This particular morphology of the constituents could be an essential factor in order for such huge structures to be able to assemble efficiently even in the absence of a scaffold. These insights might be particularly relevant for experiments trying to mimic the self-assembly of artificial capsids for biotechnological applications [5].

## ACKNOWLEDGMENTS

We thank Severin Angerpointner for stimulating discussions. This research was supported by the German Excellence Initiative via the program 'NanoSystems Initiative Munich'(NIM) and was funded by the Deutsche Forschungsgemeinschaft (DFG, German Research Foundation) under Germany's Excellence Strategy – EXC-2094–390783311 as well as under – Project-ID 364653263 – TRR 235. FMG was supported by a DFG fellowship through the Graduate School of Quantitative Biosciences Munich (QBM).

## Appendix A: Methods

### 1. Stochastic simulation

The simulations were performed using Gillespie's stochastic algorithm [37]. In the simulation complexes are represented as boolean arrays of size $S$, which contain ones at sites that are occupied by a particle and zeros otherwise. For simplicity, one can imagine the structures as two-dimensional arrays although internally, of course, all data structures are represented as one-dimensional memory sequences and two-dimensional subscript indices must be converted to linear indices. The neighboring- or adjacency relations between the sites in the two-dimensional array thereby determine the morphology and are defined as follows: In the square system, site $(i, j)$ is adjacent to sites $(i \pm 1 \mod L, j)$ and $(i, j \pm 1 \mod L)$, where $L = \sqrt{S}$ is the linear extension of the target structure and by taking the modulo periodic boundary conditions are implied. Accordingly, in the hexagonal system, site $(i, j)$ is adjacent to the six sites $(i\pm1 \mod L, j)$, $(i, j\pm1 \mod L)$ and $(i\pm1 \mod L, j\mp1 \mod L)$ and in the triangular system, site $(i, j)$ has three neighbors $(i \pm 1 \mod L, j)$ and $(i, j + 1 \mod L)$ if $j$ is even or $(i, j - 1 \mod L)$ if $j$ is odd (see Fig. 1A for the logic behind these definitions).

As soon as a dimer forms, such a boolean array is reserved for the complex and two arbitrary neighboring sites are chosen and set to 1 in order to represent the initial dimer. Due to the periodic boundary conditions, it is irrelevant which two neighboring positions are chosen because the structure is translationally invariant. Subsequently, each unoccupied site in the complex which has at least one occupied neighbor is itself occupied by a monomer at rate $\nu n$, where $n$ is the number of monomers in the system (monomer attachment). The reaction rate $\nu$ is typically set to 1. Similarly, a site that is occupied becomes disoccupied again with rate $\delta_i$, where $i$ denotes the number of occupied neighboring sites (monomer detachment). Each attachment (detachment) event decreases (increases) the number $n$ of monomers in the system. In this way, the simulation respects all possible configurations of clusters that can emerge. By counting the number $M$ of complete structures, i.e. structures with $S$ occupied sites, the yield is calculated as yield $= \frac{MS}{N}$.

It is important to optimize the code for efficiency because, since the detachment rate $\delta_1$ is typically much larger than the reaction rate $N\nu$, many Gillespie steps are generally needed until a yield of 90% is reached even for intermediate particle numbers $N$ (typically, we simulated the system with N between 100S and 1000S so that a maximum number of 100 to 1000 target structures is built). In particular, the simulation of the triangular system is computationally expensive due to the comparatively large number of intermediate steps between two stable configurations with the triangular morphology and the longer time spans required to be simulated in order to reach 90% yield. Partly, several billion Gillespie steps

were needed for a single run to complete. The computational cost of the simulation strongly increases with the size of the target structure because both the detachment rate $\delta_1$ and the required simulation time $T_{90}$ increase with $S$. Furthermore, the particle number $N$ should typically be increased with $S$ in order to keep the number of assembled structures constant. Hence, in order to be able to simulate also large system sizes up to a size of $S = 1000$, efficiency of the simulation is crucial. By associating additional data structures with the complexes that allow to choose and update attachment and detachment events efficiently, our simulation written in C++ was able to perform more than one million Gillespie steps per second on a 3,1 GHz CPU. The C++ code of the simulation is available online.

### 2. Effective model

In order to better understand the determinants of self-assembly kinetics, an effective model was described in the main text (cf. Eq. (1)). Here we discuss the model and show how it can be derived. The essence of the theory is the restriction to the most likely assembly pathways, i.e. pathways that traverse a minimal number of unstable states in order to arrive from one stable configuration to the next. The process starts with the formation of a stable nucleus, which requires a minimal number of $\sigma$ monomers (see Fig. 1C for an illustration of the nucleation process in the triangular system). Consequently, to form the nucleus, the system must traverse $\sigma - 2$ unstable states, each of which decays to the previous state with rate $\sim \delta_1$. Hence, according to classical nucleation theory [38], if $\delta_1$ is large compared to the forward rates $C\nu$ and $C\mu$, respectively, nucleation can be described as an effective reaction of order $\sigma$,

$$r_{(\sigma c_1 \to c_\sigma)} = \bar{\mu} c_1^\sigma \qquad \text{with} \qquad \bar{\mu} = \mu \left(\frac{\nu}{\delta}\right)^{\sigma-2} . \tag{A1}$$

Here $c_i$ denotes both, an oligomer of size $i$ as well as its concentration. The effective rate constant $\bar{\mu}$ thereby equals the product of the forward rates divided by the backward rates. The rates in Appendix Fig. 7 show that - with the definitions of our model - all numeric factors in the forward and backward rates, which account for equivalent assembly pathways, cancel out and so the above expression for $\bar{\mu}$ defines not just a proportionality but really an equality (the same holds true also for the square and triangular system).

Attachment processes typically proceed in two steps (see Fig. 1C): In the first step, a leading order reaction of order $\gamma$ leads to the formation of a new stable configuration. Similar as for nucleation, if $\delta_1$ is large compared to $C\nu$ the first step can be described as an effective reaction with rate constant $\sim \nu \left(\frac{\nu}{\delta}\right)^{\gamma-1}$. Subsequently, in the second step, a number of subleading order reactions may follow 'filling up the row' until the process can only proceed by another reaction of order $\gamma$. If $\delta_1$ is large compared to the forward rate $C\nu$, the subleading order reactions can be assumed to be fast compared to the leading order reaction. Hence, denoting by $n_s$ the total number of particles that are attached through the first and second step on average for a cluster of size $s$, the rate of the entire attachment process is approximately given by:

$$r_{(c_s + n_s c_1 \to c_{s+n_s})} \sim b_s \left[\nu \left(\tfrac{\nu}{\delta}\right)^{\gamma-1}\right] c_1^\gamma c_s \, . \tag{A2}$$

Here, $b_s$ scales with the size of the boundary of an average cluster of volume $s$ and accounts for the number of binding sites at which the leading order reaction can be initiated. For the analysis, however, it is convenient to consider the (harmonic) average rate for the attachment of a single monomer:

$$r_{(c_s + c_1 \to c_{s+1})} = n_s r_{(c_s + n_s c_1 \to c_{s+n_s})} := s^\omega \bar{\nu} c_1^\gamma c_s \qquad \text{with} \qquad \bar{\nu} = a\nu \left(\frac{\nu}{\delta}\right)^{\gamma-1} , \tag{A3}$$

where $a s^\omega := n_s b_s$ such that $s^\omega$ captures the scaling of the rate with the cluster size and the constant $a$ combines the numerical prefactors of $n_s$ and $b_s$. We fitted the constant $a$ but its values can also be estimated analytically. For example, in the square system, assuming that typical clusters have the shape of a square, the cluster boundary is $b_s = 4\sqrt{s}$ and the number of particles attached per attachment sequence corresponds to one quarter of the boundary, $n_s = \sqrt{s}$, implying $a = 4$ and $\omega = 1$. The best fit was obtained with a slightly larger prefactor of $a = 5.3$, which makes sense considering that clusters most likely do not grow in perfect square shape and thus have a slightly larger boundary-to-volume ratio. For the triangular system, the best fit was obtained with $a = 4$, which is slightly smaller compared to the square system, probably because a typical cluster has six edges instead of four and so $n_s$ is slightly smaller than in the square system. In the hexagonal system, there are no subleading order reaction because $\gamma = 1$ and thus $n_s = 1$. Consequently, we have $\omega = 1/2$ and the best fit was obtained with a rather small prefactor $a = 2.3$, which probably accounts for the fact that, to leading order, particles only bind to sites at which they have two neighbors, which amounts to only a fraction of all boundary sites. The constant $a$ influences the minimal assembly time and the optimal detachment rate but it does not affect their scaling as we show in the next section. We determined the respective values of $a$ by fitting the optimal detachment rate predicted by the theory with the stochastic simulation for target structures of size $S = 100$.

With the definitions for the nucleation rate and average attachment rate, Eqs. (A1) and (A3), it is straight forward to formulate the ordinary differential equations (1) that constitute the leading order theory. Note, however, that for the triangular system, the first attachment reaction after formation of the nucleus has a higher order $\gamma = 4$ compared to all subsequent attachment reactions, which have order $\gamma = 3$ (see Fig. 1A). As it turned out,

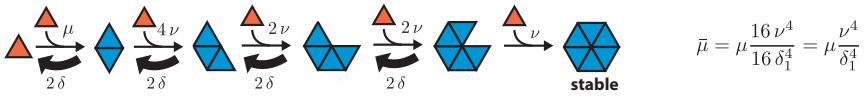


FIG. 7. Depiction of the nucleation process including all prefactors for the transition rates. Prefactors account for the degeneracy of attachment or detachment reactions leading to equivalent configurations. The prefactors of the forward and backward rates cancel each other so that the effective nucleation rate $\bar{\mu}$ has prefactor 1.

the fit to the simulation is significantly improved if the higher order of the initial attachment reaction is taken into account. Specifically, by accounting for all equivalent assembly pathways that lead from the nucleus to the next stable configuration, we determine the effective rate of the initial attachment reaction as

$$r(c_\sigma + 4c_1 \to c_{\sigma+4}) = 24\,\bar{\nu}' c_\sigma c_1^4 \qquad \text{with} \qquad \bar{\nu}' = \nu \left(\frac{\nu}{\delta}\right)^3 . \tag{A4}$$

Consequently, the (harmonic) average attachment rate per monomer for $\sigma \le s \le \sigma + 3$ is given by

$$r(c_s + c_1 \to c_{s+1}) = 96\,\bar{\nu}' c_s c_1^4 . \tag{A5}$$

We modified the effective theory of the triangular system accordingly in order to account for the higher order of the initial attachment reaction.

Eq. (1) describes the basic reaction kinetics of reversible self-assembly. The basic theory can easily be extended by accounting for additional effects. For example, in order to estimate the effect invoked by the interactions of larger oligomers (see Fig. 4B), we additionally accounted for the reactions of any two clusters of size $i \ge \sigma$ and $j \ge \sigma$ with $i + j \le S$ to a cluster of size $i + j$ at rate $\nu$:

$$r(c_i + c_j \to c_{i+j}) = \nu c_i c_j . \tag{A6}$$

To this end, we augmented the right hand side of Eq. (1) by the following terms:

$$\partial_t c_s = ... + \frac{1}{2}\nu \sum_{\substack{i,j \ge \sigma \\ i+j=s}} c_i c_j - \nu c_s \sum_{\substack{i \ge \sigma \\ i+s \le S}} c_i , \tag{A7}$$

for all $\sigma \le s \le S$, where the factor of $\frac{1}{2}$ in front of the first sum avoids double counting and serves as stoichiometric factor in the case $i = j$.

Similarly, the right hand side of Eq. (1) can be augmented to account for the effect of higher order reversibility as shown explicitly for the square system in Eq. (5). In general, the effect of higher order reversibility can be included in the theory by accounting for detachment reactions at a rate of the general form

$$r(c_s \to c_{s-1} + c_1) = \bar{\delta} s^\beta c_s . \tag{A8}$$

Here $s^\beta$ describes how the detachment rate invoked by $\delta_2$ scales with the cluster size and $\bar{\delta} \sim \delta_2$ is the proportionality constant. For example, for the square system, we determined $\beta = 0$ and $\bar{\delta} = 4\delta_2$. In contrast, in the triangular and hexagonal system, the number of particles that can detach at rate $\delta_2$ from the cluster boundary increases proportional to the size of the boundary, implying $\beta = 1/2$. As discussed in the main text, however, the extended theory is able to predict the behavior of the system only qualitatively in the regime of small $\delta_1$ and small $r = \delta_2/\delta_1$.

Finally, we used the effective theory in order to simulate the hierarchical self-assembly scenario by formally distinguishing weak and strong bonds of the particles (see Fig 6). To this end, we

In the first case, we simulated the irreversible dimerization of two (triangular) monomers via strong bonds into squares at rate $\mu = \nu$. In the second case, we considered the formation of hexagons by explicitly simulating the nucleation process in the triangular system illustrated in Appendix Fig. 7 with detachment rate $\delta_{\text{str}} = 10^{-4} * \delta_1$. The squares and hexagons, once formed, are stable and react in the usual way as described by Eq. (1) mediated by the weak bonds. Interactions between (triangular) monomers as well as incomplete hexagons with larger oligomers are fully neglected, which is motivated by the time scale separation between reactions mediated by strong and weak bonds. In the hexagonal case, it is important that the detachment rate $\delta_{\text{str}}$ of the strong bonds is neither too large nor too small relative to $\delta_1$: In both cases, formation of the hexagons would be slow and lead to an increase of the overall assembly time. We found that a ratio of $r_h := \frac{\delta_{\text{str}}}{\delta_1} \approx 10^{-4}$ between the detachment rates of the strong and weak bonds approximately minimizes $T_{90}$.

### 3. Derivation of the scaling exponents

In order to derive the scaling exponents of the minimal assembly time and the optimal parameter as a function of target structure size, we exploit that the leading order theory, Eq. (1), describes self-assembly as an irreversible process. In particular, thanks to irreversibility one can define the final yield, which is plotted in Fig. 2B in dependence of $\delta_1$. Rescaling $\delta_1$ by the optimal detachment rate $\delta_1^{\text{opt}}$ approximately makes the yield curves collapse onto a single curve (Fig. 2B inset) and thereby shows that $\delta_1^{\text{opt}}$ scales identically as the threshold rate $\delta_1^{\text{th}}$, i.e. the minimal detachment rate for which nonzero yield is obtained. Analyzing the threshold rate instead of the

optimal rate allows for a great simplification because, as we will show in the following, detailed information about the distribution of cluster sizes is not required in order to derive the scaling of the threshold rate.
Specifically, one can rewrite the sum on the right hand side of Eq. (1), governing the evolution of the concentration of monomers, as

$$\sum_{s=\sigma}^{S} s^{\omega} c_s = K \sum_{s=\sigma}^{S} s^{\omega} \frac{c_s}{K} = K \langle s^{\omega} \rangle \,, \tag{A9}$$

where $K := \sum_{s=\sigma}^{S} c_s$ denotes the total concentration of complexes above nucleation size and $\langle s^{\omega} \rangle$ the $\omega$ - moment of the distribution of cluster sizes. In the case $\omega = 1$, which applies for the square and triangular system, as long as the yield is zero, the average cluster size $\langle s \rangle$ corresponds to the total number of bound monomers divided by the total number of clusters: $\langle s \rangle = \frac{C-m}{K}$, where for notational simplicity here and in the following we denote the concentration of monomers by $m := c_1$. For general $\omega$, there is no such exact identity but in order to make progress we approximate the $\omega$ - moment by $\langle s^{\omega} \rangle = \langle s \rangle^{\omega} \approx \left(\frac{C-m}{K}\right)^{\omega}$. Because $\omega$ is typically close to 1 (for example, for the hexagonal system $\omega \approx 1/2$), we expect the approximation to be quite accurate in general. Hence, it follows for the evolution of the concentration of monomers as long as the yield is zero,

$$\frac{dm}{dt} = -\bar{\nu} m^{\gamma} \left(C - m\right)^{\omega} K^{1-\omega} - \sigma \bar{\mu} m^{\sigma} \,. \tag{A10}$$

Furthermore, the total concentration of complexes $K$ increases as a consequence of nucleation events and thus obeys:

$$\frac{dK}{dt} = \bar{\mu} m^{\sigma} \,. \tag{A11}$$

Nonzero yield is achieved if the foremost front of the density profile that describes the distribution of cluster sizes and evolves according to Eq. (1) reaches the target structure size $S$. In order to find a simple condition for the onset of the yield we first make a hydrodynamic approximation of the evolution of the cluster size concentration. To this end, as the cluster size is typically large compared to 1, we approximate the prefactor $(s-1)^{\omega}$ in the third line of Eq. (1) by $s^{\omega}$ and subsequently Taylor expand the concentration profile by interpreting $c$ as continuous function of $s$: $c_{s-1} \approx c(s) - \partial_s c(s) + \frac{1}{2}\partial_s^2 c(s) + ....$ Hence, in this continuity approximation, the evolution of the cluster size concentrations follows

$$\partial_t c_s = -\bar{\nu} s^{\omega} m^{\gamma} \partial_s c + \frac{1}{2} \bar{\nu} s^{\omega} m^{\gamma} \partial_s^2 c \,. \tag{A12}$$

This partial differential equation describes an advection-diffusion equation with coefficients depending on the cluster size $s$ and the momentary monomer concentration $m$. A similar approach of approximating the system of ordinary differential equations by a continuous advection-diffusion equation was used previously in order to describe virus capsid assembly [14, 39, 40]. Thus, the foremost front of the density profile advectively travels a distance $\Delta s_{\mathrm{advec}} = \bar{\nu} \int_0^{\infty} s(t)^{\omega} m(t)^{\gamma} dt$, which equals the square of the diffusively travelled dsitance $\Delta s_{\mathrm{advec}} = (\Delta s_{\mathrm{diff}})^2$, since the advection and diffusion coefficient are the same. Hence, as we are interested in the asymptotic scaling for large target sizes $S$, we neglect the diffusive contribution against the advective contribution. As it turns out, however, the diffusive contribution is one of the main reasons why the assembly time for small structure sizes deviates from its asymptotic scaling. Considering only the advective contribution and assuming that a number of complexes nucleates at $s = \sigma$ at time $t = 0$, the tip of the density profile evolves according to

$$\frac{ds}{dt} = \bar{\nu} s^{\omega} m^{\gamma} \,, \tag{A13}$$

with $s(0) = \sigma$ and the yield threshold is arrived if $s(\infty) = S$.
Hence, the closed system consisting of three ordinary differential equations (A10), (A11) and (A13) predicts the threshold of the yield. We were able to find an analytic solution to this problem only for the case of the square system ($\omega = 1$ and $\gamma = 2$) using elementary calculus. Specifically, in this case we find $s(\infty) = \sigma \frac{1+\sqrt{1-4\tilde{\eta}}}{1-\sqrt{1-4\tilde{\eta}}}$, with $\tilde{\eta} := \frac{\sigma \bar{\mu} C}{\bar{\nu}}$, which, for large $S$ (and $\eta \ll 1$) implies $\delta_1^{\mathrm{th}}/(C\nu) \sim \frac{\mu}{\nu} S$.
However, in order to determine the asymptotic scaling exponents, there is a much simpler way which does not even require to solve the equations. To this end, we note that in the limit of large structure size $S$, the nucleation term in Eq. (A10) is negligible for the dynamics of the monomer concentration because the number of nucleation events is significantly smaller than the number of attachment events. Furthermore, we non-dimensionalize the system by measuring concentrations in units of $C$ and time in units of the effective time scale $(\bar{\nu} C^{\gamma-1})^{-1}$: $m \to mC, \quad K \to KC, \quad t \to t(\bar{\nu} C^{\gamma-1})^{-1}$, which reduces the system to:

$$\begin{aligned} \dot{m} &= -m^{\gamma}(1-m)^{\omega} K^{1-\omega} \\ \dot{K} &= \eta m^{\sigma} \\ \dot{s} &= s^{\omega} m^{\gamma} \,, \end{aligned} \tag{A14}$$

with dimensionless parameter $\eta := \bar{\mu} C^{\sigma-\gamma-1}/\bar{\nu}$. Using a scaling ansatz for the three variables by defining $m = \tilde{m}(\eta^z t)$, $K = \eta^x \tilde{K}(\eta^z t)$ and $s = \eta^y \tilde{s}(\eta^z t)$ with $z = (1-\omega)/(2-\omega)$, $x = (2-\omega)^{-1}$ and $y = -(2-\omega)^{-1}$, one can easily verify that the system becomes independent of $\eta$:

$$\begin{aligned} \tilde{m}' &= -\tilde{m}^{\gamma}(1-\tilde{m})^{\omega} \tilde{K}^{1-\omega} \\ \tilde{K}' &= \tilde{m}^{\sigma} \\ \tilde{s}' &= \tilde{s}^{\omega} \tilde{m}^{\gamma} \,. \end{aligned} \tag{A15}$$

Hence, the scaling forms $\tilde{m}$, $\tilde{K}$ and $\tilde{s}$, while still depending on $\sigma$, $\gamma$ and $\omega$, are independent of $\eta$. In particular,

as condition for the yield onset in dependence of the detachment rate one obtains: $S \stackrel{!}{=} s(\infty) = \eta^y \tilde{s}(\infty) \sim \eta^y$, and hence

$$\eta^{-1} \sim S^{2-\omega}\,. \tag{A16}$$

With the definitions for $\bar{\mu}$ and $\bar{\nu}$ from Eqs. (A1) and (A3), we thus find the detachment rate scaling as

$$\frac{\delta_1^{\mathsf{opt}}}{C\nu} \sim \frac{\delta_1^{\mathsf{th}}}{C\nu} \sim \left(\frac{\mu}{\nu}\right)^{\frac{1}{\sigma-\gamma-1}} S^{\frac{2-\omega}{\sigma-\gamma-1}}\,, \tag{A17}$$

with parameter exponent $\phi = \frac{2-\omega}{\sigma-\gamma-1}$, consistent with the solution above for the square system. Since nucleation is the time limiting step, the assembly time $T_{90}$ can be estimated as the time it takes for $0.9C/S$ nucleation events to happen. Hence,

$$T_{90}^{\mathsf{min}} \sim \frac{\frac{C}{S}}{\bar{\mu}^{\mathsf{opt}} C^{\sigma}} \sim (C\nu)^{-1} \left(\frac{\mu}{\nu}\right)^{\frac{\gamma-1}{\sigma-\gamma-1}} S^{\frac{(1-\omega)\sigma+\gamma+2\omega-3}{\sigma-\gamma-1}}\,, \tag{A18}$$

where $\bar{\mu}^{\mathsf{opt}}$ denotes the effective nucleation rate resulting from $\delta_1 = \delta_1^{\mathsf{opt}}$. Thus, we obtain as asymptotic time complexity exponent $\theta = \frac{(1-\omega)\sigma+\gamma+2\omega-3}{\sigma-\gamma-1}$.

Interestingly, the same scaling behavior for $T_{90}$ is obtained when considering the extreme case of very slow nucleation that typically applies if $\delta_1 \gg \delta_1^{\mathsf{opt}}$. To see this, we note that in this regime the concentration of unfinished structures is low at any time and thus, approximately, one can assume that each complex is completed before the next one nucleates. Each nucleation event then reduces the number of monomers by $S$ units and hence the evolution of the monomer concentration obeys $\dot{m} = -S\bar{\mu}m^{\sigma}$. Separating variables and integrating $m$ from $C$ to $0.1C$ and $t$ from 0 to $T_{90}$, we obtain $T_{90} \sim \frac{C/S}{\bar{\mu}C^{\sigma}}$ as above (Eq. (A18)). This result confirms the asymptotic scaling of $T_{90}^{\mathsf{min}}$ and, moreover, suggests that the typical shape of the $T_{90}$ curves does not depend on $S$ as the different parts of the curve scale identically with the target structure size. The invariance of the shape of the curves in turn implies that the time complexity exponent $\theta$ not only describes the scaling of the minimal assembly time but of the entire curve and hence the scaling law can be formulated much more generally as:

$$\delta_1 \sim S^{\phi} \qquad \text{implies} \qquad T_{90} \sim S^{\theta}\,, \tag{A19}$$

as long as all higher order detachment rates are negligible: $\delta_{n\geq 2} = 0$.


[1] G. M. Whitesides, J. P. Mathias, and C. T. Seto, Molecular self-assembly and nanochemistry: a chemical strategy for the synthesis of nanostructures., Science (New York, N.Y.) **254**, 1312 (1991).

[2] G. M. Whitesides and B. Grzybowski, Self-assembly at all scales, Science **295**, 2418 (2002).

[3] S. Zhang, Fabrication of novel biomaterials through molecular self-assembly, Nature Biotechnology **21**, 1171 (2003).

[4] A. C. Mendes, E. T. Baran, R. L. Reis, and H. S. Azevedo, Self-assembly in nature: using the principles of nature to create complex nanobiomaterials, Wiley Interdisciplinary Reviews: Nanomedicine and Nanobiotechnology **5**, 582 (2013).

[5] C. Sigl, E. M. Willner, W. Engelen, J. A. Kretzmann, K. Sachenbacher, A. Liedl, F. Kolbe, F. Wilsch, S. A. Aghvami, U. Protzer, M. F. Hagan, S. Fraden, and H. Dietz, Programmable icosahedral shell system for virus trapping, Nature Materials 10.1038/s41563-021-01020-4 (2021).

[6] G. M. Whitesides and M. Boncheva, Beyond molecules: Self-assembly of mesoscopic and macroscopic components, Proceedings of the National Academy of Sciences of the United States of America **99**, 4769 (2002).

[7] R. Freeman, M. Han, Z. Álvarez, J. A. Lewis, J. R. Wester, N. Stephanopoulos, M. T. McClendon, C. Lynsky, J. M. Godbe, H. Sangji, E. Luijten, and S. I. Stupp, Reversible self-assembly of superstructured networks, Science **362**, 808 (2018).

[8] P. Ceres and A. Zlotnick, Weak protein-protein interactions are sufficient to drive assembly of hepatitis B virus capsids, Biochemistry **41**, 11525 (2002).

[9] J. Grant, R. L. Jack, and S. Whitelam, Analyzing mechanisms and microscopic reversibility of self-assembly, Journal of Chemical Physics **135**, 10.1063/1.3662140 (2011).

[10] A. Zlotnick, Are weak protein-protein interactions the general rule in capsid assembly?, Virology **315**, 269 (2003).

[11] D. C. Rapaport, Role of reversibility in viral capsid growth: A paradigm for self-assembly, Physical Review Letters **101**, 1 (2008), arXiv:0803.0115.

[12] M. F. Hagan, Modeling Viral Capsid Assembly., Advances in chemical physics **155**, 1 (2014).

[13] J. D. Perlmutter and M. F. Hagan, Mechanisms of virus assembly, Annual Review of Physical Chemistry **66**, 217 (2015), arXiv:1407.3856.

[14] D. Endres and A. Zlotnick, Model-Based Analysis of Assembly Kinetics for Virus Capsids or Other Spherical Polymers, Biophysical Journal **83**, 1217 (2002).

[15] M. F. Hagan, O. M. Elrad, and R. L. Jack, Mechanisms of kinetic trapping in self-assembly and phase transformation, Journal of Chemical Physics **135**, 10.1063/1.3635775 (2011).

[16] E. J. Deeds, J. A. Bachman, and W. Fontana, Optimizing ring assembly reveals the strength of weak interactions, Proceedings of the National Academy of Sciences of the United States of America **109**, 2348 (2012).

[17] S. Whitelam and R. L. Jack, The statistical mechanics of dynamic pathways to self-assembly, Annual Review of Physical Chemistry **66**, 143 (2015), arXiv:1407.2505.

[18] W. M. Jacobs and D. Frenkel, Self-Assembly of Structures with Addressable Complexity, Journal of the American Chemical Society **138**, 2457 (2016).

[19] K. Baek, I. Hwang, I. Roy, D. Shetty, and K. Kim, Self-Assembly of Nanostructured Materials through Irreversible Covalent Bond Formation, Accounts of Chemical Research **48**, 2221 (2015).

[20] A. Murugan, J. Zou, and M. P. Brenner, Undesired usage and the robust self-assembly of heterogeneous structures, Nature Communications **6**, 6203 (2015).

[21] F. M. Gartner, I. R. Graf, and E. Frey, The time complexity of self-assembly, Proceedings of the National Academy of Sciences **119** (2022).

[22] K. F. Wagenbauer, C. Sigl, and H. Dietz, Gigadalton-scale shape-programmable DNA assemblies, Nature **552**, 78 (2017).

[23] S. Katen and A. Zlotnick, *Methods in Enzymology*, 1st ed., Vol. 455 (Elsevier Inc., 2009) pp. 395–417.

[24] B. A. Grzybowski, C. E. Wilmer, J. Kim, K. P. Browne, and K. J. Bishop, Self-assembly: From crystals to cells, Soft Matter **5**, 1110 (2009).

[25] W. M. Gelbart, A. Ben-Shaul, and D. Roux, *Micelles, membranes, microemulsions, and monolayers* (Springer Science & Business Media, 2012).

[26] L. O. Hedges, R. V. Mannige, and S. Whitelam, Growth of equilibrium structures built from a large number of distinct component types, Soft Matter **10**, 6404 (2014).

[27] M. F. Hagan and G. M. Grason, Equilibrium mechanisms of self-limiting assembly, Reviews of Modern Physics **93**, 25008 (2021), arXiv:2007.01927.

[28] J. N. Israelachvili, D. J. Mitchell, and B. W. Ninham, Theory of self-assembly of hydrocarbon amphiphiles into micelles and bilayers, Journal of the Chemical Society, Faraday Transactions 2: Molecular and Chemical Physics **72**, 1525 (1976).

[29] P. C. Hiemenz and T. P. Lodge, *Polymer chemistry* (CRC press, 2007).

[30] C. G. Evans and E. Winfree, Physical principles for DNA tile self-assembly, Chemical Society Reviews **46**, 3808 (2017).

[31] F. M. Gartner, I. R. Graf, P. Wilke, P. M. Geiger, and E. Frey, Stochastic Yield Catastrophes and Robustness in Self-Assembly, bioRxiv , 1 (2019).

[32] C. Chen, C. C. Kao, and B. Dragnea, Self-assembly of brome mosaic virus capsids: Insights from shorter time-scale experiments, Journal of Physical Chemistry A **112**, 9405 (2008).

[33] A. Ben-Shaul and W. M. Gelbart, Statistical thermodynamics of amphiphile self-assembly: structure and phase transitions in micellar solutions, in *Micelles, Membranes, Microemulsions, and Monolayers* (Springer, 1994) pp. 1–104.

[34] P. Masson, C. Hulo, E. De Castro, H. Bitter, L. Gruenbaum, L. Essioux, L. Bougueleret, I. Xenarios, and P. Le Mercier, ViralZone: http://viralzone.expasy.org, Nucleic acids research **41**, D579 (2012).

[35] S. Li, P. Roy, A. Travesset, and R. Zandi, Why large icosahedral viruses need scaffolding proteins, Proceedings of the National Academy of Sciences of the United States of America **115**, 10971 (2018).

[36] C. A. Kerfeld and M. R. Melnicki, Assembly, function and evolution of cyanobacterial carboxysomes, Current Opinion in Plant Biology **31**, 66 (2016).

[37] D. T. Gillespie, Stochastic Simulation of Chemical Kinetics, Annual Review of Physical Chemistry **58**, 35 (2007).

[38] R. P. Sear, Nucleation: theory and applications to protein solutions and colloidal suspensions, Journal of Physics: Condensed Matter **19**, 33101 (2007).

[39] A. Zlotnick, J. M. Johnson, P. W. Wingfield, S. J. Stahl, and D. Endres, A theoretical model successfully identifies features of hepatitis B virus capsid assembly, Biochemistry **38**, 14644 (1999).

[40] A. Y. Morozov, R. F. Bruinsma, and J. Rudnick, Assembly of viruses and the pseudo-law of mass action, Journal of Chemical Physics **131**, 10.1063/1.3212694 (2009).

# Part II

# Stochastic effects and fidelity in heterogeneous self-assembly

## General motivation

In the first part of this thesis, we analyzed the time efficiency of self-assembly processes, assuming that the particle number $N$ is sufficiently large so that finite size effects do not affect the physics of the system. In contrast, in this second part we investigate how self-assembly systems behave in the limit in which the particle number becomes a relevant factor for the dynamics of the system. The biological motivation is that, for example, within cells, many components are available only in relatively small copy numbers [146]. Hence, it is not clear whether the assumption of 'sufficiently large' particle numbers used in the previous part is justified in the cellular context. Furthermore, slow diffusion could limit the local availability of constituents, causing noise in the local concentrations to become an important factor. Therefore, in order to fully understand biological self-assembly systems and the mechanisms that have evolved in order to guarantee their robust and resilient functioning, we believe that it is indispensable to understand not only the *deterministic* but also the *stochastic* dynamics of self-assembly processes.
Another assumption made throughout the first part of this thesis was that all binding reactions are specific, i.e. constituents can only bind with their designated binding partners. Correspondingly, the final assembly products are uniquely defined. In biological and experimental systems, however, non-specific or incorrect bonds between the constituents might also lead to malformed or defective structures if the control parameters like temperature, binding strength etc. are chosen unfavourably [34, 147, 129]. In other words, the yield in finished structures alone might not be enough to characterize the quality of the assembly process, but the number or frequency of assembly errors in the final structures must also be considered.

Subject of this second part of the thesis is hence a characterization of stochastic effects in self-assembly if the particle number is not abundant, as well as the susceptibility of self-assembly systems to errors and defects in the case when binding is not fully specific. Furthermore, we will discuss ways and strategies in order to avoid as far as possible the deleterious effects arising from stochasticity and error susceptibility.
Specifically, in chapter 5 we will discuss the role of stochastic effects for the activation and dimerization scenario, the factors that promote their emergence and how their deleterious effects can be alleviated. We thereby focus entirely on stochastic effects that arise intrinsically from the stochastic dynamics of the self-assembly processes but not due to external noise caused, for example, by external variations in the overall particle numbers [148, 149]. Furthermore, in this stochastic context, we will specify the role of the heterogeneity of the building blocks as an important factor that promotes the emergence of stochastic effects.
Subsequently, in chapter 6, we develop a more in depth mathematical understanding of the stochastic yield catastrophe which affects the activation scenario if particle numbers are not abundant. Furthermore, we discuss various distinct strategies in order to overcome stochastic yield catastrophes and achieve robust self-assembly also for small particle numbers.
Finally, in chapter 7, the robustness of the just-in-sequence scenario against stochastic effects is quantified. Furthermore, we discuss the susceptibility of the different self-assembly scenarios to errors in the case of reduced binding specificities, both in the deterministic (abundant particle numbers) and the stochastic (non-abundant particle numbers) regime. In particular, we demonstrate that the just-in-sequence supply strategy offers an effective and robust way

to avoid stochastic effects and assembly errors and hence might be a useful strategy to control non-equilibrium self-assembly processes.

# 5 Stochastic yield catastrophes and robustness in self-assembly

This chapter summarizes the most important findings of our project on the self-assembly of heterogeneous structures. The corresponding manuscript has been published in *eLife*. This chapter is based on and uses parts of this publication [141], which is also reprinted in section 5.6.

## 5.1 Motivation

In the first part of this thesis we analyzed the time efficiency of various self-assembly scenarios. Although we found that the time efficiency of these scenarios sometimes differs by orders of magnitudes and depends differently on the size of the target structure, all four scenarios, in principle, exhibited a similar behavior: in all cases, by varying the respective control parameter, the final yield increases from 0 to the perfect value of 1 in a strictly monotonic, sigmoidal fashion. The implicit assumption thereby is that the particle copy number $N$ is large. However, in cells, many components are available only in relatively small numbers [146]. Furthermore, cells are rather crowded and, thus, concentrations might also be subject to local fluctuations. For those reasons, in order to better understand biological self-assembly systems and the obstacles that had to be overcome by evolution in order to guarantee their robust functioning, it might be necessary to understand self-assembly dynamics also in the stochastic regime in which particle numbers are low and subject to fluctuations.
Another particularly interesting question in this context is how heterogeneity affects the assembly efficiency and the robustness of the process if the particle number is low. Deterministically, we found that three out of the four scenarios discussed in the previous part (namely the activation-, dimerization- and reversible binding scenario), which allow to slow down nucleation, treat all constituent species equivalently and therefore are invariant to the heterogeneity of the system. But does this remain true also in the limit of small particle numbers? In other words, are the various strategies to slow down nucleation really equivalent (when considering only the yield and neglecting time efficiency) or are there fundamental differences regarding their stability and robustness to noise?
In order to answer these questions, we investigate a conceptual model that describes the self-assembly of a number of constituents into ring structures of variable sizes and variable heterogeneity. We study the behavior of the activation and the dimerization scenario, which were introduced already in the previous part, in the limit of small particle numbers. We show that, while the dimerization scenario is robust for small particle numbers, the activation scenario is strongly affected by a stochastic effect, which can strongly reduce or even completely suppress the yield of the assembly process. We call this effect *stochastic yield catastrophe* and we identify irreversibility and heterogeneity as the driving forces behind it. We show that this

phenomenon leads to intriguing effects in which the final yield can become a non-monotonic function of the deterministic nucleation speed. Furthermore, we identify possible ways in order to mitigate the detrimental effect of stochasticity.
Importantly, in studying the effect of noise in this chapter, we constrain ourselves exclusively to effects arising from *internal* noise. Internal noise defines noise that arises exclusively from the stochastic dynamics of the system itself and therefore constitutes an intrinsic constraint on the assembly yield. External noise, in contrast, refers to variability of the concentrations in which the different species are provided. While effects of external noise have been studied previously, for example in [148, 149], we are not aware of any previous study that explicitly quantifies the effects of internal noise in self-assembly processes.

## 5.2 Model

The model that we use to study the effects of noise is similar to the model we introduced in chapter 2 in the 1D case and similar to the system studied in [53], which was also the original motivation for our model. To investigate the effect of noise in its simplest form, we restrict ourselves to one-dimensional target structures that form closed rings, see Fig. 8.1. This choice is motivated by the fact that rings are the simplest objects in which all species have equivalent binding properties. This symmetry and simplicity of the model thereby allow us to study in isolation the effects arising intrinsically from the stochastic dynamics. Superposing effects that could possibly arise from irregularities due to the presence of a boundary in the structures or due to more complex reaction schemes can thereby be ruled out.
Similar as before, we assume that $N$ monomers, each of $S$ different species, start in an inactive state and become activated at per capita rate $\alpha$. Once active, monomers start to assemble in periodically consecutive order to form closed ring structures of size $L$, see Fig. 8.1. Here, $L$ is a multiple of the number of species $S$, so that each species is represented equally often in a fully assembled structure. Choosing different values of $S$ while keeping the size $L$ of the rings constant, allows us to vary the heterogeneity of the structures without changing their size. The extreme cases $S = 1$, and $S = L$ are also referred to as the *homogeneous* and the *fully heterogeneous* case, respectively. The homogeneous case, in which structures are built from identical particles of only one species, can be interpreted as a simplified, one-dimensional model for virus capsid assembly [127, 34] or linear protein filament assembly [150, 151], because both systems typically assemble from only one or a very small number of different protein species. On the other hand, fully heterogeneous self-assembly systems forming so-called 'information-rich' structures are often represented in DNA-brick based nanotechnology [33, 53, 152].
We assume that growth of the structures occurs only by attachment of single monomers. Structures with size smaller than a criticial nucleation size $L_{\text{nuc}}$ grow with size dependent rates $\mu_1, \mu_2, ...$, while structures of a size larger than or equal to $L_{\text{nuc}}$ grow with a constant attachment rate $\nu \equiv 1$. Furthermore, we assume that structures with a size smaller than $L_{\text{nuc}}$ are unstable and decay back into monomers at a size dependent (per capita) rate $\delta_i$. Hence, the critical nucleation size can be interpreted in terms of classical nucleation theory as the structure size at which the free energy barrier becomes maximal [73]. Regarding the kinetics of the process, by altering the nucleation size and the decay rates, we can vary the level of reversibility in the assembly process in order to study its effect on the robustness of

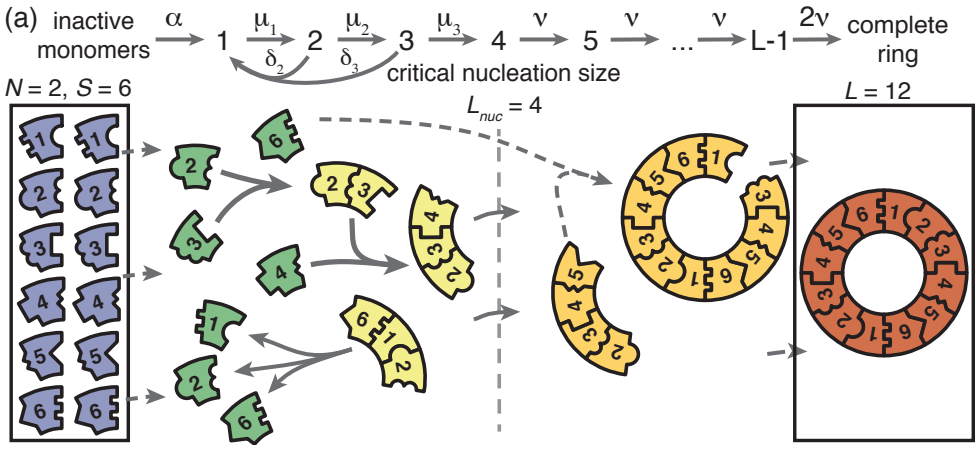


**Figure 5.1 | Illustration of the model (slightly adapted from [141]).** Ring structures of size $L$ assemble from $S$ different species. $N$ monomers of each species are initially in an inactive state (blue) and are activated at per-capita rate $\alpha$. Once active (green), species with periodically consecutive index can bind to each other. Structures only grow by addition of single monomers. Below a critical nucleation size ($L_{\mathrm{nuc}}$), structures (yellow) are unstable and decay again into monomers. In contrast, above the critical size, polymers (dark yellow) are stable and grow irreversibly until the ring is complete (the absorbing state; red). Since the structure size $L$ is restricted to multiples of the number of species $S$, each species appears equally often in a ring and all species have equivalent properties.

the assembly yield. For convenience, we typically assume that all sub-nucleation growth and decay rates are constant, $\mu_i = \mu$ and $\delta_i = \delta \; \forall \; i < L_{\mathrm{nuc}}$, but we also consider other cases in the appendix of the publication reprinted in section 5.6.
Furthermore, in order to show that our results are not an artefact of the one-dimensional geometry of the structures or the simplified assembly kinetics, we also study variations of the model by simulating the assembly of two-dimensional structures and a more complicated assembly kinetics that takes interactions between polymers into account, see section 5.6.
As a big advantage, the simplicity of the model furthermore allows us to simulate the reaction kinetics of the ring model with kinetic rate equations (ordinary differential equations), which represent the mean-field equations of the stochastic process. By comparing the outcome of the stochastic simulation with that of the mean-field equations, we are thus able to identify unambiguously the effects arising from stochasticity in the system.

## 5.3 Results and discussion

With the model we investigate the effect of noise in the activation and dimerization scenario, which have already been introduced in chapter 2. In the dimerization scenario, we set the critical nucleation size $L_{\mathrm{nuc}} = 2$ and $\delta = 0$ and we control the nucleation speed by the dimerization rate $\mu_1 := \mu$. In contrast, in the activation scenario, we set $\mu = \nu = 1$ and $\delta = 0$ and control the effective nucleation speed by the activation rate $\alpha$.
First, we characterize the behavior of the system for large particle numbers $N$ (for example $N \geq 10^5$). We find that, by decreasing either the activation or the dimerization rate below a respective threshold value, the final yield increases until it becomes perfect in the limit of small activation or dimerization rates; see Fig. 2 in the publication reprint in chapter 5.6.

Both in the activation and dimerization scenario, the final yield obtained from the stochastic simulation coincides perfectly with the yield obtained from solving the kinetic rate equations, which, by their nature, neglect noise in the system. Furthermore, the yield is found to be independent of the heterogeneity of the system. In other words, the parameter $S$, which determines the number of species, is irrelevant for the final yield.
This independence from the heterogeneity in the deterministic limit can also be shown analytically with the chemical rate equations by a symmetry argument (see supplement of the publication reprint in chapter 5.6): since the rate equations are invariant to relabelling of the species index, mathematically, the assembly process decouples into $S$ independent and identical processes for the $S$ different species. Hence, the yield and also the assembly time are independent of $S$ in the deterministic limit. This simplification furthermore enables us to calculate the threshold rate constants $\alpha_{\mathrm{th}}$ and $\mu_{\mathrm{th}}$, which mark the onset of the yield. Specifically, we find $\alpha_{\mathrm{th}} \sim \frac{\nu}{\mu}\frac{C\nu}{L^3}$ and $\mu_{\mathrm{th}} \sim \frac{\nu}{L^2}$ in agreement with the result from chapter 2, which has been derived in a different way using a scaling argument.

Intriguingly, a markedly different behavior is observed if the particle number $N$ is reduced. Figure 3a and b in the publication reprint in chapter 5.6 show the final yield in the activation and dimerization scenario for decreasing numbers of particles. While a perfect yield of 1 is achieved in the dimerization scenario even for $N = 1$, the yield in the activation scenario saturates at an imperfect value $y_{\max} < 1$, if the particle number becomes too small. Decreasing $N$ reduces the maximum yield $y_{\max}$ further until the yield is zero for any value of $\alpha$. This behavior is in sharp contrast to the deterministic theory, which still predicts a perfect yield in the limit of small $\alpha$ even for small particle numbers. Importantly, the reduction of the yield can be observed in the stochastic simulation already for rather large particle numbers up to several thousands, for example, for a structure of size $L = 60$.
Due to the strength of this effect and its stochastic origin, we termed this phenomenon *stochastic yield catastrophe*. The strength of the stochastic yield catastrophe strongly increases with the size of the (heterogeneous) target structure: the minimal particle number $N_y^{\mathrm{crit}}$ that is necessary in order to achieve a fixed yield $y$ increases strongly with the structure size $L$ (see Fig. 3c in the publication reprint and Fig. 5.2 below). Approximately, the dependence of $N_y^{\mathrm{crit}}$ on $L$ is described by a power law with exponent $\approx 2.6$. This strong nonlinear dependence of the strength of the stochastic yield catastrophe on the structure size emphasizes its significance and motivated us to use the term 'catastrophe' to describe it.
We find that the stochastic yield catastrophe can be alleviated by increasing the critical nucleation size $L_{\mathrm{nuc}}$, which enhances reversibility of the process, or by decreasing heterogeneity (i.e. by building the same number of structures more homogeneously with less different species), see Fig. 3d in the publication reprint. Therefore, we identify (partial) irreversibility and heterogeneity as the driving factors behind the stochastic yield catastrophe. Note that the fully homogeneous case ($S = 1$) is not affected at all by the stochastic yield catastrophe and a maximal yield of 1 is achieved robustly even for arbitrarily small particle numbers.
Higher dimensionality of the target structures or interactions among larger polymers are other factors that would mitigate the stochastic yield catastrophe but the reduction of the yield is still considerable in these cases. Therefore, the stochastic yield catastrophe is not an artefact of the one-dimensional geometry of the structures or the simplified reaction kinetics.

How can the occurrence of this strong stochastic effect be explained? Since the yield does not reach the perfect value of 1, the effective dimerization speed must be bounded from below

as a result of the stochastic dynamics. Intuitively, this can be explained as follows: In the limit of small $\alpha$, activation will be much slower than binding and hence the random order of activation events determines the availability of monomers and, therefore, the order of binding. Hence, monomers dimerize more frequently if momentarily no other binding sites with larger structures are available, see Fig. 4a in the publication reprint. As a result of the enhanced dimerization rate, more complexes are initiated than predicted by the deterministic theory, and hence, only a fraction of all complexes can be completed (Fig. 4b publication reprint). We analyze this intriguing stochastic dynamics in much more detail in the next chapter. Furthermore, the mitigating effect of increasing $L_{\mathrm{nuc}}$ or decreasing heterogeneity $S$ can be explained as follows: If $L_{\mathrm{nuc}}$ is increased, smaller complexes can decay again into monomers and so the system can correct the excessive number of dimerization events that occurred at early stages of the assembly process. On the other hand, building the structure with fewer different species allows for more binding possibilities for each species and so mitigates the stochastic effect that drives the enhancement of the dimerization rate.

The stochastic yield catastrophe leads to a very intriguing behavior of the yield in the activation scenario if the dimerization rate $\mu/\nu < 1$ is kept at a fixed value smaller than 1. Because $\mu/\nu < 1$ is a characteristic of the dimerization scenario, we can also regard this case as a 'mixed type' scenario. We find that, depending on the ratio $\mu/\nu$ and the structure size $S$, the yield can become a non-monotonic function of $\alpha$ and hence a non-monotonic or increasing function of the deterministic nucleation rate (see Fig. 4 of the publication reprint). The shape of the yield curves is thereby the result of the behavior of the yield in three distinct regimes: the deterministic regime (large $\alpha$), in which the dimerization rate $\mu$ controls the assembly process; the stochastic regime (small $\alpha$), in which activation is the time-limiting step and thus a stochastic yield catastrophe occurs; and an intermediate regime, at which $\alpha$ and $\mu$ synergistically control the nucleation speed but stochastic effects are still week. Depending on the setting of the parameters, the maximum in the yield can be attained in either of the three regimes, giving rise to the counterintuitive shapes of the yield curves observed in Fig. 4 of the publication reprint.

## 5.4 The stochastic exponent $\xi$

The strength of the stochastic yield catastrophe can informatively be characterized by the dependence of the minimal particle number $N_y^{\min}$ required to achieve a fixed yield $y$ on the number of species $S$. We found that for one-dimensional structures, the relation between $N_y^{\min}$ and $S$ can approximately be described by a power law, see Fig. 3c in the publication reprint. Hence, we define the *stochastic exponent* or *particle number exponent* $\xi$ in order to characterize this dependence:

$$N_y^{\min} \sim S^{\xi}\,. \tag{5.1}$$

For one-dimensional structures, we found $\xi \approx 2.6$. Note that for the range of structure sizes sampled, the power law dependence is only approximate and the curves flatten for larger sizes, indicating that the asymptotic exponent might still be a bit smaller. Interestingly, the exponent is roughly independent of the yield $y$ (for large enough $S$), see Fig. 3c in the publication reprint. In order to further examine the robustness of the stochastic exponent,

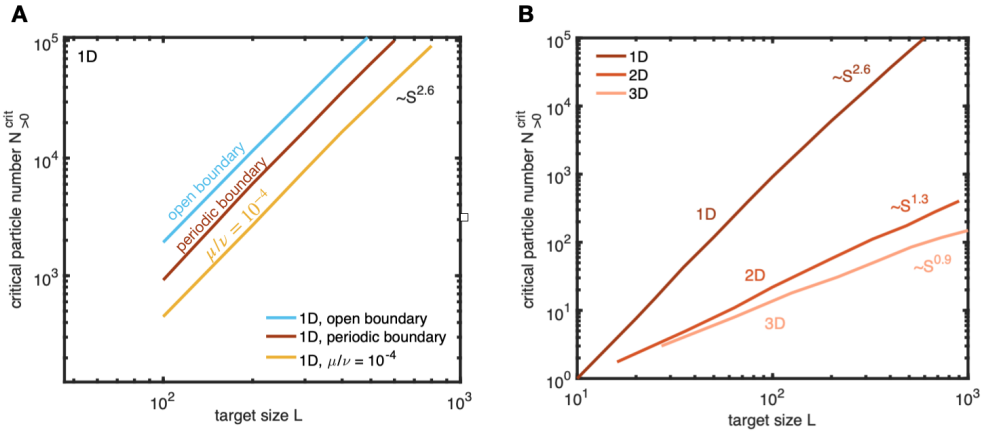


**Figure 5.2 | Robustness and dimensionality dependence of the stochastic exponent.** **A** The minimal particle number $N_{>0}^{\text{crit}}$ required to achieve a non-zero yield in the limit $\alpha \to 0$ is plotted against the structure size $L$ for different boundary conditions of the one-dimensional structures and a smaller nucleation barrier $\mu/\nu = 10^{-4}$ (instead of $\mu/\nu = 1$). The scaling of the critical particle number is the same in all three cases, which shows the robustness of the stochastic exponent to modifications of the model and variations in its parameters. **B** Dependence of $N_{>0}^{\text{crit}}$ on $L$ for different dimensionality of the target structure (periodic boundaries in each case): The critical particle number and the stochastic exponent strongly depend on the dimensionality of the target structure as explained in the main text.

we plot the minimal particle number $N_{>0}^{\text{min}}$ to obtain nonzero yield also for one-dimensional structures with non-periodic boundaries and with a smaller value for the dimerization rate $\mu$ (Fig. 5.2A). In both cases, we find that the stochastic exponent remains invariant to such variations of the model and the parameters. However, the exponent strongly depends on the dimensionality of the structures, as we verify by plotting $N_{>0}^{\text{min}}$ against $S$ likewise for two- and three-dimensional structures (Fig. 5.2B). Specifically, we obtain for two-dimensional structures $\xi \approx 1.3$ and for three-dimensional structures $\xi \approx 0.9$. This suggests that the impact of the stochastic yield catastrophe is determined by the linear dimension (diameter) of a heterogeneous structure rather than its total size: Since the diameter of a $d$-dimensional structure scales as $\sim S^{1/d}$, this implies a stochastic exponent of $\xi \approx \frac{2.6}{d}$, which reproduces roughly the exponents measured for one-, two- and three-dimensional structures.

Another possible interpretation of this result is found by noting that the number of binding sites of a $d-$dimensional structure (which is proportional to its boundary) scales as $\sim S^{\frac{d-1}{d}}$. Hence, the probability $f$ that a randomly chosen complex and a randomly chosen species can bind to each other scales as $f \sim S^{\frac{d-1}{d}}/S = S^{-1/d}$. Intuitively, we explained the stochastic yield catastrophe by the enhancement of the dimerization probability resulting from a lack of binding possibilities of species with existing complexes. Therefore, it is a plausible assumption that the minimal particle number $N_y^{\text{min}}$ can be described as a function of the (inverse) probability $f$ that a random monomer and a cluster can bind. Indeed, from the one-dimensional case, in which $f$ is a constant independent of $S$, we learn that the dependence on $f$ must be given by $N_y^{\text{min}} \sim f^{-2.6} = S^{\frac{2.6}{d}}$, which reproduces the correct stochastic exponents also for the higher-dimensional cases.

What still remains elusive is the exponent $\xi = 2.6$ for one-dimensional structures. Simple scaling arguments that we tried to understand this dependence all underestimated the stochastic

exponent. However, this could also be because the real asymptotic exponent might still be significantly smaller than the values we measured for finite values of $S$.

## 5.5 Key points

In my opinion, the key results of this project are the following:

- Heterogeneous self-assembly processes are strongly affected by stochasticity if the availability of monomers is subject to noise. These stochastic effects are not captured by a deterministic description in terms of chemical rate equations and they can lead to a strong reduction of the final yield.
- Different scenarios or strategies that slow down nucleation are not equivalent in the limit of small particle numbers: While the dimerization scenario is highly robust to noise, the activation scenario is strongly affected by noise and suffers a stochastic yield catastrophe.
- The stochastic yield catastrophe is jointly triggered by irreversibility and heterogeneity of the assembly process. Hence, while heterogeneity of the target structure is irrelevant if resources are abundant, it can play an essential role if resources are scarce.
- The effect of the stochastic yield catastrophe can informatively be characterized by the stochastic exponent $\xi$, which measures the (approximate) scaling of the minimal number of particles necessary to achieve a certain yield with the number of species. The exponent $\xi$ depends on the dimensionality of the structure but is robust to modifications of the parameter settings and other details of the model.
- For biologically relevant subunit numbers, stochastic effects might pose a potential threat for self-assembly. Hence, it is to be assumed that assembly schemes and control mechanisms have evolved in cells so that the occurrence of stochastic effects is suppressed.

## 5.6 Publication: Stochastic yield catastrophes and robustness in self-assembly, eLife 9, e51020 (2020)

This section is a publication reprint of the following manuscript published in **eLife** 9, e51020 (2020).

### Stochastic yield catastrophes and robustness in self-assembly

by

Florian M. Gartner,[1,*] Isabella R. Graf,[1,*] Patrick Wilke,[1,*] Philipp M. Geiger[1], and Erwin Frey[1]

[1] *Arnold-Sommerfeld-Center for Theoretical Physics and Center for NanoScience, Department of Physics, Ludwig-Maximilians-Universität München*

[*] *These authors contributed equally to this work.*



DOI: 10.7554/eLife.51020

RESEARCH ARTICLE

# Stochastic yield catastrophes and robustness in self-assembly

**Florian M Gartner†, Isabella R Graf†, Patrick Wilke†, Philipp M Geiger, Erwin Frey***

Arnold Sommerfeld Center for Theoretical Physics (ASC) and Center for NanoScience (CeNS), Department of Physics, Ludwig-Maximilians-Universität München, München, Germany

**Abstract** A guiding principle in self-assembly is that, for high production yield, nucleation of structures must be significantly slower than their growth. However, details of the mechanism that impedes nucleation are broadly considered irrelevant. Here, we analyze self-assembly into finite-sized target structures employing mathematical modeling. We investigate two key scenarios to delay nucleation: (i) by introducing a slow activation step for the assembling constituents and, (ii) by decreasing the dimerization rate. These scenarios have widely different characteristics. While the dimerization scenario exhibits robust behavior, the activation scenario is highly sensitive to demographic fluctuations. These demographic fluctuations ultimately disfavor growth compared to nucleation and can suppress yield completely. The occurrence of this stochastic yield catastrophe does not depend on model details but is generic as soon as number fluctuations between constituents are taken into account. On a broader perspective, our results reveal that stochasticity is an important limiting factor for self-assembly and that the specific implementation of the nucleation process plays a significant role in determining the yield.

***For correspondence:** frey@lmu.de

†These authors contributed equally to this work

**Competing interests:** The authors declare that no competing interests exist.

**Funding:** See page 16

**Received:** 12 August 2019
**Accepted:** 04 February 2020
**Published:** 05 February 2020

**Reviewing editor:** Frank Jülicher, Max Planck Institute for the Physics of Complex Systems, Germany



## Introduction

Efficient and accurate assembly of macromolecular structures is vital for living organisms. Not only must resource use be carefully controlled, but malfunctioning aggregates can also pose a substantial threat to the organism itself (***Jucker and Walker, 2013***; ***Drummond and Wilke, 2009***). Furthermore, artificial self-assembly processes have important applications in a variety of research areas like nanotechnology, biology, and medicine (***Zhang, 2003***; ***Whitesides and Grzybowski, 2002***; ***Whitesides et al., 1991***). In these areas, we find a broad range of assembly schemes. For example, while a large number of viruses assemble capsids from identical protein subunits, some others, like the Escherichia virus T4, form highly complex and heterogeneous virions encompassing many different types of constituents (***Zlotnick et al., 1999***; ***Zlotnick, 2003***; ***Hagan, 2014***; ***Leiman et al., 2010***). Furthermore, artificially built DNA structures can reach up to Gigadalton sizes and can, in principle, comprise an unlimited number of different subunits (***Ke et al., 2012***; ***Reinhardt and Frenkel, 2014***; ***Gerling et al., 2015***; ***Wagenbauer et al., 2017***). Notwithstanding these differences, a generic self-assembly process always includes three key steps: First, subunits must be made available, for example by gene expression, or rendered competent for binding, for example by nucleotide exchange (***Alberts and Johnson, 2015***; ***Chen et al., 2008***; ***Whitelam, 2015***) ('activation'). Second, the formation of a structure must be initiated by a nucleation event ('nucleation'). Due to cooperative or allosteric effects in binding, there might be a significant nucleation barrier (***Chen et al., 2008***; ***Jacobs and Frenkel, 2015***; ***Sear, 2007***; ***Lazaro and Hagan, 2016***; ***Hagan and Elrad, 2010***). Third, following nucleation, structures grow via aggregation of substructures ('growth'). To avoid kinetic traps that may occur due to irreversibility or very slow disassembly of substructures (***Hagan et al., 2011***; ***Grant et al., 2011***), structure nucleation must be significantly slower than growth

**eLife digest** The self-assembly of a large biological molecule from small building blocks is like finishing a puzzle of magnetic pieces by shaking the box. Even though each piece of the puzzle is attracted to its correct neighbours, the limited control makes it very hard to finish the puzzle in a short amount of time.

The problem becomes even more difficult if several copies of the same puzzle are assembled in one box. If several puzzles start at the same time, the different parts might steal pieces from each other, making it impossible to successfully complete any of the puzzles. This is called a depletion trap. If the box is only shaken and there is no real control over individual pieces, these traps occur at random.

Overcoming these random depletion traps is an important challenge when assembling nanostructures and other artificial molecules designed by humans without wasting many, potentially expensive, components. Previous studies have shown that when multiple copies of the same structure are assembled simultaneously, slowing the rate of initiation increases the yield of correctly-made structures. This prevents new structures from stealing pieces from existing structures before they are fully completed.

Now, Gartner, Graf, Wilke et al. have used a mathematical model to show that changing the way initiation is delayed leads to different yields. This was especially true for small systems where fluctuations in the availability of the different pieces strongly enhanced the initiation of new structures. In these cases, the self-assembly process terminated undesirably with many incomplete structures.

Nanostructures have various applications ranging from drug delivery to robotics. These findings suggest that in order to efficiently assemble biological molecules, the concentrations of the different building blocks need to be tightly controlled. A question for further research is to investigate strategies that reduce fluctuations in the availability of the building blocks to develop more efficient assembly protocols.

(*Zlotnick et al., 1999*; *Ke et al., 2012*; *Reinhardt and Frenkel, 2014*; *Wei et al., 2012*; *Jacobs et al., 2015*; *Hagan and Elrad, 2010*). Physically speaking, there are no irreversible reactions. However, in the biological context, self-assembly describes the (relatively fast) formation of long-lasting, stable structures. Therefore, at least part of the assembly reactions are often considered to be irreversible on the time scale of the assembly process. In this manuscript we investigate, for a given target structure, whether the nature of the specific mechanism employed in order to slow down nucleation influences the yield of assembled product. To address this question, we examine a generic model that incorporates the key elements of self-assembly outlined above.

## Model definition

We model the assembly of a fixed number of well-defined target structures from limited resources. Specifically, we consider a set of $S$ different species of constituents denoted by $1,\ldots,S$ which assemble into rings of size $L$. The cases $S=1$ and $1<S\leq L$ ($S=L$) are denoted as homogeneous and partially (fully) heterogeneous, respectively. The homogeneous model builds on previous work on virus capsid (*Chen et al., 2008*; *Hagan et al., 2011*), linear protein filament assembly (*Michaels et al., 2016*; *Michaels et al., 2017*; *D'Orsogna et al., 2012*) and aggregation and polymerization models (*Krapivsky et al., 2010*). The heterogeneous model in turn links to previous model systems used to study, for example, DNA-brick-based assembly of heterogeneous structures (*Murugan et al., 2015*; *Hedges et al., 2014*; *D'Orsogna et al., 2013*). We emphasize that, even though strikingly similar experimental realizations of our model exist (*Gerling et al., 2015*; *Wagenbauer et al., 2017*; *Praetorius and Dietz, 2017*), it is not intended to describe any particular system. The ring structure represents a general linear assembly process involving building blocks with equivalent binding properties and resulting in a target of finite size. The main assumption in the ring model is that the different constituents assemble linearly in a sequential order. In many biological self-assembling systems like bacterial flagellum assembly or biogenesis of the ribosome subunits the assumption of a linear binding sequence appears to be justified (*Peña et al., 2017*; *Chevance and Hughes, 2008*). In order

to test the validity of our results beyond these constraints we also perform stochastic simulations of generalized self-assembling systems that do not obey a sequential binding order: i) by explicitly allowing for polymer-polymer bindings and ii) by considering the assembly of finite sized squares that grow independently in two dimensions (see Figures 6 and 7).

The assembly process starts with $N$ inactive monomers of each species. We use $C = N/V$ to denote the initial concentration of each monomer species, where $V$ is the reaction volume. Monomers are activated independently at the same per capita rate $\alpha$, and, once active, are available for binding. Binding takes place only between constituents of species with periodically consecutive indices, for example 1 and 2 or $S$ and 1 (leading to structures such as $\ldots 1231 \ldots$ for $S = 3$); see ***Figure 1***. To avoid ambiguity, we restrict ring sizes to integer multiples of the number of species $S$. Furthermore, we neglect the possibility of incorrect binding, for example species 1 binding to 3 or $S-1$. Polymers, that is incomplete ring structures, grow via consecutive attachment of monomers. For simplicity, polymer-polymer binding is disregarded at first, as it is typically assumed to be of minor importance (***Zlotnick et al., 1999***; ***Chen et al., 2008***; ***Murugan et al., 2015***; ***Haxton and Whitelam, 2013***). To probe the robustness of the model, later we consider an extended model including polymer-polymer binding for which the results are qualitatively the same (see Figure 6 and the discussion). Furthermore, it has been observed that nucleation phenomena play a critical role for self-assembly processes (***Ke et al., 2012***; ***Wei et al., 2012***; ***Reinhardt and Frenkel, 2014***; ***Chen et al., 2008***). So it is in general necessary to take into account a critical nucleation size, which marks the transition between slow particle nucleation and the faster subsequent structure growth (***Michaels et al., 2016***; ***Lazaro and Hagan, 2016***; ***Morozov et al., 2009***; ***Murugan et al., 2015***). We denote this critical nucleation size by $L_{\mathrm{nuc}}$, which in terms of classical nucleation theory corresponds to the structure size at which the free energy barrier has its maximum. For $l<L_{\mathrm{nuc}}$ attachment of monomers to existing structures and decay of structures (reversible binding) into monomers take place at size-dependent reaction rates $\mu_l$ and $\delta_l$, respectively (***Figure 1***). Here, we focus on identical rates $\mu_l = \mu$ and $\delta_l = \delta$. A discussion of the general case is given in Appendix 4. Above the nucleation size, polymers grow by attachment of monomers with reaction rate $\nu \geq \mu$ per binding site. As

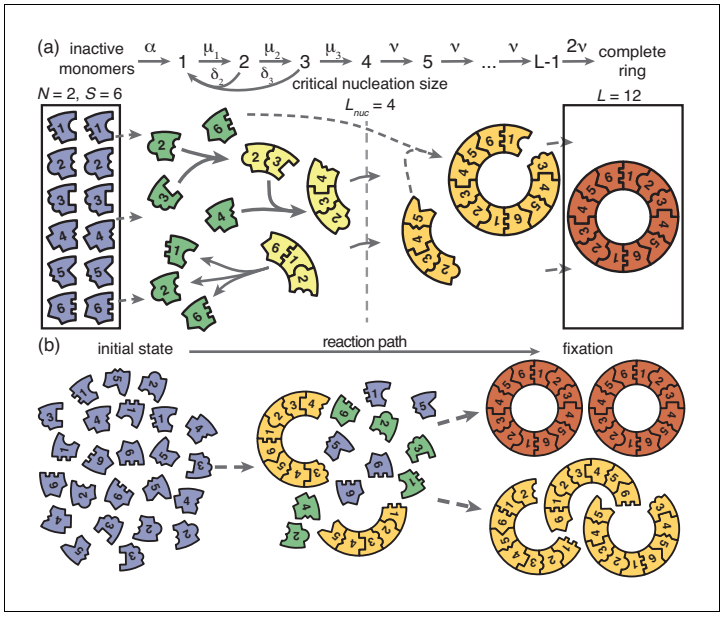


**Figure 1.** Schematic description of the model. (**a**) Rings of size $L$ are assembled from $S$ different particle species. $N$ monomers of each species are initially in an inactive state (blue) and are activated at the same per-capita rate $\alpha$. Once active (green), species with periodically consecutive index can bind to each other. Structures grow by attachment of single monomers. Below a critical nucleation size ($L_{\mathrm{nuc}}$), structures of size $l$ (light yellow) grow and decay into monomers at size-dependent rates $\mu_l$ and $\delta_l$, respectively. Above the critical size, polymers (dark yellow) are stable and grow at size-independent rate $\nu$ until the ring is complete (the absorbing state; red). (**b**) Illustration of depletion traps. If nucleation is slow compared to growth, initiated structures are likely to be completed. Otherwise, many stable nuclei will form that cannot be completed before resources run out.

we consider successfully nucleated structures to be stable on the observational time scales, monomer detachment from structures above the critical nucelation size is neglected (irreversible binding) (**Murugan et al., 2015**; **Chen et al., 2008**). Complete rings neither grow nor decay (absorbing state).

We investigate two scenarios for the control of nucleation speed, first separately and then in combination. For the 'activation scenario' we set $\mu = \nu$ (all binding rates are equal) and control the assembly process by varying the activation rate $\alpha$. For the 'dimerization scenario' all particles are inherently active ($\alpha \to \infty$) and we control the assembly process by varying the dimerization rate $\mu$ (we focus on $L_{\mathrm{nuc}} = 2$). It has been demonstrated previously in **Chen et al. (2008)** and (**Endres and Zlotnick, 2002**; **Hagan and Elrad, 2010**; **Morozov et al., 2009**) that either a slow activation or a slow dimerization step are suitable in principle to retard nucleation and favour growth of the structures over the initiation of new ones. We quantify the quality of the assembly process in terms of the assembly yield, defined as the number of successfully assembled ring structures relative to the maximal possible number $NS/L$. Yield is measured when all resources have been used up and the system has reached its final state. We do not discuss the assembly time in this manuscript, however, in Appendix 5 we show typical trajectories for the time evolution of the yield in the activation and dimerization scenario. If the assembly product is stable (absorbing state), the yield can only increase with time. Consequently, the final yield constitutes the upper limit for the yield irrespective of additional time constraints. Therefore, the final yield is an informative and unambiguous observable to describe the efficiency of the assembly reaction.

We simulated our system both stochastically via Gillespie's algorithm (**Gillespie, 2007**) and deterministically as a set of ordinary differential equations corresponding to chemical rate equations (see Appendix 1).

# Results

## Deterministic behavior in the macroscopic limit

First, we consider the macroscopic limit, $N \gg 1$, and investigate how assembly yield depends on the activation rate $\alpha$ (activation scenario) and the dimerization rate $\mu$ (dimerization scenario) for $L_{\mathrm{nuc}} = 2$. Here, the deterministic description coincides with the stochastic simulations (**Figure 2a and b**). For both high activation and high dimerization rates, yield is very poor. Upon decreasing either the activation rate (**Figure 2a**) or the dimerization rate (**Figure 2b**), however, we find a threshold value, $\alpha_{\mathrm{th}}$ or $\mu_{\mathrm{th}}$ , below which a rapid transition to the perfect yield of 1 is observed both in the deterministic and stochastic simulation. By exploiting the symmetries of the system with respect to relabeling of species, one can show that, in the deterministic limit, the behavior is independent of the number of species $S$ (for fixed $L$ and $N$, see Appendix 1). Consequently, all systems behave equivalently to the homogeneous system and yield becomes independent of $S$ in this limit. Note, however, that equivalent systems with differing $S$ have different total numbers of particles $SN$ and hence assemble different total numbers of rings.

Decreasing the activation rate reduces the concentration of active monomers in the system. Hence growth of the polymers is favored over nucleation, because growth depends linearly on the concentration of active monomers while nucleation shows a quadratic dependence. Likewise, lower dimerization rates slow down nucleation relative to growth. Both mechanisms therefore restrict the number of nucleation events, and ensure that initiated structures can be completed before resources become depleted (see **Figure 2c and d**).

Mathematically, the deterministic time evolution of the polymer size distribution $c(l,t)$ is described by an advection-diffusion equation (**Endres and Zlotnick, 2002**; **Yvinec et al., 2012**) with advection and diffusion coefficients depending on the instantaneous concentration of active monomers (see Appendix 2). Solving this equation results in the wavefront of the size distribution advancing from small to large polymer sizes (**Figure 2e**). Yield production sets in as soon as the distance travelled by this wavefront reaches the maximal ring size $L$. Exploiting this condition, we find that in the deterministic system for $L_{\mathrm{nuc}} = 2$, a non-zero yield is obtained if either the activation rate or the dimerization rate remains below a corresponding threshold value, that is if $\alpha < \alpha_{\mathrm{th}}$ or $\mu < \mu_{\mathrm{th}}$, where

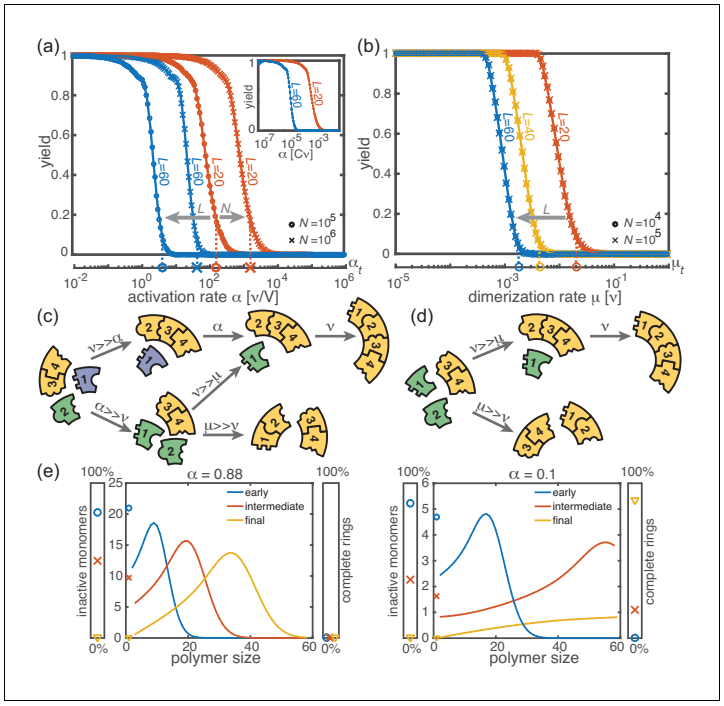


**Figure 2.** Deterministic behavior in the macroscopic limit $N \gg 1$. (**a, b**) Yield for different particle numbers $N$ (symbols) and ring sizes $L$ (colors) for $L_{\mathrm{nuc}} = 2$. Decreasing either (**a**) the activation rate ('activation scenario': $\mu = \nu$ ) or (**b**) the dimerization rate ('dimerization scenario': $\alpha \to \infty$) achieves perfect yield. The stochastic simulation results (symbols) average over 16 realizations and agree exactly with the integration of the chemical rate equations (lines). The threshold values (***Equation 1***) are indicated by the vertical dashed lines. Plotting yield against the dimensionless quantity $\alpha/(\nu C)$ causes the curves for different $C$ to collapse into a single master curve (inset in a). For both scenarios there is no dependency on the number of species $S$ in the deterministic limit. (**c, d**) Illustration showing how depletion traps are avoided by either slow activation (**c**) or slow dimerization (**d**). If the activation or the dimerization rate is small (large) compared to the growth rate, assembly paths leading to complete rings are favored (disfavored). The color scheme is the same as in ***Figure 1***. (**e**) Deterministically, the size distribution of polymers behaves like a wave, and is shown for large and small activation rate for $L = 60$, $L_{\mathrm{nuc}} = 2$, $N = 10000$ and $\mu = \nu = 1$. The distributions are obtained from a numerical integration of the deterministic mean-field dynamics, ***Equation 6***, and are plotted for early, intermediate and final simulation times. The respective percentage of inactive monomers and complete rings is indicated by the symbols in the scale bar on the left or right.

$$\alpha_{\mathrm{th}} = P_\alpha \frac{\nu}{\mu} \frac{\nu C}{(L-\sqrt{L})^3} \quad \text{and} \quad \mu_{\mathrm{th}} = P_\mu \frac{\nu}{(L-\sqrt{L})^2} \tag{1}$$

(see Appendix 3) with proportionality constants $P_\alpha = [\sqrt{\pi}\Gamma(2/3)/\Gamma(7/6)]^3/3 \approx 5.77$ and $P_\mu = \pi^2/2 \approx 4.93$. These relations generalize previous results (***Morozov et al., 2009***) to finite activation rates and for heterogeneous systems. A comparison between the threshold values given by ***Equation 1*** and the simulated yield curves is shown in ***Figure 2a,b***. The relations highlight important differences between the two scenarios (where $\alpha \to \infty$ and $\mu = \nu$, respectively): While $\alpha_{\mathrm{th}}$ decreases cubically with the ring size $L$, $\mu_{\mathrm{th}}$ does so only quadratically. Furthermore, the threshold activation rate $\alpha_{\mathrm{th}}$ increases with the initial monomer concentration $C$. Consequently, for fixed activation rate, the yield can be optimized by increasing $C$. In contrast, the threshold dimerization rate is independent of $C$ and the yield curves coincide for $N \gg 1$. Finally, if $\alpha$ is finite and $\mu < \nu$, the interplay between the two slow-nucleation scenarios may lead to enhanced yield. This is reflected by the factor $\nu/\mu$ in $\alpha_{\mathrm{th}}$, and we will come back to this point later when we discuss the stochastic effects.

In summary, for large particle numbers ($N \gg 1$), perfect yield can be achieved in two different ways, independently of the heterogeneity of the system - by decreasing either the activation rate (activation scenario) or the dimerization rate (dimerization scenario) below its respective threshold value.

## Stochastic effects in the case of reduced resources

Next, we consider the limit where the particle number becomes relevant for the physics of the system. In the activation scenario, we find a markedly different phenomenology if resources are sparse. ***Figure 3a*** shows the dependence of the average yield on the activation rate for different, low particle numbers in the completely heterogeneous case ($S = L$). Here, we restrict our discussion to the average yield. The error of the mean is negligible due to the large number of simulations used to calculate the average yield. Still, due to the randomness in binding and activation, the yield can differ between simulations. A figure with the average yield and its standard deviation is shown in Appendix 6. For very low and very high average yield, the standard deviation has to be small due to the boundedness of the yield. For intermediate values of the average, the standard deviation is highest but still small compared to the average yield. Thus, the average yield is meaningful for the essential understanding of the assembly process. Whereas the deterministic theory predicts perfect yield for small activation rates, in the stochastic simulation yield saturates at an imperfect value $y_{\max}<1$. Reducing the particle number $N$ decreases this saturation value $y_{\max}$ until no finished structures are produced ($y_{\max} \to 0$). The magnitude of this effect strongly depends on the size of the target structure $L$ if the system is heterogeneous. ***Figure 3c*** shows a diagram characterizing different regimes for the saturation value of the yield, $y_{\max}(N, L)$, in dependence of the particle number $N$ and the size of the target structure $L$ for fully heterogeneous systems ($S = L$). We find that the threshold particle number $N_y^{th}$ necessary to obtain a fixed yield $y$ increases nonlinearly with the target size $L$. For the depicted range of $L$, the dependence of the threshold for nonzero yield, $N_{>0}^{th}$, on $L$ can approximately be described by a power-law: $N_{>0}^{th} \sim L^{\xi}$, with exponent $\xi \approx 2.8$ for $L \leq 600$. Consequently, for

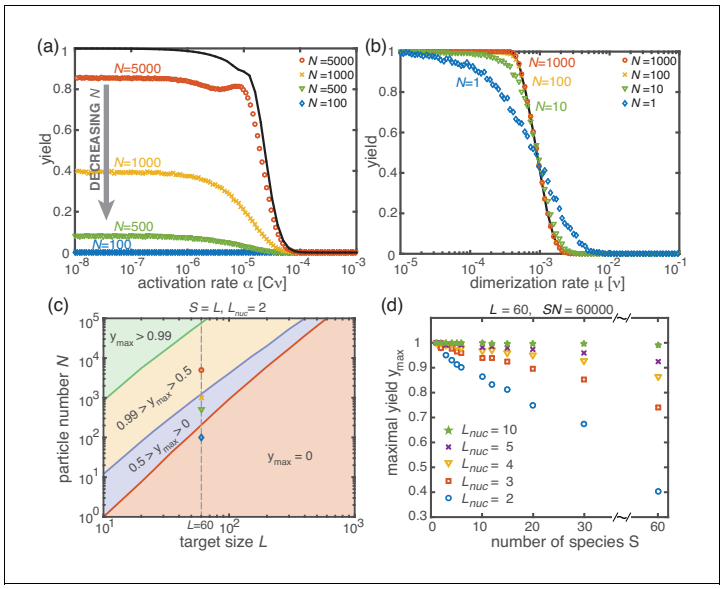


**Figure 3.** Stochastic effects in the case of reduced resources. (**a, b**) Yield of the fully heterogeneous system ($S = L$) for reduced number of particles (symbols) for $L = 60$ and $L_{\text{nuc}} = 2$ averaged over 1024 ensembles. In the activation scenario, at low activation rates the yield saturates at an imperfect value $y_{\max}$, which decreases with the number of particles (**a**). This finding disagrees with the deterministic prediction (black line) of perfect yield for $\alpha \to 0$. In contrast, the dimerization scenario robustly exhibits the maximal yield of 1 for small $N$, in agreement with the deterministic prediction (black line) (**b**). (**c**) Diagram showing different regimes of $y_{\max}(N, L)$ in dependence of the particle number $N$ and target size $L$ (for the fully heterogeneous system $S = L$) as obtained from stochastic simulations in the limit $\alpha \to 0$. The minimal number of particles necessary to obtain a fixed yield increases in a strongly nonlinear way with the target size. The symbols along the line $L = 60$ represent the saturation values of the yield curves in (**a**). (**d**) Dependence of $y_{\max}$ on the number of species $S$ for fixed $L = 60$ and fixed number of ring structures $NS/L$. Symbols indicate different values of the critical nucleation size $L_{\text{nuc}}$. The impact of stochastic effects strongly depends on the number of species under the constraint of a fixed total number of particles $NS$ and fixed target size $L$. The homogeneous system is not subject to stochastic effects at all. Higher reversibility for larger $L_{\text{nuc}}$ also mitigates stochastic effects.

$L = 600$ already more than $10^5$ rings must be assembled in order to obtain a yield larger than zero. In Appendix 8 we included two additional plots that show the dependence of $y_{\max}$ on $N$ for fixed $L$ and the dependence on $L$ for fixed $N$, respectively. The suppression of the yield is caused by fluctuations (see explanation below) and is not captured by a deterministic description. Because these stochastic effects can decrease the yield from a perfect value in a deterministic description to zero (see ***Figure 3a***), we term this effect 'stochastic yield catastrophe'. For fixed target size $L$ and fixed maximum number of target structures $\frac{NS}{L}$, $y_{\max}$ increases with decreasing number of species, see ***Figure 3d***. In the fully homogeneous case, $S = 1$, a perfect yield of 1 is always achieved for $\alpha \to 0$. The decrease of the maximal yield with the number of species $S$ thus suggests that, in order to obtain high yield, it is beneficial to design structures with as few different species as possible. In large part this effect is due to the constraint $SN = \text{const}$, whereby the more homogeneous systems (small $S$) require larger numbers of particles per species $N$ and, correspondingly, exhibit less stochasticity. If $N$ is fixed instead of $SN$, the yield still initially decreases with increasing number of species $S$ but then quickly reaches a stationary plateau and gets independent of $S$ for $S \gg 1$, see Appendix 7. Moreover, increasing the nucleation size $L_{\text{nuc}}$, and with it the reversibility of binding, also increases $y_{\max}$, see ***Figure 3(d)***. This indicates that, beside heterogeneity of the target structure, irreversibility of binding on the relevant time scale makes the system susceptible to stochastic effects.

The stochastic yield catastrophe is mainly attributable to fluctuations in the number of active monomers. In the deterministic (mean-field) equation the different particle species evolve in balanced stoichiometric concentrations. However, if activation is much slower than binding, the number of active monomers present at any given time is small, and the mean-field assumption of equal concentrations is violated due to fluctuations (for $S>1$). Activated monomers then might not fit any of the existing larger structures and would instead initiate new structures. ***Figure 4a*** illustrates this effect and shows how fluctuations in the availability of active particles lead to an enhanced nucleation and, correspondingly, to a decrease in yield. Due to the effective enhancement of the nucleation rate, the resulting polymer size distribution has a higher amplitude than that predicted deterministically (***Figure 4b***) and the system is prone to depletion traps. A similar broadening of the size distribution has been reported in the context of stochastic coagulation-fragmentation of identical particles (***D'Orsogna et al., 2015***).

In the dimerization scenario, in contrast, there is no stochastic activation step. All particles are available for binding from the outset. Consequently, stochastic effects do not play an essential role in the dimerization scenario and perfect yield can be reached robustly for all system sizes, regardless of the number of species $S$ (***Figure 3(b)***).

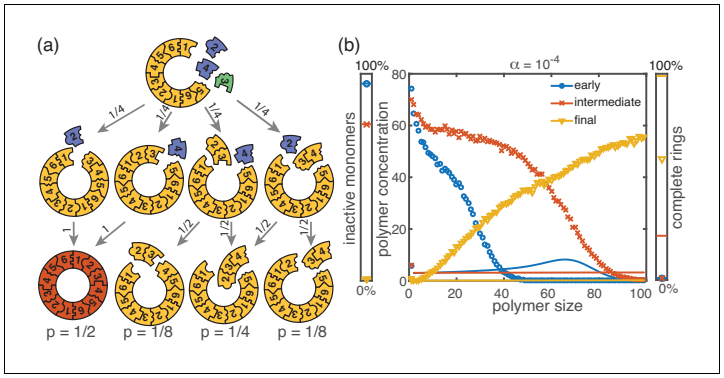


**Figure 4.** Cause and effect of stochasticity in the activation scenario. (**a**) Illustration of the significance of stochastic effects when resources are sparse. Arrows indicate possible transitions and the probabilities in the depicted situation for sufficiently small activation rate $\alpha$. For small $\alpha$, the random order of activation alone determines the availability of monomers and therefore the order of binding. In the depicted situation, the complete structure is assembled only with probability 1/2. In all other cases, only fragments of the structure are assembled such that the final yield is decreased. (**b**) Polymer size distribution for the activation scenario (symbols) as obtained from stochastic simulations, in comparison with its deterministic prediction (lines) for $S = L = 100$, $N = 1000$ and $L_{\text{nuc}} = 2$. Due to the enhanced number of nucleation events, the stochastic wave encompasses far more structures and moves more slowly. As a result, it does not quite reach the absorbing boundary.

## Non-monotonic yield curves for a combination of slow dimerization and activation

So far, the two implementations of the 'slow nucleation principle' have been investigated separately. Surprisingly, we observe counter-intuitive behavior in a mixed scenario in which both dimerization and activation occur slowly (i.e., $\mu<\nu$, $\alpha<\infty$). ***Figure 5*** shows that, depending on the ratio $\mu/\nu$, the yield can become a non-monotonic function of $\alpha$. In the regime where $\alpha$ is large, nucleation is dimerization-limited; therefore activation is irrelevant and the system behaves as in the dimerization scenario for $\alpha \to \infty$. Upon decreasing $\alpha$ we then encounter a second regime, where activation and dimerization jointly limit nucleation. The yield increases due to synergism between slow dimerization and activation (see $\mu/\nu$ dependence of $\alpha_{\mathrm{th}}$, ***Equation 1***), whilst the average number of active monomers is still high and fluctuations are negligible. Finally, a stochastic yield catastrophe occurs if $\alpha$ is further reduced and activation becomes the limiting step. This decline is caused by an increase in nucleation events due to relative fluctuations in the availability of the different species ('fluctuations between species'). This contrasts the deterministic description where nucleation is always slower for smaller activation rate. Depending on the ratio $\mu/\nu$, the ring size $L$ and the particle number $N$, maximal yield is obtained either in the dimerization-limited (red curves, ***Figure 5***), activation-limited (blue curve, ***Figure 5b***) or intermediate regime (green and orange curves, ***Figure 5***).

## Robustness of the results to model modifications

In our model, the reason for the stochastic yield catastrophe is that - due to fluctuations between species - the effective nucleation rate is strongly enhanced. Hence, if binding to a larger structure is temporarily impossible, activated monomers tend to initiate new structures, causing an excess of

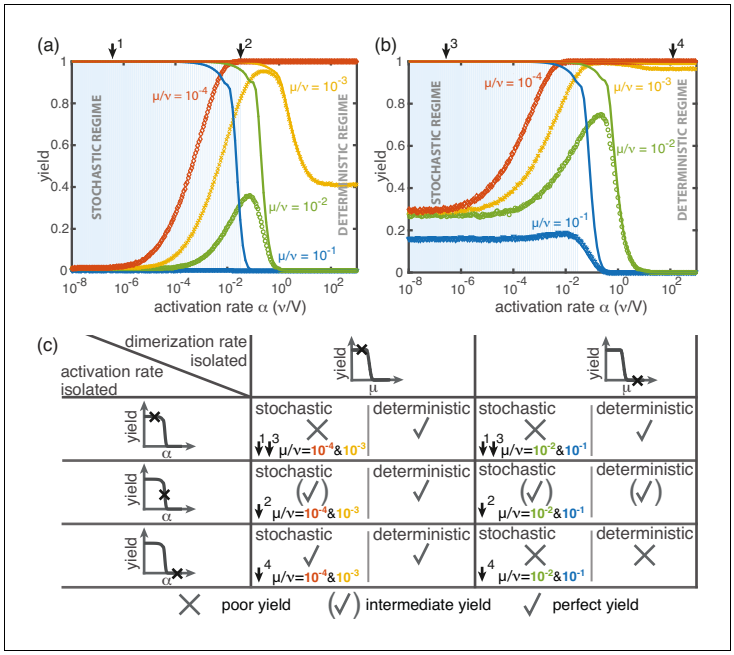


**Figure 5.** Yield for a combination of slow dimerization and activation. (**a, b**) Dependence of the yield of the fully heterogeneous system on the activation rate $\alpha$ for $N = 100$ and different values of the dimerization rate (colors/symbols) for $L = 60$ (**a**) and $L = 40$ (**b**) (averaged over 1024 ensembles). For large activation rates the yield behaves deterministically (lines). In contrast, for small activation rates, stochastic effects (blue shading) lead to a decrease in yield. Depending on the parameters, the yield maximum is attained in either the deterministic, stochastic or intermediate regime. (**c**) Table summarizing the qualitative behavior of the yield (poor/intermediate/perfect) for a combination of dimerization and activation rates for both the deterministic and the stochastic limit. The columns correspond to low and high values of the dimerization rate, as indicated by the marker in the corresponding deterministic yield curve at the top of the column. Similarly, the rows correspond to low, intermediate and high activation rates. Arrows and colors indicate where and for which curve this behavior can be observed in (**a**) and (**b**). Deviations between the deterministic and stochastic limits are most prominent for low activation rates.

structures that ultimately cannot be completed. Natural questions that arise are whether (i) relaxing the constraint that polymers cannot bind other polymers or (ii) abandoning the assumption of a linear assembly path, will resolve the stochastic yield catastrophe. To answer these questions, we performed stochastic simulations for extensions of our model system showing that the stochastic yield catastrophe indeed persists. We start by considering the ring model from the previous section but take polymer-polymer binding into account in addition to growth via monomer attachment (***Figure 6***). In detail, we assume that two structures of arbitrary size (and with combined length $\leq L$) bind at rate $\nu$ if they fit together, that is if the left (right) end of the first structure is periodically continued by the right (left) end of the second one. Realistically, the rate of binding between two structures is expected to decrease with the motility and thus the sizes of the structures. In order to assess the effect of polymer-polymer binding, we focus on the worst case where the rate for binding is independent of the size of both structures. If a stochastic yield catastrophe occurs for this choice of parameters, we expect it to be even more pronounced in all the 'intermediate cases'. ***Figure 6*** shows the dependence of the yield on the activation rate in the polymer-polymer model. As before, yield increases below a critical activation rate and then saturates at an imperfect value for small activation rates. Decreasing the number of particles per species, decreases this saturation value. Compared to the original model, the stochastic yield catastrophe is mitigated but still significant: For structures of size $S = L = 100$, yield saturates at around 0.87 for $N = 100$ particles per species and at around 0.33 for $N = 10$ particles per species. We thus conclude that polymer-polymer binding indeed alleviates the stochastic yield catastrophe but does not resolve it. Since binding only happens between consecutive species, structures with overlapping parts intrinsically can not bind together and depletion traps continue to occur. Taken together, also in the extended model, fluctuations in the availability of the different species lead to an excess of intermediate-sized structures that get kinetically trapped due to structural mismatches. Note that in the extreme case of $N = 1$, incomplete polymers can always combine into one final ring structure so that in this case the yield is always 1. Analogously, for high activation rates yield is improved for $N = 10$ compared to $N \geq 50$ (***Figure 6b***).

Kinetic trapping due to structural mismatches can occur in every (partially) irreversible heterogeneous assembly process with finite-sized target structure and limited resources. From our results, we thus expect a stochastic yield catastrophe to be common to such systems. In order to further test this hypothesis, we simulated another variant of our model where finite sized squares assemble via monomer attachment from a pool of initially inactive particles, see ***Figure 7***. In contrast to the

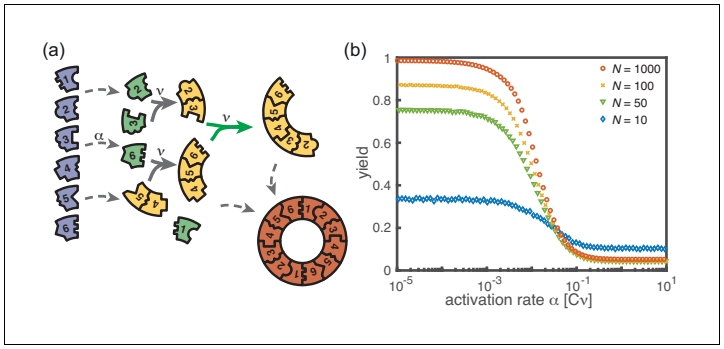


**Figure 6.** Extended model including polymer-polymer binding. (**a**) In the extended model, structures not only grow by monomer attachment but also by binding with another polymer (colored arrow). As before, binding only happens between periodically consecutive species with rate $\nu$ per binding site. So, the reaction rate for two polymers is identical to the one for monomer-polymer binding, $\nu$. Furthermore, only polymers with combined length $\leq L$ can bind. All other processes and rules are the same as in the original model described in ***Figure 1***. (**b**) The yield of the extended model as obtained from stochastic simulations is shown in dependence of the activation rate $\alpha$ for $S = L = 100$, $\mu = \nu = 1$, $L_{\text{nuc}} = 2$ and different values of the number of particles per species, $N$ (averaged over 1024 ensembles). The qualitative behavior is the same as for the original model. In particular, yield saturates (in the stochastic limit) at an imperfect value for slow activation rates. Note that for small particle numbers polymer-polymer binding results in an increase of the minimal yield (here for large activation rates). This is due to the fact that even in the case where a priori too many nucleation events happen, polymers can combine into final structures.

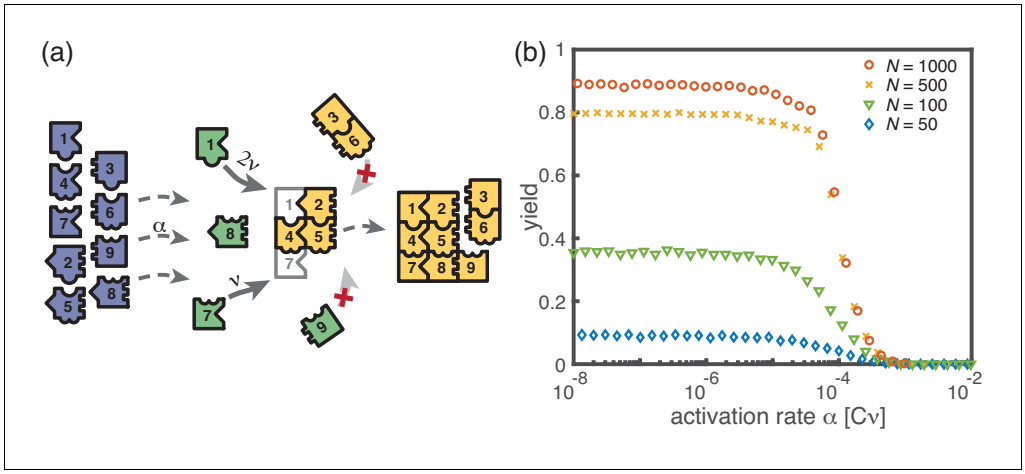


**Figure 7.** Assembly of squares of size $\sqrt{L} \times \sqrt{L}$ from $L$ different particle species. (**a**) As in the ring models, there are $N$ monomers of each species in the system. All particles are initially in an inactive state (blue) and are activated at the same per-capita rate $\alpha$. Once active (green), species with neighboring position within the square (left/right, up/down) can bind to each other. Structures grow by attachment of single monomers until the square is complete (absorbing state). Depending on the number $b$ of contacts between the monomer and the structure, the corresponding rate is $b\nu$. For simplicity, all polymers (yellow) are stable ($L_{\mathrm{nuc}} = 2$) and we do not consider polymer-polymer binding. (**b**) The yield of the square model as obtained from stochastic simulations is shown in dependence of the activation rate $\alpha$ for $S = L = 100$, $\mu = \nu = 1$ and different values of the number of particles per species, $N$ (averaged over 256 ensembles). The qualitative behavior is the same as for the previous models: Whereas the yield is poor for large activation rates, it strongly increases below a threshold value and saturates (in the stochastic limit) at an imperfect value < 1 for small activation rates. The saturation value decreases with decreasing number of particles in the system.

original model, the assembled structures are non-periodic and exhibit a non-linear assembly path where structures can grow independently in two dimensions. While the ring model assumes a sequential order of binding of the monomers, the square allows for a variety of distinct assembly paths that all lead to the same final structure. Note that, because of the absence of periodicity, the square model is only well defined for the completely heterogeneous case. ***Figure 7*** depicts the dependence of the yield on the activation rate for a square of size $S = 100$. Also in this case, we find that the yield saturates at an imperfect value for small activation rates. Hence, we showed that the stochastic yield catastrophe is not resolved neither by accounting for polymer-polymer combination nor by considering more general assembly processes with multiple parallel assembly paths. This observation supports the general validity of our findings and indicates that stochastic yield catastrophes are a general phenomenon of (partially) irreversible and heterogeneous self-assembling systems that occur if particle number fluctuations are non-negligible.

## Discussion

Our results show that different ways to slow down nucleation are indeed not equivalent, and that the explicit implementation is crucial for assembly efficiency. Susceptibility to stochastic effects is highly dependent on the specific scenario. Whereas systems for which dimerization limits nucleation are robust against stochastic effects, stochastic yield catastrophes can occur in heterogeneous systems when resource supply limits nucleation. The occurrence of stochastic yield catastrophes is not captured by the deterministic rate equations, for which the qualitative behavior of both scenarios is the same. Therefore, a stochastic description of the self-assembly process, which includes fluctuations in the availability of the different species, is required. The interplay between stochastic and deterministic dynamics can lead to a plethora of interesting behaviors. For example, the combination of slow activation and slow nucleation may result in a non-monotonic dependence of the yield on the activation rate. While deterministically, yield is always improved by decreasing the activation rate, stochastic fluctuations between species strongly suppress the yield for small activation rate by

effectively enhancing the nucleation speed. This observation clearly demonstrates that a *deterministically* slow nucleation speed is not sufficient in order to obtain good yield in heterogeneous self-assembly. For example, a slow activation step does not necessarily result in few nucleation events although deterministically this behavior is expected. Thus, our results indicate that the slow nucleation principle has to be interpreted in terms of the stochastic framework and have important implications for yield optimization.

We showed that demographic noise can cause stochastic yield catastrophes in heterogeneous self-assembly. However, other types of noise, such as spatiotemporal fluctuations induced by diffusion, are also expected to trigger stochastic yield catastrophes. Hence, our results have broad implications for complex biological and artificial systems, which typically exhibit various sources of noise. We characterize conditions under which stochastic yield catastrophes occur, and demonstrate how they can be mitigated. These insights could usefully inform the design of experiments to circumvent yield catastrophes: In particular, while slow provision of constituents is a feasible strategy for experiments, it is highly susceptible to stochastic effects. On the other hand, irrespective of its robustness to stochastic effects, the experimental realization of the dimerization scenario relies on cooperative or allosteric effects in binding, and may therefore require more sophisticated design of the constituents (***Sacanna et al., 2010***; ***Zeravcic et al., 2017***). Our theoretical analysis shows that stochasticity can be alleviated either by decreasing heterogeneity (presumably lowering realizable complexity) or by increasing reversibility (potentially requiring fine-tuning of bond strengths and reducing the stability of the assembly product). Alternative approaches to control stochasticity include the promotion of specific assembly paths (***Murugan et al., 2015***; Gartner, Graf and Frey, in preparation) and the control of fluctuations (Graf, Gartner and Frey, in preparation). One possibility to test these ideas and the ensuing control strategies could be via experiments based on DNA origami. Instead of building homogeneous ring structures as in ***Wagenbauer et al. (2017)***, one would have to design heterogeneous ring structures made from several different types of constituents with specified binding properties. By varying the opening angle of the 'wedges' (and thus the preferred number of building blocks in the ring) and/or the number of constituents, both the target structure size $L$ as well as the heterogeneity of the target structure $S$ could be controlled.

Moreover, the ideas presented in this manuscript are relevant for the understanding of intracellular self-assembly. In cells, provision of building blocks is typically a gradual process, as synthesis is either inherently slow or an explicit activation step, such as phosphorylation, is required. In addition, the constituents of the complex structures assembled in cells are usually present in small numbers and subject to diffusion. Hence, stochastic yield catastrophes would be expected to have devastating consequences for self-assembly, unless the relevant cellular processes use elaborate control mechanisms to circumvent stochastic effects. Further exploration of these control mechanisms should enhance the understanding of self-assembly processes in cells and help improve synthesis of complex nanostructures.

## Materials and methods

All our simulation data was generated with either C++ or MATLAB. The source code is available at the eLife website.

Here we show the derivation of ***Equation 1*** in the main text, giving the threshold values for the rate constants below which finite yield is obtained. The details can be found in Appendices 1–3.

### Master equation and chemical rate equations

We start with the general Master equation and derive the chemical rate equations (deterministic/mean-field equations) for the heterogeneous self-assembly process. We renounce to show the full Master equation here but instead state the system that describes the evolution of the first moments. To this end, we denote the random variable that describes the number of polymers of size $\ell$ and species $s$ in the system at time $t$ by $n_\ell^s(t)$ with $2 \leq \ell < L$ and $1 \leq s \leq S$. The species of a polymer is defined by the species of the respective monomer at its left end. Furthermore, $n_0^s$ and $n_1^s$ denote the number of inactive and active monomers of species $s$, respectively, and $n_L$ the number of complete rings. We signify the reaction rate for binding of a monomer to a polymer of size $\ell$ by $\nu_\ell$. $\alpha$ denotes the activation rate and $\delta_\ell$ the decay rate of a polymer of size $\ell$. By $\langle \ldots \rangle$ we indicate (ensemble)

averages. The system governing the evolution of the first moments (the averages) of the $\{n_\ell^s\}$ is then given by:

$$\frac{d}{dt}\langle n_0^s\rangle = -\alpha\,\langle n_0^s\rangle\,, \tag{2a}$$

$$\frac{d}{dt}\langle n_1^s\rangle = \alpha\,\langle n_0^s\rangle - \sum_{\ell=1}^{L-1}\nu_\ell\big(\langle n_1^s n_\ell^{s+1}\rangle + \langle n_1^s n_\ell^{s-\ell}\rangle\big) + \sum_{\ell=2}^{L_{\mathrm{nuc}}-1}\sum_{k=s+1-\ell}^{k=s}\delta_\ell\langle n_\ell^k\rangle\,, \tag{2b}$$

$$\frac{d}{dt}\langle n_2^s\rangle = \nu_1\,\langle n_1^s\, n_1^{s+1}\rangle - \nu_2\,\langle n_2^s\, n_1^{s+2}\rangle - \nu_2\,\langle n_2^s\, n_1^{s-1}\rangle - \delta_2\,\langle n_2^s\rangle\,\mathbf{1}_{\{2<L_{\mathrm{nuc}}\}}\,, \tag{2c}$$

$$\frac{d}{dt}\langle n_\ell^s\rangle = \nu_{\ell-1}\,\langle n_{\ell-1}^s\, n_1^{\ell+s-1}\rangle + \nu_{\ell-1}\,\langle n_{\ell-1}^{s+1}\, n_1^s\rangle - \nu_\ell\,\langle n_\ell^s\, n_1^{s+\ell}\rangle - \nu_\ell\,\langle n_\ell^s\, n_1^{s-1}\rangle - \delta\,\langle n_\ell^s\rangle\,\mathbf{1}_{\{\ell<L_{\mathrm{nuc}}\}}\,, \tag{2d}$$

$$\frac{d}{dt}\langle n_L^s\rangle = \nu_{L-1}\,\langle n_{L-1}^s\, n_1^{L+s-1}\rangle + \nu_{L-1}\,\langle n_{L-1}^{s+1}\, n_1^s\rangle\,. \tag{2e}$$

The different terms of this equation are illustrated graphically in ***Figure 8***. The first equation describes loss of inactive particles due to activation at rate $\alpha$. ***Equation 2b*** gives the temporal change of the number of active monomers that is governed by the following processes: activation of inactive monomers at rate $\alpha$, binding of active monomers to the left or to the right end of an existing structure of size $\ell$ at rate $\nu_\ell$, and decay of below-critical polymers of size $\ell$ into monomers at rate $\delta_\ell$ (disassembly). ***Equations 2c and 2d*** describe the dynamics of dimers and larger polymers of size $3 \leq \ell < L$, respectively. The terms account for reactions of polymers with active monomers (polymerization) as well as decay in the case of below-critical polymers (disassembly). The indicator function $\mathbf{1}_{\{x<L_{\mathrm{nuc}}\}}$ equals 1 if the condition $x<L_{\mathrm{nuc}}$ is satisfied and 0 otherwise. Note that a polymer of size $\ell \geq 3$ can grow by attaching a monomer to its left or to its right end whereas the formation of a dimer of a specific species is only possible via one reaction pathway (dimerization reaction). Finally, polymers of length $L$ – the complete ring structures – form an absorbing state and, therefore, include only the respective gain terms (cf ***Equation 2e***).

We simulated the Master equation underlying ***Equation 2*** stochastically using Gillespie's algorithm. For the following deterministic analysis, we neglect correlations between particle numbers $\{n_\ell^s\}$, which is valid assumption for large particle numbers. Then the two-point correlator can be approximated as the product of the corresponding mean values (mean-field approximation)

$$\langle n_i^s n_j^k\rangle = \langle n_i^s\rangle\langle n_j^k\rangle\ \forall s,k \tag{3}$$

Furthermore, for the expectation values it must hold

$$\langle n_\ell^s\rangle = \langle n_\ell^1\rangle\ \forall s \tag{4}$$

because all species have equivalent properties (there is no distinct species) and hence the system is invariant under relabelling of the upper index. By

$$c_\ell := \frac{\langle n_\ell^s\rangle}{V}, \tag{5}$$

we denote the concentration of any monomer or polymer species of size $\ell$, where $V$ is the reaction volume. Due to the symmetry formulated in ***Equation 4***, the heterogeneous assembly process decouples into a set of $S$ identical and independent homogeneous assembly processes in the deterministic limit. The corresponding homogeneous system then is described by the following set of equations that is obtained by applying (***Equation 3***, ***Equation 4***) and (***Equation 5***) to (***Equation 2***)

$$\frac{d}{dt}c_0 = -\alpha\,c_0\,, \tag{6a}$$

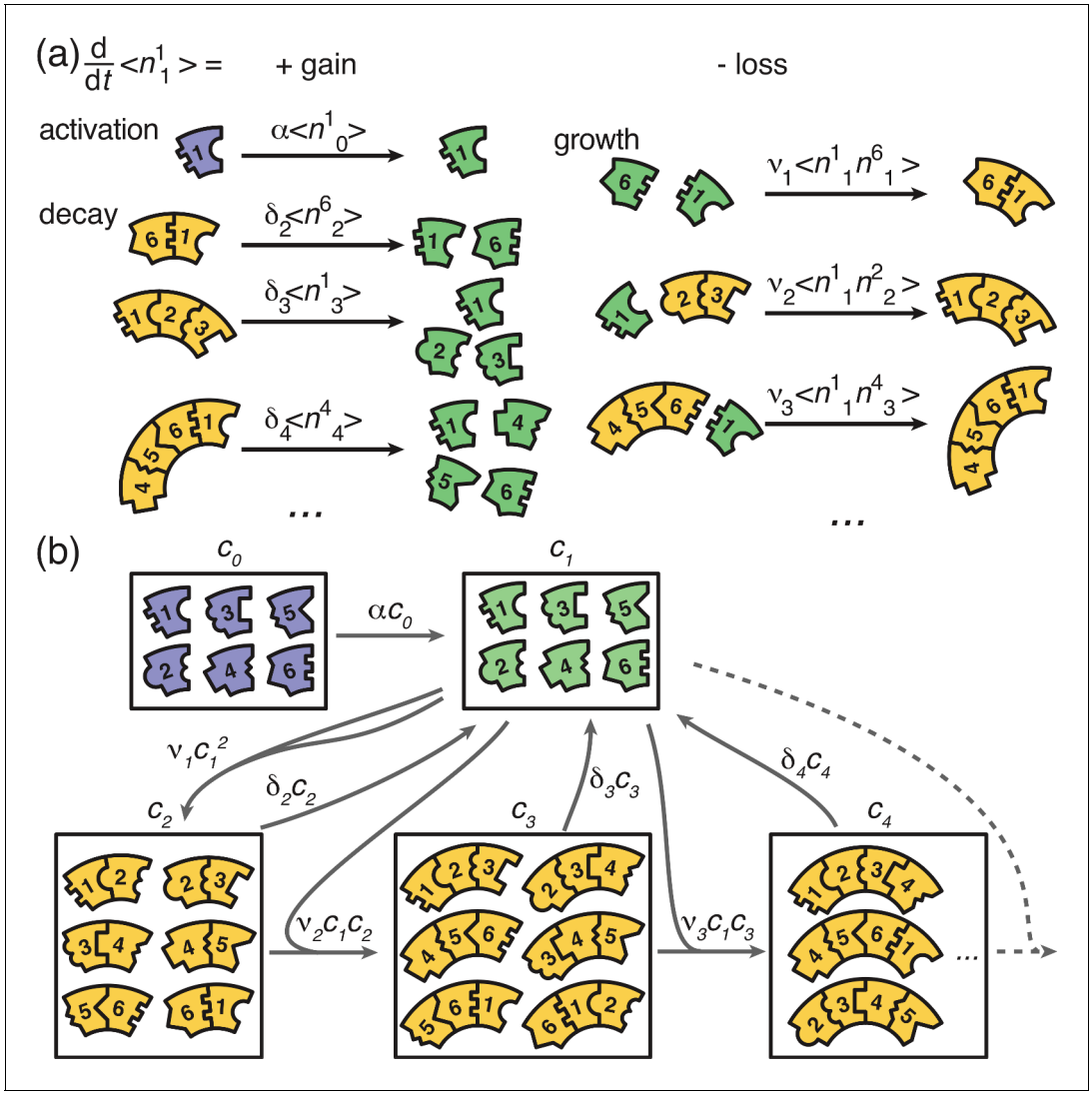


**Figure 8.** Graphical illustration of ***Equations 2 and 6***. (a) Visualization of the gain and loss terms in the dynamics of the active monomers in ***Equation 2b***. Gain of active monomers is due to activation of inactive monomers as well as decay of unstable polymers. Loss of active monomers is due to dimerization and attachment of monomers to larger polymers. (b) Visualization of the transitions between clusters of different sizes (without distinction of species). The first and second box represent the inactive and active monomers in the system, the subsequent boxes each represent the ensemble of polymers of a certain size. The arrows between the boxes show possible reactions and transitions with the reaction rates indicated accordingly. Each arrow starting from or leading to a box is associated with a corresponding loss or gain term on the right hand side of ***Equation 2*** and ***Equation 6***.

$$\frac{d}{dt}c_1 = \alpha\, c_0 - 2c_1 \sum_{\ell=1}^{L-1} \nu_\ell\, c_\ell + \sum_{\ell=2}^{L_{\mathrm{nuc}}-1} l\delta_\ell\, c_\ell\,, \tag{6b}$$

$$\frac{d}{dt}c_2 = \nu_1\, c_1^2 - 2\,\nu_2\, c_1\, c_2 - \delta_2\, c_2\, \mathbf{1}_{\{2<L_{\mathrm{nuc}}\}}\,, \tag{6c}$$

$$\frac{d}{dt}c_\ell = 2\,\nu_{\ell-1}\, c_1\, c_{\ell-1} - 2\nu_\ell\, c_1\, c_\ell - \delta_\ell\, c_\ell\, \mathbf{1}_{\{\ell<L_{\mathrm{nuc}}\}}\,, \qquad \text{for} 3 \le \ell < L, \tag{6d}$$

$$\frac{d}{dt}c_L = 2\,\nu_{L-1}\, c_1\, c_{L-1}\,. \tag{6e}$$

The rate constants $\nu_\ell$ in ***Equations 6 and 2*** differ by a factor of $V$. For convenience, we use however the same symbol in both cases. The rate constants $\nu_\ell$ in ***Equation 6*** can be interpreted in the usual units $[\frac{\text{liter}}{\text{molsec}}]$. Due to the symmetry, the yield, which is given by the quotient of the number of completely assembled rings and the maximum number of complete rings, becomes independent of the number of species $S$

$$\text{yield(t)} = \frac{Sc_L(t)V}{SNL^{-1}} = \frac{c_L(t)VL}{N}. \tag{7}$$

Hence, it is enough to study the dynamics of the homogeneous system, ***Equation 6***, to identify the condition under which non zero yield is obtained.

## Effective description by an advection-diffusion equation

The dynamical properties of the evolution of the polymer-size distribution become evident if the set of ODEs, ***Equation 6***, is rewritten as a partial differential equation. This approach was previously described in the context of virus capsid assembly (***Zlotnick et al., 1999***; ***Morozov et al., 2009***). For simplicity, we restrict ourselves to the case $L_{\text{nuc}} = 2$ and let $\nu_1 = \mu$ and $\nu_{\ell\geq 2} = \nu$. Then, for the polymers with $\ell$>2 we have

$$\partial_t c_\ell = 2\nu c_1 \left[c_{\ell-1} - c_\ell\right]. \tag{8}$$

As a next step, we approximate the index $\ell \in \{2,3,\ldots,L\}$ indicating the length of the polymer as a continuous variable $x \in [2,L]$ and define $c(x=\ell) := c_\ell$. By $A := c_1$ we denote the concentration of active monomers in the following to emphasize their special role. Formally expanding the right-hand side of ***Equation 8*** in a Taylor series up to second order

$$c(\ell-1) = c(\ell) - \partial_x c(\ell) + \frac{1}{2}\partial_x^2 c(\ell), \tag{9}$$

one arrives at the advection-diffusion equation with both advection and diffusion coefficients depending on the concentration of active monomers $A(t)$

$$\partial_t c(x) = -2\nu A\,\partial_x c(x) + \nu A\,\partial_x^2 c(x). \tag{10}$$

***Equation 10*** can be written in the form of a continuity equation $\partial_t c(x) = -\partial_x J(x)$ with flux $J = 2\nu A\, c - \nu A\,\partial_x c$. The flux at the left boundary $x=2$ equals the influx of polymers due to dimerization of free monomers $J(2,t) = \mu A^2$. This enforces a Robin boundary condition at $x=2$

$$2\nu A\, c(2,t) - \nu A\,\partial_x c(2,t) = \mu A^2. \tag{11}$$

At $x=L$ we set an absorbing boundary $c(L,t)=0$ so that completed structures are removed from the system. The time evolution of the concentration of active monomers is given by

$$\partial_t A = \alpha C e^{-\alpha t} - 2\mu A^2 - 2\nu A \int_2^L c(x,t)\,dx. \tag{12}$$

The terms on the right-hand side account for activation of inactive particles, dimerization, and binding of active particles to polymers (polymerization).

Qualitatively, ***Equation 10*** describes a profile that emerges at $x=2$ from the boundary condition ***Equation 11,*** moves to the right with time-dependent velocity $2\nu A(t)$ due to the advection term, and broadens with a time-dependent diffusion coefficient $\nu A(t)$. In Appendices 2–3 we show how the full solution of ***Equations 10 and 11*** can be found assuming knowledge of $A(t)$. Here, we focus only on the derivation of the threshold activation rate and threshold dimerization rate that mark the onset of non-zero yield. Yield production starts as soon as the density wave reaches the absorbing boundary at $x=L$. Therefore, finite yield is obtained if the sum of the advectively travelled distance $d_{\text{adv}}$ and the diffusively travelled distance $d_{\text{diff}}$ exceeds the system size $L-2$

$$d_{\text{adv}} + d_{\text{diff}} \geq L - 2. \tag{13}$$

According to **Equation 10**, $d_{\mathrm{adv}} = 2\nu \int_0^\infty A(t)dt$ and $d_{\mathrm{diff}} = \sqrt{2\nu \int_0^\infty A(t)dt}$, giving as condition for the onset of finite yield

$$2\nu \int_0^\infty A(t)dt \stackrel{!}{=} \frac{1}{4}\left(\sqrt{1+4(L-2)}-1\right)^2 \approx L - \sqrt{L}, \tag{14}$$

where the last approximation is valid for large $L$.

In order to obtain $\int_0^\infty A(t)dt$ we derive an effective two-component system that governs the evolution of $A(t)$. To this end, we denote the total number of polymers in **Equation 12** by $B(t) := \int_2^\infty c(x,t)\,dx$ (as long as yield is zero the upper boundary is irrelevant and we can consider $L = \infty$). **Equation 12** then reads

$$\frac{d}{dt}A = \alpha C e^{-\alpha t} - 2\mu A^2 - 2\nu A\,B\,, \tag{15}$$

and the dynamics of $B$ is determined from the boundary condition, **Equation 11**

$$\frac{d}{dt}B = \int_2^\infty \partial_t c(x,t)\,dx = \int_2^\infty -\partial_x J(x,t)\,dx = -\underbrace{J(\infty,t)}_{=0} + J(2,t) = \mu A(t)^2. \tag{16}$$

Measuring $A$ and $B$ in units of the initial monomer concentration $C$ and time in units of $(\nu C)^{-1}$ the equations are rewritten in dimensionless units as

$$\frac{d}{dt}A = \omega e^{-\omega t} - 2\eta A^2 - 2A\,B, \tag{17a}$$

$$\frac{d}{dt}B = \eta A^2, \tag{17b}$$

where $\omega = \frac{\alpha}{\nu C}$ and $\eta = \frac{\mu}{\nu}$. **Equation 17** describes a closed two-component system for the concentration of active monomers $A$ and the total concentration of polymers $B$. It describes the dynamics exactly as long as yield is zero. In order to evaluate the condition (14) we need to determine the integral over $A(t)$ as a function of $\omega$ and $\eta$

$$\int_0^\infty A_{\omega,\eta}(t)dt := g(\omega,\eta)\,. \tag{18}$$

To that end, we proceed by looking at both scenarios separately. The numerical analysis, confirming our analytic results, is given in Appendix 3.

## Dimerization scenario

The activation rate in the dimerization scenario is $\alpha \to \infty$, and instead of the term $\omega e^{-\omega t}$ in $\mathrm{d}A/\mathrm{d}t$, we set the initial condition $A(0) = 1$ (and $B(0) = 0$). Furthermore, $\eta = \mu/\nu \ll 1$ and we can neglect the term proportional to $\eta$ in $\mathrm{d}A/\mathrm{d}t$. As a result,

$$\frac{\mathrm{d}A}{\mathrm{d}B} = -\frac{2B}{\eta A}.$$

Solving this equation for $A$ as a function of $B$ using the initial condition $A(B=0) = 1$, the totally travelled distance of the wave is determined to be

$$2g(\omega,\eta) = 2\frac{\pi}{2\sqrt{2}}\frac{1}{\sqrt{\eta}}, \tag{19}$$

where for the evaluation of the integral we used the substitution $\eta A^2 \mathrm{d}t = \mathrm{d}B$.

### Activation scenario

In the activation scenario, yield sets in only if the activation rate and thus the effective nucleation rate is slow. As a result, in addition to $\omega \ll 1$, we can again neglect the term proportional to $\eta$ in $\mathrm{d}A/\mathrm{d}t$. This time, however, we have to keep the term $\omega e^{-\omega t}$. As a next step, we assume that $\mathrm{d}A/\mathrm{d}t$ is much smaller than the remaining terms on the right-hand side, $\omega e^{-\omega t}$ and $-2AB$. This assumption might seem crude at first sight but is justified a posteriori by the solution of the equation (see Appendix 3). Hence, we get the algebraic equation $A(t) = \omega e^{-\omega t}/(2B(t))$. Using it to solve $\mathrm{d}B/\mathrm{d}t = \eta A^2$ for $B$, and then to determine $A$, the totally travelled distance of the wave is deduced as

$$2g(\omega,\eta) = 2\frac{3^{2/3}\sqrt{\pi}\Gamma(2/3)}{6\Gamma(7/6)}(\omega\eta)^{-1/3}. \tag{20}$$

Taken together, we therefore obtain two conditions out of which one must be fulfilled in order to obtain finite yield

$$2a(\eta\omega)^{-\frac{1}{3}} \geq L - \sqrt{L} \Rightarrow \quad \alpha < \alpha_{\mathrm{th}} := P_\alpha \frac{\nu}{\mu}\frac{\nu C}{(L-\sqrt{L})^3} \tag{21}$$

$$\text{or} \quad 2b\eta^{-\frac{1}{2}} \geq L - \sqrt{L} \Rightarrow \quad \mu < \mu_{\mathrm{th}} := P_\mu \frac{\nu}{(L-\sqrt{L})^2}, \tag{22}$$

where $a$ and $b$ are numerical factors, and $P_\alpha = 8a^3 \approx 5.77$ and $P_\mu = 4b^2 \approx 4.93$. This verifies ***Equation 1*** in the main text.

## Acknowledgements

We thank Nigel Goldenfeld for a stimulating discussion, and Raphaela Geßele and Laeschkir Hassan for helpful feedback on the manuscript. This research was supported by the German Excellence Initiative via the program 'NanoSystems Initiative Munich'(NIM) and was funded by the Deutsche Forschungsgemeinschaft (DFG, German Research Foundation) under Germany's Excellence Strategy – EXC-2094–390783311. FMG and IRG are supported by a DFG fellowship through the Graduate School of Quantitative Biosciences Munich (QBM). We also gratefully acknowledge financial support by the DFG Research Training Group GRK2062 (Molecular Principles of Synthetic Biology). Finally, EF thanks the Aspen Center for Physics, which is supported by National Science Foundation grant PHY-1607611, for their hospitality and inspiring discussions with colleagues.

## Additional information

### Funding


| Funder | Grant reference number | Author |
|---|---|---|
| Deutsche Forschungsgemeinschaft | GRK2062 | Patrick Wilke |
| Deutsche Forschungsgemeinschaft | QBM | Florian M Gartner<br>Isabella R Graf |
| Aspen Center for Physics | PHY-160761 | Erwin Frey |
| Deutsche Forschungsgemeinschaft | EXC-2094 - 390783311 | Erwin Frey |

The funders had no role in study design, data collection and interpretation, or the decision to submit the work for publication.


### Author contributions

Florian M Gartner, Isabella R Graf, Patrick Wilke, Conceptualization, Data curation, Software, Formal analysis, Validation, Investigation, Visualization, Methodology, Project administration; Philipp M Geiger, Conceptualization, Validation, Investigation, Visualization, Project administration; Erwin Frey,

Conceptualization, Resources, Supervision, Funding acquisition, Validation, Methodology, Project administration


### Author ORCIDs

Florian M Gartner https://orcid.org/0000-0002-9801-4288
Isabella R Graf https://orcid.org/0000-0001-9169-9109
Erwin Frey https://orcid.org/0000-0001-8792-3358



### Decision letter and Author response

Decision letter https://doi.org/10.7554/eLife.51020.sa1
Author response https://doi.org/10.7554/eLife.51020.sa2


## Additional files

### Supplementary files

- Source code 1. C++ code for original ring model without polymer-polymer binding.
- Source code 2. C++ code for extended ring model with polymer-polymer binding.
- Source code 3. C++ code for square model.
- Source code 4. MATLAB code for original ring model.
- Transparent reporting form

### Data availability

All data was generated from stochastic simulations in C++ and deterministic simulations in Matlab. The source code files are included with the article.

## References


**Alberts B**, Johnson A. 2015. *Molecular Biology of the Cell*. New York: Garland Science.

**Chen C**, Kao CC, Dragnea B. 2008. Self-assembly of brome mosaic virus capsids: insights from shorter time-scale experiments. *The Journal of Physical Chemistry A* **112**:9405–9412. DOI: https://doi.org/10.1021/jp802498z, PMID: 18754598

**Chevance FF**, Hughes KT. 2008. Coordinating assembly of a bacterial macromolecular machine. *Nature Reviews Microbiology* **6**:455–465. DOI: https://doi.org/10.1038/nrmicro1887, PMID: 18483484

**D'Orsogna MR**, Lakatos G, Chou T. 2012. Stochastic self-assembly of incommensurate clusters. *The Journal of Chemical Physics* **136**:084110. DOI: https://doi.org/10.1063/1.3688231, PMID: 22380035

**D'Orsogna MR**, Zhao B, Berenji B, Chou T. 2013. Combinatoric analysis of heterogeneous stochastic self-assembly. *The Journal of Chemical Physics* **139**:121918. DOI: https://doi.org/10.1063/1.4817202, PMID: 24089730

**D'Orsogna MR**, Lei Q, Chou T. 2015. First assembly times and equilibration in stochastic coagulation-fragmentation. *The Journal of Chemical Physics* **143**:014112. DOI: https://doi.org/10.1063/1.4923002, PMID: 26156470

**Drummond DA**, Wilke CO. 2009. The evolutionary consequences of erroneous protein synthesis. *Nature Reviews Genetics* **10**:715–724. DOI: https://doi.org/10.1038/nrg2662, PMID: 19763154

**Endres D**, Zlotnick A. 2002. Model-based analysis of assembly kinetics for virus capsids or other spherical polymers. *Biophysical Journal* **83**:1217–1230. DOI: https://doi.org/10.1016/S0006-3495(02)75245-4, PMID: 12124301

**Gerling T**, Wagenbauer KF, Neuner AM, Dietz H. 2015. Dynamic DNA devices and assemblies formed by shape-complementary, non-base pairing 3D components. *Science* **347**:1446–1452. DOI: https://doi.org/10.1126/science.aaa5372, PMID: 25814577

**Gillespie DT**. 2007. Stochastic simulation of chemical kinetics. *Annual Review of Physical Chemistry* **58**:35–55. DOI: https://doi.org/10.1146/annurev.physchem.58.032806.104637, PMID: 17037977

**Grant J**, Jack RL, Whitelam S. 2011. Analyzing mechanisms and microscopic reversibility of self-assembly. *The Journal of Chemical Physics* **135**:214505. DOI: https://doi.org/10.1063/1.3662140, PMID: 22149800

**Hagan MF**, Elrad OM, Jack RL. 2011. Mechanisms of kinetic trapping in self-assembly and phase transformation. *The Journal of Chemical Physics* **135**:104115. DOI: https://doi.org/10.1063/1.3635775, PMID: 21932884

**Hagan MF**. 2014. Modeling viral capsid assembly. *Advances in Chemical Physics* **155**:1. DOI: https://doi.org/10.1002/9781118755815.ch01, PMID: 25663722

**Hagan MF**, Elrad OM. 2010. Understanding the concentration dependence of viral capsid assembly kinetics–the origin of the lag time and identifying the critical nucleus size. *Biophysical Journal* **98**:1065–1074. DOI: https://doi.org/10.1016/j.bpj.2009.11.023, PMID: 20303864

**Haxton TK**, Whitelam S. 2013. Do hierarchical structures assemble best via hierarchical pathways? *Soft Matter* **9**: 6851–6861. DOI: https://doi.org/10.1039/c3sm27637f

**Hedges LO**, Mannige RV, Whitelam S. 2014. Growth of equilibrium structures built from a large number of distinct component types. *Soft Matter* **10**:6404–6416. DOI: https://doi.org/10.1039/C4SM01021C, PMID: 25005537

**Jacobs WM**, Reinhardt A, Frenkel D. 2015. Rational design of self-assembly pathways for complex multicomponent structures. *PNAS* **112**:6313–6318. DOI: https://doi.org/10.1073/pnas.1502210112

**Jacobs WM**, Frenkel D. 2015. Self-assembly protocol design for periodic multicomponent structures. *Soft Matter* **11**:8930–8938. DOI: https://doi.org/10.1039/C5SM01841B, PMID: 26404794

**Jucker M**, Walker LC. 2013. Self-propagation of pathogenic protein aggregates in neurodegenerative diseases. *Nature* **501**:45–51. DOI: https://doi.org/10.1038/nature12481, PMID: 24005412

**Ke Y**, Ong LL, Shih WM, Yin P. 2012. Three-dimensional structures self-assembled from DNA bricks. *Science* **338**: 1177–1183. DOI: https://doi.org/10.1126/science.1227268, PMID: 23197527

**Krapivsky PL**, Redner S, Ben-Naim E. 2010. *A Kinetic View of Statistical Physics*. Cambridge University Press.

**Lazaro GR**, Hagan MF. 2016. Allosteric control of icosahedral capsid assembly. *The Journal of Physical Chemistry B* **120**:6306–6318. DOI: https://doi.org/10.1021/acs.jpcb.6b02768, PMID: 27117092

**Leiman PG**, Arisaka F, van Raaij MJ, Kostyuchenko VA, Aksyuk AA, Kanamaru S, Rossmann MG. 2010. Morphogenesis of the T4 tail and tail fibers. *Virology Journal* **7**:355. DOI: https://doi.org/10.1186/1743-422X-7-355, PMID: 21129200

**Michaels TC**, Dear AJ, Kirkegaard JB, Saar KL, Weitz DA, Knowles TP. 2016. Fluctuations in the kinetics of linear protein Self-Assembly. *Physical Review Letters* **116**:258103. DOI: https://doi.org/10.1103/PhysRevLett.116.258103, PMID: 27391756

**Michaels TCT**, Bellaiche MMJ, Hagan MF, Knowles TPJ. 2017. Kinetic constraints on self-assembly into closed supramolecular structures. *Scientific Reports* **7**:12295. DOI: https://doi.org/10.1038/s41598-017-12528-8, PMID: 28947758

**Morozov AY**, Bruinsma RF, Rudnick J. 2009. Assembly of viruses and the pseudo-law of mass action. *The Journal of Chemical Physics* **131**:155101. DOI: https://doi.org/10.1063/1.3212694, PMID: 20568884

**Murugan A**, Zou J, Brenner MP. 2015. Undesired usage and the robust self-assembly of heterogeneous structures. *Nature Communications* **6**:6203. DOI: https://doi.org/10.1038/ncomms7203, PMID: 25669898

**Peña C**, Hurt E, Panse VG. 2017. Eukaryotic ribosome assembly, transport and quality control. *Nature Structural & Molecular Biology* **24**:689–699. DOI: https://doi.org/10.1038/nsmb.3454, PMID: 28880863

**Praetorius F**, Dietz H. 2017. Self-assembly of genetically encoded DNA-protein hybrid nanoscale shapes. *Science* **355**:eaam5488. DOI: https://doi.org/10.1126/science.aam5488, PMID: 28336611

**Reinhardt A**, Frenkel D. 2014. Numerical evidence for nucleated self-assembly of DNA brick structures. *Physical Review Letters* **112**:238103. DOI: https://doi.org/10.1103/PhysRevLett.112.238103, PMID: 24972230

**Sacanna S**, Irvine WT, Chaikin PM, Pine DJ. 2010. Lock and key colloids. *Nature* **464**:575–578. DOI: https://doi.org/10.1038/nature08906, PMID: 20336142

**Sear RP**. 2007. Nucleation: theory and applications to protein solutions and colloidal suspensions. *Journal of Physics: Condensed Matter* **19**:033101. DOI: https://doi.org/10.1088/0953-8984/19/3/033101

**Wagenbauer KF**, Sigl C, Dietz H. 2017. Gigadalton-scale shape-programmable DNA assemblies. *Nature* **552**:78–83. DOI: https://doi.org/10.1038/nature24651, PMID: 29219966

**Wei B**, Dai M, Yin P. 2012. Complex shapes self-assembled from single-stranded DNA tiles. *Nature* **485**:623–626. DOI: https://doi.org/10.1038/nature11075, PMID: 22660323

**Whitelam S**. 2015. Hierarchical assembly may be a way to make large information-rich structures. *Soft Matter* **11**: 8225–8235. DOI: https://doi.org/10.1039/C5SM01375E, PMID: 26350267

**Whitesides GM**, Mathias JP, Seto CT. 1991. Molecular self-assembly and nanochemistry: a chemical strategy for the synthesis of nanostructures. *Science* **254**:1312–1319. DOI: https://doi.org/10.1126/science.1962191, PMID: 1962191

**Whitesides GM**, Grzybowski B. 2002. Self-assembly at all scales. *Science* **295**:2418–2421. DOI: https://doi.org/10.1126/science.1070821, PMID: 11923529

**Yvinec R**, D'Orsogna MR, Chou T. 2012. First passage times in homogeneous nucleation and self-assembly. *The Journal of Chemical Physics* **137**:244107. DOI: https://doi.org/10.1063/1.4772598, PMID: 23277928

**Zeravcic Z**, Manoharan VN, Brenner MP. 2017. *Colloquium* : Toward living matter with colloidal particles . *Reviews of Modern Physics* **89**:031001. DOI: https://doi.org/10.1103/RevModPhys.89.031001

**Zhang S**. 2003. Fabrication of novel biomaterials through molecular self-assembly. *Nature Biotechnology* **21**: 1171–1178. DOI: https://doi.org/10.1038/nbt874, PMID: 14520402

**Zlotnick A**, Johnson JM, Wingfield PW, Stahl SJ, Endres D. 1999. A theoretical model successfully identifies features of hepatitis B virus capsid assembly. *Biochemistry* **38**:14644–14652. DOI: https://doi.org/10.1021/bi991611a, PMID: 10545189

**Zlotnick A**. 2003. Are weak protein-protein interactions the general rule in capsid assembly? *Virology* **315**:269–274. DOI: https://doi.org/10.1016/S0042-6822(03)00586-5, PMID: 14585329

# Appendix 1

## Chemical reaction equations and the equivalence of models with different numbers of species

In this section we derive the chemical rate equations (deterministic equations) for the self-assembly process as described in the main text. Furthermore, we show that for general $S$ in the deterministic limit the model is equivalent to a set of $S$ independent assembly processes with only one species.

## Homogeneous structures

First, we consider the homogeneous model ($S=1$). By $c_\ell(t)$ we denote the concentration of complexes of length $\ell$ ($\ell \geq 2$) at time $t$, $c_1(t)$ is the concentration of active monomers and $c_0(t)$ the concentration of inactive monomers at time $t$. In the following we will usually skip the time argument for better readability. We denote the reaction rate for binding of a monomer to a polymer of size $\ell$ by $\nu_\ell$. The model from the main text is recovered by setting $\nu_\ell := \mu_\ell$ if $\ell<L_{\mathrm{nuc}}$, and $\nu_\ell := \nu$ otherwise. The ensuing set of ordinary differential equations then reads:

$$\frac{d}{dt}c_0 = -\alpha\, c_0\,, \tag{A1a}$$

$$\frac{d}{dt}c_1 = \alpha\, c_0 - 2c_1 \sum_{\ell=1}^{L-1} \nu_\ell\, c_\ell + \sum_{\ell=2}^{L_{\mathrm{nuc}}-1} l\delta_\ell\, c_\ell\,, \tag{A1b}$$

$$\frac{d}{dt}c_2 = \nu_1\, c_1^2 - 2\,\nu_2\, c_1\, c_2 - \delta_2\, c_2\, \mathbf{1}_{\{2<L_{\mathrm{nuc}}\}}\,, \tag{A1c}$$

$$\frac{d}{dt}c_\ell = 2\,\nu_{\ell-1}\, c_1\, c_{\ell-1} - 2\nu_\ell\, c_1\, c_\ell - \delta_\ell\, c_\ell\, \mathbf{1}_{\{\ell<L_{\mathrm{nuc}}\}}\,, \qquad \text{for} 3 \leq \ell<L\,, \tag{A1d}$$

$$\frac{d}{dt}c_L = 2\,\nu_{L-1}\, c_1\, c_{L-1}\,. \tag{A1e}$$

The indicator function $\mathbf{1}_{\{x<L_{\mathrm{nuc}}\}}$ equals 1 if the condition $x<L_{\mathrm{nuc}}$ is satisfied and 0 otherwise. The first equation describes loss of inactive particles due to activation at rate $\alpha$. It is uncoupled from the remainder of the equations and is solved by $c_0(t)=Ce^{-\alpha t}$, with $C$ denoting the initial concentration of inactive monomers. The temporal change of the active monomers is governed by the following processes (***Equation A1b***): activation of inactive monomers at rate $\alpha$, binding of active monomers to existing structures at rate $\nu_\ell$ (polymerization), and decay of below-critical polymers into monomers at rate $\delta_\ell$ (disassembly). All binding rates appear with a factor of 2 because a monomer can attach to a polymer on its left or on its right end.

Note that there is a subtlety with the dimerization term $2\,\nu_1\, c_1^2$ in ***Equation A1b***: the dimerization term as well bears a factor of 2 because two identical monomers $A$ and $B$ can form a dimer in two possible ways, either as $AB$ or $BA$. Additionally, there is a stoichiometric factor of 2 for the monomers in this reaction. However, one factor of 2 is cancelled again because, assuming there are $n$ monomers, the number of ordered pairs of monomers that describe possible reaction partners is $\frac{1}{2}n(n-1)\approx n^2/2$ (if $n$ is large) rather than $n^2$ (the number of reaction partners when two different species react). This leaves us with a single factor of 2 like for all the other binding reactions.

***Equations A1c and A1d*** describe the dynamics of dimers and larger polymers of size $3 \leq \ell<L$, respectively. The terms account for reactions of polymers with active monomers (polymerization) as well as decay in the case of below-critical polymers (disassembly). The dimerization term in the equation for $\partial_t c_2$ lacks the factor of 2 because the stoichiometric

factor is missing for the dimers as compared with the dimerization term for the monomers in the line above. Finally, polymers of length $L$ – the complete ring structures – form an absorbing state and therefore only include a reactive gain term (***Equation A1e***).

## Heterogeneous structures

Next we consider systems with more than one particle species ($S>1$). The heterogeneous system can be described by dynamical equations equivalent to the homogeneous system. We show this starting from a full description that distinguishes both monomers and polymers into a set of different species $1,\ldots,S$. The species of a polymer is defined by the species of the respective monomer at its left end. As polymers assemble in consecutive order of species, a polymer is uniquely determined by its length and species (i.e. species of leftmost monomer). In that sense, $c_\ell^s$ with $0 \leq \ell<L$ and $1 \leq s \leq S$ denotes the concentration of a polymer of length $\ell$ and species $s$ ($c_0^s$ and $c_1^s$ again denote inactive and active monomers of species $s$, respectively). For example, $c_4^5$ denotes the concentration of polymers [5678] if $S \geq 8$, or of polymers [5612] if $S = 6$. Upper indices are always assumed to be taken modulo $S$ whenever they lie outside the range $[1, S]$. Therefore, the dynamics of the concentrations $c_\ell^s$ with $3 \leq \ell<L$ is given by

$$\frac{d}{dt}c_\ell^s = \nu_{\ell-1}\, c_{\ell-1}^s\, c_1^{\ell+s-1} + \nu_{\ell-1}\, c_{\ell-1}^{s+1}\, c_1^s - \nu_\ell\, c_\ell^s\, c_1^{s+\ell} - \nu_\ell\, c_\ell^s\, c_1^{s-1} - \delta\, c_\ell^s\, \mathbf{1}_{\{\ell<L_{\mathrm{nuc}}\}}\,. \tag{A2}$$

The terms on the right-hand side account for the influx due to binding of the respective polymers of length $\ell-1$ with a monomer either on the right or on the left (first and second term), and for the outflux due to reactions of a polymer of length $\ell$ and species $s$ with a monomer on the right or on the left (third and fourth term), as well as for decay into monomers for $\ell<L_{\mathrm{nuc}}$ (last term). For the dynamics of the dimers, however, there is only one gain term arising from dimerization:

$$\frac{d}{dt}c_2^s = \nu_1\, c_1^s\, c_1^{s+1} - \nu_2\, c_2^s\, c_1^{s+2} - \nu_2\, c_2^s\, c_1^{s-1} - \delta_2\, c_2^s\, \mathbf{1}_{\{2<L_{\mathrm{nuc}}\}}\,. \tag{A3}$$

Equivalently, for the active monomers we find:

$$\frac{d}{dt}c_1^s = \alpha\, C e^{-\alpha t} - c_1^s \sum_{\ell=1}^{L-1} \nu_\ell \left(c_\ell^{s+1} + c_\ell^{s-\ell}\right) + \sum_{\ell=2}^{L_{\mathrm{nuc}}-1} \sum_{k=s+1-\ell}^{k=s} \delta_\ell c_\ell^k\,.$$

Now we exploit the symmetry of the system with respect to the species index, that is, the upper index in $\{c_\ell^s\}$: Since all species in the system are equivalent, the dynamic equations are invariant under relabelling of the upper indices. Consequently, it must hold that:

$$c_\ell^s(t) = c_\ell^k(t), \qquad \text{for any s, k} \leq \text{S at any time t.} \tag{A5}$$

In other words, the upper index is irrelevant and can also be discarded. The variable $c_\ell$ then denotes the concentration of *any* one polymer species of length $\ell$. Taking advantage of this symmetry for the equations of the heterogeneous system, (***Equation A2***, ***Equation A3*** and ***Equation A4***), and collecting equal terms leads to a set of equations fully identical to those for the homogeneous system (***Equation A1***). We show the equivalence to the homogeneous model exemplarily for the dynamics of the polymers with size $\ell \geq 3$ in ***Equation A2***. Applying $c_\ell^s(t) = c_\ell(t)$ to ***Equation A2*** yields for the dynamics of the concentration of an arbitrary polymer species of size $\ell$:

$$\begin{aligned}\frac{d}{dt}c_\ell &= \nu_{\ell-1}\, c_{\ell-1}\, c_1 + \nu_{\ell-1}\, c_{\ell-1}\, c_1 - \nu_\ell\, c_\ell\, c_1 - \nu_\ell\, c_\ell\, c_1 - \delta\, c_\ell\, \mathbf{1}_{\{\ell<L_{\mathrm{nuc}}\}}\,. \\ &= 2\nu_{\ell-1}\, c_{\ell-1}\, c_1 - 2\nu_\ell\, c_\ell\, c_1 - \delta\, c_\ell\, \mathbf{1}_{\{\ell<L_{\mathrm{nuc}}\}},\end{aligned}$$

which is identical to the respective dynamic ***Equation A1d*** for the homogeneous model. The other equations for the heterogeneous system reduce to those for the homogeneous system in an analogous manner.

Summarizing, we have shown that the (deterministic) heterogeneous assembly process decouples into a set of $S$ identical and independent homogeneous processes. In particular, yield, which is given by the quotient of the number of completely assembled rings and the maximal possible number of complete rings, becomes independent of $S$:

$$\mathrm{yield(t)} = \frac{Sc_L(t)}{SNL^{-1}} = \frac{c_L(t)L}{N}. \tag{A6}$$

# Appendix 2

## Effective description of the evolution of the polymer size distribution as an advection-diffusion equation

The dynamical properties of the evolution of the polymer size distribution become evident if the set of ODEs, ***Equation 1,*** is rewritten as a partial differential equation. This approach was previously described in the context of virus capsid assembly (***Morozov et al., 2009***; ***Zlotnick et al., 1999***; ***Endres and Zlotnick, 2002***) but we will restate the essential steps here for the convenience of the reader. To this end we interpret the length index of the polymer $\ell \in \{2,3,\ldots,L\}$ as a continuous variable that we rename $x \in [2,L]$. With such a continuous description in view we write $c(x=\ell) := c_\ell$ to denote the concentration of polymers of size $\ell$.

Since the active monomers play a special role, we denote their concentration in the following by $A$. For simplicity we restrict our discussion to the case $L_{\rm nuc}=2$ and let $\nu_1=\mu$ and $\nu_{\ell\geq 2}=\nu$. Generalizations to $L_{\rm nuc}>2$ can be done in a similar way. Then, for the polymers with $\ell \geq 3$ we have:

$$\partial_t c(\ell) = 2\nu A\,[c(\ell-1)-c(\ell)]\,. \tag{A7}$$

Formally, expanding the right-hand side in a Taylor series up to second order

$$c(\ell-1) = c(\ell) - \partial_x c(\ell) + \frac{1}{2}\partial_x^2 c(\ell)\,, \tag{A8}$$

we arrive at an advection-diffusion equation with both advection and diffusion coefficients depending on the concentration of active monomers $A(t)$,

$$\partial_t c(x) = -2\nu A\,\partial_x c(x) + \nu A\,\partial_x^2 c(x)\,. \tag{A9}$$

***Equation A9*** can be written in the form of a continuity equation $\partial_t c(x) = -\partial_x J(x)$ with flux $J = 2\nu A\, c - \nu A\,\partial_x c$. The flux at the left boundary, $x=2$, equals the influx of polymers due to dimerization of free monomers, $J(2,t)=\mu A^2$. This enforces a Robin boundary condition at $x=2$,

$$2\nu A\, c(2,t) - \nu A\,\partial_x c(2,t) = \mu A^2\,. \tag{A10}$$

At $x=L$, we have an absorbing boundary $c(L,t)=0$ so that completed structures are removed from the system. Furthermore, the time evolution of the concentration of active particles is given by

$$\partial_t A = \alpha C e^{-\alpha t} - 2\mu A^2 - 2\nu A \int_2^L c(x,t)\,dx\,. \tag{A11}$$

The terms on the right-hand side account for activation of inactive particles, dimerization, and binding of active particles to polymers (polymerization).

Qualitatively, ***Equation A9*** describes a profile that emerges at $x=2$ from the boundary condition, ***Equation A10***, moves to the right with time dependent velocity $2\nu A(t)$ due to the advection term, and broadens with a time-dependent diffusion coefficient $\nu A(t)$. The concentration of active particles $A$ determines both the influx of dimers at $x=2$, as well as the speed and diffusion of the wave profile.

Next, we derive an expression that solves ***Equation A9***, assuming that we know $A(t)$. We start by solving ***Equation A9*** at the left boundary $c(2,t)$, and then translate the resulting expression to obtain a solution for $c(x,t)$. To obtain $c(2,t)$ in dependence of $a(t)$ we can solve $\frac{d}{dt}c(2,t) = \mu A^2 - 2\nu A c(2,t)$ (see ***Equation A1c***) by 'variation of the constants' as

$$c(2,t) = \int_0^t \mu A(\tilde{t})^2 \exp\left[-2\int_{\tilde{t}}^t \nu A(t')dt'\right] d\tilde{t}\,. \tag{A12}$$

With help of this expression we find $c(x,t)$: Given $c(2,t)$, the advective part of ***Equation A9***,

$$\partial_t \tilde{c}(x) = -2\nu A\,\partial_x \tilde{c}(x)\,. \tag{A13}$$

is solved by

$$c_{\mathrm{advec}}(x,t) = c(2,\tau(x,t))\,. \tag{A14}$$

Here, $\tau(x,t)$ denotes the time when a particle now at position $x$ and time $t$ was at $x=2$. In other words, a particle at time $t$ and position $x$ has entered the system at $x=2$ at time $\tau(x,t)$. This ansatz solves the PDE (***Equation A13***) if and only if $\tau(x,t)$ satisfies

$$\tau(x,t) = \tilde{A}^{-1}\left(\tilde{A}(t) - \frac{x-2}{2\nu}\right) \tag{A15}$$

with $\tilde{A}$ being an arbitrary integral of $A$ such that $\partial_t \tilde{A}(t) = A(t)$ and $\tilde{A}^{-1}$ denoting its inverse. More easily, we find this form of $\tau$ by requiring that the integral over the velocity from time $\tau$ to $t$ equals the travelled distance $x-2$:

$$\int_\tau^t 2\nu\, A(t')dt' = x-2\,. \tag{A16}$$

To include the diffusive contribution in ***Equation A13***, we use the diffusion kernel,

$$k(x,y,t) = \left(4\pi\int_{\tau(y,t)}^t D(t)\right)^{-1/2} \exp\left(\frac{-x^2}{4\int_{\tau(y,t)}^t D(t)}\right), \tag{A17}$$

with the time dependent diffusion constant $D(t) = \nu A(t)$. The kernel $k(x,y,t)$ accounts for the mass that has been diffusively transported from $y$ over a distance of $x$. Because the mass has entered the system at $x=2$ at time $\tau(y,t)$, it diffused for the time $t-\tau(y,t)$. The complete expression for $c(x,t)$ is then obtained as the convolution of $c_{\mathrm{advec}}(x,t)$ (***Equation A14***), that is obtained from ***Equation A12*** and ***Equation A15***, and the diffusion kernel $k(x,y,t)$ (***Equation A17***):

$$c(x,t) = \int c_{\mathrm{advec}}(s,t)k(x-s,s,t)ds = \int c(2,\tau(s,t))k(x-s,s,t)ds\,. \tag{A18}$$

Interpreting the terms in the equations and the general form of the solution, we are able to understand the qualitative behavior of the system. If both the activation and the dimerization rate are large, the system produces zero yield: both advection and diffusion are driven by the concentration of active monomers $A$. If activation is fast, the concentration of active monomers $A$ will become large initially since activation is faster than the reaction dynamics. Consequently, provided $\mu \sim \nu$, dimerization dominates over binding because it depends quadratically on $A$, see ***Equation A11***. The reservoir of free particles then depletes quickly and cannot sustain the motion of the wave for long enough to reach the absorbing boundary, resulting in a very low yield. Only if either the activation rate is low enough or if $\mu \ll \nu$, the motion of the wave can be sustained until it reaches the absorbing boundary.

# Appendix 3

## Threshold values for the activation and dimerization rate

Based on the analysis from the previous section, we will now determine the threshold activation rate and threshold dimerization rate which mark the onset of non-zero yield. Yield production starts as soon as the density wave reaches the absorbing boundary at $x = L$. Therefore, finite yield is obtained if and only if the sum of the advectively travelled distance $d_{\mathrm{adv}}$ and the diffusively travelled distance $d_{\mathrm{diff}}$ exceeds the system size $L - 2$:

$$d_{\mathrm{adv}} + d_{\mathrm{diff}} \geq L - 2\,. \tag{A19}$$

The condition for the onset of non-zero yield is obtained by assuming equality in this relation. The advectively travelled distance is obtained from ***Equation A16*** by setting the borders of the integral over the velocity to $\tau = 0$ and $t = \infty$:

$$d_{\mathrm{adv}} = \int_0^\infty 2\nu A(t')dt'. \tag{A20}$$

The diffusively travelled distance is approximately given by the standard deviation of the Gaussian diffusion kernel, ***Equation A17***, again with $\tau = 0$ and $t = \infty$,

$$d_{\mathrm{diff}} = \sqrt{2\nu \int_0^\infty A(t)dt}. \tag{A21}$$

Taken together, we obtain a condition for the onset of finite yield:

$$2\nu \int_0^\infty A(t)dt + \sqrt{2\nu \int_0^\infty A(t)dt} = L - 2\,. \tag{A22}$$

Substituting $y = \sqrt{2\nu \int A}$ and requiring that $y$ is positive, we solve the quadratic equation and find that ***Equation A22*** is equivalent to

$$2\nu \int_0^\infty A(t)dt = y^2 = \frac{1}{4}\left(\sqrt{1 + 4(L-2)} - 1\right)^2 \approx L - \sqrt{L}, \tag{A23}$$

where the last approximation is valid for large $L$.

We determine the threshold values for the activation rate $\alpha$ and the dimerization rate $\mu$ by finding solutions of the dynamical equation for the active particles $A(t)$, ***Equation A11***, such that the condition, ***Equation A23***, is fulfilled. Thus, we start by deriving the dependence of $\int_0^\infty A(t)dt$ on $\alpha$ and $\mu$.

The concentration $c(x,t)$ appears in ***Equation A11*** only in terms of an integral $\int_2^L c(x,t)\,dx$, counting the total number of polymers in the system. As long as yield is zero there is no outflux of polymers at the absorbing boundary $x = L$ and the total number of polymers in the system only increases due to the influx at the left boundary $x = 2$. As long as yield is zero we can therefore equivalently consider the limit $L \to \infty$. We denote the total number of polymers in ***Equation A11*** by $B(t) := \int c(x,t)\,dx$ for which the dynamics is determined from the boundary condition, ***Equation A10***:

$$\frac{d}{dt}B = \int_2^\infty \partial_t c(x,t)\,dx = \int_2^\infty -\partial_x J(x,t)\,dx = -\underbrace{J(\infty,t)}_{=0} + J(2,t) = \mu A(t)^2. \tag{A24}$$

Hence, as long as yield is zero, the total number of polymers increases with the rate of the

dimerization events. The system then simplifies to a set of two coupled ordinary differential equations for $A$ and $B$:

$$\frac{d}{dt}A = \alpha C e^{-\alpha t} - 2\mu A^2 - 2\nu A B \tag{A25a}$$

$$\frac{d}{dt}B = \mu A^2. \tag{A25b}$$

The dynamics of $A$ and $B$ is equivalent to a two-state activator-inhibitor system, where $A$ dimerizes into $B$ at rate $\mu$, and $B$ degrades (inhibits) $A$ at rate $2\nu$. Note that ***Equation A25*** describes the exact dynamics of the active monomers $A$ and total number of polymers $B$ in the deterministic system as long as yield is zero. The system has therefore been greatly reduced from originally $SN$ coupled ODEs to now only two coupled ODEs.

For the further analysis it is useful to non-dimensionalize ***Equation A25*** by measuring $A$ and $B$ in units of the initial concentration of inactive monomers $C$ and time in units of $(\nu C)^{-1}$:

$$\frac{d}{dt}A = \omega e^{-\omega t} - 2\eta A^2 - 2A B, \tag{A26a}$$

$$\frac{d}{dt}B = \eta A^2, \tag{A26b}$$

with the remaining dimensionless parameters $\omega = \frac{\alpha}{\nu C}$ and $\eta = \frac{\mu}{\nu}$. We are interested in the integral over $A(t)$ as a function of $\omega$ and $\eta$,

$$\int_0^\infty A_{\omega,\eta}(t)dt := g(\omega,\eta)\,, \tag{A27}$$

which relates to the totally travelled distance of the wave. Note that, in case of zero yield, $2g(\omega,\eta)$ is the total advectively travelled distance of the wave (cf. ***Equation A20***) and the square of the diffusively travelled distance (cf. ***Equation A21***).

## Analysis of the dimerization scenario

The dimerization scenario is characterized by fast activation $\alpha \gg C\nu$ and slow dimerization $\mu \ll \nu$. For the dimensionless parameters these assumptions translate to $\eta \ll 1$ and $\eta \ll \omega$. Because for small $\eta \ll 1$ nucleation is much slower than growth we neglect the dimerization term in ***Equation A26a*** against the growth term. Furthermore, because $\eta \ll \omega$ activation happens on a fast time scale compared with nucleation and we may therefore integrate out the fast time scale assuming that all particles are activated instantaneously at the beginning. The system ***Equation A26*** then reduces to

$$\frac{d}{dt}A = -2A B, \tag{A28a}$$

$$\frac{d}{dt}B = \eta A^2, \tag{A28b}$$

with the initial condition $A(0) = 1$ and $B(0) = 0$. We divide the first equation by the second one (formally applying the chain rule and the inverse function theorem) to obtain a single equation for the dynamics of $A(B)$:

$$\frac{dA}{dB} = -\frac{2}{\eta}\frac{B}{A}\,, \tag{A29}$$

where $A(B{=}0) = 1$. This first order ODE can be solved by separation of variables and subsequent integration, yielding

$$A(B) = \sqrt{1 - \frac{2}{\eta}B^2}\,. \tag{A30}$$

Because the number of active monomers $A(t)$ must vanish for $t \to \infty$, the final value of $B$ is

$$B_\infty := B(t{=}\infty) = \sqrt{\frac{\eta}{2}}. \tag{A31}$$

Thereby, we calculate the function $g(\eta)$ via variable substitution $dt = \frac{dB}{\eta A^2}$:

$$g(\eta) = \int_0^\infty A(t)dt = \int_0^{B_\infty} A(B)\frac{dB}{\eta A(B)^2} = \frac{1}{\eta}\int_0^{B_\infty} \frac{dB}{\sqrt{1 - \frac{2}{\eta}B^2}} = \frac{\pi}{2\sqrt{2}}\,\eta^{-\frac{1}{2}}\,. \tag{A32}$$

So, the dependence of the travelled distance of the wave on $\eta$ obeys a power law with exponent $-\frac{1}{2}$, confirming the previous result (***Morozov et al., 2009***). For the coefficient we find $\frac{\pi}{2\sqrt{2}} \approx 1.1107$.

Additionally, we can determine the time dependent solutions $A(t)$ and $B(t)$. Using the solution for $A(B)$ from ***Equation A30*** in ***Equation A28b*** we obtain $B(t)$ as

$$B(t) = \sqrt{\frac{\eta}{2}}\tanh\left(\sqrt{2\eta}t\right). \tag{A33}$$

We use this expression for $B(t)$ in ***Equation A28a*** to obtain $A(t)$. The resulting ODEs can again be solved by separation of variables as

$$A(t) = \frac{1}{\cosh\left(\sqrt{2\eta}t\right)}. \tag{A34}$$

## Analysis of the activation scenario

In the activation scenario, $\alpha \ll C\nu$, such that $\omega \ll 1$ and $\omega \ll \eta$. As we know already that decreasing $\omega$ will slow down nucleation relative to growth we can again neglect the dimerization term in ***Equation A26a***. In contrast to the dimerization scenario, however, we have to keep the activation term. Transforming time via $\tau := 1 - e^{-\omega t}$ such that $\tau \in [0, 1]$ and writing $a(\tau) = a(1 - e^{-\omega t}) := A(t)$ and $b(\tau) = b(1 - e^{-\omega t}) := B(t)$ the system in ***Equation A26*** becomes:

$$\frac{d}{d\tau}a = 1 - \frac{2}{\omega(1-\tau)}ab, \tag{A35a}$$

$$\frac{d}{d\tau}b = \frac{\eta}{\omega(1-\tau)}a^2, \tag{A35b}$$

with the initial condition $a(0) = b(0) = 0$. The function $g(\omega, \eta)$ transforms as

$$g(\omega, \eta) = \int_0^\infty A(t)dt = \frac{1}{\omega}\int_0^1 \frac{a(\tau)}{1-\tau}d\tau. \tag{A36}$$

In the following we derive the asymptotic solution for $a(\tau)$ in the limit of small $\omega$ in order to evaluate the integral in ***Equation A36***. In the limit $\tau \to 1$ ($\Leftrightarrow t \to \infty$) both $a(\tau)$ and $\frac{d}{d\tau}a(\tau)$ will become small whereas $b(\tau)$ increases monotonically. The reaction term in ***Equation A35a*** is furthermore weighted by a factor $\frac{1}{\omega}$ which will become large if $\omega \ll 1$. We therefore postulate that for sufficiently large $\tau$ the derivative $\frac{d}{d\tau}a(\tau)$ is much smaller than the two terms on the right-hand side of ***Equation A35a*** and hence negligible. This assumption has to be justified a

posteriori with the obtained solution. Neglecting the derivative term $\frac{d}{d\tau}a$ in (***Equation A35a***) reduces the equation to an algebraic equation and we find

$$a = \frac{\omega(1-\tau)}{2b}. \tag{A37}$$

Using this result in ***Equation A35b*** we can solve for $b$ by separation of variables and subsequent integration:

$$b(\tau) = (\omega\eta)^{\frac{1}{3}} \cdot \left(\frac{3}{4}\tau - \frac{3}{8}\tau^2\right)^{\frac{1}{3}}. \tag{A38}$$

From ***Equation A37*** we immediately obtain $a(\tau)$:

$$a(\tau) = \frac{\omega^{\frac{2}{3}}}{\eta^{\frac{1}{3}}} \cdot \frac{1-\tau}{(6\tau - 3\tau^2)^{\frac{1}{3}}} := \frac{\omega^{\frac{2}{3}}}{\eta^{\frac{1}{3}}} h(\tau)\,, \tag{A39}$$

where by $h(\tau)$ we denote the part of the solution that depends only on $\tau$. Hence, we find that $a$ and hence also $\frac{d}{d\tau}a$ scale like $\sim\omega^{\frac{2}{3}}$, and will thus become small if $\omega \ll 1$ and $\tau$ is large enough. Therefore the solution is consistent and justifies the approximation in which we neglected the derivative term in the limit of small $\omega$ and sufficiently large $\tau$.
Note that consistency of the solution with the approximation is a sufficient criterion for the validity of the approximation: We can solve the system for $A$ and $B$ in ***Equation A35*** iteratively by defining

$$\frac{d}{d\tau}a_{i-1} = 1 - \frac{2}{\omega(1-\tau)}a_i b_i,$$

$$\frac{d}{d\tau}b_i = \frac{\eta}{\omega(1-\tau)}a_i^2.$$

Assuming that for $i \to \infty$, $a_i$ and $b_i$ converge to the correct solutions $a(\tau)$ and $b(\tau)$ when starting with $a_0 = 0$, we obtain $a_1$ and $b_1$ as given by ***Equation A39*** and ***Equation A38*** and can iteratively refine the approximation. The next iteration step then reads: $\frac{d}{d\tau}a_1 = 1 - \frac{2}{\omega(1-\tau)}a_2 b_2$. As $a_1 \sim \omega^{\frac{2}{3}}$ we know that the left-hand side will be small and $a_1$ and $b_1$ solve the system if the left-hand side equals 0. Writing $a_2 = a_1 + \tilde{a}_2$ and $b_2 = b_1 + \tilde{b}_2$ this gives:

$$\frac{d}{d\tau}a_1 = 1 - \frac{2}{\omega(1-\tau)}(a_1+\tilde{a}_2)(b_1+\tilde{b}_2) \approx \frac{-2}{\omega(1-\tau)}(a_1\tilde{b}_2 + b_1\tilde{a}_2)\,. \tag{A40}$$

From dimensional analysis it follows that the correction terms $\tilde{a}_2$ and $\tilde{b}_2$ must scale like $\tilde{a}_2 \sim \omega^{\frac{4}{3}}$ and $\tilde{b}_2 \sim \omega$ and are hence much smaller than the first order approximations $a_1$ and $b_1$. Higher order corrections will give even smaller contributions showing that if $\frac{d}{d\tau}a_1 \ll 1$, $a_1$ is indeed a very good approximation.

In the limit $\tau \to 0$, however, the expression for $a(\tau)$ in ***Equation A39*** diverges and consistency is violated. Hence, the obtained solution is valid only for sufficiently large $\tau$.

We fix some small $\epsilon > 0$ such that the approximation can be assumed to be sufficiently good if $\frac{d}{dt}a < \epsilon$. Furthermore, we define $\tau_\epsilon$ such that $\frac{d}{d\tau}a < \epsilon$ for all $\tau > \tau_\epsilon$. Using ***Equation A39*** we can write this as $\frac{d}{d\tau}h < \epsilon\eta^{\frac{1}{3}}/\omega^{\frac{2}{3}}$ for all $\tau > \tau_\epsilon$, where the left-hand side, $\frac{d}{d\tau}h$, depends only on $\tau$. Hence, by decreasing $\omega$ we can make $\tau_\epsilon$ arbitrarily small: $\lim_{\omega\to 0}\tau_\epsilon = 0$. In order to calculate $g(\omega,\eta)$ the integral in ***Equation A36*** can be separated in a domain where the approximation $a(\tau)$ is accurate and a domain where the correct solution $\tilde{a}(\tau)$ deviates strongly from $a(\tau)$:

$$g(\omega,\eta)=\frac{1}{\omega}\int_0^{\tau_\epsilon}\frac{\tilde{a}(\tau)}{1-\tau}d\tau+\frac{1}{\omega}\int_{\tau_\epsilon}^{1}\frac{a(\tau)}{1-\tau}d\tau. \tag{A41}$$

We see from ***Equation A35a*** that $\frac{d}{d\tau}\tilde{a}=1$ describes an upper bound to $\tilde{a}$ showing that $\tilde{a}(\tau)\leq\tau$. Therefore we can bound the contribution of the first integral as $\int_0^{\tau_\epsilon}\frac{\tilde{a}(\tau)}{1-\tau}d\tau\leq\int_0^{\tau_\epsilon}\frac{\tau}{1-\tau_\epsilon}d\tau=\frac{1}{2}\frac{\tau_\epsilon^2}{1-\tau_\epsilon}$. Because this upper bound for the integral goes to 0 if $\omega$ and hence $\tau_\epsilon$ become small the first integral will become negligible against the second one. Asymptotically, we therefore only need to consider the second integral with the solution for $a(\tau)$ as given by ***Equation A39***:

$$\begin{aligned}g(\omega,\eta)\;&=(\omega\eta)^{-\frac{1}{3}}\int_0^1(6\tau-3\tau^2)^{-\frac{1}{3}}d\tau=(\omega\eta)^{-\frac{1}{3}}\int_0^3\frac{dz}{6z^{\frac{1}{3}}\sqrt{1-\frac{z}{3}}}=\\&=\frac{3^{\frac{2}{3}}\sqrt{\pi}\,\Gamma(\frac{2}{3})}{6\,\Gamma(\frac{7}{6})}(\omega\eta)^{-\frac{1}{3}}\approx0.8969\cdot(\omega\eta)^{-\frac{1}{3}},\end{aligned} \tag{A42}$$

where we used the substitution $\tau=1-\sqrt{1-z/3}$ and $\Gamma(x)$ is the (Euler) Gamma function. So, in the limit of small $\omega$, $g$ scales with $\omega$ and $\eta$ with identical exponent $-\frac{1}{3}$. This contrasts the dimerization scenario where $g$ as well as $A$ and $B$ depend only on $\eta$ and are independent of $\omega$ (cf. ***Equation A32, A33 and A34***).

## Numerical analysis and the threshold values for the rate constants

In order to confirm the results of the last two paragraphs and to see how $g(\omega,\eta)$ behaves in the intermediate regime where $\omega$ and $\eta$ are of the same order of magnitude we also investigate the function $g(\omega,\eta)$ numerically. For that purpose we numerically integrate the ODE-system for $A(t)$ and $B(t)$ in ***Equation A26*** for different values of $\omega$ and $\eta$ with a semi-implicit method. Subsequently, we integrate the solution $A(t)$ using an adaptive recursive Simpson's rule. Plotting $g$ in dependence of $\omega$ for fixed $\eta$ on a double-logarithmic scale reveals a rather simple bipartite form of $g$, see ***Appendix 3—figure 1a***:

$$g(\omega,\eta)=\begin{cases}g_1(\eta)\omega^{-\frac{1}{3}} & \omega\ll 1\\ g_2(\eta) & \omega\gg 1.\end{cases} \tag{A43}$$

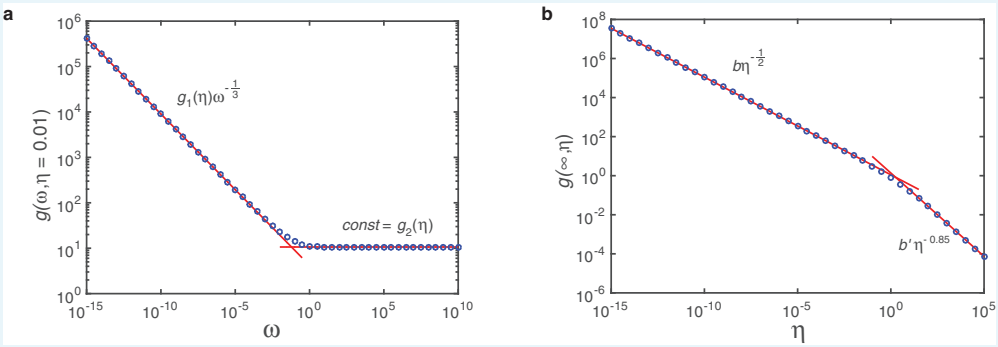


**Appendix 3—figure 1.** Fit of $g(\omega,\eta)$ on log-log scale. The function $g(\omega,\eta)=\int_0^\infty A_{\omega,\eta}(t)dt$ describes (half) the travelled distance of the profile of the polymer size distribution in dependence of $\omega=\frac{\alpha}{\nu C}$ and $\eta=\frac{\mu}{\nu}$. Marker points show solutions for $g(\omega,\eta)$ as obtained numerically from integration of ***Equation A26***. Red lines are linear fits on log-log scale. In (**a**) we plot $g(\omega,\eta)$ for fixed $\eta$ (here exemplarily for $\eta=0.01$) over 25 orders of magnitude in $\omega$ and find a markedly bipartite behavior: For small $\omega$ the dependence on $\omega$ is perfectly matched by a

power law with exponent $-\frac{1}{3}$ and $\eta$-dependent coefficient $g_1(\eta)$, whereas for large $\omega$ it is a constant $g_2(\eta)$. (**b**) Plotting $g_2(\eta)=g(\omega=\infty,\eta)$ in dependence of $\eta$ reveals again strictly bipartite behavior. Here, however, only the branch for small $\eta\leq 1$ is relevant. With the coefficient $g_1(\eta)$ that can be determined in a similar way this leads to the final form of $g(\omega,\eta)$ as given by ***Equation A46***.

The transition between these two regimes is rather sharp so that $g$ is best described in a piecewise fashion

$$g(\omega,\eta)=\max\left(g_1(\eta)\omega^{-\frac{1}{3}},g_2(\eta)\right). \tag{A44}$$

Next, we plot the coefficients $g_1(\eta)$ and $g_2(\eta)$ against $\eta$. Here we find that $g_1(\eta)=a\eta^{-\frac{1}{3}}$ with $a=\text{const}\approx 0.90$ and $g_2(\eta)$ is again bipartite with a sharp kink in between (***Appendix 3—figure 1b***):

$$g_2(\eta)=\min\left(b\eta^{-\frac{1}{2}},b'\eta^{-0.85}\right), \tag{A45}$$

where $b\approx 1.11$ and $b'\approx 1.37$. The transition between both regimes is at $\eta\approx 1.82$. The second regime is not relevant for self-assembly since it refers to both large $\omega$ and large $\eta$, hence the travelled distance $2g$ is too small to give finite yield in this regime. Therefore, we discard the second regime and obtain as final result

$$g(\omega,\eta)=\max\left(a(\eta\omega)^{-\frac{1}{3}},b\eta^{-\frac{1}{2}}\right), \tag{A46}$$

with $a\approx 0.90$ and $b\approx 1.11$. This confirms perfectly the exponents as well as the coefficients found in the last two paragraphs. It is, however, surprising that there is such a sharp transition between both regimes, which allows to define $g(\omega,\eta)$ in a piecewise fashion. This behavior must be the result of a series of lower oder terms in $g(\omega,\eta)$ which are unimportant in the limits $\omega\ll\eta$ and $\eta\ll\omega$ but cause the sharp transition when $\omega$ and $\eta$ are of the same order of magnitude.

Finally, we return to our original task of finding the threshold values of the activation and dimerization rate for the onset of yield. Using our result for $g(\omega,\eta)$ in ***Equation A23*** we find as necessary and sufficient condition to obtain finite yield in the deterministic system:

$$2\max\left(a(\eta\omega)^{-\frac{1}{3}},b\eta^{-\frac{1}{2}}\right)\geq L-\sqrt{L}. \tag{A47}$$

Alternatively, we can state this result as two separate conditions out of which at least one must be fulfilled to obtain finite yield:

$$2a(\eta\omega)^{-\frac{1}{3}}\geq L-\sqrt{L}\Rightarrow \quad \alpha<\alpha_{\text{th}}:=P_\alpha\frac{\nu}{\mu}\frac{\nu C}{(L-\sqrt{L})^3} \tag{A48}$$

$$\text{or}\quad 2b\eta^{-\frac{1}{2}}\geq L-\sqrt{L}\Rightarrow \quad \mu<\mu_{\text{th}}:=P_\mu\frac{\nu}{(L-\sqrt{L})^2} \tag{A49}$$

where $P_\alpha=8a^3\approx 5.77$ and $P_\mu=4b^2\approx 4.93$. This verifies ***Equation 1*** in the main text.

# Appendix 4

## Impact of the implementation of sub-nucleation reactions

In the main text we focused our discussion on irreversible binding $L_{nuc} = 2$. In this section we investigate the effect of different implementations of the sub-nucleation reactions.

In general, perfect yield is trivially achieved if the complete ring is the only stable structure. However, yield can be maximal already for smaller nucleation sizes $L_{nuc}$ depending on the explicit decay rate $\delta$. In the deterministic limit without the dimerization and activation mechanisms ($\mu = \nu$, $\alpha \to \infty$ ) a rapid transition from zero yield to perfect yield occurs in dependence of the critical nucleation size (see ***Appendix 4—figure 1***). The threshold value in this case is approximately half the ring size and is weakly affected by the decay rate $\delta$. In order to obtain finite yield for small nucleation sizes, an extremely high decay rate would be necessary. Hence, maximizing the yield solely by increasing the nucleation size is not very feasible.

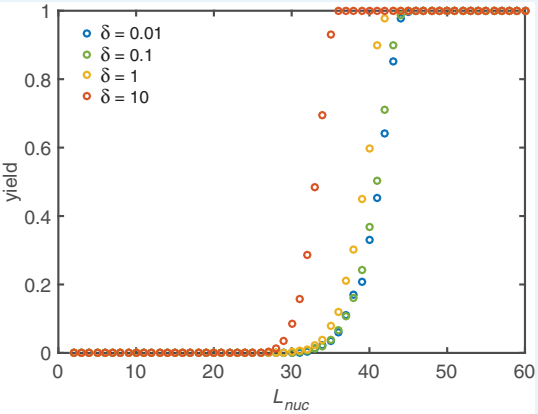


**Appendix 4—figure 1.** Yield maximization due to increased nucleation size. Without activation and dimerization mechanism $(\alpha \to \infty, \mu = \nu)$ the yield can still be optimized by increasing the critical nucleation size $L_{nuc}$. However, a significant improvement is only achieved for critical sizes larger than half the ring size. Above, a rapid transition to perfect yield takes place. Below no effect is observed at all. Increasing $\delta$ shifts the onset of yield to slightly smaller critical nucleation sizes. Other parameters: $L = 60$, $N = 10000$.

In our model, the subcritical reaction rates $\mu_i$ may take different values. Here, we want to restrict our discussion to two scenarios. First, all rates have an identical value $\mu_i = \mu$ and second, the rates increase linearly up to the super-nucleation reaction rate: $\mu_i = \mu + (\nu - \mu)\frac{i-1}{L_{nuc}-1}$.

In the deterministic limit, both implementations show the same qualitative behavior as the dimerization mechanism with $L_{nuc} = 2$ in the main text (see ***Appendix 4—figure 2***). The only relevant aspect for the final yield is the extend to which nucleation is slowed down in total. In the constant scenario all reaction steps contribute equally. As a results there is a strong dependence on the number of such reaction steps, that is on the critical nucleation size. If however, the reaction rates increase linearly with the size of the polymers, the dimerzation rate dominates. Only in the case $\mu \ll \nu$ finite yield is observed at all. In this limit the dimerization rate is much smaller than the subsequent growth rates. The explicit form of the different $\mu_i$ is not of major importance for the yield. The total slowdown of nucleation is the central feature. Structure decay does not play any role for intermediate nucleation sizes.

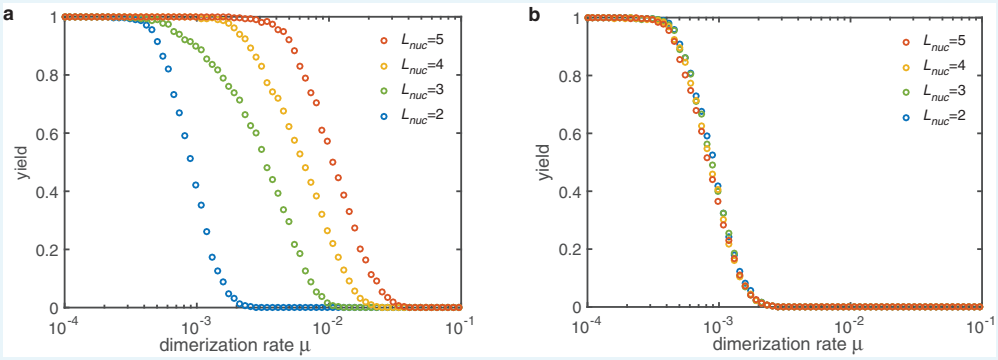


**Appendix 4—figure 2.** Yield for the dimerization mechanism ($\alpha \to \infty$) with different nucleation sizes (colors). (**a**) If all sub-nucleation growth rates are identical ($\mu_i = \mu$) increasing the nucleation size increases the threshold value $\mu_{th}$. The slow down of nucleation due to the individual sub-nucleation steps in total determines the yield. (**b**) If the sub-nucleation growth rates increase linearly $\left(\mu_i = \mu + (\nu - \mu)\frac{i-1}{L_{nuc}-1}\right)$ no dependence on the nucleation size is observed. The dimerization rate $\mu_1 = \mu$ (which is the most limiting step) dominates entirely. Other parameters: $L = 60$, $N = 10000$, $\delta = 1$.

The last question we want to address is how the combination of activation and dimerization mechanism and the corresponding non-monotonic behavior is affected by the nucleation size. Again, we compare constant sub-nucleation growth with a linearly increasing growth rate (see ***Appendix 4—figure 3***). In the deterministic regime both implementations behave qualitatively similar as the dimerization mechanism discussed in the main text. However, in both cases the stochastic yield catastrophe is less pronounced. For the constant growth rates a saturation of the maximal yield is observed for sufficiently low $\mu$. If the profile is linear this effect is weaker as compared to the constant case and a dependency on the explicit value of $\mu$ is still observed. The saturation value is not reached for these reactions rates.

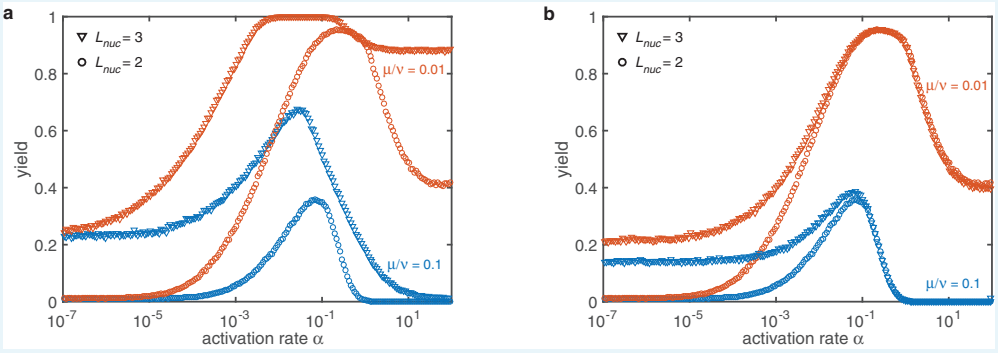


**Appendix 4—figure 3.** Combined mechanisms for different nucleation sizes (symbols) and dimerization rates (color). (**a**) If the sub-nucleation growth rates are identical ($\mu_i = \mu$) the stochastic yield catastrophe is weakened but still has a drastic impact. The qualitative behavior remains unchanged. (**b**) For a linearly increasing sub-nucleation growth rate $\left(\mu_i = \mu + (\nu - \mu)\frac{i-1}{L_{nuc}-1}\right)$ in the deterministic regime no changes are observed at all. The effect of the stochastic yield catastrophe is less pronounced. This improvement is mainly caused by structure decay which mitigates stochastic fluctuations. However, a slight dependency of the saturation value on the rate $\mu$ is observed. Other parameters: $L = 60$, $S = L$, $N = 100$, $\delta = 0.1$.

Taking all our results for the sub-nucleation behavior together we draw the following conclusions: First, structure decay by itself it not very efficient in order to maximize yield. Second, the explicit choice of the sub-nucleation rates is of minor importance for the

qualitative behavior. The system behaves similarly to the case $L_{nuc} = 2$. Third, larger nucleation sizes mitigate the stochastic yield catastrophe in general.

# Appendix 5

## Time evolution of the yield in the activation and dimerization scenario

In the main text we focus on the final yield, which represents the maximal yield that can be obtained in the assembly reaction for $t \to \infty$. Here, we briefly discuss the temporal evolution of the yield in the two scenarios. ***Appendix 5—figure 1*** shows the yield as a function of time for the dimerization scenario (blue) and the activation scenario (red) for the corresponding parameters indicated in the plot. Drawn lines show the evolution of the yield in the stochastic simulation whereas dashed lines represent its deterministic evolution obtained by integrating the corresponding mean-field rate equations (only shown for the activation scenario). In both scenarios, yield production sets in after a short lag time (***Hagan and Elrad, 2010***). The emergence of a lag time can be understood in terms of the interpretation of the assembly process as the progression of a travelling wave (see Sec. B). The travelling wave thereby describes the polymer size distribution and the time that is needed for the wave to reach the absorbing boundary equals the lag time for yield production observed in ***Appendix 5—figure 1***. After the lag time, the yield increases very abruptly in the dimerization scenario and a bit more continually in the activation scenario. Since monomers are provided gradually in the activation scenario, the emerging wave is flatter and extends over a larger range (in polymer size space) as compared to the dimerization scenario. Consequently, yield production is more gradual in the activation scenario than in the dimerization scenario. For the same reason, the dimerization scenario is generally 'faster' or more time efficient than the activation scenario. For a detailed analysis of the time efficiency of these and other self-assembly scenarios we refer the reader to our manuscript in preparation (Gartner, Graf and Frey, in preparation).

In all depicted situations, the yield increases monotonically with time. This is, of course, generally true since the completed ring structures define an absorbing state in our system. The final yield, which is indicated in the right bar, therefore represents the upper limit for the yield that can be achieved in the assembly reaction. ***Appendix 5—figure 1*** shows that the temporal yield curves initially are rather steep and quickly reach a value that lies within 10% of the final yield ('quickly' thereby refers to the respective time scale), before the curves flatten and increase more slowly. This underlines that the final yield is a meaningful observable that not only describes the upper limit for the yield but also approximates the typical yield of the assembly reaction under appropriate time constraints that are not too restrictive (on the time scale set by the respective lag time).

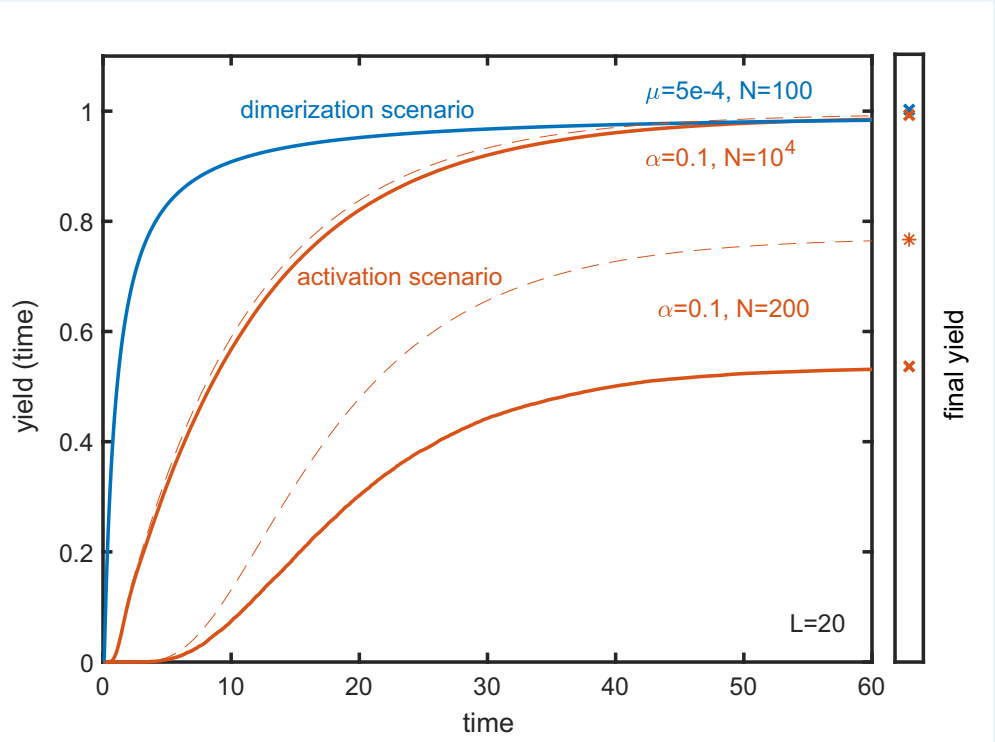


**Appendix 5—figure 1.** Time evolution of the yield in the activation and dimerization scenario. The time dependence of the yield is depicted for a dimerization scenario (blue) with $\mu = 5 \times 10^{-4}$ and $N = 100$ and for two activation scenarios (red) with $\alpha = 0.1$ and $N = 2 \times 10^2$ and $N = 10^4$, respectively, for target structures of size $L = 20$. Drawn lines show the time evolution of the stochastic systems while dashed lines describe the time evolution in the corresponding deterministic systems (where the final yield may be higher in the activation scenario). In all cases the yield increases monotonically with time. The final yield, that is indicated in the right bar, represents the upper limit of the yield at any time. Yield production in the activation scenario is generally more gradual than in the dimerization scenario. Therefore, the dimerization scenario is, in general, more time efficient than the activation scenario.

# Appendix 6

## Standard deviation of the yield

In the main text, the analysis focuses on the average yield. A priori it is, however, not apparent that this average quantity is informative, in particular due to the strong effect of stochasticity in the system. Here, we thus take a step forward to complement this picture by additionally considering a simple measure for the fluctuations of the yield, its standard deviation. ***Appendix 6—figure 1*** is an extension of ***Figure 3a*** in the main text, showing the dependence of the average yield and its sample standard deviation on the activation rate. Since yield is always positive, the standard deviation of the yield has to be small if the average yield is close to 0 ($N = 500$ in ***Appendix 6—figure 1***). The same holds true for average yield close to 1 as the yield is bounded by one from above ($N = 5000$ in ***Appendix 6—figure 1***). For intermediate values of the average yield, the standard deviation is highest but still small compared to the average yield ($N = 1000$ in ***Appendix 6—figure 1***). The average yield is, thus, meaningful. Naturally the ratio of the standard deviation compared to the average yield also depends on the number of particles per species $N$ and on the number of species $S$. Generally speaking, for higher $N$ and $S$, this ratio decreases (see ***Appendix 7—figure 1*** for the dependency on $S$).

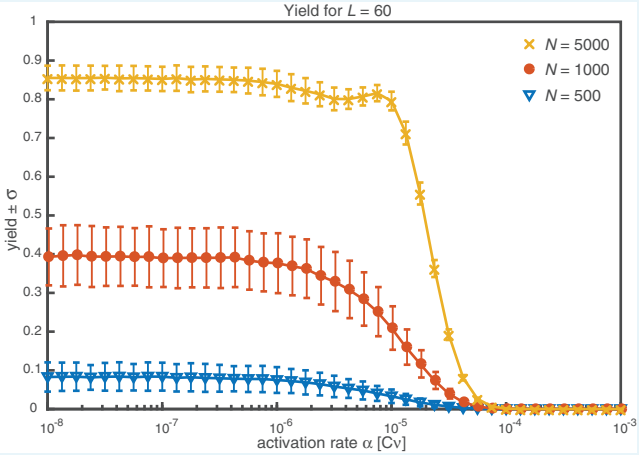


**Appendix 6—figure 1.** Average yield and its sample standard deviation. For average yield close to 0 or close to 1, the standard deviation has to be small due to the boundedness of the yield to the interval [0, 1]. For intermediate values, the standard deviation is highest. Its value is, however, still considerably smaller than the average yield. The parameters are $L = 60$, $S = L$, $\mu = \nu = 1$ and different particle numbers $N$ (colors/symbols). To obtain the average yield, the yield has been averaged over 1000 simulations. The standard deviation corresponds to the unbiased sample standard deviation.

# Appendix 7

## Influence of the heterogeneity of the target structure for fixed number of particles per species

***Figure 3d*** in the main text shows how the maximal yield $y_{\max}$ depends on the number of species $S$ if the ring size $L$ and the number of possible ring structures $NS/L$ is fixed. This comparison for fixed $NS$ is motivated by the question which role the heterogeneity of a structure plays for assembly efficiency if a certain number of structures should be realized. ***Figure 3d*** illustrates that a higher number of species $S$ (more heterogeneous structures) leads to a lower maximally possible yield, suggesting that it is beneficial to build structures with as few different species as possible. However, this situation does not correspond to the deterministically equivalent case of fixed number of particles per species $N$ (note, though, that in the deterministic case the maximally possible yield is always 1, namely for $\alpha \to 0$). Instead, for higher number of species $S$, the number of particles per species $N \propto 1/S$ decreases. How does the heterogeneity of the structures $S$ alter the maximally possible yield if $L$ and $N$ (instead of $L$ and $NS$) are fixed? ***Appendix 7—figure 1*** shows how the maximal yield $y_{\max}$ and its standard deviation (obtained as average yield and sample standard deviation for $\alpha = 10^{-8}$ when the yield has well saturated and the dynamics (except for the timescale) get independent of the exact value of the rate-limiting activation rate) depend on the number of species $S$. For homogeneous structures $S = 1$ yield is always perfect since in this case there can be no fluctuations between species. As a result, the average yield is 1 and the standard deviation is 0. For increasing $S$, the average yield decreases until it levels off for $S \gg 1$. This behavior indicates that indeed the decreasing number of particles per species $N$ for larger $S$ is essential for the decrease of the maximal yield with $S$ in ***Figure 3d***. As mentioned above, the standard deviation is largest for small $S$>1 and decreases with $S$.

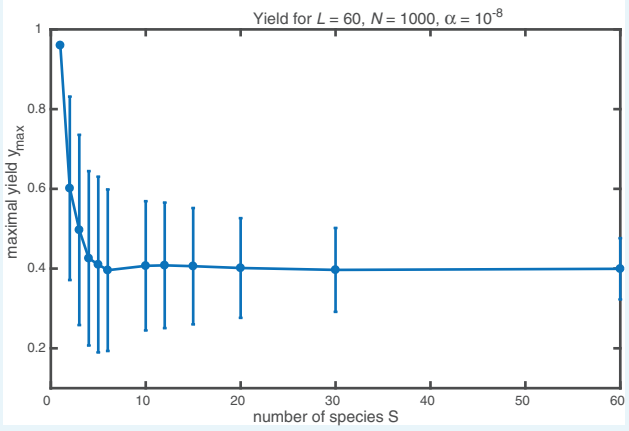


**Appendix 7—figure 1.** Influence of the heterogeneity of the target structure on the yield for fixed number of particles per species $N$. The maximal yield and its standard deviation (obtained as average yield and sample standard deviation for $\alpha = 10^{-8}$) are plotted against the number of species $S$ making up the structure of size $L = 60$. The number of particles per species $N = 1000$ is fixed. Yield drops from a perfect value of 1 for $S = 1$ to a smaller value and levels off for $S \gg 1$. The standard deviation is largest for small $S$ (except for $S = 1$ where the yield is always perfect) and decreases with increasing number of species.

# Appendix 8

## Dependence of the maximal yield $y_{\max}$ in the activation scenario on $N$ and $L$

***Figure 3c*** in the main text characterizes the dependence of the maximal yield $y_{\max}$ in the activation scenario as a 'phase diagram' distinguishing different regimes of $y_{\max}$ in dependence of the particle number $N$ and target size $L$. Supplementing this figure in the main text, ***Appendix 8—figure 1*** shows the maximum yield that is obtained in the activation scenario in the limit $\alpha \to 0$ for fixed $L$ in dependence of $N$ (***Appendix 8—figure 1a***) as well as for fixed $N$ in dependence of $L$ (***Appendix 8—figure 1b***). For larger particle number $N$, the maximal yield exhibits a transition from 0 to 1 over roughly three orders of magnitude. Increasing $L$ shifts the transition to larger $N$. The threshold particle number where the transition starts is characterised by $N_{\rm th}^{>0}(L)$ (see main text). Approximately, for $L \leq 600$, we find $N_{\rm th}^{>0}(L) \sim L^{2.8}$ (cf. main text, ***Figure 3c***). Similarly, decreasing the target size $L$ for fixed $N$, the maximal yield exhibits a transition from 0 to 1 over roughly one order of magnitude in $L$. The corresponding threshold value $L_{\rm th}^{>0}$ as a function of $N$ is obtained as the inverse function of $N_{\rm th}^{>0}(L)$. Hence, at least for $N \leq 10^5$, approximately it holds $L_{\rm th}^{>0}(N) \sim N^{0.36}$. Since $y_{\max}$ is largely independent of the number of species $S$ for fixed $N$ and $L$ (see Appendix 7), the maximal yield in the activation scenario (for $L_{\rm nuc} = 2$) can be fully characterized as a function $y_{\max}(N,L)$ of $N$ and $L$. Hence, $y_{\max}$ can roughly be expressed in terms of the threshold particle number $N_{\rm th}^{>0}(L)$ as

$$y_{\max}(N,L)\begin{cases} \approx 1 & \text{if} N > 10^3 N_{\rm th}^{>0}(L) \\ <1 & \text{if} N_{\rm th}^{>0}(L) < N < 10^3 N_{\rm th}^{>0}(L) \\ =0 & \text{if} N < N_{\rm th}^{>0}(L) \end{cases} \tag{A50}$$

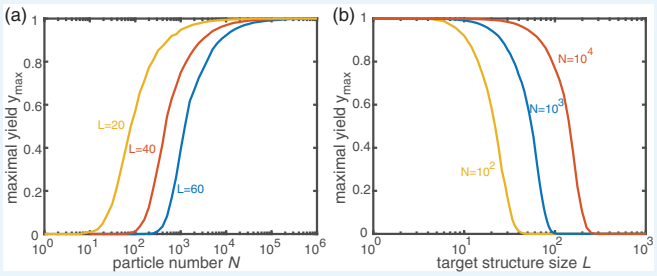


**Appendix 8—figure 1.** Dependence of the maximal yield $y_{\max}$ in the activation scenario on $N$ and $L$. For each data point, $y_{\max}$ was determined as the average yield of 100 independent stochastic simulations of the activation scenario with $\alpha = 10^{-12}$. (**a**) Variation of the particle number $N$ for different target sizes $L$. The maximal yield increases from 0 to 1 over roughly three order of magnitude in $N$. The onset of the transition depends on $L$. (**b**) Variation of the target size $L$ for different particle numbers $N$. Increasing the target size $L$ with $N$ being fixed causes the maximal yield to drop to 0. The transition from 1 to 0 spans roughly one order of magnitude in $L$ and its position is determined by $N$.

As can be seen from ***Figure 3c*** in the main text, the transition line between zero and nonzero yield slightly flattens with increasing $L$. Hence, the power law $N_{\rm th}^{>0}(L) \sim L^{2.8}$ (and similarly for $L_{\rm th}^{>0}$) only holds approximately and for a restricted range in $L$ and $N$. The asymptotic behavior of $N_{\rm th}^{>0}$ in the limit $L \to \infty$ remains elusive.

# 6 Understanding and controlling stochastic heterogeneous self-assembly

This chapter summarizes the most important findings of our project on understanding and guiding robust self-assembly of heterogeneous structures, which directly links to the previous project and seeks to establish a deeper understanding of the stochastic yield catstrophe in the activation scenario. The corresponding manuscript is currently in preparation for submission. This chapter is based on and uses parts of the manuscript preprint in section 6.5.

## 6.1 Motivation

In the last chapter, we discussed how heterogeneous self-assembly systems are affected by stochastic effects if particle concentrations are low and subject to fluctuations. As a result of these stochastic effects, we found that the activation scenario undergoes a stochastic yield catastrophe, which can completely suppress the yield despite the deterministic theory would predict a perfect yield. Several questions about this strong stochastic effect still remain unclear. For example: how can fluctuations between the concentrations of species, which are typically of the order of $1/\sqrt{N}$, can have such a drastic, deleterious effect? How can the strong, nonlinear dependence of the strength of the stochastic yield catastrophe on the number of species be explained? In order to be able to find efficient strategies to mitigate stochastic yield catastrophes, it might furthermore be useful to understand which kind of noise causes the effect in the first place: Is demographic noise in the particle concentrations the primary cause of the stochastic yield catastrophe or rather the random order in which particles bind to each other, also referred to as 'reaction noise'? Finally, having achieved a deeper understanding of the effect and its underlying causes, it would be interesting to see if a similar effect could also arise in other systems different from self-assembly, like, for example, general complex reaction networks, or if the effect is specific to self-assembling systems.
In order to answer these questions and to gain a deeper understanding of the stochastic yield catastrophe, we will formulate an effective theory of the stochastic dynamics in the activation scenario. An effective theory typically provides a coarse-grained view on a physical system and thereby allows one to understand the essential factors that cause or contribute to an effect.
The value of an effective theory is nicely illustrated with the example of superconductivity: When superconductivity was discovered, it was assumed that the effect is caused by a special from of transport of electrons between atoms [153, 154]. A much deeper understanding was established later with the help of Ginzburg-Landau theory, which relates the phenomenon of superconductivity to the breaking of a global U(1) gauge symmetry in the effective field theory [155, 156]. This conception enabled the prediction of other systems with superconducting properties - among those, most astonishingly, systems which do not even consist of atoms

or electrons, like, for example, deconfined quark matter in neutron stars exhibiting colour superconductivity [157].
This kind of abstraction or generalization achieved by the effective theory, which provides the deepest level of understanding of a physical effect, is the result of the identification of the essential 'degrees of freedom' of a system and their interactions. By formulating an effective theory of our stochastic system, we likewise seek to gain a deeper understanding of the essential factors that cause stochastic yield catastrophes and to find answers to the above mentioned questions. With the help of this understanding, we will be able to propose various strategies in order to mitigate or suppress stochastic effects and to improve self-assembly efficiency in the stochastic limit.

## 6.2 Model

The model that we studied in this project is the same as the one used in the previous chapter. We therefore do not discuss the model again but refer the reader to section 5.2 of the previous chapter. Here we set the critical nucleation size to $L_{\text{nuc}} = 2$, so that growth is completely irreversible. Furthermore, in the manuscript preprint in section 6.5, we also introduce the ability for particles to bind incorrectly with a small error rate $\nu_{\text{def}}$. Incorrect binding, however, was only treated incidentally in this project and, in general, we set the error rate $\nu_{\text{def}}$ to zero. Therefore, we will not go more into detail about incorrect binding here but discuss its consequences in-depth in the next chapter.

## 6.3 Results and Discussion

As has been discussed in detail in the last chapter, several unexpected effects are observed in the model if the activation rate $\alpha$ is decreased and the particle number $N$ is not abundant. First, if the activation rate is decreased, the final yield increases only up to an imperfect value (which can also be zero), whereas a perfect yield, as predicted by the deterministic theory, can only be achieved if the particle number $N$ is very large.
Second, if $\mu < \nu$, the yield can even become a non-monotonic function of the activation rate, and hence - quite counterintuitively - a non-monotonic function of the deterministic nucleation speed. Third, the strength of the stochastic yield catastrophe strongly increases with the number of species $S$, while for $S = 1$ (homogeneous case) the system behaves deterministically.

The idea of this project is to formulate an effective theory that describes the stochastic behavior of the system by taking fluctuations in the concentrations of the different species into account (demographic noise) while neglecting noise arising from randomness in choosing a binding partner (reaction noise). Hence, the assumption of the theory is that the stochastic yield catastrophe is primarily a result of demographic noise in the species' concentrations arising from randomness in the order of their activation. Specifically, nucleation events are expected to be triggered if individual species are currently underrepresented as a result of their retarded activation. We call those species that are currently not available for binding *unavailable* species. The idea is illustrated in Fig. 6.1. Here, activation of species 6 and 2 are retarded and hence these species are momentarily unavailable. As a consequence, complexes

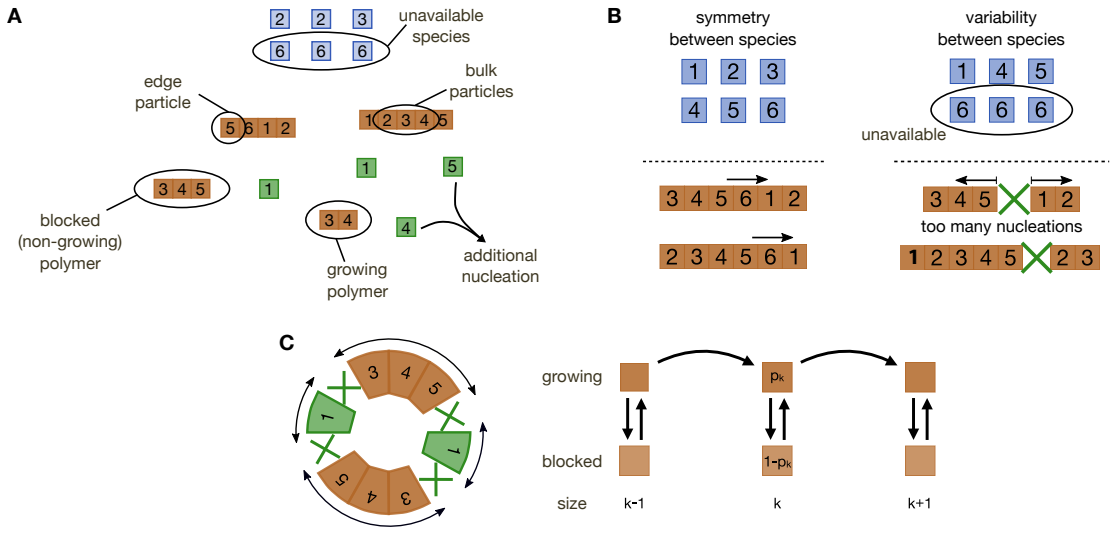


**Figure 6.1 | Illustration of the effective theory.** **A** Species which are currently unavailable for binding ('unavailable species') lead to additional nucleation events: If certain species ('unavailable species'; here e.g. species 6) have been activated less than average, the growth of existing structures (here e.g. the complex 3-4-5) may be blocked as a result of their shortage and, consequently, additional nucleation events between neighboring species might be triggered (here e.g. species 4 and 5). **B** In contrast, in the deterministic description (B left), species are activated uniformly and, hence, the number of nucleation events is strongly underestimated by the deterministic theory as compared to the stochastic case (B right). **C** By averaging the distribution of unavailable species, we calculate the probability for a complex to be in the blocked state, which is used in order to formulate the effective theory. The effective theory describes transitions between the 'blocked' and 'growing' states of complexes during their growth. Integration of the theory yields a description of the stochastic dynamics that accounts for the effects arising as a consequence of demographic noise.

like 1-2-3-4-5 or 3-4-5 that would required these unavailable species in order to further grow are prevented from growing. These complexes are called *blocked*. At the same time, available monomer species like 4 and 5, which cannot bind to the existing complexes because a connecting species like 6 is unavailable, instead nucleate new structures. Supposing species 6 were available, it could bind to the complex 1-2-3-4-5 to form a complex 6-1-2-3-4-5, to which subsequently species 5 and 4 could attach. Without species 6, however, nucleation of 4 and 5 is much more likely. In this way, fluctuations between the concentrations of species trigger additional nucleation events. The deterministic theory, in contrast, assumes that all species are activated uniformly and, hence, does not capture the additional nucleation events arising from fluctuations in the availability of species (see Fig. 6.1B).

The statistics that describe the number and distribution of unavailable species therefore promise to be key in a quantitative description of the stochastic system. Since activation of monomers is independent of the reaction dynamics, the (time dependent) probability of a species to be unavailable can be estimated with a 'fluctuation-corrected mean-field' ansatz. In a next step, the probability of a complex of length $\ell$ to be in a blocked state is related to the probability of a species to be unavailable. To this end, again in the spirit of a 'fluctuation-corrected mean-field' approach, we perform a weighted average over all possible configurations in which a certain number of species is missing (see Fig. 6.1C) and from its statistics derive the average probability for a complex of length $\ell$ to be in the blocked state. As it turned out,

the probability for a complex to be blocked generally increases with its size because larger complexes are more likely to have stopped growing due to a missing species. Consequently, the average growth rate of a cluster decreases with its size, which is in sharp contrast to the deterministic theory, where all clusters grow with the same rate. This finding suggests that fluctuations suppress the yield by favouring the emergence of small structures while at the same time blocking the growth of larger ones, which, over time, leads to a strong competition for resources. Herein we also find an explanation for the strong dependence of stochastic effects on the number of species: Since larger clusters grow increasingly slower, the total amount of resources needed to reach a specified yield increases nonlinearly with the size of the target structure (i.e. the number of species it consists of).
In the last step, in order to fully quantify the stochastic dynamics, we formulate an effective theory, which, for each cluster size, distinguishes a blocked and a growing state, and accordingly characterizes the transition probabilities between these two states (see Fig. 6.1C). With the help of the effective theory, the evolution of the full cluster size distribution can be predicted. Despite several simplifications that were made in order to derive the effective theory, its predictions qualitatively fit the behavior of the stochastic system very well (see Fig. 2 in the publication preprint in section 6.5). For example, the saturation of the yield for small activation rates, as well as its non-monotonicity as a function of $\alpha$ in the case where $\mu < \nu$ are described very well by the effective theory. This confirms that demographic noise in the concentrations of the different species is the main cause of the stochastic yield catastrophe while reaction noise appears to be less significant. The essential variable that characterizes the level of demographic noise is thereby the variance $\sigma_0^2$ of the number of activated particles of a (randomly chosen) species. Finding strategies in order to decrease this variance is tantamount to increasing assembly efficiency.

The understanding gained from the effective theory enabled us to conceptualize four control strategies to mitigate or suppress stochastic effects and enhance resource efficiency of self-assembly in the stochastic limit. Since demographic noise in the concentrations of the various species was identified as the main cause of the stochastic yield catastrophe, all four strategies aim to control fluctuations in the species' concentrations. There are, however, two principally different ways how this can be achieved: Two of the four strategies aim to equilibrate the concentrations of the different species while the other two reduce randomness by promoting a specific order in which the species are activated. As a further criterium, we distinguished whether external or self-organized, internal control is used to reduce the level of noise.
For example, in order to reduce the variance between the concentrations of species, inactive particles can be provided in successive 'bursts'. This means that, instead of providing all monomers at once, only a fraction of the monomers is supplied, with the different species being distributed as evenly as possible (in their stoichiometric ratios). After some waiting time, the next such burst of particles is supplied until all $N$ particles per species have been provided. If the variability of the concentrations within each burst is sufficiently low, demographic noise can thus be reduced and the final yield be increased (see Fig. 5a,b in the manuscript preprint in section 6.5). Since the composition of the bursts is not regulated by the system itself but requires some external control mechanism, we consider this as an *external* control strategy. For example, cells could realize a similar strategy by controlling a number of genes that code for the various constituents by a common promoter region (so-called gene cassettes). In this way, transcription of the genes could proceed in 'bursts', thereby decreasing the level of noise

in the constituents. However, translation might still be an additional source of noise in this system.
A different way to reduce variability in the species' concentrations can be achieved with internal feedback. Specifically, a mechanism by which active monomers inhibit the activation of their own species could likewise decrease variability since species which are available in lower numbers would thus be activated more often than species that are available in large numbers. For example, cells could realize such a mechanism by endowing the constituents with gene-regulatory functions controlling their own expression. In our system, we modelled this case by assuming that the activation rate of species $i$ is given by $\alpha_{(i)} = \alpha_0 e^{-qm_i^a}$, where $\alpha_0$ is a basal activation rate, $q$ the inhibition strength and $m_i^a$ the concentration of active monomers of species $i$. Indeed we find that by increasing the inhibition strength $q$, the yield in the limit of small $\alpha_0$ increases as a result of the reduction of demographic noise in the system (see Fig. 5c,d in the manuscript preprint in section 6.5).
Taken together, these findings confirm that demographic noise plays an important role for assembly efficiency, as suggested by the effective theory. Control strategies that reduce demographic noise can thereby enhance resource efficiency in heterogeneous self-assembly.

Another possibility in order to reduce stochastic effects and enhance self-assembly efficiency is by promoting a specific order in which the species are activated, similar to the just-in-sequence supply strategy discussed in part 1 of this thesis. At first glance, this approach seems to be counterproductive in mitigating stochastic effects since consecutive activation of the species apparently increases the variability between their concentrations. The crucial point, however, is that variability between species must be increased in a very coordinated fashion so as to promote a specific assembly path, inhibiting spurious nucleation events.
One way to activate the species in consecutive order is by using inhomogeneous activation rates for the different species. For example, in the linear ring structure that we consider, activation rates can be chosen to decrease exponentially with the species index: $\alpha^{(i)} = \alpha_0 \omega^{-i}$, where $\alpha_0$ is the basal activation rate and $\omega$ is a constant (in the manuscript we chose a slightly different activation order in which $\alpha^{(i)}$ decreases symmetrically to both sides of the ring). In this way, species with a lower index tend to be activated earlier than those with a larger index. By choosing the parameters $\alpha_0$ and $\omega$ suitably, we find indeed that the final yield can be improved significantly in this way (see Fig. 6(b) in the manuscript preprint in section 6.5).
A just-in-sequence supply strategy as introduced in chapter 2 allows for even further reduction of the noise level and thus permits us to achieve even higher resource efficiency in the stochastic limit. For example, particles can be provided in 'batches', whose composition and timing is controlled externally as described in part 1. Alternatively, just-in-sequence supply can also be implemented in a self-organized way, for example, by assuming that the monomers of each species inhibit activation of the species that follows next in the supply sequence. This scenario and its implications will be discussed at length in the subsequent chapter, which is why we do not go further into detail here but refer the reader to chapter 7.

In another project [6], which was conducted by our Master student Frederik Träuble but is not part of this thesis, we investigated if an effect similar to the stochastic yield catastrophe could also occur in other complex reaction networks, like enzymatic or metabolic networks. This, however, is apparently not the case because the competition between nucleation of new structures and growth of existing structures, which is a hallmark specifically of self-assembling

systems and has no analogue in general reaction networks, is crucial to the emergence of stochastic yield catastrophes. Therefore, we believe that the phenomenon of stochastic yield catastrophes is restricted to self-assembly systems.

## 6.4 Key points

In my opinion, the key results of this project are the following:

- Fluctuations in the availability of different species (demographic noise) is the origin of the stochastic yield catastrophe in the activation scenario and can thus be a severe limiting factor for heterogeneous self-assembly.
- The stochastic dynamics of the system is well described by an effective theory that accounts for demographic noise between the species but neglects noise arising from the random binding kinetics (reaction noise).
- Stochastic effects can be mitigated either by controlling the level of demographic noise or by supplying the species in sequence so as to favour a particular assembly path. We examined specific examples to implement both of these strategies. All examples rely on supply regulation conducted either by external control or self-inhibitory feed-back. We furthermore discussed concrete ideas how these strategies could be realized in a biological context.

## 6.5 Manuscript preprint: Understanding and guiding robust self-assembly of heterogeneous structures

This section is a preprint of the following manuscript.

### Understanding and guiding robust self-assembly of heterogeneous structures

by

Isabella R. Graf,[1,*] Florian M. Gartner,[1,*] and Erwin Frey[1]
[1] *Arnold-Sommerfeld-Center for Theoretical Physics and Center for NanoScience, Department of Physics, Ludwig-Maximilians-Universität München*
[*] *These authors contributed equally to this work.*

# Understanding and guiding robust self-assembly of heterogeneous structures

Isabella R. Graf,[1,*] Florian M. Gartner,[1,*] and Erwin Frey[1,†]

[1] *Arnold Sommerfeld Center for Theoretical Physics and Center for NanoScience, Department of Physics, Ludwig-Maximilians-Universität München, Theresienstrasse 37, D–80333 München, Germany*

Self-assembly is not only crucial for living organisms but also an important component for the technological production of functional nanostructures. For these structures to be versatile, they must be heterogeneous and consist of a number of different modules that are responsible for specific functions or tasks. Recently, however, a conceptual model has demonstrated that the self-assembly of heterogeneous structures can be subject to strong stochastic effects that significantly suppress yield. Given that self-assembly is an essential process in living systems and in nanotechnological applications, this finding raises two immediate questions: How do heterogeneous structures assemble efficiently in living organisms? Which guiding strategies could be implemented into the design of artificial assembly systems in order to achieve high assembly yield? An answer to these questions requires a thorough understanding of the occurrence of the detrimental stochastic effects ("stochastic yield catastrophe"). To make progress, here we formulate an effective theory for the aforementioned conceptual model that enables us to unravel the various sources of stochasticity in terms of their relevance to assembly efficiency. From this effective theory, we identify the fluctuations in the availability of the different constituents for binding as the major cause of the stochastic yield catastrophe. We use this insight to propose and implement two control strategies to improve yield by reducing the variance in the relative availability of constituents. These are based on supply control by providing particles in bursts or by implementing self-inhibitory feedback. Remarkably, also a strong increase in the variance between constituents enhances assembly yield, provided it is coordinated and favors a specific assembly path. We discuss possible limitations and applications of all control strategies and place our findings in a broader perspective.

## I. INTRODUCTION

One of the defining features of living systems is their ability to autonomously generate complex structures and macro-molecular machineries. Underlying this ability are self-assembly and self-organization processes. These rely on local interactions between constituents but are generically not driven by external guidance or a global control system [1, 2]: Unlike someone who assembles bricks in the correct order to create a predefined structure, the assembly of cellular structures such as microtubules [3–5], ribosomes [6, 7], flagellar motors [8, 9] or intracellular viruses [10–12] must work without an externally provided construction plan. How do local interactions between constituents suffice to build macroscopic structures? In particular, it is still an open question why assembly yield can be high although the free energy landscape may exhibit many local minima [2, 13–15] in which the dynamics can get kinetically trapped on the relevant timescales. As a result of such kinetic trapping, only fragments of structures might be formed but no complete structures [2, 16, 17].

Elucidating principles for the kinetics of self-assembly processes is expected to be useful not only for the understanding of intracellular self-assembly but also for the design of artificial self-assembly systems [13]. These artificial assembly processes are based on techniques such as DNA nanotechnology, including DNA origami [18, 19], DNA bricks [20], or single-stranded tiles [21], and allow for a rich variety of possible large-scale structures. As a result, artificial self-assembly is believed to be a promising route towards functional nanostructures [2, 22], with proof-of-principle achievements ranging from nanoboxes with programmable lids [23] to micrometer-sized colloids [24].

The problem of kinetic trapping has long been studied in these systems and has been described both in experiments reproducing natural assembly processes of, for example, virus capsids [10, 25, 26], as well as in artificial self-assembly systems based on DNA nanotechnology [27, 28]. It has been pointed out by several studies that reversibility of binding is a possibility to overcome kinetic trapping [29–34]. However, for virus capsids and other functional biological structures it has been shown that at least part of the reactions are not reversible on the time scale of the assembly process [35, 36]. From a biological point of view, this (partial) irreversibility is reasonable since, for instance, virus shells must be stable to protect their cargo in adverse environments, which requires sufficiently strong and stable bonds. Allosteric control has therefore been proposed as a viable mechanism to actively suppress nucleation and thereby avoid kinetic trapping in weakly reversible self-assembly [36–39]. And indeed, it has been demonstrated that allosteric effects play an important role in the self-assembly of viruses, flagellar motors and actin filaments [37, 38, 40–43].

Furthermore, the principle of "slow nucleation but fast growth" has become a guiding rule for self-assembly [10, 16, 20, 44, 45]. It is based on the idea that if nucle-

* These authors contributed equally to this work.
† Please send correspondence to frey@lmu.de.

ation of new structures is slow compared to the growth of existing structures, the structures are formed one after the other and there is no competition for resources. One would expect that such a situation could be induced by allosteric effects, which are assumed to control the nucleation speed. However, a recent study shows that for heterogeneous systems, the way in which allosteric control is implemented plays a critical role [46]. In particular, if fluctuations in the availability of the different kinds of building blocks are relevant, a severe stochastic effect termed 'stochastic yield catastrophe' can cause kinetic trapping in weakly reversible self-assembly. This type of kinetic trapping is special in that it constitutes a genuinely stochastic effect that is not captured by mean-field chemical rate equations.

Since fluctuations in the relative concentrations of particles can arise in multiple different ways ranging from diffusion to stochastic production of the building blocks, stochastic yield catastrophes might represent a major limitation for self-assembly efficiency. Hence, it is crucial to gain a deeper understanding about the underlying causes of stochastic yield catastrophes in order to propose effective strategies to mitigate their detrimental effect. These insights could enhance our understanding of cellular self-assembly processes and usefully inform experiments and nanotechnological implementations. To this end, here we revisit a conceptual model of a linear, heterogeneous assembly process as introduced in Ref. [46] and focus on a quantitative understanding of the role of fluctuations. In line with Einstein's demand on what a proper model should be like [47], we find that this model is conceptually rich enough to show all essential features of self-assembly processes and – at the same time – as simple as possible to allow for an in-depth theoretical analysis. We develop an effective stochastic theory that extends a previously formulated mean-field description [46]. In contrast to this mean-field description, it captures the observed phenomenology, including the stochastic yield catastrophe, qualitatively correctly. Our analysis reveals that the main contribution to the stochastic yield catastrophe is indeed due to demographic noise, rather than inherent reaction noise. Based on this insight, we propose different strategies to suppress the detrimental effect of fluctuations and discuss their possible implementations. Concretely, these strategies prevent stochastic effects either by reducing fluctuations in the availability of the different species or by controlling the supply in a way to favor specific assembly paths. We expect that these strategies could be implemented in systems based on modern nanotechnological devices in rather straightforward ways. Hence, these strategies might constitute viable ways to realize irreversible self-assembly of complex information-rich nanostructures.

## II. MODEL DEFINITION AND RESULTS FROM STOCHASTIC SIMULATIONS

### A. Stochastic model

We consider a conceptual irreversible self-assembly process with a unique target structure (ring) of finite size $L$ composed of monomers of $S$ different species, as illustrated in Fig. 1, which summarizes the key processes during self-assembly. Specifically, we take into account a stochastic activation step and irreversible binding reactions as introduced in Refs. [46, 48]. All monomers are inactive initially and are activated at a per capita rate $\alpha$. Once active, monomers of species $i \in \{1, \dots, S\}$ bind other monomers of the (periodically) neighboring species $(i\pm1)\mathrm{mod}S$ to form dimers at rate $\mu$ (*dimerization*), e.g. active monomers 3 and 4 in Fig. 1. Furthermore, monomers can also attach to larger structures by binding to a periodically consecutive species (*correct binding*) at rate $\nu$, e.g. active monomer 5 and polymer 3-4. Alternatively, binding may also occur between polymers and monomers of the next-nearest-neighbor species at a reduced rate $\nu_{\mathrm{def}} \ll \nu$, creating a defect in the structure (*defect formation*, e.g. active monomer 4 and polymer 6-1-2, creating a defect at species 3 (or 5). Since polymer-polymer binding is typically assumed to be less relevant as compared to binding between monomers and polymers [10, 17, 49, 50], we assume that structures only grow by the attachment of monomers. Once the structure has reached the target size $L$ (including the defects; see the final target structures in Fig. 1), the ring closes and no further growth of this ring is possible.

A typical assembly pathway proceeds as follows: As soon as some monomers have been activated, monomers dimerize and polymers start to grow by monomer attachment of correct (neighboring) or defect-forming (next-nearest neigbhboring) species. These polymers then all continue to grow until they have either reached the target size or until all monomers are bound in polymers.

The quality of the assembly process (*"yield"*) is measured at exactly this time when no further growth is possible any more as all monomers have been activated and are depleted (bound in larger structures). The yield $Y$ is defined as the number of finished target structures, $N_{\mathrm{target}}$, compared to the maximally possible number of defect-free target structures, $N^*_{\mathrm{target}}$. In a perfect assembly process each species occurs exactly $L/S$ times in each finished structure. Hence, the number of possible defect-free target structures is given by $N^*_{\mathrm{target}} = N/(L/S)$. Hence, the yield is defined as

$$Y = \frac{LN_{\mathrm{target}}}{SN}\,. \tag{1}$$

Analogously, the defect-free yield, $Y^{(0)}$ is defined as the number of defect-free target structures, $N^{(0)}_{\mathrm{target}}$, com-

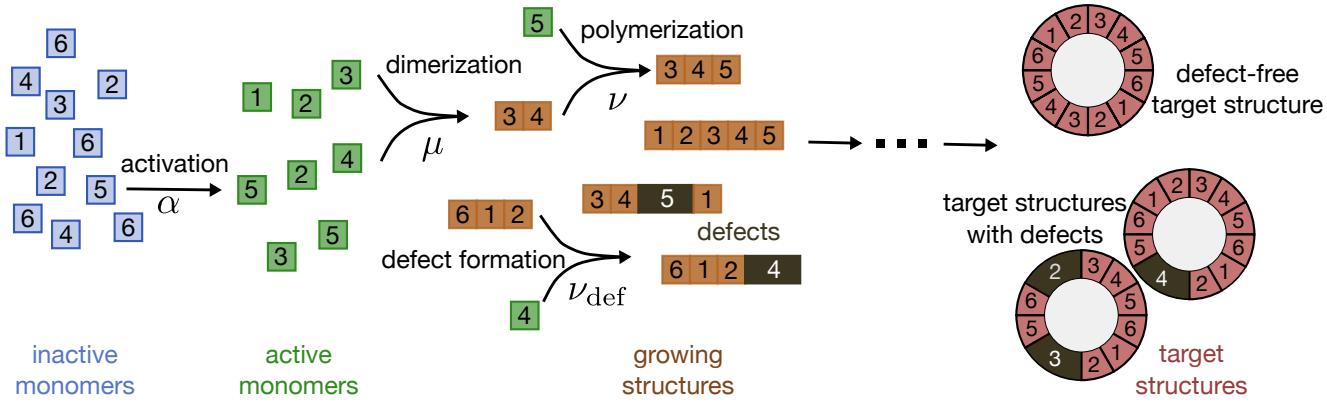


FIG. 1. **Schematic of the conceptual self-assembly model** Rings of target size $L$ are assembled from $S$ different species of particles (here $L = 12$ and $S = 6$). All monomers start in an inactive state (blue) and have to be activated before being able to bind. This activation happens at a per-capita rate $\alpha$. Structures grow by attachment of active monomers (green). Defect-free binding happens only between nearest-neighbor species (in a periodically consecutive ordering), so species $i$ can bind to $i \pm 1$ (modulo $S$). Dimerization happens at rate $\mu$ whereas monomer binding to larger structures (orange) happens at rate $\nu$. Defect formation occurs at a much lower rate $\nu_{\rm def} \ll \nu$ between next-nearest neighbors, leaving out one species and thereby creating a defect (black). A structure is finished (red) once its size (including the defects) has reached the target size $L$. There are $N$ particles of each species, so that in total the system could build $NS/L$ defect-free target structures.

pared to $N^*_{\rm target}$:

$$Y^{(0)} = \frac{LN^{(0)}_{\rm target}}{SN}\,. \tag{2}$$

If many structures are completed during the process (irrespective of whether they contain defects or not), the yield is high. In contrast, the defect-free yield is high only if many defect-free structure are produced. It thus quantifies the quality and amount of target structures.

### B. Mean-field behavior (abundant resources)

In this section we summarize the most important findings of the previous studies [46, 48] to gain a first intuition about the self-assembly process. We discuss the more intuitive deterministic limit of large system size $N \to \infty$ first and focus on the case of finite resources afterwards.

A well-known principle for efficient self-assembly is the 'slow-nucleation principle' [10, 20, 21, 44–46, 51] which states that the assembly yield is high if nucleation of new structures is slow compared to the growth of structures. In this case, it is very likely that a structure that has been nucleated grows into the target structure before a new structure is nucleated. As a result, structures are assembled one after the other and the assembly yield is high. Conversely, if nucleation of new structures is fast, many structures will be nucleated simultaneously. These polymers then compete for the same resources and resources run out before the structures are completed ('depletion trap').

In the deterministic limit of many particles per species $N \to \infty$, the self-assembly process in our model, Fig. 1, behaves according to the slow-nucleation principle [46]. For high activation rate (large $\alpha$) and fast dimerization ($\mu \approx \nu$), the number of active monomers is high and nucleation of new structures (dimerization) occurs more frequently than growth of larger structures. Correspondingly, the yield is very low. In agreement with the slow-nucleation principle, the efficiency of the assembly process can be improved by either decreasing the dimerization rate $\mu$ or the activation rate $\alpha$ compared to the growth rate $\nu \equiv 1$: Yield is a monotonic function of both $\alpha$ and $\mu$ and perfect yield is always achieved in the limit of small $\alpha$ or $\mu$, irrespective of the number of particles $N \gg 1$ or species $S$ [46, 48]. Indeed, for fixed number of particles $N$ per species and fixed target size $L$ yield is independent of the number of species $S$.
As discussed in the next section II C, stochastic effects do, however, qualitatively alter the self-assembly process.

### C. Stochastic effects for finite resources

For reduced resources (smaller $N$) and heterogeneous structures $S > 1$, fluctuations in the dynamics become relevant and the behavior of the system is qualitatively different from the behavior in the deterministic limit [46, 48]. In this case, stochastic simulations of the system based on Gillespie's algorithm [52] demonstrate that the yield saturates at an imperfect value $Y_{\rm max}$ in the limit of small $\alpha$ if $N$ is not large enough (Fig. 2 (a, d)). Previously, we have shown that below a threshold value of $N$, which depends on the size of the target structure, this saturation value $Y_{\rm max}$ is in fact zero and the system produces no yield although yield is perfect in the corresponding deterministic description ('stochastic yield catastrophe') [46]. Furthermore, we have shown that yield can be a non-monotonic function of the activation rate both

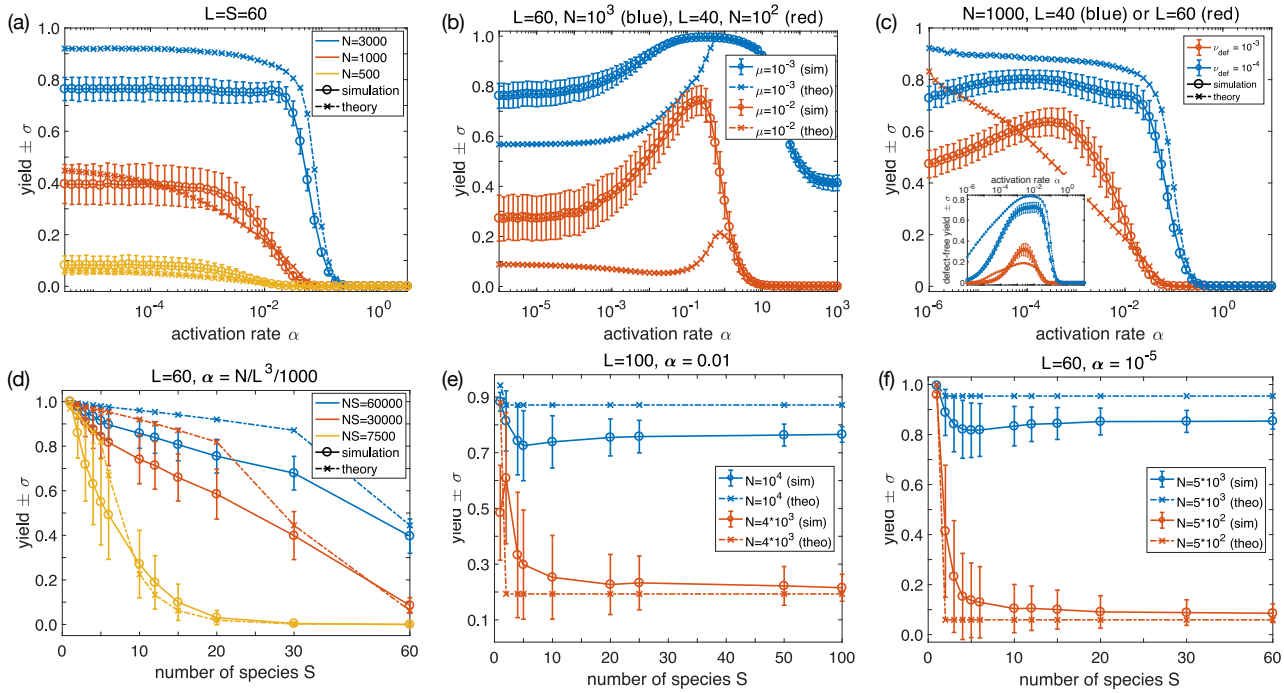


FIG. 2. **Stochastic yield catastrophe as observed in stochastic simulations (circles) and results of the effective theory (crosses).** (a) The average yield and its standard deviation (in stochastic simulations) are plotted against the activation rate $\alpha$ for different numbers of particles per species $N = 3000$ (blue), $N = 1000$ (red) and $N = 500$ (yellow). Yields saturates at an imperfect value for $\alpha \to 0$. The parameters are $L = S = 60$, $\mu = \nu = 1$ and $\nu_{\rm def} = 0$. (b) For small dimerization rate, here $\mu = 10^{-3}$ (blue; $L = S = 60$, $N = 10^3$) or $\mu = 10^{-2}$ (red; $L = S = 40$, $N = 10^2$), the average yield can become a non-monotonic function of the activation rate $\alpha$. The other parameters are $\nu = 1$ and $\nu_{\rm def} = 0$. (c) For finite defect formation rate, here $\nu_{\rm def} = 10^{-4}$ (blue) or $\nu_{\rm def} = 10^{-3}$ (red), both the defect-free yield (inset), i.e. the yield of all target structures without defects, as well as the total yield (main figure), i.e. the yield of all target structures with and without defects, can be a non-monotonic function of the activation rate $\alpha$. The other parameters are $N = 1000$, $\mu = \nu = 1$ and $L = S = 60$ (red) or $L = S = 40$ (blue). (d) The average yield and its standard deviation are plotted against the number of species $S$ for fixed total number of particles $NS = 60000$ (blue), $NS = 30000$ (red) and $NS = 7500$ (yellow). In this case, the average yield decreases with increasing heterogeneity of the structure (number of species $S$ that make up the ring). The parameters are $L = 60$, $\alpha = N/L^3/1000$, $\mu = \nu = 1$ and $\nu_{\rm def} = 0$. The activation rate is chosen small enough that the yield has already reached its saturation value $Y_{\rm max}$ for $\alpha \to 0$. (e, f) The average yield and its standard deviation are plotted against the number of species $S$. In contrast to (d), here the number of particles per species $N$ (and not $NS$) is fixed. Yield is highest for homogeneous structures $S = 1$ and levels off at an imperfect value for $S \gg 1$ (e) The parameters are $L = 100$, $\alpha = 10^{-2}$, $\mu = \nu = 1$, $\nu_{\rm def} = 0$ and $N = 10^4$ (blue) or $N = 4 * 10^3$ (red) as indicated. (f) The parameters are $L = 60$, $\alpha = 10^{-5}$, $\mu = \nu = 1$, $\nu_{\rm def} = 0$ and $N = 5 * 10^3$ (blue) or $N = 5 * 10^2$ (red) as indicated.

for $\mu < \nu$ or $\nu_{\rm def} > 0$ (Fig. 2 (b,c)), a feature that does not occur in the limit $N \to \infty$. In the case $\nu_{\rm def} > 0$, also the defect-free yield shows non-monotonic behavior with respect to the activation rate $\alpha$ (inset in Fig. 2 (c)). Finally, for fixed number $N$ of particles per species and fixed target structure size $L$, the yield is not independent of the number of species $S$ (Fig. 2 (e,f)). Instead, the yield is large for $S = 1$ but then drops for $S > 1$ and saturates for $S \gg 1$. It remained, however, elusive why these stochastic effects are so strong and which sources of stochasticity (demographic noise or reaction noise) contribute mostly to the observed phenomenology. One goal of this manuscript is to gain a deeper insight into which physical principles underlie the stochastic yield catastrophe.

### D. Fundamental difference between the deterministic and the stochastic limit

What is the fundamental difference between the deterministic limit ($N \to \infty$) and the case of reduced resources? For $N \to \infty$, the randomness of binding and fluctuations in the relative number of the different constituents (demographic noise) are negligible [46, 48]. This is, however, not true for reduced resources. Heuristically, if certain species are temporarily less available than others due to random fluctuations in the activation of particles, the neighboring species will tend to nucleate additional structures or to form defects (Fig. 3 (a, b)). For instance, if a species required for correct growth is temporarily not available as an active monomer (e.g. species

6 in Fig. 3 (a)), a monomer of the next species might form a defect (species 1 in the figure). Similarly, active monomers of this next species might dimerize with a monomer of their other neighboring species instead. As a result, there will be too many nucleation events or too many defective structures, suppressing the (defect-free) yield. While it is intuitive that fluctuations in the availability of the different species may lead to additional nucleation events or defect formation, a quantitative understanding is still lacking. Due to the central limit theorem, demographic fluctuations or shot noise are typically expected to scale as $1/\sqrt{N}$ compared to the mean $N$. So, why do demographic fluctuations in the relative availability of the different species lead to such strong stochastic effects even in cases when the number of particles per species $N$ is large? To which extent do the different sources of stochasticity (demographic noise, reaction noise due to randomness in binding) contribute to the observed effects? To address these questions, we next formulate an effective theory. This effective description of the self-assembly process focuses on stochasticity introduced by demographic fluctuations in the relative number of active monomers of the different species and neglects reaction noise. It will turn out that effectively putting in this source of stochasticity can indeed qualitatively account for the observed strong deviations from the deterministic description.

## III. EFFECTIVE THEORY: IDEA

The goal of this section is to provide a first motivation for the formulation of the effective theory. Since the effective theory will be based on the deterministic description of the system in Ref. [46], we summarize the most important aspects of this deterministic picture first. In addition, this summary is intended to give insights into which additional aspects might be important for a description of the stochastic effects. Building on these insights, we will then argue for our particular approach to extend the deterministic description.

### A. Reduction to one-species problem in the deterministic limit

The deterministic description of the process as presented in Ref. [46] is based on the assumption that the number $N$ of particles per species is large. Accordingly, it neglects chemical noise due to randomness in choosing a binding partner and demographic fluctuations in the number of active particles of the different species. Consequently, all species are equivalent and all structures of equal size can be treated on the same footing, irrespective of which species they are composed of. Using symmetry arguments, it is thus possible to characterize the assembly dynamics only in terms of the size $l$ of the different structures (for simplicity, we restrict our discussion to the case without defect formation $\nu_{\mathrm{def}} = 0$). Polymers of all sizes $l \in \{2, \dots, L-1\}$ (except for the target size $l = L$) grow by attachment of monomers at rate $\nu$ per monomer at either end. In the time evolution of the number $c_l$ of polymers of size $l$ per species, this process corresponds to a loss term of $-2\nu m^a c_l$ where $m^a$ denotes the number of active monomers per species. The factor of 2 comes from the two configurations in which a monomer can bind to a polymer (namely from the left or right). This loss term appears as a gain term for the number $c_{l+1}$ of structures of size $l+1$ since attachment of a monomer to a structure of size $l$ leads to a structure of size $l+1$. Furthermore, two active monomers dimerize at per capita rate $\mu$. For $m^a$ active monomers per species, this yields a gain term $\mu(m^a)^2$ for the dimers. In contrast to the gain term due to polymer growth, there is no factor of 2 here. This is due to the fact that there is only one possibility to create a dimer from two monomers. Taken together, the time evolution of the number of structures $c_l$ of size $l \geq 2$ per species is thus given by [46]

$$\partial_t c_2 = \mu(m^a)^2 - 2\nu m^a c_2\,, \tag{3a}$$

$$\partial_t c_l = 2\nu m^a (c_{l-1} - c_l)\,, \tag{3b}$$

$$\partial_t c_L = 2\nu m^a c_{L-1}\,. \tag{3c}$$

Initially there are $N$ inactive monomers of each species. All of these are activated at the per-capita rate $\alpha$. The survival probability up to time $t$ is thus $e^{-\alpha t}$ and the average number of inactive monomers at time $t$ is $Ne^{-\alpha t}$. Hence, the gain term for active monomers at time $t$ (which is given by the total activation rate) is $\alpha N e^{-\alpha t}$. The loss term has two contributions, one from dimerization and one from growth of polymers. Analogously to the corresponding loss/gain terms for the polymers, these are given by $-2\nu m^a c_l$ for $l \in \{2, \dots, L-1\}$ for polymer growth and $-2\mu(m^a)^2$ for dimerization. The additional factor of 2 in the dimerization loss term is a stoichiometric factor (two monomers participate in the dimerization). In summary, the time evolution of the monomers is given by [46]

$$\partial_t m^a = N\alpha e^{-\alpha t} - 2\mu(m^a)^2 - 2\nu m^a \sum_{l=2}^{L-1} c_l\,. \tag{4}$$

Note that here and in the following we always consider the number of structures *per species*. For better readability, we will not explicitly mention this in the following.

As mentioned before, in the deterministic limit, the assembly yield is independent of the number of species $S$ (for fixed $N$ and $L$). This equivalency is apparent from the time evolution of the structures, Eqs. 3 and 4, into which the number of species $S$ does not enter. It is, however, in conflict with stochastic simulations where heterogeneous systems ($S > 2$) are subject to strong fluctuation effects but the homogeneous system ($S = 1$) is not (Fig. 2 (e,f)). The reason for the equivalency in the deterministic description lies in the assumption that all species behave identically. Extending the deterministic

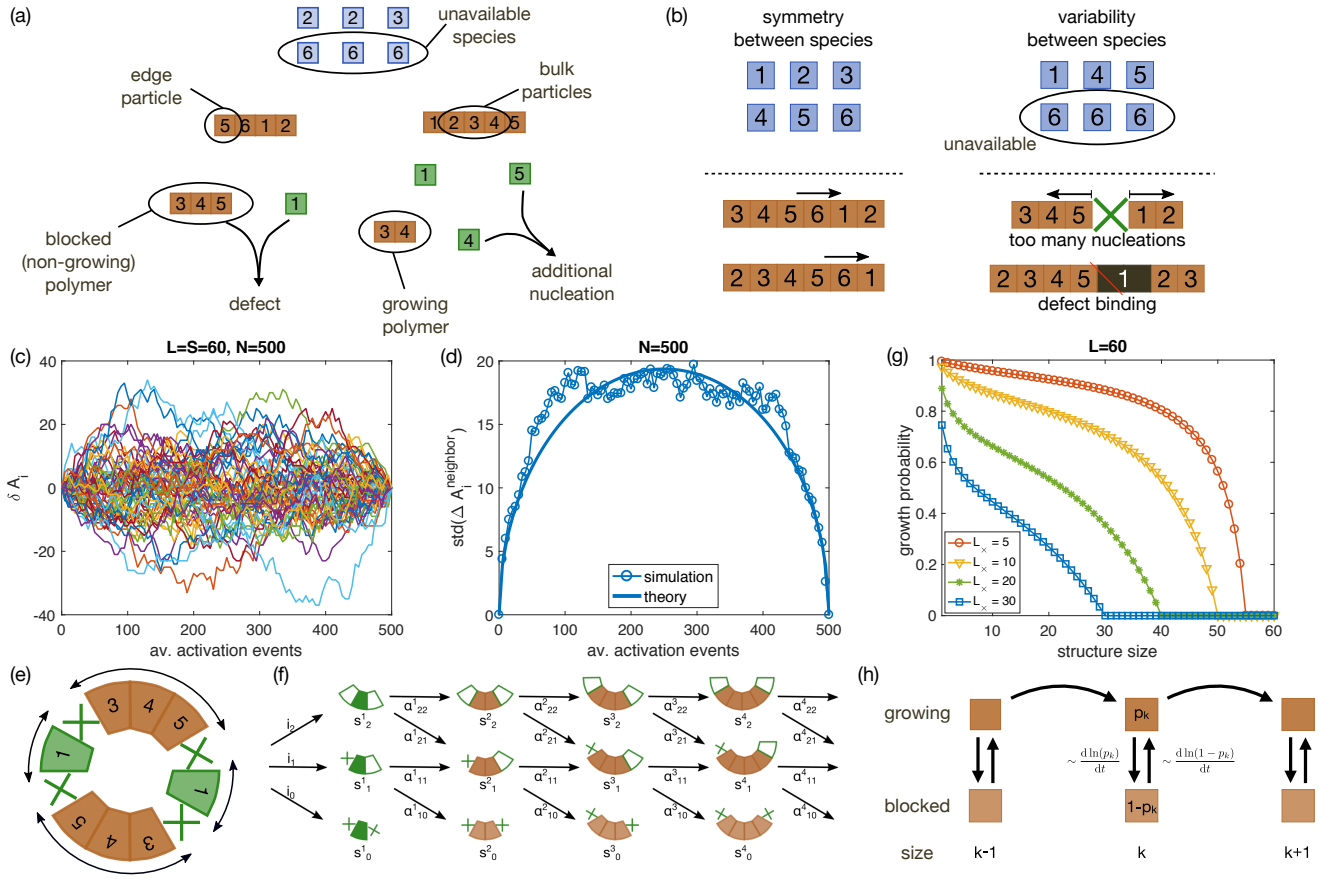


FIG. 3. **Illustration of the effective theory and the terminology.** (a, b) Species which are currently unavailable for binding (in short: "unavailable species") lead to additional nucleation events and defect formation. If a species ("unavailable species"; here e.g. species 6) has been activated much less than its neighbors, these neighbors tend to nucleate new structures (e.g. excess of active monomers of species 4 and 5 in (a) or missing link between polymers 3-4-5 and 1-2 in (b)) or to form defects (e.g. active monomer 1 binds erroneously to polymer 3-4-5 due to a lack of other binding partners, thereby forming a defect). In the deterministic description, which assumes symmetry between the species, all species are equally available and large structures form. (c) The number of activated particles of the different species $A_i$ (different colors) relative to their mean, $\delta A_i = A_i - \bar{A}$, is shown in dependence of the average number of activation events per species $\bar{A}$. The data are shown for one simulation with parameters $L = 60$, $N = 500$, $\nu = \mu = 1$, $\nu_{\rm def} = 0$ and $\alpha = 0.01$. (d) The simulated (symbols) and theoretical values (line) of the standard deviation of the neighbor fluctuations $\sigma = \mathrm{std}(\Delta A_i^{\rm neighbor} = A_{i+1} + A_{i-1} - A_i - \bar{A}) = \sqrt{3\bar{A}(1 - \bar{A}/N)}$, are plotted against the average number of activation events per species, $\bar{A}$, and for the same parameter values as in (a). The standard deviation is calculated with respect to all species $i$ in a single realization of the process. (e) Unavailable species (crosses) act as obstacles for growth. The distribution of segment sizes between unavailable species depends on the probability that species are unavailable. (f) Illustration of the assembly paths into structures with different numbers of "growing ends". If structures grow by attachment of monomers of an available species, the number of growing ends either stays the same or decreases by one. (g) Prediction for the steady-state probability $p_l$ that a structure that grows to size $l$ ends up in a state where it can grow by attachment of monomers of available species. This probability depends on the number $S_\times$ of unavailable species. The relevant parameters are $L = 60$ and $L_\times = (L/S)S_\times = 5$ (red circles), $L_\times = 10$ (yellow triangles), $L_\times = 20$ (green stars) and $L_\times = 20$ (blue squares). (h) In the effective theory, structures can be either in a state where both neighboring species are unavailable ("blocked") or in a state where at least one neighbor is available ("growing"); see also (a). Structures in the blocked state can only grow once an unavailable species is activated, whereas structures in the growing state can also grow by available species. Over time, the number of unavailable species changes. As a result, structures can change from being blocked to being able to grow or vice versa.

picture with the goal to capture the stochastic limit, will thus require to reconsider this assumption. In the next subsection, we will motivate our particular choice for extending the deterministic description.

### B. Effective description of the stochastic system as one-species problem

A fully stochastic description of our system would require a high-dimensional master equation, including all

possible structure configurations (lengths and compositions). Such a master equation is not very revealing *per se* since it reflects the complexity of the dynamics one-to-one. However, by finding an (effective) representation in a lower-dimension space, one can hope to get important insights into which features of the full process are crucial for the dynamics and which are not. A typical approach for finding such a lower-dimensional representation are moment-closure techniques [53]. For this purpose, one derives a hierarchy of equations that relates the different moments to each other. For large systems with many interacting elements, this hierarchy is typically extensive and it is necessary to define a closure relation that truncates the hierarchy. In the simplest case, only the first moment (i.e. the average) is taken into account while all correlations are neglected. Implementing this procedure rigorously [46] leads to the deterministic description, Eqs. 3 and 4. We tried to refine this closure relation by considering second-order moments. However, due to the large number of combinatorial possibilities, there is no canonical choice for the closure relation and we did not succeed to define a reasonable one. Is there another possibility to effectively reduce the high-dimensional system to a lower-dimensional space? Potentially yes, at least if one assumes that only demographic fluctuations in the relative number of active monomers between species but not reaction noise are crucial. In this case, it might not be necessary to resolve the exact composition of the structures. Instead one could try to classify structures into two different states per given size of a structure: one for structures which currently cannot grow due to a lack of neighboring particles ("blocked polymers") and one for the structures that can grow by monomer attachment of neighboring species ("growing polymers"); see Fig. 3 (a) for an illustration. In that way, the description is still "close" to the deterministic description in the sense that only an additional state has to be introduced. If this were successful, it would reduce the original set of $(L+1)\times S$ ordinary, stochastic differential equations [54] to a system of $2(L+1)$ ordinary differential equations (see also below for details) compared to $L$ in the deterministic case (Eqs. 3 and 4).

Of course, to formulate such an effective theory it is necessary to define more precisely what we mean by "blocked" and "growing polymers". To do this and to develop a good intuition for the system, in the next section, we will look more closely at the system's properties and, in particular, the variations between species.

### C. Origin of stochastic yield catastrophe: Inter-species variability and "unavailable species"

As mentioned above, intuitively, fluctuations in the availability of the different species can lead to undesirable nucleation events or defect formation if the species necessary for correct growth are currently unavailable for binding. So, how distinct is the availability of the different species? Or, more concretely, how much do the numbers of activated particles $A_i$ of the different species vary compared to each other and compared to the mean value $\bar{A}=\sum_i A_i/S$? Fig. 3(a) shows the deviation $\delta A_i = A_i - \bar{A}$ of the number of activated particles for all species (colors) relative to their mean value, as measured in one single stochastic simulation with parameters $L=60$ and $N=100$. The deviation is plotted against the average number of activation events per species $\bar{A}$ (which is a monotonic function of time). As expected, the deviation is zero at the beginning ($\bar{A}=0$) and at the end ($\bar{A}=N$) since then no particles of either species or all particles of all species are activated, respectively. In between these two limits, it attains values of typically 2-3 % of the total number of particles per species $N$. This value can be understood analytically: There are $N$ particles of each species and $NS$ particles in total. Furthermore, if the average number of activation events per species is $\bar{A}$, in total $S\bar{A}$ activation events have happened. Thus, since activation of particles occurs independently for all particles and species, the number of activated particles of one species $A_i$ is determined by the following random process: Take $S\bar{A}$ random draws without replacement from a population of size $SN$ that contains $N$ "successes" (particles of species $i$). The distribution corresponding to this random process is called hypergeometric distribution [55] with parameters $SN$, $N$ and $S\bar{A}$:

$$A_i \sim \mathrm{HypGeo}(SN, N, S\bar{A}). \tag{5}$$

Its variance is given by

$$\mathrm{Var}_0 = \bar{A}\left(1-\frac{1}{S}\right)\left(1-\frac{\bar{A}}{N}\right)\frac{NS}{NS-1} \approx \bar{A}\left(1-\frac{\bar{A}}{N}\right), \tag{6}$$

where the approximation is valid for large $S$. As a result, the standard deviation is maximal when half of the particles have been activated on average, $\bar{A}=N/2$, with a value of $\sqrt{N}/2$ which is roughly 11 (or 2.2 %) for $N=500$.

Since the average number of particles per species $\bar{A}\propto N$, this scaling of the variance shows that the fluctuations in the relative particle number of the different species are indeed of the order $1/\sqrt{N}$ compared to the total number of particles $N$ per species. As mentioned above, this scaling is expected for demographic noise. But how can these order $1/\sqrt{N}$ fluctuations have such a strong effect even for large $N$? There are several possible reasons: First, the dynamics of the process triggers a kind of reinforcing effect ("snowball effect") where the effect of fluctuations gets amplified due to the dynamics it causes itself. If fluctuations at the beginning of the dynamics result in too many nucleation events, too many structures form. In the worst case, none of these structures is then completed due to competition for resources. So, a small fluctuation in the beginning has a large effect on the outcome and whether a fluctuation changes the self-assembly process considerably is thus history- and time-dependent. This dependence on time is amplified even more since the population size is non-constant. As a result, it is

not necessarily the standard deviation compared to the total number of particles $N$ that is relevant for the process but rather the standard deviation compared to the mean number of activated particles, $\bar{A}$. So, the quantity to look at is not $\mathrm{Var}_0/N^2 = \bar{A}\,(1-\bar{A}/N)/N^2$ but rather the coefficient of variation,

$$CV^2 = \frac{\mathrm{Var}_0}{\bar{A}^2} = \frac{\bar{A}(1-\bar{A}/N)}{\bar{A}^2} = \frac{1-\bar{A}/N}{\bar{A}}\,. \qquad (7)$$

This coefficient of variation is indeed very large at the beginning (it diverges for $\bar{A} \to 0$ due to the zero mean), suggesting that in particular at the beginning, there can be too many undesirable nucleation events. In conclusion, the effect of fluctuations is strongly time- and history-dependent.

In this section, we tried to motivate our approach to extend the deterministic description of the self-assembly process by its "essential" ingredients. It is based on the idea that it is mainly the demographic noise that is decisive for the dynamics of the assembly process. So, inspired by the species symmetry in the deterministic description, we assume that it is not necessary to keep track of all possible configurations of structures but that it is sufficient to characterize structures only in terms of whether they can grow by monomer attachment or whether they are blocked due to unavailable species. The probabilities to be in either state are expected to depend on the variability between species which is quantified by the distribution of the number of active particles, Eq. 5. We will revisit this distribution when we set up the effective theory in the next section.

## IV. EFFECTIVE THEORY: QUANTIFICATION

The goal of this section is to make the effective theory for the model in Fig. 1 explicit. As we formulate the theory, we also try to give an answer to the following questions: How does variability between species influence the dynamics of the assembly process? How does a species that is currently not available for binding alter the self-assembly dynamics?

We will proceed as follows: First, we introduce some terminology (Sec. IV A) that will make the formulation of the effective theory more convenient; see also Fig. 3 (a). Next, we determine the probability of species $i$ to be currently unavailable for binding; for a precise definition see Sec. IV A and Fig. 3 (a). This can be due to low activation of species $i$ itself or due to high activation of the neighboring species $i \pm 1$ and thus a high likelihood for species $i$ to be bound to these neighboring species on both sides already; for instance, species 6 in Fig. 3 (a) has been activated less than average and, at the same time, its neighbors, species 5 and 1, have been activated more than average. From the probability of being unavailable for binding and the corresponding number of "unavailable species" we then determine the probability for a structure to be able to further grow, depending on the length of the structure. Finally, we write down an *effective one-species theory* for the polymer-size distribution that considers two states, one "blocked" and one "growing" state for each polymer size (for a precise definition see Sec. IV A; in Fig. 3 (a) the polymer 3-4-5 is blocked because there is neither an active monomer of species 2 nor one of species 6 whereas 3-4 can grow by attachment of an active monomer of species 5). A reader not interested in the mathematical details is referred to Sec. IV F for a summary.

### A. Terminology

To begin with we define some terminology that will be useful in formulating the effective theory; for an illustration see also Fig. 3(a):

- "*Monomers*" denote particles that are not bound to any other particle, yet.
- "*Edge particles*" are defined as particles attached to either end of unfinished polymers, e.g. particles of species 5 and 2 in the polymer 5-6-1-2.
- In contrast, "*bulk particles*" are defined as those particles that are part of a larger polymer but are not edge particles, e.g. particles of species 2, 3 and 4 in the polymer 1-2-3-4-5.
- "*Growing polymers*" in a given system are defined as those polymers that have available binding partners in the pool of active monomers which (upon binding to the polymer) lead to the correct assembly of the structure, without creating a defect, e.g. polymer 3-4 to which active monomer 5 could bind to.
- "*Blocked polymers*", on the other hand, are those polymers in the system that lack correct binding partners in the monomer pool, e.g. polymer 3-4-5 can only grow by attachment of an active monomer which is out-of-sequence and would create a defect (monomer of species 1) since there are no active monomers of species 2 or 6 available.
- Finally, we denote a species as "*unavailable*" if it is currently not available for binding to any structure (monomer or polymer) in the system. For this to be the case two conditions need to be fulfilled: First, there is no active monomer of that species present. Second, there are no edge particles of that species. If there are neither active monomers nor edge particles, all activated particles are bulk particles and, thus, already have binding partners on both sides. Hence, in this case there are currently no processes possible that would lead to further binding of a particle of an unavailable species to another monomer

or polymer. Note that this definition does not necessarily imply that the unavailable species has not been activated, at all, but rather that its activation is small compared to its neighboring species (see also below) and, as a result, it is not available for binding (any more).

### B. Probability for the unavailability of species

How do fluctuations in the relative number of particles of the different species translate into species currently not being available for binding? To address this question, we will employ a fluctuation-corrected mean-field argument in the following: Denote by $N_i^{(b)}$ the number of particles of species $i$ a neighboring species can bind to. This number has two contributions, namely the edge particles and active monomers of this species. Deterministically, the number of edge particles per species is given by $2\,u$ where

$$u = \sum_{k=2}^{L-1} c_k \tag{8}$$

is the total number of all unfinished polymers (of size $k \in \{2, \ldots, L-1\}$) per species. The reason is that each unfinished polymer has two ends, implying that there are in total $2\,S\,\sum_{k=2}^{L-1} c_k$ edge particles or on average $2\,\sum_{k=2}^{L-1} c_k$ per species. As a result, deterministically (i.e. in a mean-field description) $N_i^{(b)}$ is given by

$$\bar{N}_i^{(b)} = 2\,u + m^a \tag{9}$$

where $m^a$ is the number of active monomers per species. Due to the species symmetry in the deterministic mean-field description [46], this result is independent of the species index $i$.

This will not be the whole story in a stochastic description since fluctuations in the activation of the different species are expected to influence the number of active monomers and edge particles of the different species. Heuristically, if species $i$ is activated less (more) than average, there will be less (more) active monomers and/or edge particles, so $N_i^{(b)}$ will be smaller (larger). To quantify this heuristic picture, we apply a fluctuation-corrected mean-field argument which conceptually corresponds to a lowest-order perturbation theory in the fluctuations: We assume that $N_i^{(b)}$ increases (decreases) by 1 for each particle that species $i$ is activated more (less) than average. That is, $N_i^{(b)}$ has an additional term

$$\delta A_i = A_i - \bar{A}, \tag{10}$$

where $A_i$ is the number of activated particles of species $i$ and $\bar{A} = \sum_i A_i/S$ is the average over all species, as above. The idea is that each additionally activated particle is either present as an active monomer or bound to a polymer as an edge particle. Conversely, if one had to remove one particle of one species from a mean-field configuration with the goal to change "as little as possible", one would remove an active monomer or an edge particle. Removing or adding an edge particle also changes the number of edge particles of the neighboring species. Thus, $N_i^{(b)}$ is also affected by the activation levels of the neighboring species $i\pm1$. For simplicity, we assume that each additionally (less) activated particle of one of the neighboring species reduces (augments) the number of edge particles or the number of active monomers of species $i$ by 1 [56]. Thus, from this direct dependency of the number of edge particles of species $i$ on the activation levels of the neighboring species $i \pm 1$, $N_i^{(b)}$ gets reduced by

$$-(\delta A_{i+1} + \delta A_{i-1}). \tag{11}$$

Taken together, we find the following fluctuation-corrected mean-field expression for the number of active monomers and edge particles of species $i$

$$\begin{aligned} N_i^{(b)} &= 2\,u + m^a + \delta A_i - (\delta A_{i+1} + \delta A_{i-1}) \\ &= 2\,u + m^a + \bar{A} + A_i - (A_{i+1} + A_{i-1})\,. \end{aligned} \tag{12}$$

In principle, this expression can become negative. This is an artefact of the above mentioned procedure which *per se* only makes sense for small fluctuations with respect to the mean-field configuration. We elaborate on this point in the following: In a mean-field configuration, the number of particles of species $i$ a neighboring species can bind to is given by $N_i^{(b)} = \bar{N}_i^{(b)} = 2\,u + m^a$. Decreasing the activation level of species $i$, $A_i$, or increasing the levels of $i\pm1$, $A_{i\pm1}$, will effectively remove active monomers and edge particles of species $i$, thus decreasing $N_i^{(b)}$. Of course, if at all, this procedure only makes sense until there are no more active monomers and edge particles of species $i$ left: $N_i^{(b)} = 0$. Further reduction of $A_i$ or increase $A_{i\pm1}$ will certainly also affect the bulk particles of species $i$, potentially "breaking up" larger polymers. Then, we formally have $N_i^{(b)} < 0$. Intricately, it is exactly this tail statistics when formally $N_i^{(b)} < 0$ that is presumably most relevant for the strength of the stochastic effects: As soon as fluctuations are large enough to trigger a qualitatively different growth behavior ("breaking up larger polymers"), strong stochastic effects are expected. Since it appears infeasible to us to derive this tail statistics from first principles, we try to gauge its effect through the probability that $N_i^{(b)} \leq 0$. More concretely, we use this "lowest-order perturbation theory procedure" and its prediction of the transition from $N_i^{(b)} > 0$ to $N_i^{(b)} \leq 0$ as a proxy for when a species qualitatively changes the growth behavior of the neighboring species because it is unavailable for binding.

In this picture, the probability of species $i$ to be unavailable ("unavailability probability") is

$$\begin{aligned} p_\times &= \mathrm{Prob}(N_i^{(b)} \leq 0) \\ &= \mathrm{Prob}(A_{i+1} + A_{i-1} - A_i - \bar{A} \geq 2\,u + m^a). \end{aligned} \tag{13}$$

Does this formula for the probability meet the intuitive criteria for when a species should be unavailable? Which characteristics should such a probability of species $i$ to be currently unavailable for binding have intuitively? First, it should increase if species $i$ has been activated less than average because then it is likely that the species is unavailable for binding. Indeed, the smaller $A_i$, the larger $p_\times$ according to Eq. 13. Moreover, if the neighboring species $i\pm1$ are present in excess, they also effectively reduce the number of active monomers and edge particles of species $i$ by binding to them. Thus, the probability for species $i$ to be unavailable should increase. Also this correlation is reflected in Eq. 13: The larger $A_{i+1}+A_{i-1}$, the larger $p_\times$. Finally, if the average number of unfinished structures and active monomers, $2\,u+m^a$, increases, the probability to be unavailable should decrease. This is because then the deviation from the mean and, thus, the fluctuations must be larger. In fact, for larger $2\,u+m^a$ in Eq. 13, the unavailability probability $p_\times$ decreases. In sum, the effective probability given in Eq. 13 at least captures our intuitive expectations.

In order to find an explicit expression for $p_\times$ from Eq. 13, we next determine the distribution of the number of activated particles, $A_i$, up to time $t$. For each particle the survival probability up to time $t$, i.e. the probability not to become activated until time $t$, is given by $e^{-\alpha t}$. Thus, since all particles are activated independently, the number of activated particles of species $i$ is binomially distributed with number of trials $N$ and probability $1-e^{-\alpha t}$:

$$A_i \sim \mathrm{Bin}(N, 1-e^{-\alpha t}). \tag{14}$$

The variance of this distribution ("single-species variance") is given by

$$\sigma_0^2 = N\,(1-e^{-\alpha t})\,e^{-\alpha t}\,. \tag{15}$$

Moreover, the number of activated particles of each species is independent for all species, that is, the $A_i$ are independent for all $i$. As a result, the fluctuations in the relative activation levels between neighboring species $\Delta A_i^{\mathrm{neighbor}} := A_{i+1}+A_{i-1}-A_i-\bar{A}$ exhibit a variance

$$\sigma^2 \approx 3\sigma_0^2. \tag{16}$$

Note that here we assumed $\bar{A}$ to be deterministic: $\bar{A}=N(1-e^{-\alpha t})$ which is a reasonable assumption if $S\gg1$. Interestingly, this predicted standard deviation of $\Delta A_i^{\mathrm{neighbor}}$,

$$\sqrt{3}\sigma_0 = \sqrt{3N(1-e^{-\alpha t})e^{-\alpha t}}\,, \tag{17}$$

already captures the standard deviation in a *single* realization of the stochastic process when averaged over all species $i$ quite well; see Fig. 3(d). This observation indicates that the system is self-averaging, at least for large numbers of species $S\gg1$. Such a self-averaging property of the system is reassuring because this whole idea for the quantification of the effective theory is based on a (fluctuation-corrected) mean-field argument that should ultimately capture the typical behavior of single realizations of the self-assembly process. If there would not be any "internal averaging" in a single realization, there would not be much hope that the fluctuation-corrected mean-field argument for the unavailability probability, Eq. 13, is informative.

Combining all of the above and approximating the distribution of $\Delta A_i^{\mathrm{neighbor}}$ as a Gaussian distribution with mean zero and standard deviation $\sigma$, Eq. 16, we find the following expression for the probability of species $i$ to be unavailable:

$$\begin{aligned} p_\times &= \mathrm{Prob}(\Delta A_i^{\mathrm{neighbor}} \geq 2u+m^a) \\ &= \frac{1}{2}\left[1-\mathrm{erf}\left(\frac{2u+m^a}{\sqrt{6}\sigma_0}\right)\right], \end{aligned} \tag{18}$$

where erf is the error function.

This equation makes sense intuitively: If there are on average more active monomers and edge particles per species (larger number of unfinished structures $2u+m^a$), larger fluctuations are required to find a species without active monomers and edge particles. As a consequence, the probability of a species to be unavailable for binding decreases.

So far, we only considered a single species and asked what the probability is that this particular species is unavailable. For the dynamics of the self-assembly process it is, however, relevant to know *how many* species are unavailable, since this determines which fraction of structures can grow. It is a nontrivial problem to determine the overall number of unavailable species from the single-species probability, due to correlations between species. For simplicity, we neglect these correlations and assume that the probability for species to be unavailable is independent for all species [57]. Then, the number of unavailable species scales with the number of species and is given by

$$S_\times = S\,p_\times = \frac{S}{2}\left[1-\mathrm{erf}\left(\frac{2u+m^a}{\sqrt{6}\sigma_0}\right)\right]. \tag{19}$$

If the number of species $S$ does not equal the size of the target structure $L$ ($S<L$) it is useful to also define the number of "unavailable sites" in the full ring structure,

$$L_\times = \frac{L}{S}S_\times = \frac{L}{2}\left[1-\mathrm{erf}\left(\frac{2u+m^a}{\sqrt{6}\sigma_0}\right)\right]. \tag{20}$$

This number does not equal the number of unavailable species if each species occurs repeatedly in the ring, i.e. if $L/S>1$. Each unavailable species, thus, has to be associated with $L/S$ unavailable sites along the ring.

### C. Size-dependent probability for a growing polymer to be able to further grow

Suppose there are $S_\times$ unavailable species and, correspondingly, $L_\times$ unavailable sites along the ring. What is

the probability $p_l$ that a structure that has reached size $l \in \{2, \dots, L-1\}$ can further grow by attachment of an available species? To answer this question, let us look at segments of size $l$ (Fig. 3(e-f)). These segments can be in three states: i) available species can bind to both ends (denoted by $S_2^l$; two "growing" ends), ii) an available species can bind to one end, whereas the other end would require an unavailable species to grow ($S_1^l$; one "growing" end, one "blocked" end), and iii) both ends require an unavailable species to grow and are, correspondingly, blocked by the unavailability of the neighboring species ($S_0^l$; two "blocked" ends).

What are the abundances of these states, denoted by $s_2^l$, $s_1^l$ and $s_0^l$, respectively? And what do the (relative) abundances tell us about the probability that a structure that has reached size $l$ can grow further by attachment of available species?

We will proceed as follows: First, as illustrated in Fig. 3(f), we define a simplified assembly process that is supposed to reflect the original assembly process in a stationary state in which the number of unavailable sites $L_\times$ is fixed. For this simplified assembly process, we then derive effective transition probabilities and determine the steady-state configuration by considering all possible assembly/growth paths into a structure of size $l$ in state $S_j^l$, $j = 0, 1, 2$. Finally, this configuration will be used to determine the probabilities $p_l$ that a structure which has grown to size $l$ ends up in state where it has at least one growing end.

### 1. *Simplified assembly process*

Assuming for simplicity that structures only grow by attachment of available species, in the simplified assembly process, we consider the following transitions between structures of different sizes (see also Fig. 3(f)):

$$S_2^l \xrightarrow{\alpha_{22}^l} S_2^{l+1}\,, \tag{21a}$$

$$S_2^l \xrightarrow{\alpha_{21}^l} S_1^{l+1}\,, \tag{21b}$$

$$S_1^l \xrightarrow{\alpha_{11}^l} S_1^{l+1}\,, \tag{21c}$$

$$S_1^l \xrightarrow{\alpha_{10}^l} S_0^{l+1}\,. \tag{21d}$$

Here, $\alpha_{ij}^l$ denotes the transition rate from a structure of size $l$ and state $i$ to size $l+1$ and state $j = i$ or $j = i-1$. The basic idea to just consider these transitions in the simplified assembly process depicted in Fig. 3(f) is as follows: Available species only bind to so-called "growing" ends of structures. If an available species binds to a growing end of a structure $S_2^l$ or $S_1^l$ of size $l$, this growing end is replaced by a new end in the structure of size $l+1$, namely the subsequent species. This new end can be either growing (if another available species could subsequently bind) or blocked (if the next required species for growth is an unavailable species). Thus, by binding of an available species, the number of growing ends either stays the same or decreases by 1 but can never increase. As a result, there are only transitions between $S_i^l$ and $S_i^{l+1}$, $S_{i-1}^{l+1}$ for $i = 1, 2$.

Note that the simplified assembly process assumes that unavailable species are not present at all (instead of being present as bulk particles). Correspondingly, the transition rates $\alpha_{ij}^l$ automatically entail that all structures in the simplified assembly process are made up from available species only. Certainly, this is not satisfied in the original assembly process. Unfortunately, however, we were not successful in incorporating this aspect directly into the simplified assembly process, for instance, by additionally considering the possibility that blocked structures grow at a reduced rate (corresponding to activation events of unavailable species). One reason is that it was not clear to us how one should choose such a reduced rate in comparison to the other transition rates. Furthermore, even with a given reduced rate, we did not manage to derive an analytic expression for the probabilities $p_l$ that a structure that has grown into size $l$ can grow further, which is what we need to formulate the effective theory (see later). This effective theory will then indeed include the aspect that the number of available species changes over time but will be based on the quasi-stationary approximation of a fixed number of unavailable species $L_\times$ in the simplified assembly process. It will turn out that the fact that structures in the simplified assembly process only contain available species leads to a strict length cutoff in the dynamics above which there is no growth at all. We will come back to this point at the end of the section when we compare the predictions of the effective theory to results from stochastic simulations.

### 2. *Transition rates*

In order to determine the transition rates explicitly, consider a structure of size $l$ with two available species next to both ends (two growing ends). For such a structure, there are $\binom{L-(l+2)}{L_\times}$ possibilities to distribute the $L_\times$ unavailable sites to the $L-(l+2)$ remaining sites on the ring. This number of possibilities decreases to $\binom{L-(l+3)}{L_\times}$ possibilities if the structure grows in a way that after growth there are still two growing ends. As a result, if the unavailable species (and sites [58]) are randomly distributed around the ring, the probability that this happens is $\binom{L-(l+3)}{L_\times}/\binom{L-(l+2)}{L_\times}$. Correspondingly, the probability that the structure grows into a structure with one growing and one blocked end is $1 - \binom{L-(l+3)}{L_\times}/\binom{L-(l+2)}{L_\times}$. Translating this probability into a transition rate yields $2\gamma(1 - \binom{L-(l+3)}{L_\times}/\binom{L-(l+2)}{L_\times})$ where $\gamma$ corresponds to the total rate of attachment of an active monomer of an available species to one end. The factor of 2 is due to the fact that the rate that a monomer binds to a structure with two growing ends is twice as large as the rate that it binds to a structure with one growing end. Employing an

analogous argument for structures with one growing and one blocked end, we find the following transition rates (see Appendix for details)

$$\alpha_{22}^l = 2\gamma \frac{\binom{L-(l+3)}{L_\times}}{\binom{L-(l+2)}{L_\times}} = 2\gamma\left(1 - \frac{L_\times}{L-(l+2)}\right) = 2\gamma - \alpha_{21}^l, \tag{22a}$$

$$\alpha_{11}^l = \gamma \frac{\binom{L-(l+3)}{L_\times-1}}{\binom{L-(l+2)}{L_\times-1}} = \gamma\left(1 - \frac{L_\times - 1}{L-(l+2)}\right) = \gamma - \alpha_{10}^l. \tag{22b}$$

To determine the steady-state configuration of the simplified assembly process, we do not only need the transition rates between the states in the network but we also have to define a boundary condition which specifies at which rates ("influx rates") active monomers enter the system at the left boundary $l = 1$. For this purpose, we will denote by $i_2$, $i_1$ and $i_0$ the influx of active monomers that can grow at both ends (corresponding to state $s_2^1$), at only one end ($s_1^1$) and at no end ($s_0^1$), respectively. The total influx of active monomers $I = i_2 + i_1 + i_0$ is not crucial for the growth probabilities because it just scales the occupancy in the network and will drop out at the end. What is relevant are the relative influx rates for the different states. Similarly to above, the explicit forms we use come from considering the probabilities for a random monomer of an available species to have two, one or zero available neighbors, respectively: If the monomer has two available neighbors, there are $\binom{L-3}{L_\times}$ possibilities to distribute the remaining unavailable sites along the ring. For one or zero available neighbors, the number of possibilities are $2\binom{L-3}{L_\times-1}$ and $\binom{L-3}{L_\times-2}$, respectively. If the unavailable sites are randomly distributed around the ring, the influx rates have to scale with exactly these numbers of possibilities and we get

$$i_2 = \binom{L-3}{L_\times} I\,, \tag{23a}$$

$$i_1 = 2\binom{L-3}{L_\times-1} I\,, \tag{23b}$$

$$i_0 = \binom{L-3}{L_\times-2} I\,. \tag{23c}$$

### 3. *Steady-state configuration and growth probabilities*

From the influx rates, Eq. 23, and the transitions rates, Eq. 21, one can determine the steady-state numbers $s_j^l$ of structures of size $l$ with $j = 1, 2$ growing ends (see Appendix B). How is the probability $p_l$ that a structure that grows into size $l$ has at least one growing end expressed in terms of these steady-state numbers? It is given as the ratio of (1) the rate $\gamma_1$ at which structures of size $l-1$ grow into structures of size $l$ that are still able to further grow by attachment of an available species compared to (2) the overall rate $\gamma_2$ at which structures of size $l-1$ grow into structures of size $l$:

$$p_l = \frac{\gamma_1}{\gamma_2}. \tag{24}$$

$\gamma_2$ has two contributions, namely the rate at which a monomer of an available species attaches to any structure of size $l-1$ with one growing end, $(\alpha_{11}^{l-1}+\alpha_{10}^{l-1})s_1^{l-1}$, and the corresponding one for attachment to a structure with two growing ends $(\alpha_{22}^{l-1}+\alpha_{21}^{l-1})s_2^{l-1}$. According to Eq. 22, $\alpha_{11}^{l-1}+\alpha_{10}^{l-1} = \gamma$ and $\alpha_{22}^{l-1}+\alpha_{21}^{l-1} = 2\gamma$, so we find

$$\gamma_2 = (\alpha_{11}^{l-1} + \alpha_{10}^{l-1})s_1^{l-1} + (\alpha_{22}^{l-1} + \alpha_{21}^{l-1})s_2^{l-1} \tag{25}$$

$$= \gamma(s_1^{l-1} + 2s_2^{l-1}). \tag{26}$$

$\gamma_1$ only counts the growth events for which the resulting structure is still able to grow by attachment of an available species (at least at one end). Correspondingly, it has the same contributions as $\gamma_2$ except that is does not include the transition $s_1^{l-1} \to s_0^l$ which produces a structure that cannot grow further. Compared to $\gamma_2$ the rate is thus reduced by $\alpha_{10}^{l-1}s_1^{l-1}$ and we have

$$\gamma_1 = \alpha_{11}^{l-1}s_1^{l-1} + (\alpha_{22}^{l-1} + \alpha_{21}^{l-1})s_2^{l-1} \tag{27}$$

$$= \alpha_{11}^{l-1}s_1^{l-1} + 2\gamma s_2^{l-1}. \tag{28}$$

It follows that

$$p_l = \frac{\alpha_{11}^{l-1}s_1^{l-1} + 2\gamma s_2^{l-1}}{\gamma s_1^{l-1} + 2\gamma s_2^{l-1}}\,. \tag{29}$$

Combining the above and using $\gamma - \alpha_{11}^{l-1} = \alpha_{10}^{l-1}$ yields the following expression for the probability $p_l$ that a structure that has reached size $l$ can grow further by attachment of available species:

$$p_l = 1 - \frac{\alpha_{10}^{l-1}}{\gamma}\ \frac{s_1^{l-1}}{s_1^{l-1} + 2s_2^{l-1}} \tag{30}$$

Finally, and as explained in detail in Appendix B, considering all possible assembly/growth paths to determine $s_j^l$ gives an explicit expression of $p_l$

$$p_l = \begin{cases} 1 - \frac{lL_\times(L_\times-1)}{[L-(l+1)]\,[L+(l-1)L_\times-l]}\,, & l < L - L_\times \\ 0 & \text{else,} \end{cases} \tag{31}$$

if $L_\times > 1$. Otherwise, $p_l = 1$ for all $l$.

Figure 3(g) shows $p_l$ as a function of the structure size $l$ for a ring size $L = 60$ and for different, fixed numbers of unavailable sites $L_\times = 5$, $L_\times = 10$, $L_\times = 20$, and $L_\times = 30$. Intriguingly, $p_l$ decreases for larger structure size $l$, implying that it becomes increasingly difficult for structures to grow further once they get larger. This suggests that unavailable species foster growth of small structures compared to large ones, which, generally speaking, leads to lower yield.

In closing this section, we would like to critically assess the validity of the simplified assembly process. First,

we assumed that always the same species are unavailable for binding. As can be seen in Fig 3(c) this assumption that always the same species are unavailable describes the right trend: If a species has a very low activation level compared to the mean at one point in time $t_0$, it is more likely to still have a very low activation level later, as compared to a species with high activation level at $t_0$. However, it is also evident from the figure that this statement is not strictly true. Indeed, there are species that have an average activation level at first but then over time change to having a low activation level compared to the mean and become unavailable for binding. Related to the first assumption, we furthermore hypothesized that these unavailable species are entirely unavailable, meaning that they are not incorporated in any structure. As a result, only structures of size $l \leq L - L_\times - 1$ can grow and the growth probability is identical to zero for all other structures. This assumption cannot be quite true since unavailable for binding only refers to not being present as active monomer or as edge particles but not to being absent completely. Nonetheless, from comparison of this theory with stochastic simulations it seems that ultimately this is a reasonable approximation for understanding the qualitative behavior (see Sec. V).

### D. Two-state ansatz

The probability $p_l$ determined in the last section represents the probability that a *specific* polymer that has *just* reached size $l$ is able to grow further by monomer attachment of available species, i.e. has at least one growing end when it has reached size $l$. This probability is, however, *not* the same as the fraction of structures of size $l$ that has at least one growing end. The reason is a bit subtle and has to do with what we condition on.

In the way we determined $p_l$ in the previous section (Eq. 31), it corresponds to the probability that a *specific* structure that has *just* grown from size $l-1$ to size $l$ is in a state with at least one growing end, i.e. is (in the terminology of the previous section) in state $S^l_{i=1}$ or $S^l_{i=2}$. We, thus, condition on the fact that the specific structure *just grows* from size to $l-1$ to $l$. We could also have looked at the fraction $f_l = (S^l_{i=1} + S^l_{i=2})/(S^l_{i=0} + S^l_{i=1} + S^l_{i=2})$ of structures of size $l$ in a state with one or two growing ends, $S^l_{i=1}$ or $S^l_{i=2}$, as compared to a state with two blocked ends, $S^l_{i=0}$. This fraction $f_l$ would describe the probability that a *randomly picked* structure *of size* $l$ can, in principle, grow. Hence, $f_l$ would correspond to conditioning the probability on the fact that the structure *has* a size $l$ (irrespective of when it reached this size).

These two probabilities $p_l$ and $f_l$ are, in general, not the same. The reason is that structures of size $l$ with at least one growing end continue to grow while the structures of size $l$ with no growing end accumulate. As a result, over time the number of structures of size $l$ that cannot grow increases compared to the one of size $l$ that can grow. This can be seen very nicely in the simplified assembly process mentioned in the previous section: Indeed, $f_l$ would be ill-defined there because there is a continuous influx of monomers and the states $S^l_0$ would get more and more populated. In contrast, the numbers of structures in the states $S^l_{1,2}$ converge to a steady-state value because there is not only influx into these states but also outflux from them (due to the growth of structures).

Taken together, the probabilities $p_l$ determined in Eq. 31 do not correspond to the fraction of structures of size $l$ that can grow.

As a result, if there are now $c_l$ structures of size $l$, one cannot conclude that a fraction $p_l$ of those grows by monomer attachment and, correspondingly, that there are $p_l \cdot c_l$ structures of size $l$ (per species) available for binding.

One approach to resolve this issue would be to try to determine the momentary fraction $f_l$ of structures of size $l$ that can grow. Since, however, many factor would influence how exactly $f_l$ should change over time (including the growth dynamics itself!), we chose an alternative approach: Instead of treating all structures of a certain size as one "population" – as one does in a mean-field description [46] – we introduce two populations $G_l$ and $B_l$ (for growing and blocked) with corresponding concentrations $g_l$ and $b_l$ (Fig. 3(h)). The first population $G_l$ includes all structures that grow by attachment of monomers of available species (i.e. those with at least one growing end), whereas $B_l$ denotes those that are blocked (meaning they only grow if currently unavailable species get activated).

The respective probabilities of these populations correspond to the growth probabilities $p_l$ determined in Eq. 31 which quantify how likely it is that a structure that has just reached size $l$ can grow further by attachment of an available species. Thus, if a structure of size $l-1$ grows to size $l$, with probability $p_l$ it ends up in $G_l$ and with probability $1-p_l$ in $B_l$:

$$G_{l-1} \longrightarrow \begin{cases} G_l & \text{with probability } p_l \\ B_l & \text{with probability } 1-p_l. \end{cases} \tag{32}$$

If now structures in $G_l$ grow, this does not influence the population $B_l$ and there is no need to determine a momentary fraction $f_l$ of structures that can, in principle, grow.

Due to activation and binding events, the number of unavailable species $S_\times$ and thus $p_l$ (Eq. 31) change over time. If the number of unavailable species increases, structures previously in the growing state might get blocked and, vice versa, if the number of unavailable species decreases, structures that were in the blocked state might transition to the growing state. As a result, there has to be an exchange between the populations $G_l$ and $B_l$ if $\mathrm{d}S_\times/\mathrm{d}t \neq 0$. In order to formulate the effective theory, it is necessary to quantify this exchange. For this purpose, we define the flux between the two states $B_l$ and $G_l$ as the number of structures that transition from $B_l$ to $G_l$ per time. How does this flux depend on the derivative of the probability $p_l$, $\mathrm{d}p_l/\mathrm{d}t$?

Since this dependency is not entirely intuitive, we consider a much simpler system first. In this simpler system, it is straightforward to derive the fluxes and the resulting formulas for the fluxes can then be generalized for our purpose. Consider a system with $N$ particles where each can be in either of two states, with $p(t)$ denoting the fraction in state $g$ at time $t$: Then we have

$$N_g(t) = Np(t)\,, \text{ and } N_g(t+\Delta t) = Np(t+\Delta t)\,. \quad (33)$$

Consequently,

$$N_g(t+\Delta t) - N_g(t) = N_g(t)\,\frac{p(t+\Delta t) - p(t)}{p(t)}\,, \quad (34)$$

and hence

$$\frac{\mathrm{d}N_g(t)}{\mathrm{d}t} = N_g \frac{\mathrm{d}\ln p(t)}{\mathrm{d}t} = (N_g - N)\,\frac{\mathrm{d}}{\mathrm{d}t}\ln\left(1-p(t)\right), \quad (35)$$

where we used $(N - N_g)/(1 - p) = N - N_g/p$ in the last step. Equation 35 implies that the per-capita rate of exchange between the two states is not equal to the change in probability but rather to the change in the logarithm of the probability. Intuitively, in order for the probability $p$ to change by a fixed value, always the same number of particles has to transition from one state to the other, irrespective of the number of particles in the original state. As a result, if the number of particles was high (low) in the original state, a small (large) fraction of them needs to be exchanged.

In our system, there are not only two states but particles can transition between different states (growing/blocked and different polymer sizes). Nonetheless, the exchange dynamics relative to the number of particles in each state should be the same as in the simple system. Thus, the fluxes between the "growing" $G_l$ and "non-growing/blocked" $B_l$ populations (i.e. the number of structures that transition from $B_l$ to $G_l$ per time) are given by

$$J_l^{B\to G} = -J_l^{G\to B} = \begin{cases} g_l \frac{\mathrm{d}}{\mathrm{d}t}\log p_l & \text{if } \frac{\mathrm{d}p_l}{\mathrm{d}t} < 0 \\ -b_l \frac{\mathrm{d}}{\mathrm{d}t}\log(1-p_l) & \text{if } \frac{\mathrm{d}p_l}{\mathrm{d}t} > 0. \end{cases} \quad (36)$$

These equations imply that if the probability $p_l$ decreases ($\mathrm{d}p_l/\mathrm{d}t < 0$) a part of the structures of size $l$ currently in the growing state will transition to the non-growing (blocked) state: $J_l^{G\to B} > 0$. Conversely, if $p_l$ increases ($\mathrm{d}p_l/\mathrm{d}t < 0$) structures of size $l$ can grow again and will transition from the blocked to the growing state: $J_l^{B\to G} > 0$.

Before we discuss the last aspect of the effective theory, namely the monomer dynamics, we give a short summary of the mathematical analysis so far. Starting from the fluctuations in the relative availability of the different species due to the random activation process, we aimed to quantify how these fluctuations modify the growth dynamics of self-assembling structures. Intuitively, the idea is the following: If certain species are less activated than their neighboring species, these species can become unavailable for binding. This unavailability of some species then blocks the growth of those structures that need the unavailable species for the next step of the assembly process. Assuming a random distribution of these unavailable species along the ring structure, we quantified this blockade effect through the probabilities $p_l$ that a structure that has just reached size $l$ can continue to grow (i.e. is not blocked by unavailable species), Eq. 31. These growth probabilities are large if the number of unavailable species is small, as one would intuitively expect; see also Fig. 3 (g). Importantly, one has to distinguish between the probability ($p_l$) that a single structure that has *just* reached size $l$ can continue to grow and the probability $f_l$ that a randomly picked structure *of this size* $l$ is able to grow. The reason is that structures that can continue to grow have a different growth dynamics than those that cannot: While structures in the growing state can grow as usual, structures in the non-growing (blocked) state can only grow if a currently unavailable species is activated. As a result of this diverging growth dynamics, there is generally an accumulation of non-growing structures (compared to growing ones). This accumulation entails that the probability $f_l$ that a randomly picked structure of size $l$ cannot grow is much higher than the probability $p_l$ that a single structure that has just reached size $l$ can grow further. To account for this difference, we introduced two distinct states for each structure size, corresponding to the growing and non-growing (blocked) polymers.

What remains to be discussed before we can write down the full dynamics of the self-assembly process is the effective behavior of the monomers. This will be done in the next subsection.

### E. Monomer dynamics

So far, we have identified two different states for the polymers, namely blocked (non-growing) and growing ones, depending on whether the species they need for further growth are currently unavailable or not. This separation already implies that there need to be at least two different states of active monomers, namely those monomers belonging to currently unavailable species and those that belong to species that are currently available for binding. Furthermore, in analogy with the polymer states, also a third state is reasonable, namely a "blocked" (non-growing) monomer which would need monomers of unavailable species on both sides to be able to form a dimer. What are the respective probabilities for these states of monomers if there are $S_\times$ unavailable species in the system? We denote them by capital letters $P$ to avoid confusion with the probabilities $p_l$ that a structure that reached size $l$ ended up in the growing state.

The probability of monomers to belong to an unavail-

able species can be approximated by

$$P_\times = \frac{S_\times}{S} = \frac{L_\times}{L}, \tag{37}$$

since there is the same total number $N$ of particles of each species and a randomly chosen monomer thus corresponds with probability $S_\times/S$ to an unavailable species [59]. The probability of a monomer to be blocked is given by

$$P_\mathrm{b} = 1 - p_1 \tag{38}$$

with $p_1$ determined by Eq. 31, analogously to the probability $1-p_l$ that a polymer of size $l$ is in the blocked (non-growing) state. Finally, the probability of all other monomers ("normal monomers") is given by the remaining probability

$$P_\mathrm{n} = 1 - P_\mathrm{b} - P_\times \,. \tag{39}$$

Since $P_\times$ and $P_\mathrm{b}$ increase with the number of unavailable species, the probability of a monomer to be in the "normal" state decreases with increasing $L_\times$ or increasing fluctuations in the relative availability of species. Indeed, one can interpret the normal monomers as the equivalent to the monomers in the deterministic description: If the fluctuations between the species are small and there are no unavailable species, $L_\times = 0$, we have $P_\times = P_\mathrm{b} = 0$ and all monomers are in the normal state: $P_\mathrm{n} = 1$. In fact, we then have $p_l = 1$ for all $l$ implying that also all polymers are in the "growing" state which is the equivalent to the (unique) polymer state in the deterministic description.

When we explored a dynamics with these three states of monomers (combined with the polymer dynamics as stated below), it turned out that these are sufficient to capture the qualitative behavior of the stochastic model. However, in particular for self-assembly processes with a small dimerization rate, $\mu \ll \nu$, where the monomer dynamics plays an important role, the quantitative agreement with the result from stochastic simulations can be improved considerably by the introduction of an additional monomer state. This "unblocked" state comprises all monomers that have been in the blocked state but then got unblocked due to a decrease in the number of unavailable species over time, $\mathrm{d}L_\times/\mathrm{d}t < 0$; see also Fig. 4 for an illustration of the monomer dynamics. Such a decrease in $L_\times$ eventually happens in each system, since after activation of all particles, there is no variability between species and, thus, no species with less activation compared to the other species. The reason why this additional state changes the dynamics is that it can prevent the different monomers that have been blocked before from instantaneously dimerizing with each other once they are unblocked. Such a behavior would not make much sense since the different species in the blocked state either correspond to exactly the same species or are separated by at least one unavailable species. In both cases, they are not supposed to bind to each other. With the introduction of the unblocked state, it is possible to eliminate this binding pattern by not allowing the monomers in the unblocked state to dimerize with each other. If they would just transition back to the normal state instead, such a rule could not be implemented since monomers need to be able to dimerize. In summary, we take into account a forth monomer state that, however, is not directly accessible if monomers are activated but gets populated by the originally blocked monomers. Based on these effective states of monomers and the description of polymers in two different state (non-growing/blocked and growing), we will next formulate the full effective theory.

### F. Effective theory

In the last sections, we have discussed several aspects of the effect of stochasticity and the resulting variability between species. First, we have introduced the concept of a currently unavailable species. It is a species that does not have any (already activated) particles with free binding sites on the left or right. Roughly speaking, if a species is considerably less activated than other species it is likely that it becomes an unvailable species. The unavailability of such a species then effectively blocks the growth of structures. Employing a fluctuation-corrected mean-field argument, relating fluctuations in the random activation of the different species to the availability of particles for binding, we have then deduced the probability of a structure to further grow by attachment of monomers of an available species. Importantly, this probability $p_l$, of being in the "growing state", Eq. 31, depends on the size $l$ of the structure so that larger structures are less likely to grow by attachment of available species. Instead they need to "wait" for a monomer of a currently unavailable species to be activated before they can grow ("blocked state").

To sum up, the picture is as follows: There are two types of species, available and unavailable ones, and each structure can be in either of two states, a growing and a blocked state (see also Fig. 3 (a)). Unavailable species have been activated less compared to their neighboring species and due to their unavailability block the growth of structures. Once they get activated, they bind to all structures because most structures can grow by attachment of a monomer of an unavailable species – at least at one end [60]. In contrast, monomers of available species can principally only bind to structures in the growing state (Fig. 4), i.e. to structures that are not completely blocked by the unavailability of the neighboring species but instead can grow at least at one end by attachment of an available species. If structures of size $l-1$ grow by monomer attachment, with a certain probability $1-p_l$ they end up in the non-growing (blocked) state in which both ends need a monomer of an unavailable species to grow further. This probability $1-p_l$, Eq. 31, increases with increasing number of unavailable species and with increasing size of the structure $l$. With the inverse probability $p_l$, structures end up in the growing state. As a result, during the growth process more and more structures

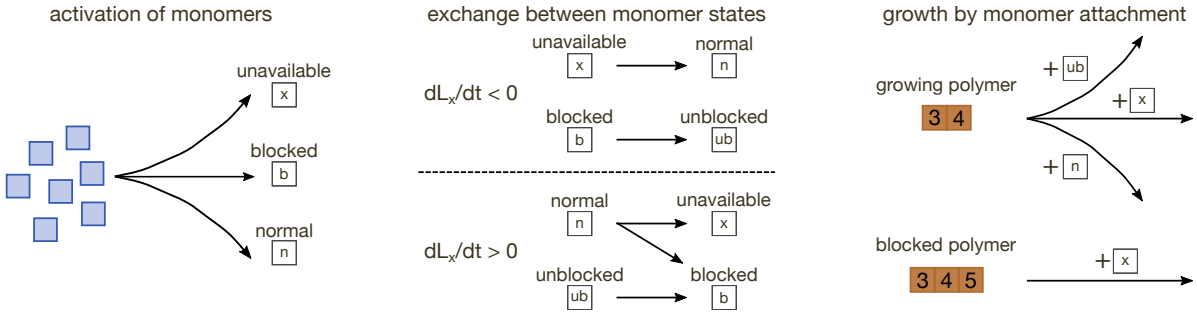


FIG. 4. **Illustration of the monomer dynamics.** There are four monomer states: an unavailable, blocked, unblocked and normal one. Monomers in the unavailable, blocked and normal state are activated at rates $N\alpha e^{-\alpha t}P_\times$, $N\alpha e^{-\alpha t}P_\mathrm{b}$ and $N\alpha e^{-\alpha t}P_\mathrm{n}$, respectively. If the number of unavailable species decreases, monomers in the unavailable state transition to the normal state and monomers in the blocked state transition to the unblocked state. Conversely, if the number of unavailable species increases, monomers in the normal state either transition to the unavailable or to the blocked state. Monomers in the unblocked state transition back to the blocked state. Polymers in the growing state can bind to monomers in the normal, unavailable and unblocked state. In contrast, polymers in the non-growing state can only bind to monomers in the unavailable state.

will transition from the growing to the blocked state in which activation of a monomer of an unavailable species is necessary for further growth.

Taken together, we can now build up the effective growth dynamics of the self-assembly process with no defect formation, $\nu_\mathrm{def}=0$; for an analysis of the more general case, we refer the reader to Appendix C. For better readability, we will explain the different contributions to the dynamics in separate paragraphs: activation of monomers (proportional to $\alpha$), dimerization between monomers (proportional to $\mu$), growth dynamics of polymers by monomer attachment (terms proportional to $\nu$), and the exchange dynamics between the different states of each structure size (denoted by $\rho$ and $\varrho$). The full dynamics is shown in Sec. IV F 5. We use the following notation: $g_l$ ($b_l$) denotes the concentration of polymers of size $l\geq 2$ in the growing (blocked) state. The concentrations $m_\mathrm{n}$, $m_\times$, $m_\mathrm{b}$ and $m_\mathrm{ub}$ denote the concentration of monomers in the normal, unavailable, blocked and unblocked state, respectively; see also Sec. IV E. All concentrations always refer to one species.

### 1. *Activation of monomers (see also Fig. 4)*

Each of the $N$ particles for each species is activated at a per-capita rate $\alpha$. Hence, at time $t$, on average $Ne^{-\alpha t}$ particles per species are still inactive, and the overall rate of monomer activation per species is thus $\alpha Ne^{-\alpha t}$. As we have discussed in detail in Sec. IV E, there are four different monomers states, one for monomers belonging to unavailable species $m_\times$, one for monomers that are blocked by an unavailable species on each end $m_\mathrm{b}$, one for monomers that had been blocked but were "freed" (unblocked) due to a decrease in the number of unavailable species, $m_\mathrm{ub}$, and the remaining one for normal monomers $m_\mathrm{n}$. At activation, monomers either end up in the normal, unavailable or blocked state with respective probabilities $P_\mathrm{n}$, $P_\times$ and $P_\mathrm{b}=1-P_\mathrm{n}-P_\times$. The corresponding gain terms in the monomer dynamics are, thus, $\alpha Ne^{-\alpha t}P_\mathrm{n}$, $\alpha Ne^{-\alpha t}P_\times$ and $\alpha Ne^{-\alpha t}P_\mathrm{b}$, respectively. There is no gain term for unblocked monomers due to activation because this type of monomer only includes the monomers that have been in the blocked state before and then got unblocked as fluctuations between species (or, equivalently, $L_\times$) decreased.

### 2. *Dimerization between monomers*

In general, dimerization happens at rate $\mu$. However, not all monomers can dimerize with all other monomers. More concretely, monomers in the blocked state can only dimerize with monomers in the unavailable state (because by definition they are blocked on both sides by an unavailable species). There are $2m_\times m_\mathrm{b}$ different combinations of monomers for such dimerization events where the factor of 2 takes into account that monomer 1 can bind from the left or from the right to monomer 2. Thus, the overall rate for this process is $2\mu m_\mathrm{b}m_\times$ and it occurs as loss terms in the dynamics of both $m_\mathrm{b}$ and $m_\times$. In the gain term for the dimers $g_2$ and $b_2$, these terms are multiplied by the probabilities $p_2$ and $1-p_2$, respectively, to account for the fact that a newly formed dimer is with probability $p_2$ in the growing state and with inverse probability $1-p_2$ in the non-growing (blocked) one. Monomers in the unavailable state not only dimerize with monomers in the blocked state but also with monomers in the normal and unblocked state because monomers of the unavailable species are supposed to be "required" by all other structures. Analogous to the previous case, the corresponding rates are $2\mu m_\mathrm{n}m_\times$ and $2\mu m_\mathrm{ub}m_\times$, respectively, again with additional factors $p_2$ and $1-p_2$ for the gain terms. Finally, monomers in the unavailable state dimerize among themselves. Due to the indistinguishability between monomers of one state, there are only $m_\times^2$

combinations for two monomers in the unavailable state to dimerize. Since two monomers are lost in the process, the overall loss rate for the monomers is still $2\mu m_\times^2$. The gain term for the dimers is, however, just $\mu m_\times^2$, again weighted with the probabilities $p_2$ and $1-p_2$. Monomers in the normal state not only dimerize with the monomers in the unavailable state but also with themselves (as is the case in the deterministic description where there are only "normal" monomers) and with the unblocked monomers (which are basically the same as normal monomers only that they have been in the blocked state before). Similarly to above, the corresponding loss terms are $2\mu m_\mathrm{n}^2$ and $2\mu m_\mathrm{n} m_\mathrm{ub}$ and the gain terms are $\mu m_\mathrm{n}^2 p_2$ or $\mu m_\mathrm{n}^2(1-p_2)$ and $2\mu m_\mathrm{n} m_\mathrm{ub} p_2$ or $2\mu m_\mathrm{n} m_\mathrm{ub}(1-p_2)$, respectively. Finally, monomers in the unblocked state behave similarly as the monomers in the normal state only that they do not dimerize among themselves. Thus, there are just the loss terms from dimerization of monomers in the unblocked state with monomers in either the normal or the unavailable state, as described above.

#### 3. *Growth dynamics (see also Fig. 4)*

As mentioned above, monomers of the unavailable type (i.e. monomers of an unavailable species) bind to all polymers. These binding processes are represented by the terms

$$2\nu m_\times g_l p_{l+1} + 2\nu m_\times g_l(1-p_{l+1}) = 2\nu m_\times g_l \tag{40a}$$
$$2\nu m_\times b_l p_{l+1} + 2\nu m_\times b_l(1-p_{l+1}) = 2\nu m_\times b_l\,. \tag{40b}$$

For instance, each monomer of the unavailable type can bind at rate $\nu$ to each structure of size $l$ in the growing state. Overall, there are $2m_\times g_l$ possible combinations because the monomer can attach from both sides to the structure. So, the overall binding for a monomer of the unavailable type to a structure of size $l$ in the growing state is $2\nu m_\times g_l$. With probability $p_{l+1}$ the newly formed structure of size $l+1$ is in the growing state and with the inverse probability $1-p_{l+1}$ in the blocked state. As a result, the rate of formation of a structure of size $l+1$ in the growing or blocked state due to binding of a monomer in the unavailable state to a growing structure of size $l$ is given by $2\nu m_\times g_l p_{l+1}$ or $2\nu m_\times g_l(1-p_{l+1})$, respectively. Similarly, the overall binding rate for a monomer in the unavailable state to a structure of size $l$ in the blocked state is $2\nu m_\times b_l$. Again, the thereby formed structures of size $l+1$ are in the growing (non-growing) state with probability $p_{l+1}$ (inverse probability $1-p_{l+1}$) and the respective rates are $2\nu m_\times b_l p_{l+1}$ and $2\nu m_\times b_l(1-p_{l+1})$.

#### 4. *Exchange dynamics*

The strength of stochastic fluctuations and with it the number of unavailable species changes over time. For instance, as shown above in Fig. 3(d), the standard deviation of the availability of different species as compared to their neighbors is maximal when just half the particles have been activated and is zero at the beginning and at the end of the process. As a result, the probability for a structure of size $l$ to be in the growing state, $p_l$, changes over time. If $p_l$ changes there needs to be an exchange of structures of size $l$ between the corresponding growing ($G_l$) and blocked state ($B_l$). A structure in the blocked state that was blocked by the unavailability of its two neighboring species might, for instance, transition to the growing state once one of the originally unavailable neighboring species gets available. As motivated in Sec. IV D, the corresponding fluxes between the states are proportional to the derivative of the logarithm of the respective probability $p_l$ or $1-p_l$ (depending on the direction of the exchange). Thus, we have

$$\rho_l = J_l^{B\to G} = \begin{cases} \frac{g_l}{p_l}\frac{\mathrm{d}p_l}{\mathrm{d}t} & \text{if } \frac{\mathrm{d}p_l}{\mathrm{d}t} < 0 \\ \frac{b_l}{1-p_l}\frac{\mathrm{d}p_l}{\mathrm{d}t} & \text{if } \frac{\mathrm{d}p_l}{\mathrm{d}t} > 0, \end{cases} \tag{41}$$

where we defined $\rho_l$ as the flux from the blocked to the growing state, $J_l^{B\to G}$ (compare also Eq. 36). So, if the probability to be in the growing state $p_l$ increases (decreases), there is positive flow from the blocked (growing) to the growing (blocked) state.

The fluxes between the monomer states are a bit more involved because there are not only two different states but, in principle, four of them. We denote them by a slightly different letter, $\varrho$, to avoid confusion with the other fluxes. If the number of unavailable species decreases, $\mathrm{d}L_\times/\mathrm{d}t < 0$, the generalization is straightforward: Monomers of the unavailable type transition to the normal state and monomers that had been blocked by unavailable species will become unblocked (see also Fig. 4). Thus, there are only transitions from one state to one other state. As motivated in Sec. IV D, the per-capita transition rates are proportional to the derivative of the logarithm of the probability of the respective state. In the case $\mathrm{d}L_\times/\mathrm{d}t < 0$, we thus have

$$\varrho_\mathrm{n} = -\varrho_\times = -\frac{m_\times}{P_\times}\frac{\mathrm{d}P_\times}{\mathrm{d}t} \tag{42a}$$
$$\varrho_\mathrm{ub} = -\varrho_\mathrm{b} = -\frac{m_\mathrm{b}}{P_\mathrm{b}}\frac{\mathrm{d}P_\mathrm{b}}{\mathrm{d}t}. \tag{42b}$$

Here $\mathrm{d}P_\times/\mathrm{d}t < 0$ and $\mathrm{d}P_\mathrm{b}/\mathrm{d}t < 0$, so that the flux into the normal, $\varrho_\mathrm{n}$, and unblocked state, $\varrho_\mathrm{ub}$, is positive, as expected.

In contrast, if the number of unavailable species increases, both the number of active monomers in the unavailable state as well as the number of active monomers in the blocked state increases. This implies that monomers in the normal state can either transition to the unavailable or to the blocked state (see also Fig. 4). Furthermore, monomers in the unblocked state transition back to the blocked state. As we show in Appendix B 2,

these transitions for $\mathrm{d}L_\times/\mathrm{d}t > 0$ are realized by

$$\varrho_\mathrm{n} = \frac{m_\mathrm{n}}{P_\mathrm{n}}\frac{\mathrm{d}P_\mathrm{n}}{\mathrm{d}t} = -\frac{m_\mathrm{n}}{P_\mathrm{n}}\frac{\mathrm{d}p_\times}{\mathrm{d}t} - \frac{m_\mathrm{n}}{P_\mathrm{n}}\frac{\mathrm{d}P_\mathrm{b}}{\mathrm{d}t} \tag{43a}$$

$$\varrho_\times = \frac{m_\mathrm{n}}{P_\mathrm{n}}\frac{\mathrm{d}P_\times}{\mathrm{d}t} \tag{43b}$$

$$\varrho_\mathrm{ub} = -\frac{m_\mathrm{ub}}{1-P_\mathrm{b}}\frac{\mathrm{d}P_\mathrm{b}}{\mathrm{d}t} \tag{43c}$$

$$\varrho_\mathrm{b} = \frac{m_\mathrm{n}}{P_\mathrm{n}}\frac{\mathrm{d}P_\mathrm{b}}{\mathrm{d}t} + \frac{m_\mathrm{ub}}{1-P_\mathrm{b}}\frac{\mathrm{d}P_\mathrm{b}}{\mathrm{d}t}. \tag{43d}$$

Now, $\mathrm{d}P_\times/\mathrm{d}t > 0$, $\mathrm{d}P_\mathrm{b}/\mathrm{d}t > 0$ and $\mathrm{d}P_\mathrm{n}/\mathrm{d}t < 0$, so that there is indeed flux from the normal to the unavailable and blocked state and from the unblocked to the blocked state. The influx from the normal into the unavailable state $\varrho_\times$ is proportional to the number of monomers in the normal state $m_\mathrm{n}$ and to the change in the likelihood of species to be unavailable, $\mathrm{d}P_\times/\mathrm{d}t$. This term appears as a gain term for the monomers of unavailable species, $\varrho_\times$, and as a loss term for monomers in the normal state, $\varrho_\mathrm{n}$. Monomers in the normal state also transition to the blocked state. This flux is again proportional to $m_\mathrm{n}$ and to the change in the likelihood of species to be blocked, $\mathrm{d}P_\mathrm{b}/\mathrm{d}t$. This term appears in $\varrho_\mathrm{n}$ as loss term and as gain term in $\varrho_\mathrm{b}$. Finally, monomers in the unblocked state transition back to the blocked state. The corresponding flux is proportional to the number of monomers in the unblocked state $m_\mathrm{ub}$, and to the change in the likelihood of species to be unblocked, $\mathrm{d}P_\mathrm{ub}/\mathrm{d}t = \mathrm{d}(1-P_\mathrm{b})/\mathrm{d}t = -\mathrm{d}P_\mathrm{b}/\mathrm{d}t$.

Irrespective of the sign of $\mathrm{d}L_\times/\mathrm{d}t$, we have

$$\varrho_\mathrm{n} + \varrho_\times + \varrho_\mathrm{b} + \varrho_\mathrm{ub} = 0 \tag{44}$$

due to conservation of particles.

#### 5. *Full dynamics*

Combining all of these contributions to the dynamics, the full dynamics reads as follows:
Monomer dynamics (see also Secs. IV F 1, IV F 2, IV F 3 and IV F 4):

$$\partial_t m_\mathrm{n} = \alpha N e^{-\alpha t} P_\mathrm{n} - 2\mu D_\mathrm{n} - 2\nu m_\mathrm{n}\gamma + \varrho_\mathrm{n} \tag{45a}$$

$$\partial_t m_\times = \alpha N e^{-\alpha t} P_\times - 2\mu D_\times - 2\nu m_\times(\gamma+\beta) + \varrho_\times \tag{45b}$$

$$\partial_t m_\mathrm{b} = \alpha N e^{-\alpha t} P_\mathrm{b} - 2\mu D_\mathrm{b} + \varrho_\mathrm{b} \tag{45c}$$

$$\partial_t m_\mathrm{ub} = -2\mu D_\mathrm{ub} - 2\nu m_\mathrm{ub}\gamma + \varrho_\mathrm{ub} \tag{45d}$$

where

$$2D_\mathrm{n} = 2\left(m_\mathrm{n}^2 + m_\mathrm{n}m_\times + m_\mathrm{n}m_\mathrm{ub}\right) \tag{46a}$$

$$2D_\times = 2\left(m_\times^2 + m_\times m_\mathrm{n} + m_\times m_\mathrm{ub} + m_\times m_\mathrm{b}\right) \tag{46b}$$

$$2D_\mathrm{b} = 2m_\mathrm{b}m_\times \tag{46c}$$

$$2D_\mathrm{ub} = 2\left(m_\mathrm{ub}m_\mathrm{n} + m_\mathrm{ub}m_\times\right), \tag{46d}$$

denote the number of ways in which a monomer in the normal, unavailable, blocked or unblocked state can dimerize with another monomer, respectively. Here, $m_\mathrm{n}$, $m_\times$, $m_\mathrm{b}$ and $m_\mathrm{ub}$ denote the numbers of monomers in the normal, unavailable, blocked and unblocked state (per species), respectively; see also Sec. IV E. Furthermore, $\gamma = \sum_{l=2}^{L-1} g_l$ and $\beta = \sum_{l=2}^{L-1} b_l$ denote the total number of unfinished polymers in the growing and blocked state, respectively. Here, $g_l$ and $b_l$ denote the numbers of polymers of size $l \geq 2$ (per species) in the growing and blocked state, respectively.
Polymer dynamics (see also Secs. IV F 2, IV F 3 and IV F 4):

$$\partial_t g_2 = \mu\left(D_\mathrm{n} + D_\times + D_\mathrm{b} + D_\mathrm{ub}\right)p_2 - 2\nu g_2 M_\mathrm{G} + \rho_2 \tag{47a}$$

$$\partial_t b_2 = \mu\left(D_\mathrm{n} + D_\times + D_\mathrm{b} + D_\mathrm{ub}\right)(1-p_2) - 2\nu b_2 m_\times - \rho_2 \tag{47b}$$

for the dimers and

$$\partial_t g_l = 2\nu\left(g_{l-1}M_\mathrm{G} + b_{l-1}m_\times\right)p_l - 2\nu g_l M_\mathrm{G} + \rho_l \tag{48a}$$

$$\partial_t b_l = 2\nu\left(g_{l-1}M_\mathrm{G} + b_{l-1}m_\times\right)(1-p_l) - 2\nu b_l m_\times - \rho_l \tag{48b}$$

for all polymers with $l \in \{3,\ldots,L-1\}$ where $M_\mathrm{G} = (m_\mathrm{n} + m_\times + m_\mathrm{ub})$ denotes the number of monomers that can bind to structures in the growing state. Finally, for the final target structures there is only one state (since they do not grow further) which we denote by $G_L$ with concentration $g_L$:

$$\partial_t g_L = 2\nu\left(g_{L-1}M_\mathrm{G} + b_{L-1}m_\times\right). \tag{49}$$

The probabilities $p_{l\geq 2}$ are defined in Eq. 31 and the probabilities for the monomers in Eqs. 37, 38 and 39. The full dynamics (Eqs. 45, 47, 48, 49) is solved numerically using MATLAB.

## V. COMPARISON TO STOCHASTIC SIMULATIONS AND DETERMINISTIC THEORY

Does this effective theory capture the strong stochastic effects as observed in stochastic simulations of the system? Figure 2 shows the result of a numerical integration of the effective theory (Eqs. 45, 47, 48, 49), in comparison with the stochastic simulations. While the effective theory does not coincide fully quantitatively with the stochastic simulations, it correctly predicts the qualitative behavior of the system, in contrast to the deterministic theory [46] (not shown). First, the effective theory correctly predicts that the yield saturates at an imperfect value $Y_\mathrm{max} < 1$ in the limit of small activation rate (Fig. 2 (a)). This imperfect value decreases for smaller numbers $N$ of particles per species and for larger target structure sizes $L$. Furthermore, we recover the non-monotonic behavior of the (defect-free) yield with the activation rate,

if the dimerization rate is small ($\mu \ll \nu$; Fig. 2 (b)) or if defect formation is allowed ($\nu_{\text{def}} > 0$; Fig. 2(c)). Note that in the case of defect formation, we do recover the non-monotonic behavior of the defect-free yield (yield of all defect-free target structures) but not of the total yield (yield of all target structures). This is presumably because in our theory defect formation is always possible and since we do not account for additional fluctuations in the availability of the different species due to defect formation [48]; for details on the effective theory with defect formation, $\nu_{\text{def}} > 0$, please refer to Appendix C. Finally, for fixed target size $L$ and fixed total number of particles $NS$ (or, equivalently, fixed number of rings $NS/L$ if assembly proceeds perfectly), the yield decreases for larger heterogeneity of the target structure (corresponding to the number of species $S$ in the system) (Fig. 2 (d)). In contrast, yield becomes independent of the number of species $S$ for $S \gg 1$ if the number of particles per species $N$ is kept constant (Fig. 2 (e) and (f)). This implies that, as long as the structures are not fully homogeneous and variability between different species exists ($S \gg 1$), for constant $N$ and $L$ the number of species is not decisive for the process. In the effective theory, this can be seen from the fact that only the number of unavailable sites along the ring, $L_\times$, enters but not the number of unavailable species, $S_\times$ itself (at least if we assume that the periodicity of the arrangement does not change the length of segments of available species considerably, see Sec. IV C). As a result, the redundancy $L/S$ of the structure does not influence the assembly process in the effective theory, as long as $N$ and $L$ are constant. In this case of fixed $N$ and $L$, the average yield can even be a non-monotonic function of the number of species (blue (upper) curves in Figs. 2(e) and (f)). We speculate that this is a consequence of the variance of the yield being dependent on the number of species in the system and of the yield being bounded between 0 and 1: Our effective theory suggests that the single-species fluctuations are one of the decisive factors for the strength of stochastic effects. These fluctuations are quantified by the average variance between neighboring species. This variance, however, is also subject to stochasticity itself: The fewer species there are in the system, the more we expect the average variance between neighboring species (where the average is taken with respect to the different species) to fluctuate between single realizations of the assembly process. As a result, it is intuitive that also the yield fluctuates more if there are less species. Since, furthermore, yield is bounded by 0 and 1, this could imply that for systems with yield "close to" 1, fluctuations might actually decrease the average yield, whereas for yields close to 0, the opposite happens. This suggests that in cases where the yield for $S \gg 1$ is "close to" 0, systems with few species actually exhibit a higher average yield (as they are subject to more fluctuations) (red (lower) curves in Figs. 2(e) and (f)), whereas for the case where the average yield is "close to" 1, the opposite is true, and yield can indeed be a non-monotonic function of the number of species $S$ (blue (upper) curves in Figs. 2(e) and (f)) It would be very interesting to check more rigorously whether this speculation is indeed true.

So far, we have focused on the final yield of the assembly process. In order to check whether the effective theory captures the dynamics of the polymer size distribution qualitatively correctly (and not only the final yield), we compare the temporal evolution of the polymer size distribution as predicted by the effective theory and as measured in stochastic simulations in Appendix A. While there exist obvious differences (such as, for instance, the dynamics of the monomers and the resulting dynamics for the smaller structures), the front of the wave in the stochastic simulations seems to be predicted quite reliably by the effective theory. This front is mainly determined by the probabilities $p_l$, Eq. 31, that determine which portion of structures of size $l$ ends up in the growing state. These probabilities predict that there is a sharp transition between structures of size $l > L - L_\times - 1$ that do not grow at all and smaller structures $l \leq L - L_\times - 1$ that have a high likelihood to grow (see also Sec. IV C and Fig. 3). As a result of the sharp transition and the fact that large structures do not grow much, the waves produced by the effective theory build up much larger and, correspondingly, move much more slowly through the system (as more structures grow simultaneously), as compared to the waves predicted by the deterministic theory [46]. This higher amplitude and slower speed of the wave predicted by the effective theory is in agreement with the waves from the stochastic simulations, suggesting that the probabilities $p_l$ capture the dynamics reasonably well although they were determined from a much simplified assembly process (see Sec. IV C). Finally, although there are quantitative deviations in the monomer dynamics, in both the stochastic simulations and in the effective theory the number of monomers is high until very late in the process.

Taken together, these results suggest that the effective theory captures the most important aspects of the self-assembly process. In order to suggest ways how to improve yield in the system, it thus seems promising to analyze the integral new aspects of the effective theory as compared to a deterministic description of the system as given in Sec. III A.

## VI. REDUCE FLUCTUATIONS IN THE AVAILABILITY OF THE DIFFERENT SPECIES IN ORDER TO IMPROVE YIELD

How can we use the insights gained from the formulation of the effective theory to suggest viable ways to improve the yield in the self-assembly process? Since, deterministically, the yield is always perfect for small enough activation rate, we take a closer look at the difference between the deterministic and effective theory. This difference is in the additional blocked state $B_l$ in the effective theory. This state describes structures that would need a

particle of an unavailable species to grow and thus, generally speaking, tend not to grow due to variability between species. These fluctuations are quantified by the single-species standard deviation $\sigma_0$, Eq. 15. Our effective theory thus suggests that reducing the single-species standard deviation should improve the yield in the system. In the following, we will consider two specific ways to achieve this goal.

### A. Provision in bursts

As shown in Fig. 3(d), where $\sqrt{3\sigma_0}$ (black) is plotted against the average number of activation events per species, the single-species standard deviation has a pronounced maximum when on average half the particles have been activated. Our effective theory, thus, suggests that in order to improve the assembly yield one could constrain the system in a way that the single-species standard deviation takes on a value of zero from time to time. This can be achieved by providing particles in bursts: Instead of providing all $N$ particles of each species right from the beginning, the particles are put into the system in $b$ bursts, where each burst contains a number of $N/b$ particles per species. This means that at first only $N/b$ particles of each species are put into the system. Only when these particles have been activated and the binding processes have been completed, the next burst of particles is provided - and so on until all $N$ particles per species have been provided. Figure 5(a) shows the resulting single-species standard deviation measured in stochastic simulations when a total number of $N = 500$ particles is provided in 1, 2, 10 or 20 subsequent bursts (the x-axis represents time in units of activation events). The standard deviation decreases for larger numbers of bursts since it is reduced to zero at the end of each burst: After the $i$-th burst exactly $iN/b$ particles of each species have been activated and there is no variability between species at this point in time. Consequently, the maximum of the single-species standard deviation decreases from $\frac{1}{2}\sqrt{N}$ in the original system to $\frac{1}{2}\sqrt{N/b}$; see Appendix D for more details. According to the effective theory, the yield is expected to increase as a result of the reduced single-species standard deviation. Fig. 5(b) shows the final yield curves in dependence of the activation rate $\alpha$ for the different numbers of bursts. Indeed, it is found that the yield strongly increases with increasing number of bursts. As one can infer upon inspection of Fig. 5(a), this increase in the yield correlates with a smaller standard deviation of the neighbor fluctuations.

In order to improve the yield by providing the particles in bursts it is necessary that the bursts are sufficiently deterministic, i.e. the number of particles per species per burst has to be subject to little fluctuations. Otherwise, the single-species standard deviation cannot be reduced effectively. Indeed, we show in Appendix E that if the number of particles per species per burst is drawn randomly from a Poisson distribution with mean $N/b$, the process is independent of the number of bursts. There, we also discuss some aspects of bursts for which the number of particles per species per burst is drawn independently from a Gaussian or Binomial distribution, respectively. We find that, for provision of particles in bursts to be effective, the width of the distribution of the particles per species per bursts need not be too large (Fano factor $F < 1$).

### B. Self-inhibitory feedback

As indicated by the effective theory, the large single-species variance is detrimental because it favors growth and nucleation of small structures as compared to large structures. The reason is that, when species are unavailable, active monomers of the neighboring species can accumulate as there are no fitting polymers to bind. Subsequently, this accumulation of active particles strongly increases the tendency to form new nuclei. A very direct way to avoid this problem would be to introduce a self-inhibition mechanism that suppresses the accumulation of these active monomers. Explicitly, we will consider a variant of the system ("self-inhibition scenario") where the activation rate of species $i$ is given by

$$\alpha^{(i)} = \alpha_0 \exp\left(q m_i^a\right), \tag{50}$$

where $m_i^a$ is the number of active monomers of species $i$, $\alpha_0$ is the bare activation rate and $q \leq 0$ is the inhibition strength. If one species has been activated more (less) than average, it will typically have more (less) active monomers than average. In the self-inhibition scenario with $q < 0$, this implies that the activation of additional monomers is suppressed (enhanced) for over-represented (under-represented) species and so the different levels of activation are expected to converge. Fig. 5(c) shows how for increasing inhibition strength $q$ the standard deviation of the neighbor fluctuations decreases. The effect of the inhibition strength $q$ on reducing the neighbor fluctuations is pronounced already in the early stages of the assembly process where not as many structures and monomers are present. This is particularly useful because fluctuations in the beginning are expected to suppress yield most considerably. We thus anticipate from the effective theory that yield should improve. Indeed, Fig. 5(d) shows that higher inhibition strengths improve yield significantly. Again, we see that there is a clear correlation between higher yield and smaller neighbor fluctuations; compare Figs. 5(c) and (d).

Taken together, decreasing the variance between the species by either directly influencing the single-species variance or by self-adjusting the activation levels of different species due to feedback, can strongly improve yield, as suggested by the effective theory.

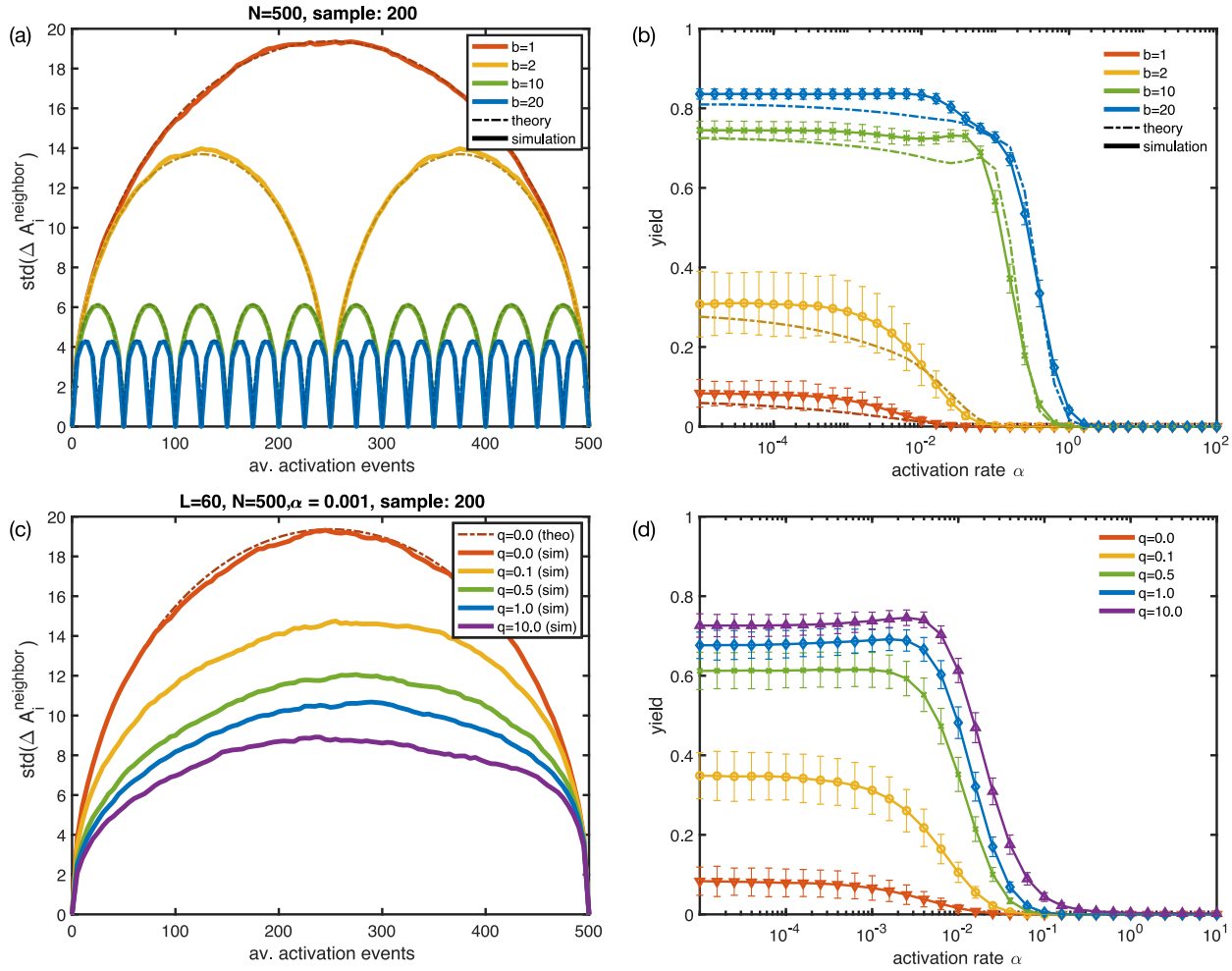


FIG. 5. **Decreasing the variance in the relative number of available particles per species improves yield.** (a) Burst scenario: The standard deviation of the neighbor fluctuations $\mathrm{std}(\Delta A_i^{\mathrm{neighbor}})$ for the original system and for systems with $b = 2$, 10 and 20 bursts, respectively, are plotted against the average number of activation events per species. The theoretical predictions are shown with dotted-dashed lines and the results from stochastic simulations (averaged over 200 samples) with solid lines (and slightly lighter color to ease the comparison). The parameter values are $L = 60$, $N = 500$, $\nu = \mu = 1$, $\nu_{\mathrm{def}} = 0$ and $\alpha = 10^{-4}$. Note that for the stochastic simulations with several bursts, we measured the standard deviation in one burst and concatenated it $b$ times with itself. Since the assembly dynamics does not influence the activation of particles, the standard deviations should statistically be the same in all bursts. (b) Burst scenario: The average assembly yield and its standard deviation obtained from stochastic simulations (1000 samples; solid lines with markers) is shown in dependence of the activation rate for different number of bursts. The theoretical predictions from the effective theory with bursts (see Appendix D) are shown for comparison (dotted-dashed lines). The parameters are $L = 60$, $N = 500$, $\nu = \mu = 1$, $\nu_{\mathrm{def}} = 0$ and number of bursts as indicated in the plot. (c) Self-inhibition scenario: The standard deviation of the neighbor fluctuations $\mathrm{std}(\Delta A_i^{\mathrm{neighbor}})$ as obtained from stochastic simulations (averaged over 200 samples) is shown for different inhibition strengths $q$ (different colors, solid lines). The theoretical prediction for zero inhibition strength is shown as dotted-dashed line in red. The parameters are $L = 60$, $N = 500$, $\nu = \mu = 1$, $\nu_{\mathrm{def}} = 0$, $\alpha_0 = 10^{-3}$ and inhibition strength as indicated in the plot. (d) Self-inhibition scenario: the average assembly yield and its sample standard deviation obtained from stochastic simulations (1000 samples) is plotted as a function of the bare activation rate $\alpha_0$ for different inhibition strength $q$ (different colors). The other parameters are $L = 60$, $N = 500$, $\nu = \mu = 1$, $\nu_{\mathrm{def}} = 0$.

## VII. CONTROLLED VARIABILITY BETWEEN SPECIES

Remarkably, not only decreasing the variance between species but also increasing it in a controlled fashion can improve yield [17, 48]. In this section, we will shortly discuss two suggestions of recent studies [17, 48] as well as a third possibility to increase the yield by increasing the variance between the relative concentrations of the different species. Key to all of these strategies is that

by inducing differences in the concentrations of active monomers specific assembly paths are favored.

### A. Non-stoichiometric concentrations: specific assembly path

Recently, it has been shown that one can considerably enhance assembly efficiency by using non-stoichiometric concentrations for the different building blocks [17]. Specifically, it was suggested to provide building blocks of a small region of the target structure in excess compared to the remaining species. In light of our results, this is surprising at first glance: Rather than decreasing the variability between different species, this setup actually increases the inter-species variation. How can the observed increase in efficiency be reconciled with the finding that fluctuations in the relative concentrations of species favor kinetic trapping? The key insight that solves this riddle is that one has to use non-stochiometric concentrations in a highly coordinated fashion. Instead of indiscriminately over-expressing species randomly, one has to specifically select a set of species in a single connected region of the structure [17]. This procedure then favors a specific assembly path by favoring the formation of nucleation seeds in that chosen region. As a result, all structures grow from these more or less identical seeds without competition for resources; the assembly yield is high.

### B. Non-homogeneous activation rates

A very similar effect can be achieved by using non-homogeneous activation rates for the different species. For randomly distributed rates along the ring, this would increase fluctuations in the relative availability of species and thus lead to a lower yield; see Appendix F, Figs. 14, 15. If, however, a specific assembly path is favored by specifying a particular order of species activation, yield can be increased. Figure 6(a) illustrates such a choice of activation rates

$$\alpha^{(i)} = \begin{cases} \alpha_0\, w^i & \text{for } i \leq S/2 \\ \alpha_0\, w^{S-(i-1)} & \text{for } i > S/2, \end{cases} \tag{51}$$

where $\alpha_0$ scales all rates homogeneously and $w$ determines the relative magnitude of the activation rates. The two species with indices $S/2$ and $S/2+1$ have the largest activation rates, their neighbors the second largest and so on. In this way, this specific choice of activation rates favors assembly paths that proceed in the same order by starting with nucleation of species $S/2$ and $S/2+1$ and subsequently grow to larger and smaller indices to the right and to the left. Correspondingly, due to reduced competition for resources, the yield increases [61] if $w > 1$; see Fig. 6(b). Increasing the exponential weight $w$ enhances the tendency of particles to be activated in the chosen order and hence improves the yield. However, once $w$ becomes so large that activation of some species is faster than binding, active monomers of those species would accumulate and form new nuclei. Consequently, the yield decreases again once $w$ exceeds this threshold. The maximal (total) activation rate in the system is the activation rate of species $L/2$ and $L/2+1$ and is given by $\alpha_{\max} \sim N\alpha_0 w^{L/2}$. In contrast, the time scale for binding is $\nu N$. Hence, the threshold can be estimated by equating $\alpha_{\max} = \nu N$, resulting in an expected yield drop if $w > w_{\max} := \alpha_0^{-2/L}$. As the maximal activation rate and therefore $w_{\max}$ depend on $\alpha_0$, the range of values of $w$ for which yield improves increases with decreasing $\alpha_0$. Therefore, the maximum yield rises if $\alpha_0$ is reduced, see Fig. 6(b).

### C. Just-in-sequence mechanism

The purpose of using non-stoichiometric concentrations or non-homogeneous activation rates is to control the order in which particles become available for binding and thereby to favor specific assembly pathways. We recently presented a mechanism for efficient self-assembly that implements such a 'supply control strategy' in a similar but more effective way, based on inhibitory feedback between neighboring species [48]. To that end, we assume that the inactive (and optionally active) monomers of species $i < L$ inhibit the activation of the subsequent species $i+1$. In this way, species $i+1$ gets activated 'just-in-sequence' after species $i$ has been activated and has, in large part, been assembled already. Only species 1 is not inhibited. The resulting inhibition cascade that ensures that the particles are provided and assembled in the specified sequence is illustrated in Fig. 6. We termed this supply control strategy 'just-in-sequence', or short, JIS mechanism. Similar to Eq. 50, we assume that the activation rate of species $i+1$ with $i < L$ is given by

$$\alpha^{(i+1)} = \alpha_0 e^{q m_i^i}, \tag{52}$$

where $\alpha_0$ denotes the basal activation rate, $q < 0$ the parameter that controls the strength of inhibition and $m_i^i$ the concentration of inactive monomers of species $i$. Optionally, one could also account for inhibition by active monomers by replacing $m_i^i$ with $m_i^i + m_i^a$ as this would only have a negligible effect on the assembly process [48]. Figure 6 shows the yield in dependence of the activation rate $\alpha$ for different values of the inhibition strength $q$ and for $S = 60$ and $N = 500$. Interestingly, a small nonzero $q$ reduces the yield compared to the original case with $q = 0$, because weak inhibition amplifies stochastic effects [48]. However, by further increasing the inhibition strength, the yield quickly rises up to the perfect value of 1 in the respective regime of $\alpha$. Moreover, the threshold activation rate below which the yield rises increases due to a finite inhibition strength. Note that, in comparison with the self-inhibitory mechanism, a much

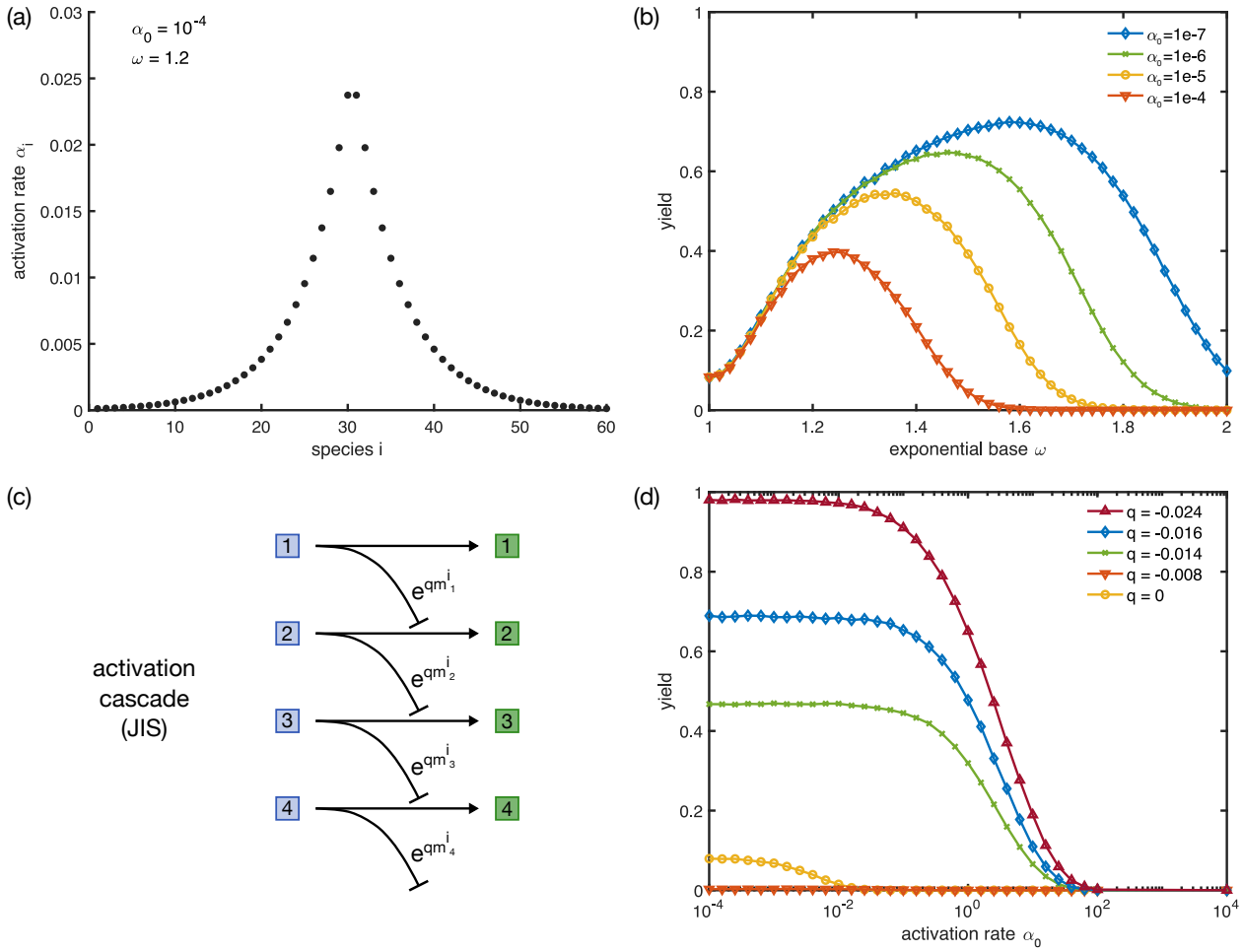


FIG. 6. **Increasing the variance in a coordinated fashion improves yield.** (a,b) Non-homogeneous activation rates. Yield can be improved by choosing the activation rates non-homogeneously. (a) Activation rates plotted against the species index according to Eq. 51 for $\alpha_0 + 10^{-4}$, $\omega = 1.2$ and $L = 60$. The activation rate is highest for the two species in the middle, $i = S/2$ and $i = S/2+1$, and decreases exponentially to the left and to the right. Therefore, assembly pathways that start with the dimerization of species $S/2$ and $S/2+1$ are strongly favored. (b) Yield plotted against the magnitude of the exponential base $\omega$ for different basal activation rates $\alpha_0$ and $S = 60$, $N = 500$. The yield increases with increasing $\omega$ and attains a maximum. Then yield drops again because for large $\omega$ activation of the species becomes fast compared to the growth dynamics. (c,d) JIS scenario. Just-in-sequence supply can be realized effectively with inhibitory feedback, thereby greatly enhancing the yield. (c) Inhibition cascade. The inactive monomers of each species $i$ inhibit the activation of the subsequent species $i+1$ as described by Eq. 52. Only species 1 is not inhibited and is therefore activated first. This triggers an activation cascade which provides the particles in sequence with the specified assembly pathway. (d) Yield in dependence of $\alpha_0$ for different inhibition strengths $q$ and $S = 60$, $N = 500$. For small, nonzero values of $q$ the yield decreases due to an amplification of stochastic effects. For larger values of $q$, however, the yield quickly rises up to the perfect value of 1. For increasing $q$, the threshold activation rate is shifted towards higher values of $\alpha_0$.

lower inhibition strength $q$ is required to achieve high yield. This is because in the self-inhibitory mechanism inhibition is effectuated by the active monomers while in the JIS mechanism it is accomplished by the inactive monomers, which are usually present in much larger numbers. Hence, the JIS mechanism is a very effective strategy to increase self-assembly efficiency and to avoid stochastic yield catastrophes.

## VIII. CHARACTERIZATION OF THE MITIGATION MECHANISMS

As noted in this and earlier studies [46, 48], there exists a variety of methods how to mitigate the stochastic yield catastrophe in heterogeneous self-assembly systems. Depending on the system, one may have access to manipulate or control different elements of the assembly

process and hence some strategies can be more feasible than others. For instance, if one has direct control over the binding properties of the constituents, it might be most efficient to reduce the ratio between the molecular rates for nucleation and growth by relying on allosteric effects. As long as the availability of constituents is not rate-limiting, stochastic effects then do not severely limit the yield of the assembly process [46, 48]. However, controlling the assembly process via the molecular binding rates might be effortful and not very versatile since the constituents would need to be specially tailored for a specific target structure and the corresponding assembly process. Furthermore, allosteric control might require an elaborate design of the constituents, hard to be realized in a controlled fashion in nanotechnological applications. In these applications, it might be more viable to execute control on a systemic level via supply regulation [48]. Supply regulation exerts control over the assembly process by governing the way, specifically the order and amount, in which particles are provided. Elaborate binding properties enabling e.g. allosteric effects are thereby not required. Furthermore, supply regulation provides a way to realize effective self-assembly even if the binding reactions are not or only weakly reversible on the time scale of the assembly process. This is convenient since not relying on reversibility of binding allows to maximize the bond strengths in order to assemble stable and long-living structures. On the downside, however, stochastic effects can easily jeopardize the assembly efficiency if the availability of binding particles is constrained. In order to overcome the limitation arising from the stochastic yield catastrophe, we have discussed several possibilities to implement efficient supply control strategies. Here we want to briefly mention these different possibilities and discuss their respective advantages and drawbacks. We classify these mechanisms by two main distinguishing features: type of regulation and effect on the inter-species variance; see Fig. 7.

Regarding the type of regulation, we have encountered two principally different strategies: the JIS mechanism [48] and the self-inhibitory feedback mechanism both rely on feedback that returns information about the specific state of the assembly process (specifically how many active and/or inactive monomers there are). This information is used to regulate the supply in a self-organized, autonomous fashion. In contrast, in the burst scenario, no such feedback was implemented. Instead, we assumed that the bursts were provided automatically after long enough time spans so that all particles of the previous burst had enough time to bind. Similarly, in the scenarios with non-homogeneous activation rates or non-stoichiometric concentrations [17], no feedback of information about the state of the system was needed.

A second distinguishing characteristic of the presented supply control strategies is their respective effect on the inter-species variance. Processes like bursts or self-inhibition decrease the variance between the species' concentrations and thereby reduce stochastic effects without favoring specific assembly paths. Conversely, strategies including just-in-sequence supply [48], engineering inhomogeneous activation rates or choosing non-stoichiometric concentrations [17] increase the variance in a coordinated way. In this fashion, certain assembly paths are favored which leads to reduced competition for resources and consequently suppresses stochastic effects. The advantage of using a strategy that decreases the inter-species variance is that such a strategy is expected to be applicable independently of the heterogeneity and design of the target structure: Irrespective of whether certain species occur several times in the target structure, decreasing inter-species fluctuations reduces undesirable nucleation events [62]. Conversely, for those strategies that favor specific assembly paths, supply regulation has to be adapted accordingly if species occur several times in the target structure and hence in the assembly path. Specifically, this would demand a higher degree of regulation as it must be assured then that species are delivered not only in the correct order but also in the correct amount. The specific mechanisms discussed here are not directly suitable for this purpose: there is no control over the portion of each species that is delivered at once (specifically, constituents cannot be activated in fractions of their total numbers). However, more sophisticated supply regulatory mechanisms based

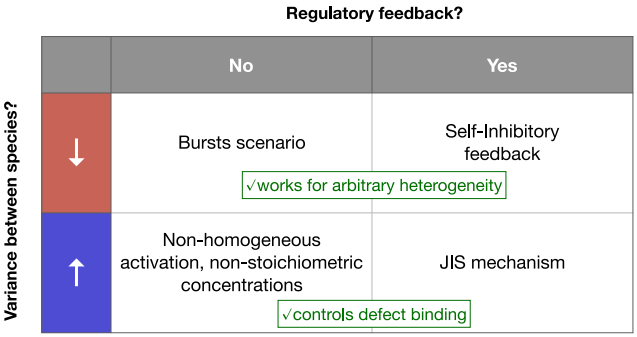


FIG. 7. **Summary of the different control strategies to improve yield and guide the assembly process.** In essence, the control strategies discussed in this manuscript in order to improve yield can be classified into two categories. First, the variance between species is either decreased (burst scenario and self-inhibitory feedback) or increased in a coordinated fashion (non-homogeneous activation rates, non-stoichiometric concentrations [17] and coordinated inhibition of neighboring species (JIS mechanism) [48]). Second, these strategies either rely on regulatory feedback (self-inhibitory feedback and coordinated inhibition of neighboring species (JIS mechanism) [48]) or not (non-homogeneous activation rates, non-stoichiometric concentrations [17] and burst scenario). Increasing the variance in a controlled manner by either non-homogeneous activation rates or in the JIS mechanism not only improves yield but also controls defect formation. In contrast, reducing the variance is generally useful for heterogeneous structures, irrespective of whether species occur several times in one target structure or not.

on feedback might be able to support the self-assembly of structures also with repeated patterns of constituents. A major advantage of providing constituents in a way to favor a specific assembly path lies in the reduction of assembly errors and defects that would result form incorrect binding events [48]. This is plausible because if particles are delivered specifically as they are needed in the assembly process the probability for cross-specific binding reactions is minimized and correct growth fostered.

In conclusion, depending on whether structures are fully heterogeneous or show repeated patterns and whether or not defect control is essential, a coordinated increase or a general decrease of inter-species variability may be beneficial.

## IX. SUMMARY AND DISCUSSION

The goal of this manuscript was to understand the role of stochastic effects in heterogeneous self-assembly processes. To this end, we formulated an effective theory for a conceptual model for the assembly of heterogeneous ring structures. Previously it was shown that stochastic effects can be detrimental for the yield of the self-assembly process ("stochastic yield catastrophe") [46, 48]. However, it remained elusive why stochastic fluctuations do have such a strong effect and which role the different sources of stochasticity play for the assembly process. The main insights gained from our analysis are the following: First, we have shown that fluctuations in the relative availability of species are the main cause for the stochastic yield catastrophe. An effective theory incorporating only this source of stochasticity and neglecting other fluctuations such as randomness in binding captures the phenomenology of the full stochastic model. Second, the effective theory allowed us to pinpoint the consequences of inter-species variability on the fidelity of the assembly process: If certain species are activated less than their binding partners, they can become temporarily unavailable for the assembly process. Their unavailability then blocks the growth of neighboring structures. Growth is biased towards small structures, which accumulate in the system. This accumulation is detrimental because a substantial amount will not be completed before resources run out. As a result, the assembly yield is low [10, 20, 21, 44–46, 51]. This effect that may lead to kinetic trapping is not captured in a deterministic description but constitutes a genuine stochastic effects caused by fluctuations in the relative concentrations of the different species.

Importantly, our theoretical analysis also reveals that the strength of the fluctuations in the relative availability of the different species is, to a large extent, set by the single-species variance in the supply. This key insight enabled us to identify different ways to significantly increase assembly efficiency by reducing variability between species. All of these strategies use supply regulation to suppress stochastic effects and avoid kinetic trapping. We distinguished these strategies according to two relevant criteria: whether or not feedback or information about the system is used to regulate the supply (*type of regulation*) and whether the variance between different species is reduced or specific assembly paths are favored (*effect on inter-species variance*). Corresponding to this classification scheme we discussed five different strategies to improve the yield. The first two strategies reduce the inter-species variance with or without the help of feedback:

- Burst scenario: inactive monomers are provided in several bursts, each of which contains a fraction of the total number of monomers in stoichiometric ratios. The time intervals between subsequent bursts are sufficiently long so that all possible binding reactions of the previous burst have taken place before the next burst is provided.

- Self-inhibition scenario: activation is inhibited by active monomers of the same species. The accumulation of active monomers of single species is thereby inhibited.

We found that improving the yield by providing particles in bursts requires the bursts to be sufficiently deterministic, i.e. the number of particles per species per burst must be tightly controlled to obey stoichiometric ratios; see Appendix E. We believe that cells could, in principle, effectuate such a strategy by controlling the composition of bursts via a regulation of several genes by a common promoter. Interesting open questions in the context of whether this would be a realistic possibility for cells concern the dependence of the yield on the exact (deterministic or stochastic) timing between the bursts. Furthermore, it might be enlightening to consider bursts of different size and to ask to what extend the order of bursts of different sizes matters.

Two recent studies demonstrated that also the opposite strategy, namely increasing the variation between species, can increase yield [17, 48]. However, increasing the inter-species variability only leads to an improved assembly process if it occurs in a very coordinated way that favors a specific assembly path (see also Appendix F). Then, competition of different structures for the same resources is reduced to a minimum and the assembly process leads to completed target structures. The following strategies have been proposed to favor specific assembly paths, where only the last one relies on feedback:

- Non-stoichiometric concentrations [17]: certain species are heavily over-represented to trigger nucleation events specifically between these species and to favor assembly paths that emanate from these nuclei.

- Inhomogeneous activation rates: exponentially increasing or decreasing activation rates provide active monomers in sequence with a specific assembly path.

- Just-in-sequence scenario [48]: activation is inhibited by inactive monomers of the neighboring species. The resulting inhibition cascade between the species favors a specific assembly path and delivers active monomers just-in-sequence with this chosen path.

From a theoretical perspective, there are several other interesting aspects about the described stochastic effects in self-assembling systems. Naively, one might ask how fluctuations between the concentrations of species, which are typically of the order of $1/\sqrt{N}$ (compared to the number of particles per species $N$), can lead to such dramatic effects. To answer this question, two aspects should be considered: First, at early stages of the assembly process, the relevance of stochastic effects must be evaluated with respect to the number of particles that have been activated to that point, rather than the total number of particles. Hence fluctuations at the beginning of the assembly process might not be suppressed as $\sim 1/\sqrt{N}$ but rather as $\sim 1/\sqrt{N_{\text{eff}}}$ where $N_{\text{eff}}$ is some effective particle number which can be much smaller than $N$. Hence at the onset of the assembly process fluctuations are indeed much more substantial even if $N$ is large. Second, it is exactly the first part of the assembly process that is most crucial for the final state. If too many structures nucleate in the beginning, too many structures compete for the same resources and none of them can be finished. This implies that especially fluctuations at the beginning of the assembly process may have a big impact since their influence determines the fate of the system. A similar phenomenology is observed, for instance, in self-reinforcing processes [63].

On a broader perspective, we demonstrate that demographic noise can be an important limiting factor for the self-assembly of heterogeneous structures. In our model, demographic noise is due to an additional activation step that renders particles competent for binding. This can be either interpreted in terms of an actual activation step (such as for instance due to allosteric effects [39, 49, 64]) or in terms of co-translational [65] or co-transcriptional assembly [66]: While the building blocks are still produced, the assembly process already takes place simultaneously. The effects of simultaneous production and assembly of building blocks is expected to be relevant both for self-assembly in living organisms as well as in nanotechnological applications: In particular, it has been suggested that combining *in vivo* transcription with simultaneous RNA-based assembly techniques might be a promising route for the further development of nanotechnology [66–69]. In light of our findings, it will be interesting to see whether such approaches applied to the assembly of large and heterogeneous structures need further regulation mechanisms to circumvent strong stochastic effects. Our proposed control strategies may then provide a first step to improve assembly efficiency.

## ACKNOWLEDGMENTS

We thank Philipp Geiger and Patrick Wilke for helpful comments. This research was funded via the Excellence Cluster "ORIGINS" by the Deutsche Forschungsgemeinschaft (DFG, German Research Foundation) under Germany's Excellence Strategy – EXC-2094 – 390783311. IRG and FG were supported by a DFG fellowship through the Graduate School of Quantitative Biosciences Munich (QBM).

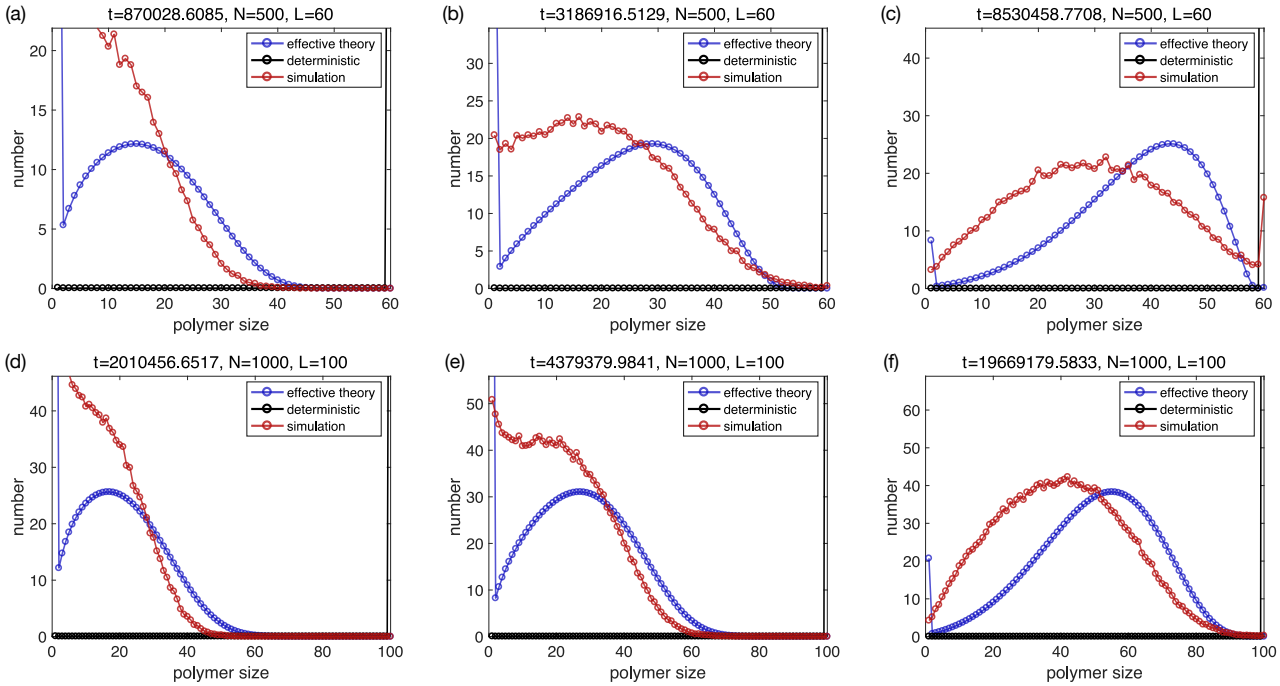


FIG. 8. **Temporal evolution of the polymer size distribution in the limit $\alpha \to 0$.** The polymer size distribution (of all species combined) as measured in stochastic simulations (red; averaged over 100 simulations each) is shown in comparison to the prediction of the effective theory ($Sc_l(t) = S(g_l(t) + b_l(t))$ as obtained by a numerical integration of Eqs. 45, 47, 48, 49; blue) and in comparison to the prediction of the deterministic theory ($Sc_l(t)$ as obtained by a numerical integration of Eqs. 3, 4; see also Ref. [46]; black). For each parameter combination ($L = 60$, $N = 500$ in (a,b,c) and $L = 100$, $N = 1000$ in (d,e,f)) the polymer size distribution is shown for small (a,d), intermediate (b,e) and large time (c,f), respectively. The other parameters are $L = S$, $\mu = \nu = 1$, $\nu_{\text{def}} = 0$ and $\alpha = 10^{-4}N/L^3$. The wave predicted by the deterministic theory has an extremely small amplitude and is therefore not visible.

## Appendix A: Temporal evolution of the polymer size distribution

Figs. 8, 9 show the time evolution of the structure size distribution (of all species combined) in the stochastic simulations and in the effective theory (with $c_l(t) = g_l(t) + b_l(t)$ according to Eqs. 45, 47, 48, 49), in comparison to the deterministic prediction ($c_l$ according to Eqs. 3, 4) as presented in Ref. [46]. We make the following observations: On the one hand, the monomer dynamics does not seem to be reproduced very well by the effective theory. Correspondingly, the back of the wave decays more rapidly in the effective theory as compared to the stochastic simulations. In relation to the deterministic wave, however, the waves produced by the effective theory and by the stochastic simulations are quite similar. This is true in particular in the limit $\alpha \to 0$ (Fig. 8) where the deterministic wave is not really visible because it exhibits a very small amplitude. In both the stochastic simulations and in the effective theory the number of monomers is high until very late in the process and the waves move much more slowly as compared to the deterministic wave because many structures compete for the same resources. Furthermore, while the effective theory does not capture the front of the wave perfectly, it does describe the right trend. As a result, the approximations made to determine the probabilities $p_l$ in terms of the simplified assembly process appear to be justifiable in retrospect.

## Appendix B: Detailed mathematical analysis

In this section, we will present the details of the parts of the mathematical analysis that have been skipped in the main text.

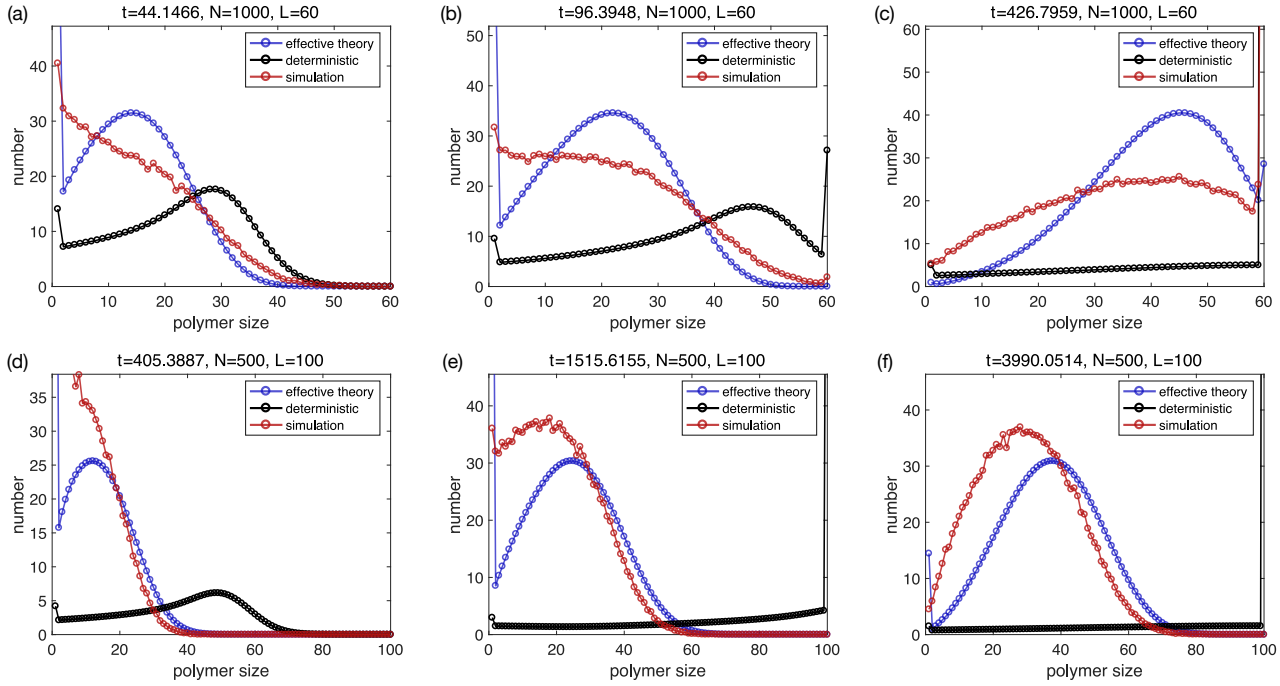


FIG. 9. **Temporal evolution of the polymer size distribution for $\alpha = N/L^3$.** The polymer size distribution (of all species combined) as measured in stochastic simulations (red; averaged over 100 simulations each) is shown in comparison to the prediction of the effective theory ($Sc_l(t) = S(g_l(t) + b_l(t))$ as obtained by a numerical integration of Eqs. 45, 47, 48, 49; blue) and in comparison to the prediction of the deterministic theory ($Sc_l(t)$ as obtained by a numerical integration of Eqs. 3, 4; see also Ref. [46]; black). For each parameter combination ($L = 60$, $N = 1000$ in (a,b,c) and $L = 100$, $N = 500$ in (d,e,f)) the polymer size distribution is shown for small (a,d), intermediate (b,e) and large time (c,f), respectively. The other parameters are $L = S$, $\mu = \nu = 1$, $\nu_{\text{def}} = 0$.

### 1. Derivation of the growth probabilities $p_l$

In this subsection, we will explain our choice of transition rates $\alpha^l_{jk}$ more thoroughly. From the resulting formulas (which are also given in the main text, Eq. 22), we derive the steady-state occupancy in the effective assembly network (Eq. 21 and Fig. 3 (f)). This steady-state occupancy will then be used to calculate the growth probabilities $p_l$, Eq. 31.

#### *a. Transition rates $\alpha^l_{jk}$*

To determine the transition rates between the different states $S^l_i$ of the simplified assembly process described in section IV C and illustrated in Fig. 3(f), we proceed as follows: First, we derive the probability $\Pi^l_{ij}$ that a structure of size $l$ with $i = 1$ or $i = 2$ growing ends has $j = 0, 1$ or 2 growing ends after attachment of a monomer to one of the original growing ends. Then, we use this probability to calculate the transition rates.

To determine $\Pi^l_{ij}$, it is convenient to consider the ways in which a monomer can attach to a structure of size $l$ with $i = 1$ or $i = 2$ growing ends: We begin with a structure that has two growing ends. Then, a monomer can attach either to the left or to the right. In order to calculate the probability that the structure still has two growing ends after the monomer attachment, we consider the probabilities of the following configurations ("embeddings"; see Fig. 10 A for an illustration):

a) The two neigboring sites of the structure of size $l$ with two growing ends both correspond to species that can grow further in the direction away from the structure (left configuration in A). That is, regardless of which end of the structure a monomer attaches to, the new end will also be in a growing state.

b) One neighboring site corresponds to a species that can grow further in the direction away from the structure, whereas the other one does not (middle configurations in A). In this case, the probability that the new end is in the growing state is 1/2 and the probability that the new end is in the blocked state is also 1/2.

c) Both neighboring sites correspond to species that cannot grow further in the direction away from the structure

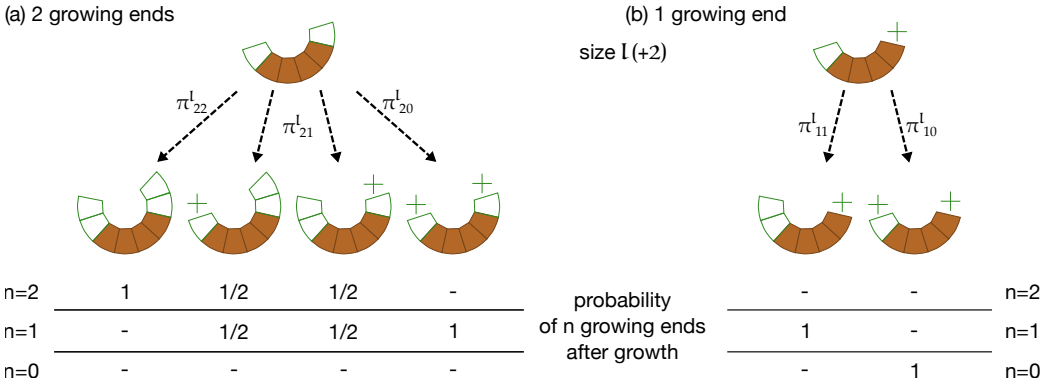


FIG. 10. **Illustration of the probabilities $\pi^l_{ij}$ that a structure of size $l$ with $i$ growing ends is embedded in configurations with additional growing or blocked ends.** (a) A structure of size $l$ with two growing ends $i = 2$ can be embedded in four different configurations of structures: one structure with an additional growing end at both ends ($j = 2$; left), two structures with one additional growing and one additional blocked end ($j = 1$; middle) and one structure with two additional blocked ends ($j = 0$; right). If the original structure of size $l$ is embedded in the structure on the left ($j = 2$), it will with probability 1 still have two growing ends after growth by one monomer. If it is embedded in one of the middle structures ($j = 1$), after growth by one monomer it will have either one or two growing ends (depending on which monomer attached to it). The probability is 1/2 for both cases. Finally, if the original structure was embedded in the structure on the right ($j = 0$), after growth it will in both cases have one growing and one blocked end. Thus the probability to end up in a configuration with one growing end and one blocked end is 1. (b) A structure of size $l$ with one growing end $i = 1$ can be embedded in two configurations: one structure with an additional growing site next to the original growing end ($j = 1$; left) and one structure with a blocked site next to the growing end ($j = 0$; right). If it is embedded in the structure on the left ($j = 1$), after growth (which can only happen at one end) it will still have one growing end. In contrast, if it is embedded in the structure on the right ($j = 0$), it will be blocked after growth.

(left configurations in A). Then, the probability that the new end is in the blocked state is 1.
What are the probabilities for either of these configuration? If we assume that the unavailable species are distributed randomly along the ring, the number of configurations in which the next-nearest neighbor species at each end of the structure of size $l$ are available (configuration a) is given by

$$X^l_{22} = \binom{L-(l+4)}{L_\times}$$

since the $L_\times$ unavailable species can be distributed to the remaining $L-(l+4)$ sites along the ring (the configuration we consider comprises the original structure of size $l$, the two neighboring species and the two next-nearest neighboring species). Similarly, the number of configurations in which the next-nearest neighbor species at one end of the structure of size $l$ is available but the next-nearest neighbor at the other end is unavailable (configuration b) is given by

$$X^l_{21} = 2\binom{L-(l+4)}{L_\times - 1}$$

because one of the unavailable species is already part of the complex of size $l$ plus the four surrounding next and next-nearest neighbors. Thus, only $L_\times - 1$ unavailable species are distributed among the remaining $L-(l+4)$ sites along the ring. The factor 2 comes from the fact that there are two equivalent configurations of this type (the available next-nearest species can be on the left or on the right). Finally, the number of configurations in which the next-nearest neighbor species at both ends of the structure of size $l$ are unavailable (configuration c) is given by

$$X^l_{20} = \binom{L-(l+4)}{L_\times - 2}$$

because two of the unavailable species are already part of the complex of size $l$ plus the four surrounding next and next-nearest neighbors.

From the number of configurations we can determine the respective probabilities by normalizing the number of

configurations by the overall number of configurations:

$$\pi_{22}^l = \frac{X_{22}^l}{X_{22}^l + X_{21}^l + X_{20}^l}$$
$$\pi_{21}^l = \frac{X_{21}^l}{X_{22}^l + X_{21}^l + X_{20}^l}$$
$$\pi_{20}^l = \frac{X_{20}^l}{X_{22}^l + X_{21}^l + X_{20}^l}.$$

As mentioned before, in configuration a ($\pi_{22}^l$), the probability that after growth by a monomer the structure still has two growing ends is 1. In configuration b ($\pi_{21}^l$) it is 1/2 and in configuration c ($\pi_{20}^l$) it is zero. The overall probability $\Pi_{22}^l$ that a structure of size $l$ with two growing ends has still two growing ends after attachment of a monomer to one of the original growing ends is given by

$$\Pi_{22}^l = \pi_{22}^l + \frac{1}{2}\pi_{21}^l = 1 - \frac{L_\times}{L - l - 2}.$$

In the last step, we plugged in the explicit formulas in terms of the binomial coefficients.
Analogously, the overall probability $\Pi_{21}^l$ that a structure of size $l$ with two growing ends has still one growing end after attachment of a monomer to one of the original growing ends is given by

$$\Pi_{21}^l = \pi_{20}^l + \frac{1}{2}\pi_{21}^l = \frac{L_\times}{L - l - 2}.$$

For structures with only one growing end, the situation is simpler because attachment of a monomer can only occur at one end (see Fig. 10 B for an illustration). Then the only question is whether the next-nearest neighbor at the growing end is available or not. Analogously to above, the number of configurations in which the next-nearest neighboring species at the growing end of the structure of size $l$ is available (left in panel B) is given by

$$X_{11}^l = \binom{L - (l+3)}{L_\times - 1}.$$

In this case, the size of the relevant complex is $l+3$, namely the original size $l$ plus the two nearest neighbors plus the next-nearest neighbor at the growing end. Since one end of the structure is blocked, one of the neighboring species is unavailable and, thus, there remain $L_\times - 1$ unavailable species that can be distributed among $L - (l+3)$ sites along the ring. Similarly, the number of configurations in which the next-nearest neighboring species at the growing end of the structure of size $l$ is unavailable (right in panel B) is given by

$$X_{10}^l = \binom{L - (l+3)}{L_\times - 2}.$$

In this case one of the neighboring species and the next-nearest neighboring species at the growing end are unavailable; there remain $L_\times - 2$ unavailable species that can be distributed among $L - (l+3)$ sites along the ring.

The respective probabilities for these configurations are

$$\pi_{11}^l = \frac{X_{11}^l}{X_{11}^l + X_{10}^l} = 1 - \frac{L_\times - 1}{L - l - 2} = \Pi_{11}^l$$
$$\pi_{10}^l = \frac{X_{10}^l}{X_{11}^l + X_{10}^l} = \frac{L_\times - 1}{L - l - 2} = \Pi_{10}^l,$$

where we plugged in the explicit expressions in terms of the binomial coefficients. Furthermore, due to the way in which the configurations were defined, the overall probabilities $\Pi_{1j}^l$ that a structure of size $l$ with one growing end has $j = 0$ or 1 growing ends after attachment of a monomer are in this case directly given by the probabilities of the respective configuration (see also the table at the bottom of Fig. 10 B).

How can we use these probabilities $\Pi_{ij}^l$ to determine the transition rates? $\Pi_{ij}^l$ denotes the conditional probability that a structure of size $l$ with $i = 1$ or $i = 2$ growing ends has $j = 0, 1, 2$ growing ends after a monomer has attached, if we already know that attachment happens. So, to translate these conditional probabilities, we need to multiply them by the rate at which monomer attachment occurs.
In the main text, we defined $\gamma$ as the total rate of attachment of a monomer to one growing end. Thus, the overall rate

for attachment of a monomer to a structure with two growing ends is $2\gamma$ and the one for attachment to a structure with one growing end is $\gamma$. Therefore, the probabilities for structures with two growing ends have to be multiplied by $2\gamma$ and the ones for structures with one growing end by $\gamma$. The transition rates are thus given by

$$\begin{aligned}
\alpha_{22}^l &= 2\gamma\Pi_{22}^l = 2\gamma\left(1 - \frac{L_\times}{L-l-2}\right)\\
\alpha_{21}^l &= 2\gamma\Pi_{22}^l = 2\gamma\frac{L_\times}{L-l-2}\\
\alpha_{22}^l &= \gamma\Pi_{22}^l = \gamma\left(1 - \frac{L_\times - 1}{L-l-2}\right)\\
\alpha_{22}^l &= \gamma\Pi_{22}^l = \gamma\frac{L_\times - 1}{L-l-2},
\end{aligned}$$

as stated in the main text, Eq. 22.

### *b. Steady-state occupancy $s_j^l$ in the effective assembly network for fixed number of unavailable sites $L_\times$*

In this section, we will determine the steady-state occupancy $s_j^l$ in the simplified assembly network described in section IV C and illustrated in Fig. 3(f).

To this end, we consider the in- and outfluxes into the states $S_j^l$ for $l \geq 2$ and $j = 1, 2$ ($l$ denotes the size of the structure and $j$ the number of growing ends). Since the number of growing ends cannot increase in the simplified assembly network, the influx into state $S_2^l$ is solely from state $S_2^{l-1}$ at rate $\alpha_{22}^{l-1}$. Outflux occurs at rates $\alpha_{22}^l$ into state $S_2^{l+1}$ and $\alpha_{21}^l$ into state $S_1^{l+1}$. Thus, the temporal evolution of the number $s_2^l$ of particles in state $S_2^l$ is given by

$$\frac{\mathrm{d}s_2^l}{\mathrm{d}t} = \alpha_{22}^{l-1}s_2^{l-1} - \left(\alpha_{22}^l + \alpha_{21}^l\right)s_2^l = \alpha_{22}^{l-1}s_2^{l-1} - 2\gamma s_2^l.$$

Regarding state $S_1^l$, there is influx from state $S_2^{l-1}$ at rate $\alpha_{21}^{l-1}$ and from $S_1^{l-1}$ at rate $\alpha_{11}^{l-1}$. Outflux occurs at rates $\alpha_{11}^l$ into state $S_1^{l+1}$ and $\alpha_{10}^l$ into state $S_0^{l+1}$. The temporal evolution of the number $s_1^l$ of particles in state $S_1^l$ is thus

$$\frac{\mathrm{d}s_1^l}{\mathrm{d}t} = \alpha_{21}^{l-1}s_2^{l-1} + \alpha_{11}^{l-1}s_1^{l-1} - \left(\alpha_{11}^l + \alpha_{10}^l\right)s_1^l = \alpha_{21}^{l-1}s_2^{l-1} + \alpha_{11}^{l-1}s_1^{l-1} - \gamma s_1^l.$$

In steady-state, $\mathrm{d}s_j^l/\mathrm{d}t = 0$, these equations are rewritten in terms of a recursion relation as

$$\begin{aligned}
s_2^l &= \frac{\alpha_{22}^{l-1}}{2\gamma}s_2^{l-1}\\
s_1^l &= \frac{\alpha_{21}^{l-1}}{\gamma}s_2^{l-1} + \frac{\alpha_{11}^{l-1}}{\gamma}s_1^{l-1}.
\end{aligned}$$

The solution to this recursion relation for $l \geq 3$ is given by

$$s_2^l = \frac{(L-L_\times-3)(L-L_\times-4)\dots(L-L_\times-l)}{(L-3)(L-4)\dots(L-(l+1))}\left(L-L_\times-(l+1)\right)s_2^1 = \tag{B1a}$$

$$= \left(L-L_\times-(l+1)\right)s_2^1\phi_l, \tag{B1b}$$

$$s_1^l = \frac{(L-L_\times-3)(L-L_\times-4)\dots(L-L_\times-l)}{(L-3)(L-4)\dots(L-(l+1))}\left((L-L_\times-2)s_1^1 + 2(l-1)L_\times s_2^1\right) = \tag{B1c}$$

$$= \left((L-L_\times-2)s_1^1 + 2(l-1)L_\times s_2^1\right)\phi_l, \tag{B1d}$$

where we defined

$$\phi_l = \frac{(L-L_\times-3)(L-L_\times-4)\dots(L-L_\times-l)}{(L-3)(L-4)\dots(L-(l+1))}.$$

These expressions depend on the steady-state numbers $s_j^1$ of monomers with either $j=1$ or $j=2$ growing ends. To make progress, we thus need to determine these steady-state numbers. This can be done by considering the steady-state dynamics of the monomer states. Into state $S_2^1$ there is an influx $i_2$ (as defined in the main text in Eq. 23), and the monomers transition to states $S_1^2$ and $S_2^2$ at rates $\alpha_{21}^1$ and $\alpha_{22}^1$, respectively. As a result,

$$\frac{\mathrm{d}s_2^1}{\mathrm{d}t} = i_2 - \left(\alpha_{22}^1 + \alpha_{21}^1\right) s_2^1 = i_2 - 2\gamma s_2^1.$$

Similarly, we have

$$\frac{\mathrm{d}s_1^1}{\mathrm{d}t} = i_1 - \left(\alpha_{11}^1 + \alpha_{10}^1\right) s_1^1 = i_1 - \gamma s_1^1.$$

In steady-state, these equations reduce to

$$s_2^1 = \frac{i_2}{2\gamma} \tag{B2a}$$

$$s_1^1 = \frac{i_1}{\gamma}. \tag{B2b}$$

*c. Growth probabilities $p_l$*

Finally we plug in the expressions, Eqs. B1, B2, for the steady-state number $s_j^l$ of particles in state $S_j^l$ into the equation for the probability $p_l$, Eq. 30. Using the explicit form of the influx rates $i_2$ and $i_1$, Eq. 23, yields after some algebra

$$p_l = \begin{cases} 1 - \frac{lL_\times(L_\times - 1)}{[L-(l+1)]\,[L+(l-1)L_\times - l]}\,, & l < L - L_\times \\ 0 & \text{else,} \end{cases} \tag{B3}$$

as given in the main text, Eq. 31. As it is derived here, it is only valid for $l \geq 4$ (since Eq. B1 is only valid for $l \geq 3$). By explicitly calculating $p_l$ for $l = 1, 2$ and 3 from the recursion relation, one can, however, show that the same formulas also apply in these cases. More generally, if there is less than one species unavailable, $L_\times < 1$, all structures can grow. Then we have $p_l = 1\ \forall l$.

### 2. Exchange dynamics between the different monomer states

In this subsection, we give details on how we determined the fluxes between the different monomer states if the number of unavailable sites $L_\times$ changes.

For this purpose, it is illustrative to consider a system with three states $A$, $B$ and $C$ and total number of particles $N$. We assume that the probability to be in state $A$ at time $t$ is $p_A(t)$ and analogously for $B$ and $C$ the probabilities are $p_B(t)$ and $p_C(t)$ with $p_A(t) + p_B(t) + p_C(t) = 1$. Furthermore, we assume that the total number is conserved: $N = \text{const}$. Then, we have for the numbers of particles $N_A$, $N_B$ and $N_C$ at time $t$:

$$N_A(t) = Np_A(t) \qquad N_B(t) = Np_B(t) \qquad N_C(t) = Np_C(t).$$

For the derivatives, we thus find analogously to the main text

$$\frac{\mathrm{d}N_A}{\mathrm{d}t} = N\frac{\mathrm{d}p_A}{\mathrm{d}t} = \frac{N_A}{p_A}\frac{\mathrm{d}p_A}{\mathrm{d}t} = N_A\frac{\mathrm{d}\,\ln(p_A)}{\mathrm{d}t},$$

and similarly for $B$ and $C$. As a result, for a three-state system we get exactly the same per-capita rates of exchange $r_A^{\mathrm{pc}}$ as for the two-state system discussed in the main text in Sec. IV D:

$$r_A^{\mathrm{pc}} = \frac{\mathrm{dln}(p_A)}{\mathrm{d}t}.$$

It is given by the time derivative of the logarithm of the corresponding probability. The only difference now is that it is not clear, yet, which portion of $A$ transforms to $B$ and $C$, respectively, if $\mathrm{d}p_A/\mathrm{d}t < 0$.

To answer this question, we consider two cases:
For the first case, we assume that $\mathrm{d}p_A/\mathrm{d}t < 0$ and $\mathrm{d}p_B/\mathrm{d}t > 0$ and $\mathrm{d}p_C/\mathrm{d}t > 0$, so there is only outflux from state $A$ into states $B$ and $C$. In this case, it is useful to rewrite the time derivatives of $N_B$ and $N_C$ as follows:

$$\frac{\mathrm{d}N_B}{\mathrm{d}t} = N\frac{\mathrm{d}p_B}{\mathrm{d}t} = \frac{N_A}{p_A}\frac{\mathrm{d}p_B}{\mathrm{d}t}$$
$$\frac{\mathrm{d}N_C}{\mathrm{d}t} = N\frac{\mathrm{d}p_C}{\mathrm{d}t} = \frac{N_A}{p_A}\frac{\mathrm{d}p_C}{\mathrm{d}t}.$$

Thus, the fractions of particles that transition from state $A$ to the states $B$ and $C$ are proportional to the corresponding changes in the probability, $\mathrm{d}p_B/\mathrm{d}t$ and $\mathrm{d}p_C/\mathrm{d}t$, respectively.
For the second case, we assume that $\mathrm{d}p_A/\mathrm{d}t < 0$ and $\mathrm{d}p_B/\mathrm{d}t < 0$ whereas $\mathrm{d}p_C/\mathrm{d}t > 0$, so there is outflux from states $A$ and $B$ into state $C$. The time derivative of $N_C$ is then conveniently rewritten as

$$\frac{\mathrm{d}N_C}{\mathrm{d}t} = N\frac{\mathrm{d}p_C}{\mathrm{d}t} = -N\left(\frac{\mathrm{d}p_A}{\mathrm{d}t} + \frac{\mathrm{d}p_B}{\mathrm{d}t}\right) = -\frac{N_A}{p_A}\frac{\mathrm{d}p_A}{\mathrm{d}t} - \frac{N_B}{p_B}\frac{\mathrm{d}p_B}{\mathrm{d}t},$$

where the second equality follows from conservation of probability $p_A + p_B + p_C = 1$. As expected, the flux into state $C$ then just corresponds to the sum of the two outfluxes from states $A$ and $B$, respectively.

These "rules" can now be applied to the exchange of monomers between the different states:
Consider first the case where the number of unavailable species decreases, $\mathrm{d}L_\times/\mathrm{d}t < 0$. Some monomers of the blocked state will then transition to the unblocked state and some monomers that have been unavailable previously will transition to the normal state. In this case, there are only interactions between two states each and we can immediately conclude that the fluxes between the states are given by

$$\varrho_\times = \frac{m_\times}{P_\times}\frac{\mathrm{d}P_\times}{\mathrm{d}t} \qquad \varrho_\mathrm{n} = -\varrho_\times \tag{B4a}$$
$$\varrho_\mathrm{b} = \frac{m_\mathrm{b}}{P_\mathrm{b}}\frac{\mathrm{d}P_\mathrm{b}}{\mathrm{d}t} \qquad \varrho_\mathrm{ub} = -\varrho_\mathrm{b}, \tag{B4b}$$

as given in the main text, Eq. 42.

In the case where the number of unavailable species increases, $\mathrm{d}L_\times/\mathrm{d}t > 0$, some monomers of the unblocked state transition back to the blocked state and some monomers of the normal state either transition to the unavailable state or also to the blocked state. In this case, we thus have according to the above rules:

$$\varrho_\times = \frac{m_\mathrm{n}}{P_\mathrm{n}}\frac{\mathrm{d}P_\times}{\mathrm{d}t} \tag{B5a}$$
$$\varrho_\mathrm{n} = \frac{m_\mathrm{n}}{P_\mathrm{n}}\frac{\mathrm{d}P_\mathrm{n}}{\mathrm{d}t} \tag{B5b}$$
$$\varrho_\mathrm{b} = \frac{m_\mathrm{n}}{P_\mathrm{n}}\frac{\mathrm{d}P_\mathrm{b}}{\mathrm{d}t} + \frac{m_\mathrm{ub}}{1-P_\mathrm{b}}\frac{\mathrm{d}P_\mathrm{b}}{\mathrm{d}t} \tag{B5c}$$
$$\varrho_\mathrm{ub} = \frac{m_\mathrm{ub}}{P_\mathrm{ub}}\frac{\mathrm{d}P_\mathrm{ub}}{\mathrm{d}t} = -\frac{m_\mathrm{ub}}{1-P_\mathrm{b}}\frac{\mathrm{d}P_\mathrm{b}}{\mathrm{d}t}, \tag{B5d}$$

where we used that the unblocked state effectively corresponds to a probability $1 - P_\mathrm{b}$ because all outflux from the blocked state goes into it (instead of going into the unavailable or the normal state). These equations correspond to Eq. 43 as given in the main text.

## Appendix C: Effective theory with defect formation

In the main text, we presented the effective theory for the case of no defect formation $\nu_\mathrm{def} = 0$. Here, we explain our approach to generalize the theory by effectively including erroneous binding. We make several (crude) simplifications:

- Erroneous binding (defect formation) is not subject to stochastic effects. That is, all monomers in states in which they cannot regularly bind to a polymer can bind at rate $\nu_\mathrm{def}$ to this polymer, thereby creating a defect in the structure. The essential idea is that it is unlikely that a polymer or monomer in the blocked state is blocked

by two unavailable species in a row: Say species $i$ and $j > i$ were unavailable, then a structure $(i{+}1)\ldots(j{-}1)$ is in the blocked state. We assume that it is unlikely that simultaneously also species $i{-}1$ and $j{+}1$ are unavailable, so the structure $(i{+}1)\ldots(j{-}1)$ can grow by erroneous binding by either species $i{-}1$ or $j{+}1$.

- Although structures with defects will effectively include unavailable species (because these species have typically been left out if erroneous binding occurs), we take the probabilities that these structures end up in a growing or blocked state to be the same as for the structures with defects: $p_l$. This certainly is a simplification because in the "derivation" of $p_l$ on the basis of the simplified assembly process described in section IV C and illustrated in Fig. 3(f), we assumed that all structures only grow by attachment of available species.
  As a result, the further growth dynamics of a polymer does not depend on whether it contains defects or not.

- We do not take into account that erroneous binding can lead to additional stochastic effects (see also [48]).

In order to write down the ensuing dynamics of all the structures, we define the following quantities:

- $g_l^D$ for $l \geq 4$ denotes the concentration of polymers with at least one defect and size $l$ in the growing state. The size $l$ always refers to the number of subunits in the structure plus the number of defects. If, for instance, a polymer of size $l$ grows by erroneous binding (creating a defect in the structure), the size of the resulting polymer is taken to be $l+2$. This convention is convenient because it ensures that it is always the structures of size $L$ that do not grow further. Since we do not keep track of the number of defects in a structure, this would be difficult to achieve otherwise.
  Since erroneous binding only occurs from the dimers onwards (there is no erroneous dimerization), polymers with defects have at least a size $l = 4$.

- Analogously, $b_l^D$ for $l \geq 4$ denotes the concentration of polymers with at least one defect and size $l$ in the blocked state.

- As before, $g_l$ and $b_l$ are defined as the concentration of polymers of size $l$ with no defect in the growing and blocked state, respectively.

How does the dynamics of monomers change due to the defect formation? First, the monomers that could bind regularly to the (defect-free) polymers in either the growing and/or blocked state, can now additionally grow to the corresponding defect-containing polymers in either the growing and/or blocked state because we assume that defect-free structures and defect-containing structures in the growing and or blocked state do not differ in their growth dynamics.
Second, the monomers that previously could not bind to a polymer in a certain state, can now erroneously bind to these polymers at rate $\nu_{\mathrm{def}}$, irrespective of whether the polymers in question already contain defects or not. In this case, an (additional) defect is created in the structure.
With these ingredients the monomer dynamics reads as follows:

$$\partial_t m_{\mathrm{n}} = \alpha N e^{-\alpha t} P_{\mathrm{n}} - 2\mu D_{\mathrm{n}} - 2\nu m_{\mathrm{n}}\gamma + \varrho_{\mathrm{n}} - \left[2\nu_{\mathrm{def}} m_{\mathrm{n}} \left(\beta_{\mathrm{def}} + \beta_{\mathrm{def}}^D\right) + 2\nu m_{\mathrm{n}}\gamma^D\right] \tag{C1a}$$

$$\partial_t m_{\times} = \alpha N e^{-\alpha t} P_{\times} - 2\mu D_{\times} - 2\nu m_{\times}\left(\gamma + \beta\right) + \varrho_{\times} - \left[2\nu m_{\times}\left(\gamma^D + \beta^D\right)\right] \tag{C1b}$$

$$\partial_t m_{\mathrm{b}} = \alpha N e^{-\alpha t} P_{\mathrm{b}} - 2\mu D_{\mathrm{b}} + \varrho_{\mathrm{b}} - \left[2\nu_{\mathrm{def}} m_{\mathrm{b}} \left(\beta_{\mathrm{def}} + \beta_{\mathrm{def}}^D + \gamma_{\mathrm{def}} + \gamma_{\mathrm{def}}^D\right)\right] \tag{C1c}$$

$$\partial_t m_{\mathrm{ub}} = -2\mu D_{\mathrm{ub}} - 2\nu m_{\mathrm{ub}}\gamma + \varrho_{\mathrm{ub}} - \left[2\nu_{\mathrm{def}} m_{\mathrm{ub}} \left(\beta_{\mathrm{def}} + \beta_{\mathrm{def}}^D\right) + 2\nu m_{\mathrm{ub}}\gamma^D\right] \tag{C1d}$$

Here, the expressions $[\ldots]$ in the brackets at the end of each line correspond to the new terms with respect to the equations presented in the main text where $\nu_{\mathrm{def}} = 0$ was assumed. Furthermore, we defined

$$\gamma^D = \sum_{l=4}^{L-1} g_l^D \qquad \beta^D = \sum_{l=4}^{L-1} b_l^D \tag{C2a}$$

$$\gamma_{\mathrm{def}} = \sum_{l=2}^{L-2} g_l \qquad \beta_{\mathrm{def}} = \sum_{l=2}^{L-2} b_l \tag{C2b}$$

$$\gamma_{\mathrm{def}}^D = \sum_{l=4}^{L-2} g_l^D \qquad \beta_{\mathrm{def}}^D = \sum_{l=4}^{L-2} b_l^D \tag{C2c}$$

as i) all the unfinished polymers with defects (superscript $D$) in either the growing ($\gamma^D$) or blocked state ($\beta^D$)
ii) all unfinished polymers without defects (no superscript) in either the growing ($\gamma_{\mathrm{def}}$) or blocked state ($\beta_{\mathrm{def}}$) whose

size is less than or equal to $L-2$ so that they still grow by erroneous binding (subscript "def") without surpassing the target structure size
iii) all unfinished polymers with defects (superscript $D$) in either the growing ($\gamma^D_{\mathrm{def}}$) or blocked state ($\beta^D_{\mathrm{def}}$) whose size is less than or equal to $L-2$ so that they still grow by erroneous binding (subscript "def") without surpassing the target structure size.

Before going to the polymers, we shortly illustrate the above "rules" for $m_{\mathrm{n}}$: Previously, the monomers in the normal state could only bind to unfinished polymers in the growing state $\gamma$. So now they additionally bind to the unfinished polymers in the growing state $\gamma^D$ with defects and erroneously to the polymers in the blocked states with size $l \leq L-2$ ($\beta_{\mathrm{def}}$ and $\beta^D_{\mathrm{def}}$).

How does the dynamics of the dimers change? Dimers cannot contain defects, so there are no polymers $g_2^D$ or $b_2^D$ and the only new terms in $g_2$ and $b_2$ come from erroneous binding of dimers with monomers with which they do not bind correctly:

$$\partial_t g_2 = \mu\left(D_{\mathrm{n}} + D_{\times} + D_{\mathrm{b}} + D_{\mathrm{ub}}\right) p_2 - 2\nu g_2 M_{\mathrm{G}} + \rho_2 - \left[2\nu_{\mathrm{def}} g_2 m_{\mathrm{b}}\right] \tag{C3a}$$
$$\partial_t b_2 = \mu\left(D_{\mathrm{n}} + D_{\times} + D_{\mathrm{b}} + D_{\mathrm{ub}}\right)(1-p_2) - 2\nu b_2 m_{\times} - \rho_2 - \left[2\nu_{\mathrm{def}} b_2 M_D\right], \tag{C3b}$$

where the new terms [...] are again in the brackets. Furthermore, we defined

$$M_D = m_{\mathrm{n}} + m_{\mathrm{ub}} + m_{\mathrm{b}} \tag{C4}$$

as all the monomers that bind erroneously to polymers in the blocked state, thereby creating a defect. These are exactly monomers in the normal, unblocked and blocked state because these cannot bind to polymers in the growing state.

These additional terms for the monomers appear equivalently for all other polymers without defects that are of size $l \leq L-2$ and, thus, are small enough to potentially bind erroneously:

$$\partial_t g_l = 2\nu\left(g_{l-1} M_{\mathrm{G}} + b_{l-1} m_{\times}\right) p_l - 2\nu g_l M_{\mathrm{G}} + \rho_l - \left[2\nu_{\mathrm{def}} g_l m_{\mathrm{b}}\right] \tag{C5a}$$
$$\partial_t b_l = 2\nu\left(g_{l-1} M_{\mathrm{G}} + b_{l-1} m_{\times}\right)(1-p_l) - 2\nu b_l m_{\times} - \rho_l - \left[2\nu_{\mathrm{def}} b_l M_D\right]. \tag{C5b}$$

Finally, the dynamics of the polymers of size $L-1$ and $L$ without defects does not change because only a correct monomer can bind to these structures and they cannot be made by erroneous binding:

$$\partial_t g_{L-1} = 2\nu\left(g_{L-2} M_{\mathrm{G}} + b_{L-2} m_{\times}\right) p_{L-1} - 2\nu g_{L-1} M_{\mathrm{G}} + \rho_{L-1} \tag{C6a}$$
$$\partial_t b_{L-1} = 2\nu\left(g_{L-2} M_{\mathrm{G}} + b_{L-2} m_{\times}\right)(1-p_{L-1}) - 2\nu b_{L-1} m_{\times} - \rho_{L-1}. \tag{C6b}$$
$$\partial_t g_L = 2\nu\left(g_{L-1} M_{\mathrm{G}} + b_{L-1} m_{\times}\right) \tag{C6c}$$

What is the dynamics of the polymers with defects? To address this question, we distinguish several cases for the growth into the structures and for the growth out of them. We begin with the growth into the structures:

- Polymers of size $l = 4$ with defect can only result from erroneous binding of a dimer with a monomer (total size: 2 (from dimer) + 1 (from monomer) + 1 (from defect)).
- Polymers of size $l = 5$ with defect(s) can result from correct growth of a polymer of size $l = 4$ with defect or from erroneous binding of a monomer with a polymer of size $l = 3$ without defects (there are no polymers of size $l = 3$ with defects).
- Polymers of size $6 \leq l \leq L$ with defect(s) can result from correct growth of a polymer of size $l-1$ with defect or from erroneous binding of a monomer with a polymer of size $l-2$ with or without defects.

For the growth out of the structures we have

- Polymers of size $4 \leq l \leq L-2$ can either grow correctly or erroneously by binding of a monomer in the respective state(s) (see also the dynamics of the monomers).
- Polymers of size $l = L-1$ can only grow correctly by binding of a monomer in the respective state(s) because they are too large to incorporate another defect.
- Polymers of size $l = L$ do not grow any more.

Taken together, these aspects yield the following dynamics of polymers with defects: For structures of size $l = 4$:

$$\partial_t g_4^D = 2\nu_{\text{def}}\left(g_2 m_{\text{b}} + b_2 M_D\right) p_4 - 2\nu g_4^D M_G - 2\nu_{\text{def}} g_4^D m_{\text{b}} + \tilde{\rho}_4^D \tag{C7a}$$

$$\partial_t b_4^D = 2\nu_{\text{def}}\left(g_2 m_{\text{b}} + b_2 M_D\right)(1 - p_4) - 2\nu b_4^D m_\times - 2\nu_{\text{def}} b_4^D M_D - \tilde{\rho}_4^D, \tag{C7b}$$

where the flux $\tilde{\rho}_4^D$ between the blocked and growing state is defined analogously to the fluxes between the blocked and growing states for the polymers without defects (see below). For structures of size $l = 5$ we have

$$\partial_t g_5^D = \left(2\nu_{\text{def}}\left(g_3 m_{\text{b}} + b_3 M_D\right) + 2\nu\left(g_4^D M_G + b_4^D m_\times\right)\right) p_5 - 2\nu g_5^D M_G - 2\nu_{\text{def}} g_5^D m_{\text{b}} + \tilde{\rho}_5^D \tag{C8a}$$

$$\partial_t b_5^D = \left(2\nu_{\text{def}}\left(g_3 m_{\text{b}} + b_3 M_D\right) + 2\nu\left(g_4^D M_G + b_4^D m_\times\right)\right)(1 - p_5) - 2\nu b_5^D m_\times - 2\nu_{\text{def}} b_5^D M_D - \tilde{\rho}_5^D, \tag{C8b}$$

and for all structures with $6 \leq l \leq L - 2$:

$$\partial_t g_l^D = \left(2\nu_{\text{def}}\Big(\left(g_{l-2} + g_{l-2}^D\right) m_{\text{b}} + \left(b_{l-2} + b_{l-2}^D\right) M_D\Big) + 2\nu\Big(g_{l-1}^D M_G + b_{l-1}^D m_\times\Big)\right) p_l - \tag{C9a}$$

$$- 2\nu g_l^D M_G - 2\nu_{\text{def}} g_l^D m_{\text{b}} + \tilde{\rho}_l^D$$

$$\partial_t b_5^D = \left(2\nu_{\text{def}}\Big(\left(g_{l-2} + g_{l-2}^D\right) m_{\text{b}} + \left(b_{l-2} + b_{l-2}^D\right) M_D\Big) + 2\nu\Big(g_{l-1}^D M_G + b_{l-1}^D m_\times\Big)\right)(1 - p_l) - \tag{C9b}$$

$$- 2\nu b_l^D m_\times - 2\nu_{\text{def}} b_l^D M_D - \tilde{\rho}_l^D.$$

Finally, we find for the structures of size $l = L - 1$

$$\partial_t g_{L-1}^D = \left(2\nu_{\text{def}}\Big(\left(g_{L-3} + g_{L-3}^D\right) m_{\text{b}} + \left(b_{L-3} + b_{L-3}^D\right) M_D\Big) + 2\nu\Big(g_{L-2}^D M_G + b_{L-2}^D m_\times\Big)\right) p_{L-1} - 2\nu g_{L-1}^D M_G + \tilde{\rho}_{L-1}^D$$

$$\partial_t b_{L-1}^D = \left(2\nu_{\text{def}}\Big(\left(g_{L-3} + g_{L-3}^D\right) m_{\text{b}} + \left(b_{L-3} + b_{L-3}^D\right) M_D\Big) + 2\nu\Big(g_{L-2}^D M_G + b_{L-2}^D m_\times\Big)\right)(1 - p_l) - 2\nu b_{L-1}^D m_\times - \tilde{\rho}_{L-1}^D,$$

and of size $l = L$:

$$\partial_t g_L^D = 2\nu_{\text{def}}\Big(\left(g_{L-2} + g_{L-2}^D\right) m_{\text{b}} + \left(b_{L-2} + b_{L-2}^D\right) M_D\Big) + 2\nu\Big(g_{L-1}^D M_G + b_{L-1}^D m_\times\Big). \tag{C11}$$

The only thing left to determine is the exchange dynamics between the polymers with defect in the growing and blocked state, respectively. Since we assumed that the dynamics of polymers in the growing and blocked state does not depend on whether the polymers include defects or not, these fluxes for the polymers with defects are entirely analogous to the fluxes for the polymers without defects. We thus have:

$$\tilde{\rho}_l^D = J_l^{B^D \to G^D} = \begin{cases} \frac{g_l^D}{p_l}\frac{\mathrm{d}p_l}{\mathrm{d}t} & \text{if } \frac{\mathrm{d}p_l}{\mathrm{d}t} < 0 \\ \frac{b_l^D}{1-p_l}\frac{\mathrm{d}p_l}{\mathrm{d}t} & \text{if } \frac{\mathrm{d}p_l}{\mathrm{d}t} > 0. \end{cases} \tag{C12}$$

As one can observe in Fig 2 (c), a numerical integration of the full dynamics presented in this section in MATLAB captures the non-monotonic behavior of the defect-free yield (inset) but not of the overall yield. This is presumably due to two of the simplifications we made: First, erroneous binding is always possible, irrespective of the state of the polymers (growing/blocked). As a result, if stochastic effects are strong, erroneous binding is very likely and in the limit of small activation $\alpha \to 0$, structures acquire more and more defects, leading to a higher yield. (In principle, the maximal possible yield is $L/(L/2+1) \approx 2$ because from the dimer state onwards all structures might only bind erroneously and then only $2+(L-2)/2 = L/2+1$ (instead of $L$) particles would make up one final structure.) Second, we did not consider that erroneous binding might itself enhance stochastic effects: If species $i$ is unavailable for a long time, the neighboring species $i \pm 1$ might bind erroneously instead of species $i$. In the end, however, this means that there will be too many particles of species $i$ available because the defects have already taken the original places of species $i$.

## Appendix D: Effective theory with bursts

The effective theory as given in the main text, Eqs. 45, 47, 48, 49, can be straightforwardly generalized to the burst scenario if the bursts are well-separated as described in the main text: The particles of the $i$-th burst are provided to

the system only once all binding reactions of the previous $i-1$-th burst have taken place and no more reactions are possible.

For $b$ bursts in total, the dynamics of the $i$-th burst is then determined by the original dynamics as given in the main text, 45, 47, 48, 49, except for two small modifications.
First, the influx of active particles into the monomer states $\mu \in \{\mathrm{n}, \times, \mathrm{b}\}$ due to the activation process is modified by

$$\alpha N e^{-\alpha t} P_\mu \longrightarrow \alpha \frac{N}{b}\, e^{-\alpha\left(t - t_{i-1}^{\mathrm{final}}\right)} P_\mu \tag{D1}$$

for all $t \in [t_{i-1}^{\mathrm{final}}, t_i^{\mathrm{final}}]$ where $t_i^{\mathrm{final}}$ denotes the time after which all reactions after the $i$-th burst have taken place (and $t_0^{\mathrm{final}} = 0$ by convention). This is just due to the fact that in each burst not $N$ but $N/b$ particles are provided. Furthermore, at $t = t_{i-1}^{\mathrm{final}}$ the number of inactive particles is increased to $N$ again and a new round of activation starts.
Second, one has to rescale the time and the number of particles in $\sigma_0$ with respect to the formula Eq. 15 given in the main text:

$$\sigma_0^2 = N\left(1 - e^{-\alpha t}\right) e^{-\alpha t} \longrightarrow \frac{N}{b}\left(1 - e^{-\alpha\left(t - t_{i-1}^{\mathrm{final}}\right)}\right) e^{-\alpha\left(t - t_{i-1}^{\mathrm{final}}\right)}. \tag{D2}$$

Again, this is due to the fact that at $t = t_{i-1}^{\mathrm{final}}$, there is no variability between the species because exactly $N/b$ particles per species per preceding burst have been provided. Furthermore, per burst there are only $N/b$ (instead of $N$) particles per species, so the Binomial distribution is with respect to $N/b$ (and not $N$ as before). As a result, over time the maximal standard deviation is given by $\sqrt{N/b}/2$ for $b$ bursts instead of $\sqrt{N}/2$ for only one burst (see also Fig. 5(a)).

The full dynamics is then obtained by a piecewise integration of this dynamics where the initial configuration of the $i$-th burst is given by the final configuration of the $i-1$-th burst (and by convention the initial configuration of the 1st burst corresponds to the original configuration of the system: all particles are inactive).

## Appendix E: Random bursts (limit $\alpha \to 0$)

In the main text, we restricted our discussion to the case of deterministic bursts with exactly $N/b$ particles per species per burst (where $b$ denotes the number of bursts). Here, we will touch upon some features of random bursts where the numbers of particles per species per burst are drawn independently from a random distribution. We will focus on three types of distributions: Poisson, Gaussian and Binomial statistics. As in the main text, we will restrict our discussion to the case where the bursts are well-separated in time, meaning that particles of the $i$-th burst are only provided once all binding reactions between the particles of the previous bursts have taken place. Furthermore, we consider the limit $\alpha \to 0$, i.e. the limit where particles are provided one after the other with all possible binding reactions taking place in between. In this limit, only the ordering of particles matters.

The yield is determined as the number of particles in the target structures relative to the total number $N_{\mathrm{tot}}$ of particles (of all species) provided to the system:

$$Y = \frac{L N_{\mathrm{target}}}{N_{\mathrm{tot}}}\,. \tag{E1}$$

In the case of a deterministic number of particles, the total number is $N_{\mathrm{tot}} = NS$ and we recover the definition of the yield as given in the main text.

### 1. Poisson bursts: no advantage due to several bursts

In this subsection, we illustrate that for bursts for which the particles per species and per burst are drawn independently from a Poisson distribution with parameter (mean) $N/b$ per species per burst, the number of bursts does not have any influence in the limit $\alpha \to 0$.

In Figure 11 the average yield (and its standard deviation) is shown for systems with $b$ bursts for which the number of particles per species per burst is drawn independently from a Poisson distribution with mean $N_0/b$. We observe that in this case the yield is independent of the number $b$ of bursts, in contrast to the case of deterministic bursts discussed in the main text; Fig. 5(b)).

In more mathematical terms, this can be understood as follows: Suppose there are two species $V$ and $W$ whose numbers of particles are independently Poisson distributed with mean $\bar{V}$ and $\bar{W}$, respectively. Then the distribution

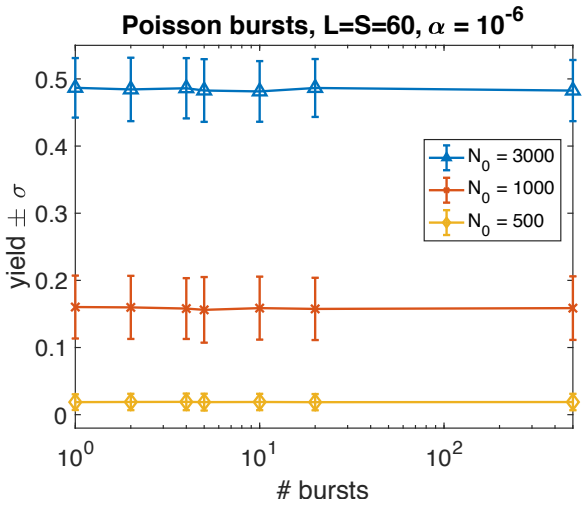


FIG. 11. **Different numbers of bursts with Poisson distributed numbers of particles.** Particles are provided in $b$ bursts for which the number of particles per species per burst is each drawn independently according to a Poisson distribution with mean $N_0/b$.The average yield and its standard deviation (averaged over 1000 samples each) is plotted against the number of bursts for different values of $N_0$: $N_0 = 3000$ (blue triangles), $N_0 = 1000$ (red crosses), $N_0 = 3000$ (yellow diamonds). The other parameters are $L = S = 60$, $\mu = \nu = 1$, $\nu_{\text{def}} = 0$ and $\alpha = 10^{-6}$.

of the number $v$ of particles of species $V$ conditioned on the total number of particles of species $V$ and $W$ being $v + w = z$ is given as Binomial distribution with sample size $z$ and probability $\bar{V}/(\bar{V} + \bar{W})$:

$$\text{Prob}(V = v|V + W = z) = \frac{\text{Prob}(V = v, V + W = z)}{\text{Prob}(V + W = z)} = \frac{\text{Prob}(V = v, W = z - v)}{\text{Prob}(V + W = z)} = \frac{\text{Prob}(V = v)\text{Prob}(W = z - v)}{\text{Prob}(V + W = z)} =$$
$$= \frac{\frac{\bar{V}^v}{v!}e^{-\bar{V}}\ \frac{\bar{W}^{z-v}}{(z-v)!}e^{-\bar{W}}}{\frac{(\bar{V}+\bar{W})^z}{z!}e^{-\bar{V}-\bar{W}}} = \binom{z}{v}\left(\frac{\bar{V}}{\bar{V}+\bar{W}}\right)^v\left(\frac{\bar{W}}{\bar{V}+\bar{W}}\right)^{z-v}, \tag{E2}$$

where the third equation is due to the independence of $V$ and $W$. Furthermore, since the sum of independent Poisson distributions is again a Poisson distribution with the summed average, $V + W$ is Poisson distributed with mean $\bar{V} + \bar{W}$. Equation E2 shows that the distribution of the number $v$ of particles of species $V$ conditioned on the total number of particles of species $V$ and $W$ being $v + w = z$ only depends on the ratio of the averages of the two Poisson distributions but not on their absolute values.

This argument can be transferred to the self-assembly process with Poisson distributed bursts. The total number of particles of each species up to burst $i$ is Poisson distributed since the individual numbers of particles per burst are Poisson distributed as well. For all these Poisson distributions, the ratio between the mean of the number of particles of one species and the mean of the number of particles of all the $S-1$ other species is always $1/(S-1)$ (or in terms of $\bar{V}/(\bar{V} + \bar{W}) = 1/S$), irrespective of how many bursts are used and in which burst the system currently is. So, the single-species variance after $\bar{A}$ activation events (or $S\bar{A}$ total activation events) is given by

$$\sigma^2_{\text{Poisson}} = S\bar{A}\frac{1}{S}\left(1 - \frac{1}{S}\right) \approx \bar{A}, \tag{E3}$$

irrespective of the number of bursts. Taken together, this (non-rigorous) argument underpins that in the case of Poisson bursts, the variances in the relative availabilities of the different species is independent of the number of bursts. Furthermore, Equation E3 suggests that, in contrast to the deterministic case where the number of particles per species (per burst) is fixed, the variance increases linearly with the number of activation events and does not decrease again.

### 2. Gaussian and Binomial bursts

So far, we have considered two cases: deterministic bursts (with zero variability or zero Fano factor, $F_{\text{d}} = 0$) and Poisson bursts (with Fano factor, $F_{\text{Poisson}} = 1$). This raises the question how the yield depends, more generally, on

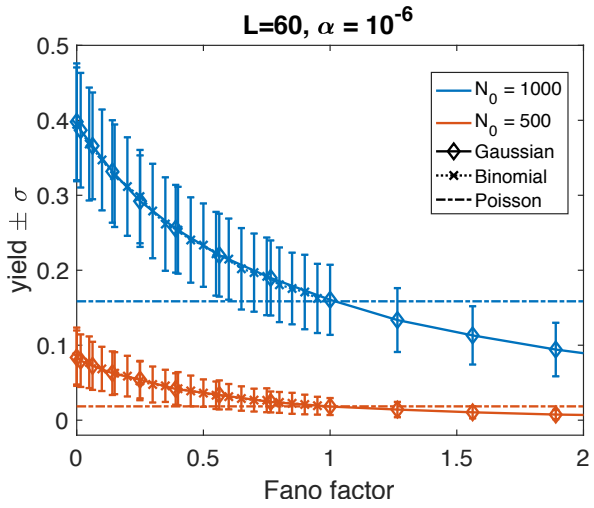


FIG. 12. **Single random burst with different distributions.** The yield and its standard deviation (averaged over 1000 samples each) for systems with one single burst for which the number of particles per species is drawn according to different distributions is plotted against the Fano factor of the respective distribution. In the Gaussian (Binomial) burst, the number of each species is drawn independently according to a Gaussian (Binomial) distribution with mean $N_0 = 1000$ (blue; Gaussian: diamonds; Binomial: crosses) or $N_0 = 500$ (red; Gaussian: diamonds; Binomial: crosses) and Fano factor $F = \sigma^2/N_0$. In the Poisson burst, the number of each species is drawn according to a Poisson distribution with mean $N_0$. In this case, the Fano factor is always 1. For better comparison, we nonetheless plot the corresponding average value of the yield (dotted-dashed line) as a function of the "Fano factor" although the Fano factor does not change. The other parameters are $L = S = 60$, $\mu = \nu = 1$, $\nu_{\text{def}} = 0$ and $\alpha = 10^{-6}$.

the Fano factor which is defined as the ratio between the variance $\sigma^2(X)$ and the mean $\langle X\rangle$ of a random variable $X$:

$$F(X) = \frac{\sigma^2(X)}{\langle X\rangle}.$$

Since the Fano factor for a Poisson distribution is always 1, we consider two other distributions to address this question: a Binomial distribution and a Gaussian distribution. More concretely, we performed simulations for well-separated bursts for which the number of particles per species per burst is drawn independently from a Binomial or Gaussian distribution, respectively. In the case of $b$ bursts, the mean is taken to be $N_0/b$ per burst per species. Furthermore, the variance per burst per species is chosen as $\sigma^2 = FN_0/b$, so the Fano factor is $F$. These expressions for the mean and the variance directly define the Gaussian distribution. For the Binomial distributions, the mean and variance translate into a probability $p$ and a sample size $N_S$ as follows:

$$N_S p \stackrel{!}{=} \frac{N_0}{b} \quad \text{and} \quad N_s p(1-p) \stackrel{!}{=} F\frac{N_0}{b} \implies p = 1 - F \quad \text{and} \quad N_S = \frac{N_0}{b(1-F)}. \tag{E4}$$

Correspondingly, the Binomial distribution can only be defined for a Fano factor $F < 1$.

### *a. Single random burst*

We consider a system with $b = 1$ burst first. Figure 12 shows how the yield depends on the Fano factor $F$ for a single burst for which the number of particles per species is drawn independently from a Gaussian or Binomial distribution with mean $N_0$ and Fano factor $F$. For comparison, we also show the average yield of a single Poisson burst with mean $N_0$. In this case, the Fano factor is always $F = 1$ and we only plot it as a line for better comparison. As expected, the yield is smaller for higher Fano factor or larger variance $\sigma^2$. Furthermore, it does not depend on whether the burst is drawn from a Gaussian or Binomial distribution since these two distributions align for large enough sample size: The curves for the two cases lie on top of each other (note, though, that the Binomial distribution is only defined for Fano factors $F < 1$; see Eq. E4). At a Fano factor $F = 1$, these curves cross the average yield for the corresponding Poisson distribution which also exhibits a Fano factor of 1. Taken together, this suggests that even a single burst with "controlled variance" (Fano factor $F < 1$) improves the yield as compared to a system where the particles are provided according to a Poisson process.

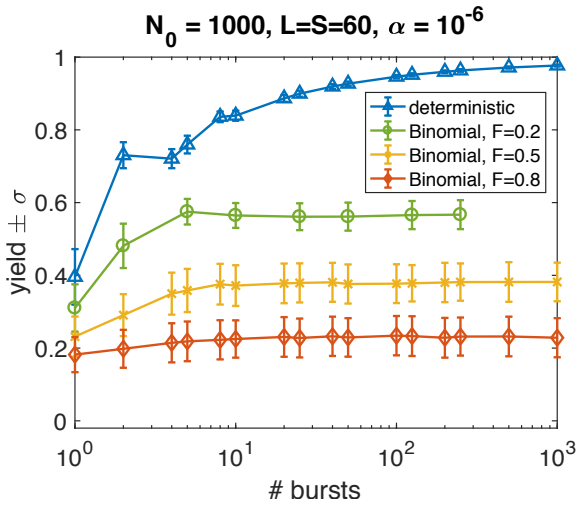


FIG. 13. **Different numbers of bursts with binomially distributed numbers of particles.** The yield and its standard deviation (averaged over 1000 samples each) for systems with $b$ bursts for which the numbers of particles per species per burst are drawn independently from a Binomial distribution with mean $N_0/b = 1000/b$ and Fano factor $F = 0.2$ (green circles), $F = 0.5$ (yellow crosses) and $F = 0.8$ (red diamonds) is plotted against the number of bursts $b$. For comparison, we also show the yield and its standard deviation (averaged over 1000 samples each) for "deterministic" bursts with exactly $N_0/b$ particles per species per burst. The other parameters are $L = S = 60$, $\mu = \nu = 1$, $\nu_{\text{def}} = 0$ and $\alpha = 10^{-6}$. Note that for a Fano factor $F = 0.2$ the maximal number of bursts that ensures that the sample size $N_S$ of the binomial distribution (see Eq. E4) is an integer value is $b_{\max} = 250$.

### *b. Several bursts*

As discussed in the main text, a higher number of bursts improves assembly efficiency if the number of particles per species per burst is deterministic (and equal for all species; compare Fig. 5(a,b)). How does this change if the number of particles per burst is drawn according to a distribution with non-zero variance? To address this question, we considered the case where the number of particles per species is drawn independently according to a Binomial distribution with mean $N_0/b$ per burst (for $b$ bursts) and Fano factor $F$. We restrict our discussion to the case of the Binomial distribution: For large numbers of bursts the number of particles per species per burst is small and then one has to be careful to use a Gaussian distributions due to two reasons:
First, a Gaussian distribution can, in principle, generate negative values. Second, and more importantly, we would have to convert the continuous Gaussian distribution into a discrete distribution (since the number of particles of each species should be a natural number). For small averages, this conversion would lead to artefacts.

Fig. 13 shows how the yield depends on the number of bursts if the number of particles per species per burst is drawn independently from a Binomial distribution with mean $N_0 = 1000$ and Fano factor as indicated in the legend. In the deterministic case $F = 0$, the yield increases considerably with the number of bursts (apart from the kink). For larger values of the Fano factor, this increase is less pronounced but still present. Note, however, that the Binomial distribution only allows for Fano factors $F < 1$ (see Eq. E4).

Taken together, this suggests that as long as the bursts are "deterministic enough", i.e. exhibit a small Fano factor, yield indeed increases for larger numbers of bursts.

## Appendix F: Random non-homogeneous activation rates

As discussed in the main text, non-homogeneous activation rates can considerably increase the yield (compare Fig. 6(a,b)) if they favor a specific assembly path. In this section, we briefly illustrate that a system with non-homogeneous activation rates that are randomly distributed over the species generally strongly decreases the assembly efficiency.

We consider two scenarios.
In the first case, the activation rate of species $i$ is determined by

$$\alpha^{(i)} = \alpha_0(1 + \epsilon U_{[0,1)})$$

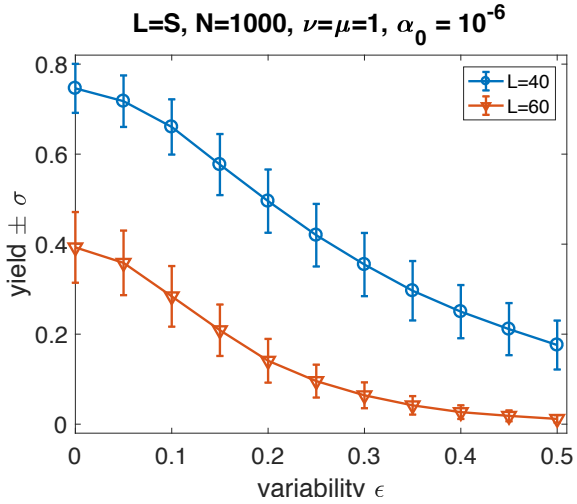


FIG. 14. **Random inhomogeneous activation rates with uniformly distributed variability.** The average yield and its standard deviation (for a sample of size 1000 each) is plotted against the variability $\epsilon$ in the activation rate. The activation rate of species $i$ is given by $\alpha^{(i)} = \alpha_0(1 + \epsilon U_{[0,1)})$ where $U_{[0,1)}$ is uniformly distributed between $[0, 1)$ and is chosen independently for all species and all samples. The parameters are $L = 40$ (blue circles) or $L = 60$ (red triangles) and $S = L$, $N = 1000$, $\alpha_0 = 10^{-6}$, $\mu = \nu = 1$

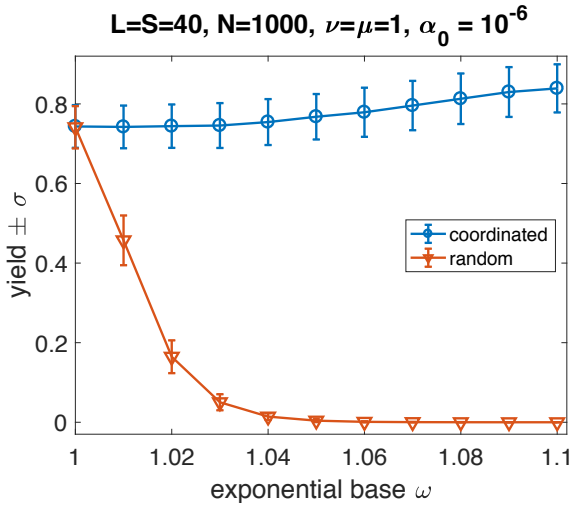


FIG. 15. **Random inhomogeneous activation rates with exponentially faster species.** The average yield and its standard deviation (for a sample of size 1000 each; red triangles) are plotted against the exponential base $w$. The activation rate of species $i$ is given by $\alpha^{(i)} = \alpha_0 f(\text{perm}(i))$ where perm creates a random permutation of the species $1, 2, \ldots, S$, independently for all samples. $f$ is the scaling function that was also chosen for the case with coordinated inhomogeneous activation rates as described in the main text: $f(i) = w^i$ for $i \leq S/2$ and $f(i) = w^{S-i}$ for $i > S/2$. For comparison, the coordinated case without permutation, perm $\equiv$ identity, is also shown (blue circles). The parameters are $L = S = 40$, $N = 1000$, $\alpha_0 = 10^{-6}$, $\mu = \nu = 1$.

where $U_{[0,1)}$ is uniformly distributed between $[0, 1)$ and is chosen independently for all species and all samples. $\epsilon$ controls the typical variability between two species.

Figure 14 shows how the yield depends on the variability $\epsilon$. For larger variability between the species, the average yield decreases. This is expected as higher variability generally leads to larger fluctuations in the availability of the different species and, thus, to stronger stochastic effects that suppress the yield.

In the second case, we taken the same functional form as in the main text (exponential) only that these activation rates are not coordinated among the species to yield a favored assembly path but instead are randomly distributed among the different species. That is, the activation rate of species $i$ is given by

$$\alpha^{(i)} = \alpha_0 f\left(\mathrm{perm}(i)\right)$$

where $f$ is the scaling function that was also chosen for the case with coordinated inhomogeneous activation rates as described in the main text: $f(i) = w^i$ for $i \leq S/2$ and $f(i) = w^{S-i}$ for $i > S/2$. However, in contrast to the situation in the main text, perm now creates a random permutation of the species $1, 2, \ldots, S$, independently for all samples.

Fig. 14 shows how the yield depends on the exponential base $w$. Since in this case the variability between species is extremely large (due to the exponential functional form of the scaling function $f$), the yield strongly decreases with $w$ and is zero already for $w \approx 1.05$. For comparison, we show again the dependency of the yield on $w$ if the inhomogeneous activated rates are coordinated as described in the main text: perm $\equiv$ identity. Due to the small range of $w$ shown, the yield only slightly increases.

[1] George M Whitesides and Bartosz Grzybowski, "Self-assembly at all scales," Science **295**, 2418–2421 (2002).
[2] Stephen Whitelam and Robert L Jack, "The statistical mechanics of dynamic pathways to self-assembly," Annual review of physical chemistry **66**, 143–163 (2015).
[3] Marc Kirschner and Tim Mitchison, "Beyond self-assembly: From microtubules to morphogenesis," Cell **45**, 329–342 (1986).
[4] Eva Nogales and Hong Wei Wang, "Structural intermediates in microtubule assembly and disassembly: How and why?" Current Opinion in Cell Biology **18**, 179–184 (2006).
[5] Johanna Roostalu and Thomas Surrey, "Microtubule nucleation: Beyond the template," Nature Reviews Molecular Cell Biology **18**, 702–710 (2017).
[6] Dieter Kressler, Ed Hurt, and Jochen Baßler, "Driving ribosome assembly," Biochimica et Biophysica Acta - Molecular Cell Research **1803**, 673–683 (2010).
[7] Alessandro Fatica and David Tollervey, "Making ribosomes," Current Opinion in Cell Biology **14**, 313–318 (2002).
[8] Howard C. Berg, "The Rotary Motor of Bacterial Flagella," Annual Review of Biochemistry **72**, 19–54 (2003).
[9] Tohru Minamino and Katsumi Imada, "The bacterial flagellar motor and its structural diversity," Trends in Microbiology **23**, 267–274 (2015).
[10] Adam Zlotnick, Jennifer M Johnson, Paul W Wingfield, Stephen J Stahl, and Dan Endres, "A theoretical model successfully identifies features of hepatitis b virus capsid assembly," Biochemistry **38**, 14644–14652 (1999).
[11] Adam Zlotnick, "Are weak protein–protein interactions the general rule in capsid assembly?" Virology **315**, 269–274 (2003).
[12] Michael F Hagan, "Modeling viral capsid assembly," Advances in chemical physics **155**, 1 (2014).
[13] Zorana Zeravcic, Vinothan N Manoharan, and Michael P Brenner, "Colloquium: Toward living matter with colloidal particles," Reviews of Modern Physics **89**, 031001 (2017).
[14] Thomas CT Michaels, Lucie X Liu, Samo Curk, Peter G Bolhuis, Andela Saric, and Tuomas PJ Knowles, "Reaction rate theory for supramolecular kinetics: application to protein aggregation," arXiv preprint arXiv:1803.04851 (2018).
[15] Samuel I.A. Cohen, Risto Cukalevski, Thomas C.T. Michaels, A. Šarić, Mattias Törnquist, Michele Vendruscolo, Christopher M. Dobson, Alexander K. Buell, Tuomas P.J. Knowles, and Sara Linse, "Distinct thermodynamic signatures of oligomer generation in the aggregation of the amyloid-$\beta$ peptide," Nature Chemistry **10**, 523–531 (2018).
[16] Michael F Hagan, Oren M Elrad, and Robert L Jack, "Mechanisms of kinetic trapping in self-assembly and phase transformation," The Journal of chemical physics **135**, 104115 (2011).
[17] Arvind Murugan, James Zou, and Michael P Brenner, "Undesired usage and the robust self-assembly of heterogeneous structures," Nature Communications **6**, 6203 (2015).
[18] PWK Rothemund, Nature **440**, 297 (2006).
[19] Klaus F Wagenbauer, Christian Sigl, and Hendrik Dietz, "Gigadalton-scale shape-programmable dna assemblies," Nature **552**, 78–83 (2017).
[20] Yonggang Ke, Luvena L Ong, William M Shih, and Peng Yin, "Three-dimensional structures self-assembled from dna bricks," Science **338**, 1177–1183 (2012).
[21] Bryan Wei, Mingjie Dai, and Peng Yin, "Complex shapes self-assembled from single-stranded dna tiles," Nature **485**, 623 (2013).
[22] Shuguang Zhang, "Fabrication of novel biomaterials through molecular self-assembly," Nature Biotechnology **21**, 1171–1178 (2003).
[23] ES Andersen, M Dong, MM Nielsen, K Jahn, R Subramani, and XXX, "Self-assembly of a nanoscale dna box with a controllable lid," Nature **459**, 73–76 (2009).
[24] MP Valignat, O Theodoly, JC Crocker, WB Russel, and PM Chaikin, "Reversible self-assembly and directed assembly of dna-linked micrometer-sized colloids," Proceedings of the National Academy of Sciences **102**, 4225–29 (2005).
[25] Adam Zlotnick, Ryan Aldrich, Jennifer M Johnson, Pablo Ceres, and Mark J Young, "Mechanism of capsid assembly for an icosahedral plant virus," Virology **277**, 450–456 (2000).
[26] Masanori Nakagawa, Shumpei Kai, Tatsuo Kojima, and Shuichi Hiraoka, "Energy-landscape-independent kinetic trap of an incomplete cage in the self-assembly of a pd2l4 cage," Chemistry–A European Journal **24**, 8804–8808 (2018).
[27] Benedict EK Snodin, Flavio Romano, Lorenzo Rovigatti, Thomas E Ouldridge, Ard A Louis, and Jonathan PK Doye, "Direct simulation of the self-assembly of a small dna origami," ACS nano **10**, 1724–1737 (2016).
[28] Hannah K Wayment-Steele, Daan Frenkel, and Aleks Reinhardt, "Investigating the role of boundary bricks in dna brick self-assembly," Soft Matter **13**, 1670–1680 (2017).
[29] George M. Whitesides and Mila Boncheva, "Beyond molecules: Self-assembly of mesoscopic and macroscopic components," Proceedings of the National Academy of Sciences of the United States of America **99**, 4769–4774 (2002).
[30] Michael F. Hagan and David Chandler, "Dynamic pathways for viral capsid assembly," Biophysical Journal **91**, 42–54 (2006), arXiv:0511006 [q-bio].
[31] Adam Zlotnick, "Distinguishing reversible from irreversible virus capsid assembly," Journal of molecular biology **366**, 14–18 (2007).
[32] Robert L. Jack, Michael F. Hagan, and David Chandler, "Fluctuation-dissipation ratios in the dynamics of self-assembly," Physical Review E - Statistical, Nonlinear, and Soft Matter Physics **76**, 1–8 (2007).
[33] Hung D. Nguyen, Vijay S. Reddy, and Charles L. Brooks, "Deciphering the kinetic mechanism of spontaneous self-assembly of icosahedral capsids," Nano Letters **7**, 338–344 (2007).

[34] D. C. Rapaport, "Role of reversibility in viral capsid growth: A paradigm for self-assembly," Physical Review Letters **101**, 1–4 (2008), arXiv:0803.0115.
[35] Sushmita Singh and Adam Zlotnick, "Observed hysteresis of virus capsid disassembly is implicit in kinetic models of assembly," Journal of Biological Chemistry **278**, 18249–18255 (2003).
[36] Alexander Yu Morozov, Robijn F Bruinsma, and Joseph Rudnick, "Assembly of viruses and the pseudo-law of mass action," The Journal of chemical physics **131**, 10B607 (2009).
[37] D. L. Caspar, "Movement and self-control in protein assemblies. Quasi-equivalence revisited," Biophysical Journal **32**, 103–138 (1980).
[38] C. Packianathan, S. P. Katen, C. E. Dann, and A. Zlotnick, "Conformational Changes in the Hepatitis B Virus Core Protein Are Consistent with a Role for Allostery in Virus Assembly," Journal of Virology **84**, 1607–1615 (2010).
[39] Guillermo R Lazaro and Michael F Hagan, "Allosteric control of icosahedral capsid assembly," The Journal of Physical Chemistry B **120**, 6306–6318 (2016).
[40] FRANK Birnbaum and MICHAEL Nassal, "Hepatitis b virus nucleocapsid assembly: primary structure requirements in the core protein." Journal of virology **64**, 3319–3330 (1990).
[41] M. C. Johnson, H. M. Scobie, Y. M. Ma, and V. M. Vogt, "Nucleic Acid-Independent Retrovirus Assembly Can Be Driven by Dimerization," Journal of Virology **76**, 11177–11185 (2002).
[42] Yu May Ma and Volker M Vogt, "Rous sarcoma virus gag protein-oligonucleotide interaction suggests a critical role for protein dimer formation in assembly," Journal of virology **76**, 5452–5462 (2002).
[43] Siddhartha AK Datta, Zhuojun Zhao, Patrick K Clark, Sergey Tarasov, Jerry N Alexandratos, Stephen J Campbell, Mamuka Kvaratskhelia, Jacob Lebowitz, and Alan Rein, "Interactions between hiv-1 gag molecules in solution: an inositol phosphate-mediated switch," Journal of molecular biology **365**, 799–811 (2007).
[44] Aleks Reinhardt and Daan Frenkel, "Numerical evidence for nucleated self-assembly of dna brick structures," Phys. Rev. Lett. **112**, 238103 (2014).
[45] William M Jacobs, Aleks Reinhardt, and Daan Frenkel, "Rational design of self-assembly pathways for complex multicomponent structures," Proceedings of the National Academy of Sciences **112**, 6313–6318 (2015).
[46] Florian M Gartner, Isabella R Graf, Patrick Wilke, Philipp M Geiger, and Erwin Frey, "Stochastic yield catastrophes and robustness in self-assembly," arXiv preprint arXiv:1905.09912 (2019).
[47] "A model should be as simple as it can be but no simpler", *Albert Einstein*.
[48] Florian M. Gartner, Isabella R. Graf, and Erwin Frey, "Controlling fidelity and time-efficiency in self-assembly," (2019).
[49] Chao Chen, C Cheng Kao, and Bogdan Dragnea, "Self-assembly of brome mosaic virus capsids: insights from shorter time-scale experiments," The Journal of Physical Chemistry A **112**, 9405–9412 (2008).
[50] Thomas K Haxton and Stephen Whitelam, "Do hierarchical structures assemble best via hierarchical pathways?" Soft Matter **9**, 6851–6861 (2013).
[51] Michael F Hagan and Oren M Elrad, "Understanding the concentration dependence of viral capsid assembly kinetics?the origin of the lag time and identifying the critical nucleus size," Biophysical journal **98**, 1065–1074 (2010).
[52] Daniel T Gillespie, "A general method for numerically simulating the stochastic time evolution of coupled chemical reactions," Journal of Computational Physics **22**, 403–434 (1976).
[53] Christian Kuehn, "Moment closure—a brief review," in *Control of Self-Organizing Nonlinear Systems*, edited by Eckehard Schöll, Sabine H. L. Klapp, and Philipp Hövel (Springer International Publishing, Cham, 2016) pp. 253–271.
[54] There are $(L+1)\times S$ different types of active and inactive monomers and structures of size $l \in \{2,\dots,L\}$ if $\nu_{def}=0$. If $\nu_{def}>0$ and one only distinguishes between defective and non-defective structures, this number roughly doubles.
[55] John A Rice, *Mathematical statistics and data analysis* (Cengage Learning, 3rd edition, 2006).
[56] Note that one could also argue that each additionally (less) activated particle of each neighboring species $i\pm1$ reduces (augments) this number by $1/2$, splitting its effect between species $i$ and $i\pm2$. The qualitative results are the same in both cases.
[57] Whether different species are unavailable for binding is, of course, not entirely independent. For instance, an excess activation of one species will make it more likely for both neighboring species to be unavailable for binding. Conversely, however, if one species is unavailable, the neighboring species is less likely to be unavailable as well. Taken together, an independence assumption might be reasonable.
[58] Note that in this derivation, we neglect that if $L/S>1$ the segments along the ring are correlated due to the periodic design of the structures.
[59] In this argument, we neglect that the different species are not all equally available at all times. However, as we have seen before, the relative deviation is only of the order $1/\sqrt{N}$ and, thus, not expected to be crucial in this step.
[60] In more technical terms, the probability for structures in the simplified assembly process to have two growing ends (Fig. 3(f)), i.e. two ends to which an available species binds, is quite low for $L_\times \geq 2$ and large structure sizes. So, most larger structures in the growing state actually bind an unavailable species on one end and an available one on the other end; see also Eq. B1 for an expression of the steady-state occupancies of the states with two or one growing end, respectively.
[61] Also $0<w<1$ would improve the yield as it would only reverse the order of activation and the corresponding assembly path compared to $w>1$.
[62] Of course, fluctuations should be minimized with respect to the stoichiometrically given concentration ratios. If a species occurs twice as many times in the final structure, it should also be available twice as many times.
[63] Robin Pemantle, "A survey of random processes with reinforcement," Probability Surveys **4**, 1–79 (2007).
[64] Adam Zlotnick and Suchetana Mukhopadhyay, "Virus assembly, allostery and antivirals," Trends in Microbiology **19**,

14–23 (2011).
[65] Eviatar Natan, Jonathan N. Wells, Sarah A. Teichmann, and Joseph A. Marsh, "Regulation, evolution and consequences of cotranslational protein complex assembly," Current Opinion in Structural Biology **42**, 90–97 (2017).
[66] Jaimie Marie Stewart and Elisa Franco, "Self-assembly of large RNA structures: learning from DNA nanotechnology," DNA and RNA Nanotechnology **2**, 23–35 (2015).
[67] Camille J Delebecque, Ariel B Lindner, Pamela A Silver, and Faisal A Aldaye, "Organization of Intracellular Reactions with Rationally Designed RNA Assemblies," Science **333**, 470–474 (2011).
[68] Florian Praetorius, Benjamin Kick, Karl L. Behler, Maximilian N. Honemann, Dirk Weuster-Botz, and Hendrik Dietz, "Biotechnological mass production of DNA origami," Nature **552**, 84–87 (2017).
[69] Mo Li, Mengxi Zheng, Siyu Wu, Cheng Tian, Di Liu, Yossi Weizmann, Wen Jiang, Guansong Wang, and Chengde Mao, "In vivo production of RNA nanostructures via programmed folding of single-stranded RNAs," Nature Communications **9**, 2196 (2018).

# 7 Controlling fidelity in heterogeneous self-assembly

This chapter summarizes the most important findings of our project on error-proneness and fidelity in heterogeneous self-assembly. The corresponding manuscript is currently in preparation for submission. This chapter is based on and uses parts of the manuscript preprint in section 7.5.

## 7.1 Motivation

In the previous chapters, we have considered kinetic traps that arise from an excess of nucleation events resulting in a large amount of incomplete structures. Another important threat for self-assembling systems is posed by kinetic traps that arise due to the assembly of erroneous or malformed structures. In particular, errors or defects that occur in highly functional structures can lead to dysfunctional behavior and thereby pose a substantial threat to the entire organism [158]. It is therefore not surprising that various human diseases can be related to errors or defects in relevant structures like ribosomes, nuclear pore complexes or proteasomes [159, 160, 161]. For example, defective ribosomes are associated with a broad range of diseases, collectively termed ribosomopathies [159] and proteasome dysfunction is especially related to neurodegenerative [162, 163], cardiovascular [164, 165] and autoimmune diseases [166] as well as cancer [167]. In order to ensure the correct assembly of such complex structures, elaborate control- and proofreading mechanisms have evolved that initiate degradation of malformed structures or intermediates. For example, nuclear pore complex assembly is surveilled by a protein called *Heh2*, which destabilizes and clears defective complex intermediates [160]. Malfunctioning of this control mechanism leads to malformed nuclear pore complexes and is associated with neurodegenerative diseases, ageing and cancer [160].

Despite the existence of such elaborate proof reading mechanisms, however, self-assembly would be very inefficient if the assembly processes were not optimized to avoid errors and defects in the first place as far as possible. Therefore, in this chapter we investigate how effective the simple control strategies for irreversible self-assembly introduced in part 1 (specifically, the activation, dimerization and just-in-sequence scenario) are in avoiding assembly errors. We restrict our attention to the irreversible scenarios here, because complex molecular machines like ribosomes, nuclear pore complexes or flagellae are broadly assumed to assemble irreversibly. Error susceptibility in reversible self-assembly is, of course, an equally important subject but needs to be discussed in depth in a separate project (which is not part of this thesis).
It should be noted that self-assembly of complex biological structures is typically highly

regulated, relying on a large number of assembly factors and elaborate mechanisms, and is certainly not exclusively described by one of our simple scenarios. Nevertheless, these elaborate mechanisms might possibly realize or build upon a simpler strategy and might have evolved to overcome the remaining deficiencies of the simpler strategy. By studying the simple scenarios, we therefore hope to gain a better understanding of the challenges that had to be overcome by evolution in order to achieve robust and resilient self-assembly and get an idea of how elaborate control mechanisms would need to function.
The emergence of complex structures and their assembly processes thereby poses a chicken-egg-problem: Without reliable assembly factors no reliable assembly of machinery like ribosomes, nuclear pore complexes etc., and without the latter no reliable assembly of the former [168]. A possible solution to this apparent paradox could be that assembly processes initially were much simpler, then evolved to optimize their reliability and gradually increased their complexity by including additional assembly factors. Studying simple control mechanisms for self-assembly could therefore also make an important contribution to the understanding of the origin of complex structures and of life in general.

An important source of errors and uncertainty in heterogeneous self-assembly is caused by imperfect binding specificities between the constituents. For example, if monomers attach incorrectly or at a wrong site in the structure - even if this happens only with a small rate - errors might accumulate and compromise the functionality of the structure. Another possibility might be due to monomers attaching prematurely to the structure and thereby hindering the attachment of other species that should have bound earlier, causing a defect (for an illustration of this process see Fig. 1 in the preprint in section 7.5).
Here we investigate a simple model that accounts for both these kinds of errors or defects by considering structures that assemble via a linear assembly path. A linear assembly path amounts to assuming that, under normal conditions, the different species attach one by one in a given order, as it typically applies to the self-assembly of complex structures like ribosomes, flagellae or nuclear pore complexes [20, 126, 24, 169]. We assume that, with a finite error probability, the typical assembly path can be disrupted, causing an error, and we ask how the frequency of errors depends on the control scenario. In particular, we investigate to which extent errors can be avoided by effectively regulating the supply of the constituents.
To this end, we study a slightly modified version of the just-in-sequence scenario, in which the monomers are activated slowly and activation of a species is inhibited by the species prior in the sequence. In this form, the just-in-sequence scenario might be able to be realized in a biological context with the help of inhibitory feedback. Finally, we compare the time efficiency of the just-in-sequence scenario based on inhibitory feedback with that of the Jis scenario relying on external supply control as discussed in chapter 2, as well as with the time efficiency of the other scenarios.

## 7.2 Model

The model we used in this project builds on the models for heterogeneous self-assembly studied in the former chapters of this thesis and expands those by accounting for assembly errors and by implementing a feedback mechanism for supply control. Specifically, as illustrated in Fig. 8.1, we consider a set of $S = L$ different species of constituents labeled by indices $i$ from

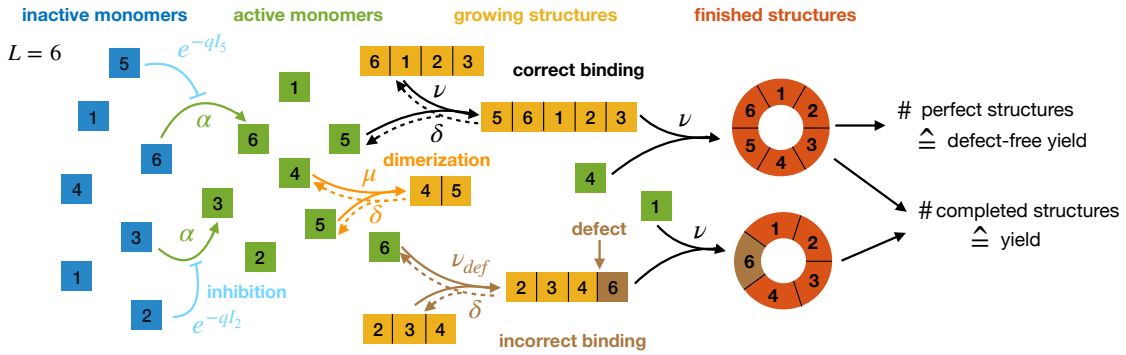


**Figure 7.1 | Illustration of the model.** Rings of size $L$ are assembled from $S = L$ different species of monomers. $N$ monomers of each species are initially in an inactive state and are activated at a maximum per-capita rate $\alpha$. Activation of species $i \leq 2$ is inhibited by the inactive monomers of species $i-1$ as detailed in the main text. Once active, species with periodically consecutive indices can bind to each other. Dimerization of two monomers happens at rate $\mu$ and attachment of monomers to polymers at rate $\nu$. Furthermore, monomers can bind incorrectly to a polymer at rate $\nu_{\text{def}}$, thereby omitting one species (defect). More precisely, a monomer of species $i$ binds incorrectly with rate $\nu_{\text{def}}$ to a complex with species $i-2$ ($i+2$) at its right (left) end, thereby omitting species $i-1$ ($i+1$), respectively. There is no incorrect dimerization. If the difference between the left and the right end of a polymer is 1 (modulo $L$) the polymer closes to a ring which constitutes an absorbing state. The yield measures the number of completed rings relative to their maximum number $N$, whereas the defect-free yield measures the number of completed rings without any defects relative to $N$.

the set $\{1, \ldots, L\}$, which assemble into rings. The ring structure thereby represents a general linear assembly process in which monomers attach in a given order (the resulting structure could also be higher-dimensional). The periodicity of the ring allows us to analyze the system mathematically.

As before, we assume that any two species with (periodically) consecutive indices can dimerize with a rate $\mu$. Once a dimer has formed, it serves as a nucleus for further growth by sequential addition of monomers with rate $\nu$. Furthermore, monomers can bind incorrectly with rate $\nu_{\text{def}}$, where upon binding a single-species defect is created in the structure (see Fig. 8.1 and Fig. 2a,c in the publication preprint in section 7.5). As incorrect binding is typically much less likely than binding in the correct sequence order, we assume $\nu_{\text{def}} \ll \nu$. Moreover, it is assumed that (correctly and incorrectly assembled) monomers detach from the ends of an (incomplete) structure at rate $\delta$. Typically, however, we set $\delta = 0$, thereby considering a process that is irreversible on the relevant time scale. The yield is defined as the number of completed, correctly or incorrectly assembled rings relative to their maximum number $N$. In contrast, the defect-free yield is defined as the number of completed rings without any defects relative to $N$ and quantifies the robustness of the assembly process to errors (fidelity).

Initially, $N$ monomers per species are in an inactive state and need to get activated in order to be able to bind. Activation of species $i$ is inhibited by species $i-1$. Specifically, we assume that species $i \geq 2$ is activated at rate $\alpha_i = \alpha e^{-qI_{i-1}}$, where $q$ is called the *inhibition strength*, $\alpha$ is the basal activation rate and $I_{i-1}$ denotes the concentration of inactive monomers of species $i-1$ (only species 1 is not inhibited, which implies that the process starts with activation of species 1). If the inhibition strength $q$ is large, activation of species $i$ is strongly suppressed

as long as species $i-1$ has not been activated in considerable amounts. Hence, increasing the strength of inhibition enforces the species to be activated in a sequence similar to the just-in-sequence scenario studied in chapter 2. While in chapter 2 supply regulation required external control, here supply regulation is promoted internally via inhibitory feedback. In this feedback-based Jis scenario, (unless $q$ is unrealistically large) the different species will not be activated perfectly in sequence, but there will always be some temporal 'overlap' between the activation of consecutive species. Therefore, in order to avoid spurious nucleation events, the basal activation rate $\alpha$ must additionally be controlled as will be discussed in detail below.
The limiting case without inhibition ($q = 0$) corresponds to the activation scenario. Since the activation scenario is strongly affected by stochastic effects, it will be particularly interesting to see how stochastic effects behave when $q$ is gradually increased from zero. Furthermore, the dimerization scenario corresponds to setting $\alpha = \infty$ and controlling the assembly process by the dimerization rate $\mu$.
We will investigate the proneness of these three scenarios (activation, dimerization and just-in-sequence scenario) to assembly errors and analyze the behavior of the yield and defect-free yield as functions of the respective control parameters.

## 7.3 Results and Discussion

First, we determine how effectively the number of defects can be controlled in the dimerization and activation scenario. To this end we study the behavior of the defect-free yield. Since deterministically, the monomer concentrations of all species are the same in both scenarios, a simple mean field argument predicts the ratio between the yield and the defect-free yield: Since all species are available in equal concentrations, the probability that a defect occurs at a given site is $p_{\mathrm{def}} = \nu_{\mathrm{def}}/(\nu + \nu_{\mathrm{def}})$. Hence, the probability that a completed structure is free from defects equals the probability that in $L-2$ subsequent binding steps no defect occurs and thus,

$$\frac{\text{defect-free yield}}{\text{yield}} = (1 - p_{\mathrm{def}})^{L-2} \approx e^{-(L-2)p_{\mathrm{def}}}, \tag{7.1}$$

assuming that $p_{\mathrm{def}} \ll 1$. Hence, the defect-free yield is expected to decrease exponentially with the size of the target structure and the defect probability $p_{\mathrm{def}}$.
Indeed, plotting the yield and defect-free yield against the dimerization rate shows that the dimerzation scenario behaves according to this mean-field prediction also in the limit of small particle numbers $N$, see Fig. 3a in the publication preprint in section 7.5.

In contrast, the activation scenario shows a more intricate behavior: Upon decreasing the activation rate, the yield rises up to a maximal value that is generally smaller than 1 due to the stochastic yield catastrophe (see chapter 5). The defect-free yield also increases at first but then reaches a maximum and subsequently drops again to a stationary plateau if $\alpha$ is further decreased. This non-monotonic behavior of the defect-free yield is not captured by the mean-field theory, Eq. (7.1), which only predicts the maximum of the defect-free yield in the limit $N \to \infty$. In analogy with the term 'stochastic yield catastrophe', we refer to the drop of the defect-free yield in the limit of small $\alpha$ as 'stochastic defect catastrophe'. Similar to the stochastic yield catastrophe, the defect catastrophe originates from fluctuations in the relative copy numbers of the different species if the activation rate is small: If a shortage

in the supply of one species persists long enough, incorrect binding by the wrong building blocks becomes more likely as the proper building blocks are not readily available. The defect catastrophe occurs once the activation rate decreases below the characteristic rate at which incorrect binding occurs, which is determined by $\nu_{\mathrm{def}}$. Since $\nu_{\mathrm{def}} \ll \nu$, where $\nu$ determines the threshold activation rate, the defect-free yield first rises to a maximum when decreasing $\alpha$ before the defect catastrophe occurs, which thereby causes the non-monotonic behaviour.

Together, this shows that the error proneness of self-assembly cannot be efficiently controlled neither in the dimerization nor in the activation scenario. While the dimerization scenario behaves as predicted by mean-field theory, the activation scenario is additionally affected by stochastic effects, which strongly increase the error rate. Similarly, stochastic effects could also arise in a spatial system due slow diffusion causing demographic noise in the local concentrations. This suggests that defects and errors might be a strong limitation for self-assembling systems, in particular if, additionally, fluctuations in the relative concentrations of the different species are relevant.

Next, we investigated whether by increasing the inhibition strength $q$, the frequency of assembly errors can be reduced. Interestingly, plotting the yield and defect-free yield against the inhibition strength $q$ for a fixed activation rate $\alpha$ reveals that the (defect-free) yield initially declines when $q$ is increased but finally almost reaches the perfect value of 1 if $q$ becomes large and $\alpha$ is sufficiently small, see Fig. 4a in the publication preprint in section 7.5. Hence, with the help of inhibition, the impact of noise can be regulated: A small value of $q$ increases stochastic effects because species are activated 'out-of-sequence', i.e. before the previous species has been activated, which causes strong demographic noise in the species' concentrations. If, however, $q$ is large enough so that out-of-sequence activation is sufficiently suppressed, the strict sequential activation of the constituents reduces randomness and thereby decreases the probability for monomers to bind incorrectly, which leads to an enhancement of the (defect-free) yield.
In order to obtain a high (defect-free) yield, it is furthermore crucial that the basal activation rate $\alpha$ is small enough: Keeping $q$ fixed and varying $\alpha$ shows that the yield is zero if $\alpha$ is large and starts to increase only if the activation rate is reduced below a threshold value $\alpha_{\mathrm{th}}^{\mathrm{JIS}}$, see Fig. 4b in the publication preprint. A small basal activation rate is important because inhibition is imperfect for any finite $q$ and thus there is always a certain temporal overlap in the activation of consecutive species, which would trigger additional nucleation events (also see Fig. 5 in the publication preprint). By decreasing $\alpha$, however, the concentration of active monomers is reduced, similar as in the activation scenario, and thus attachment of monomers to already existing structures is favoured over nucleation of new structures. Due to the influence of inhibition, the threshold activation rate to obtain non-zero yield is generally larger in the Jis scenario than the threshold rate in the activation scenario. Specifically, we find the former scaling with the size of the target structure as $\alpha_{\mathrm{th}}^{\mathrm{Jis}} \sim L^1$ while the later scales as $\alpha_{\mathrm{th}}^{\mathrm{Act}} \sim L^3$.

Approximating the inhibition function as a step function, $e^{-qI_i} \approx \Theta(1/q - I_i)$, and considering the coarse-grained dynamics of the concentrations of active, inactive and bound monomers, analytic expressions for several key quantities of the assembly process in the just-in-sequence

scenario can be derived; for details see Supplement of the publication preprint in section 7.5. For example, the probability for a defect to occur at a specified site is approximately given by $p_{\mathrm{def}} = \frac{\nu_{\mathrm{def}}}{(qC-1)\nu}$, and the total assembly time follows as $T_{90} = \frac{L}{\alpha} \ln(qC)$. This shows that the defect probability can be efficiently suppressed by increasing the inhibition strength $q$, while the assembly time depends only logarithmically on $q$ and thus increases only slightly when $q$ is augmented. This implies that in an effective implementation of the JIS scenario the inhibition strength should be maximized.
Furthermore, the minimal time required to achieve 90% yield can be shown analytically to scale roughly like $T^{\mathrm{min}}_{90,\mathrm{Jis}} \sim \frac{L^2}{\nu C}$. Hence, the Jis scenario based on inhibitory feedback has the same time complexity as the Jis scenario that relies on external supply control, compare chapter 2. This result again demonstrates the robustness of the time complexity exponents. By explicitly simulating both cases, however, we find that the minimal assembly time in the Jis scenario with external supply control is roughly 1.5 orders of magnitude smaller compared to the Jis scenario with inhibitory feedback. The reason for this discrepancy in the time efficiency is that the feedback-based Jis mechanism requires slow activation in order to prevent spurious nucleation events, which makes it less efficient than the externally controlled Jis mechanism, in which all monomers of a 'batch' are provided simultaneously.

In total, these results suggest that temporal supply regulation as effectuated in the Jis scenario can mitigate stochastic effects and greatly enhance the robustness of the assembly process to errors compared to the activation and dimerization scenario.
Generally speaking, in the self-assembly of heterogeneous structures, information is required to specify the location and connectivity of the building blocks within the assembled structure ('information-rich' structures). This information can, for example, be stored in the constituents themselves (through their binding specificities, allosteric effects to avoid kinetic traps or fine-tuned bond strength to find free energy minima). We call such strategies that rely on sophisticated molecular binding properties of the constituents 'molecular' control strategies. Supply regulation constitutes an alternative way to provide this assembly information that helps the constituents to assemble correctly ('supply control strategy'). The information provided through the supply sequence allows to decrease the information content of the constituents, which may thus become less specific and less specialized.
Hypothetically, this could have been an important factor enabling the evolution of complex macromolecules: If, for example, a regulatory program ensures that the constituents are made competent for binding in a specified sequence and thereby supports the correct self-assembly of these subunits, the constituents themselves might have more flexibility to mutate and acquire additional functions. Evidence for supply regulation in biological self-assembly are indeed found, for instance, in the bacterial flagellum, where gene-expression programs coordinate the expression of the relevant genes in correspondence with specific stages of the assembly process [24]. Hence, as a hypothetical idea, it might be thinkable that it was the interplay between these redundant or 'orthogonal' strategies, the molecular- and supply control strategy, that enabled the evolution of those complex macromolecules and sophisticated assembly processes that we observe in nature.

## 7.4 Key points

In my opinion, the key results of this project are the following:

- Supply regulation in the just-in-sequence scenario can be realized either by external control (see chapter 2) or in a self-organized way with the help of inhibitory feedback. The latter case describes a possible scenario that could be realized in a biological system and it requires the monomers to be activated slowly, similarly as in the activation scenario. Both implementations of the just-in-sequence scenario exhibit the same time complexity exponent.
- In the activation and dimerization scenario, in the limit of large particle numbers, the number of structures without errors/defects decreases exponentially with the rate for incorrect binding $\nu_{\mathrm{def}}$ as well as with the size of the target structure. If particle numbers are not abundant, the activation scenario suffers a stochastic defect catastrophe, which further decreases the defect-free yield. Assembly errors might therefore pose a strong limitation in these systems, in particular if fluctuations in particle concentrations are relevant (e.g. due to slow diffusion).
- In the just-in-sequence scenario, the defect-free yield can be enhanced efficiently by increasing the strength of inhibition between consecutive species, while at the same time the required assembly time increases only slightly. Supply regulation might therefore offer an effective and viable way to increase the fidelity of self-assembly processes both in biological and artificial systems. Hypothetically, this might have been an important factor enabling the evolution of complex macromolecules.

## 7.5 Manuscript preprint: Controlling fidelity and time-efficiency in self-assembly

This section is a preprint of the following manuscript.

**Controlling fidelity and time-efficiency in self-assembly**

by

Florian M. Gartner,[1] Isabella R. Graf, [1,2] and Erwin Frey[1]
[1] *Arnold-Sommerfeld-Center for Theoretical Physics and Center for NanoScience, Department of Physics, Ludwig-Maximilians-Universität München*
[2] *Present address: Department of Physics, Yale University, New Haven, CT 06520, USA.*

# Controlling fidelity and time-efficiency in self-assembly

**Florian Gartner[1], Isabella Graf[l] & Erwin Frey[1*]**

[1] Ludwig-Maximilians-Universität München, Department of Physics, Arnold-Sommerfeld-Center for Theoretical Physics (ASC) and Center for NanoScience (CeNS), Theresienstrasse 37, D-80333 München, Germany.

[*] Corresponding authors: frey@lmu.de

## *Abstract*

**Self-assembly is a fundamental concept used to explain the astonishing ability of living systems to autonomously generate complex structures and machineries. Yet, it remains largely unclear how nature achieves such high reliability and reproducibility in these processes. Using a conceptual and generic model we examine different strategies to effectuate the self-assembly of finite-sized heterogeneous target structures. These different strategies are compared with respect to their yield, error-proneness and time-efficiency. In particular, we discuss supply regulation as a powerful yet simple mechanism to enhance the efficiency and fidelity of heterogeneous self-assembly processes. Supply regulation requires the assembling constituents to be provided in accordance with the most favorable assembly pathway ('just-in-sequence supply'). Since this method has several benefits but does not rely on optimized molecular binding properties, it constitutes a promising possibility for artificial self-assembly.**

## *Introduction*

The self-assembly of functional structures on the nanometer scale from smaller subunits or elementary building blocks plays a fundamental role in biology (Whitesides, 2002; Mendes, 2013). Understanding and being able to imitate these processes will give rise to novel applications in engineering, biotechnology and medicine (Whitesides, 1991; Whitesides 2002; Zhang, 2003). The obstructions to efficient and reliable self-assembly are, however, numerous: For example, a self-assembling system might get trapped in a local minimum of the free energy landscape which is different from its optimal state, known as kinetic trap (Hagan, 2011; Grant, 2011). Furthermore, we have recently shown that the dynamics of self-assembling systems can be strongly affected by stochastic effects that emerge due to a slow activation or production step of the constituents and can completely suppress the yield (termed "stochastic yield catastrophe") (Gartner, 2019). These stochastic effects were shown to arise when fluctuations in the concentrations of the various species become large, thereby enhancing the effective nucleation rate.

Moreover, in this work we discuss two further central aspects of self-assembly processes: *Error proneness* and *time efficiency*. In particular, we ask to which extend fidelity in self-assembly can be achieved if there is a (small) chance for particles to bind incorrectly. Additionally, we characterize the time efficiency of self-assembly processes by examining the minimal time needed to reach a certain yield in an assembly product for various self-assembly scenarios. Based on our findings, we argue that both, error proneness and poor time efficiency, can constitute major limitations of general self-assembling systems.

In order to overcome these limitations, elaborate mechanisms have evolved in cellular systems whose function is to guide the assembly processes and increase their efficiency. For example, in ribosomal assembly, specialized assembly factors coordinate the assembly process and control the finished structures for errors and defects (Nerurkar, 2015; Peña, 2017). In bacterial flagellum assembly, membrane proteins and chaperons form an export system that, by switching its export specificity, determines the exact order in which flagellar components are exported through the membrane to assemble the external parts of the flagellum (Macnab, 2004; Chevance, 2008; Vonderviszt, 2013). Finally, in virus capsid assembly, allosteric binding effects prevent the spontaneous dimerization of molecules and favor growth of the capsids over nucleation, thereby avoiding kinetic traps (Caspar, 1980; Packianathan, 2010; Lazaro, 2016).

While those mechanism have evolved over evolutionary time scales and rely on specialized molecules with precisely adopted binding properties, for artificial self-assembly one would like to implement simpler control mechanisms (Zhang, 2001). Optimally, such control mechanisms should make minimal demands on molecular properties of the constituents in order to allow for a flexible design of the building blocks. In line with these requirements, we show that the efficiency and reliability of heterogeneous assembly processes can be greatly enhanced by coordinating the supply

of the assembling constituents. This assembly strategy relies on the intuition that, for optimal efficiency, the different types of molecules should be made available for binding in the same order in which they are assembled. In a very similar way, industrial assembly processes, in particular in the automotive industry, profit in various ways from an organizational principle referred to as *'just-in-sequence' supply* (Werner, 2003; Roser, 2017). This principle demands that the different pieces are delivered to the assembly line in the exact sequence in which they are built in. Thereby, the efficiency of the workflow can be increased, human errors resulting from incorrect assembly reduced and storage costs minimized (Roser, 2017).

We propose a simple feedback mechanism for molecular self-assembly by which each species inhibits the availability of its successor in order to achieve just-in-sequence supply in a self-organized way. Alternatively, the supply could be controlled externally, e.g. by an appropriate supply protocol in an experiment. By comparing with other assembly scenarios, we show that a 'just-in-sequence' supply strategy is effective in minimizing the number of assembly errors, avoids stochastic yield catastrophes and kinetic traps, and also enhances the time efficiency.

## *Model*

### *Model motivation*

In this work we focus on *heterogeneous linear assembly processes*. A *linear* assembly process presupposes that the constituents bind to the growing structure one by one, in a preferred linear order with one or two independent growth directions (Zlotnik, 1999; Endres, 2002; Morozov, 2009). Please note, however, that the emerging structure itself does not necessarily have to be a spatially linear (one-dimensional) object. It may as well have a more complex, three-dimensional geometry as long as there is a unique assembly pathway (or several topologically equivalent ones). With this in mind, assembly line models have been used extensively to study the formation of virus capsids (Zlotnik, 1994; Zlotnik, 1999; Endres, 2002; Morozov, 2009; Hagan 2010; Chen, 2008; Hagan, 2014). Furthermore, many other biological systems like the bacterial flagellum or the subunits of ribosomes assemble in a linear order (Chevance, 2008; Vonderviszt, 2013; Peña, 2017), probably because a linear binding sequence constitutes the easiest way to realize the formation of such complex structures. These complex macromolecular machineries typically represent 'information-rich' structures, i.e. they consist of multiple different types of constituents where each constituent has a well-defined locus within the structure (Cademartiri, 2015; Whitelam, 2015). Here, for simplicity, we consider systems that are fully heterogeneous, i.e. all constituents are assumed to be different.

Generally, before an assembly process starts, the constituents need to be supplied or produced, e.g. by gene expression, or rendered competent for binding, e.g. by a biochemical process like nucleotide exchange (Chen, 2008; Alberts, 2015; Lazaro,

2016). We model this *'activation' step* as a transition from an inactive state to an active state for each constituent. The inactive state can be thought of as representing a different molecular conformation or a precursor of the corresponding molecule/protein that is not yet competent for binding. In a synthetic system, it might also represent the state before the particle has entered the system. A major theme in our analysis concerns the question how supply can be effectively regulated through (simple) interactions between the various constituents.

Once the constituents start to assemble, occasionally binding events might happen that lead to incorrectly assembled structures (Hedges, 2014; Whitelam, 2015). Here, for specificity, we consider assembly errors that result if a constituent binds prematurely and thereby disrupts the intended assembly order; see Fig. 1 for an illustration. These assembly errors might occur because of similarities in the binding domains of the constituents. In particular, in the self-assembly of a three-dimensional structure, structural stability is often achieved by numerous bonds between the different constituents (high inter-species connectivity), see Fig. 1. Hence, in a naive implementation of the assembly process, the geometry of the structure may easily allow for deviations from the desirable assembly path that then lead to defects in the structure as shown in the lower panel of Fig. 1. Here, for example, species F adheres prematurely before the predecessor species E has bound. Thereby, species F hinders the accessibility of species E to its binding spot due to steric effects and prevents its binding, resulting in a defect in the final structure.

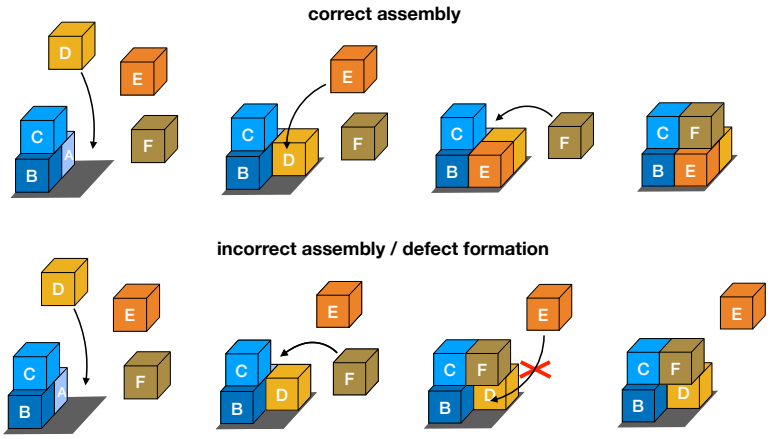


**Figure 1: Sketch of a generic assembly process illustrating the occurrence of assembly errors (defects).** We depict the assembly of 6 constituents (denoted as A…F) on top of a substrate. The favorable assembly path is A-B-C-D-E-F. The upper line shows the assembly of the last three constituents (D,E,F) in the correct order. The lower line illustrates the occurrence of an assembly error: constituent F binds prematurely sticking only to D and C while E is still missing. Subsequent binding of E is hindered by F and therefore prevented. This causes a defect of particle E in the structure.

***Model description***

We build on previous models describing the self-assembly of heterogeneous, finite-sized target structures (D'Orsogna, 2013; Murugan, 2015; Gartner, 2019) and expand those by accounting for assembly errors and by implementing a feedback mechanism for supply control. Specifically, as illustrated in Fig. 2, we consider a set of $L$ different species of constituents labeled by indices $i$ from the set $\{1, \dots, L\}$, which assemble into rings. The ring structure thereby ought to represent a general linear assembly process with two independent growth directions. We choose the ring as model for the target structure because the periodicity of the ring allows to analyze the system mathematically by exploiting its symmetry without otherwise affecting the qualitative behavior. The completed rings form an absorbing state of the system which do no longer participate in any reactions.

In detail, we assume that any two species with (periodically) consecutive indices (like 1 and 2 or $L$ and 1) can dimerize with a rate $\mu$. Once a dimer has formed, it serves as a nucleus for further growth by sequential addition of monomers. In the following, we will refer to the ensuing structure as a polymer, keeping in mind that the actual structure may as well be three-dimensional. The rightmost (leftmost) species of a polymer will be referred to as the right (left) end of that polymer. Binding of additional monomers to either end of that polymer in correct sequence order occurs with a fixed rate $\nu$. There may also be incorrect binding of species violating the sequence order. For specificity, we consider single species defects, where upon binding a gap is created in the sequence order; see Fig. 2a,c. As incorrect binding is typically much less likely than correct binding we assume $\nu_{\mathrm{def}} \ll \nu$. Finally, to be able to also consider assembly dynamics where binding is reversible we introduce a process where monomers detach from the ends of a structure with a detachment rate $\delta$. If not stated otherwise, we set $\delta = 0$, thus considering a process that is irreversible on the time scale at which the assembly reaction takes place (cf. section "Time efficiency"). The ring closes when the sequence indices between the left and right end differ by 1 (modulo $L$). Then, the structure is completed and no further attachment or detachment processes are possible. If a completed structure is free of defects, we call it `perfect' otherwise `imperfect'; see Fig. 2a.

Initially, $N$ monomers per species are assumed to be in an inactive state where they are still unable to form bonds. The initial concentration of each monomer species is denoted by $C = N/V$, where $V$ is the reaction volume. In order to be able to bind, monomers have to undergo an activation step. We are interested in how self-assembly efficiency is affected by inhibitory feedback. Specifically, we consider a kinetic process where activation of species tends to occur in the desired sequence order. Given a basal activation rate $\alpha$ for the first species (which we take[1] as i = 1), we implement such a

[1] Since the ring model is symmetric, it is an arbitrary choice from which species the activation sequence is started. In assembly processes with only one growth direction there would be a unique sequence.

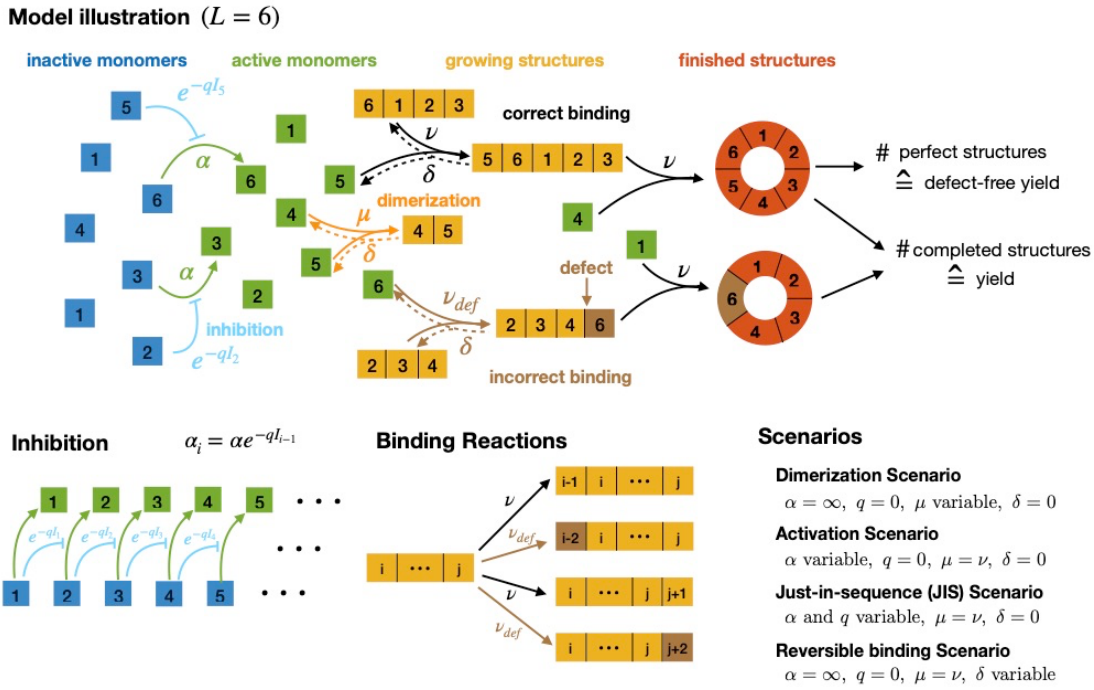


**Figure 2: Schematic description of the model and the different scenarios. (a)** Rings of size $L$ are assembled from $L$ different particle species. $N$ monomers of each species are initially in an inactive state and are activated at a maximum per-capita rate $\alpha$. Activation of species $i$ is inhibited by the monomers of species $i-1$ (if $i \geq 2$) as detailed in Eq. (1). Once active, species with periodically consecutive indices can bind to each other. Dimerization of two monomers happens at rate $\mu$ and attachment of monomers to polymers at rate $\nu$. Furthermore, monomers can bind incorrectly to a polymer at rate $\nu_{\text{def}}$, thereby omitting one species (defect). There is no incorrect dimerization. If the difference between the left and the right end of a polymer is 1 (modulo $L$) the polymer closes to a ring which constitutes an absorbing state. The yield measures the number of completed structures (closed rings) relative to the maximum number $N$ of perfect rings (completed and without defects). The defect-free yield measures the number of perfect rings relative to $N$. **(b)** Inhibition cascade that realizes just-in-sequence supply in the JIS scenario. In the JIS scenario, the inactive monomers of each species inhibit the activation of the subsequent species. This inhibition cascade effectuates that the different species are provided just-in-sequence for the assembly process along a chosen assembly path. **(c)** Possible binding reactions of a polymer $(i,j)$ with left end $i$ and right end $j$. Species indices are understood modulo $L$. To the left end of the polymer, a monomer of species $i-1$ can bind correctly, $(i,j) \to (i-1,j)$, with rate $\upsilon$ or species $j-2$ can bind incorrectly, $(i,j) \to (i-2,j)$, with rate $\nu_{\text{def}}$. In the case of incorrect binding, a defect of species $i-1$ is created. Analogously, to the right end a monomer of species $j+1$ can bind correctly, $(i,j) \to (i,j+1)$, or species $j+2$ can bind incorrectly. **(d)** Specification of the parameters for the four different assembly scenarios studied in this work. The respective parameter(s) declared as 'variable' in each scenario will be tuned in order to optimize the (defect-free) yield and the time-efficiency. The default parameters which are not declared 'variable' are set as follows: $\alpha = \infty, q = 0, \mu = \nu, \delta = 0$.

sequential inhibitory feedback by assuming that the activation rate of the subsequent species is reduced with respect to the basal value:

$$\alpha_i = \alpha \cdot H(I_{i-1})\,. \tag{1}$$

The inhibition function $H$ with $0 \leq H \leq 1$ depends on the concentration of the inactive monomers, $I_{i-1}$, of the preceding species $i-1$ in such a way that inhibition of species $i$ is strong if there is no significant number of active monomers of the preceding species

available yet; see below for specific choices of the inhibition function. Heuristically, this is expected to lead to a 'just-in-sequence' assembly process, where the activation of the subsequent species starts only when a large fraction of the species just preceding in sequence order is already bound; for an illustration see Fig. 2b.

For the numerical analysis we choose the inhibition function $H_1(I) := e^{-qI}$, that suppresses activation of a species exponentially with the number $I$ of inactive preceding monomers. The parameter $q$, that we will refer to as the inhibition strength, can be thought of as describing an inhibition threshold: activation is inhibited if $I \gg I_0$ and unhindered if $I \ll I_0$, where $I_0 = \frac{1}{q}$. In order to make the system amenable for an analytic treatment we will use a (Heaviside) step function $H_2(I) := \Theta(I_0 - I)$. We will show later that in the relevant regime where self-assembly is efficient, the precise form of the inhibition function is not important but different inhibition functions lead to quantitatively very similar results, suggesting that the results and findings apply in general.

***Scenarios and observables***

We will analyze the model in various limiting cases (called 'scenarios') that are informative about the respective role of activation, dimerization, inhibitory feedback (implementing a 'just-in-sequence' supply of constituents) and reversibility of binding, regarding the efficiency and fidelity of the self-assembly process. These different scenarios are listed in Fig. 2c. The first three scenarios are irreversible and rely on different mechanisms to impede nucleation and thereby favor growth of existing structures over the initiation of new ones ('slow nucleation principle') (Zlotnik, 1999; Hagan, 2010; Ke, 2012; Reinhardt, 2014; Jacobs, 2015; Gartner, 2019). This ensures that initiated structures can get finished before resources run out ('depletion trap') (Grant, 2011; Hagan, 2011; Nakagawa, 2018). In the '*dimerization scenario',* the number of nucleation events is restricted by controlling the nucleation rate $\mu$ while all monomers are active right from the outset ($\alpha = \infty, q = 0$). In contrast, in the '*activation scenario',* all species are activated slowly and uniformly with a constant rate $\alpha$ while the nucleation rate is taken as identical to the growth rate ($\mu = \nu, q = 0$). Slow activation can have a similar effect as slow dimerization in that it restricts the number of nucleation events (Lazaro, 2016; Gartner, 2019). Both of these implementations of the slow nucleation principle limit early stages of the assembly process in a way that does not discriminate between the various species. As motivated in the introduction, the efficiency and fidelity of the assembly process might be improved by introducing some element of coordination in the supply of the different species. In the '*Just-In-Sequence scenario'* (*JIS-scenario*) the different species get activated 'one after the other' as effectuated by a non-zero inhibition strength $q$ that reduces the basal activation rate $\alpha$ as detailed above. Finally, in the discussion of the time efficiency of assembly processes, we investigate a fourth scenario that is distinguished by a finite monomer detachment rate $\delta$ while all particles are active from

the outset and nucleation is not disfavored relative to growth ($\alpha = \infty$, $\mu = \nu$). While the first three scenarios are irreversible and rely on some mechanism to suppress nucleation, this '*reversible binding*' scenario does not actively prevent nucleation. Rather, in a random process bound monomers can detach from some structures and attach to others until a sufficient amount of structures has been completed.

In the following, we perform stochastic simulations for all four scenarios using the Gillespie algorithm (Gillespie, 2007), as well as numeric integration of the deterministic mean-field equations (chemical rate equations, see SI). We quantify the assembly process using three key observables. The *yield* measures the number of completed structures (closed rings), relative to the initial number $N$ of monomers per species (that corresponds to the maximum number of perfect rings), irrespective of the number of defects. In contrast, the *defect-free yield* counts only perfect structures, i.e. those that are completed and without any defects, again relative to $N$. While the defect-free yield is always bounded by 1, the yield can exceed the value of 1 if many defects in the structures provide additional resources for further structures to be completed. In order to evaluate the effectiveness of an assembly process, we measure its *final* yield and defect-free yield when all resources are consumed and the system has reached its final state. Furthermore, in order to quantify the time-efficiency, we define the (deterministic) *assembly time* $T_{90}$ as the elapsed time until the (deterministic) yield reaches a value of 90%. If the final yield remains smaller than 90% we set $T_{90} = \infty$. The deterministic assembly time (obtained from integrating the chemical rate equations) corresponds to the mean stochastic assembly time if the number of particles $N$ is sufficiently large. We compare the different scenarios with respect to their time efficiency by determining for each scenario the minimal deterministic assembly time, $T_{90}^{\min}$, that can be achieved by optimizing the respective variable parameter(s).

## *Results*

We start by discussing the final yield and defect-free yield in the dimerization, activation and JIS scenario. In particular, we are interested in how effectively the number of defects can be controlled in the different scenarios, and to which extend the yield and defect-free yield are affected by stochastic effects. For specificity, we fix the defect rate to $\nu_{\mathrm{def}}/\nu = 0.01$.

***The dimerization scenario***. The stochastic simulations show that upon decreasing the dimerization rate below a threshold value, the yield increases towards the perfect value of 1 (or even slightly larger than 1, if $\nu_{\mathrm{def}}$ is sufficiently large); see Fig. 3a. This is a manifestation of the slow nucleation principle: If nucleation is sufficiently retarded, an increasing number of structures gets finished (Morozov, 2009; Hagan, 2010; Gartner, 2019). Furthermore, we find that the defect-free yield is always a constant fraction of the yield. It can be estimated by a mean-field argument neglecting fluctuations between

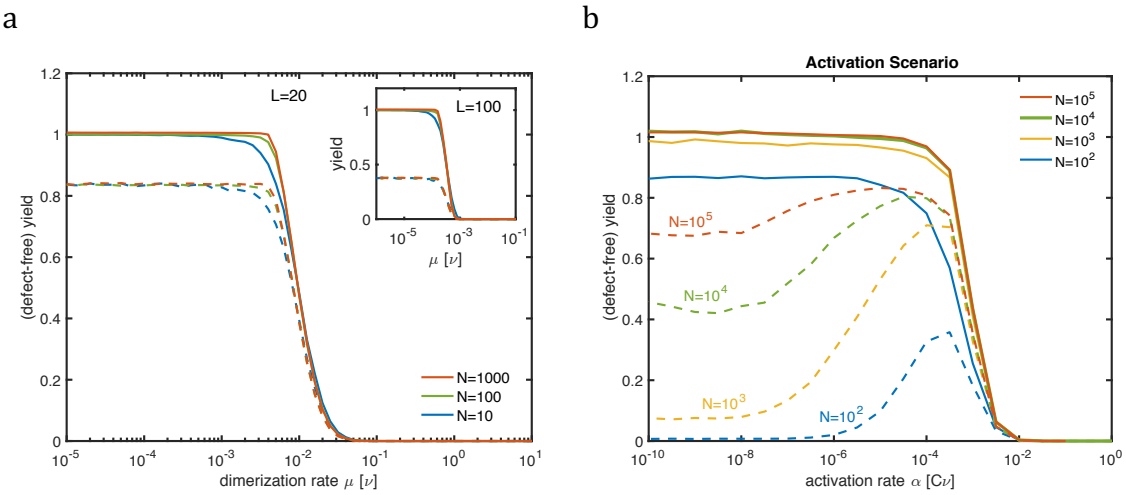


**Figure 3:** Dependence of the yield (drawn line) and defect-free yield (dashed line) on the dimerization rate ('dimerization scenario', (a)) and activation rate ('activation scenario', (b)) for L=20 and $\upsilon_{\mathrm{def}}/\upsilon = 0.01$. Different particle numbers N are indicated by different colors. **(a)** Decreasing the dimerization rate achieves perfect yield. The defect-free yield is always a constant fraction of the yield as described by the mean-field identity in Eq. (2). Varying the initial concentration $C$ of monomers or the copy number $N$ has an insignificant effect on the final (defect-free) yield. Larger target structure size $L$ (inset) shifts the transition to smaller dimerization rates and reduces the defect-free yield. **(b)** Decreasing the activation rate enhances the yield as well, however, as a result of stochastic effects a perfect yield cannot be achieved in general. Also due to stochastic effects, the defect-free yield becomes a non-monotonic function of $\alpha$, which exhibits a maximum at intermediate activation rates. Both the yield and defect-free yield decrease with decreasing number of particles N as stochastic effects become more pronounced. While the yield behaves fully deterministic for $N \geq 10^4$, the defect-free yield shows a significant drop still for $N = 10^5$.

the copy numbers of different species: Assuming that all species are available in equal concentrations, the probability that a defect occurs at a given binding site is $p_{\mathrm{def}} = \nu_{\mathrm{def}}/(\nu + \nu_{\mathrm{def}})$. The probability that a completed structure is perfect (defect-free), then, equals the probability that in $L-2$ subsequent binding steps no defect occurs. Therefore,

$$\frac{\text{defect free yield}}{\text{yield}} = (1-p_{\mathrm{def}})^{L-2} \approx \exp\left[-(L-2)p_{\mathrm{def}}\right] \ , \qquad (2)$$

where in the last step we assumed $p_{\mathrm{def}} \ll 1$. As can be inferred from Fig. 3a, the defect-free yield in the dimerization scenario is well approximated by this mean-field result. We attribute this to the fact that for $\alpha = \infty$ the concentration of active monomers is typically large and, therefore, fluctuations in the relative copy numbers of the different species are negligible. This is no longer the case for the activation scenario, as we will see in the next paragraph. Equation (2) states that the number of completed structures without defects decreases exponentially with the defect probability $p_{\mathrm{def}}$, as well as with the structure size $L$. Therefore, in the dimerization scenario, incorrect binding severely limits the correct assembly of large objects.

***The activation scenario***. The activation scenario shows a more intricate behavior. By decreasing the activation rate, the yield rises as in the dimerization scenario; see Fig. 3b. As a consequence of the stochastic yield catastrophe, however, it generally does not reach a perfect value of 1 unless $N$ is very large (Gartner, 2019). The defect-free yield also initially rises with decreasing activation rate. While with further decreasing $\alpha$ the yield stays constant, the defect-free yield decreases again to a constant value that depends on $N$. This non-monotonic behavior of the defect-free yield is not captured by mean-field theory, Eq. (2); however, it correctly predicts the maximum value of the defect-free yield in the limit $N \to \infty$. In analogy with the term 'stochastic yield catastrophe', we refer to the drop of the defect-free yield due to defect formation as '*stochastic defect catastrophe'*. It originates from the large fluctuations in relative copy numbers of the different species at low activation rates: if a shortage in supply of one species persists long enough, incorrect binding by the wrong building blocks becomes more likely as the proper building blocks are not readily available. Accordingly, one expects stochastic effects in the defect-free yield if the time scale for incorrect binding of an active monomer in the system, $(\nu_{\mathrm{def}} C)^{-1}$, is small compared to the time scale for activation of a specific species, $(\alpha N)^{-1}$. The characteristic scale of the activation rate that marks the onset of the stochastic defect catastrophe, therefore, equals $\alpha_{\mathrm{def}} \sim \nu_{\mathrm{def}}\, C/N$. In systems that achieve a non-zero defect-free yield, this scale is typically smaller than the threshold value $\alpha_{\mathrm{th}} \sim \nu C/L^3$ below which the deterministic yield rises (Gartner, 2019). Hence, the defect-free yield is usually a non-monotonic function of $\alpha$, taking a maximum in the interval $\alpha_{\mathrm{def}} \leq \alpha \leq \alpha_{\mathrm{th}}$. Interestingly, for large target sizes $L$ and nonzero defect rate $\nu_{\mathrm{def}} > 0$, the yield also becomes a non-monotonic function of the activation rate. The reduction of yield for small $\alpha$ thereby is caused by incorrectly binding particles occupying the regular binding sites of their neighboring species, which enhances the effective nucleation rate. As this is only an incidental finding, however, we will not go more into detail about this effect causing non-monotonic yield curves here.

Summarizing, we find that the error proneness of assembly processes cannot be efficiently controlled in neither the dimerization nor the activation scenario. While the (defect-free) yield in the dimerization scenario is well described by mean-field theory, both the yield and defect-free yield are strongly reduced by stochastic effects in the activation scenario with respect to the expected mean-field values. This suggests that reduction in yield is a general feature of 'far-from-equilibrium' self-assembly processes if fluctuations in the relative concentrations of the different species are relevant; this might likewise be the case in spatial systems due to diffusion.

***The Just-In-Sequence Scenario.***

Next, we investigate the effect of just-in-sequence supply on the effectiveness of the assembly process. We first consider a fixed activation rate $\alpha$ and discuss how the yield depends on the inhibition strength $q$ (Fig. 4a). In the limit $q = 0$ (activation scenario), the values of the yield and defect-free yield depend on $N$, $L$ and $\alpha$. The stochastic simulations show that increasing the inhibition strength initially amplifies stochastic

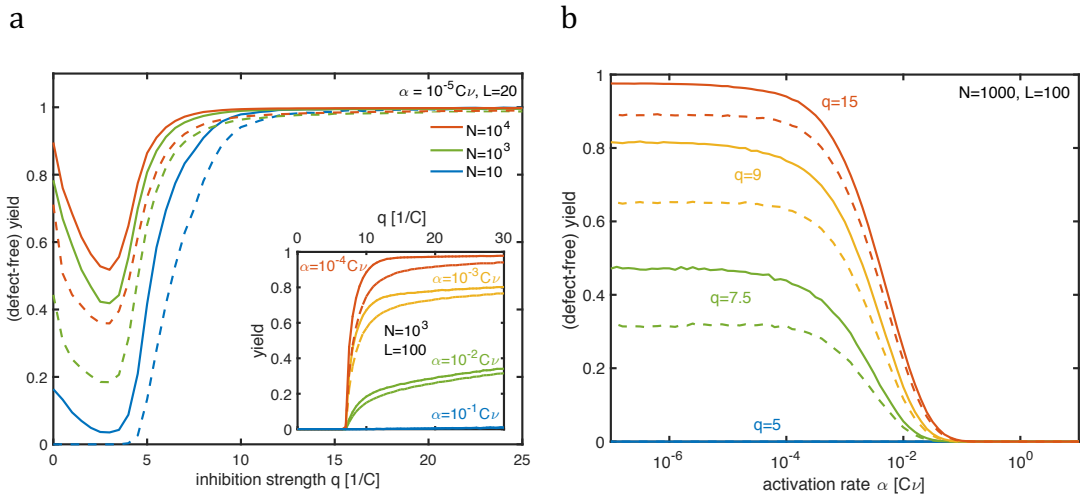


**Figure 4:** Dependence of the yield (drawn line) and defect-free yield (dashed line) on the inhibition strength and activation rate ('JIS scenario'). **(a)** Main plot: Variation of the inhibition strength for different particle numbers $N$ and constant activation rate $\alpha = 10^{-5}C\upsilon$, $\mathrm{L} = 20$ and $\upsilon_{\mathrm{def}} = 0.01$. Increasing the inhibition strength first leads to a drop of the yield and defect-free yield due to stochastic effects. Sufficiently strong inhibition, however, achieves near perfect yield and defect-free yield for arbitrary particle numbers $N$. Inset: Variation of the inhibition strength for larger target structure size $L = 100$ with fixed $N = 1000$ and different $\alpha$. The yield is zero at q=0 because $\alpha$ is above the threshold value for the activation scenario ($\alpha_{\mathrm{th}}^{\mathrm{act}} \sim 10^{-6}C\upsilon$) and stochastic effects suppress yield. Increasing the inhibition strength, however, leads to an abrupt rise of the (defect-free) yield here as well. If the activation rate becomes too large, though, no nonzero yield can be achieved any more by varying the inhibition strength. **(b)** Variation of the activation rate for different inhibition strengths q and constant $\mathrm{L} = 100, N = 1000$ and $\upsilon_{\mathrm{def}} = 0.01$. The (defect-free) yield increases if the activation rate is reduced below a threshold level provided inhibition is strong enough. Increasing the inhibition strength suppresses stochastic effects and leads to a rise of the (defect-free) yield.

effects with an ensuing decline in the (defect-free) yield. Intuitively, this decline is caused by premature activation events if inhibition between species is not strong enough. Instead of activation of all species in the right (just-in-sequence) order, monomers are activated 'out-of-sequence', thereby causing additional, undesirable nucleation events. To determine the scale of q on which the yield drop occurs, we estimate the number of monomers that are activated 'out-of-sequence' (i.e. before the preceding species has been activated). Premature activation of inactive monomers obeys $\frac{d}{dt}I_i = -\alpha_i^{\min} I_i$ , where $\alpha_i^{\min} := \alpha_i(I_{i-1} = C) = \alpha e^{-qC}$ is the maximally inhibited, premature activation rate. Integrated over the time span T of the assembly process this results in $C(1 - e^{-\alpha_i^{\min} T})$ monomers per species being activated prematurely (see Fig 5). The time span T of the assembly process scales as $T \sim L^2\alpha^{-1}$ (see SI). Hence, for $\alpha_i^{\min} T \sim e^{-qC}L^2 \gtrsim 1$ (i.e. $qC \lesssim 2\ln(L)$), a substantial concentration of monomers gets activated 'out-of-sequence'. These monomers cannot be used in the regular assembly path and may instead facilitate nucleation of new structures and, correspondingly, resource depletion. In contrast, for larger $q$ this effect is negligible. Therefore, upon further increasing $q$, both the yield and defect-free yield are observed to rise again and reach values close to 1. This shows that temporal supply

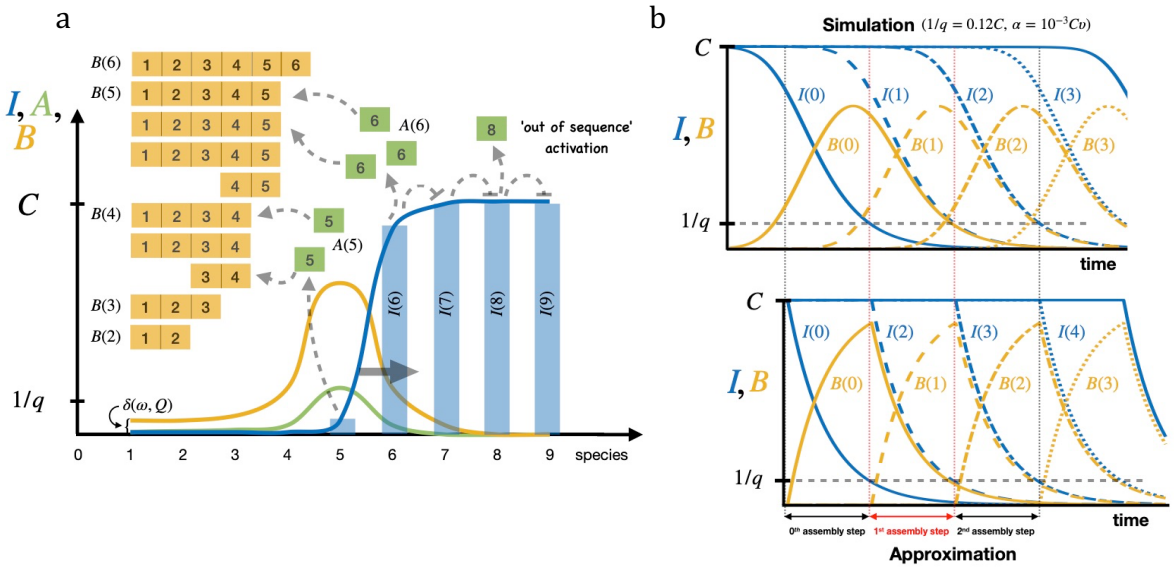


**Figure 5: Dynamics in the JIS scenario. (a)** The inhibition cascade (cf. Fig 3) causes travelling wave front and travelling pulse-like solutions for the concentrations of inactive monomers ($I$, blue), active monomers ($A$, green) and polymers with a determined right end ($B$, orange) after coarse-graining in species space. The inactive monomers get activated species after species as soon as the concentration of inactive monomers of the previous species has dropped to $\sim 1/q$. The activated monomers bind to the right ends of the polymers, thereby translating the $B$ field to higher species indices. Premature or 'out-of-sequence' activation ahead of the wave front occurs if inhibition is insufficiently strong. The stationary value of $B$ after the wave has passed is identical to the dimerization probability $\delta(\omega, Q)$ per assembly step (cf. Eq (4)) and indicatory of the final yield (cf. Eq (5)). **(b)** Time dependence of the concentrations of inactive monomers ($I$, blue) and polymers with a determined right end ($B$, orange) for four consecutive species. Species indices are counted from 0 to 3 for consistency with the notation in the analytic section. The upper panel shows the trajectories in the deterministic simulation with $1/q = 0.12\,C$, $\alpha = 10^{-3}Cv$ and inhibition function $H_1$. The lower panel shows the corresponding approximations for $I$ and $B$, resulting from replacing H1 with H2, which are used in the mathematical analysis to derive A(t) (cf. SI). The approximated $I_i$ are simple exponentials that start to decay when $I_{i-1}$ has dropped to $1/q$ and the $B_i$ are approximated as $B_i \approx I_{i-1} - I_i$. To derive the analytic results, we study the kinetics of the 1st assembly step indicated in red.

regulation, effectuated by a finite inhibition strength, can mitigate stochastic effects and greatly enhance the fidelity of the assembly process compared to the activation and dimerization scenario.

Besides inhibition of premature activation via the inhibition strength $q$ also the magnitude of the basal activation rate $\alpha$ has an important effect on the final yield. Figure 4b shows the yield and defect-free yield in dependence of $\alpha$ for different inhibition strengths $q$ and $L = 100$. We find that nonzero yield is obtained only if the activation rate is below a threshold value $\alpha_{\mathrm{th}}^{\mathrm{JIS}}$, independently of the value of q (cf. Fig. 4b). The significance of the basal activation rate $\alpha$ for the yield is explained as follows: Considerable activation of a given species $i$ starts, roughly, when the inactive monomer concentration of the preceding species $i-1$ drops below the inhibition threshold $I_0 = 1/q$. Therefore, there is always a certain temporal overlap in the activation of consecutive species; for an illustration see Fig. 5. Decreasing $\alpha$ reduces the concentration of active monomers, similar as in the activation scenario, and thereby

favors attachment of the monomers to already existing structures over nucleation of new structures. In contrast to the activation scenario, however, the impact of stochastic effects for $\alpha < \alpha_{\mathrm{th}}^{\mathrm{JIS}}$ can be controlled in the JIS scenario by increasing the inhibition strength. Consequently, if q is large enough, near perfect yield and defect-free yield are achieved for $\alpha \ll \alpha_{\mathrm{th}}^{\mathrm{JIS}}$ even for small particle numbers. Furthermore, we find $\alpha_{\mathrm{th}}^{\mathrm{JIS}} \sim L^{-1}$ (see SI) while the threshold rate in the activation scenario scales as $\alpha_{\mathrm{th}}^{\mathrm{act}} \sim L^{-3}$ (Gartner, 2019). This difference in the scaling exponent has important consequences regarding time efficiency, as we will see below.

Indeed, the precise implementation of the inhibition mechanism is not crucial for these findings. To understand this robustness property, it is insightful to think of the assembly process as a dynamic process in species space, where the concentrations of inactive, active, and bound monomers are considered as time-dependent functions of the species index. The ensuing coarse-grained dynamics of the concentration profiles then describes travelling wave fronts and pulses (see Fig. 5). Intriguingly, these wave fronts are generally very steep for strictly sequential inhibition cascades, irrespective of the details of the inhibition mechanism. This observation can be exploited by approximating the inhibition function $H_1$ by a step function $H_2(I) := \Theta(1/q - I)$, which enables one to obtain closed mathematical expressions for several key quantities of the assembly process. In the following, we discuss these results on an intuitive basis; for the formal calculations we refer the reader to the SI. Intuitively, the assembly process works well only if it is unlikely for two neighboring species $i$ and $i+1$ to dimerize before species $i$ attaches to the growing polymer $[1 \dots i-1]$. The dimerization probability $p_{\mathrm{dim}}$ of two subsequent monomers grows linearly with the number of possible dimerization partners for a monomer. To lowest order, the momentary monomer concentration is linear in the basal activation rate and hence, one expects $p_{\mathrm{dim}} \sim \alpha$. A detailed calculation (see SI) indeed shows

$$p_{\mathrm{dim}} = \frac{\alpha}{\nu C} \ln\left(\frac{\nu}{q\alpha}\right). \tag{3}$$

Such a dimerization event could occur in each step of the assembly process. Hence, the yield is equal to the probability that no dimerization events occurs in the L-2 subsequent growth steps between the dimer and the target structure:

$$\text{yield} = (1 - p_{\mathrm{dim}})^{L-2}. \tag{4}$$

Likewise, the defect-free yield is the fraction of the yield that has not acquired any defect in the relevant L-3 assembly steps:

$$\frac{\text{defect-free yield}}{\text{yield}} = (1 - p_{\mathrm{def}})^{L-3}, \tag{5}$$

with the defect probability $p_{\mathrm{def}}$ per assembly step given by

$$p_{\mathrm{def}} = \frac{\nu_{\mathrm{def}}}{(qC-1)\nu}. \tag{6}$$

The defect probability is proportional to the ratio of the per-capita rates $\nu_{\mathrm{def}}/\nu$ weighted with the ratio between defective and regular binding sites for a monomer: When

activation of species $i+1$ begins, roughly $C-1/q$ monomers of species $i$ have already been activated and bound. Hence, a monomer of species $i+1$ has approximately $C-1/q$ possibilities to bind correctly versus the remaining 1/q possibilities to bind incorrectly. The corresponding ratio, $\frac{1/q}{(C-1/q)}=\frac{1}{(qC-1)}$, accounts for the additional factor in Equation (6).

Furthermore, the time of a single assembly step equals the time it takes for the concentration of inactive monomers of a given species to drop from C to 1/q. The total assembly time bears an additional factor of $L$, summing the time of all individual assembly steps:

$$T_{90}=\frac{L}{\alpha}\ln(qC). \tag{7}$$

Thus, we find that the dimerization probability must be controlled by decreasing the activation rate since variation of the inhibition strength only has a small effect on $p_{\mathrm{dim}}$, cf. Eq. (3). Decreasing the activation rate, however, as a side effect increases the assembly time according to Eq. (7). Correspondingly, the minimal possible assembly time to achieve 90% yield is determined by solving Eqs. (3) and (4) for $\alpha$ and using the result in Eq. (7). Approximately, we find for large $L$:

$$T_{90,\mathrm{JIS}}^{\min}\sim\frac{L^2}{\nu C}. \tag{8}$$

Hence, the minimal assembly time in the JIS scenario increases quadratically with the size of the target structure. In contrast, the defect probability can be efficiently suppressed by increasing the inhibition strength $q$, while the assembly time depends only logarithmically on $q$. This implies that in an effective implementation of the JIS scenario the inhibition strength should be maximized.

In Figures S3 - S5 of the SI we compare these analytic results, Eqs.(3)-(7), with numeric simulations of the original process. We find that the analytic expressions are indeed very accurate for sufficiently small $\omega$ and large enough $q$. Therefore, we conclude that the approximations done in the analysis are justified in the regime where self-assembly is effective. The fact that with rather crude approximations an accurate description of the system can be achieved suggests that many model details, such as the exact implementation of the inhibition mechanism and the precise form of the inhibition function, are irrelevant for the successful realization of a JIS supply strategy.

***The optimized JIS scenario***. According to Eq. (7), the assembly time is mainly constrained by the basal activation rate whereas inhibition affects the assembly time only logarithmically. This raises the question whether we can trade slow activation (small $\alpha$) for large inhibition $q$ in order to improve the time efficiency. In the previous section we found that a small basal activation rate was necessary to keep the concentration of active monomers low and thus prevent nucleation between consecutive species, which are activated in overlapping time intervals (see Fig. 5). Intuitively, we expect that increasing the inhibition strength and assuming that both inactive and active monomers inhibit activation of the next species will make slow activation obsolete ($\alpha_{\mathrm{th}}^{\mathrm{JIS}}\to\infty$) and allow to regulate the supply solely via inhibition. In

a real-world system, this may hardly be realized via direct inhibitory feedback, because inhibition might need to be unrealistically strong. A supply mechanism that does not rely on feedback but activates the different species at fixed time intervals, though, could achieve a similar effect. In the framework of our model, we describe this case with an inhibition function $H_3$ similar to $H_2$ that additionally takes inhibition by the active monomers into account:

$$H_3(I_{i-1}, A_{i-1}) := \Theta\left(\frac{1}{q} - (I_{i-1} + A_{i-1})\right). \quad (9)$$

We find that the inhibition strength must fulfill $qC \geq L/\ln(y^{-1})$, where $y$ is the yield to be realized with $\alpha \to \infty$ (see SI). The minimal total assembly time, then, is obtained as

$$T_y^{\min} = \frac{L^2}{C\nu \ln(y^{-1})}. \quad (10)$$

Surprisingly, the exponent 2 that describes the scaling of the minimal assembly time with the target size is robust and cannot be altered by such modifications to the feedback (cf. Eq. (8)). This is because binding of the monomers, which now constitutes the time constraining process of an individual assembly step, leads to the same scaling behavior (see SI). However, we will see in the next paragraph that the minimal assembly time is reduced by a constant (L-independent) factor as a consequence of this kind of feedback.

A further possibility to increase the time efficiency in the JIS scenario consists in choosing non-stoichiometric concentrations for the different species (Murugan, 2015). Nonstoichiometric concentrations allow to compensate the resource consumption caused by undesired nucleation events more effectively and thereby contribute to enhance the time efficiency (see SI). Specifically, by choosing an initial concentration profile that, in our model, increases linearly with the species index reduces the minimal assembly time by roughly 50%. In the following, we refer to the JIS scenario with improved supply coordination (strong inhibition in combination with an inhibition function like $H_3$) and optimized resource distribution as *optimized JIS scenario*.

### *Time Efficiency*

In a biological context, the relevant question might not so much concern the final yield that can be achieved after arbitrarily long time but rather the time scale at which a sufficiently high yield in assembly product can be achieved. Therefore, we now compare the different scenarios with respect to their time-efficiency. Beside the three irreversible scenarios discussed above we also evaluate the time efficiency of the '*reversible binding'* scenario that has a variable detachment rate $\delta$. We restrict the analysis to a discussion of the deterministic assembly time (that is obtained by integrating the ensuing set of ordinary differential equations, see SI). The deterministic assembly time corresponds to the average stochastic assembly time provided the particle number $N$ is large enough so that stochastic effects are negligible (primarily concerning the activation scenario). For convenience we set $\nu_{\text{def}} = 0$, as a small defect

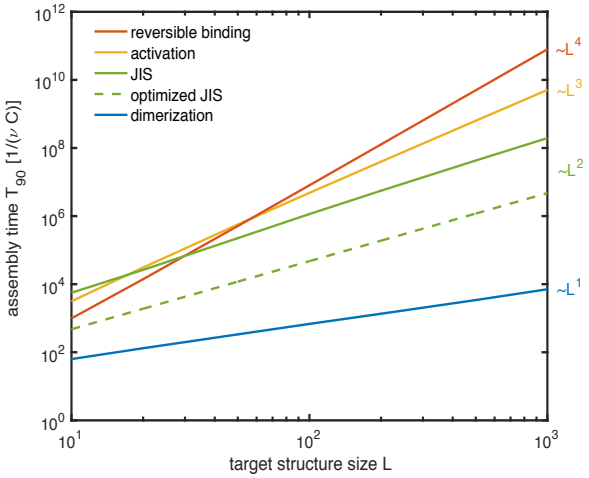


| Scenario | optimal parameter value | minimal assembly time $T_{90}^{min}$ |
|---|---|---|
| Reversible Binding | $\delta_{opt} \sim L^{-2}$ | $\sim L^4$ |
| Activation | $\alpha_{opt} \sim L^{-3}$ | $\sim L^3$ |
| JIS | $\alpha_{opt} \sim L^{-1}$ | $\sim L^2$ |
| Optimized JIS | $Q_{opt} \sim L$ | $\sim L^2$ |
| Dimerization | $\mu_{opt} \sim L^{-2}$ | $\sim L^1$ |

**Figure 6: Time Efficiency. (a)** Dependence of the minimal assembly time to achieve 90% yield on the size of the target structure for the different scenarios. The assembly time is minimized using a constrained optimization algorithm on the variable parameter of the respective scenario. The minimal assembly time exhibits a power law dependence on the target structure size. The exponents are integer numbers that characterize the different scenarios. The largest exponent of 4 is found for the 'scenario of reversible binding' where the assembly time is minimized over a variable detachment rate $\delta$. The 'activation scenario' is characterized by an exponent of 3. The 'JIS scenario' and 'optimized JIS scenario' (using maximally strong inhibition and an optimized resource distribution) both scale with $L$ to the power of 2, however, the 'optimized JIS scenario' exhibits a smaller prefactor. The dimerization scenario scales with $L$ to the power 1 and is the most time-efficient of all four scenarios. **(b)** The table summarizes the exponents for the minimal assembly time and the optimal parameter values that achieve the minimization. All exponents are derived analytically in the SI.

rate would only have a negligible effect on the assembly time. In each scenario, we determine the minimal time span $T_{90}^{\min}$ to obtain a yield of 90% by optimizing the value(s) of the respective variable parameter(s), cf. Fig.2.

The basic time scale in all scenarios is set by the reactive time scale $(C\nu)^{-1}$. Hence, the minimal assembly time is proportional to $(C\nu)^{-1}$ times a dimensionless factor $f_{\text{scenario}}(L)$ that is scenario-specific and depends only on the target structure size

$$T_{90}^{\min,\text{scenario}} = (C\nu)^{-1} f_{\text{scenario}}(L)\,. \qquad (11)$$

Consequently, in each scenario, the absolute assembly time can be reduced by increasing the initial concentration or the reaction rate. In order to determine the target size dependence $f_{\text{scenario}}(L)$ of $T_{90}^{\min}$, an optimization algorithm is used to minimize the assembly time $T_{90}$ for each scenario in the deterministic simulation under the constraint that the yield is larger or equal 90%. Figure 6 shows the result of this minimization, corresponding to the minimal assembly time in units of the typical reaction time, $T_{90}^{\min}[(C\nu)^{-1}]$, as a function of the target size $L$ for all four scenarios on a double logarithmic scale. For each scenario, we find a power-law dependence of the minimal assembly time on L: $f_{\text{scenario}}(L) \sim L^{\chi(\text{scenario})}$. Interestingly, the exponents $\chi$ that characterize the target size dependence in the four scenarios are the integer numbers $\{1,2,3,4\}$. Hence, a clear hierarchy in time-efficiency at large $L$ can be identified: The dimerization scenario is the most time efficient scenario at large target

sizes exhibiting the exponent $\chi(\text{dimerization}) = 1$. Controlling the dimerization rate is efficient as it allows to initiate just as many structures as needed, each of which can be completed very quickly since all constituents are available in active form. The second most time efficient scenario is the optimized JIS scenario with $\chi(\text{JIS}) = 2$. The JIS scenario also exhibits an exponent of 2, but has a larger prefactor compared to its optimized version. The activation scenario has an exponent of $\chi(\text{activation}) = 3$ because for large target structures uncoordinated activation is less time efficient than coordinated activation in the JIS scenario. Finally, for the scenario of reversible binding we find $\chi(\text{reversible binding}) = 4$. Here, nucleation events are not a priori prevented but initiated structures can be degraded again in order to free the resources for other structures to grow and get finished. Since structure degradation due to reversibility is a random process, the scenario of reversible binding is very time inefficient at large $L$. For small structure sizes, on the other hand, reversible binding is quite effective and may even outperform the other scenarios in terms of time efficiency. The exponents characterizing the target size dependence of the minimal assembly time in the different scenarios together with the scaling of the parameter values that minimize $T_{90}$ are summarized in Fig. 6b. All exponents can also be derived analytically (see SI). Importantly, the exponents do not depend on the value of the yield that we choose in the definition of the assembly time, as long as this value is smaller than 100% (e.g. $T_{95}^{\min}$ and $T_{70}^{\min}$ would exhibit the same exponents).

## *Conclusion*

In this work we discussed four different scenarios that effectuate the self-assembly of finite-sized heterogeneous target structures. These scenarios exemplify two principally different control strategies by which the assembly processes are regulated. On the one hand, control of the assembly process can be achieved on a molecular level by optimizing the molecular binding properties of the constituents. Alternatively, we showed that control of the assembly process can be attained on a systemic level via supply regulation. This suggests to distinguish between 'molecular control strategies' and 'systemic control strategies' in the context of self-assembly. The dimerization scenario corresponds to a molecular control strategy that relies on allostery, a sophisticated molecular mechanism, to avoid kinetic trapping (Caspar, 1980; Packinathan, 2010). Allosteric control enables cooperative binding effects and thereby allows to reduce the ratio between the dimerization and the growth rate. Consequently, the dimerization scenario is the most time efficient of all four scenarios. Reversible binding also exemplifies a molecular control strategy since it demands optimized bond strengths that are sufficiently stable but at the same time reversible on the relevant time scale (Ceres,2002; Rapaport, 2008; Grant, 2011, Hagan 2014). This scenario is time-efficient for small structure sizes but inefficient at large sizes. Besides the avoidance of kinetic traps, assembly errors represent a major threat for the assembly

product. Hence, a maximization of the binding specificity is vital in these scenarios in order to minimize the molecular rate for errors and defects.

As an alternative to a molecular control strategy, we found that the assembly process can also be controlled on a systemic level via supply regulation. The activation scenario constitutes a first step in this direction as it avoids kinetic traps by slow provisioning of the constituents. However, our analysis shows that – due to randomness in the order of supply – the activation scenario is prone to unfavorable stochastic effects that may manifest themselves as stochastic yield and defect catastrophes. To overcome these deficiencies, we have proposed a just-in-sequence supply strategy, where, in addition, the supply sequence is regulated. We find that this leads to a strong attenuation of stochastic effects as well as an effective reduction of the error frequency, even in case of a large molecular error rate. Furthermore, for large target structures, the time efficiency can be significantly increased in comparison to the activation scenario or reversible-binding scenario.

A purely molecular control strategy requires optimized molecular properties which might compromise the functionality of the structure or pose severe restrictions on the design of the constituents and the structure. For example, in assembly processes with reversible bindings, the requirement of reversibility demands optimized bond strengths rather than maximally stable bonds. A reduced molecular bond strength, however, might diminish the stability of the structure as a whole – unless a special design of the structure that realizes a high number of intermolecular bonds establishes collective stability. Hence, in this case, the molecular control strategy relying on reversibility of binding either compromises the functionality of the structure (its stability) or restricts its design by demanding high intermolecular connectivity. In contrast, a just-in-sequence supply strategy can be realized without the need to modify the components and thereby compromise the functionality of the structure. For example, one can envision an experimental protocol in which the different constituent species are given into solution one-by-one after experimentally indicated time intervals. JIS supply strategies might therefore constitute a viable way to realize large structures in irreversible artificial self-assembly. Furthermore, evidence have amounted in recent years that in the assembly of complex cellular organelles, such as the bacterial flagellum, temporal gene expression is coupled to specific stages of the assembly process (Chevance, 2008). This might hint at a role of JIS supply strategies also in cellular self-assembly processes.

The two control strategies on the molecular and on the systemic level are, of course, not mutually exclusive but can be combined to enhance the efficiency of self-assembly. In this sense, molecular control mechanisms and supply regulation can be regarded as ‘orthogonal’ strategies, that can synergize but still be implemented independently from each other. Such redundant, independent control mechanisms can enhance robustness to mutations and are thus often considered a promoting factor for evolution. Hence, it might be thinkable that it was the interplay between molecular and systemic control strategies that has enabled the evolution of such complex machineries and sophisticated assembly processes that we observe in nature.

**Acknowledgements.** We would like to thank Patrick Wilke and Philipp Geiger for useful discussions. This research was funded via the Excellence Cluster "ORIGINS" by the Deutsche Forschungsgemeinschaft (DFG, German Research Foundation) under Germany's Excellence Strategy – EXC-2094 – 390783311. FG and IRG were supported by a DFG fellowship through the Graduate School of Quantitative Biosciences Munich (QBM).

## References

1. Alberts, B., Johnson, A., Lewis, J., Morgan, D., Raff, M., Roberts, K., Walter, P., Wilson, J., and Hunt, T. *Molecular Biology of the Cell.* (Garland Science, 2015).

2. Baek, K., Hwang, I., Roy, I., Shetty, D. & Kim, K. Self-Assembly of Nanostructured Materials through Irreversible Covalent Bond Formation. *Acc. Chem. Res.* **48**, 2221–2229 (2015).

3. Cademartiri, L. & Bishop, K. J. M. Programmable self-assembly. *Nat. Mater.* **14**, 2–9 (2015).

4. Caspar, D. L. Movement and self-control in protein assemblies. Quasi-equivalence revisited. *Biophys. J.* **32**, 103–138 (1980).

5. Ceres, P. & Zlotnick, A. Weak protein-protein interactions are sufficient to drive assembly of hepatitis B virus capsids. *Biochemistry* **41**, 11525–11531 (2002).

6. Chen, C., Kao, C. C. & Dragnea, B. Self-assembly of brome mosaic virus capsids: Insights from shorter time-scale experiments. *J. Phys. Chem. A* **112**, 9405–9412 (2008).

7. Chevance, F. F. V. & Hughes, K. T. Coordinating assembly of a bacterial macromolecular machine. *Nat. Rev. Microbiol.* **6**, 455–465 (2008).

8. D'Orsogna, M. R., Zhao, B., Berenji, B. & Chou, T. Combinatoric analysis of heterogeneous stochastic self-assembly. *J. Chem. Phys.* **139**, (2013).

9. Endres, D. & Zlotnick, A. Model-Based Analysis of Assembly Kinetics for Virus Capsids or Other Spherical Polymers. *Biophys. J.* **83**, 1217–1230 (2002).

10. Gartner, F. M., Graf, I. R., Wilke, P., Geiger, P. M. & Frey, E. Stochastic Yield Catastrophes and Robustness in Self-Assembly. *bioRxiv* 660340 (2019) doi:10.1101/660340.

11. Gillespie, D. T. Stochastic Simulation of Chemical Kinetics. *Annu. Rev. Phys. Chem.* **58**, 35–55 (2007).

12. Grant, J., Jack, R. L. & Whitelam, S. Analyzing mechanisms and microscopic reversibility of self-assembly. *J. Chem. Phys.* **135**, (2011).

13. Hagan, M. F. Modeling Viral Capsid Assembly. *Adv. Chem. Phys.* **155**, 1–68 (2014).

14. Hagan, M. F. & Elrad, O. M. Understanding the Concentration Dependence of Viral Capsid Assembly Kinetics—the Origin of the Lag Time and Identifying the Critical Nucleus Size. *Biophys. J.* **98**, 1065–1074 (2010).

15. Hagan, M. F., Elrad, O. M. & Jack, R. L. Mechanisms of kinetic trapping in self-assembly and phase transformation. *J. Chem. Phys.* **135**, (2011).

16. Hedges, L. O., Mannige, R. V. & Whitelam, S. Growth of equilibrium structures built from a large number of distinct component types. *Soft Matter* **10**, 6404–6416 (2014).

17. Jacobs, W. M., Reinhardt, A. & Frenkel, D. Rational design of self-assembly pathways for complex multicomponent structures. *Proc. Natl. Acad. Sci. U. S. A.* **112**, 6313–6318 (2015).

18. Ke, Y., Ong, L. L., Shih, W. M. & Yin, P. Three-dimensional structures self-assembled from DNA bricks. *Science (80-. ).* **338**, 1177–1183 (2012).

19. Klajn, R., Bishop, K. J. M. & Grzybowski, B. A. Light-controlled self-assembly of reversible and irreversible nanoparticle suprastructures. *Proc. Natl. Acad. Sci. U. S. A.* **104**, 10305–10309 (2007).

20. Lazaro, G. R. & Hagan, M. F. Allosteric Control of Icosahedral Capsid Assembly. *J. Phys. Chem. B* **120**, 6306–6318 (2016).

21. Linko, V. & Dietz, H. The enabled state of DNA nanotechnology. *Curr. Opin. Biotechnol.* **24**, 555–561 (2013).

22. Macnab, R. M. Type III flagellar protein export and flagellar assembly. *Biochim. Biophys. Acta - Mol. Cell Res.* **1694**, 207–217 (2004).

23. Mendes, A. C., Baran, E. T., Reis, R. L. & Azevedo, H. S. Self-assembly in nature: using the principles of nature to create complex nanobiomaterials. *Wiley Interdiscip. Rev. Nanomedicine Nanobiotechnology* **5**, 582–612 (2013).

24. Morozov, A. Y., Bruinsma, R. F. & Rudnick, J. Assembly of viruses and the pseudo-law of mass action. *J. Chem. Phys.* **131**, (2009).

25. Murugan, A., Zou, J. & Brenner, M. P. Undesired usage and the robust self-assembly of heterogeneous structures. *Nat. Commun.* **6**, 6203 (2015).

26. Nakagawa, M., Kai, S., Kojima, T. & Hiraoka, S. Energy-Landscape-Independent Kinetic Trap of an Incomplete Cage in the Self-Assembly of a $Pd_2L_4$ Cage. *Chem. - A Eur. J.* **24**, 8804–8808 (2018).

27. Nerurkar, P. *et al.* Eukaryotic Ribosome Assembly and Nuclear Export. *Int. Rev. Cell Mol. Biol.* **319**, 107–140 (2015).

28. Packianathan, C., Katen, S. P., Dann, C. E. & Zlotnick, A. Conformational Changes in the Hepatitis B Virus Core Protein Are Consistent with a Role for Allostery in Virus Assembly. *J. Virol.* **84**, 1607–1615 (2010).

29. Peña, C., Hurt, E. & Panse, V. G. Eukaryotic ribosome assembly, transport and quality control. *Nat. Struct. Mol. Biol.* **24**, 689–699 (2017).

30. Rapaport, D. C. Role of reversibility in viral capsid growth: A paradigm for self-assembly. *Phys. Rev. Lett.* **101**, 1–4 (2008).

31. Reinhardt, A. & Frenkel, D. Numerical evidence for nucleated self-assembly of DNA brick structures. *Phys. Rev. Lett.* **112**, 1–5 (2014).

32. Roser, C. Just in Sequence | AllAboutLean.com. https://www.allaboutlean.com/just-in-sequence-definition/ (2017).

33. Vonderviszt, F. & Namba, K. Structure, Function and Assembly of Flagellar Axial Proteins. (2013).

34. Werner, S., Kellner, M., Schenk, E. & Weigert, G. Just-in-sequence material supply—a simulation based solution in electronics production. *Robot. Comput. Integr. Manuf.* **19**, 107–111 (2003).

35. Whitelam, S. Hierarchical assembly may be a way to make large information-rich structures. *Soft Matter* **11**, 8225–8235 (2015).

36. Whitesides, G. M., Mathias, J. P. & Seto, C. T. Molecular self-assembly and nanochemistry: a chemical strategy for the synthesis of nanostructures. *Science* **254**, 1312–9 (1991).

37. Whitesides, G. M. & Grzybowski, B. Self-assembly at all scales. *Science (80-. ).* **295**, 2418–2421 (2002).

38. Zhang, S. Molecular Self-assembly. *Encycl. Mater. Sci. Technol.* 5822–5828 (2001) doi:10.1016/B0-08-043152-6/01012-3.

39. Zhang, S. Fabrication of novel biomaterials through molecular self-assembly. *Nat. Biotechnol.* **21**, 1171–1178 (2003).

# Supplementary Information for

# "Controlling fidelity and time-efficiency in self-assembly"

Florian M. Gartner, Isabella R. Graf and Erwin Frey

(Dated: December 28, 2021)

**CONTENTS**

We discuss the stochastic Master equations that have been simulated by Gillespie's algorithm and derive the chemical rate equations (deterministic/mean-field equations) for the full self-assembly system. Furthermore, we outline the calculations that led to the analytic results presented in the main text.

### A. Master equation and chemical rate equations

We start with the general Master equation and derive the chemical rate equations (deterministic/mean-field equations) for the self-assembly system. We will not show the full Master equation here but instead discuss the system that describes the evolution of the first moments. To this end, we denote by $n_\ell^s(t)$ the number of polymers of size $\ell$ and species $s$ that are present in the system at time $t$, where $2 \leq \ell < L$ and $1 \leq s \leq S$. The species of a polymer is defined by the species of the respective monomer at its right end. Furthermore, $n_0^s$ and $n_1^s$ denote the number of inactive and active monomers of species $s$, respectively, and $n_L$ the number of complete rings. In the following, species indices are always assumed to be taken modulo $L$ in case they lie outside the range $1 \leq s \leq L$. We denote the dimerization rate of two monomers by $\mu$ and the rate for binding of a monomer to a polymer by $\nu$. Furthermore, $\delta$ denotes the rate for detachment of a monomer from the end of a polymer. Finally, $\alpha_s = \alpha H(n_0^{s-1})$ is the activation rate for a monomer of species $s$, where $\alpha$ is the basal activation rate and $H(n_0^{s-1}) := e^{-qn_0^{s-1}(1-\delta_{s1})}$ the inhibition function, which implements inhibition by the left neighbouring species except for $s = 1$. By $\langle ... \rangle$ we indicate (ensemble) averages. The system governing the evolution of the first moments (the averages) of the numbers $\{n_\ell^s\}$ is then given by:

$$\frac{d}{dt}\langle n_0^s \rangle = -\alpha \, \langle H(n_0^{s-1}) n_0^s \rangle \,, \tag{1a}$$

$$\begin{aligned}\frac{d}{dt}\langle n_1^s \rangle = {} & \alpha \, \langle H(n_0^{s-1}) n_0^s \rangle - \mu \left( \langle n_1^s n_1^{s+1} \rangle + \langle n_1^s n_1^{s-1} \rangle \right) - \nu \sum_{\ell=2}^{L-1} \left( \langle n_1^s n_\ell^{s+\ell} \rangle + \langle n_1^s n_\ell^{s-1} \rangle \right) \\ & - \nu_{\text{def}} \sum_{\ell=2}^{L-1} \left( \langle n_1^s n_\ell^{s+\ell+1} \rangle + \langle n_1^s n_\ell^{s-2} \rangle \right) + \delta \sum_{\ell=2}^{L-1} \left( \langle n_\ell^{s+\ell-1} \rangle + \langle n_\ell^s \rangle \right) \,,\end{aligned} \tag{1b}$$

$$\begin{aligned}\frac{d}{dt}\langle n_2^s \rangle = {} & \mu \, \langle n_1^s \, n_1^{s+1} \rangle - \nu \, \left( \langle n_2^s \, n_1^{s-2} \rangle + \, \langle n_2^s \, n_1^{s+1} \rangle \right) \\ & - \nu_{\text{def}} \, \left( \langle n_2^s \, n_1^{s-3} \rangle + \, \langle n_2^s \, n_1^{s+2} \rangle \right) - \delta \, \langle n_2^s \rangle \,,\end{aligned} \tag{1c}$$

$$\begin{aligned}\frac{d}{dt}\langle n_\ell^s \rangle = {} & \nu \, \left( \langle n_{\ell-1}^s \, n_1^{s-\ell+1} \rangle + \langle n_{\ell-1}^{s-1} \, n_1^s \rangle - \langle n_\ell^s \, n_1^{s-\ell} \rangle - \langle n_\ell^s \, n_1^{s+1} \rangle \right) \\ & + \nu_{\text{def}} \, \left( \langle n_{\ell-2}^s \, n_1^{s-\ell+1} \rangle + \langle n_{\ell-2}^{s-2} \, n_1^s \rangle - \langle n_\ell^s \, n_1^{s-\ell-1} \rangle - \langle n_\ell^s \, n_1^{s+2} \rangle \right) \\ & + \delta \, \left( \langle n_{\ell+1}^s \rangle + \langle n_{\ell+1}^{s+1} \rangle \right) \mathbf{1}_{\{\ell \leq L-2\}} - 2\delta \langle n_\ell^s \rangle \,, \qquad 3 \leq \ell < L \,,\end{aligned} \tag{1d}$$

$$\frac{d}{dt}\langle n_L \rangle = \sum_{s=1}^{L} \left[ 2\nu \, \langle n_{L-1}^s \, n_1^{s+1} \rangle + \nu_{\text{def}} \left( \langle n_{L-2}^s \, n_1^{s+2} \rangle + \langle n_{L-2}^s \, n_1^{s+1} \rangle \right) \right] \,. \tag{1e}$$

The first equation describes loss of inactive particles due to activation. Eq. (1b) gives the temporal change of the number of active monomers that is governed by the following processes: activation of inactive monomers, dimerization of active monomers at rate $\mu$, correct and incorrect binding of active monomers to the left and to the right end of existing polymers at rate $\nu$ and $\nu_{\mathrm{def}}$, respectively, and detachment of monomers from the left and right end of polymers with rate $\delta$.
Equations (1c) and (1d) describe the dynamics of dimers and larger polymers of size $3 \leq \ell < L$, respectively. The terms account for dimerization of active monomers (only in Eq (1c)) as well as all possible kinds of reactions of polymers with active monomers along with detachment of monomers from polymers. Note that a polymer of size $\ell \geq 3$ can grow by attaching a monomer to its left or to its right end whereas the formation of a dimer of a specific species is only possible via one reaction pathway (dimerization reaction). The indicator function $\mathbf{1}_{\{\ell \leq L-2\}}$ in Eq. (1d) (which equals 1 if the condition $\ell \leq L-2$ is satisfied and 0 otherwise) excludes source terms that would account for detachment from completed rings, which we always assume as stable. Finally, the complete ring structures form an absorbing state and, therefore, include only the respective gain terms (cf. Eq (1e)).
We simulated the Master equation underlying Eq. (1) stochastically using Gillespie's algorithm and in the simulation additionally kept track of the number of defects that a polymer has acquired.
For sufficiently large particle copy numbers $N$, correlations between the particle numbers $\{n_\ell^s\}$ in Eq. (1) can be neglected and the two-point correlator can be approximated as the product of the corresponding mean values (mean-field approximation):

$$\langle n_i^s n_j^k \rangle = \langle n_i^s \rangle \langle n_j^k \rangle \ \forall s, k \tag{2}$$

Applying this to Eq. (1) and defining the concentrations $c_\ell^s := \frac{\langle n_\ell^s \rangle}{N_A V}$, where $V$ is the reaction volume and $N_A$ is Avogadro's constant, we arrive at the (deterministic) chemical rate equations for the concentrations $\{c_\ell^s\}$.
In order to further simplify the analysis, we exploit the symmetry of the system and take into account the nature of the dynamical processes involved. To this end, as we will explain in the following, we can discard either the species index (if $q = 0$) or the length index (if $q > 0$) and thereby reduce the effective number of degrees of freedom. First we discuss the case $q = 0$.

### B. Reduction in the case $q = 0$ (activation, dimerization and reversible binding scenario)

When inhibition is absent ($q = 0$), all species have equivalent properties (there is no distinct species). In fact, the term $(1 - \delta_{s1})$ in the inhibition function is the only term that explicitly depends on the species index in Eq. (1) if $q > 0$. For $q = 0$, however, the system

is invariant under relabelling the upper index and for the expectation values it consequently holds

$$\langle n_\ell^s \rangle = \langle n_\ell^k \rangle := \langle n_\ell \rangle \quad \forall s, k \tag{3}$$

This symmetry is relevant for the activation, dimerization and reversible binding scenario where $q = 0$. By discarding the species index, the number of degrees of freedom in these scenarios can be reduced from $L^2 + 1$ to $L + 1$. Mathematically, the heterogeneous assembly process thereby decouples into $L$ identical and independent homogeneous assembly processes in the deterministic limit. The corresponding homogeneous system is described by the following set of equations that is obtained from Eq. (1) by applying (2), (3) and the definition of the $\{c_\ell\}$. The quantities $\{c_\ell\}$ thereby describe the concentrations of structures of size $\ell$ of any species:

$$\frac{d}{dt}c_0 = -\alpha\, c_0\,, \tag{4a}$$

$$\frac{d}{dt}c_1 = \alpha\, c_0 - 2\mu c_1^2 + 2\left(-\nu c_1 - \nu_{\text{def}} c_1 + \delta\right)\sum_{\ell=2}^{L-1} c_\ell\,, \tag{4b}$$

$$\frac{d}{dt}c_2 = \mu\, c_1^2 - 2\nu\, c_1 c_2 - 2\nu_{\text{def}}\, c_1 c_2 - \delta\, c_2\,, \tag{4c}$$

$$\frac{d}{dt}c_\ell = 2\nu c_1\left(c_{\ell-1} - c_\ell\right) + 2\nu_{\text{def}} c_1\left(c_{\ell-2} - c_\ell\right) + 2\delta\left(c_{\ell+1}\mathbf{1}_{\{\ell \le L-2\}} - c_\ell\right)\,, \tag{4d}$$

$$\frac{d}{dt}c_L = 2\nu\, c_1 c_{L-1} + 2\nu_{\text{def}} c_1 c_{L-2}\,. \tag{4e}$$

The rate constants $\nu_\ell$ in Eq. (4) and (1) differ by a factor of $V$. For convenience, however, we use the same symbol in both cases. The rate constants $\nu_\ell$ in Eq. (4) can be interpreted in the usual units $[\frac{\text{liter}}{\text{mol sec}}]$. In the last equation we omitted a factor of $L$ that should be present according to Eq. (1) but is left out here because we only consider the contribution to $c_L$ per species.

Note that this dynamical system describes an equivalent homogeneous self-assembly process, i.e. one where the structures are assembled from identical particles (cf. [1] ). By integrating Eq. (4) numerically, the deterministic self-assembly system can be simulated efficiently. We used this approach to determine the minimal assembly time in dependence of $L$ for the activation, dimerization and reversible binding scenario.

### C. Continuity approximation for q=0

The system for $q = 0$ can be further simplified by a continuity approximation in which the ODE system is written as a partial differential equation. A similar approach was used previously in [1–3]. To this end, we approximate the index $\ell \in \{2, 3, \ldots, L\}$ indicating the length of the polymer as a continuous variable $x \in [2, L]$ and define $c(x = \ell) := c_\ell$. By $A := c_1$ we denote the concentration of active monomers in the following to emphasize their

special role. Formally expanding the terms on the right-hand side of Eq. (4d) in a Taylor series up to second order,

$$c(\ell \pm 1) = c(\ell) \pm \partial_x c(\ell) + \frac{1}{2}\partial_x^2 c(\ell)\,, \tag{5}$$

$$c(\ell - 2) = c(\ell) - 2\partial_x c(\ell) + \partial_x^2 c(\ell)\,, \tag{6}$$

one arrives at the following advection-diffusion equation

$$\partial_t c(x) = \left[2\delta - 2A(\nu + 2\nu_{\rm def})\right]\, \partial_x c(x) + \left[\delta + A(\nu + 2\nu_{\rm def})\right]\, \partial_x^2 c(x)\,. \tag{7}$$

Note that both the advection and the diffusion coefficient depend on the concentration $A$ of active monomers. Equation (7) can be written in the form of a continuity equation $\partial_t c(x) = -\partial_x J(x)$ with flux $J = \left[2\delta - 2A(\nu + 2\nu_{\rm def})\right]\, c - \left[\delta + A(\nu + 2\nu_{\rm def})\right]\, \partial_x c$. The flux at the left boundary $x = 2$ equals the influx of polymers due to dimerization of free monomers $J(2,t) = \mu A^2$. This enforces a Robin boundary condition at $x = 2$

$$\left[2\delta - 2A(\nu + 2\nu_{\rm def})\right]\, c(2) - \left[\delta + A(\nu + 2\nu_{\rm def})\right]\, \partial_x c(2) = \mu A^2\,. \tag{8}$$

At $x = L$ we set an absorbing boundary $c(L,t) = 0$, so that completed structures are removed from the system. The time evolution of the concentration of active monomers is given by

$$\partial_t A = \alpha C e^{-\alpha t} - 2\mu A^2 - 2A(\nu + \nu_{\rm def}) \int_2^L c(x,t)\, dx + 2\delta \left[2c(2) + \int_3^L c(x,t)\, dx\right]\,. \tag{9}$$

The terms on the right-hand side account for activation of inactive particles, dimerization, binding of active particles to polymers (polymerization) and detachment of monomers.

Qualitatively, Eq. (7) describes a profile that emerges at $x = 2$ from the boundary condition Eq. (8), moves to the right with time-dependent velocity $\left[2\delta - 2A(\nu + 2\nu_{\rm def})\right]$ due to the advection term, and broadens with a time-dependent diffusion coefficient $\left[\delta + A(\nu + 2\nu_{\rm def})\right]$. Assuming $A(t)$ is known, the full solution of Eqs. (7) and (8) can be constructed, as we show explicitly in [1]. Here, however, we are mainly interested the scaling exponents that describe the dependence of the minimal assembly time and the control parameters on the structure size $L$. For the reversible binding scenario, the analysis has been performed in [4] by using a first passage time approach to the random walk process described by Eq. (7). The exponent $\phi = 4$ for the structure size dependence of the minimal assembly time in the reversible binding scenario could thereby be confirmed analytically.
Also for the activation and dimerization scenario, the exponent $\phi$ can be derived analytically. This is done in the easiest way by deriving the scaling exponent of the threshold rate for the onset of non-zero yield. It can be verified that in the limit of large structure sizes $L$, the threshold activation or dimerization rate scales identically as the optimal activation or dimerization rate that minimizes the assembly time [4]. Deriving the scaling of the threshold activation or dimerization rate has the advantage that the outflux of structures

through the absorbing boundary can be neglected and therefore the system can be strongly simplified. We have derived scaling laws for the threshold dimerization and activation rate previously [1], but for the convenience of the reader we will reprint the essential steps of the analysis here. To this end, we set $\delta = 0$ in the following and we neglect the error rate $\nu_{\text{def}}$ against $\nu$. Then, the total advectively and diffusively travelled distance of the foremost tip of the concentration profile according to Eq. (7) is given by $d_{\text{adv}} = 2\nu \int_0^\infty A(t)dt$ and $d_{\text{diff}} = \sqrt{2\nu \int_0^\infty A(t)dt}$, respectively. Yield production starts as soon as the density wave reaches the absorbing boundary at $x = L$. Hence, in order to obtain non-zero yield, it must hold

$$d_{\text{adv}} + d_{\text{diff}} \geq L - 2\,. \tag{10}$$

As condition for the onset, we thus obtain

$$2\nu \int_0^\infty A(t)dt \stackrel{!}{=} \frac{1}{4}\left(\sqrt{1 + 4(L-2)} - 1\right)^2 \approx L - \sqrt{L}\,, \tag{11}$$

where the last approximation is valid for large $L$.
In order to obtain $\int_0^\infty A(t)dt$, we derive an effective two-component system that governs the evolution of $A(t)$. To this end, we denote the total number of polymers in Eq. (9) by $B(t) := \int_2^\infty c(x,t)\,dx$ (as long as yield is zero the upper boundary is irrelevant and we can consider $L = \infty$). Eq. (9) then reads

$$\frac{d}{dt}A = \alpha C e^{-\alpha t} - 2\mu A^2 - 2\nu A\ B\,, \tag{12}$$

and the dynamics of $B$ is determined from the boundary condition, Eq. (8)

$$\frac{d}{dt}B = \int_2^\infty \partial_t c(x,t)\,dx = \int_2^\infty -\partial_x J(x,t)\,dx = -\underbrace{J(\infty,t)}_{=0} + J(2,t) = \mu A(t)^2. \tag{13}$$

Measuring $A$ and $B$ in units of the initial monomer concentration $C$ and time in units of $(\nu C)^{-1}$, the equations are rewritten in dimensionless units as

$$\frac{d}{dt}A = \omega e^{-\omega t} - 2\eta A^2 - 2A\ B\,, \tag{14a}$$

$$\frac{d}{dt}B = \eta A^2\,, \tag{14b}$$

where $\omega = \frac{\alpha}{\nu C}$ and $\eta = \frac{\mu}{\nu}$. Eq. (14) describes a closed two-component system for the concentration of active monomers $A$ and the total concentration of polymers $B$. It describes the dynamics exactly as long as the yield is zero. In order to evaluate the condition (11) we need to determine the integral over $A(t)$ as a function of $\omega$ and $\eta$

$$\int_0^\infty A_{\omega,\eta}(t)dt := g(\omega,\eta)\,. \tag{15}$$

To that end, we proceed by looking at both scenarios separately. We only give an outline of the results; Details of the analysis can be found in [1]

`Dimerization scenario`

The activation rate in the dimerization scenario is $\alpha \to \infty$, and so the term $\omega e^{-\omega t}$ in $\mathrm{d}A/\mathrm{d}t$ can be dismissed, if instead we set the initial condition $A(0) = 1$ (and $B(0) = 0$). Furthermore, $\eta = \mu/\nu \ll 1$ and we can neglect the term proportional to $\eta$ in $\mathrm{d}A/\mathrm{d}t$. As a result,

$$\frac{\mathrm{d}A}{\mathrm{d}B} = -\frac{2B}{\eta A}.$$

Solving this equation for $A$ as a function of $B$ by using the initial condition $A(B = 0) = 1$, the totally travelled distance of the wave is determined to be

$$2g(\omega, \eta) = 2\frac{\pi}{2\sqrt{2}}\frac{1}{\sqrt{\eta}}, \tag{16}$$

where for the evaluation of the integral we used the substitution $\eta A^2 \mathrm{d}t = \mathrm{d}B$.

`Activation scenario`

In the activation scenario, yield sets in only if the activation rate and thus the effective nucleation rate is slow. As a result, we can again neglect the term proportional to $\eta$ in $\mathrm{d}A/\mathrm{d}t$. This time, however, we have to keep the term $\omega e^{-\omega t}$. As a next step, we assume that $\mathrm{d}A/\mathrm{d}t$ is much smaller than the remaining terms on the right-hand side, $\omega e^{-\omega t}$ and $-2AB$. This assumption might seem crude at first sight but is justified *a posteriori* with the solution of the equation. Hence, we get the algebraic equation $A(t) = \omega e^{-\omega t}/(2B(t))$. Using it to solve $\mathrm{d}B/\mathrm{d}t = \eta A^2$ for $B$, and then to determine $A$, the totally travelled distance of the wave is deduced as

$$2g(\omega, \eta) = 2\frac{3^{2/3}\sqrt{\pi}\Gamma(2/3)}{6\Gamma(7/6)}(\omega\eta)^{-1/3}. \tag{17}$$

Taken together, from the analysis of the activation and dimerization scenario we obtain two conditions out of which one must be fulfilled in order to obtain a finite yield

$$2a(\eta\omega)^{-\frac{1}{3}} \geq L - \sqrt{L} \qquad \Rightarrow \qquad \alpha < \alpha_{\mathrm{th}} := P_\alpha \frac{\nu}{\mu}\frac{\nu C}{(L - \sqrt{L})^3} \tag{18}$$

$$\text{or} \qquad 2b\eta^{-\frac{1}{2}} \geq L - \sqrt{L} \qquad \Rightarrow \qquad \mu < \mu_{\mathrm{th}} := P_\mu \frac{\nu}{(L - \sqrt{L})^2}\,, \tag{19}$$

where $a$ and $b$ are numerical factors, and $P_\alpha = 8a^3 \approx 5.77$ and $P_\mu = 4b^2 \approx 4.93$. Because in the activation scenario monomer activation defines the rate limiting step, the assembly time

scales inversely to the activation rate. Since the optimal activation rate that minimizes the assembly time scales identically as the threshold rate, we obtain the minimal assembly time scaling as

$$T_{90}^{\min} \sim \frac{1}{\alpha_{\text{th}}} \sim (C\nu)^{-1}\frac{\mu}{\nu}L^3\,, \tag{20}$$

in the limit of large $L$. Therefore, $\chi(\text{activation}) = 3$, in agreement with the numerical result in the main text. Similarly, dimerization is the rate limiting step in the dimerization scenario and thus the minimal assembly time scales like the inverse dimerization rate,

$$T_{90}^{\min} \sim \frac{C}{\mu_{\text{th}}} \sim (C\nu)^{-1}L^1\,. \tag{21}$$

Therefore, $\chi(\text{dimerization}) = 1$. Hence, all scaling exponents for the minimal assembly time could be derived correctly for the three scenarios with $q = 0$ with the reductionist approach and the continuity approximation. Next, we analyze the case $q > 0$, corresponding to the Jis scenario.

### D. Reduction in the case $q > 0$ (Jis scenario)

In the Jis scenario, the symmetry of species is broken due to the presence of inhibition ($q > 0$). However, here we can argue on physical grounds that the length index is irrelevant: Because of inhibition, monomers are activated in sequence and binding to the right end of the polymers is strongly favoured over binding to the left end. Whereas the right end of a polymer is described by its species index, the length index serves to keep track of its left end in Eq. (1). Therefore, if binding to the left and detachment of monomers are neglected, the length index can be disregarded. To this end, we introduce the variables $I_s := c_0^s$, $A_s := c_1^s$ and $B_s := \sum_{\ell=2}^{L} c_\ell^s$ which denote, respectively, the concentrations of inactive and active monomers of species $s$, as well as the total concentration of polymers of species $s$ and arbitrary length $\ell$. The governing set of equations for $A_s, I_s$ and $B_s$ can then be derived from Eq. (1) by setting $\delta = 0$ and disregarding binding to the left end of polymers:

$$\frac{d}{dt}I_s = -\alpha I_s e^{-qI_{s-1}(1-\delta_{1s})}\,, \tag{22a}$$

$$\frac{d}{dt}A_s = \alpha I_s e^{-qI_{s-1}(1-\delta_{1s})} - \mu\left(A_sA_{s+1} + A_sA_{s-1}\right) - \nu A_sB_{s-1} - \nu_{\text{def}}A_sB_{s-2}\,, \tag{22b}$$

$$\frac{d}{dt}B_s = \mu A_sA_{s-1} + \nu\left(A_sB_{s-1} - A_{s+1}B_s\right) + \nu_{\text{def}}\left(A_sB_{s-2} - A_{s+2}B_s\right)\,. \tag{22c}$$

Thereby, the number of degrees of freedom has been reduced from $L^2 + 1$ in Eq. (1) to $3L$. Note that $B_L$ does not measure the concentration of complete structures and, therefore, the yield cannot be assessed in a direct way. However, the final concentration of polymers, $B_s(\infty)$ for any $1 \ll s < L$, is directly related to the dimerization probability by $p_{\text{dim}} = B_s(\infty)/N$. This holds because each dimerization event consumes a monomer which

is then missing for the growth of a structure. The yield is equal to the probability that in $L-2$ subsequent assembly steps no dimerization event happens and hence can be calculated from the dimerization probability as $\mathit{yield} = (1 - p_{\mathrm{dim}})^{L-2}$ (cf. Eq. (4) in the main text). Similarly, the defect probability $p_{\mathrm{def}} = \frac{\nu_{\mathrm{def}}}{N^2} \int_0^\infty A_s B_{s-2}\, dt$ can be calculated from the solution of Eq. (22) by evaluating the temporal correlator of $A_s$ with $B_{s-2}$ for any $1 \ll s < L-2$. Initially, for small $s$, there might be a short transient before stationary values for the dimerization and defect probability can be obtained. Therefore, we included the condition $s \gg 1$ when $s$ is the species index for which the corresponding concentrations of $A$ and $B$ are measured. Typically, however, the transient is short so that the effect caused by a deviant transient dimerization and defect probability on the yield and defect-free yield is negligible for large $L$. Hence, Eq. 22 can be used to efficiently simulate the JIS scenario and determine all relevant quantities from the simulation.

In both cases, for $q = 0$ and $q \neq 0$, we could therefore reduce the description of the system in the deterministic limit to only a single set of indices. The interactions and transitions between the degrees of freedom labelled by the corresponding index sets are local, meaning that transitions only occur between neighbouring degrees of freedom labelled by consecutive indices. Therefore, in both cases, we can use a hydrodynamic approach to further simplify the systems. For the case $q = 0$, as shown above, this describes the system as an effective advection diffusion process in one spatial dimension. In this case, the hydrodynamic approach works very well and yields an accurate description of the dynamics of the concentration profile. Therefore, it seems promising to use the same approach also for the case $q > 0$. We will show in the following that the ensuing partial differential equation admits travelling wave solutions for the concentration profiles $I$, $A$ and $B$ in qualitative agreement with the phenomenology observed in the system (see main text Fig. 5). However, when evaluating the speed of the wave, we find that, quantitatively, the analytic result strongly deviates from the propagation speed in the simulation. We attribute these deviations to the fact that the emerging wave profile is too steep in order for the continuity approximation and the gradient expansion to yield quantitatively correct results. Therefore, we will subsequently use a complementary approach in which we exploit the steepness of the wave front in order to derive quantitatively accurate results. Nevertheless, as we consider the analysis of the traveling wave solutions quite instructive, we start by discussing the continuum approach first.

### E. Continuity approximation and traveling wave ansatz for $q > 0$

In order to rewrite Eq. (22) as a set of partial differential equations, we interpret the length index $\ell$ as a continuous variable and expand all fields up to second order. We measure time in units of $\left[\frac{1}{C\nu}\right]$ and $I, A, B$ in units of $[C]$. Furthermore, since inhibition is never perfect, the concentration of inactive monomers on the right of the travelling wave front would slowly decrease ('out-of-sequence' activation of monomers). Hence, in order to obtain

a real travelling wave solution, we have to add a small correction term $\gamma$ to the equation for the inactive monomers, which compensates the permanent outflux of particles. In order to guarantee mass conservation and the existence of travelling wave solutions, we subtract the same term $\gamma$ from the equation for the active monomers. In order for self-assembly to be efficient, out-of-sequence activation and hence the correction have to be negligibly small; Therefore, the requirement of the correction term is merely a mathematical subtly that guarantees the existence of real travelling wave solution.
Setting $\delta$ and $\nu_{\text{def}}$ to zero, Eq.(22) then transforms to

$$\partial_t I = -\omega I e^{-Q(I-\partial_x I+\frac{1}{2}\partial_x^2 I)} + \gamma\,, \tag{23a}$$

$$\partial_t A = \omega I e^{-Q(I-\partial_x I+\frac{1}{2}\partial_x^2 I)} - \eta A(2A+\partial_x^2 A) - A(B-\partial_x B+\frac{1}{2}\partial_x^2 B) - \gamma\,, \tag{23b}$$

$$\partial_t B = A(B-\partial_x B+\frac{1}{2}\partial_x^2 B) + \eta A(A-\partial_x A+\frac{1}{2}\partial_x^2 A) - B(A+\partial_x A+\frac{1}{2}\partial_x^2 A)\,, \tag{23c}$$

where $\omega = \frac{\alpha}{C\nu}$, $\eta = \frac{\mu}{\nu}$ and $Q = qC$ are the dimensionless parameters and for the correction we set $\gamma = \omega e^{-Q}$, in order to ensure $\partial_t I = 0$ at the far right of the wave front. Assuming that a travelling wave solution exists, we make the ansatz:

$$I(z) := I(x-ct), \qquad A(z) := A(x-ct), \qquad B(z) := B(x-ct), \tag{24}$$

where $c$ is the resulting speed of the wave. The system then reads:

$$-cI' = -\omega I e^{-Q(I-I'+\frac{1}{2}I'')} + \gamma\,, \tag{25a}$$

$$-cA' = \omega I e^{-Q(I-I'+\frac{1}{2}I'')} - \eta A(2A+A'') - A(B-B'+\frac{1}{2}B'') - \gamma\,, \tag{25b}$$

$$-cB' = A(B-B'+\frac{1}{2}B'') + \eta A(A-A'+\frac{1}{2}A'') - B(A+A'+\frac{1}{2}A'')\,. \tag{25c}$$

Assuming an infinitely extended system, we imply the following asymptotic behaviour:

$$I(-\infty) = \beta, \qquad I(+\infty) = 1\,, \tag{26a}$$

$$A(-\infty) = 0, \qquad A(+\infty) = 0\,, \tag{26b}$$

$$B(-\infty) = p, \qquad B(+\infty) = 0\,. \tag{26c}$$

The final concentration of complexes $p = p_{\text{dim}}$ is interpreted as the (stationary) dimerization probability (the fraction of complexes whose growth was interrupted by a dimerization event). Furthermore, the constant $\beta$ must be such that the concentration of inactive monomers at $x = -\infty$ becomes stationary, meaning:

$$0 = -\omega\beta e^{-Q\beta} + \gamma \qquad \Rightarrow \qquad \beta e^{-Q\beta} = e^{-Q} \tag{27}$$

resulting in $\beta = -\frac{1}{Q}W_0(-Qe^{-Q})$, where $W_0$ denotes the relevant branch of the Lambert W-Function.

Knowledge of the dimerization probability $p$ and the wave speed $c$ in dependence of the parameters $\omega, \eta$ and $Q$ is sufficient in order to evaluate the quality and the efficiency of the assembly process: The yield relates to the dimerization probability via $yield = \big(1 - p_{\mathrm{dim}}(\omega, Q)\big)^{L-2}$ (see main text Eq. (4)), and the assembly time corresponds to the time it takes the wave to travel a distance $L$: $T_{90} = \frac{L}{c}$. In the following, we will therefore derive the speed of the traveling wave arising from Eq. (25a).

*Derivation of the wave speed (continuity approach)*

In order to show that traveling wave solutions exist and to determine their speed, we consider only the equation for the dynamics of the inactive monomers since it is decoupled from the other two equations for$A$ and $B$ and can be analyzed independently. Dividing both sides of Eq. (25a) by $\omega$ and defining $\tilde{c} = \frac{c}{\omega}$, the equation becomes independent of $\omega$,

$$-\tilde{c}I' = -Ie^{-Q(I-I'+\frac{1}{2}I'')} + e^{-Q}\,, \tag{28}$$

which means that $\tilde{c}$ can be a function only of $Q$ and hence:

$$c(\omega, Q) = \omega\ \tilde{c}(Q)\,. \tag{29}$$

To proceed, we make the equation amenable for phase plain analysis by rewriting it as a coupled system of two first order equations for $I$ and $S = I'$:

$$I' = S\,; \qquad S' = I'' = -\frac{2}{Q}\ln\left(\frac{e^{-Q} + \tilde{c}S}{I}\right) - 2I + 2S\,. \tag{30}$$

There are two fixed points obeying

$$S = 0\,, \qquad\qquad Q + \ln I - QI = 0. \tag{31}$$

which correspond to the asymptotic values for $I$ and $S$:

$$(I_1^*, S_1^*) = (\beta, 0) \qquad \text{and} \qquad (I_2^*, S_2^*) = (1, 0) \tag{32}$$

The solution that corresponds to a travelling wave solution is a heteroclinic orbit connecting the two fixed points.
The fixed points, however, do not change their stability when varying $\tilde{c}$ or $Q$, so a local stability analysis does not help to determine $\tilde{c}(Q)$. Furthermore, there is not only one but a bunch of different (physically meaningful) heteroclinic orbits and one has to determine the one that corresponds to the initial conditions. Solving Eq. (30) numerically shows that for fixed $Q$, the heteroclinic orbits make an increasingly larger excursion (larger amplitude) when $\tilde{c}$ becomes smaller, and finally for some minimal value of $\tilde{c}$ hits the fixed point at 1 directly from above rather than from the left, see Fig. S1. For illustration, this is plotted here for $Q = 16$ and the minimal $\tilde{c}$ is found to be approximately $\tilde{c}_{\min} \approx 0.26$.

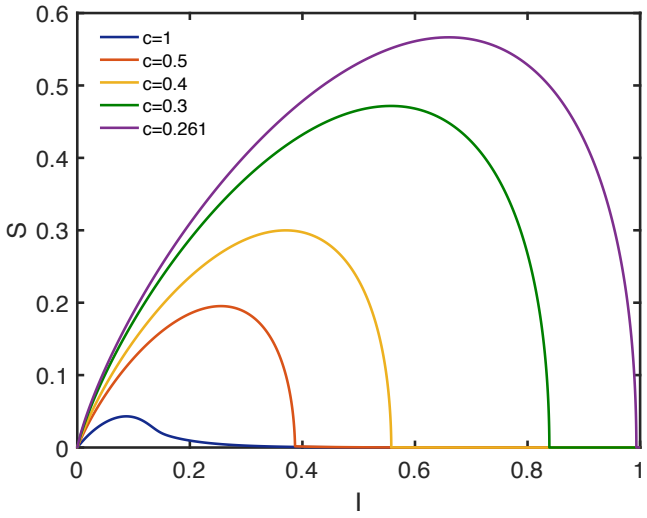


Fig. S 1: Solution of Eq. (30) obtained numerically for the heteroclinic orbits connecting the fixed points given by Eq. (32) for different values of $c$. Upon decreasing $c$, the orbits make an increasingly larger excursion (larger amplitude) until for the minimal wave speed $c_{\min} \approx 0.26$ they hit the fixed point $(1, 0)$ directly from above instead of from the left. The minimal wave speed therefore corresponds to the steepest wave front and is thus consistent with our initial conditions.

The heteroclinic orbit with the largest amplitude corresponds to the steepest wave front and, therefore, we argue that this must be the front that is realized when initially $I = 1$ everywhere except for the first site, i.e. when starting with a maximally steep gradient. Hence, $\tilde{c} = \tilde{c}_{\min}$.

Dividing $S'$ by $I'$ in Eq. (30), we obtain a differential equation for $S(I)$ that describes the trajectory in the phase plain:

$$\frac{dS}{dI} = -\frac{2}{SQ} \ln\left(\frac{e^{-Q} + \tilde{c}S}{I}\right) - 2\frac{I}{S} + 2 \tag{33}$$

The term $e^{-Q}$ is very small if $Q$ is sufficiently large and is only relevant if $S$ goes to 0. Therefore, we can neglect this term if we take as initial value some small but finite $S = \epsilon$ rather than $S = 0$ and break up if $S$ becomes smaller than $\epsilon$ again. We define $\tilde{S} = QS$ and $\tilde{I} = QI$, so that the equation becomes independent of $Q$. Furthermore, let $x := (\log \frac{1}{\tilde{c}})^{-1}$. Equation (33) then becomes

$$\frac{d\tilde{S}}{d\tilde{I}} = \frac{2}{\tilde{S}x} - \frac{2}{\tilde{S}} \ln\left(\frac{\tilde{S}}{\tilde{I}}\right) - 2\frac{\tilde{I}}{\tilde{S}} + 2\,. \tag{34}$$

Since $I$ goes to 1 asymptotically, $\tilde{I}$ goes to $Q$. Hence, for a given wave speed $\tilde{c}$, the corresponding value of $Q$ is determined as the point where the trajectory hits the $I-$axis from

above. In this way, one can easily determine the function $Q(\tilde{c})$ numerically.
Plotting the trajectories for different values of $\tilde{c}$ or $x$ reveals some interesting behaviour: Rescaling the $\tilde{I}-$ and $\tilde{S}-$axis for each trajectory individually by its maximal $\tilde{I}-$ and $\tilde{S}-$value, $\tilde{I}_{\max} = Q$ and $\tilde{S}_{\max}$, respectively, makes all curves collapse onto a single master curve (see Fig. S2). The collapse is imperfect if $\tilde{c}$ is large but becomes very accurate if $\tilde{c}$ is small.

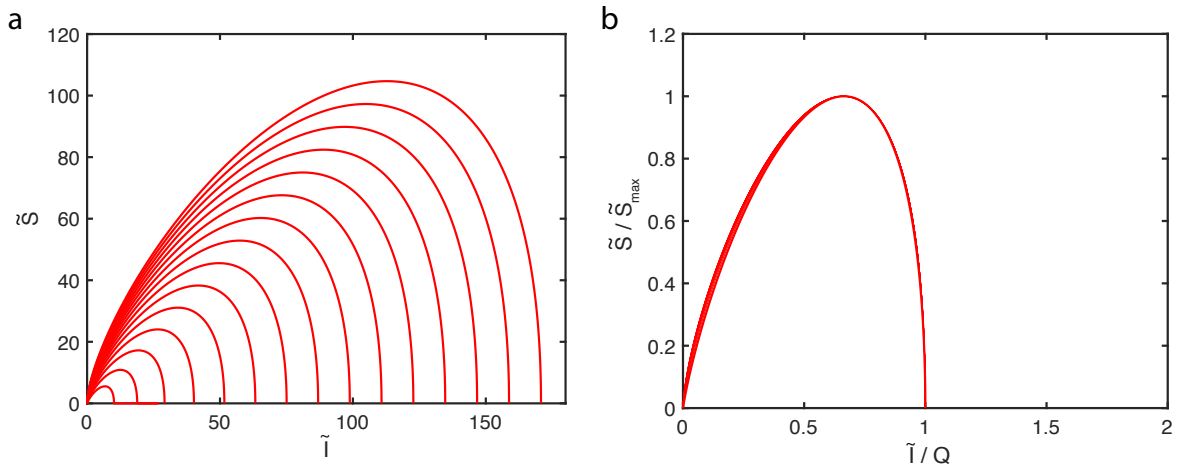


Fig. S 2: **a)** Plot of trajectories as obtained by solving Eq. (34) numerically for different $\tilde{c} = e^{-1/x}$ ($\tilde{c} = \exp(-8 : 0.5 : -1)$). The maximal $\tilde{I}-$value ($\tilde{I}_{\max}$), i.e. the point where the trajectories get down on the $\tilde{I}-$axis is identical to $Q$. **b)** Rescaling the $\tilde{I}-$ and $\tilde{S}-$axis by $\tilde{I}_{\max} = Q$ and $\tilde{S}_{\max}$ for each curve individually makes the trajectories collapse onto a single master curve.

We thus find that the trajectories described by Eq. (34) apparently obey an asymptotic scaling form for small $\tilde{c}$ or $x$. This motivates us to use the following ansatz in which we expand $\tilde{S}$ in a power series in $x$ and scale $\tilde{I}$ with $x$:

$$\tilde{I} = \frac{1}{x}\tilde{I}_0 \tag{35a}$$

$$\tilde{S}(\tilde{I}) = \frac{1}{x}\tilde{S}_0(\tilde{I}_0) + \tilde{S}_1(\tilde{I}_0) + x\tilde{S}_2(\tilde{I}_0) + ... \tag{35b}$$

Using this ansatz to order $O(1)$ in $x$ in Eq. (34) gives

$$\frac{d\tilde{S}_0}{d\tilde{I}_0} + x\frac{d\tilde{S}_1}{d\tilde{I}_0} = \frac{2}{\tilde{S}_0 + x\tilde{S}_1} - \frac{2x}{\tilde{S}_0 + \tilde{S}_1 x}\ln\left(\frac{\tilde{S}_0}{\tilde{I}_0} + x\frac{\tilde{S}_1}{\tilde{I}_0}\right) - 2\frac{\tilde{I}_0}{\tilde{S}_0 + x\tilde{S}_1} + 2\,. \tag{36}$$

Expanding the rhs in $x$ and taking together terms with equal power in $x$ yields:

$$0 = \left(-\frac{d\tilde{S}_0}{d\tilde{I}_0} + \frac{2}{\tilde{S}_0} - 2\frac{\tilde{I}_0}{\tilde{S}_0} + 2\right) + x\left(-\frac{d\tilde{S}_1}{d\tilde{I}_0} - \frac{2}{\tilde{S}_0^2}\tilde{S}_1 - \frac{2}{\tilde{S}_0}\ln\left(\frac{\tilde{S}_0}{\tilde{I}_0}\right) + 2\frac{\tilde{I}_0}{\tilde{S}_0^2}\tilde{S}_1\right) + O(x^2)\,. \tag{37}$$

So, in the limit $x \to 0$, only the leading order term is relevant and reveals the defining equation for the scaling form $\tilde{S}_0(\tilde{I}_0)$ independent of $x$:

$$\frac{d\tilde{S}_0}{d\tilde{I}_0} = \frac{2}{\tilde{S}_0} - 2\frac{\tilde{I}_0}{\tilde{S}_0} + 2\,. \tag{38}$$

With the solution for the asymptotic scaling form $\tilde{S}_0(\tilde{I}_0)$, the subleading order correction $\tilde{S}_1(\tilde{I}_0)$ could be calculated and with that one the next lower order correction and so on.
According to Eq. (35), in the limit of small $x$, the point $\tilde{I} = Q$ in which the curve hits the $\tilde{I}$ axis from above obeys $Q = \frac{1}{x}a_0 = -a_0 \log(\tilde{c})$, where $a_0 := \tilde{I}_0^{\max}$ is a constant. Therefore, to leading order,

$$\tilde{c} = e^{-Q/a_0}\,, \tag{39}$$

where the constant $a_0$ is determined numerically from the scaling form described by Eq. (38) as $a_0 \approx 24.12$. For larger values of $x$ or $\tilde{c}$ (small $Q$), higher order corrections to the scaling form have to be considered $Q = \frac{1}{x}a_0 + a_1 + xa_2 + ...$, which gives a constant prefactor to the wave speed as a subleading order correction

$$\tilde{c} = e^{a_1/a_0} e^{-Q/a_0}\,. \tag{40}$$

However, numerically we find that the higher order terms only make a minor correction to the shape of the trajectory and hence also to the wave speed. Therefore, the analysis predicts that the wave speed decreases exponentially with the inhibition parameter $Q$.
Figure S3 compares the wave speed that is measured when numerically integrating the partial differential equation (23) to the speed of the wave that emerges from the original ODE system, Eq. (22). We find that the continuity approximation strongly underestimates the resulting wave speed and that $c$ can be fitted very well assuming a logarithmic dependence on $Q$ (see fits in Fig. S3) rather than an exponential dependence as predicted by the theory.

Hence, we find that while the continuity approximation correctly predicts the qualitative behavior of the system (traveling wave solutions, wave speed is a decreasing function of $Q$), it fails to give quantitatively correct results. The reason for this discrepancy is that the wave front is too steep and, therefore, the gradient expansion of the fields in Eq. (23) up to second order is not sufficient in order to obtain accurate results. We will therefore now use a complementary approach that exploits the fact that the wave front is very steep and we will find that this approach, in contrast, yields very accurate results for the wave speed, the dimerization probability and the defect probability.

### F. Steep-front-approximation (2-species-approximation) for $q > 0$

This complementary approach, which was also sketched in the main text, relies on a few approximations that are justified under the assumption that the emerging wave profile is steep and $\omega \ll 1$. With a few simplifications, we can thereby reduce the dynamical system

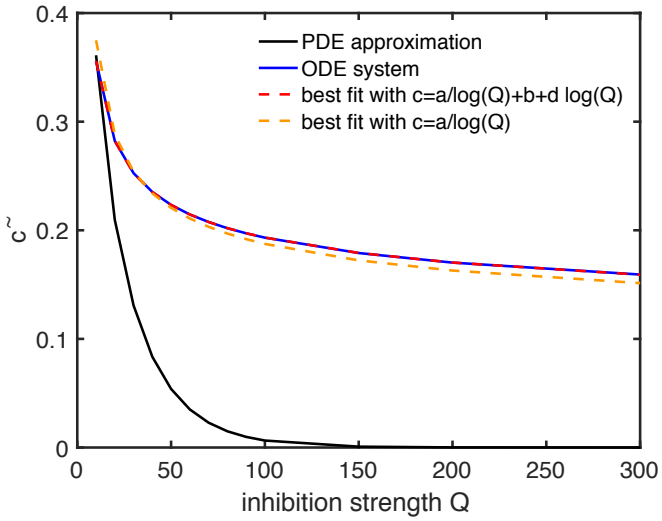


Fig. S 3: Comparison of the wave speed $\tilde{c} = c/\omega$ as a function of $Q$ obtained from numerical integration of the partial differential equation (23) (black line) with the speed measured from the original ODE system, Eq. (22) (blue line). The large discrepancy implies that the continuity approximation of the ODE system and the gradient expansion of the fields is inaccurate because the wave front is too steep. The dashed lines show fits of $c$ by functions depending inverse logarithmically on $Q$, which yield much better fits compared to the inverse exponential dependence (Eq. (39)) predicted by the hydrodynamic approach.

to a two-component system that describes the dynamics of two consecutive species in the sequence and which can be solved analytically.
First, we approximate the inhibition term $\exp(-QI_{i-1})$ as a step function $\Theta(\frac{1}{Q} - I_{i-1})$, so that inhibition of $I_i$ is assumed to be perfect while $I_{i-1}$ is larger than $\frac{1}{Q}$ and negligible below this threshold. This approximation is generally justified if the wave front is steep and thus the concentration of inactive monomers changes quickly from its maximum value (near perfect inhibition) to zero (no inhibition). The wave speed is then easily determined from the timespan $T$ of an individual assembly step, which is given by the time it takes until $I_i$ drops from 1 to $\frac{1}{Q}$ assuming that $I_{i-1}$ has already fallen below $\frac{1}{Q}$. $I_i$ then follows a simple decay dynamics $I_i = e^{-\alpha t}$ and we thus find $T = \frac{1}{\alpha} \ln Q$ and

$$c = \frac{1}{T} = \frac{\alpha}{\ln Q} \,. \tag{41}$$

This result differs strongly from the previous result, Eq. (39), obtained with the hydrodynamic approximation. We find that the actual wave speed $\tilde{c}$ as a function of $Q$, which is obtained by simulating the ODE system, is indeed very well described by $\tilde{c} = a/\ln Q$, where the optimal fit is obtained with a coefficient $a = 0.86$ only slightly smaller than one (see Fig. S3). An even more accurate fit is obtained by adding correction terms of the

form $\tilde{c} = a/\ln Q + b + d\ln Q$, with coefficients being determined as $a = 0.7, b = 0.06$ and $d = -0.0044$. Hence, the approximation apparently works very well and the wave speed depends indeed only very mildly on $Q$ .

With this correct result for the wave speed, we can also estimate the minimal inhibition strength $Q$ that is required so that 'out-of-sequence' activation does not noticeably deteriorate the yield. To this end, we estimate the number of monomers $N_L^{\text{leak}}$ of the last species $L$ that are activated out-of-sequence (i.e. before species $L-1$ was activated) with rate $N\alpha e^{-Q}$:

$$\frac{N_L^{\text{leak}}}{N} = \alpha e^{-Q} T = \alpha e^{-Q} \frac{L}{\alpha \tilde{c}} = e^{-Q} \ln Q \frac{L}{a} \sim L e^{-Q} \,, \tag{42}$$

where $T$ is the total time the assembly process takes. On the deterministic level, this ratio of 'leaked' particles $N_L^{\text{leak}}/N$ is identical to the yield deficiency resulting from out-of-sequence activation. In the stochastic system, however, the yield deficiency will be higher because there will be much more dimerization events resulting from out-of-sequence activation due to stochastic effects (stochastic yield catastrophe) than predicted deterministically. An upper bound for the detrimental effect of the stochastic yield catastrophe is therefore determined by estimating the *total* concentration of monomers of all species that are activated out-of-sequence (until each species is reached by the wave front) and equating this with the yield deficiency. This corresponds to assuming that each monomer that is activated out-of-sequence initiates a new complex, which certainly overestimates the stochastic effect:

$$1 - \text{yield} = \int_0^L l e^{-Q} dl = \frac{1}{2} L^2 e^{-Q} \sim L^2 e^{-Q} \,. \tag{43}$$

Hence, if the yield deficiency due to out-of-sequence activation should be smaller than $\epsilon$, $Q$ must be larger than

$$Q > \ln\left(\frac{L^2}{\epsilon}\right). \tag{44}$$

For example, if $L = 100$ and $\epsilon = 0.01$ then $Q$ should be larger than 13.8.

Next, we determine the dimerization probability and the defect binding probability from the simplified model. To this end, we consider the dynamics of active monomers of two subsequent species that, for simplicity, we denote by indices 1 and 2. Since in the regime in which self-assembly is efficient only a tiny fraction of monomers will dimerize or bind incorrectly, we neglect dimerization and defect binding in the dynamics. For the active monomer concentrations of species 1 and 2 it then follows:

$$\partial_t A_1 = \omega I_1 - A_1 B_0 \,, \tag{45a}$$

$$\partial_t A_2 = \omega I_2 - A_2 B_1 \,, \tag{45b}$$

with initial condition $I_1 = I_2 = B_0 = 1$ and $A_1 = A_2 = B_1 = 0$ at $t = 0$. The dimerization probability and defect binding probability are then given by $p_{\text{dim}} = \int_0^\infty A_1(t) A_2(t) dt$ and

$p_{\mathrm{def}} = \frac{\nu_{\mathrm{def}}}{\nu} \int_0^\infty B_0(t) A_2(t) dt$, respectively. Assuming that all species are supplied in equal concentrations, as described in the main text, the number $B_0$ of complexes of species 0 equals the number of unbound monomers of species 1: $B_0 = I_1 + A_1$. Similarly, $B_1$ is given by the number of monomers of species 1 that have already bound (to $B_0$) minus the number of monomers of species 2 that have already bound (and thus transformed $B_1$ to $B_2$): $B_1 = (1-I_1-A_1)-(1-I_2-A_2)$. Since in the limit of small $\omega$, where self-assembly is efficient, the number of active monomers is typically small, we neglect the concentrations of active monomers in $B_0$ and $B_1$, which would lead to nonlinear terms in the above equation. This, however, has the consequence that $A_1$ and $A_2$ in the equation above will never relax to zero because when $I_i$ becomes zero, $\partial_t A_i$ is zero as well. This is a problem when integrating the concentrations of active monomers over all time until $\infty$. In order to remedy this problem, we replace $\infty$ in the integral by an upper cutoff that is defined as the time point where $I_1$ becomes smaller than $A_1$ and thus the approximation is no longer justified. The system can then be written as follows:

$$\partial_t A_1 = \omega I_1 - A_1 I_1 \,, \tag{46a}$$

$$\partial_t A_2 = \omega I_2 - A_2(I_2 - I_1) \,. \tag{46b}$$

As long as $I_1$ is above the threshold $\frac{1}{Q}$, $I_2$ will not be activated and consequently $A_2$ will remain 0. Hence, as initial condition we set $I_1(0) = 1/Q$, $I_2(0) = 0$ and $A_1(0) = A_2(0) = 0$. Then, starting from time $t_0 = 0$, there is no inhibition on $I_2$ in this approximation and the concentrations of inactive monomers follow simple decay dynamics: $I_1 = \frac{1}{Q} e^{-\omega t}$ and $I_2 = e^{-\omega t}$:

$$\partial_t A_1 = e^{-\omega t} \frac{1}{Q} (\omega - A_1) \tag{47a}$$

$$\partial_t A_2 = e^{-\omega t} (\omega - A_2 + \frac{1}{Q} A_2) \,. \tag{47b}$$

Furthermore, it is useful to transform time via $\tau := 1 - e^{-\omega t}$ so that $\tau$ is in the integral $[0, 1]$:

$$\partial_\tau A_1 = \frac{1}{Q\omega} (\omega - A_1) \tag{48a}$$

$$\partial_\tau A_2 = \frac{1}{\omega} (\omega - A_2 + \frac{1}{Q} A_2) \tag{48b}$$

The solutions to this inhomogeneous linear system of ODEs with constant coefficients are given by

$$A_1 = \omega \left( 1 - \exp\left(-\frac{\tau}{Q\omega}\right) \right) \,, \tag{49a}$$

$$A_2 = \frac{\omega}{1 - \frac{1}{Q}} \left( 1 - \exp\left( -(1 - \frac{1}{Q}) \frac{\tau}{\omega} \right) \right) \,. \tag{49b}$$

The time point when $I_1(\tau) = \frac{1}{Q}(1-\tau)$ becomes smaller than $A_1(\tau)$, which defines the upper bound for the integrals, is thus given by $b := 1 - Q\omega\left(1 - \exp\left(-\frac{1}{\omega Q}\right)\right)$. For the dimerization probability we then obtain

$$\begin{aligned} p_{\text{dim}} &= \int_0^b A_1(\tau)A_2(\tau)\frac{d\tau}{\omega(1-\tau)} \\ &= \frac{\omega}{1-\frac{1}{Q}}\int_0^b \left(1-\exp\left(-\frac{\tau}{Q\omega}\right)\right)\left(1-\exp\left(-(1-\frac{1}{Q})\frac{\tau}{\omega}\right)\right)\frac{1}{1-\tau}d\tau\,. \end{aligned} \tag{50}$$

Since in the limit of small $\omega$ the exponentials become very small, we approximate both of them by 0 and are left with:

$$p_{\text{dim}} = \frac{\omega}{1-\frac{1}{Q}}\int_0^b \frac{1}{1-\tau}d\tau = -\frac{\omega}{1-\frac{1}{Q}}\ln(1-b) = -\frac{\omega}{1-\frac{1}{Q}}\ln\left(Q\omega(1-\exp\left(-\frac{1}{Q\omega}\right))\right). \tag{51}$$

Neglecting also here the exponential in the limit of small $\omega$, we obtain as final result for $\omega \ll \frac{1}{Q}$:

$$p_{\text{dim}}(\omega, Q) = \frac{\omega}{1-\frac{1}{Q}}\ln\left(\frac{1}{Q\omega}\right). \tag{52}$$

Comparing this result with the dimerization probability obtained from numerical integration of the ODE system Eq. (22) shows a very good agreement for $\omega < \frac{1}{Q}$, see Fig. S4 where Q=50.

Hence we find for the yield under the assumption that $Q$ is large enough and $\omega \ll \frac{1}{Q}$ (compare main text Eq. (4)):

$$\text{yield} = \left(1 - p_{\text{dim}}(\omega, Q)\right)^L = \left(1 - \frac{\omega}{1-\frac{1}{Q}}\ln\left(\frac{1}{Q\omega}\right)\right)^L, \tag{53}$$

where it was further assumed that $L$ is large, otherwise $L$ would need to be replaced by $L-2$. For example, demanding the yield to be larger or equal $y$ we have to determine $\omega$ such that

$$\omega Q \ln\left(\frac{1}{Q\omega}\right) \leq \left(1 - y^{\frac{1}{L}}\right)(Q-1) \approx -\frac{\ln y}{L}(Q-1)\,, \tag{54}$$

where we assumed that $L$ is large and $y$ is sufficiently close to 1 so that $y^{\frac{1}{L}} = \exp\left(\frac{1}{L}\ln y\right) \approx$

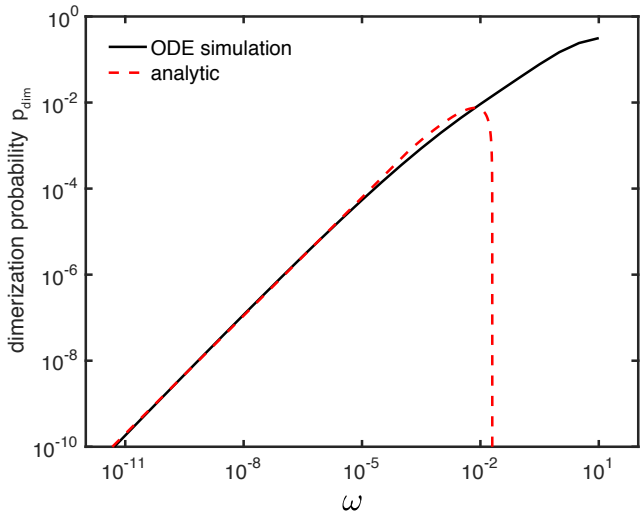


Fig. S 4: Dimerization probability versus $\omega$ for $Q = 50$: Comparison between theory, Eq. (52), (red dashed line) and the simulation of the ODE system Eq. (22) (black dawn line).

$1 + \frac{1}{L}\ln y$. The solution is given by the LambertW-function as[1]

$$\omega = \frac{\frac{\ln y}{L}(1 - \frac{1}{Q})}{\text{LambertW}\left(\frac{\ln y}{L}(Q-1)\right)}. \tag{55}$$

For a rough estimate, however, we can replace $\ln\left(\frac{1}{Q\omega}\right)$ in Eq. (54) by a constant $d$ to obtain (assuming $Q$ is large)

$$\omega \approx -\frac{\ln y}{d\ L}\,. \tag{56}$$

So $\omega$ scales approximately like $\omega \sim L^{-1}$. The total time $T_y$ that it takes to reach a yield $y$ is then given by

$$T_y = \frac{L}{c} = \frac{L}{\alpha\tilde{c}(Q)} \approx \frac{L\ln Q}{\omega\nu N} \approx -\frac{d\ln Q}{\ln y}\frac{L^2}{\nu N} \sim \frac{L^2}{\nu N}\,. \tag{57}$$

confirming the characteristic scaling exponent (time complexity exponent) of 2.

---

[1] Aside: Solution of $x\ln x = y$ (or similarly $x^x = z$):

$$\begin{aligned} & x\ln x = y \\ \Rightarrow\quad & x = \exp\left(\frac{y}{x}\right) \\ \Rightarrow\quad & \frac{y}{\ln x} = \exp\left(\frac{y}{x}\right) \\ \Rightarrow\quad & y = \frac{y}{x}\exp\left(\frac{y}{x}\right) \\ \Rightarrow\quad & \frac{y}{x} = \text{LambertW}(y) \\ \Rightarrow\ & x = \frac{y}{\text{LambertW}(y)} \end{aligned}$$

In a similar way we determine the probability for defect binding (note that here we do not need to cut off the integral because $B_0(\tau) = I_1(\tau) = \frac{1}{Q}(1-\tau)$ becomes 0 if $\tau \to 1$ and makes the integral converge):

$$\begin{aligned} p_{\text{def}} &= \frac{\nu_{\text{def}}}{\nu} \int_0^1 B_0(\tau) A_2(\tau) \frac{d\tau}{\omega(1-\tau)} = \frac{\nu_{\text{def}}}{\nu} \int_0^1 I_1(\tau) A_2(\tau) \frac{d\tau}{\omega(1-\tau)} \\ &= \frac{\nu_{\text{def}}}{(Q-1)\nu} \int_0^1 \left(1 - \exp(-(1-\frac{1}{Q})\frac{\tau}{\omega})\right) d\tau \approx \frac{\nu_{\text{def}}}{(Q-1)\nu}\,, \end{aligned} \tag{58}$$

where we again neglected the exponential in the integral in the limit of small $\omega$. Therefore, we find that $p_{\text{def}}$ can be efficiently controlled by increasing $Q$.

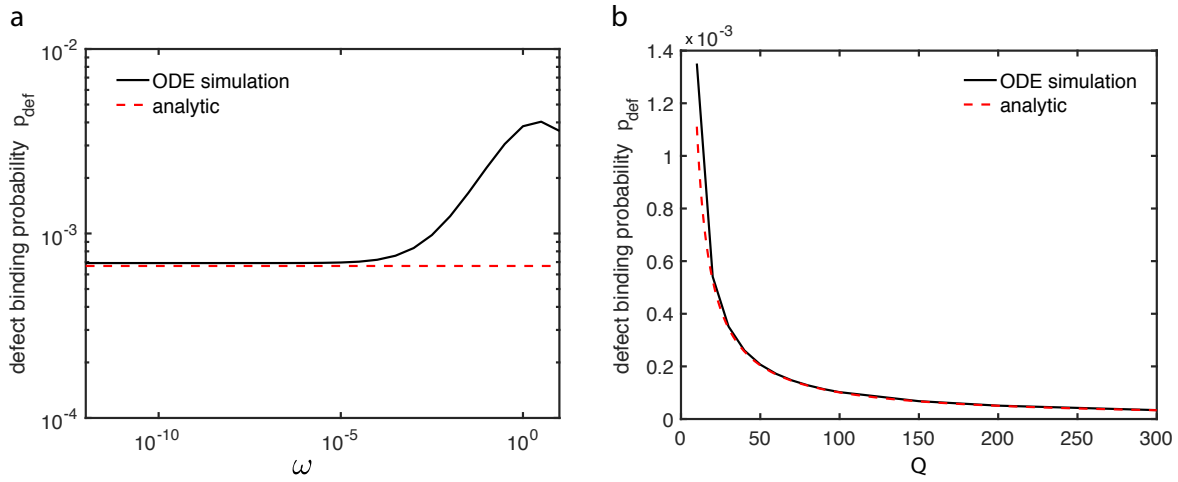


Fig. S 5: Defect binding probability versus $\omega$ with $Q = 16$ and $\nu_{\text{def}} = 0.01$ (a) and versus $Q$ with $\omega = 10^{-4}$ and $\nu_{\text{def}} = 0.01$ (b): Comparison between theory, Eq. (58), (red dashed line) and the simulation of the ODE system Eq. (22) (black drawn line).

For the defect-free yield it thus follows:

$$\text{yield}_{\text{defect-free}} = \text{yield} \cdot (1 - p_{\text{def}})^L = \left(1 - \frac{\omega}{1-\frac{1}{Q}} \ln\left(\frac{1}{Q\omega}\right)\right)^L \left(1 - \frac{\nu_{\text{def}}}{(Q-1)\nu}\right)^L . \tag{59}$$

In conclusion, while the hydrodynamic approach failed to give quantitatively correct results for the Jis scenario, the steep-front-approximation, in which we approximate the exponential inhibition term by a step function, yields very accurate results for several key quantities describing the assembly process like the wave speed, the dimerization probability and the defect probability, see Figs. S3, S4 and S5. The good agreement between the analytic results obtained with the steep-front-approximation and the numeric results obtained from ODE simulations of the original model suggest that details of the functional form of the inhibition term are not too important. The crucial point seems to be only that inhibition is generally strong enough and that out-of-sequence supply is widely suppressed. This coincidence justifies our rather arbitrary choice of the inhibition function in order to derive generic results on the just-in-sequence scenario. Furthermore, it suggests that with other inhibition terms like, e.g. a sigmoidal inhibition function, our findings and results will apply as well - at least on a qualitative basis.

[1] F. M. Gartner, I. R. Graf, P. Wilke, P. M. Geiger, and E. Frey, Elife **9**, e51020 (2020).

[2] A. Zlotnick, J. M. Johnson, P. W. Wingfield, S. J. Stahl, and D. Endres, Biochemistry **38**, 14644 (1999).

[3] A. Y. Morozov, R. F. Bruinsma, and J. Rudnick, Journal of Chemical Physics **131** (2009), 10.1063/1.3212694.

[4] F. M. Gartner, I. R. Graf, and E. Frey, bioRxiv (2021).

# Part III

# Self-assembly and gene-expression

# 8 Self-assembly and gene-expression: a hypothetical model

## 8.1 Motivation

All components that self-assemble into macromolecular structures inside cells are created via gene-expression. Furthermore, these macromolecular structures like flagellae, ribosomes or nuclear pore complexes are typically built in well-controlled numbers [170, 20, 171]. This raises the question of how cells are able to precisely count the number of molecules they need to produce in order to assemble a specific number of structures without wasting too much energy. Energy will be wasted if constituents are produced in larger numbers than are needed but also if there is much variability in the concentrations of the different species so that their numbers deviate strongly from the stoichiometric ratios. Hence, precision of molecule counting in gene expression is an essential factor that influences resource efficiency.
Furthermore, we have seen that kinetic traps can be avoided and self-assembly efficiency be increased if the constituents are provided in a temporal sequence. Therefore, another scope of gene expression could be to regulate or to support the assembly process by providing the constituents in a temporal sequence. Indeed, it has been discovered that in the assembly of large structures like the bacterial flagellum, gene expression is temporally coupled to specific stages of the organelle-assembly process [23, 24, 172, 173].
Together, this shows that self-assembly and gene-expression are closely related and can hardly be analyzed isolatedly for self-assembly processes in a cellular context. Furthermore, in synthetic biology, during the last decades, big advances have been made in producing synthetic biomolecules via artificial gene-expression and regulating their expression through synthetic gene-regulatory networks [174, 175, 176]. Hence, a promising approach to artificial self-assembly might be to produce the components that self-assemble into the structures directly in the system itself [177, 178]. If counting of molecules could be made precise enough, this would open up the path for efficient implementations of the just-in-sequence scenario (see discussion in previous chapters). Efficiency and fidelity of the assembly process could then be controlled by regulation of the supply, whereas fine-tuning of the reaction rate constants and other sophisticated molecular properties would no longer be required.

In this chapter, we study a hypothetical model of how gene-expression and self-assembly could work together in order to create a specified number of heterogeneous target structures. To this end, we show how basic gene-regulatory functions like activation and inhibition can be used in order to coordinate the supply of constituents in a temporal sequence. More specifically, we consider a sequence of genes, each of which activates its successor and inhibits its own activity. As a result, a travelling wave in gene activity emerges, which travels down the gene sequence and produces the building blocks of the structures in a temporal sequence. We

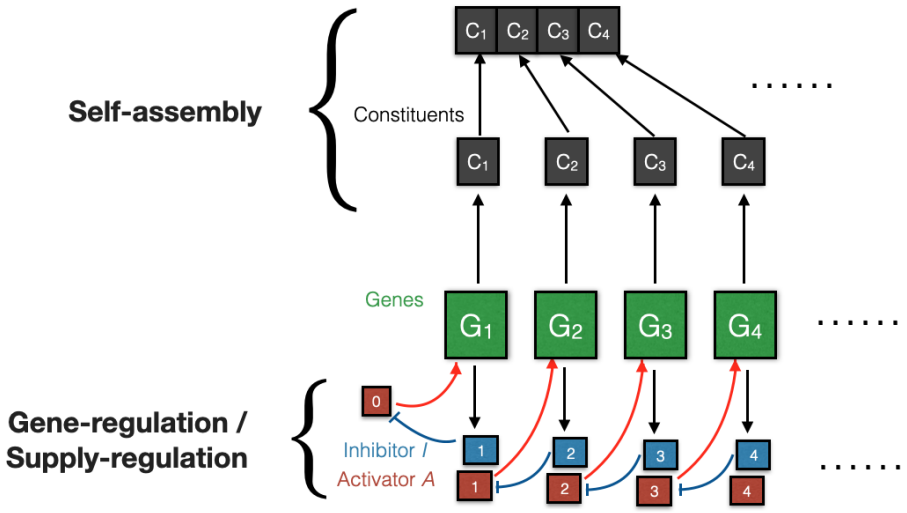


**Figure 8.1 | Illustration of the model.** We assume that a bunch of genes $G_1$, $G_2$, ... (green) express the constituents $C_1$, $C_2$, ... (black), which assemble into a heterogeneous structure. Together with the respective constituent, each gene expresses an activator $A_i$ (red) and an inhibitor $I_i$ (blue). The activator is a transcription factor that activates the subsequent gene in the sequence. Instead, the inhibitor is an enzyme that degrades the activator produced by the previous gene. Therefore, by expressing the activator and inhibitor, a gene activates the next gene in the sequence and inhibits its own activity. The initial activator $A_0$ is regarded as an external signal to start the assembly process. The system is described by the rate equations given in Eq. 8.1.

show that the count of molecules produced per gene can be described by an iterative map that relates the concentration of gene-product to the concentration of activator produced by the preceding gene in this sequence. The stationary molecule count corresponds to a stable fixed point of this iterative map.
Furthermore, in order for this mechanism to be useful in a biological or artificial context, two criteria of robustness must be fulfilled: First, the existence of an activation barrier must prevent the mechanism from accidental release due to small fluctuations in the particle numbers. Second, the stationary molecule count should be stable to noise in the particle numbers and rate constants. With the help of the iterative map we identify conditions that must be met in order for these two criteria to be fulfilled. In identifying these conditions, we find some interesting overlap with specificities of the regulatory network that controls expression of the building blocks of the flagellar motor in Gram-negative bacteria. This suggests that regulation of the flagellar motor protein components might be identified with a single segment of our proposed multi-gene cascade.

## 8.2 Model

We consider a number of genes $G_1$, $G_2$, ... $G_S$ which express the constituents $C_1$, $C_2$, ... $C_S$ that assemble in a linear sequence. The linear assembly pathway only represents a specific assembly order but it does not necessarily imply a one-dimensional geometry of the final structure. Examples of biological macromolecules that are assembled in a strictly linear

fashion include the bacterial flagellum or the subunits of the ribosome [24, 20]. The focus in this chapter, however, is not on the assembly process as such but only on the gene regulatory mechanism that coordinates the supply of constituents. Therefore, we assume that each gene $G_i$ along with the constituent expresses an activator $A_i$ and an inhibitor $I_i$. The activator activates the expression of the subsequent gene $G_{i+1}$, while the inhibitor degrades the activator $A_{i-1}$ of the preceding gene and thereby inhibits the activity of gene $G_i$, see Fig. 8.1. $I_i$ could, for example, act by catalyzing the phosphorylation or dimerization of $A_{i-1}$, assuming that in phosphorylated or dimerized form the activator loses its activating effect. The idea behind this regulatory gene cascade is that each gene is activated by its predecessor and - as soon as a specified expression level has been achieved - stops the production as a consequence of the self-inhibitory feedback. We assume that expression of a gene is described by a sigmoidal function of the activator concentration with maximum rate $\alpha$ and Hill coefficient $b$. The Hill coefficient thereby models a preceding $b$-merization of the activator molecules prior to attaching to the promoter region of the corresponding gene. Similarly, we assume that the inhibitor first forms a $d$-mer before degrading the activator at a rate $\rho$. Denoting concentrations by lower case letters, the model is hence represented by the following set of differential equations:

$$\begin{aligned} \frac{d}{dt}a_i &= \frac{\alpha}{1+a_{i-1}^{-b}} - \rho a_i i_{i+1}^d \,, \\ \frac{d}{dt}i_i &= \frac{d}{dt}c_i = \frac{\alpha}{1+a_{i-1}^{-b}} \,. \end{aligned} \tag{8.1}$$

Activation of the first gene $G_1$ is triggered by an initial activator $A_0$, which is interpreted as an external signal to initiate the gene cascade and to start the assembly process. Our initial condition will therefore be some finite concentration of $a_0$ and all other concentrations set to zero.
It should be noted that this model does not represent any particular biological or artificial system. Rather, it describes a hypothetical mechanism of how a temporal supply sequence of constituents can be achieved by means of basic gene regulatory functions. It can give an idea of how biological systems could possibly work and inspire the design of artificial systems.

A characteristic of the model is that supply regulation is not facilitated by the constituents themselves but by separate transcription factors, which we call activators $A_i$ and inhibitors $I_i$. This separation of tasks could have various advantages: First, gene-regulation can take place even if a part of the constituents has already assembled and can no longer fulfill gene-regulatory tasks. Second, the activators and inhibitors could be produced in larger numbers than the constituents themselves. This would improve the precision with which the regulation factors can be detected by the promoter regions of the genes according to the Berg-Purcell limit [179, 180]. As a consequence, the counting precision and the robustness of the mechanism can be enhanced. Lastly, regulating the supply with independent transcription factors extricates the constituents from additional tasks associated with gene-regulation and with the avoidance of kinetic traps in the assembly process (see chapter 7). This allows for more flexibility in the design of the constituents as well as the gene-regulatory mechanisms and could increase evolvability for a biological system or adaptability/versatility for artificial systems.

## 8.3 Results

For the analysis of the model it is useful to consider the dynamics, Eq. (8.1), in dimensionless form by measuring time in units of the inverse maximal expression rate $\alpha^{-1}$:

$$\begin{aligned} \frac{d}{dt}a_i &= \frac{1}{1+a_{i-1}^{-b}} - \varphi a_i i_{i+1}^d \,, \\ \frac{d}{dt}i_i &= \frac{d}{dt}c_i = \frac{1}{1+a_{i-1}^{-b}} \,, \end{aligned} \tag{8.2}$$

where $\varphi := \rho/\alpha$ is a dimensionless parameter. Equation (8.2) has been integrated numerically using Matlab. Figure 8.2 shows snapshots of the concentration profiles of the constituents, activators and inhibitors for a system with $S = 50$ genes, simulated for different initial concentrations $a_0$ and different $\varphi$. For suitable values of the parameters, a solitary wave in gene activity is triggered by the initial activator. The triggered wave travels down the cascade of genes and produces the constituents of the structures in a temporal sequence (Fig. 8.2A and B). While the concentration profile of the activator has a pulse-like shape, the constituent and inhibitor concentrations form a travelling wave front. The final concentration of constituents (and inhibitors) thereby approaches a constant value for large $i$, independent of the initial activator concentration. If $a_0$ is large, the stationary concentration is approached from above (Fig. 8.2A), otherwise it is approached from below (Fig. 8.2B).
However, if $a_0$ is too small and the Hill coefficient $b$ large enough, the wave cannot be triggered. The activator concentration then decreases too quickly and the wave cannot proceed beyond the first few genes (Fig. 8.2C). Hence, we find that the Hill coefficient $b$ generates an activation barrier for the trigger wave which can protect it from accidental release due to noise. Only an initial signal that is strong enough will be able to trigger the wave. Moreover, the wave can not be triggered if the ratio $\varphi$ between the inhibition rate $\rho$ and the maximal expression rate $\alpha$ becomes too large (Fig. 8.2D). In this case, the wave is not released no matter how large the initial activator concentration is.

In the following, we will try to understand the behavior of the system analytically. In particular, we would like to understand the following three quantities, which are highly relevant from a biophysical point of view:

- the speed $v$ of the travelling wave,
- the stationary constituent concentration $c_s$ and
- the activation barrier $a_{\text{th}}$ (activation threshold).

The wave speed is an essential parameter in order to control the assembly process. Implementation of the just-in-sequence mechanism requires the constituents to be provided slowly enough and hence necessitates a sufficiently low speed of the travelling wave. The stationary constituent concentration represents the count in which molecules are produced. In order to be resource efficient or to avoid kinetic traps in the assembly process with the just-in-sequence strategy, it is essential that this counting mechanism is sufficiently robust to noise. Finally, the activation barrier prevents the trigger wave from accidental release due to noise. Therefore, its existence is an essential prerequisite for this mechanism to be relevant in a biological

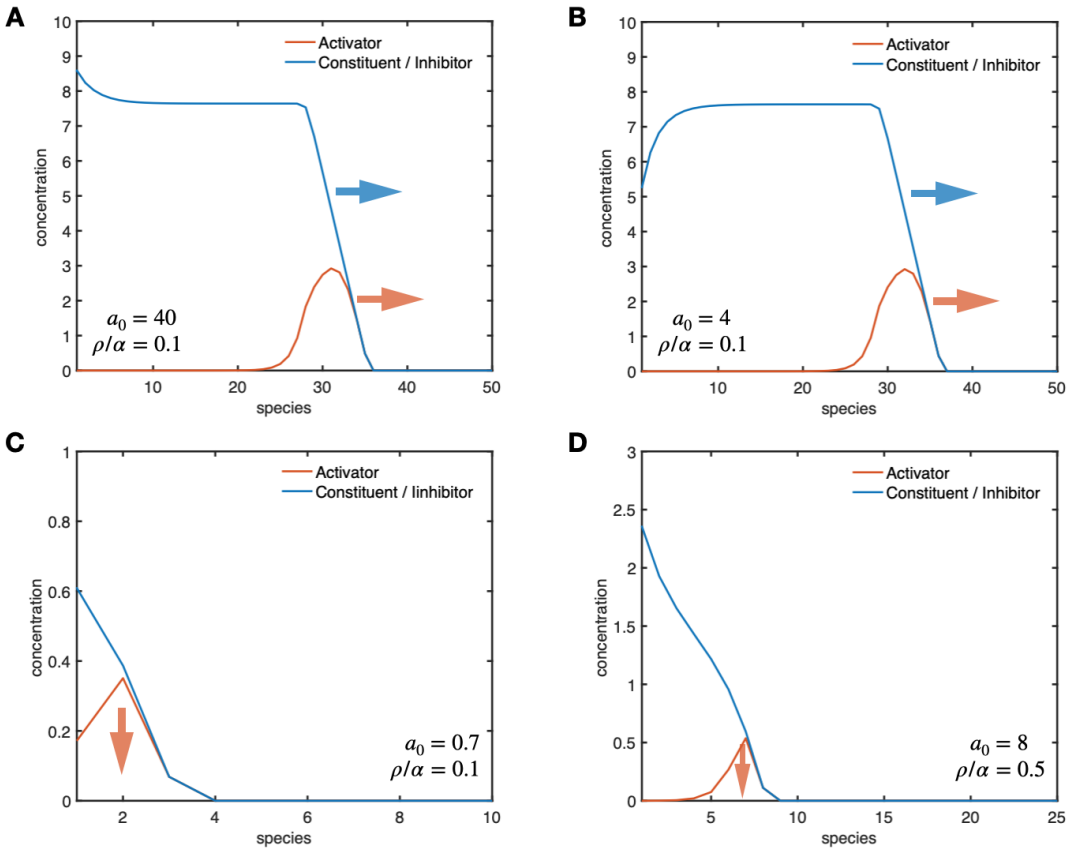


**Figure 8.2 | Snapshots of the temporal dynamics.** The momentary concentrations of constituents, activators and inhibitors are plotted as profiles over all species. Arrows indicate the direction of propagation of the profiles. **A,B** For suitable parameter settings and sufficiently large initial activator concentrations, travelling wave fronts and pulses emerge, which travel down the gene sequence. If the initial activator concentration is large (low), the stationary constituent concentration is approached from above (A) (or below (B)). **C,D** If the initial activator concentration is too low (C) or the ratio $\varphi = \rho/\alpha$ between the inhibition and activation rate is too large (D), the wave cannot be triggered. Instead of propagating as a solitary wave, the activator concentration then quickly decays.

or experimental context.

### 8.3.1 Insights from dimensional anaylsis

Before we analyze the system more in depth, an immediate result from dimensional analysis informs about the functional form of the wave speed $v$ and how the system is optimally controlled: Because $\varphi = \rho/\alpha$ is the only relevant parameter (for fixed $b$ and $d$), the wave speed $\tilde{v}$ in dimensionless units can only be a function of $\varphi$: $\tilde{v} = \tilde{v}(\varphi)$. Hence, transforming back to physical units, the wave speed has the form

$$v = \alpha \tilde{v}(\varphi)\,. \tag{8.3}$$

In contrast, the stationary constituent concentration and threshold activator concentration are functions only of $\varphi$ (again for fixed $b$ and $d$),

$$c_s = c_s(\varphi) \tag{8.4}$$
$$a_{\mathrm{th}} = a_{\mathrm{th}}(\varphi)\,. \tag{8.5}$$

Hence, by changing $\alpha$ but keeping the ratio $\varphi = \rho/\alpha$ constant, the speed $v$ of the wave can be adapted while the other properties of the wave and the counting mechanism remain constant. This is an important result on biological grounds, because the speed $v$ of the wave is an important parameter to be tuned in order to overcome kinetic traps in the assembly process according to the just-in-sequence scenario.

In the following, we investigate the behavior of the system more in depth and derive analytic expressions for $c_s$ and $a_{\mathrm{th}}$. Since travelling wave solutions can be observed, one might suspect that a good approach to the problem would be to use a continuum (hydrodynamic) approximation of the ordinary differential equation and then describe its solutions with a travelling wave ansatz [181]. However, similarly as in chapter 7, the continuum approximation fails in the physically relevant regime because the wave front is too steep. Therefore, we use a complementary approach, which exploits the steepness of the wave front. In this approximation, we assume that only one gene is active at a time. Only as soon as the activator of a gene is degraded and the gene has become inactive again, expression of the next gene in the sequence starts. This divides the whole gene cascade into individual segments which can be analyzed separately. Each of these gene segments is characterized by a map that relates the activator input to the concentration of produced constituent / inhibitor. The whole process is then described iteratively by reapplying the map for subsequent gene segments. Analyzing the fixed point structure of this iterative map informs about the stationary constituent concentration $c_s$, and the activation barrier $a_{\mathrm{th}}$.

### 8.3.2 Analysis via an iterative map

In order to describe the gene cascade via an iterative map, we approximate the process by assuming that the expression of a gene $G_{i+1}$ starts only as soon as the previous gene $G_i$ is fully expressed and has become inactive again. Consequently, during the expression of $G_i$, the inhibitor $I_{i+1}$ will not yet be produced and both transcription factors $A_i$ and $I_i$ and the constituent $C_i$ will thus be present in equal amounts. Denoting the equal concentrations of gene products (activator $a_i$, inhibitor $i_i$ and constituent $c_i$) by $p$ and the activator concentration $a_{i-1}$ by $a$, Eq. (8.2) simplifies for an individual segment in the cascade to

$$\frac{d}{dt}a = -\varphi a p^d\,, \tag{8.6}$$
$$\frac{d}{dt}p = \frac{1}{1+a^{-b}}\,. \tag{8.7}$$

Note that the production term in the first line is missing because, according to the approximation, production of $a$ has already stopped before production of $p$ by the subsequent starts. In the next segment, the final product concentration $p_\infty := p(t=\infty)$ of the last step will be identical to the new initial activator concentration $a_0 := a(t=0)$. This process is iterated to

the last gene segment. Hence, knowing the final product concentration $p_\infty$ as a function of the initial activator concentration $a_0$, the process is described iteratively by reapplying the function on itself. In order to derive the function $p_\infty(a_0)$, we divide Eq. (8.6) by Eq. (8.7):

$$\frac{da}{dp} = -\varphi a p^d (1 + a^{-b}) \,, \tag{8.8}$$

which can be solved by separation of variables:

$$\int_{a_0}^{0} \frac{1}{a(1+a^{-b})} da = \int_{0}^{p^\infty} -\varphi p^d dp \,, \tag{8.9}$$

$$\Rightarrow p_\infty(a_0) = \left( \frac{d+1}{b} \frac{1}{\varphi} log(a_0^b + 1) \right)^{1/(d+1)} . \tag{8.10}$$

This equation defines the iterative map [182]. The dynamics of successive steps in the map can be visualized graphically by plotting $p_\infty(a_0)$ together with a bisecting line of slope one through the origin (Fig. 8.3A): Starting from an arbitrary initial activator concentration $a_0$ on the x-axis, the corresponding final product concentration $p_\infty(a_0)$ is found as the y-coordinate of the point in which a vertical line through $a_0$ intersects with the curve. In order to apply the function a second time, $p_\infty(p_\infty(a_0))$, the argument $p_\infty(a_0)$ first has to be mapped on the x-axis by intersecting the bisector with a horizontal line through $p_\infty(a_0)$. The new function value $p_\infty(p_\infty(a_0))$ is then found by intersecting the curve with a vertical line through the point on the bisector. This process can be iterated arbitrarily. The final constituent concentrations $p^i_\infty(a_0)$ produced by the genes are thereby indicated by the tips of the vertical arrows. Points in which the curve intersects with the bisector are called fixed points. In these points, the outcome remains the same if the map is applied repeatedly. Fixed points also organize the flow of the map: The dynamics approaches stable fixed points and moves away from unstable ones.

In the scenario depicted in Fig. 8.3A, there are three fixed points in total, an unstable and two stable ones (one of which is the trivial fixed point). We also show the flow for two different initial activator concentrations, which qualitatively correspond to the two cases depicted in Fig. 8.2A and B. In both cases, the final constituent concentration flows to the same stable fixed point.
In contrast, the unstable fixed point corresponds to the activation barrier: If the initial activator concentration lies below the x-value of the unstable fixed point, the flow goes to 0 and the wave cannot be triggered as has been seen in Fig. 8.2C.
Decreasing $b$ or increasing $d$, we find that the curve loses its typical S-shape and so the unstable fixed point disappears (Fig. 8.3B). The trivial fixed point then becomes unstable and the slightest perturbation or activator input could trigger the wave. This case is therefore very unfavorable in a biological context.
Furthermore, if the parameter $\varphi$ becomes too big, a saddle node bifurcation occurs and eliminates the nontrivial stable and unstable fixed points (Fig. 8.3C). Then the wave cannot be triggered no matter how large the initial activator concentration is. This case corresponds to the scenario depicted in Fig. 8.2D.
In contrast, decreasing the parameter $\varphi$, there will always be a nontrivial stable fixed point, which, however, at some point starts to increase very quickly if $\varphi$ becomes too small (Fig.

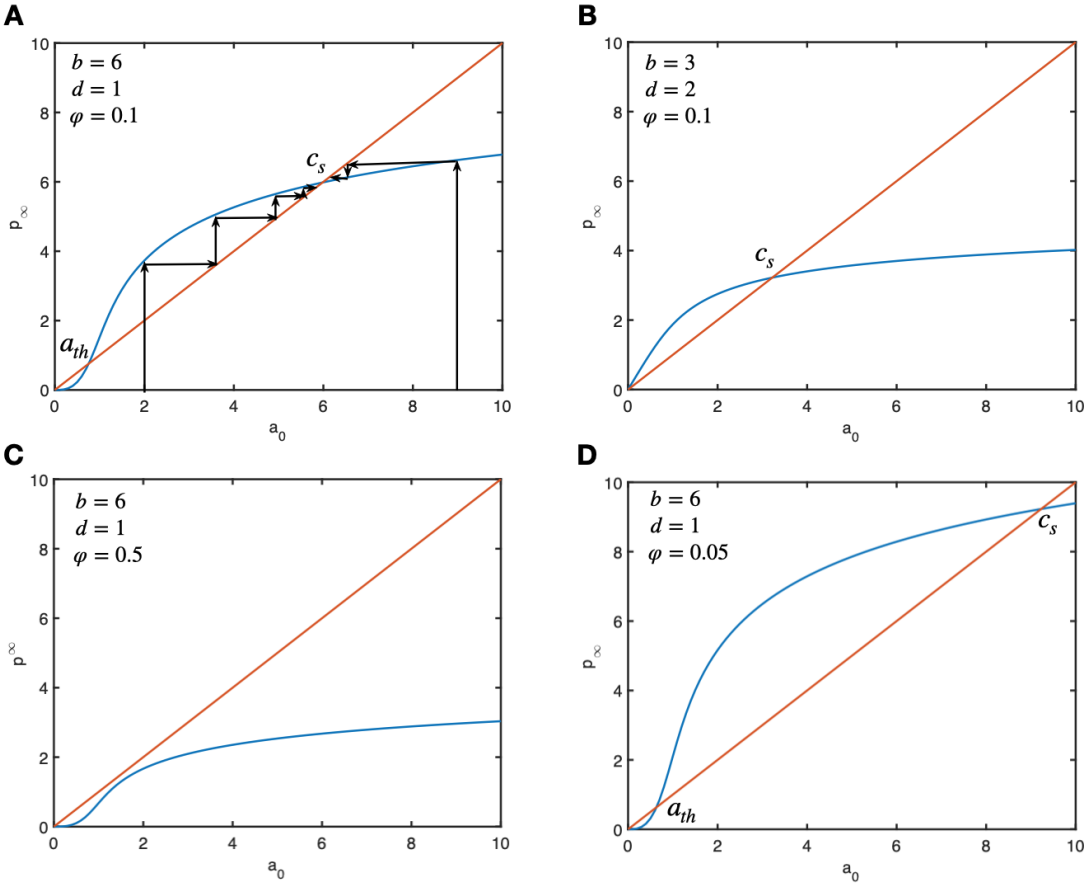


**Figure 8.3 | Analysis of the system via an iterative map.** **A** Visualization of the flow resulting from repeated application of the function $p_\infty(a_0)$. The points where the vertical arrows hit the blue curve correspond to the final constituent concentrations in subsequent gene segments. Intersections of the curve (blue) with the bisector (red) represent fixed points of the map. The flow goes towards a stable fixed point (stationary constituent concentration $c_s$) and away from the unstable fixed point (activation barrier $a_{\mathrm{th}}$). **B** Decreasing the Hill coefficient $b$ or increasing $d$, the intermediate unstable fixed point disappears in a transcritical bifurcation. Then, there is no activation barrier and slightest perturbation in the activator concentration can trigger the wave. **C** Increasing the ratio $\varphi = \rho/\alpha$, the stable and the unstable fixed point get eliminated in a saddle node bifurcation. The wave then cannot be triggered no matter how large the initial concentration of activator is. **D** If $\varphi$ becomes small, the stable fixed point becomes very large and the curve intersects the bisector at a sharp angle. Consequently, many steps may be required in the iterative map until the stable fixed point is approached.

8.3D). This implies that the curve will intersect with the bisector at a sharp angle, and, consequently, many steps may be needed for a general initial activator concentration until the stable fixed point is reached. The molecule count is less robust then. Increasing the parameter $d$ increases the range in $\varphi$ for which $c_s$ is well-behaved and, hence, $d$ plays an important role in enhancing robustness of the system (also see Fig. 8.4 and discussion below).

From Eq. (8.10) it follows that all fixed points $a_*$ are solutions of the equation

$$\left(\frac{d+1}{b}\frac{1}{\varphi}log(a_*^b+1)\right)^{1/(d+1)} = a_*\,. \tag{8.11}$$

In the following, we will derive analytic expressions for the two nontrivial fixed points, which describe the activation barrier $a_{\text{th}}$ and the stationary constituent concentration $c_s$, and derive conditions for their existence.

### The activation barrier

The existence of the unstable fixed point is indicated by the slope of the curve $p_\infty(a_0)$ at $a_0 = 0$. If $p'_\infty(0) > 1$, there is no unstable fixed point but only an additional stable one (see Fig. 8.3B). If $p'_\infty(0) < 1$, there are either two additional fixed points (Fig. 8.3A and D) or none (Fig. 8.3C). In order to calculate the initial slope, we approximate the function $p_\infty(a_0)$ (Eq. (8.10)) for small $a_0$, then take the derivative and evaluate it at $a_0 = 0$:

$$p_\infty(a_0) \approx \left(\frac{d+1}{b}\frac{1}{\varphi}a_0^b\right)^{1/(d+1)} \tag{8.12}$$

$$\Rightarrow\quad p'_\infty(a_0) \approx \left(\frac{d+1}{b}\frac{1}{\varphi}\right)^{1/(1+d)} \frac{b}{d+1}a_0^{\frac{b-(d+1)}{d+1}} \tag{8.13}$$

$$\Rightarrow\quad \lim_{a_0\to 0} p'_\infty(a_0) = \begin{cases} \infty & b \le d+1 \\ \varphi^{-1/(d+1)} & b = d+1 \\ 0 & b > d+1 \end{cases} \tag{8.14}$$

In the case $b = d + 1$, it can be shown that the curve has no inflection point and, therefore, an unstable fixed point does not exist. Hence, only for $b > d+1$ does the unstable fixed point and the activation barrier exist. This result could indeed be verified with simulations of the full system, Eq. (8.2). Assuming that $a_{\text{th}}^b$ is small, we can use the same approximation for $p_\infty(a_0)$ as above in order to find an approximate expression for the activation barrier:

$$a_{\text{th}} = p^\infty(a_{\text{th}}) = \left(\frac{d+1}{b}\frac{1}{\varphi}\log(a_{\text{th}}^b+1)\right)^{1/(d+1)} \approx \left(\frac{d+1}{b}\frac{1}{\varphi}a_{\text{th}}^b\right)^{1/(d+1)} \tag{8.15}$$

$$\to a_{\text{th}} = \left(\frac{d+1}{b}\frac{1}{\varphi}\right)^{1/(d+1-b)} \qquad \text{for } d+1-b<0\,. \tag{8.16}$$

For $d + 1 - b > 0$ we also obtain a solution which, however, in this case corresponds to the stable fixed point $c_s$ (which is more accurately described in the way shown in the next paragraph).

### The stationary constituent concentration

In order to find an analytic expression for the stationary constituent concentration, we assume that $c_s^b \gg 1$ and hence we approximate $\log(1 + c_s^b) \approx \log(c_s^b) = b \log(c_s)$ in Eq. (8.11). The fixed point condition for the stationary constituent concentration then reads

$$\log(c_s) = \frac{\varphi}{d+1} c_s^{d+1} . \tag{8.17}$$

Substituting $y := -(d+1)\log(c_s)$, this is transformed to

$$y e^y = -\varphi , \tag{8.18}$$

which constitutes the defining equation of the LambertW function. For $\varphi \in (0, e^{-1})$, there are two real solutions; for $\varphi = e^{-1}$ there is one and for $\varphi > e^{-1}$ there is none:

$$y = \begin{cases} \{W_0(-\varphi), W_{-1}(-\varphi)\} & \varphi \in (0, e^{-1}) \\ -1 & \varphi = e^{-1} \\ \emptyset & \varphi > e^{-1} \end{cases} \tag{8.19}$$

Resubstituting, we obtain:

$$c_s = \begin{cases} \left\{ e^{-W_0(-\varphi)/(d+1)}, e^{-W_{-1}(-\varphi)/(d+1)} \right\} & \varphi \in (0, e^{-1}) \\ e^{1/(d+1)} & \varphi = e^{-1} \\ \emptyset & \varphi > e^{-1} \end{cases} \tag{8.20}$$

So, the solution predicts both fixed points, the stable and the unstable one. The unstable fixed point $a_{\text{th}}$ (the solution with $W_0$) is, however, better described by the former approximation, Eq. (8.16), since the assumption $a_{\text{th}}^b \gg 1$ is not satisfied (typically even $a_{\text{th}}^b < 1$). In contrast, the stable fixed point $c_s$ of the map is accurately described as:

$$c_s = e^{-W_{-1}(-\varphi)/(d+1)} . \tag{8.21}$$

Furthermore, Eq. (8.20) predicts the value of $\varphi$ at which the saddle node bifurcation occurs as $\varphi_c = e^{-1}$, independently of $b$ and $d$.

In order to verify these results, we compare in Fig. 8.4 the analytic result (Eq. (8.21)) for the stationary constituent concentration (drawn line), with a numeric solution of the fixed point condition in the iterative map, Eq. 8.11), (dashed line), together with the actual value of $c_s$ obtained from numeric integration of the full system, Eq. (8.2), (markers). All curves are plotted for different values of $d$ and fixed $b = 6$. We find that the analytic solution, Eq. (8.21), coincides perfectly with the numeric solution of the fixed point condition. Furthermore, the iterative map describes the constituent concentration accurately in the regime of large $\varphi$, where the curves are flat. However, the approximation via the iterative map fails to describe the process quantitatively if $\varphi$ becomes too small. In this regime, the trigger waves become very long, extending over many genes, and thus the approximation that only one gene will be active at a time breaks down. Furthermore, in the regime of small $\varphi$, it takes many steps in the cascade until the stationary concentration is approached and $c_s$ is highly sensitive

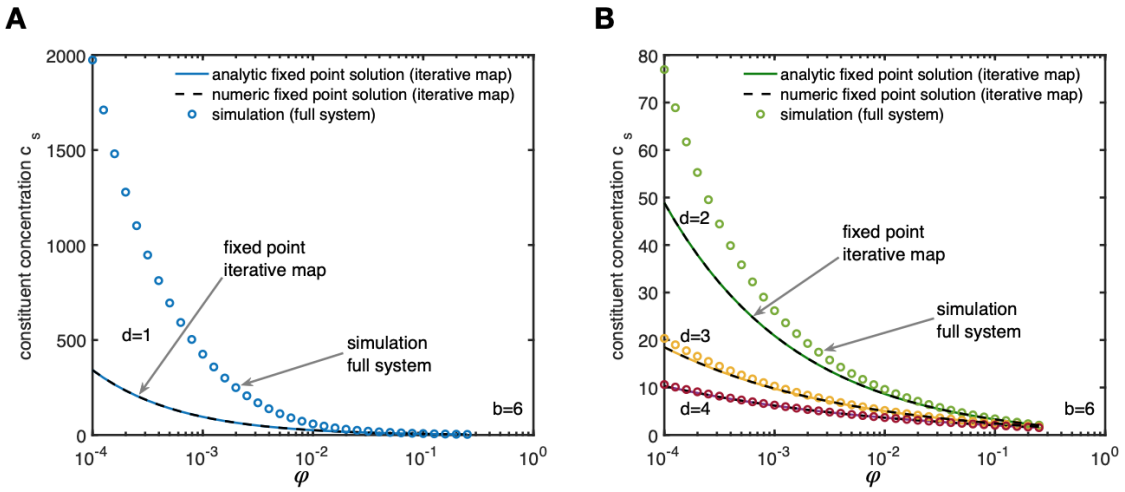


**Figure 8.4 | Stationary constituent concentration (analysis vs simulation).** The stable fixed point (drawn and dashed line) of the iterative map in dependence of $\varphi$ is plotted in comparison with the stationary constituent concentration $c_s$ obtained in the simulation after $S = 100$ gene segments (markers). Plots were obtained with a Hill coefficient $b = 6$ and $d = 1$ (A) as well as $d = 2, 3, 4$ (B). The approximative analytic solution (drawn line) and the numeric solution (dashed line) of the fixed point condition, Eq. 8.11, coincide perfectly. The iterative map predicts $c_s$ accurately, if the ratio $\varphi = \rho/\alpha$ is sufficiently large. This corresponds to the regime in which the wave profile is steep and $c_s$ is insensitive to variations in $\varphi$. Increasing $d$ enlarges this physically relevant regime and the general quality of the fit improves.

to variations in $\varphi$. Hence, we conclude that the regime of small $\varphi$ is not favorable from a biophysical point of view and a biological system would need to be operated rather at a large ratio $\varphi$ close to the bifurcation. In this regime of large $\varphi$, the iterative map constitutes an accurate description of the process. Increasing the parameter $d$ makes the curves flatter and hence increases the robustness of $c_s$ to variations in $\varphi$. The trigger waves then maintain their compact form in a large range of $\varphi$ and thus the general quality of the fit improves drastically.

In conclusion, we find that increasing cooperativity in inhibition (parameter $d$) enhances robustness of the counting mechanism and extends the parameter regime in which the system can operate. By increasing $d$, the system becomes widely insensitive to variations in the ratio $\varphi$ between the inhibition and activation rate. On the other hand, increasing cooperativity in activation (parameter $b$) enhances robustness of the system to noise in the particle numbers by generating an activation barrier which prevents the wave from accidental release. The speed $v$ of the gene wave can be controlled independently of its other properties by varying the activation rate $\alpha$ while keeping the ratio $\varphi = \rho/\alpha$ constant.

These findings suggest that the proposed mechanism could indeed be a viable way for cells or artificial systems to produce a bunch of constituents in specific numbers, which assemble into heterogeneous structures. The constituents are thereby delivered in a temporal sequence, which can enhance the efficiency and the fidelity of the self-assembly process as discussed in previous chapters of this thesis. The gene-expression mechanism discussed here is a hypothetical model and we are not aware of any specific biological system which realizes such a travelling wave of gene activity. However, intriguingly, as we discuss as a last point, some

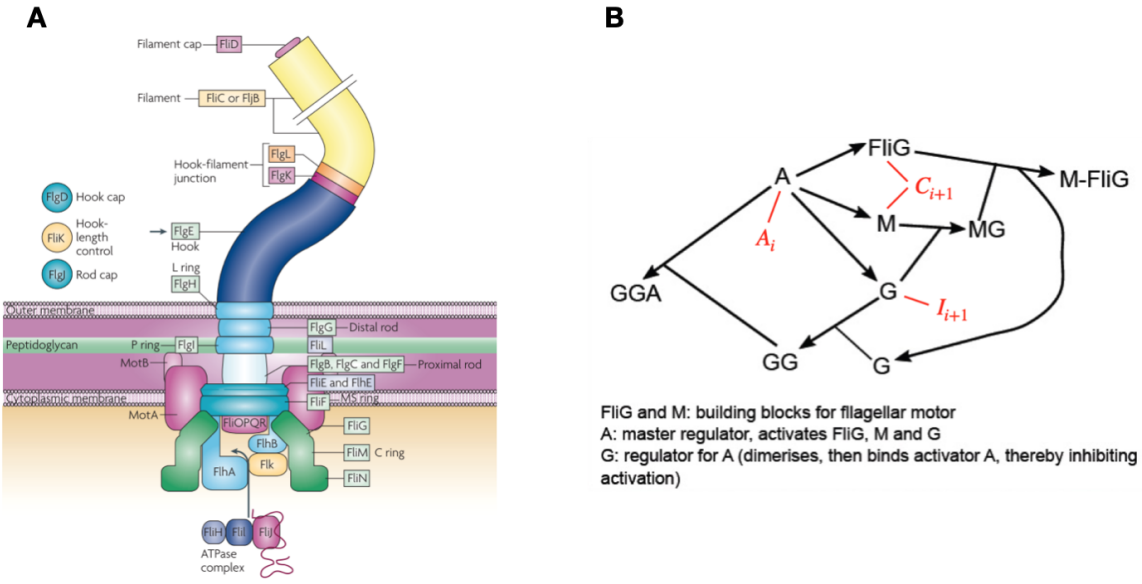


FliG and M: building blocks for filagellar motor
A: master regulator, activates FliG, M and G
G: regulator for A (dimerises, then binds activator A, thereby inhibiting activation)

**Figure 8.5 | Gene-regulation in flagellum assembly. A** Flagellar components of Salmonella enterica serovar Typhimurium. Figure taken from [24]. **B** Regulatory network that controls gene-expression of the components FliG and M of the C ring. Identifying the corresponding components as the activator $A_i$, constituent $C_{i+1}$ and inhibitor $I_{i+1}$, (indicated in red), the network can be considered as a single gene-segment in our proposed cascade (see main text for details).

striking similarities of our system can be found with the gene network that regulates expression of the flagellar motor proteins *FliG* and *FliM* in *Shewanella putrefaciens*. This suggests that expression of these motor proteins could be described as a single segment in the gene-cascade of our model.

### Expression of flagellar motor proteins as biological example for our proposed mechanism?

The bacterial flagellum poses a formidable example of a self-assembling system. The flagellum together with the motor socket is assembled out of roughly 30 thousand proteins of almost 30 different species [126]. Unique molecular mechanisms have evolved in order to coordinate the assembly of this highly complex, functional structure. In particular, recent discoveries describe mechanisms that couple temporal gene-expression of the constituents to specific stages of the organelle-assembly process [23, 172, 24, 173, 170]. Flagellar proteins are thereby organized into three classes which are expressed sequentially in a temporal sequence [23, 24]. Discussing the details of this hierarchy is beyond the scope of this chapter but our focus here lies on the regulatory subnetwork that controls expression of the proteins *FliG* and *FliM*, which form part of the C-ring of the basal body, see Fig. 8.5A. The regulatory network in *Shewanella putrefaciens* is depicted in Fig. 8.5B, following [170]. A Master regulator *FlrA* ($A$) thereby activates the expression of *FliG*, *FliM* ($M$) and *FlhG* ($G$). *FliG* and $M$ are the constituents which form part of the C-ring. Association of *FliG* with $M$ into a complex *M-FliG* is catalyzed by $G$ which dimerizes with $M$ in order to facilitate the reaction. Afterwards, $G$ acts as an inhibitor of $A$. To this end, $G$ forms a homodimer, which binds the activator $A$. Expression of the proteins that form the complex *M-FliG* can therefore be regarded as a

single segment in the gene regulatory cascade described by our model: $A$ thereby plays the role of the activator $A_i$, $M$ and *FliG* are the constituents $C_{i+1}$, and $G$ represents the inhibitor $I_{i+1}$. The cooperativity coefficient for inhibition is identified as $d = 2$, because the inhibitor $G$ first dimerizes before binding $A$. Consequently, in order for an activation barrier to exist, according to our analysis, a Hill coefficient of at least $b \leq d + 2 = 4$ is required. Indeed, it is known that the activator binds to the promoter that regulates the expression of *FliG*, $M$ and $G$ as a hexamer, implying a Hill coefficient of $b = 6$. Even though there are no evidence so far of a new activator $A_{i+1}$ which propagates the wave to a subsequent segment of genes, the depicted regulatory subnetwork appears to correspond to a single step as described by the iterative map above. In particular, our results regarding the influence of the cooperativity coefficients $b$ and $d$ on the robustness of the counting mechanism still seem to apply.

## 8.4 Key points

The deepest understanding of a thing can often be gained trying to (re)invent that thing. This is because by (re)inventing something, one also learns about the many pitfalls that lie on the road and how these pitfalls can be circumvented. In this spirit, here we tried to reinvent a small piece of biology by finding a solution to the problem of how to couple self-assembly with temporal gene-expression. The key insights gained from this analysis are the following:

- With simple regulatory functions, gene-expression of the constituents can be coordinated so that the building blocks are produced in specified numbers and in a temporal sequence.
- The implementation of the inhibitory feedback thereby seems to play an essential role in order to achieve robust counting and a propagating wave in gene activity. For example, one possibility stipulates that the inhibitor catalyzes the degradation of the activator without being consumed itself in this reaction.
- The cooperativity coefficients (Hill coefficients) for activation and inhibition are crucial determinants for the robustness of the mechanism to noise in the particle numbers and noise in the rate constants. In particular, the existence of an activation barrier that prevents the wave from accidental release requires a large Hill coefficient for activation.
- Although there is no known biological system that our model describes in detail, some analogies with the network that regulates expression of the flagellar motor proteins can be found and similar criteria for robustness seem to apply.
- Furthermore, we hope that our results may guide synthetic biology and artificial self-assembly in the attempt to generate self-assembling constituents that form macromolecular structures by artificial in vitro gene-expression.

## 8.5 Outlook

In our model, we only considered transcriptional regulation of the genes and we neglected the step of translation of the mRNA into proteins. A more detailed version of the model could therefore take translation explicitly into account. An explicit translational step will induce a

temporal delay between transcriptional regulation and its effect on the rate of protein production. Furthermore, translation will add an additional source of noise to the system, which can disturb the accuracy of counting. On the other hand, translation offers additional possibilities for regulation. In order to deal with the delay induced by the additional translational step, it might be favorable for the genes to interact on a larger range, e.g. assuming that a gene does not (only) activate its nearest neighbor but (also) its next nearest neighbor etc. (and similarly for inhibition). In this way, additional regulatory interactions could average out the effect of noise and premature activation/inhibition could counteract the delay induced by the translational step.

Moreover, until now, we have only simulated the system deterministically by integrating chemical rate equations. In order to fully specify the robustness of the system with respect to noise it would thus be a natural next step to simulate the system stochastically and verify if our conclusions remain valid also for stochastic systems with low particle numbers.

# 9 Summary: A kinetic theory of self-assembly

The goal of this final chapter is to summarize the most important results of this thesis and to formulate a concise and hopefully useful theory of non-equilibrium self-assembly processes.

We start this chapter with a little anecdote by Suárez Miranda [183] that demonstrates the importance of reductionism in science and describes the unfortunate fate of a scientific discipline that did not follow this idea of reductionism:

*... In that Empire, the Art of Cartography attained such Perfection that the map of a single Province occupied the entirety of a City, and the map of the Empire, the entirety of a Province. In time, those Unconscionable Maps no longer satisfied, and the Cartographers Guilds struck a Map of the Empire whose size was that of the Empire, and which coincided point for point with it. The following Generations, who were not so fond of the Study of Cartography as their Forebears had been, saw that that vast Map was Useless, and not without some Pitilessness was it, that they delivered it up to the Inclemencies of Sun and Winters. In the Deserts of the West, still today, there are Tattered Ruins of that Map, inhabited by Animals and Beggars; in all the Land there is no other Relic of the Disciplines of Geography.*

In my opinion, this story tells us two things. First, it shows us how important it is that a model of a physical system be reductionist. If a model is too extensive and contains too many details of the system, like the huge 1:1 map of the empire, it is unhandy and useless (except from serving as a housing for animals and beggars) and way too complicated to be appreciated by anyone except its own creators. Thus, for a model to be truly useful, it needs to be reductionist and focus on the essential aspects of a system: There might not always be agreement as to which aspects are essential. For example, geographers, geologists, meteorologists, politicians, militaries, ... all deal with very different kinds of problems and thus will have different ideas as to what is essential. Consequently, these different groups of professions typically will use different kinds of maps containing the information they rely on. Analogously, there might also be different kinds of models to the same physical system, which focus on different aspects of the system and idealize or simplify other parts of it.
The second lesson that we can learn from the story comes by interpreting the map as knowledge in general. Also a simplified, reductionist model can give rise to complex and complicated behavior. The theory that we develop from such a model, however, should likewise be useful, understandable and as simple as possible in order to be applicable by a large community of scientists, engineers, medical experts, etc. This reductionism of knowledge into a concise theory usually comes along with some kind of abstraction or generalization of the 'knowledge' that was first acquired in independent projects and is subsequently condensed into a more comprehensive and abstract theory. It is needless to say that this step of formulating a the-

ory might also comprise a decision as to which aspects are important on a broader perspective.

Throughout this thesis, we have studied simple, conceptual models of self-assembling systems, which idealize certain aspects that did not seem crucial to us (or could even be shown to be not important for the behavior of the system). Still, the analyses of these idealized model systems filled so many pages that one could tile an entire room with it and that barely anyone will ever have the time to read in detail. The goal of this last chapter is therefore to formulate a kinetic theory of ideal self-assembly that concisely summarizes the central findings and results of this thesis. We hope that in this concise form our theory will be memorizable and useful for the study as well as the experimental realization of self-assembling systems.

## 9.1 Kinetic theory of self-assembly

In the following we will formulate a kinetic theory of ideal self-assembly, which concisely summarizes the central results of this thesis. Denoting our theory as a kinetic theory, we want to contrast it with the equilibrium or thermodynamic theory of self-assembly, which assumes that the final state of the self-assembly system can be characterized as a free energy minimum. In contrast, our theory builds upon the slow nucleation principle and considers self-assembly as a kinetic process which may or may not end up in an equilibrium state. Both theories may thus be useful in different contexts like the various kinds of maps used by geologists, meteorologists and militaries as discussed in the motivation of this chapter. A central advantage of the kinetic theory is that, as a core element, it predicts the time assembly processes will take.

Specifically, our theory describes different ways how self-assembly processes can kinetically be controlled by distinguishing four self-assembly control scenarios. It specifies how the control parameters of these scenarios should be adapted in correspondence with the size of the target structure and how the observables (yield and assembly time) will behave in response to such control. To this end, the theory describes scaling relations (scaling theory) between the control parameters or the observables and the size of the target structures. However, the theory does not specify the proportionality constants for these scaling relations. The reason is that, as we have seen, the proportionality factors depend on various details of the system, whereas the scaling exponents are invariant to such details and therefore promise to achieve a reliable, robust and universally valid description of self-assembly processes.

### Scenarios and control parameters

The theory assumes that there are four different scenarios or 'driving forces' for self-assembly, which, by their regulation, allow to 'drive' the assembled structures towards larger sizes. These driving forces are: (slow) activation (act), (slow) dimerization (dim), reversible binding (rev) and just-in-sequence supply (jis) (see Fig. 9.1 and model description in chapter 2 for details). Each scenario is characterized by a (dimensionless) control parameter, which we generically call $P$, as well as a set of exponents. The control parameter describes the regulation of the driving force and, to define a dimensionless quantity, is measured relative either to the typical reaction constant $\nu$ or the (inverse) reactive time scale $C\nu$ of the system

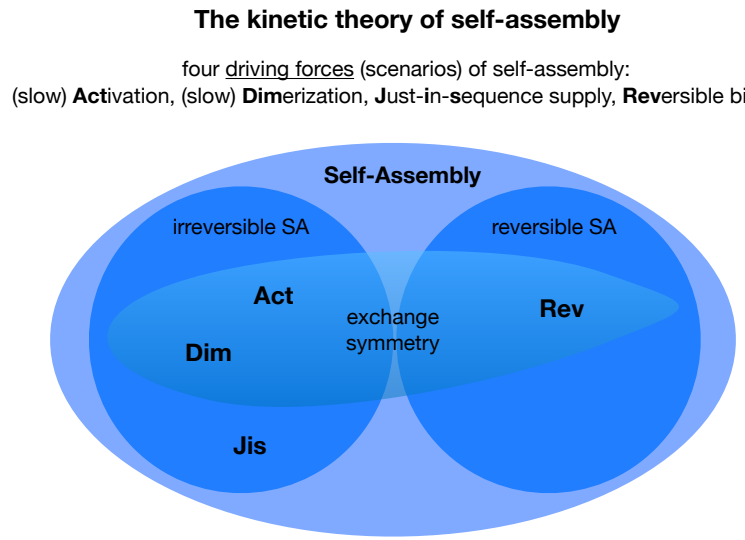


**Figure 9.1 | Four different scenarios for self-assembly.** We distinguish three irreversible and one reversible scenario (control strategy) for self-assembly. Each strategy can be used in order to retard the nucleation of new structures relative to the grow of existing structures and hence to increase the size of the resulting assemblies. Three of the four scenarios are invariant to the exchange or relabelling of species in the dynamic equations. As a consequence, these scenarios can be used to control both homogeneous as well as heterogeneous self-assembly processes. In contrast, the just-in-sequence scenario does not exhibit this symmetry and, thus, requires the constituents to be heterogeneous.

(where $C$ denotes the initial concentration of monomers).
For the activation scenario, the control parameter is the activation rate $\alpha$ relative to $C\nu$. In the dimerization scenario, the control parameter is the ratio between the dimerization rate $\mu$ and the reaction rate $\nu$. The reversible binding scenario is controlled by the ratio between the detachment rate $\delta_1$ and $C\nu$ and the JIS scenario is controlled by the time interval $\Delta T$ between successive batches relative to $(C\nu)^{-1}$ for a suitably chosen supply protocol. Alternatively, the Jis scenario can also be controlled by the activation rate $\alpha$ relative to $C\nu$ if there is inhibitory feedback between the constituent species (see chapter 7). Here we describe primarily the former realization of the Jis scenario, in which the supply is controlled externally. The corresponding scaling exponents are, however, the same in both cases.
Each scenario describes a distinct mechanism which allows to retard the rate of nucleation of new structures relative to the growth of existing structures and hence to increase the size of the resulting assemblies (see description in chapter 2). The activation, dimerization and reversible binding scenario do not discriminate between the different species (their dynamic equations are invariant to the exchange of species) and hence can be used to control both homogeneous as well as heterogeneous self-assembly processes. In contrast, the just-in-sequence scenario requires the constituents of the system to be heterogeneous.

### Growth exponent $\omega$

The scaling exponents are expressed as functions of the *growth exponent* $\omega$ (see chapter 4). The growth exponent describes how the (average) rate with which a cluster grows by one unit scales with its size. Thus, for irreversible systems, the growth exponent typically equals the

| | control parameter P | parameter exponent $\phi$ | time complexity exponent $\theta$ | stochastic exponent $\xi$ |
|---|---|---|---|---|
| act | $\frac{\alpha}{C\nu}$ | $2\omega - 3$ | $3 - 2\omega$ | $\approx 2.6 \cdot (1 - \omega)$ |
| dim | $\frac{\mu}{\nu}$ | $\omega - 2$ | $1 - \omega$ | 0 |
| jis | $\Delta TC\nu$ | $-1$ | $2 - \omega$ | 1 |
| rev $(\sigma = \gamma + 1)$ | $\frac{\delta_1}{C\nu}$ | $2\omega - 2$ | $4 - 2\omega$ | 0 |
| $(\sigma > \gamma + 1)$ | $\frac{\delta_1}{C\nu}$ | $\frac{2 - \omega}{\sigma - \gamma - 1}$ | $\frac{(1-\omega)\sigma + \gamma + 2\omega - 3}{\sigma - \gamma - 1}$ | 0 |

**Table 9.1 | Scaling exponents.** Each of the four scenarios is controlled by a dimensionless control parameter $P$ and its scaling behavior is determined by three exponents $\phi$, $\theta$ and $\xi$. Specifically, the three exponents describe how the control parameter, the assembly time and the minimal particle number scale with of the size of the target structure $S$, see Eqs. (9.1) and (9.2). The exponents are expressed in terms of the growth exponent $\omega$, which determines the scaling of the growth rate with structure size and depends primarily on the dimensionality of the assembled structure (see paragraph 'growth exponent'). Furthermore, in the reversible binding scenario, $\sigma$ denotes the nucleation size (minimal number of monomers that can form a stable arrangement) and $\gamma$ the leading effective order of attachment reactions (see chapter 4 for details). In the reversible binding scenario, we distinguish the two cases $\sigma = \gamma - 1$ and $\sigma > \gamma - 1$, which typically correspond to the assembly of one-dimensional and higher-dimensional structures, respectively. The underlying mechanisms in both cases are different (see chapter 2). The just-in-sequence scenario can also be controlled with inhibitory feedback and a slow activation rate, in which case the control parameter would be $P = \alpha/(C\nu)$ instead of $\Delta TC\nu$ (see chapter 7) but the exponents are the same in both cases.

| | $\phi_c$ | $\theta_c$ | $\xi_c$ |
|---|---|---|---|
| act | -1 | 1 | $\sim 0.35$ |
| dim | 0 | 0 | 0 |
| jis | 0 / -1 | 0 / 1 | 0 |
| rev $(\sigma = \gamma + 1)$ | $-1$ | 1 | 0 |
| $(\sigma > \gamma + 1)$ | $\frac{1}{\sigma - \gamma - 1}$ | $\frac{\gamma - 1}{\sigma - \gamma - 1}$ | 0 |

**Table 9.2 | Complementary exponents.** To each of the three exponents, we can associate a complementary exponent which likewise describes the dependence of the control parameter, assembly time and particle number on the dimerization barrier $\mu/\nu$, see Eq. (9.3). In the just-in-sequence scenario, the complementary exponents distinguish the two cases when the supply is controlled externally (first value) or internally with inhibitory feedback and a slow activation rate (second value). In the activation, dimerization and reversible binding scenario in the case $\sigma = \gamma + 1$, the exponents and complementary exponents fulfil a simple relation, see Eqs. (9.4) and (9.5).

exponent at which the boundary of a cluster scales with its size and is approximately given by $\omega = 0$ for 1D; $\omega = 1/2$ for 2D and $\omega = 2/3$ for 3D structures.
However, if binding is reversible, the growth exponent must also take the effective order of attachment reactions into account. More specifically, the growth exponent takes into account if the average effective order of attachment reactions depends on the size of a cluster. Typically, this will be the case if larger structures on average grow more frequently through fast, lower order reactions compared to smaller structures (see chapter 4 for details). As a consequence, the growth exponent for reversible binding therefore depends on the morphology of the building blocks. Relative to the estimates for irreversible systems, the growth exponent will typically either remains the same (e.g. for hexagonal building blocks) or increase by a factor of 2 ($\omega = 1$ for 2D and $\omega = 4/3$ for 3D structures; e.g. for square- or trigonal building blocks).

### Control parameter exponent $\phi$ and time complexity exponent $\theta$

The first two scaling exponents are the *control parameter exponent* $\phi$ and the *time complexity exponent* $\theta$. The exponent $\theta$ describes how the required assembly time scales with the target structure size, provided that the respective control parameter $P$ is regulated such that it scales with the target structure size to the exponent $\phi$:

$$P \sim S^{\phi} \qquad \Rightarrow \qquad T_x C\nu \sim S^{\theta}\,. \tag{9.1}$$

Here, $0 < x < 1$ is the demanded yield (resource efficiency) for which the assembly time is measured. The scaling relation is independent of the value of $x$ at least as long as $x$ is not too close to 0 or 1. The validity of the relation in this general form can be shown by plotting $T_x/S^{\theta}$ against $P/S^{\phi}$ for different target structure sizes $S$ and different values of the yield $x$ and demonstrating that the curves collapse onto a master curve; see Figure 2.2 in chapter 2. In particular, from this general relation it follows that the *minimal* assembly time that can be achieved also scales like $\sim S^{\theta}$. Hence, the exponent $\theta$ allows to effectively compare the time efficiency of the scenarios (cf. chapter 2) as well as of different implementations of the scenarios (cf. chapter 3) or morphologies of the building blocks (cf. chapter 4), which we used extensively throughout the first part of this thesis.

### Stochastic exponent $\xi$

The relation in Equation (9.1) holds under the condition that the particle number $N$ is large enough so that stochastic effects do not affect the yield. For the dimerization and reversible binding scenario, the particle number is irrelevant to realize a specified yield. However, for the supply control scenarios, i.e. the activation and Jis scenario, stochastic effects can severely limit the yield that can maximally be achieved (for the Jis scenario these stochastic effects are rather discreteness effects arising from the discreteness of particle numbers which are unable to represent the required nonstoichiometric ratios with sufficient accuracy if $N$ is too small). This requirement of a minimal particle number $N_x^{\min}$ in order to realize a yield $x$ is captured by the stochastic exponent $\xi$, which describes how $N_x^{\min}$ scales with $S$. Hence, we can summarize the theory as:

$$P \sim S^{\phi} \qquad \Rightarrow \qquad T_x C\nu \sim S^{\theta} \qquad \text{if} \qquad N \gg N_x^{\min} \sim S^{\xi}\,. \tag{9.2}$$

For the dimerization and reversible binding scenario, the stochastic exponent is 0. For the activation scenario, the value for $\xi$ given in table 9.1 is a rough estimate that has been de-

termined numerically. Presumably, the value will further decrease if it is measured for larger target structure sizes and its asymptotic value remains elusive. For structures up to a size of at least $S = 1000$, however, a presumed power law with the exponent given in table 9.1 provides a good approximation for the dependence of $N_x^{\min}$ on $S$.

### Complementary exponents $\phi_c, \theta_c$ and $\xi_c$

The exponents $\phi, \theta$ and $\xi$ describe the dependence of $P, T_x$ and $N_x^{\min}$ on the size $S$ of the target structure. We can go one step further and define for each exponent a complementary exponent $\phi_c, \theta_c$ and $\xi_c$ which analogously describes the dependence of $P, T_x$ and $N_x^{\min}$ on the dimerization barrier $\mu/\nu$. The full theory then reads:

$$P \sim S^{\phi} \left(\frac{\mu}{\nu}\right)^{\phi_c} \quad \Rightarrow \quad T_x C\nu \sim S^{\theta} \left(\frac{\mu}{\nu}\right)^{\theta_c} \quad \text{if} \quad N \gg N_x^{\min} \sim S^{\xi} \left(\frac{\mu}{\nu}\right)^{\xi_c} . \tag{9.3}$$

The relation holds under the condition that $\mu/\nu$ is not too small. For example, it is clear that by decreasing the dimerization rate $\mu/\nu$, the assembly time ($T_x$) cannot be reduced below the assembly time of the dimerization scenario. Hence, the scaling laws described by the complementary exponents are valid only in some range around $\mu/\nu = 1$.
Note that in chapter 2, in the activation and dimerization scenario, we related the parameter- and time complexity exponents for higher dimensional target structures to the one-dimensional case (corresponding to $\omega = 0$) by rescaling the reaction rate $\nu \to \nu S^{\omega}$ (where $\omega = (d-1)/d$). The transformation thereby maps the higher-dimensional growth processes to an effective one-dimensional process along the radial coordinate. Performing this transformation requires knowledge of the complementary exponents. On the other hand, using this transformation in Eq. (9.3) (note that also the parameter $P$ bears a factor of $\nu$ which must also be transformed), it follows that for the activation, dimerization, and reversible binding scenario in the case $\sigma = \gamma + 1$, the parameter- and time complexity exponent and their complementary exponents obey a simple relation[1]:

$$\phi + (\phi_c - 1)\omega = \phi(\omega = 0) =: \phi_0 , \tag{9.4}$$

as well as

$$\theta + (\theta_c + 1)\omega = \theta(\omega = 0) =: \theta_0 . \tag{9.5}$$

The exponents $\phi_0$ and $\theta_0$ (which are the exponents evaluated at $\omega = 0$ and thus correspond to the assembly of one-dimensional structures), are also called the *bare exponents*. Incidentally, the bare time complexity exponents for the dimerization-, Jis-, activation- and reversible binding scenario in the case $\sigma = \gamma + 1$ are the integer numbers 1,2, 3 and 4.

The complementary exponents are interesting because they describe the effect of a simultaneous regulation by the dimerization rate additionally with another control parameter. Hence, the complementary exponents allow to describe mixed-type scenarios for combinations between the dimerization scenario and the other scenarios. It might be possible that

[1] A similar relation does not hold for the reversible binding scenario in the case $\sigma > \gamma + 1$, because in this case effective rates for nucleation and attachment must be considered, both of which depend on $\nu$, whereas the nucleation rate should actually not be affected by altering $\omega$, which is why the rescaling argument does not work. In the Jis scenario, the relation does not hold either for the parameter exponent but it holds for the time complexity exponent in the case in which the supply is controlled externally.

further combinations, for example between the activation and the reversible binding scenario (a mixed-type scenario which appears to be highly relevant, for instance, for virus capsid assembly) can be described in a similar way and could thus be an interesting starting point for future research.

### Caveats

The exponents displayed in table 9.1 and 9.2 (with exception of the stochastic exponents) represent analytic estimates for the exponents. Their simulated values may slightly deviate from the analytic estimates. However, in most cases studied in this thesis, we found that the analytic values yield good approximations of the simulated exponents. Only in the reversible binding scenario for three-dimensional target structures, deviations between the theoretic and the measured exponents were found to be slightly more pronounced. It is possible that this discrepancy is due to an inaccurate estimation of the growth exponent $\omega$ and it would be interesting to investigate this more in depth by (numerically) determining a more accurate estimate for $\omega$.

Furthermore, the exponents for the reversible binding scenario were derived under the simplifying assumption that only single-bonded one-mers can detach again from a structure ('first order reversibility', see chapter 4). We have evidence that the exponents remain approximately the same if higher order detachment processes are additionally taken into account, provided that the ratio between detachment rates of consecutive order ('reversibility ratio', see chapter 4) remains constant[2]. However, it would be sensible to test this again carefully and also to investigate how the exponents behave if the reversibility ratio is not constant (for example if the temperature is used as the experimental control parameter).

### Analytic methods to derive the parameter- and time complexity exponents

Note that we described two different ways in order to derive the analytic estimates for the parameter- and time complexity exponents[3]. One way starts from the slow nucleation principle: $\frac{\text{total nucleation rate}}{\text{total attachment rate}} \sim S^{-1}$, and then uses scaling arguments in order to identify the dependence of the total rates at the left hand side for each scenario. This approach was used in chapter 2, see [2].
Another possibility to derive the exponents in the activation, dimerization and reversible binding scenario in higher dimensions is by exploiting that, asymptotically, the optimal parameter value scales identically as the threshold value of the parameter to obtain non-zero yield. This enabled us to reduce the dynamics to an effective two-variable-system, with one variable representing the concentration of (active) monomers and the other one the concentration of incomplete structures. In some cases, the two-variable system could be solved analytically (see chapter 5, [1]), while in other cases the exponents could be derived from the simplified system with a scaling ansatz (see chapter 4). A similar approach of reducing the dynamics

[2] A constant reversibility ratio would require the binding energy (and temperature) to be constant. This would correspond, for example, to an experimental control scenario in which the monomer concentration is used as the control parameter (see chapter 4).

[3] here we refer to the irreversible scenarios and the reversible binding scenario for higher dimensional structures. For reversible binding in the case of one-dimensional structures, which describes a profoundly different mechanism, another analytic approach was used in order to derive the exponents, see chapter 2.

to a low-dimensional system with the help of an effective model was also applied in chapters 3 and 7 in order to derive the exponents of different implementations of the just-in-sequence scenario. In all cases studied, both analytic methods yielded exactly the same estimates for the exponents and can therefore be considered equivalent.
We have not yet found a way to derive an analytic estimate for the stochastic exponent. The value given in table 9.1 relies on an estimation of the stochastic exponent from numerical simulations.

### Robustness of the exponents

A central result and an important pillar for the applicability of the scaling theory is the finding that the exponents are highly robust to various modifications of the model, the parameters or the assembly protocols. For example, in chapter 2, we showed that the exponents remain the same if we consider varying attachment rates for the different species or whether the structures are simulated with periodic or open boundary conditions. Furthermore, for large enough particle numbers, the heterogeneity (distinguishability) of the building blocks can be shown mathematically to be irrelevant except for the just-in-sequence scenario.
In the activation scenario, we could show mathematically and verify numerically that the exponents do not depend on the form of the monomer input as long as there is no discrimination between species (chapter 2). Moreover, in the reversible binding scenario, the exponents remain invariant if advanced protocols like annealing are used, in which the temperature is gradually decreased as the reservoir of monomers gets depleted (chapter 2); and the just-in-sequence scenario exhibits the same exponents whether supply regulation is controlled externally ('batches' of monomers that are supplied at distinct time points) or internally with the help of inhibitory feedback (see chapter 7).
This robustness property of the exponents suggests that the classification of self-assembly processes into the four categories or control scenarios is reasonable and informative as the scenarios broadly determine the scaling properties of the assembly processes. The robustness of the exponents furthermore could enable a 'scaling approach' to artificial self-assembly as a simple way to determine the optimal parameter values in an experiment, as we elaborate below.
In order to further probe the robustness of the exponents, it might be interesting to analyze more mixed-type scenarios in which the assembly processes are controlled by two ore more different control parameters simultaneously. The complementary exponents describe superpositions of the dimerization scenario with another scenario and the theory suggests that the scaling exponent for the other parameter and the assembly time thereby remain unaffected. The question that arises is whether other combinations of scenarios follow a similar logic and whether the scaling exponents thereby remain unaffected as well.

### Conclusions from the scaling theory

The exponents allow us to draw a number of immediate conclusions. For example, comparing the exponents of the different scenarios allows one to draw conclusions on the time efficiency of the different control strategies and to extrapolate these trends to arbitrarily large sizes of the target structure (chapter 2). We thereby found that the dimerization scenario is particularly time efficient, while the activation scenario and reversible binding for one-dimensional target structures are inefficient strategies in order to control the assembly of large objects; In con-

trast, reversible binding for higher-dimensional target structures as well as just-in-sequence supply are typically significantly more time efficient.
The exponents furthermore reveal that the time efficiency of the reversible binding scenario strongly depends on the morphology of the constituents (chapter 4): In the optimal case (for example in the case of a hexagonal morphology of the monomers), reversible binding can be as efficient as the dimerization scenario while in the worst case, it will be less efficient by several orders of magnitude.
Moreover, we applied the scaling theory in order to determine the efficiency of different implementations of the just-in-sequence scenario by calculating and comparing their time complexity exponents (see chapters 3 and 7). The analysis shows that the method in which the constituents are supplied in increasing, non-stoichiometric concentrations defines the most efficient way to realize just-in-sequence supply for higher-dimensional target structures. Whether the supply is thereby controlled externally or with the help of inhibitory feedback (maybe even coupled directly with gene-expression, see chapter 8) yields the same time complexity exponent, whereby external supply control is more efficient by roughly 1.5 orders of magnitude (see chapter 7).
The stochastic exponent furthermore gives information about the strength of stochastic effects. For example, the stochastic exponent reveals that stochasticity in the activation scenario strongly decreases with the dimensionality of the target structure and that the dimerization and reversible binding scenario are largely unaffected by stochastic effects. As a subject for future research, it would be interesting to quantify the stochastic exponents for the diverse mitigation strategies that we described in chapter 6, in order to see whether their mitigating effect is quantified by the pertinent stochastic exponent. Furthermore, as the stochastic exponents in table 9.1 have been determined numerically, a future goal for the effective stochastic theory would be to also find analytic estimates for these exponents.
Furthermore, in chapter 7, we investigated the proneness of the different scenarios to assembly errors and defects. An interesting question for future research would thus be whether the susceptibility to errors can be incorporated into the scaling theory in a meaningful way, for example by introducing an additional exponent that quantifies the expected number of defects/errors in a structure in dependence of its size. To this end, it would primarily be necessary to quantify the susceptibility of the reversible binding scenario to errors and study the error proneness for higher-dimensional target structures. As we have seen in chapter 7, assembly errors can be a substantial threat to the system. Including error susceptibility into the theory could thus be an important next step.

### Scaling approach to artificial self-assembly

Because the exponents of our kinetic scaling theory can be characterized robustly and could be shown not to depend on many details of the system, this suggests a 'scaling approach' to artificial self-assembly: Specifically, the idea is that the experimentalist first tries to realize the self-assembly of small structures, thereby optimizing the time efficiency in the experiment by regulating the pertinent control parameter(s). Subsequently, the experiment will be 'scaled up' to larger structure sizes, whereby the knowledge of the theoretic scaling exponents can help significantly in order to find the correct adjustment of the control parameter(s). Possible experimental control parameter could be, for example, the temperature or the monomer- or salt concentration in the reversible binding senario; the light intensity which induces a switch from an assembly-inactive to an active configuration in the activation scenario; or the time in-

terval between successive time points at which monomers are provided in the just-in-sequence scenario. If the time efficiency of the self-assembly of the larger structures is still far below the time efficiency obtained for the smaller system scaled with the pertinent time complexity exponent, the control parameter can be readjusted before the system is possibly scaled up again to an even larger structure size.
Such an approach could be pursued, for example, in typical experiments like those of the group of Hendrik Dietz [110]. In this concrete experiment, artificial virus shells of different sizes were built from similar types of building blocks (see introduction to part I) and the scaling approach could be a useful strategy in order to enhance the time efficiency of the self-assembly of the larger capsids (which took roughly two weeks in their experiments, while the smaller capsids self-assembled in only a few minutes).
Our theory furthermore suggests a number of very concrete possibilities how the assembly time in experiments could be reduced: For example, by changing the morphology of the building blocks, by implementing a hierarchical assembly step (see chapter 4) or by applying a different control scenario like the just-in-sequence scenario instead of reversible binding (see chapter 2). We furthermore provided an idea of how self-assembly could be coupled with (artificial) gene-expression, such that the assembling constituents are produced directly in the system itself (see chapter 8), which is considered a very promising route to nanotechnology [177, 178].

### Final conclusion

The essential conclusion of this thesis and the kinetic scaling theory is that stochasticity and poor time efficiency can be severely limiting factors for self-assembly systems, both of which, however, can be overcome in various ways. It is therefore crucial that both these factors are taken into account when studying biological self-assembly processes or when implementing artificial self-assembly systems. Considering that biological self-assembly processes will likely have evolved in a way to bypass these limiting factors, these insights could help to improve our understanding of biological self-assembly systems. In a similar way, nanotechnology can profit from these insights, for example, by allowing to speed up experiments, which, in the best case, could even lead to new technological or medical applications. I deeply wish that this kinetic theory of self-assembly will be useful for the good, help to advance our understanding of biology and contribute to the progress of nanotechnology and medicine.

# Bibliography


[1] F. M. Gartner, I. R. Graf, P. Wilke, P. M. Geiger, and E. Frey, "Stochastic yield catastrophes and robustness in self-assembly," *Elife*, vol. 9, p. e51020, 2020.

[2] F. M. Gartner, I. R. Graf, and E. Frey, "The time complexity of self-assembly," *Proceedings of the National Academy of Sciences*, vol. 119, no. 4, 2022.

[3] F. M. Gartner and E. Frey, "Self-assembly efficiency strongly depends on the morphology of the building blocks," *In preparation*, 2022.

[4] F. M. Gartner, I. R. Graf, and E. Frey, "Controlling fidelity and time efficiency in self-assembly," *In preparation*, 2022.

[5] I. R. Graf, F. M. Gartner, and E. Frey, "Understanding and guiding robust self-assembly of heterogeneous structures."

[6] F. Träuble, F. M. Gartner, I. R. Graf, and E. Frey, "Topological properties of self-assembly reaction networks determine robustness to stochastic effects."

[7] L. Würthner, F. M. Gartner, D. Muramatsu, and E. Frey, "Anomalous kinetic roughening of bulk-coupled growing interfaces," *In preparation*, 2022.

[8] D. Muramatsu, F. M. Gartner, and E. Frey, "Immune cells as active matter system," *In preparation*, 2022.

[9] S. Angerpointner, K. Kohler, O. Trapp, and E. Frey, "Kinetic models of the formose reaction in alkaline environments reveal (un)identifiable reaction pathways," *In preparation*, 2022.

[10] M. Gaimann, F. M. Gartner, and E. Frey, "In silico evolution of biological conditional memory using sequential transcription logic," *In preparation*, 2022.

[11] A. V. Dass, S. Wunnava, J. Langlais, B. von Esch, M. Krushe, L. Ufer, N. Chrisam, R. C. A. Dubini, F. M. Gartner, S. Angerpointer, C. F. Dirscherl, P. Rovó, C. B. Mast, J. Šponer, C. Ochsenfeld, E. Frey, and D. Braun, "RNA auto-polymerisation from 2',3'–cyclic nucleotides at air-water interface.," *In preparation*, 2022.

[12] J. A. Marsh and S. A. Teichmann, "Structure, dynamics, assembly, and evolution of protein complexes," *Annual review of biochemistry*, vol. 84, pp. 551–575, 2015.

[13] D. Arslan, M. Legendre, V. Seltzer, C. Abergel, and J. M. Claverie, "Distant Mimivirus relative with a larger genome highlights the fundamental features of Megaviridae," *Proceedings of the National Academy of Sciences of the United States of America*, vol. 108, no. 42, pp. 17486–17491, 2011.

[14] C. J. Jones and S.-I. Aizawa, "The bacterial flagellum and flagellar motor: structure, assembly and function," *Advances in microbial physiology*, vol. 32, pp. 109–172, 1991.

[15] P. L. Krapivsky, S. Redner, and E. Ben-Naim, *A kinetic view of statistical physics*. Cambridge University Press, 2010.

[16] J. C. Sang, J.-E. Lee, A. J. Dear, S. De, G. Meisl, A. M. Thackray, R. Bujdoso, T. P. J. Knowles, and D. Klenerman, "Direct observation of prion protein oligomer formation reveals an aggregation mechanism with multiple conformationally distinct species," *Chemical science*, vol. 10, no. 17, pp. 4588–4597, 2019.

[17] T. Weiffert, G. Meisl, P. Flagmeier, S. De, C. J. R. Dunning, B. Frohm, H. Zetterberg, K. Blennow, E. Portelius, D. Klenerman, and Others, "Increased secondary nucleation underlies accelerated aggregation of the four-residue N-terminally truncated A$\beta$42 species A$\beta$5–42," *ACS chemical neuroscience*, vol. 10, no. 5, pp. 2374–2384, 2019.

[18] F. S. Ruggeri, T. Šneideris, M. Vendruscolo, and T. P. J. Knowles, "Atomic force microscopy for single molecule characterisation of protein aggregation," *Archives of biochemistry and biophysics*, vol. 664, pp. 134–148, 2019.

[19] P. Nerurkar, M. Altvater, S. Gerhardy, S. Schütz, U. Fischer, C. Weirich, and V. G. Panse, "Eukaryotic Ribosome Assembly and Nuclear Export," *International Review of Cell and Molecular Biology*, vol. 319, pp. 107–140, jan 2015.

[20] C. Peña, E. Hurt, and V. G. Panse, "Eukaryotic ribosome assembly, transport and quality control," *Nature Structural and Molecular Biology*, vol. 24, no. 9, pp. 689–699, 2017.

[21] H. Lempiäinen and D. Shore, "Growth control and ribosome biogenesis," *Current opinion in cell biology*, vol. 21, no. 6, pp. 855–863, 2009.

[22] M. Derenzini, L. Montanaro, and D. Trere, "Ribosome biogenesis and cancer," *Acta histochemica*, vol. 119, no. 3, pp. 190–197, 2017.

[23] P. Aldridge and K. T. Hughes, "Regulation of flagellar assembly," *Current Opinion in Microbiology*, vol. 5, no. 2, pp. 160–165, 2002.

[24] F. F. Chevance and K. T. Hughes, "Coordinating assembly of a bacterial macromolecular machine," *Nature Reviews Microbiology*, vol. 6, no. 6, pp. 455–465, 2008.

[25] M. F. Hagan, "Modeling Viral Capsid Assembly," in *Advances in Chemical Physics*, vol. 155, pp. 1–68, NIH Public Access, 2014.

[26] D. Bamford and M. Zuckerman, *Encyclopedia of Virology*. Academic Press, 2021.

[27] S. Katen and A. Zlotnick, *Chapter 14 The Thermodynamics of Virus Capsid Assembly*, vol. 455. Elsevier Inc., 1 ed., 2009.

[28] B. A. Grzybowski, C. E. Wilmer, J. Kim, K. P. Browne, and K. J. Bishop, "Self-assembly: From crystals to cells," *Soft Matter*, vol. 5, no. 6, pp. 1110–1128, 2009.

[29] S. Whitelam and R. L. Jack, "The statistical mechanics of dynamic pathways to self-assembly," *Annual Review of Physical Chemistry*, vol. 66, no. February, pp. 143–163, 2015.

[30] P. Van Der Schoot and R. Zandi, "Kinetic theory of virus capsid assembly," *Physical Biology*, vol. 4, no. 4, pp. 296–304, 2007.

[31] M. F. Hagan, O. M. Elrad, and R. L. Jack, "Mechanisms of kinetic trapping in self-assembly and phase transformation," *Journal of Chemical Physics*, vol. 135, no. 10, 2011.

[32] W. M. Gelbart, A. Ben-Shaul, and D. Roux, *Micelles, membranes, microemulsions, and monolayers*. Springer Science & Business Media, 2012.

[33] L. O. Hedges, R. V. Mannige, and S. Whitelam, "Growth of equilibrium structures built from a large number of distinct component types," *Soft Matter*, vol. 10, no. 34, pp. 6404–6416, 2014.

[34] J. D. Perlmutter and M. F. Hagan, "Mechanisms of virus assembly," *Annual Review of Physical Chemistry*, vol. 66, no. February, pp. 217–239, 2015.

[35] M. F. Hagan and G. M. Grason, "Equilibrium mechanisms of self-limiting assembly," *Reviews of Modern Physics*, vol. 93, no. 2, p. 25008, 2021.

[36] D. Endres and A. Zlotnick, "Model-Based Analysis of Assembly Kinetics for Virus Capsids or Other Spherical Polymers," *Biophysical Journal*, vol. 83, pp. 1217–1230, aug 2002.

[37] E. J. Deeds, J. A. Bachman, and W. Fontana, "Optimizing ring assembly reveals the strength of weak interactions," *Proceedings of the National Academy of Sciences of the United States of America*, vol. 109, no. 7, pp. 2348–2353, 2012.

[38] W. M. Jacobs and D. Frenkel, "Self-Assembly of Structures with Addressable Complexity," *Journal of the American Chemical Society*, vol. 138, no. 8, pp. 2457–2467, 2016.

[39] A. Zlotnick, "To Build a Virus Capsid: An Equilibrium Model of the Self Assembly of Polyhedral Protein Complexes," *Journal of Molecular Biology*, vol. 241, no. 1, pp. 59–67, 1994.

[40] A. Zlotnick, J. M. Johnson, P. W. Wingfield, S. J. Stahl, and D. Endres, "A theoretical model successfully identifies features of hepatitis B virus capsid assembly," *Biochemistry*, vol. 38, no. 44, pp. 14644–14652, 1999.

[41] R. Schwartz, P. W. Shor, P. E. Prevelige, and B. Berger, "Local rules simulation of the kinetics of virus capsid self-assembly," *Biophysical Journal*, vol. 75, no. 6, pp. 2626–2636, 1998.

[42] D. C. Rapaport, J. E. Johnson, and J. Skolnick, "Supramolecular self-assembly: Molecular dynamics modeling of polyhedral shell formation," *Computer Physics Communications*, vol. 121-122, pp. 231–235, 1999.

[43] M. F. Hagan and D. Chandler, "Dynamic pathways for viral capsid assembly," *Biophysical Journal*, vol. 91, no. 1, pp. 42–54, 2006.

[44] H. D. Nguyen, V. S. Reddy, and C. L. Brooks, "Deciphering the kinetic mechanism of spontaneous self-assembly of icosahedral capsids," *Nano Letters*, vol. 7, no. 2, pp. 338–344, 2007.

[45] D. C. Rapaport, "Role of reversibility in viral capsid growth: A paradigm for self-assembly," *Physical Review Letters*, vol. 101, no. 18, pp. 1–4, 2008.

[46] J. E. Baschek, H. C. R. Klein, and U. S. Schwarz, "Stochastic dynamics of virus capsid formation: direct versus hierarchical self-assembly," *BMC Biophysics*, vol. 5, no. 22, 2012.

[47] A. Y. Morozov, R. F. Bruinsma, and J. Rudnick, "Assembly of viruses and the pseudo-law of mass action," *Journal of Chemical Physics*, vol. 131, no. 15, 2009.

[48] M. F. Hagan and O. M. Elrad, "Understanding the Concentration Dependence of Viral Capsid Assembly Kinetics—the Origin of the Lag Time and Identifying the Critical Nucleus Size," *Biophysical Journal*, vol. 98, pp. 1065–1074, mar 2010.

[49] Y. Ke, L. L. Ong, W. M. Shih, and P. Yin, "Three-dimensional structures self-assembled from DNA bricks," *Science*, vol. 338, no. 6111, pp. 1177–1183, 2012.

[50] B. Wei, M. Dai, and P. Yin, "Complex shapes self-assembled from single-stranded DNA tiles," *Nature*, vol. 485, no. 7400, pp. 623–626, 2012.

[51] A. Reinhardt and D. Frenkel, "Numerical evidence for nucleated self-assembly of DNA brick structures," *Physical Review Letters*, vol. 112, no. 23, pp. 1–5, 2014.

[52] W. M. Jacobs, A. Reinhardt, and D. Frenkel, "Rational design of self-assembly pathways for complex multicomponent structures," *Proceedings of the National Academy of Sciences of the United States of America*, vol. 112, no. 20, pp. 6313–6318, 2015.

[53] A. Murugan, J. Zou, and M. P. Brenner, "Undesired usage and the robust self-assembly of heterogeneous structures," *Nature Communications*, vol. 6, p. 6203, may 2015.

[54] P. K. Sorger, P. G. Stockley, and S. C. Harrison, "Structure and assembly of turnip crinkle virus: II. Mechanism of reassembly in vitro," *Journal of molecular biology*, vol. 191, no. 4, pp. 639–658, 1986.

[55] K. N. Parent, M. M. Suhanovsky, and C. M. Teschke, "Polyhead formation in phage P22 pinpoints a region in coat protein required for conformational switching," *Molecular microbiology*, vol. 65, no. 5, pp. 1300–1310, 2007.

[56] G. M. Whitesides and M. Boncheva, "Beyond molecules: Self-assembly of mesoscopic and macroscopic components," *Proceedings of the National Academy of Sciences of the United States of America*, vol. 99, no. 8, pp. 4769–4774, 2002.

[57] P. Ceres and A. Zlotnick, "Weak protein-protein interactions are sufficient to drive assembly of hepatitis B virus capsids," *Biochemistry*, vol. 41, no. 39, pp. 11525–11531, 2002.

[58] S. Zhang, "Fabrication of novel biomaterials through molecular self-assembly," *Nature Biotechnology*, vol. 21, no. 10, pp. 1171–1178, 2003.

[59] A. Zlotnick, "Are weak protein-protein interactions the general rule in capsid assembly?," *Virology*, vol. 315, no. 2, pp. 269–274, 2003.

[60] J. Grant, R. L. Jack, and S. Whitelam, "Analyzing mechanisms and microscopic reversibility of self-assembly," *Journal of Chemical Physics*, vol. 135, no. 21, 2011.

[61] R. Freeman, M. Han, Z. Álvarez, J. A. Lewis, J. R. Wester, N. Stephanopoulos, M. T. McClendon, C. Lynsky, J. M. Godbe, H. Sangji, E. Luijten, and S. I. Stupp, "Reversible

self-assembly of superstructured networks," *Science*, vol. 362, no. 6416, pp. 808–813, 2018.

[62] J. Louten, "Virus structure and classification," *Essential Human Virology*, p. 19, 2016.

[63] F. H. C. Crick, J. D. Watson, and Others, "Structure of small viruses.," *Nature*, vol. 177, pp. 473–475, 1956.

[64] D. L. D. Caspar and A. Klug, "Physical principles in the construction of regular viruses," in *Cold Spring Harbor symposia on quantitative biology*, vol. 27, pp. 1–24, Cold Spring Harbor Laboratory Press, 1962.

[65] P. Masson, C. Hulo, E. De Castro, H. Bitter, L. Gruenbaum, L. Essioux, L. Bougueleret, I. Xenarios, and P. Le Mercier, "ViralZone: http://viralzone.expasy.org," *Nucleic acids research*, vol. 41, no. D1, pp. D579—-D583, 2012.

[66] W. W. Newcomb, B. L. Trus, F. P. Booy, A. C. Steven, J. S. Wall, and J. C. Brown, "Structure of the herpes simplex virus capsid molecular composition of the pentons and the triplexes," *Journal of molecular biology*, vol. 232, no. 2, pp. 499–511, 1993.

[67] S. Tanaka, C. A. Kerfeld, M. R. Sawaya, F. Cai, S. Heinhorst, G. C. Cannon, and T. O. Yeates, "Atomic-level models of the bacterial carboxysome shell," *science*, vol. 319, no. 5866, pp. 1083–1086, 2008.

[68] H. Fraenkel-Conrat and R. C. Williams, "Reconstitution of Active Tobacco Mosaic Virus From Its Inactive Protein and Nucleic Acid Components," *Proceedings of the National Academy of Sciences*, vol. 41, no. 10, pp. 690–698, 1955.

[69] P. E. Prevelige, D. Thomas, and J. King, "Nucleation and growth phases in the polymerization of coat and scaffolding subunits into icosahedral procapsid shells," *Biophysical Journal*, vol. 64, no. 3, pp. 824–835, 1993.

[70] C. Chen, C. C. Kao, and B. Dragnea, "Self-assembly of brome mosaic virus capsids: Insights from shorter time-scale experiments," *Journal of Physical Chemistry A*, vol. 112, no. 39, pp. 9405–9412, 2008.

[71] S. Kler, R. Asor, C. Li, A. Ginsburg, D. Harries, A. Oppenheim, A. Zlotnick, and U. Raviv, "RNA encapsidation by SV40-derived nanoparticles follows a rapid two-state mechanism," *Journal of the American Chemical Society*, vol. 134, no. 21, pp. 8823–8830, 2012.

[72] R. Zandi, P. van der Schoot, D. Reguera, W. Kegel, and H. Reiss, "Classical nucleation theory of virus capsids," *Biophysical journal*, vol. 90, no. 6, pp. 1939–1948, 2006.

[73] R. Becker and W. Döring, "Kinetische behandlung der keimbildung in übersättigten dämpfen," *Annalen der Physik*, vol. 416, no. 8, pp. 719–752, 1935.

[74] V. L. Morton, P. G. Stockley, N. J. Stonehouse, and A. E. Ashcroft, "Insights into virus capsid assembly from non-covalent mass spectrometry," *Mass spectrometry reviews*, vol. 27, no. 6, pp. 575–595, 2008.

[75] A. Zlotnick and S. Mukhopadhyay, "Virus assembly, allostery and antivirals," *Trends in Microbiology*, vol. 19, no. 1, pp. 14–23, 2011.

[76] M. F. Hagan and R. Zandi, "Recent advances in coarse-grained modeling of virus assembly," *Current Opinion in Virology*, vol. 18, pp. 36–43, 2016.

[77] A. Ben-Shaul and W. M. Gelbart, "Statistical thermodynamics of amphiphile self-assembly: structure and phase transitions in micellar solutions," in *Micelles, Membranes, Microemulsions, and Monolayers*, pp. 1–104, Springer, 1994.

[78] R. F. Bruinsma, W. M. Gelbart, D. Reguera, J. Rudnick, and R. Zandi, "Viral Self-Assembly as a Thermodynamic Process," *Physical Review Letters*, vol. 90, no. 24, p. 4, 2003.

[79] S. A. Safran, *Statistical thermodynamics of surfaces, interfaces, and membranes*. CRC Press, 2018.

[80] K. N. Parent, M. M. Suhanovsky, and C. M. Teschke, "Phage P22 procapsids equilibrate with free coat protein subunits," *Journal of molecular biology*, vol. 365, no. 2, pp. 513–522, 2007.

[81] C. Uetrecht, N. R. Watts, S. J. Stahl, P. T. Wingfield, A. C. Steven, and A. J. R. Heck, "Subunit exchange rates in Hepatitis B virus capsids are geometry-and temperature-dependent," *Physical Chemistry Chemical Physics*, vol. 12, no. 41, pp. 13368–13371, 2010.

[82] S. Singh and A. Zlotnick, "Observed hysteresis of virus capsid disassembly is implicit in kinetic models of assembly," *Journal of Biological Chemistry*, vol. 278, no. 20, pp. 18249–18255, 2003.

[83] D. Endres, M. Miyahara, P. Moisant, and A. Zlotnick, "A reaction landscape identifies the intermediates critical for self-assembly of virus capsids and other polyhedral structures," *Protein Science*, vol. 14, no. 6, pp. 1518–1525, 2009.

[84] P. Moisant, H. Neeman, and A. Zlotnick, "Exploring the paths of (virus) assembly," *Biophysical Journal*, vol. 99, no. 5, pp. 1350–1357, 2010.

[85] J. M. Johnson, J. Tang, Y. Nyame, D. Willits, M. J. Young, and A. Zlotnick, "Regulating self-assembly of spherical oligomers," *Nano letters*, vol. 5, no. 4, pp. 765–770, 2005.

[86] M. Thomas and R. Schwartz, "Quantitative computational models of molecular self-assembly in systems biology," *Physical biology*, vol. 14, no. 3, p. 35003, 2017.

[87] P. L. Freddolino, A. S. Arkhipov, S. B. Larson, A. McPherson, and K. Schulten, "Molecular dynamics simulations of the complete satellite tobacco mosaic virus," *Structure*, vol. 14, no. 3, pp. 437–449, 2006.

[88] E. Bianchi, J. Largo, P. Tartaglia, E. Zaccarelli, and F. Sciortino, "Phase diagram of patchy colloids: Towards empty liquids," *Physical review letters*, vol. 97, no. 16, p. 168301, 2006.

[89] H. Liu, S. K. Kumar, and F. Sciortino, "Vapor-liquid coexistence of patchy models: Relevance to protein phase behavior," *The Journal of chemical physics*, vol. 127, no. 8, p. 84902, 2007.

[90] D. C. Rapaport, "Self-assembly of polyhedral shells: a molecular dynamics study," *Physical Review E*, vol. 70, no. 5, p. 51905, 2004.

[91] H. D. Nguyen, V. S. Reddy, and C. L. Brooks Iii, "Invariant polymorphism in virus capsid assembly," *Journal of the American Chemical Society*, vol. 131, no. 7, pp. 2606–2614, 2009.

[92] D. C. Rapaport, "Studies of reversible capsid shell growth," *Journal of Physics: Condensed Matter*, vol. 22, no. 10, p. 104115, 2010.

[93] S. D. Hicks and C. L. Henley, "Irreversible growth model for virus capsid assembly," *Physical Review E*, vol. 74, no. 3, p. 31912, 2006.

[94] A. Levandovsky and R. Zandi, "Nonequilibirum assembly, retroviruses, and conical structures," *Physical review letters*, vol. 102, no. 19, p. 198102, 2009.

[95] S. J. Stray, C. R. Bourne, S. Punna, W. G. Lewis, M. G. Finn, and A. Zlotnick, "A heteroaryldihydropyrimidine activates and can misdirect hepatitis B virus capsid assembly," *Proceedings of the National Academy of Sciences*, vol. 102, no. 23, pp. 8138–8143, 2005.

[96] G. M. Whitesides and B. Grzybowski, "Self-assembly at all scales," *Science*, vol. 295, no. 5564, pp. 2418–2421, 2002.

[97] H. Gu, J. Chao, S.-J. Xiao, and N. C. Seeman, "A Proximity-Based Programmable DNA Nanoscale Assembly Line," *Nature*, vol. 465, pp. 202–205, 2010.

[98] P. C. Nickels, B. Wünsch, P. Holzmeister, W. Bae, L. M. Kneer, D. Grohmann, P. Tinnefeld, and T. Liedl, "Molecular force spectroscopy with a DNA-origami – based nanoscopic force clamp," *Science*, vol. 354, no. 6310, pp. 305–307, 2016.

[99] R. Jia, T. Wang, Q. Jiang, Z. Wang, C. Song, and B. Ding, "Self-Assembled DNA Nanostructures for Drug Delivery," *Chinese Journal of Chemistry*, vol. 34, no. 3, pp. 265–272, 2016.

[100] P. Wang, T. A. Meyer, V. Pan, P. K. Dutta, and Y. Ke, "The Beauty and Utility of DNA Origami," *Chem*, vol. 2, no. 3, pp. 359–382, 2017.

[101] N. C. Seeman, "Nucleic acid junctions and lattices," *Journal of Theoretical Biology*, vol. 99, no. 2, pp. 237–247, 1982.

[102] F. C. Simmel, "DNA-based assembly lines and nanofactories," *Current Opinion in Biotechnology*, vol. 23, no. 4, pp. 516–521, 2012.

[103] I. Saaem and T. H. LaBean, "Overview of DNA origami for molecular self-assembly," *Wiley Interdisciplinary Reviews: Nanomedicine and Nanobiotechnology*, vol. 5, pp. 150–162, 2013.

[104] P. W. K. Rothemund, "Folding DNA to create nanoscale shapes and patterns," *Nature*, vol. 440, pp. 297–302, 2006.

[105] S. M. Douglas, H. Dietz, T. Liedl, B. Högberg, F. Graf, and W. M. Shih, "Self-assembly of DNA into nanoscale three-dimensional shapes," *Nature*, vol. 459, no. 7245, pp. 414–418, 2009.

[106] W. M. Shih, J. D. Quispe, and G. F. Joyce, "A 1.7-kilobase single-stranded DNA that folds into a nanoscale octahedron," *Nature*, vol. 427, pp. 618–621, 2004.

[107] E. S. Andersen, M. Dong, M. M. Nielsen, K. Jahn, R. Subramani, W. Mamdouh, M. M. Golas, B. Sander, H. Stark, C. L. P. Oliveira, and Others, "Self-assembly of a nanoscale DNA box with a controllable lid," *Nature*, vol. 459, pp. 73–76, 2009.

[108] S. M. Douglas, A. H. Marblestone, S. Teerapittayanon, A. Vazquez, G. M. Church, and W. M. Shih, "Rapid prototyping of 3D DNA-origami shapes with caDNAno," *Nucleic acids research*, vol. 37, no. 15, pp. 5001–5006, 2009.

[109] K. F. Wagenbauer, C. Sigl, and H. Dietz, "Gigadalton-scale shape-programmable DNA assemblies," *Nature*, vol. 552, no. 7683, pp. 78–83, 2017.

[110] C. Sigl, E. M. Willner, W. Engelen, J. A. Kretzmann, K. Sachenbacher, A. Liedl, F. Kolbe, F. Wilsch, S. A. Aghvami, U. Protzer, M. F. Hagan, S. Fraden, and H. Dietz, "Programmable icosahedral shell system for virus trapping," *Nature Materials*, 2021.

[111] T. J. Fu and N. C. Seeman, "DNA double-crossover molecules," *Biochemistry*, vol. 32, no. 13, pp. 3211–3220, 1993.

[112] P. W. K. Rothemund, N. Papadakis, E. Winfree, and A. Condon, "Algorithmic self-assembly of DNA Sierpinski triangles," *PLoS biology*, vol. 2, no. 12, p. e424, 2004.

[113] R. Schulman and E. Winfree, "Synthesis of crystals with a programmable kinetic barrier to nucleation," *Proceedings of the National Academy of Sciences of the United States of America*, vol. 104, no. 39, pp. 15236–15241, 2007.

[114] L. L. Ong, N. Hanikel, O. K. Yaghi, C. Grun, M. T. Strauss, P. Bron, J. Lai-Kee-Him, F. Schueder, B. Wang, P. Wang, J. Y. Kishi, C. Myhrvold, A. Zhu, R. Jungmann, G. Bellot, Y. Ke, and P. Yin, "Programmable self-assembly of three-dimensional nanostructures from 10,000 unique components," *Nature*, vol. 552, no. 7683, pp. 72–77, 2017.

[115] K. V. Gothelf, "LEGO-like DNA Structures," *Science*, vol. 338, no. 6111, pp. 1159–1161, 2012.

[116] P. W. K. Rothemund and E. S. Andersen, "The importance of being modular," *Nature*, vol. 485, pp. 584–585, 2012.

[117] L. Cademartiri and K. J. M. Bishop, "Programmable self-assembly," *Nature Materials*, vol. 14, pp. 2–9, 2015.

[118] Z. Zeravcic, V. N. Manoharan, and M. P. Brenner, "Colloquium: Toward living matter with colloidal particles," *Reviews of Modern Physics*, vol. 89, no. 3, p. 31001, 2017.

[119] E. Winfree, "DNA computing by self-assembly," in *2003 NAE Symposium on Frontiers of Engineering*, pp. 105–117, 2004.

[120] D. Doty, "Theory of algorithmic self-assembly," *Communications of the ACM*, vol. 55, no. 12, pp. 78–88, 2012.

[121] C. G. Evans and E. Winfree, "Physical principles for DNA tile self-assembly," *Chemical Society Reviews*, vol. 46, no. 12, pp. 3808–3829, 2017.

[122] J. G. Heddle, S. Chakraborti, and K. Iwasaki, "Natural and artificial protein cages: design, structure and therapeutic applications," *Current Opinion in Structural Biology*, vol. 43, pp. 148–155, 2017.

[123] B. Schwarz, M. Uchida, and T. Douglas, "Biomedical and catalytic opportunities of virus-like particles in nanotechnology," *Advances in virus research*, vol. 97, pp. 1–60, 2017.

[124] C. A. Kerfeld, M. R. Sawaya, S. Tanaka, C. V. Nguyen, M. Phillips, M. Beeby, and T. O. Yeates, "Protein structures forming the shell of primitive bacterial organelles," *Science*, vol. 309, no. 5736, pp. 936–938, 2005.

[125] B. D. Rae, B. M. Long, M. R. Badger, and G. D. Price, " Functions, Compositions, and Evolution of the Two Types of Carboxysomes: Polyhedral Microcompartments That Facilitate CO 2 Fixation in Cyanobacteria and Some Proteobacteria ," *Microbiology and Molecular Biology Reviews*, vol. 77, no. 3, pp. 357–379, 2013.

[126] E. Racker, "Structure, function, and assembly of membrane proteins," 1987.

[127] A. Zlotnick, "To Build a Virus Capsid: An Equilibrium Model of the Self Assembly of Polyhedral Protein Complexes," *Journal of Molecular Biology*, vol. 241, pp. 59–67, aug 1994.

[128] J. N. Israelachvili, D. J. Mitchell, and B. W. Ninham, "Theory of self-assembly of hydrocarbon amphiphiles into micelles and bilayers," *Journal of the Chemical Society, Faraday Transactions 2: Molecular and Chemical Physics*, vol. 72, pp. 1525–1568, 1976.

[129] Bruinsma, "Physics of viral shells,"

[130] H. D. Nguyen, V. S. Reddy, and C. L. Brooks, "Deciphering the kinetic mechanism of spontaneous self-assembly of icosahedral capsids," *Nano Letters*, vol. 7, no. 2, pp. 338–344, 2007.

[131] A. W. Wilber, J. P. Doye, A. A. Louis, E. G. Noya, M. A. Miller, and P. Wong, "Reversible self-assembly of patchy particles into monodisperse icosahedral clusters," *Journal of Chemical Physics*, vol. 127, no. 8, 2007.

[132] I. G. Johnston, A. A. Louis, and J. P. Doye, "Modelling the self-assembly of virus capsids," *Journal of Physics Condensed Matter*, vol. 22, no. 10, 2010.

[133] J. P. Mahalik and M. Muthukumar, "Langevin dynamics simulation of polymer-assisted virus-like assembly," *Journal of Chemical Physics*, vol. 136, no. 13, 2012.

[134] D. C. Rapaport, "Molecular dynamics simulation of reversibly self-assembling shells in solution using trapezoidal particles," *Physical review E*, vol. 86, no. 5, p. 51917, 2012.

[135] A. Zlotnick, J. M. Johnson, P. W. Wingfield, S. J. Stahl, and D. Endres, "A theoretical model successfully identifies features of hepatitis B virus capsid assembly," *Biochemistry*, vol. 38, no. 44, pp. 14644–14652, 1999.

[136] C. P. Goodrich, E. M. King, S. S. Schoenholz, E. D. Cubuk, and M. P. Brenner, "Designing self-assembling kinetics with differentiable statistical physics models," *Proceedings of the National Academy of Sciences of the United States of America*, vol. 118, no. 10, pp. 1–7, 2021.

[137] D. L. Caspar, "Movement and self-control in protein assemblies. Quasi-equivalence revisited," *Biophysical Journal*, vol. 32, no. 1, pp. 103–138, 1980.

[138] G. R. Lazaro and M. F. Hagan, "Allosteric Control of Icosahedral Capsid Assembly," *The Journal of Physical Chemistry B*, vol. 120, pp. 6306–6318, jul 2016.

[139] A. Reinhardt and D. Frenkel, "Numerical evidence for nucleated self-assembly of DNA brick structures," *Physical review letters*, vol. 112, no. 23, p. 238103, 2014.

[140] M. A. M. Groenen, R. P. M. A. Crooijman, A. Veenendaal, H. H. Cheng, M. S, and J. J. V. D. P, "NfwrhbWiophmbhoicrenpCL- shic rcie Wrrclaiw," *Stimulus*, vol. 274, no. 49, pp. 1–8, 1995.

[141] F. M. Gartner, I. R. Graf, P. Wilke, P. M. Geiger, and E. Frey, "Stochastic Yield Catastrophes and Robustness in Self-Assembly," *bioRxiv*, pp. 1–37, 2019.

[142] J. Boekhoven, W. E. Hendriksen, G. J. M. Koper, R. Eelkema, and J. H. van Esch, "Transient assembly of active materials fueled by a chemical reaction," *Science*, vol. 349, no. 6252, pp. 1075–1079, 2015.

[143] F. M. Gartner, I. R. Graf, and E. Frey, "Controlling fidelity and time-efficiency in self-assembly."

[144] C. Li, J. C.-Y. Wang, M. W. Taylor, and A. Zlotnick, "In Vitro Assembly of an Empty Picornavirus Capsid follows a Dodecahedral Path," 2012.

[145] C. A. Kerfeld and M. R. Melnicki, "Assembly, function and evolution of cyanobacterial carboxysomes," *Current Opinion in Plant Biology*, vol. 31, pp. 66–75, 2016.

[146] B. Alberts, D. Bray, K. Hopkin, A. D. Johnson, J. Lewis, M. Raff, K. Roberts, and P. Walter, *Essential cell biology*. Garland Science, 2015.

[147] M. F. Hagan and D. Chandler, "Dynamic pathways for viral capsid assembly," *Biophysical Journal*, vol. 91, no. 1, pp. 42–54, 2006.

[148] M. R. D'Orsogna, B. Zhao, B. Berenji, and T. Chou, "Combinatoric analysis of heterogeneous stochastic self-assembly," *Journal of Chemical Physics*, vol. 139, no. 12, 2013.

[149] M. R. D'Orsogna, Q. Lei, and T. Chou, "First assembly times and equilibration in stochastic coagulation-fragmentation," *Journal of Chemical Physics*, vol. 143, no. 1, 2015.

[150] T. C. Michaels, A. J. Dear, J. B. Kirkegaard, K. L. Saar, D. A. Weitz, and T. P. Knowles, "Fluctuations in the Kinetics of Linear Protein Self-Assembly," *Physical Review Letters*, vol. 116, no. 25, pp. 1–5, 2016.

[151] T. C. Michaels, M. M. Bellaiche, M. F. Hagan, and T. P. Knowles, "Kinetic constraints on self-assembly into closed supramolecular structures," *Scientific Reports*, vol. 7, no. 1, pp. 1–8, 2017.

[152] L. Cademartiri and K. J. Bishop, "Programmable self-assembly," *Nature Materials*, vol. 14, no. 1, pp. 2–9, 2015.

[153] A. Einstein, "Theoretical remark on the superconductivity of metals," *arXiv preprint physics/0510251*, 2005.

[154] T. Sauer, "Einstein and the early theory of superconductivity, 1919–1922," *Archive for history of exact sciences*, vol. 61, no. 2, pp. 159–211, 2007.

[155] M. Cyrot, "Ginzburg-Landau theory for superconductors," *Reports on Progress in Physics*, vol. 36, no. 2, pp. 103–158, 1973.

[156] N. Goldenfeld and C. Woese, "Life is Physics: Evolution as a Collective Phenomenon Far From Equilibrium," *Annual Review of Condensed Matter Physics*, vol. 2, no. 1, pp. 375–399, 2011.

[157] M. G. Alford, A. Schmitt, K. Rajagopal, and T. Schäfer, "Color superconductivity in dense quark matter," *Reviews of Modern Physics*, vol. 80, no. 4, p. 1455, 2008.

[158] D. A. Drummond and C. O. Wilke, "The evolutionary consequences of erroneous protein synthesis," *Nature reviews. Genetics*, vol. 10, no. 10, p. 715, 2009.

[159] K. E. Bohnsack and M. T. Bohnsack, "Uncovering the assembly pathway of human ribosomes and its emerging links to disease," *The EMBO Journal*, vol. 38, no. 13, pp. 1–20, 2019.

[160] B. M. Webster, P. Colombi, J. Jäger, and C. Patrick Lusk, "Surveillance of nuclear pore complex assembly by ESCRT-III/Vps4," *Cell*, vol. 159, no. 2, pp. 388–401, 2014.

[161] E. Jankowska, J. Stoj, P. Karpowicz, P. A. Osmulski, and M. Gaczynska, "The proteasome in health and disease," *Current pharmaceutical design*, vol. 19, no. 6, pp. 1010–1028, 2013.

[162] Y. A. Sulistio and K. Heese, "The ubiquitin-proteasome system and molecular chaperone deregulation in Alzheimer's disease," *Molecular neurobiology*, vol. 53, no. 2, pp. 905–931, 2016.

[163] Z. Ortega and J. J. Lucas, "Ubiquitin–proteasome system involvement in Huntington's disease," *Frontiers in molecular neuroscience*, vol. 7, p. 77, 2014.

[164] M. Sandri and J. Robbins, "Proteotoxicity: an underappreciated pathology in cardiac disease," *Journal of molecular and cellular cardiology*, vol. 71, pp. 3–10, 2014.

[165] O. Drews and H. Taegtmeyer, "Targeting the ubiquitin-proteasome system in heart disease: the basis for new therapeutic strategies," *Antioxidants & redox signaling*, vol. 21, no. 17, pp. 2322–2343, 2014.

[166] M. Karin and M. Delhase, "The I$\kappa$B kinase (IKK) and NF-$\kappa$B: key elements of proinflammatory signalling," in *Seminars in immunology*, vol. 12, pp. 85–98, Elsevier, 2000.

[167] M. A. Ermolaeva, A. Dakhovnik, and B. Schumacher, "Quality control mechanisms in cellular and systemic DNA damage responses," *Ageing research reviews*, vol. 23, pp. 3–11, 2015.

[168] E. Smith and H. J. Morowitz, *The origin and nature of life on earth: the emergence of the fourth geosphere*. Cambridge University Press, 2016.

[169] L. Budenholzer, C. L. Cheng, Y. Li, and M. Hochstrasser, "Proteasome Structure and Assembly," 2017.

[170] V. Blagotinsek, M. Schwan, W. Steinchen, D. Mrusek, J. C. Hook, F. Rossmann, S. A. Freibert, H. Kratzat, G. Murat, D. Kressler, R. Beckmann, M. Beeby, K. M. Thormann, and G. Bange, "An ATP-dependent partner switch links flagellar C-ring assembly with gene expression," *Proceedings of the National Academy of Sciences of the United States of America*, vol. 117, no. 34, pp. 20826–20835, 2020.

[171] S. Otsuka and J. Ellenberg, "Mechanisms of nuclear pore complex assembly – two different ways of building one molecular machine," *FEBS Letters*, vol. 592, no. 4, pp. 475–488, 2018.

[172] R. M. Macnab, "Type III flagellar protein export and flagellar assembly," *Biochimica et Biophysica Acta (BBA) - Molecular Cell Research*, vol. 1694, pp. 207–217, nov 2004.

[173] T. G. Smith and T. R. Hoover, "Deciphering bacterial flagellar gene regulatory networks in the genomic era," *Advances in applied microbiology*, vol. 67, pp. 257–295, 2009.

[174] G. Gines, A. S. Zadorin, J. C. Galas, T. Fujii, A. Estevez-Torres, and Y. Rondelez, "Microscopic agents programmed by DNA circuits," *Nature Nanotechnology*, vol. 12, no. 4, pp. 351–359, 2017.

[175] K. Montagne, R. Plasson, Y. Sakai, T. Fujii, and Y. Rondelez, "Programming an in vitro DNA oscillator using a molecular networking strategy," *Molecular Systems Biology*, vol. 7, no. 466, pp. 1–7, 2011.

[176] K. F. Murphy, R. M. Adams, X. Wang, G. Balázsi, and J. J. Collins, "Tuning and controlling gene expression noise in synthetic gene networks," *Nucleic Acids Research*, vol. 38, no. 8, pp. 2712–2726, 2010.

[177] J. M. Stewart and E. Franco, "Self-assembly of large RNA structures: learning from DNA nanotechnology," *DNA and RNA Nanotechnology*, vol. 2, no. 1, pp. 23–35, 2016.

[178] F. Praetorius, B. Kick, K. L. Behler, M. N. Honemann, D. Weuster-Botz, and H. Dietz, "Biotechnological mass production of DNA origami," *Nature*, vol. 552, no. 7683, pp. 84–87, 2017.

[179] H. C. Berg and E. M. Purcell, "Physics of chemoreception," *Biophysical Journal*, vol. 20, no. 2, pp. 193–219, 1977.

[180] K. Kaizu, W. De Ronde, J. Paijmans, K. Takahashi, F. Tostevin, and P. R. T. Wolde, "The berg-purcell limit revisited," *Biophysical Journal*, vol. 106, no. 4, pp. 976–985, 2014.

[181] J. D. Logan, *An introduction to nonlinear partial differential equations*, vol. 89. John Wiley & Sons, 2008.

[182] S. H. Strogatz, *Nonlinear dynamics and chaos with student solutions manual: With applications to physics, biology, chemistry, and engineering.* CRC press, 2018.

[183] S. Miranda, "On Exactitude in Science," *in J. L. Borges and A. Hurley: Collected fictions*, 1999.

# Acknowledgment

*Aurea prima sata est aetas, quae vindice nullo,*
*sponte sua, sine lege fidem rectumque colebat.*

*The first age sown was golden, which, without coercion, nor law,*
*was cherishing faith and the right moral through their own will.*

*Ovid, The four ages*

This excerpt from the *Metamorphoses*, with which Ovid begins his description of the golden age of humankind, has always inspired me. As the most important characteristic of the golden age, Ovid states that there was no coercion, no laws, no rules that forced people to do the right thing, but that everyone was free and decided for the good at his own will.
He didn't start his introduction - as one could have naively expected - by saying that people were free from pain and sorrow in general, from hard work and the undesirable consequences that might follow from their moral decisions for the individual. Instead, he envisioned the golden age as a world in which people decided spontaneously to follow the righteous path, which may sometimes also be cumbersome and will definitely be more demanding than the path of laziness, infamousness and immorality.

I think it was during the second year of my PhD, while I got tired from correcting exercise sheets, that I wrote this excerpt on the corner of the whiteboard in my office, where it was still there at the time I handed in my thesis (I have briefly contemplated to carve it into the pillar but I refrained since I know people at the institute are a bit touchy when it comes to the pillars ;)).
I always felt that doing research in our group very much resembled what Ovid describes as the golden age. All the projects and research I did, I always had the feeling I did due to a strong inner motivation, for curiosity or the idea that something profound could be waiting around the next corner. That doesn't mean it was all easy going. Sometimes hard work and perseverance were required, when things didn't come up as easily as I would have expected. However, I always had the feeling that I was going that path due to an inner drive and not because I was forced or urged to. At the end, nothing is more rewarding than the thrill when an abstract idea of the mind comes to work.
I deeply enjoyed the freedom to choose the topics and projects to work on that fascinated me the most. I highly appreciated having the freedom to work at the time and places I preferred and to take some more time for something when it was necessary. Also I liked that the distribution of tasks like teaching assignments, supervision of students and the group jobs occurred largely on a voluntary basis.
The golden age is clearly a collective achievement: it could not be realized if not at least the majority of a group behaved in a collaborative and supportive way. Therefore, I deeply thank

all members of the group for their commitment, their constant readiness to help and support and to fulfil their part when it was required.

There are many people to whom, in particular, I would like to express my deep gratitude for making these past years such a wonderful and rich experience.
First and foremost, of course, I cordially thank my supervisor Erwin Frey. I thank you for your continuous support, your trust and your positive attitude, which creates such a warm and supportive atmosphere in the group. I thank you for the freedom you gave all of us in pursuing our projects and your aversion against rules! I thank you for the many opportunities you gave us to visit conferences, workshops, seminars or discuss our research with invited guests. Thank you for all the time you spent discussing with me my different projects or reading through and correcting my paper drafts! You have truly been inspiring to me on many different levels.

I likewise want to thank all the other former and present members of our group for their commitment, their open-mindedness and their willingness to help and to support. I am thankful for the many joyful events we had the pleasure to experience together, like those wonderful trips to Antholz, the Christmas or barbecue parties or the various conferences we visited together, spending time talking and philosophizing. I enjoyed discussing about science and other things with you, designing exercise sheets or working together on various projects. In this context, I particularly want to thank Isabella Graf, Patrick Wilke, Phillip Geiger, Leaschkir Würthner, David Muramatsu, George Dadunashvili, Frederik Träuble, Severin Angerpointner, Mario Gaimann and Alexander Battenberg, with whom I had the pleasure to collaborate directly on different projects.
A very special thanks goes to my friend, roommate and our admin, Laeschkir Würthner, who helped me enormously with all my IT- and hardware related problems but who also always had an open ear or two for any other kind of problem and always a good advice; who furthermore recommended me the best music (Dream Theater), the best TV series (Hannibal) and the best gym in the city (Unterföhring) - Thank you Bro!

I am deeply thankful that I had the opportunity to be part of the graduate school "Quantitative Biosciences Munich" (QBM), the SFB 1032 as well as CRC 235 (origins of life) and that I could profit from the many workshops, retreats, talks and conferences planned and organized through these programs. I deeply thank all the persons who put so much effort into all these initiatives and programs, in particular, Ulrike Gaul, Filiz Civril, Markus Hohle, Mara Kieke, Marilena Pinto, Joachim Rädler, Dieter Braun and Susanne Hennig.

I special thanks also goes to the other members of my thesis advisory committee, Chase Broedersz and Dieter Braun and the members of my PhD committee, in particular, the second reviewer of my thesis, Ulrich Gerland.

I thank Henrik Weyer, Isabella Graf and Verena Gartner for proofreading parts of my thesis.

I especially thank my wife Verena for her love, her support and for always being there for me. Furthermore, I thank my daughter Alina for always playing “Nordpol-Schneesturm” with me and my son Samuel for his cute little smiles.

Finally, I deeply want to thank my brother Daniel and my parents, Margit and Peter Gartner, for their love, their positivity and their constant support. I thank you for all the possibilities you gave me in my life and for always being there for me. I am more than thankful that I have so wonderful parents, even more now that I truly understand what it means to be a parent.